THÈSE DE DOCTORAT

NNT : 2026UPASB002

université PARIS-SACLAY

Étude des régulations de la rhizodéposition et du prélèvement d'azote à différentes échelles à l'aide de la modélisation structure-fonction des plantes. Application au cas d'étude du blé (*Triticum aestivum*)

Investigating the multi-scale regulations of rhizodeposition and nitrogen uptake using Functional-Structural Plant Modeling. Application of a framework to winter wheat (Triticum aestivum)

Thèse de doctorat de l'Université Paris-Saclay

École doctorale n° 581, Agriculture, alimentation, biologie, environnement, santé (ABIES)
Spécialité de doctorat : Sciences végétales
Graduate School : BioSphERA. Référent : AgroParisTech

Thèse préparée dans l'**UMR ECOSYS**, Université Paris-Saclay, INRAE, AgroParisTech, sous la direction de **Frédéric REES**, Chargé de recherche (ADR), la co-direction d'**Alexandra JULLIEN**, et le co-encadrement de **Romain BARILLOT**, Chargé de recherche, et **Christophe PRADAL**, Ingénieur de recherche

Thèse soutenue à Paris-Saclay, le 15 janvier 2026, par

Tristan GÉRAULT

Composition du Jury

Membres du jury avec voix délibérative

Marion PRUDENT Directrice de recherche, INRAE (Université de Bourgogne)	Présidente
Soazig GUYOMARC'H Professeure, Université de Montpellier	Rapporteur & Examinatrice
Guillaume LOBET Professeur (équiv. HDR), Université Catholique de Louvain (Belgique)	Rapporteur & Examinateur
Gaëtan LOUARN Directeur de recherche, INRAE (Université de Poitiers)	Examinateur
Philippe NACRY Directeur de recherche, INRAE (Université de Montpellier)	Examinateur

université PARIS-SACLAY
ÉCOLE DOCTORALE
Agriculture, alimentation, biologie, environnement, santé (ABIES)

Titre : Étude des régulations de la rhizodéposition et du prélèvement d'azote à différentes échelles à l'aide de la modélisation structure-fonction des plantes. Application au cas d'étude du blé (*Triticum aestivum*)

Mots clés : Exsudation racinaire, FSPM, Couplage aérien-racinaire, Ecophysiologie végétale, Stockage de carbone dans les sols, Blé

Résumé : La rhizodéposition, c'est-à-dire la libération de matières organiques par les racines vivantes, a été identifiée comme un levier pour favoriser la séquestration de carbone dans les sols et l'adaptation des plantes à des conditions environnementales variables. Son intensité varie fortement selon l'âge de la plante et la disponibilité en ressources du sol, suivant des régulations encore mal comprises. La rhizodéposition dépendrait du statut métabolique de la plante, en particulier des échanges de carbone (C) et d'azote (N) au sein de la plante. Son hétérogénéité le long des racines suggère une forte dépendance vis-à-vis de l'architecture racinaire et des caractéristiques anatomiques et métaboliques de chaque segment racinaire. L'absorption de nutriments par les racines étant contrôlée par des facteurs similaires, la rhizodéposition et l'absorption d'azote pourraient co-évoluer dans l'espace et le temps, mais leur variabilité spatiale conjointe et leurs interactions restent largement inexplorées.

Cette thèse a visé à quantifier la variabilité spatiale et temporelle de la rhizodéposition et de l'absorption d'azote, à proposer une interprétation mécaniste de cette variabilité, et à évaluer son importance pour le bilan en C et N de la plante, en prenant le blé comme cas d'étude. Elle s'est appuyée sur des modèles de plantes fonction-structure (FSPM), afin d'étudier les interactions entre architecture, métabolisme et environnement. *Root-CyNAPS*, un nouveau FSPM simulant le métabolisme et le transport de l'azote dans un système racinaire 3D avec une description anatomique détaillée, a été conçu pour analyser la variabilité spatiale de l'absorption et de la rhizodéposition d'azote en lien avec les échanges de C et d'eau. *Root-CyNAPS* a ensuite été couplé à deux FSPM existants, *CN-Wheat*, qui simule la croissance et le fonctionnement C&N du blé en tenant compte d'une architecture aérienne détaillée, et *RhizoDep*, qui simule la croissance et la rhizodéposition du C sur un système racinaire architecturé.

Le couplage de ces trois FSPM, rendu possible par le nouvel outil *MetaFSPM,* a conduit au modèle *Wheat-BRIDGES*. En complément, des essais en rhizotrons ont été conçus pour suivre l'évolution de l'architecture et de l'anatomie du blé au cours du temps et mesurer les flux de rhizodéposition le long des racines.

Les simulations de *Root-CyNAPS* ont montré que la contribution au bilan en N de la plante des régions les plus actives (e.g. pointes racinaires et zones d'émergence des racines latérales) dépend de la disponibilité en N du sol et de l'âge de la plante. *Wheat-BRIDGES* confirme que ces régions actives se caractérisent à la fois par une rhizodéposition et une absorption d'azote accrues, en raison de leur dépendance similaire aux concentrations en métabolites et à l'anatomie racinaire le long d'une racine donnée. Ces simulations montrent aussi qu'approximer ces deux flux à partir de la masse du système racinaire ou du taux de photosynthèse ne permet pas de quantifier précisément leur variabilité au cours du temps. Les résultats expérimentaux obtenus en rhizotrons suggèrent que l'anatomie d'une racine de blé varie peu le long d'un axe et que l'anatomie racinaire influence ces flux principalement via l'évolution de la perméabilité de l'endoderme et de la sénescence corticale. Globalement, les résultats de cette thèse montrent que les concentrations locales en métabolites et la différenciation de l'endoderme sont des déterminants clés de l'évolution de la rhizodéposition et de l'absorption d'azote le long des racines et au cours du temps, conduisant à une co-localisation partielle de ces flux. Les modèles développés dans cette thèse offrent la possibilité d'explorer des interactions complexes dans le système sol–plante–atmosphère et ouvrent de nouvelles perspectives pour identifier des idéotypes ou pratiques agroécologiques permettant d'optimiser la rhizodéposition et/ou l'absorption d'azote par les racines.

université PARIS-SACLAY

ÉCOLE DOCTORALE
Agriculture, alimentation, biologie, environnement, santé (ABIES)

Title : Investigating the multi-scale regulations of rhizodeposition and nitrogen uptake using Functional-Structural Plant Modeling. Application of a framework to winter wheat (*Triticum aestivum*)

Keywords : Root exudation, FSPM, Shoot-root coupling, Plant ecophysiology, Soil carbon sequestration, Wheat

Abstract : Rhizodeposition – the release of organic matters by living roots – has been recognized as a lever for soil carbon sequestration and plant's adaptation to contrasted environments. Yet its magnitude varies widely with plant age and soil resource availability, and the underlying regulations remain unclear. Rhizodeposition may depend on the metabolic status of the plant, in particular on the exchanges of carbon (C) and nitrogen (N) between plant compartments. Its highly heterogeneous distribution along roots suggests a strong dependency on root architecture and on the anatomical and metabolic characteristics of individual root segments. Because nutrient uptake is controlled by similar factors, one may hypothesize that rhizodeposition and N uptake are linked in space and time, but their spatial variability and interactions have remained largely unexplored. This thesis aimed to quantify the spatial and temporal variability of rhizodeposition and N uptake, to provide a mechanistic interpretation of such variability, and to assess its importance in terms of plant C & N balance, using wheat as a case study.

The thesis relied primarily on the use of functional-structural plant models (FSPM), which allow to investigate the interactions between plant architecture, metabolism and environment from organ scale to whole-plant scale. Root-CyNAPS, a new FSPM simulating N uptake, metabolism and transport in a 3D root system with a detailed anatomical description, was developed and used to investigate how N uptake and N rhizodeposition vary along roots and interact with C and water dynamics. Root-CyNAPS was then coupled to two existing FSPMS, i.e. CN-Wheat, which simulates wheat growth in interaction with C, N and water dynamics using a detailed description of shoot organs in 3D, and RhizoDep, which simulates root growth and rhizodeposition in interaction with root C metabolism in a 3D root system. Wheat-BRIDGES, the whole-plant model resulting from the coupling of these three FSPM, was made possible by the development of *MetaFSPM*, a new generic toolkit that facilitates FSPM coupling and inter-comparison. To complement this modeling approach, experiments were conducted in large soil-filled rhizotrons in order to monitor the evolution of wheat architecture and root anatomy over time and to measure rhizodeposition rates along wheat roots.

Root-CyNAPS simulations showed that the contribution of most active root regions - e.g. root tips and sites of lateral root emergence - to plant N balance is highly sensitive to soil N availability and plant age. *Wheat-BRIDGES* simulations confirmed that the same root regions dominate both rhizodeposition and mineral N uptake, with local metabolite concentrations and root anatomy resulting in a co-location of these flows along individual roots. However, differences between root types and age-dependent changes in the root system generate complex dynamics at plant scale, showing that simple approaches such as assuming a proportionality of rhizodeposition or N uptake with root system biomass or C input are not accurate enough. Experimental results obtained in rhizotrons suggested that root anatomical characteristics do not significantly vary along the roots of wheat, aside the evolution of endodermis' apoplastic barrier and cortical senescence. Altogether, the results of this thesis show that local metabolite concentrations and endodermis differentiation are key drivers of rhizodeposition and N uptake evolution along the roots and over time, leading to a partial co-location of these flows. The models developed in this thesis offer the opportunity to explore complex links between C, N and water dynamics in the plant-soil-atmosphere system and to identify new ideotypes or agroecological practices that optimize rhizodeposition and/or root N uptake.

Résumé en français

Contexte scientifique, problématique et stratégie générale

Agriculture, transition agroécologique et rôle des flux racinaires de C et de N

L'agriculture intensive mise en place au cours de la seconde moitié du XXe siècle a permis des gains de rendement majeurs, mais au prix d'externalités environnementales, sanitaires et sociales désormais bien documentées [Evenson and Gollin, 2003, Malézieux, 2012, Gomiero, 2016, Gliessman, 2014, Cellier et al., 2020]. La simplification des rotations, le recours massif aux fertilisants et aux pesticides, la dépendance aux énergies fossiles et la dégradation progressive des sols soulignent les limites structurelles de ce modèle [M. Tahat et al., 2020, Hatt et al., 2016, Keesstra et al., 2024]. Dans le même temps, l'agriculture contribue de manière importante aux émissions de gaz à effet de serre et demeure particulièrement vulnérable à l'augmentation de la variabilité climatique et à l'intensification des extrêmes [Tubiello et al., 2022, Kahiluoto et al., 2019, Coumou and Rahmstorf, 2012, Asseng et al., 2015, Kornhuber et al., 2023, Baffes and Etienne, 2024]. Dans ce contexte, la transition agroécologique vise moins l'adoption d'un ensemble figé de pratiques que la reconception des agroécosystèmes à partir des processus écologiques qui soutiennent durablement la production [Altieri, 1999, Francis et al., 2003, Wezel et al., 2009, Duru et al., 2015, Altieri, 2018].

Parmi ces processus, la relocalisation et le couplage local des cycles du carbone et de l'azote constituent un levier central [Drinkwater and Snapp, 2007]. Le stockage de carbone organique dans les sols est devenu un enjeu majeur à la fois pour la fertilité des agroécosystèmes et pour l'atténuation du changement climatique [Minasny et al., 2017, Guenet et al., 2021, Don et al., 2024], et les racines y occupent une place particulière. Les apports racinaires contribuent à la formation de matière organique stable de manière souvent plus efficace que des masses équivalentes de résidus aériens [Rasse et al., 2005, Jackson et al., 2017]. Au-delà de la nécromasse racinaire, les racines vivantes transfèrent continuellement vers le sol des composés organiques carbonés et azotés par rhizodéposition. Cette dernière, longtemps qualifiée de *hidden half of the hidden half*, représente une fraction quantitativement importante mais extrêmement variable du bilan de la plante [Gregory, 2022, Nguyen, 2009, Pausch and Kuzyakov, 2018, Fustec et al., 2010, Jones et al., 2009, Wichern et al., 2008]. Loin d'être une perte de ressources inutile pour la plante, la rhizodéposition participe à la structuration de l'environnement biotique et abiotique de la racine, module l'accès à l'eau et aux nutriments et peut stimuler l'activité microbienne du sol, en particulier la minéralisation de l'azote du sol [Canarini et al., 2019, Usyskin-Tonne et al., 2021, Dijkstra et al., 2013, Ai et al., 2020, Gan et al., 2022].

Un problème multiscalaire encore mal résolu

Si l'importance fonctionnelle de la rhizodéposition est bien établie, ses déterminants restent mal compris, en particulier lorsque l'on cherche à relier les flux locaux à l'échelle du segment racinaire aux bilans carbone et azote de la plante entière. La

littérature suggère que les échanges racine-sol ne sont pas uniformément distribués dans l'architecture racinaire, mais concentrés dans des zones préférentiellement "actives", par exemple au voisinage des apex ou des zones d'émergence des racines latérales [Hodge et al., 2009, Bechmann et al., 2014, Le Deunff et al., 2019, Canarini et al., 2019]. Cependant, la localisation précise, l'intensité relative et surtout la contribution effective de ces zones à l'échelle du système racinaire entier restent difficiles à établir. Les approches expérimentales localisées en conditions de sol sont lourdes, souvent invasives, et ne donnent accès qu'à des instantanés partiels [Buckley et al., 2020, Wacker et al., 2024, Nguyen et al., 2016]. À cette difficulté expérimentale s'ajoute un verrou conceptuel: les flux observés localement dépendent à la fois du statut physiologique local des tissus, des gradients de métabolites, des propriétés anatomiques, des transports axiaux d'eau et de solutés, des allocations entre organes et de la dynamique d'architecture racinaire elle-même [Gratani, 2014, Bollard, 1960, Dodd et al., 2008, 2009].

Cette articulation entre échelles rend la modélisation mécaniste particulièrement pertinente. Les modèles de culture ou de surface continentale représentent généralement les racines de façon agrégée en un seul compartiment et décrivent la rhizodéposition ou l'absorption d'azote comme des fractions imposées de compartiments végétaux globaux. Ces approches permettent l'intégration dans des cadres plus larges, mais elles peinent à représenter explicitement l'hétérogénéité des échanges dans l'architecture racinaire [Dunbabin et al., 2013, Postma et al., 2017, Schnepf et al., 2018, Giraud et al., 2023]. À l'inverse, les Functional-Structural Plant Models (FSPM), ou modèles structure-fonction, permettent de relier géométrie de la plante, processus locaux et interactions avec l'environnement [Sievänen et al., 2014, Louarn and Song, 2020, Schäfer et al., 2022]. Ils offrent donc un cadre approprié pour étudier comment des processus localisés, dépendants des concentrations en métabolites et de l'anatomie des tissus, émergent à l'échelle de la plante entière. Néanmoins, aucun modèle existant ne permet actuellement de représenter simultanément, dans une architecture racinaire explicite, la rhizodéposition carbonée, les flux d'azote minéral et organique, les transports hydriques et la rétroaction de ces processus sur le bilan C-N de la plante entière.

Objectifs et hypothèses de la thèse

Dans cette thèse, j'ai abordé cette question en utilisant le blé (*Triticum aestivum*) comme plante modèle, à la fois pour son importance agronomique et parce que sa nutrition azotée est fortement sensible aux contraintes environnementales [Martre et al., 2024]. L'objectif général a été de comprendre comment la rhizodéposition et l'absorption évoluent le long des racines d'une plante en croissance, quels sont les déterminants mécanistes de cette hétérogénéité spatiale et temporelle, et dans quelle mesure cette hétérogénéité rejaillit sur le fonctionnement C-N de la plante entière et, à plus long terme, sur les interactions plante-sol. Plus précisément, j'ai formulé cinq hypothèses directrices. J'ai d'abord posé que la rhizodéposition ne pouvait pas être réduite à une simple proportion de biomasse racinaire ou d'allocation de photoassimilats vers les racines (H1). J'ai ensuite supposé que le concept binaire d'*active root zones* était trop simplificateur et que la contribution relative des différentes portions du système racinaire devait varier avec l'âge de la plante

et l'environnement (H2). J'ai également fait l'hypothèse que les processus dominants au sein des échanges racine-sol pouvaient se substituer les uns aux autres selon les conditions, en particulier pour l'absorption d'azote transportée par les flux d'eau (H3). Enfin, j'ai considéré que les concentrations locales en métabolites et l'anatomie des tissus constituaient des régulateurs communs de la rhizodéposition et de l'absorption d'azote (H4), tout en supposant que, à l'échelle de la plante, ces flux pouvaient être synchronisés avec l'activité photosynthétique (H5).

Pour tester ces hypothèses, j'ai combiné le couplage et le développement de modèles mécanistes avec des expérimentations originales en rhizotrons. La thèse s'organise ainsi autour de deux développements méthodologiques centraux. Le premier consiste en la construction de modèles mécanistes capables de relier les processus C-N locaux de segments racinaires à la plante entière. Le second correspond à la mise en place d'un dispositif expérimental en rhizotron destiné à caractériser l'architecture racinaire, l'anatomie des racines et la rhizodéposition dans des conditions contrôlées tout en restant en contact avec un sol non stérile.

Chapitre 2. *Root-CyNAPS*: modéliser les échanges d'azote, d'eau et l'anatomie à l'échelle du segment racinaire

Positionnement du chapitre et principes du modèle

Le premier développement de la thèse a consisté à construire *Root-CyNAPS*, un FSPM racinaire dédié aux échanges d'azote et d'eau, intégrant explicitement l'anatomie du segment racinaire et les concentrations locales en métabolites. Ce modèle répond à un manque identifié dans la littérature. Les modèles hydrauliques architecturés, issus notamment des travaux de Doussan et al. [1998] puis de leurs prolongements, permettent de représenter les conductances radiales et axiales de l'eau dans une architecture 3D, tandis que d'autres cadres plus récents comme *OpenSimRoot* ou *CPlantBox* permettent de coupler architecture racinaire et absorption de ressources [Javaux et al., 2008, Postma et al., 2017, Schnepf et al., 2018, Giraud et al., 2023]. Cependant, ces modèles restent généralement limités lorsqu'il s'agit de représenter le rôle régulateur du statut C-N local de la racine. À l'inverse, des approches plus fines de type *MECHA* ont montré l'importance de l'anatomie explicite dans la détermination des propriétés hydrauliques [Couvreur et al., 2018], sans pour autant intégrer la totalité des flux d'azote et leurs interactions avec le carbone.

Root-CyNAPS a été conçu pour articuler ces dimensions. Le modèle représente, pour chaque segment d'une architecture racinaire 3D, les pools labiles d'azote minéral, d'acides aminés et de protéines de réserve, ainsi que les volumes d'eau des compartiments symplasmique, xylémien et phloémien. Il simule simultanément l'absorption active d'azote minéral par les transporteurs membranaires, l'entrée apoplastique d'azote portée par les flux d'eau, l'exsudation d'azote organique, des biosynthèses locales, les échanges radiaux entre symplasme et vaisseaux, le transport axial dans le xylème et le phloème, ainsi que l'effet de l'anatomie locale sur les surfaces d'échange et sur la différenciation progressive des barrières apoplastiques. Dans ce cadre, la surface d'échange avec le sol n'est pas assimilée à une simple surface cylindrique, mais dépend des surfaces tissulaires pertinentes, des poils absorbants et de la conductance des barrières endodermiques et exodermiques [Clarkson et al., 1971, Hose

et al., 2001, Enstone et al., 2002, Schreiber et al., 2005, Ouyang et al., 2020]. Le modèle s'inscrit ainsi dans la continuité des FSPM racinaires existants, tout en introduisant une représentation couplée de l'azote, de l'eau et de l'anatomie apte à analyser des bilans nets d'azote, c'est-à-dire la différence entre absorption brute et pertes par rhizodéposition.

Scénarios de simulation et apports du chapitre

J'ai utilisé *Root-CyNAPS* sur des architectures racinaires de blé produites par le modèle *RhizoDep*, pour différents âges de plante et différentes concentrations externes en nitrate, de façon à explorer l'hétérogénéité spatiale de l'absorption nette d'azote dans un cadre contrôlé. L'intérêt de cette étape était double. D'une part, il s'agissait d'identifier les zones préférentielles d'échanges au sein du système racinaire. D'autre part, je cherchais à quantifier la contribution effective de ces zones dites *les plus actives* au bilan global de la plante, plutôt que de les définir de façon qualitative.

Les simulations ont mis en évidence deux zones préférentielles d'absorption nette d'azote, l'une proche des apex, l'autre au niveau des zones d'émergence des racines latérales. Dans ces zones, l'activité d'absorption pouvait être environ dix fois supérieure à celle des segments adjacents. Toutefois, la contribution de ces zones au bilan global n'était pas constante. Lorsqu'elles étaient définies comme les 10 % de longueur racinaire présentant les flux unitaires les plus élevés, leur contribution à l'absorption nette d'azote variait fortement avec l'âge de la plante et la concentration en nitrate du sol, ce qui remet directement en cause une définition prédéfinie et statique de "zones racinaires actives". Les résultats ont également montré que l'absorption d'azote médiée par les flux d'eau pouvait atteindre jusqu'aux deux tiers de l'absorption brute d'azote, tandis que les pertes d'azote par exsudation pouvaient en compenser plus de la moitié. Autrement dit, l'absorption nette d'azote ne peut pas être interprétée sans expliciter simultanément les voies d'entrée et de sortie. Cette conclusion est importante, car de nombreux travaux ciblent des traits d'absorption sans les recontextualiser dans un bilan net incluant la rhizodéposition azotée [Holz et al., 2024, Lynch et al., 2024, Griffiths and York, 2020].

Ce chapitre apporte donc trois résultats majeurs pour la suite de la thèse. Premièrement, il confirme que l'hétérogénéité des échanges d'azote le long des racines est un phénomène structuré par une hétérogénéité locale des concentrations métaboliques et anatomiques. Deuxièmement, il montre que la dominance relative des processus peut se déplacer selon les conditions, ce qui appuie l'idée d'un fonctionnement plastique et composite des échanges racine-sol. Troisièmement, il fournit un socle mécaniste et numérique pour coupler ensuite ces flux d'azote et d'eau avec les dynamiques carbonées, la croissance racinaire et les échanges trophiques C-N aérien-racinaire effectués par la plante entière.

Chapitre 3. *MetaFSPM*: une infrastructure de couplage pour relier modèles racinaires, aériens et environnementaux

Nécessité d'un outil de couplage

L'ambition de relier des processus locaux de rhizodéposition et d'absorption d'azote au bilan C-N de la plante entière supposait de coupler plusieurs modèles développés indépendamment: *CN-Wheat* pour le fonctionnement C-N des organes aériens de blé [Barillot et al., 2016, Gauthier et al., 2020], *RhizoDep* pour les processus carbonés et de croissance du système racinaire [Rees et al., 2025], *Root-CyNAPS* pour l'azote, l'eau et l'anatomie racinaire, ainsi que des composantes environnementales de lumière et de sol. Or, malgré des hypothèses physiologiques partiellement convergentes, ces modèles différaient par leur structure de code, leur granularité spatiale, leurs schémas numériques et leur gestion des entrées-sorties. Les pratiques de couplage ad hoc deviennent rapidement difficiles à maintenir dans un contexte où des centaines de variables sont échangées et où les hypothèses de couplage doivent rester inspectables et modifiables.

Dans ce contexte, j'ai développé *MetaFSPM*, un outil léger de modularisation et de couplage conçu pour l'écosystème *OpenAlea* [Pradal et al., 2008, 2015]. Son objectif n'était pas de proposer un cadre de modélisation universel, mais d'opérationnaliser, dans le cadre de cette thèse, une stratégie de couplage explicite entre modèles structure-fonction et composantes environnementales. Ce travail s'inscrit dans un mouvement plus large de formalisation des composants, des contrats d'échange et des orchestrations de modèles, tel qu'on le retrouve dans *Crop2ML* ou *xarray-simlab* [Midingoyi et al., 2021, Benoit Bovy et al., 2021, Post et al., 2024, Vaillant et al., 2022].

Architecture de *MetaFSPM* et rôle dans la thèse

Le principe central de *MetaFSPM* est de représenter chaque sous-modèle comme un *composant* déclarant explicitement les variables qu'il lit, celles qu'il écrit, ses paramètres, son ou ses solveurs et ses règles d'ordonnancement. Un deuxième utilitaire de *MetaFSPM* permet d'assembler plusieurs composants dans un modèle composite, en centralisant les correspondances de variables, les conversions d'unités, les agrégations nécessaires et l'ordonnancement d'exécution des composants au sein d'un pas de temps. Cette séparation entre formalismes écophysiologiques et utilitaires d'exécution permet à la fois de préserver la logique interne des modèles existants et de rendre leurs interfaces lisibles, testables et réutilisables [Henke et al., 2016, Soualiou et al., 2021].

Pour la réalisation de cette thèse, *MetaFSPM* a joué un rôle méthodologique déterminant. Il a permis de refactoriser *CN-Wheat*, *RhizoDep*, *Root-CyNAPS* et les modèles environnementaux en composants interopérables, puis de les réassembler progressivement en modèles plus complexes. C'est dans ce cadre qu'a été construit *Root-BRIDGES*, couplant les processus carbonés de *RhizoDep* et les processus azote-eau-anatomie de *Root-CyNAPS*, puis *Wheat-BRIDGES*, qui ferme les cycles C-N à l'échelle de la plante entière. Au-delà de cette thèse, ce chapitre montre que le couplage de FSPM peut être documenté comme un objet scientifique à part entière:

les hypothèses d'interfaçage, les choix de résolution et les dépendances entre composants ne sont plus cachés dans un code monolithique, mais explicités dans des contrats de couplage et des graphes d'exécution. Cette explicitation améliore la reproductibilité, facilite l'exploration d'hypothèses alternatives et prépare des usages futurs comme l'analyse de sensibilité, la calibration orientée par des motifs expérimentaux ou la construction de métamodèles [Pagès et al., 2020, Blanc et al., 2023, Gawinowski et al., 2024].

Chapitre 4. *Wheat-BRIDGES*: du segment racinaire à la plante entière

Construction du modèle composite

Le chapitre 4 constitue le coeur intégrateur de la thèse, utilisant *MetaFSPM* pour construire *Wheat-BRIDGES*, un FSPM de plante entière capable de représenter explicitement les processus C-N-eau dans les organes aériens et souterrains du blé, tout en tenant compte de l'architecture végétale, sa croissance, et des interactions avec des composantes de lumière et de sol. Pour cela, j'ai d'abord construit *Root-BRIDGES*, modèle intermédiaire racinaire couplant *RhizoDep* et *Root-CyNAPS*. *Root-BRIDGES* permet de simuler conjointement la croissance racinaire, la distribution des hexoses, des acides aminés et de l'azote minéral, les flux d'eau, les transports dans le xylème et le phloème, ainsi que la rhizodéposition carbonée et azotée le long d'une architecture racinaire en croissance. J'ai ensuite remplacé, dans *CN-Wheat*, le compartiment racinaire homogène par ce module architecturé, de manière à fermer les cycles de carbone et d'azote entre racines et parties aériennes.

Cette étape n'était pas purement technique. Elle revenait à remplacer des règles d'allocation globales par des transports spatialisés dans des tissus conducteurs, et donc à faire émerger les bilans de la plante à partir des activités locales des organes. La stabilisation numérique d'un tel système a nécessité l'articulation de plusieurs solveurs, certains explicites, d'autres implicites ou fondés sur des résolutions de type Newton-Raphson, selon les composantes concernées. J'ai appliqué *Wheat-BRIDGES* à un scénario réaliste de croissance végétative du blé d'hiver déjà utilisé pour la validation de *CN-Wheat*, de manière à pouvoir comparer les sorties des deux modèles sans introduire de différences d'environnement qui auraient brouillé l'interprétation [Ljutovac, 2002].

Validation relative et apports sur le bilan C-N de la plante

Les premières simulations ont montré que *Wheat-BRIDGES* préserve les grandes dynamiques de développement aérien simulées par *CN-Wheat*, en particulier pour la cinétique d'allongement foliaire, même si certaines divergences apparaissent sur les dernières feuilles et sur les bilans d'azote des parties aériennes. Cette cohérence relative est importante, car elle montre que l'introduction d'un système racinaire explicitement architecturé ne compromet pas les propriétés émergentes déjà validées du modèle aérien. Dans le même temps, elle révèle que cette explicitation modifie effectivement les allocations et les bilans C-N de la plante, ce qui permet de questionner les objectifs scientifiques initiaux de la thèse.

À l'échelle de la plante entière, *Wheat-BRIDGES* montre que la rhizodéposition carbonée simulée représente environ 6 % de la photosynthèse brute, ce qui se situe dans l'intervalle rapporté dans la littérature [Nguyen, 2009, Pausch and Kuzyakov, 2018]. Surtout, les sorties du modèle ne confirment pas l'idée d'une relation simple entre rhizodéposition et photosynthèse, biomasse racinaire ou allocation carbonée vers les racines. Les flux totaux covarient avec la croissance de la plante au cours du temps, mais il n'émerge pas de synchronisation robuste lorsqu'on exprime ces flux par unité de masse ou de surface d'échange. Cette absence de proportionnalité simple appuie directement la première hypothèse de la thèse. Elle suggère que la variabilité rapportée dans la littérature entre espèces, génotypes ou conditions de culture ne peut pas être interprétée seulement comme une dispersion expérimentale, mais aussi comme la conséquence attendue d'une structuration interne très hétérogène des flux [Pausch and Kuzyakov, 2018, Canarini et al., 2019, Pausch et al., 2024].

Hétérogénéité spatiale des échanges et statut des *active root zones*

L'apport majeur du chapitre 4 réside dans l'analyse spatiale des échanges le long du système racinaire. *Wheat-BRIDGES* retrouve, pour la rhizodéposition carbonée comme pour l'absorption nette d'azote minéral, deux zones d'activité préférentielle: une zone apicale et une zone associée à l'émergence des racines latérales. Ces zones ne sont toutefois ni fixes, ni équivalentes entre processus, ni homogènes entre types de racines. Leur distance à l'apex, leur intensité relative et leur persistance varient avec le type de racine, l'âge de l'axe, le rythme de croissance et le contexte environnemental. Cette observation prolonge et renforce les résultats obtenus avec *Root-CyNAPS*. Elle montre que la notion de *zone active* peut être utile comme outil descriptif, mais qu'elle devient trompeuse dès qu'on lui attribue un statut invariant.

Quantitativement, les simulations montrent qu'environ 10 % de la longueur racinaire la plus active concentre près de 90 % de la rhizodéposition carbonée, mais seulement environ 50 % de l'absorption minérale d'azote, 45 % de l'exsudation organique d'azote et 25 % de l'absorption d'eau. Cette différence signifie que tous les processus ne partagent pas le même degré de polarisation spatiale, et qu'une représentation homogène du système racinaire manquerait une part importante de l'organisation fonctionnelle interne. Elle montre aussi que l'absorption d'eau, beaucoup plus diffuse, ne se superpose pas mécaniquement aux autres flux. Les résultats appuient donc l'idée que les zones apicales et les zones d'émergence latérale sont des points structurants, mais non des catégories suffisantes pour décrire l'ensemble de la plasticité fonctionnelle du système racinaire.

Co-localisation des flux et déplacement des processus dominants

Un autre résultat important concerne la co-localisation entre rhizodéposition et absorption d'azote. À l'échelle d'un axe racinaire pris isolément, les deux processus tendent bien à se maximiser dans les mêmes régions, notamment près de l'apex et des points d'émergence des racines latérales. Cette co-localisation émerge dans le modèle du fait de régulations communes par les concentrations locales en hexoses et en acides aminés, par l'état de différenciation des tissus et par les surfaces d'échange accessibles. Elle apporte donc un soutien mécaniste à l'idée qu'une partie des in-

teractions entre rhizodéposition et nutrition minérale pourrait être organisée par des régulations locales [Bilyera et al., 2021, Liu et al., 2022, Pausch et al., 2024]. Néanmoins, cette co-localisation n'est pas parfaite. Les maxima de rhizodéposition et d'absorption d'azote ne coïncident pas systématiquement pour tous les axes et à tous les pas de temps. Selon les cas, l'un des deux processus peut être plus marqué à l'apex, l'autre davantage près des émergences latérales. La co-localisation dépend donc de l'axe considéré, de son âge et du processus étudié, ce qui invite à se méfier des raisonnements à partir d'agrégations globales.

Le chapitre 4 montre également que les processus dominants de l'absorption d'azote peuvent changer avec les conditions. Dans certaines situations, l'entrée d'azote transportée par l'eau atteint des niveaux comparables à ceux de l'absorption active transmembranaire. Ce résultat est cohérent avec l'idée d'un continuum eau-solutés où les flux hydriques ne servent pas seulement de support de transport axial, mais participent directement à la dynamique radiale d'acquisition [Bauget et al., 2023]. De la même façon, l'absorption d'eau se révèle minimale près de l'apex et maximale plus en arrière, en particulier au voisinage des jeunes émergences latérales, de sorte que sa co-localisation avec la rhizodéposition et l'absorption d'azote n'est que partielle. Ce déplacement relatif des processus dominants soutient donc l'hypothèse d'une plasticité fonctionnelle des échanges racine-sol qui ne se résume ni à une seule zone, ni à un seul mécanisme d'échange sol-racine.

Chapitre 5. Caractérisation expérimentale de l'architecture racinaire, de l'anatomie et de la rhizodéposition du blé

Un volet expérimental conçu pour évaluer et calibrer les modèles développés

Le chapitre 5 apporte le contrepoint expérimental de la thèse. Son objectif n'était pas uniquement de produire une quantification exhaustive des gradients de rhizodéposition le long de racines de blé, mais de construire un dispositif capable de générer des observations localisées sur lesquelles appuyer et discuter les hypothèses des chapitres de modélisation. Pour cela, j'ai conduit deux expériences en rhizotrons remplis de sol et installés en chambres de culture. Une première expérience visait à documenter la croissance racinaire du blé et l'évolution de l'anatomie radiale le long de racines séminales. Une seconde expérience était dédiée au développement d'une méthode non destructive de piégeage répété des rhizodépôts au moyen de patchs de sable appliqués localement sur des segments racinaires ciblés, en parallèle d'un suivi temporel de l'architecture racinaire et du phénotype aérien.

Ce dispositif s'appuie sur plusieurs briques méthodologiques complémentaires. Les rhizotrons à fenêtres mobiles permettent l'accès répété à des portions ciblées du système racinaire. Les images temporelles sont utilisées pour reconstruire l'architecture racinaire au cours du temps, estimer l'âge des segments et replacer les mesures locales dans l'histoire de croissance de la plante. L'analyse d'images de sections racinaires a été menée en s'appuyant sur une adaptation de *GRANAR* [Heymans et al., 2020], tandis que l'annotation et la segmentation des images de rhizotron mobilisent des outils issus de la phénotypie racinaire et de l'apprentissage profond [Lobet et al., 2011, 2015, Smith et al., 2022, Schnepf et al., 2023]. Ainsi, le chapitre

5 ne constitue pas un simple ajout expérimental, mais une tentative de mise en cohérence des échelles d'observation avec celles des modèles.

Stabilité de l'anatomie radiale et portée pour la modélisation

Les observations histologiques réalisées sur racines séminales de blé ont montré qu'entre quelques millimètres et 40 cm de distance à l'apex, l'organisation radiale reste remarquablement stable. Une fois normalisée par le rayon de la racine, la surface externe totale des cellules par unité de longueur varie peu le long de l'axe. Les tissus corticaux représentent la majeure partie de cette surface d'échange, alors que seules les sections les plus basales présentent une réduction nette compatible avec une perte corticale. Ce résultat est important pour l'interprétation des simulations. Il suggère que, sur la majeure partie de la racine séminale, les variations longitudinales des échanges racine-sol ne peuvent pas être expliquées principalement par de grandes variations de surface géométrique disponible. Elles renvoient plutôt à l'état des barrières apoplastiques, aux gradients de métabolites et au statut de croissance des tissus. Cette observation soutient donc le choix, fait dans *RhizoDep*, *Root-CyNAPS* et *Wheat-BRIDGES*, de représenter la surface d'échange comme proportionnelle au rayon local pour l'essentiel de la longueur racinaire, tout en soulignant l'importance future de mieux mesurer la sénescence corticale et la différenciation de l'endoderme et de l'exoderme [Watt et al., 2003, Henry and Deacon, 1981, Tixier et al., 2023, Bohm et al., 2025].

Mesure locale de la rhizodéposition: faisabilité, limites et interprétation

Concernant la rhizodéposition, le piégeage par patchs de sable s'est révélé techniquement faisable, mais proche des limites analytiques lorsque les échantillons étaient analysés uniquement en carbone et azote totaux. Les quantités de carbone détectées dans les patchs après quatre heures de contact avec les racines étaient très faibles et souvent à peine supérieures à celles des témoins sans contact racinaire. Malgré ce signal faible, une partie des échantillons significativement au-dessus du bruit de fond provenait majoritairement de zones apicales, ce qui est cohérent avec l'idée d'apex comme points chauds de rhizodéposition, déjà suggérée par le modèle et par la littérature [Ryan et al., 1995, Nielsen et al., 1994, Haase et al., 2007, Shi et al., 2011, Akatsuki and Makita, 2020]. En revanche, la variabilité des mesures et le faible rapport signal sur bruit n'ont pas permis de reconstruire avec robustesse des profils complets selon le type de racine et la distance à l'apex.

Ces difficultés expérimentales et analytiques soulignent l'utilité des modèles comme outils d' exploration de motifs difficilement accessibles expérimentalement. Elles identifient aussi très concrètement les améliorations nécessaires: méthodes analytiques plus sensibles, comme la GC-MS/MS ciblée ou non ciblée appliquée à des extraits de sable, temps d'exposition plus longs mais contrôlés vis-à-vis de la dégradation microbienne, ou modification du design des pièges. En parallèle, des tests préliminaires de pulse labeling localisé au $^{15}NO_3^-$ montrent qu'il existe une voie prometteuse pour quantifier expérimentalement l'hétérogénéité spatiale de l'absorption d'azote dans le même type de dispositif. Enfin, le jeu de données temporel acquis sur l'architecture racinaire et la phénologie aérienne constitue une ressource

importante pour mieux contraindre les règles d'émergence des racines nodales et les vitesses d'allongement, qui se sont révélées déterminantes dans le fonctionnement de *Wheat-BRIDGES*.

Conclusion générale

Cette thèse montre que la rhizodéposition et l'absorption d'azote minéral ne peuvent pas être assimilés à des flux constants ou simplement proportionnels à la masse des racines. La dynamique de ces flux émerge au contraire d'une combinaison de régulations locales par les métabolites, l'anatomie, les transports d'eau et de solutés, la croissance racinaire et les allocations entre organes, combinaison dont les effets changent au cours du temps et selon les axes du système racinaire. En développant successivement *Root-CyNAPS*, *MetaFSPM*, *Root-BRIDGES* et *Wheat-BRIDGES*, puis en confrontant ces approches à des expériences en rhizotrons, j'ai pu montrer que la rhizodéposition ne se réduit ni à une proportion fixe de la photosynthèse ni à une proportion fixe de biomasse racinaire, que le concept d'*active root zones* doit être utilisé avec prudence, que l'absorption d'azote au travers des flux d'eau peut devenir aussi importante que l'absorption active selon les conditions, et que la rhizodéposition et l'absorption d'azote peuvent être colocalisés ou non, suivant le type de racines et les conditions de croissance de la plante.

D'un point de vue méthodologique, la thèse apporte un cadre de modélisation réutilisable pour explorer conjointement fonctionnement racinaire local, bilan C-N de la plante entière et interactions avec l'environnement. *MetaFSPM* formalise une stratégie de couplage qui rend les hypothèses de modélisation plus explicites et plus modulaires. *Wheat-BRIDGES* fournit un premier prototype cohérent de plante entière architecturée couplant les cycles de carbone et d'azote entre parties aériennes et racinaires. Le dispositif expérimental en rhizotron, malgré ses limites analytiques actuelles, ouvre des perspectives concrètes pour mieux décrire qualitativement et quantitativement l'évolution des fluxs de rhizodéposition le long des racines, un ensemble de données nécessaire à une calibration plus quantitative des modèles. Ensemble, ces contributions posent les bases d'une exploration mécaniste des interactions plante-sol où la dynamique locale des flux, la plasticité architecturale et le fonctionnement C-N global de la plante peuvent être analysés dans un même cadre.

Perspectives

Les résultats obtenus ouvrent plusieurs perspectives. À court terme, l'une des priorités est de renforcer la calibration quantitative de *Wheat-BRIDGES*, en particulier pour la respiration racinaire, l'exsudation azotée et certains paramètres de perméabilité phloémienne, puis de compléter cette calibration par des analyses de sensibilité structurées et des approches de calibration orientée par motifs expérimentaux. Il sera également nécessaire d'explorer des scénarios environnementaux plus contrastés que ceux utilisés ici, notamment pour le nitrate, la disponibilité en eau, la température et la lumière, afin de mieux tester l'hypothèse d'une plasticité des flux gouvernée avant tout par le déplacement spatio-temporel des zones de forte activité.

À plus long terme, plusieurs enrichissements du cadre de modélisation apparais-

sent prometteurs. Le couplage avec des modèles de sol plus détaillés, qu'il s'agisse de biogéochimie C-N, de transport des solutés ou de structure physique du sol, permettrait d'évaluer plus finement comment les points chauds de rhizodéposition et d'absorption d'azote interagissent avec la dynamique microbienne et la disponibilité locale des ressources [Kyker-Snowman et al., 2020, Zhang et al., 2021, Daly et al., 2016, Rötzer et al., 2025]. De même, l'introduction d'une représentation métabolique plus explicite, distinguant davantage d'espèces chimiques plutôt que des pools moyens, offrirait un lien plus direct avec les données métabolomiques et les variations génotypiques [Shaw and Cheung, 2018, Hunt et al., 2023, Fiehn, 2016, Rao and Liu, 2025]. Enfin, la modularité acquise pendant cette thèse ouvre la voie à des simulations multi-espèces et à des changements d'échelle, par exemple vers l'interculture, les mélanges variétaux ou l'upscaling au champ via des métamodèles, de façon à relier plus directement les mécanismes identifiés ici à des questions d'agroécologie appliquée [Perthame et al., 2023, Pagès et al., 2020, Blanc et al., 2023, Gawinowski et al., 2024].

Funding

This PhD was funded by the french doctoral school *Agriculture, alimentation, BIologie, Environnement et Santé* (ABIES) and benefited from a complementary funding from the *MIXROOT-C* project (2021-2024) supported by the European Union program *Horizon 2020* according to the funding No. 862695 *EJP SOIL*.

Remerciements

Sur cette page, je voudrais marquer un temps d'arrêt pour celles et ceux qui me liront afin d'insister sur le fait que ce travail de thèse a été profondément collectif et que je souhaite chaleureusement remercier toutes les personnes qui ont pu, de près ou de loin, y prendre part.

Tout d'abord, je tiens vraiment à remercier mes quatre encadrants, Frédéric Rees, Alexandra Jullien, Romain Barillot et Christophe Pradal, de m'avoir dédié de votre temps dès que nécessaire, pour votre positivité permanente, pour vos conseils d'orientation avisés face à la complexité des sujets abordés, tout en étant toujours attentifs à ma liberté scientifique à chaque étape de la réalisation de cette thèse. Au delà d'une relation hiérarchique de supervision, j'ai toujours eu le sentiment de travailler main dans la main avec vous et j'espère vraiment pouvoir continuer sur cette voie dans les années à venir. Aussi, vous êtes tous un exemple sur lequel je m'appuierai sans aucun doute quant à la manière d'enseigner, d'encadrer et de collaborer humainement au sein de la communauté scientifique, tout en trouvant un équilibre entre une vie de recherche et sa vie privée.

Je remercie bien sûr toute ma famille qui a suivi de très près et avec grand intérêt chaque étape du déroulement de cette thèse, et qui a éclairé les tunnels de travail en étant toujours d'un soutien infaillible sans lequel je n'aurait jamais pu aller aussi loin.

Je veux aussi remercier chaque personne qui a été impliquée dans les phases de préparation, réalisation et d'analyse des expérimentations en conditions contrôlées présentées dans ce manuscrit: Josianne Jean-Jacques, Rozenn Le Hir, Alain Fortineau, Didier Charpentier, Florian Perrault, Nathalie Lecorneur, Marina Berthet, Marie-Reine Hoffmann, Léo Tumoine, Xavier Cornilleau, Baptiste Esnault, Céline Richard-Molard et Laurène Perthame. Nous obtiendrons bientôt les résultats associés dans les mois à venir et ce sera un plaisir de les partager avec vous!

Enfin, je veux aussi remercier toutes les personnes d'ECOSYS avec lesquelles j'ai pu échanger au-delà de mon sujet de recherche, pour m'avoir montré leur perspective de la recherche et avoir envisagé des connections plus qu'essentielles entre disciplines, mais également pour m'avoir partagé leur vision bien au-delà du cadre du travail. Je ne pourrai pas citer tout le monde tant il y a de personnes accueillantes dans ce labo, mais, Solen je ne t'oublie pas, c'était un plaisir de démarrer la thèse avec toi et je te souhaite plein de bonheur pour la suite. Pedro, merci pour ton accueil dès le premier jour, c'était un plaisir d'échanger avec toi et vraiment inspirant de constater tout le travail abattu lors de cette grande transition de la thèse à ton poste. Je reviens porter la table basse quand tu veux, et vive l'Irlande! Siwar, je suis vraiment heureux qu'on ait pu passer successivement tous les caps de la thèse

en binôme, partager notre amour du piment, et que tu t'épanouisse aujourd'hui dans ton postdoc. Sebastien, merci pour toutes ces discussions, toutes ces blagues, tes bons conseils et les rebondissements d'horaires lorsque l'on prenait la navette de Charléty tous les matins. Vive le futur président SIAFEE! Manuela, madame la doyenne, merci pour toutes ces chansons partagées, ces cours de danse, ces fous rires... Tu es aussi un modèle de maturité pour moi à réussir à gérer autant en même temps. Rachna, je n'oublie toujours pas toutes nos discussions dans le RER, on continue d'arroser la tomate! Aubin, le cross coding-sprint a payé! J'ai hâte qu'on continue de se régaler en sciences comme au restau! Tobias, it was a pleasure to hit the CROUS and the road to Edinburgh with you and Frédéric! Emilio and Shuaishuai, 兄弟, the arrival of your duo in the office was really the last step for the team to be complete, I loved working in music with you. Let's go to 西北疯 once again soon! Hajar, merci d'avoir toujours été si encourageante et pleine de positivité quelque soit la situation, on se voit bientôt! Marcelo, merci d'avoir fait en sorte de garder tout le monde connecté pour que je puisse continuer à avoir des nouvelles de la fine équipe! Nomena, jamais je n'avais rencontré une personne avec une vision aussi inspirante et partagée auparavant. Je ne te remercierai jamais assez d'avoir mis en musique la fin de la thèse, avec ton aide, ton amitié et ta confiance sans aucun détour, tu es devenue tellement importante à mes yeux. Je sais qu'on avancera ensembles sur bien des projets, c'est certain. À toute ma decabrozer!

Enfin je voudrais remercier tous les artistes qui m'ont énormément accompagné à chaque étape de cette thèse, toutes ces mélodies qui m'ont offertes des moments de suspendus face à la beauté de la réalisation et de mon objet d'étude. Un grand merci à Dakhabrakha pour *Vesna*, AC/DC pour *For those about to rock (we salute you)*, Yoshida Takuro pour 恋の歌, Stevie Wonder pour *Misstra Know It All*, Ayo pour *Without You*, Sumino Hayato pour *After Dawn*, *One Last Kiss* et *Aqua Riyuchi Sakamoto*, Ikue Asazaki pour ええうみ, Gustavo Santaolalla pour *Cordon de Plata*, John Butler pour *Spring to Come* et *Running to Keep Up*, Lianne La Havas pour *Weird Fishes*, Mdou Moctar pour *Asshet Akal*, Naâman pour *Soul Plan*, ZZ Top pour *Asleep in the desert*, Ibrahim Maalouf pour *True Sorry*, James Brown pour *People Get Up And Drive Your Funky Soul*, Esthétique Mouana pour *Elena Tomato*, Koji Kondo pour *Dire, Dire Docks*, Daniel Deluxe pour *Access Denied*, Infraction pour *Full Speed*, Talpa pour *Violently Happy*, Carpenter Brut pour *Disco Zombie Italia*, Kendrick Lamar pour *untitled 06*, *King Kuta*, *Father Time*, *Reincarnated*, Post Malone pour *Socialite* et *Hollywood's Bleeding*, Knowknow pour *Bossy* et 小生意, Doja Cat pour *AAAH MEN!*, Daddy Yankee pour *Gasolina*, Anderson Paak pour *Come Down*, Shaka Ponk pour *Alegria* et *Share a Line*, Mick Gordon pour *The Underking* et *Transistor Fist*, Gojira pour *The Gift of Guilt*, Delilah Bon pour *Dead Men Don't Rape*, Bear McCreary pour *Raeb's Lament*, Hiroyuki Sawano pour *Vogel im Käfig*, *Bird in a Cage*, *Bauklötze* et 進撃 *st-hrn-egt20130629* 巨人, Shiro Sagisu pour *La Distancia Para Un Duelo*, The Hu pour *Mother Nature*, Hanggai pour *Borulai's Lullaby* et *The Vast Grassland*, Piotr Musial pour *The Slopes of the Blessure*, Andrew Prahlow pour *Timber Hearth*, et enfin Toto pour *Manuela Run*, *White Sister*, *Kingdom of Desire*, Marcus Miller pour *Run for Cover*, Abba pour *Dancing Queen*, Beyoncé pour *Daughter* et *16 carriages* et *II Hands II Heaven*, et Steely Dan pour *Home at Last*.

Communications associated with this PhD thesis

The work presented in this PhD thesis has up to now resulted in the following scientific communications:

- Co-authorship in *"Deciphering spatiotemporal patterns of rhizodeposition with a functional-structural root model: RhizoDep"*, Rees et al. [2025], published in *Plant and Soil*
- First author of the article *"Do specific root zones shape plant net N uptake? Modeling insights from Root-CyNAPS"*, in press at *in silico Plants*
- Oral presentation at the workshop *Carbon Allocation in Plants 2023* in Versailles, France: *"How can local sugar concentrations in roots regulate the exchanges of C& N between shoots, roots and soil ? FSPM modeling at plant scale for an architectured wheat"*
- Oral presentation at the meeting of the *International Society for Root Research (ISRR)* in 2024 in Leipzig, Germany: *"Modeling carbon and nitrogen exchanges at the soil-root interface, case study of spring wheat response to a nitrate patch"*
- Oral presentation at the meeting of the *RhizosPHARE* network in 2024 in Rennes, Frace: *"How are local root uptake and rhizodeposition integrated by soil during plastic root growth? The new Wheat-BRDIGES model approach"*
- Poster communication at the international conference *Rhizosphere 6* in 2025 in Edinburgh, UK: *"Modeling C&N root-soil exchanges with 3D root and shoot growth based on plant ecophysiology: the Wheat-BRIDGES approach"*. First poster prize award.

Contents

French Summary **4**

Funding **15**

Acknowledgements **15**

Communications associated with this PhD thesis **17**

1 Context, State of the art & Objectives **11**
1.1 General context 12
1.2 State of the art 14
1.2.1 Rhizodeposition, an elusive process 14
1.2.2 Regulation of root-soil exchanges at the scale of a root segment 17
1.2.3 Experimental challenges associated to the characterization of root-soil C&N exchanges 22
1.2.4 Simulating root-soil C&N exchanges at different scales: opportunities and limits 26
1.2.5 Conclusion 34
1.3 Research questions, strategy and organization of this work 36

2 Do specific root zones shape plant net N uptake? Insights from the *Root-CyNAPS* model **39**
2.1 Chapter strategy 40
2.2 In Silico Plant Article Introduction 43
2.3 Root-CyNAPS Model Description 45
2.4 Use Case: Simulation of Wheat N Uptake 61
2.5 Results 64
2.6 Discussion 69
2.7 Chapter Contribution to Thesis Strategy 86

3 *MetaFSPM*, a new toolkit for FSPM modularization and coupling enabling the study of multiscale C&N regulations in wheat **87**
3.1 Chapter Strategy 88
3.2 Introduction 88
3.3 Material & Methods 90
3.3.1 *MetaFSPM* - a generic coupling toolkit 90
3.4 Results 92

3.5 Discussion . . . 95
3.5.1 Positioning *MetaFSPM* among existing FSPM platforms and coupling approaches . . . 95
3.5.2 Component-based coupling to foster the exploration of multiscale C – N regulations . . . 96
3.5.3 Limitations and future developments . . . 97
3.6 Conclusion . . . 98
3.7 Chapter Contribution to Thesis Strategy . . . 98

4 *Wheat-BRIDGES*, a whole-plant model to study the multiscale determinants of C&N exchanges between roots and soil 99
4.1 Chapter strategy . . . 100
4.2 Introduction . . . 102
4.3 Material & Methods . . . 103
4.3.1 Adaptation of existing FSPM components for the *Wheat-BRIDGES* model . . . 103
4.3.2 *Wheat-BRIDGES* simulation loop . . . 107
4.3.3 First *Wheat-BRIDGES* parametrization and simulation scenario under variables environmental conditions . . . 108
4.4 Results . . . 110
4.4.1 Comparison of simulation outputs between *CN-Wheat* and *Wheat-BRIDGES* . . . 110
4.4.2 Cumulated C&N plant balance over time . . . 111
4.4.3 Correlations between C & N flow rates over time at the scale of the plant . . . 113
4.4.4 Spatial variability of C&N exchanges along roots . . . 116
4.5 Discussion . . . 120
4.5.1 *Wheat-BRIDGES* outputs coherence . . . 122
4.5.2 Do we need an explicit root system architecture to understand root-soil exchanges? . . . 123
4.5.3 Methodological contribution to FSPM coupling . . . 127
4.5.4 Model limitations and targeted improvements . . . 129
4.6 Chapter conclusion and perspectives . . . 132
4.7 Chapter Contribution to Thesis Strategy . . . 133

5 Experimental characterization of wheat root architecture, root anatomy, and rhizodeposition over space and time 135
5.1 Introduction and chapter strategy . . . 136
5.2 Material & Methods . . . 136
5.2.1 Experimental design . . . 138
5.2.2 Preparation steps . . . 138
5.2.3 Repeated bolting cloth installation and rhizodeposit sampling with sand patches . . . 143
5.2.4 Repeated root and shoot phenotyping . . . 146
5.2.5 Destructive sampling protocols . . . 147
5.2.6 Analytical protocols . . . 148
5.3 Experimental results . . . 151

5.3.1 Root cross sections image analysis . . . 151
5.3.2 C&N rhizodeposition rates estimated from rhizodeposit traps 153
5.4 Discussion . . . 157
5.4.1 Anatomy of wheat roots and its possible influence on root-soil exchanges . . . 157
5.5 Conclusions . . . 160
5.6 Chapter contribution to Thesis Strategy . . . 162

6 General Discussion 163
6.1 Reminder of thesis objectives and strategy . . . 164
6.1.1 Validity of initial hypotheses . . . 164
6.2 Main scientific findings . . . 168
6.2.1 Carbon rhizodeposition is more than a simple fraction of the carbon fixed by the plant and allocated to the roots . . . 168
6.2.2 Active root zones: an oversimplified concept . . . 168
6.2.3 Studying the co-location of rhizodeposition and resource uptake hotspots . . . 170
6.2.4 Importance of the spatial heterogeneity of root-soil exchange and consequences on the functioning of the plant . . . 171
6.3 Methodological achievements and remaining challenges . . . 172
6.3.1 *MetaFSPM*, a new coupling framework for complex FSPMs . 172
6.3.2 *Root-CyNAPS*, a new root FSPM to study the heterogeneity of mineral N uptake along roots . . . 173
6.3.3 *Wheat-BRIDGES*, a new whole-plant FSPM to explore the heterogeneity and plasticity of root-soil exchanges . . . 173
6.3.4 Exploring the spatial and temporal variations of root-soil exchanges with innovative experimental approaches . . . 174
6.3.5 Towards a better understanding of plant-soil interactions . . . 176
6.4 Conclusion . . . 178

References 179

Supplementary Material 199
Chapter 2 Supplementary Material . . . 201
Chapter 4 Supplementary Material . . . 243
Chapter 5 Supplementary Material . . . 252

List of Figures

1.1 Schematic cross section of a wheat root 19
1.2 Summary of the different approaches for sampling root exudates . . . 22
1.3 Description of the main pools and compartments used in the *CN-Wheat* model 32
1.4 Overview of the *RhizoDep* model 33
1.5 Conceptual framework of the thesis 37

2.1 Conceptual scheme in Chapter 2 41
2.2 Conceptual scheme of the Root-CyNAPS model 49
2.3 3D static root system architecture of simulated properties 63
2.4 Visualization of the spatial heterogeneity of net N uptake within the 3D root system of wheat 65
2.5 Evolution of length-wise net N uptake with the distance from root tip simulated by Root-CyNAPS 66
2.6 Evolution of the cumulative contribution of roots to the net N uptake of the root system with their cumulative contribution to total root length 68
2.7 Decomposition of total root N balance into N inflows and outflows simulated by RootCyNAPS 70

3.1 Functionality of the *component* structure introduced by *MetaFSPM* . 91
3.2 Components coupling scheme for the new *Wheat-BRIDGES* model . 94

4.1 Conceptual scheme in Chapter 4 101
4.2 Environmental conditions applied at the boundary of *Wheat-BRIDGES* organs 109
4.3 Simulated evolution of the length of individual leaves on the main stem 111
4.4 Simulation of shoot and root structural mass over time 112
4.5 Simulation of shoot:root structural mass ratio 112
4.6 Simulation of the absolute C and N distribution within the plant . . 113
4.7 Simulation of the relative C and N distribution within the plant . . . 114
4.8 Simulation of the evolution of C rhizodeposition over time 114
4.9 Simulation of absolute C rhizodeposition and N uptake as a function of photosynthesis 115
4.10 Simulation of mass-related C rhizodeposition and N uptake as a function of photosynthesis 116
4.11 Simulation of the spatial distribution of net C rhizodeposition 117

4.12 Simulation of local C rhizodeposition as a function of local N uptake 118
4.13 Simulated spatial distribution of C rhizodeposition and N uptake in the first 10 cm from root tip 120
4.14 Simulated cumulative contribution of active root zones to root-soil exchange flows 121

5.1 Conceptual scheme in Chapter 5 137
5.2 Sampling planning of Experiment 2 139
5.3 Schematic representation of rhizotrons' experimental setup 141
5.4 Key steps of the protocol of rhizodeposit sampling in rhizotrons . . . 145
5.5 Illustration of images taken from a rhizotron 147
5.6 Processing pipeline for the high resolution rhizotron images dataset . 151
5.7 Illustration of the root sections observed and reconstructed by simulation 152
5.8 Evolution of cell height along the first 6 mm of a wheat seminal root 153
5.9 Amount of C measured in control samples 156

6.1 Final conceptual scheme of the thesis 167
6.2 Inputs provided to Root-CyNAPS and resolution loop 224
6.3 Evolution of input root system architecture over plant age 225
6.4 3D static root system architecture displaying the root type 226
6.5 Evolution of the hexose concentration in the root system symplasm with plant age simulated by RhizoDep 227
6.6 Temporal variations of Root-CyNAPS outputs over 24 hours of simulations 228
6.7 Evolution of length-wise net mineral N uptake with the thermal time since root tissue formation 229
6.8 Evolution of massic net mineral N uptake with the distance from tip 230
6.9 Decomposition of net N uptake between gross N uptake and N losses through diffusion with distance from root tip 231
6.10 Evolution of length-wise net N uptake with various state variables of the Root-CyNAPS model 232
6.11 Evolution of length-wise gross N uptake with various state variables of the Root-CyNAPS model 233
6.12 Evolution of length-wise N loss through diffusion with various state variables of the Root-CyNAPS model 234
6.13 Percentage of root system structural mass as a function of the percentage of root system length for plant ages from 10 to 60 days-old . 235
6.14 Contribution of the 10% most active root length in whole-plant N budget, as a function of root system age and nitrate concentration in culture solution 236
6.15 Simulated shoot N content by *CN-Wheat* and *Wheat-BRIDGES* . . . 243
6.16 Simulated C rhizodeposition and N uptake as a function of C allocation to roots 243
6.17 Simulated C rhizodeposition and N uptake as a function of massic photosynthesis 244

6.18 Simulated C rhizodeposition and N uptake as a function of massic C & N allocation to roots 244
6.19 Simulated spatial distribution of length-related net mineral N uptake along roots 245
6.20 Simulated spatial distribution of length-related N rhizodeposition along roots 246
6.21 Simulated spatial distribution of length-related water uptake along roots 247
6.22 Simulated spatial distribution of length-related C rhizodeposition and N uptake along a single root 248
6.23 Simulation scenario applied to *Root-BRIDGES* 249
6.24 Nitrate patch scenario applied to *Root-BRIDGES* 250
6.25 Data analysis workflow for FSPM time-series outputs 251
6.26 Rhizotrons' temperature profile over soil depth 252

List of Tables

1.1 Possible coupling strategy between *CN-Wheat* and *RhizoDep* 34

2.1 Description and units of the Root-CyNAPS model variables 45
2.2 Description and units of the Root-CyNAPS model parameters 58
2.3 Simulation scenarios presented in the core text of the article 61
2.4 Inputs and initial conditions estimated from literature for each scenario 62
2.5 Root-CyNAPS outputs after 24h on a static root system of wheat under 0.5 mM nitrate, as compared with values reported in the literature under similar conditions 64

3.1 Example of components structured with the *MetaFSPM* toolkit . . . 93

5.1 Average properties of a soil collected from the *Plateau de Saclay*, mixed with 30% volume of sand, and used in Exp. 1 and 2. All soil properties were measured after drying and sieving 140
5.2 Summary of anatomical features computed from root sections 154

6.1 Complete list of equations, description and units of the Root-CyNAPS model 203
6.2 Description and units of the Root-CyNAPS model parameters 214

Chapter 1

Context, State of the art & Objectives

1.1 General context

The dominant agricultural model in industrialized countries is built on technological innovations implemented soon after the Second World War to meet food demand and lower prices with an increase in yield. These practices, such as mechanization, intensive irrigation systems, or the use of synthetic herbicides, pesticides and fertilizers, were designed to optimize and standardize crops growing conditions by reducing pressures from diseases, pests, adventitious species and hydromineral resources limitations [Evenson and Gollin, 2003, Malézieux, 2012]. This intensification relied on a small number of species and varieties, selected to respond to standardized conditions with high yields. However, **agriculture intensification** has generated major environmental, health and social externalities over the last decades. Intensive agriculture has degraded soils, water and air quality, threatening food security and safety [Gomiero, 2016, Gliessman, 2014, Cellier et al., 2020]. Modern farming practices simplify rotations and rely on high fertilizer and pesticide inputs, which reduce soil fertility and disrupt rhizosphere microbiome [M. Tahat et al., 2020]. Modern crop varieties were generalized in intensified cropping rotations at the expense of a 75% loss of crop genetic diversity over the 20th century [Gliessman, 2014]. Intensive farming, as well as the pre- and post-production activities, depends heavily on fossil energy and cause the degradation of non - renewable soil resources [Hatt et al., 2016, Keesstra et al., 2024]. Worldwide, food systems contribution to CO_2, CH_4 and N_2O greenhouse gas emissions have been estimated to range between 20 and 40% of anthropogenic emissions for the 1990-2019 period [Tubiello et al., 2022], making them an important contributor to climate change. Despite large investments in technological innovation and breeding programs, the conventional model is facing intrinsic limitations. Even with global yield still increasing, climate change is expected to increase yield volatility and require new cultivars and cropping designs resilient to temperature and precipitation variability [Baffes and Etienne, 2024]. **Aside from being major contributors to climate change, conventional systems also demonstrate low resilience to climatic variability and extremes** [Kahiluoto et al., 2019]. The intensification of climate extremes projected for the coming decades highlights the vulnerability of these systems and the associated risks for food security [Coumou and Rahmstorf, 2012, Asseng et al., 2015, Kornhuber et al., 2023]. Climate change already compromises the capacity of agro - ecosystems to provide ecosystem services: high temperatures and water shortages increase evapotranspiration, reduce primary production of agroecosystems and food provisioning [Semeraro et al., 2023]. Despite the urge for adaptation strategies, intensive agriculture is locked in place by its industrial nature and international competition. Large specialized farms rely on downstream agro-industry outlets whose specifications on input-dependent practices, modern varieties, and food intrinsic properties, e.g. grain protein content, hampers the adoption of existing and new agronomic, social, and economical innovations that would alleviate the impact of climate change on crops and lower the impact of agriculture on the environment [Meynard et al., 2018, Brun et al., 2021].

Given these observations and the rising global food demand driven by a growing population [Tilman et al., 2011], the intensive agricultural model is being questioned,

calling for a systemic paradigm shift to reconcile productivity with ecosystem-based practices, environmental integrity, and social equity. The **agroecological transition** offers a pathway toward a more sustainable agricultural model that can overcome the limits of conventional systems [Altieri, 1999, Wezel et al., 2009, Duru et al., 2015, Altieri, 2018]. At the interface between the natural, economic, social, political, and action sciences, agroecology can be defined as the ecology of food systems and mainly emphasizes on the key role of transition and innovation processes rather than advocating for a fixed set of practices [Francis et al., 2003]. A central principle of the agroecological transition is to identify cropping systems adaptations that would re-localize the cycling of carbon (C) and nitrogen (N), and strengthen the interactions between these two resources locally [Drinkwater and Snapp, 2007]. As in any ecosystem, crops grow from the acquisition of mineral C and N resources and subsequently inject organic C&N into the ecosystem. Recent studies have pointed out **plant organic inputs as a key lever for cropping practices adaptations to enhance net ecosystem C sequestration**. The *4 per 1000 initiative* showed that an increase in agricultural soil C stocks by 0.4% every year could compensate 20 to 35% of anthropogenic CO_2 emissions [Minasny et al., 2017]. Recently, Guenet et al. [2021] and Don et al. [2024] showed that aside aiming for net C sequestration, all of C and N greenhouse gases, and all sequestration and emission processes, should be considered to evaluate the contribution of a given practice to climate change mitigation . Several practical guidelines have been suggested to engage soil management in the agroecological transition, such as the preservation measures of peatlands and carbon-rich soils [Nabuurs et al., 2023], usage of cover-crops and rotation diversification to increase soil C inputs and reduce fertilize requirements [Peng et al., 2023, Nouri et al., 2022], an optimization of fertilizer use, residues incorporation and irrigation [Maaz et al., 2021, Abalos et al., 2022], or a reduction of tillage intensity to preserve soil structure and microbial activity [Paustian et al., 2016]. Even though such sets of practices have been advocated by researchers for several years, consensus indicators are still lacking to evaluate and institutionally regulate these soil performances [Cornu et al., 2023, Whalen et al., 2022, Wang and Kuzyakov, 2024].

Plant roots represent an important pathway by which plants transfer carbon below ground, and root-derived C inputs to the soil have been shown to contribute to the formation of stable soil organic matter 2 to 5 times more than a similar mass of shoot residues [Rasse et al., 2005, Jackson et al., 2017], making them **a major contributor to soil C sequestration**. Roots can transfer organic C&N into the soil both as dead roots and as **rhizodeposits**, defined here as any type of organic matters released by living roots into the soil. Rhizodeposition has been considered the *hidden half of the hidden half* [Gregory, 2022] given the difficulty in characterizing it. Rhizodeposition represents a significant but variable proportion of plant C & N balance, ranging from 0% to 47% of the C fixed by the plant through photosynthesis [Nguyen, 2009, Pausch and Kuzyakov, 2018] and from 2 % to 71 % of the N taken up by the plant [Fustec et al., 2010, Jones et al., 2009, Wichern et al., 2008]. While rhizodeposition might be considered as a waste of resources by the plant, **rhizodeposition can benefit to the plant in many ways**, e.g. by optimizing nutrient and water (W) uptake by shaping roots' abiotic and biotic soil environment [Gregory, 2022]. Correspondingly, rhizodeposition has been shown

to respond to soil nutrient and water availability, usually through an increase in rhizodeposition rate when facing resource scarcity [Canarini et al., 2019, Usyskin-Tonne et al., 2021]. In particular, rhizodeposition may stimulate soil microbial activity and generate the so-called *rhizospheric priming effect* (RPE), i.e. the change in soil organic matter decomposition caused by root activity [Dijkstra et al., 2013], which can result in an increased soil N mineralization and possibly a greater N uptake by the plant [Ai et al., 2020, Gan et al., 2022]. Despite the importance of rhizodeposition for plant and soil functioning, rhizodeposition remains poorly understood as it varies depending on plant species, phenological stages, soil types, and environmental conditions [Wichern et al., 2008, Jones et al., 2009, Pausch and Kuzyakov, 2018]. Rhizodeposition has been hypothesized to depend on the tight coupling between C & N cycles at the scale of the plant, but also on very localized processes occurring at the scale of a millimetric root segment, interacting with the way the root system adapts to an heterogeneous soil environment [Gratani, 2014].

Given its link with soil C sequestration and plant nutrition, rhizodeposition could represent a significant lever in the agroecological transition. A deeper understanding is however required regarding **the significance of rhizodeposition in plant C&N balance**, and regarding **the traits and environmental drivers that can effectively regulate rhizodeposition**. The following section summarizes the current level of understanding in scientific literature regarding rhizodeposition, its variability in different contexts and at different scales, and gives an overview of various approaches used to quantify rhizodeposition and its link with plant functioning.

1.2 State of the art

This literature survey investigates first what is currently known about rhizodeposition and its variability over time in different contexts. A focus is then made on the spatial distribution of rhizodeposition together with N and water uptake within the root system architecture. Finally, experimental and modeling approaches used to characterize the spatial and temporal variations of these root-soil exchanges are presented and discussed.

1.2.1 Rhizodeposition, an elusive process

Rhizodeposition does not correspond to a single flow but encompasses **a large set of processes** and a **diversity of organic materials and compounds**, which can confuse the identification of rhizodeposition determinants. Rhizodeposition includes the release of water-soluble metabolites (i.e., exudation), the excretion of proteins and exoenzymes, the secretion of mucilage, the sloughing of border cells from the cap protecting the root tip, and the emission of volatile organic compounds [Jones et al., 2009]. However, no consensus about the exact perimeter of rhizodeposition has emerged so far. For example, some authors consider that rhizodeposition also includes the allocation of resources to symbiotic microorganisms (i.e. Rhizobium or mycorrhizal fungus) or the senescence of fine roots [Jones et al., 2009, Pausch and Kuzyakov, 2018], while the excretion of inorganic compounds (e.g. ammonium and nitrate) is sometimes associated to rhizodeposition, e.g. in the studies that use

isotopic N labeling for investigating N rhizodeposition [Wichern et al., 2008]. In this thesis, rhizodeposition is considered as *any organic material released by a living root into the surrounding environment*, which can include root cell debris but excludes inorganic compounds, fine roots, and the resources directly allocated to root symbiotic microorganisms. Nonetheless, the boundary between living and dead roots is still blur, as mature roots can contain aerenchyma or dead tissues, despite conductive elements in the stele still being functional. With the current definition, the cell metabolite content released under cell differentiation will be described as rhizodeposits and separated from the cell content of a dying root. However the two processes overlap experimentally, and in a context of extreme weather events, or invasive sampling conditions, stress related root senescence might further amplify this confusion between rhizodeposition and root mortality. A recent review of Mueller et al. [2024] emphasized the need for sampling C inputs into the soil at very short time intervals in order to capture the whole life cycle of a root, which undergoes a progressive transition from rhizosphere to detritusphere. In addition, the exact contribution of each rhizodeposition flow to the overall rhizodeposition rate of the plant has remained obscure. Mucilage secretion and cells sloughing have been suggested to contribute to rhizodeposition at least 10 times less than root exudation [Nguyen, 2009, Rees et al., 2025], but high-molecular-weight exudates were shown to constitute 14-52% of total rhizodeposited C in maize [Jones and Darrah, 1993].

A large range of rhizodeposition rates has been reported in the literature, depending on plant species and growth stage. Various studies have revealed **differences in rhizodeposition levels among distinct plant families or species** [Nguyen, 2009, Jones et al., 2009]. Moreover, experimental studies comparing closely related varieties or replicates of the same variety still expose significant variations of total rhizodeposition, as shown by Van de Broek et al. [2020] with rhizodeposition levels varying about 2 fold between recent and old wheat cultivars. Rhizodeposition has been shown to considerably **vary over time and growth stage**. As pointed by Pausch and Kuzyakov [2018], the allocation of C to the root system usually decreases over annual plant growth, resulting in a decrease in rhizodeposition rate when related to the biomass of root (i.e., a decrease in the flow rate expressed as gram of rhizodeposited C per gram of root mass per day). As the root system grows in size, this may not necessarily mean that rhizodeposition rate expressed in absolute values (gram of rhizodeposited C per day) decreases over time. For example, in the case of wheat, the peak of C rhizodeposited by the plant may occur between stem elongation and ear emergence [Swinnen et al., 1994]. On a shorter time scale, rhizodeposition also follows a **diurnal pattern**, as plant C-labeling experiments have shown that rhizodeposited C primarily originates from recent photoassimilates [Liljeroth et al., 1990, Badri and Vivanco, 2009].

Rhizodeposition also depends on plant growth environment. Shoot activity is regulated by incident PAR, temperature and humidity perceived by each photosynthetic organ, subsequently affecting C fixation and C allocation to the root system and the range of total rhizodeposition [Farquhar et al., 1980]. Rhizodeposition processes in roots are in turn regulated by soil temperature, soil physical properties, water and nutrient availability, and the activity and diversity of the microbial community [Bakhshandeh et al., 2019, Maurer et al., 2021, Robert et al., 2025]. In

particular, mineral N uptake from the soil is thought to be a key regulatory process of rhizodeposition at multiple temporal and plant scales. Indeed, photosynthesis is regulated by the amount of nitrogen available to the leaves and therefore by N uptake and allocation from the roots to the shoot. Conversely, the range of C & N rhizodeposition and active nitrogen uptake is thought to be regulated by the amount of photosynthates allocated from the shoot to the roots, with contrasted effects reported depending on the current size of the root system [Canarini et al., 2019, Bicharanloo et al., 2022, Tixier et al., 2023, Amoah et al., 2025]. These C&N interactions between roots and shoot during their exchange with environment act as a dynamic and cumulative adjustment of root and shoot development, balancing N acquisition and C reduction under heterogeneous conditions. Water acquisition also impacts C&N root-shoot allocations since it regulates N transport to shoot through the transpiration stream, photosynthesis levels under water stress, and couples xylem and phloem sap flows for allocation of photosynthates to the roots [Nakad et al., 2022]. This allocation through phloem sap movements creates preferential allocation pathways in root system topology: a variation in photosynthate production by the shoot will reach specific zones of the root system faster than others [Schultes et al., 2025].

Water acquisition by roots not only sustains transpiration for photosynthesis and shoot growth but also constrains C&N exchanges between shoot and root. In vascular plants, xylem vessels transport water and dissolved mineral N from the roots to the leaves, driven mainly by the transpiration stream, whereas phloem sieve tubes redistribute sucrose, amino acids and other assimilates from photosynthetic *source* leaves to heterotrophic *sink* organs such as roots, young leaves and grains [Tegeder and Hammes, 2018, Plett et al., 2020]. Changes in soil water status therefore alter N transport to the shoot through xylem flow, restrain photosynthesis under water stress, and, via water exchange between xylem and phloem, affect the pressure gradients that drive phloem sap flow and the allocation of photosynthates to the root system [Sevanto, 2014, Plett et al., 2020]. Because phloem conduits follow the branching topology of the plant, this long-distance transport creates preferential allocation pathways within the root system: a change in photosynthate production in the shoot will reach specific root axes earlier or more strongly than others, leading to spatially heterogeneous carbon supply [Lacointe and Minchin, 2008, Nakad et al., 2022, Schultes et al., 2025]. Unloading of phloem to local root symplasm would then be driven by the consumption rate of transported compounds, sustaining a decreasing phloem-symplasm gradient especially in active growth and exudation regions [Ross-Elliott et al., 2017, Canarini et al., 2019].

Intermediate conclusion: Rhizodeposition corresponds to several distinct processes, and is associated with a high variability in terms of rhizodeposition flows reported in the literature. This variability may be linked to the dependence of rhizodeposition on plant genotypes, plant growth stage and environmental conditions such as temperature, soil water availability and soil nutrient availability. Rhizodeposition stands at the interface of C and N cycles in the soil-plant system and needs to be considered as part of the functioning of the whole plant. In particular, rhizodeposition may directly respond to changes in photosynthesis and/or nitrogen uptake. However, rhizodeposition may also be controlled locally at the scale of a small root

segment, where the interaction between rhizodeposition, nitrogen uptake and water uptake may play a significant role for the plant.

1.2.2 Regulation of root-soil exchanges at the scale of a root segment

Rhizodeposition has been shown to be heterogeneously distributed along roots [Jones et al., 2009, Sasse et al., 2018]. Its variability at plant scale therefore closely relates to its root system architecture [Nielsen et al., 1994, Landl et al., 2021, Galindo-Castañeda et al., 2024]. This spatial and temporal plasticity superimposes with all above-mentioned sources of variability, and defines the *local* scale at which the determinants of rhizodeposition, but also N and water uptake, should be studied to disentangle systemic complexity.

Variability of rhizodeposition and N uptake along roots

Rhizodeposition has long been known to be heterogeneously distributed along roots. In particular, **root tips have been designed as a major site of rhizodeposition** [Jones et al., 2009, Sasse et al., 2018], although some studies have suggested alternative "hotspots" such as the root hair zone, lateral root emergence sites, or even the root base [Badri and Vivanco, 2009, Holz et al., 2018, Voothuluru et al., 2018]. However, the spatial evolution of rhizodeposition has remained largely unexplored [Galindo-Castañeda et al., 2024].

Nitrogen uptake is also assumed to vary along roots. The existence of high-activity N uptake zones has been reported, typically near root apices, young lateral or root hair elongation zones [Yoneyama et al., 1975, Henriksen et al., 1992, Sorgonà et al., 2011, Zhong et al., 2014]. Several overlapping concepts are found in the literature to define preferential exchange zones in the root system and measure their contribution to plant N budget. It includes *active root length* [Hodge et al., 2009, Bechmann et al., 2014], *active root biomass* [Malagoli and Le Deunff, 2014, Le Deunff et al., 2019], *cortical-senescence-free length* [Schneider et al., 2017], and *hot spots* [Kanno et al., 2016, Canarini et al., 2019]. These concepts aim to capture the long-standing observation that a relatively small, physiologically young, or anatomically specialized fraction of the root system performs the majority of root exchanges [Grasmanis and Barley, 1969]. These concepts may be summarized under the broader term ***most active root zones***. According to the review by Hodge et al. [2009], only 10% of total root length would contribute to the *majority* of N uptake, and 30% for water uptake; however, the definition of *majority* remains unclear. In another study, Cruz et al. [1995] found that, in 7 day-old carob seedlings, the first 4 cm from the root tip accounted for approximately 40% of total N uptake. Modeling work by Robinson et al. [1991] on spring wheat suggests that, for contrasted plant age and soil nitrate concentrations, between 2 to 22% of root length account for the total measured N uptake. Similarly, Le Deunff et al. [2019] estimated that 4 to 7% of the root biomass, mostly fine root apices, was *active* in terms of N uptake in winter oilseed rape, although the contribution of this *active* part over the remaining part of the root system was not specified. Overall, the location, number, and contribution

of the *most active root zones* to plant N budget vary substantially across studies and remain insufficiently quantified.

Regulation of root-soil exchanges at the scale of a root segment

At the scale of a root segment, root-soil exchanges may be determined i) by the internal concentration of metabolites within the roots and the gradient of concentration with the external concentration outside the root, and ii) by the anatomy of root tissue. Indirectly, both rhizodeposition and N uptake may also be linked through biogeochemical processes occurring in soil. These three aspects are explored below.

Regulation of root-soil exchanges by local concentrations inside and outside the roots Carbon and nitrogen resources acquisition, metabolism, and transport are strongly interrelated, and the coupling points between these two cycles have been related to the dynamics of concentration profiles and C-N exchanges along roots [Ogawa, 2005, Fernández González et al., 2024, Sasse et al., 2018, Zhong et al., 2014].

Rhizodeposition is thought to be dominated by root exudation of soluble compounds, which has been associated to the diffusion of compounds from root cells into the surrounding environment [Jones and Darrah, 1993, Personeni et al., 2007, Jones et al., 2009]. Root-soil concentration gradients of organic compounds like carbohydrates, amino acids or organic acids are therefore expected to regulate the range of exudation flows. Consequently, any other process affecting these local concentrations may also have an influence on root exudation. However, variations in the exudation rate of a metabolite does not necessarily follow variations of its concentration inside root cells [Canarini et al., 2016, Proctor and He, 2017], suggesting the existence of additional drivers of rhizodeposition.

Nitrogen uptake also depends on root's internal and external concentrations of compounds. Nitrate and ammonium uptake in symplasm and export to the xylem have been described as active processes relying on the energetic metabolism and therefore the local hexose availability in root symplasm to transport N [Lejay et al., 2003, Amoah et al., 2025]. Moreover, local concentrations in mineral N in symplasm were reported to feedback on mineral N uptake kinetics through regulations of transporters' phosphorylation, expression, composition and density on the plasma membrane [Siddiqi et al., 1989, Liu and Tsay, 2003, Le Deunff et al., 2019]. Some metabolic pathways are also at the interface between C&N cycles such as amino acids synthesis, which consumes hexoses and inorganic nitrogen. Even though the majority of amino acids synthesis occurs in leaves, up to 40% of this synthesis has been associated to roots with an important variability between species [Scheurwater et al., 2002, Andrews and Raven, 2022]. Along with C&N unloading from the phloem, this local C&N metabolism would affect the local balance of C&N metabolites and therefore impact the aforementioned regulations on rhizodeposition and mineral N uptake, as well as the regulation of growth processes and related changes in root anatomy.

Influence of root anatomy on root-soil exchanges Root anatomical traits, such as parenchyma and root hairs exchange surface, endodermis development, or

conductive elements dimensions, have been associated with local C&N root-soil exchange, transport, storage, or anchoring functions. Basic root anatomy can be summarized as follows (Fig. 1.1), looking at the root from its external surface up to its center:

- The outerlayer cells is the *epidermis*, and is in direct contact with root's surrounding environment (e.g. soil solution).
- In a transitory layer called the *exodermis* underlying the epidermis, a watertight barrier can sometimes be formed and prevent the free passage of water and solutes to and from roots through the cell walls (*apoplastic* pathway), forcing the solutes to circulate selectively through the membrane of root cells.
- The *cortex* lays below the exodermis and contains one or several layers of parenchyma cells.
- A layer called *endodermis* can also develop an apoplastic barrier (e.g. characterized by lignin-rich Casparian strips) that limits the free transfer of solutes through the interconnected cell walls between the cortex and the tissue underlying the cortex, i.e. the stele.
- The *stele* corresponds at the central cylinder of the root and contains, besides parenchyma cells, the two types of vascular tissues, i.e. the *xylem* that conveys water and compounds from roots to shoots, and the *phloem* that conveys photoassimilates and other compounds from shoots to roots.

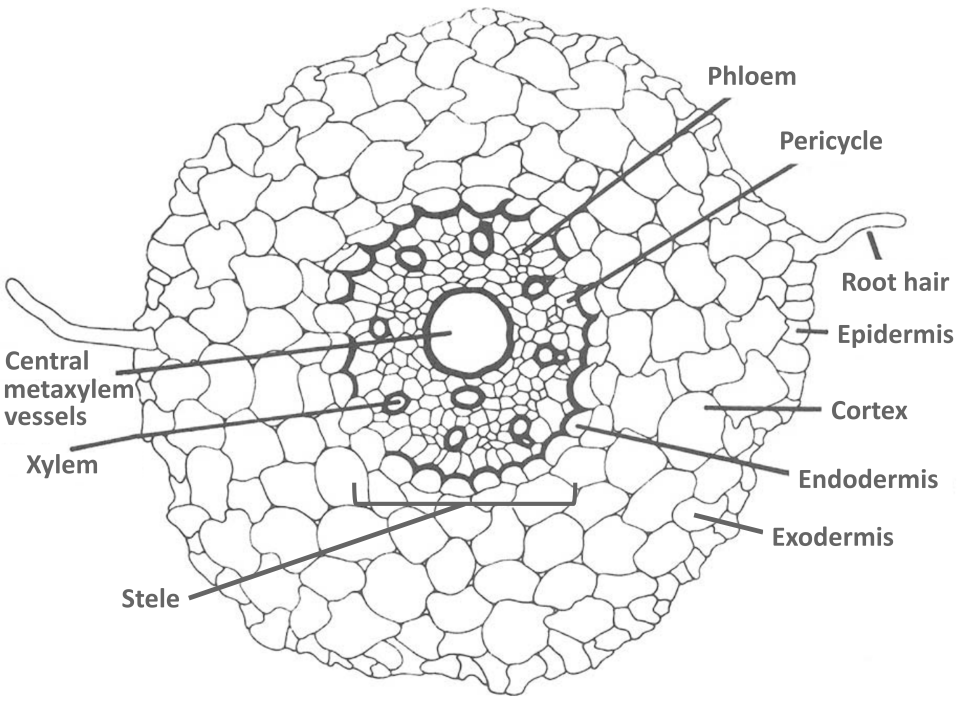

Figure 1.1: Schematic root cross section of a wheat seedling, adapted from Lersten [1987]

Primary root growth occurs at the root tip, where the meristem in which new cells are produced is protected by a *root cap*, where border cells are continuously sloughed

off and represents one specific rhizodeposition flow. Above the meristem, cells elongate within the *elongation zone*, above which *root hairs* can differentiate from specific epidermis cells and extend the capacity of the root to exchange matter with the surrounding environment. Lateral roots emerge from a primordium formed within the stele and can temporarily disturb the tightness of the endodermis apoplastic barrier. Later on, cortical senescence or the formation of aerenchyma may also modify the radial connectivity of the different root tissues [Lynch et al., 2021].

Root anatomical traits have been shown to be highly plastic under varying apex growth rate, temperature, mechanical resistance, and soil N, water and oxygen availability [Lynch et al., 2021]. Variations of these local anatomical traits with genotypes have also been reported [Namyslov et al., 2020, Lippold et al., 2021]. Local anatomical features can modify the overall root system architecture, as seen for example by a decreased rooting depth for maize mutants without cortical senescence [Lynch et al., 2021]. Conversely, these traits have a direct effect on local root-soil exchanges, though a modification of the exchange surface between root cells and the surrounding environment and of the permeability of cell walls.

The exchange surface between a root segment and the soil therefore depends on root diameter, successive tissue layers with specific cells shapes, dimensions and relative proportion between tissues, e.g. stele proportion or size of conductive elements [Heymans et al., 2020]. After root tissues formation in the meristematic region, several differentiation events occur and alter the accessible exchange surface and volume. Some processes will decrease exchange surface with root segment age and lead to root tip dominance for root-soil exchanges, e.g. cells elongation, aerenchyma formation, cortical senescence, and the progressive lignification and suberization of endodermis and exodermis which restrain the apoplastic pathway for N and water uptake [Calvo - Polanco et al., 2021, Ouyang et al., 2020]. This general decrease along root axis can however be counterbalanced by events like root hairs formation on epidermis which can account for a significant share of the exchange surface [Holz et al., 2018], root thickening, increasing cell size and layer number with thickening, or lateral apices emergence that can reopen Casparian strips. The maximal exchange surface at root tips associated with the immaturity of apoplastic barriers are assumed to contribute to the high exudation rates observed at root tips [Canarini et al., 2019].

Adding to symplastic exchange surface, the cell wall conductivity and topology defines the conductance of the whole root segment locally for N and water transport to the xylem, but also exudates diffusivity towards the soil [Couvreur et al., 2018]. Root anatomy also defines the cytosolic volume in which metabolite concentrations are defined, impacting tissues buffering capacity to metabolic and transport processes, and ultimately defining the root-soil concentration gradient for exudation [Colombi et al., 2022]. The loss of this volume can also lead to a local specialization of root tissues for transport, e.g. with cortical senescence lowering metabolic activity, phloem unloading and exudation range while keeping functional conductive elements in the stele [Schneider et al., 2017, Lynch et al., 2021].

Despite these insights, few studies have quantified how spatiotemporal variations in anatomy along roots translate into patterns of exudation and nutrient uptake. It is still unclear how the formation of boundary layers quantitatively influence C-N

root-soil exchanges. For example, the contribution of root hairs plasticity to nitrogen acquisition and exudation is debated; although hairs growth responds to nutrient stress, a direct link to increased exchanges has yet to be demonstrated [Lippold et al., 2021]. More integrated approaches combining high - resolution imaging, local C-N flux sampling and mechanistic modeling are needed to link anatomical traits with CN root – soil exchanges and rhizosphere processes.

Indirect regulation through local root-soil interactions Aside from root physiology, also interact with their environment, i.e. the soil [Gregory, 2022], and local C-N interactions affecting root concentrations also extend to the rhizosphere. Depending on the conditions in which rhizodeposits are released, they could be quickly assimilated by the microbial communities. Even though the outcomes of this assimilation on SOC sequestration versus microbial CO_2 emissions can be contrasted, for example depending on N fertilization [Bicharanloo et al., 2022], this would also increase the **N mining activity** in contact with the roots and sustain root N uptake [Pausch et al., 2024, Wiesenbauer et al., 2024]. Another indirect C-N interaction is the rhizodeposition of mucilage by root apices, **maintaining hydraulic continuity** and water uptake levels near apices, increasing their local N uptake and export compared to other root regions [Carminati et al., 2016, Bauget et al., 2023]. It is worth noting that **these C-N interactions with the soil may be decoupled spatially and temporally**. Rhizodeposition initiates a potential feedback on N availability at a specific location in the soil, but with a delay. As the root apex keeps moving forward, this suggests that the high exudation rate at a given root apex may trigger a higher soil nitrogen mineralization rate, which will subsequently result in a higher N availability to the younger lateral roots that will emerge in these zones, rather than to the main root apex itself [Wiesenbauer et al., 2024]. **N and water resources are not homogeneously distributed within the soil**, and roots have evolved to cope with such spatial heterogeneity [Hodge et al., 2009]. This spatial and temporal heterogeneity mobilize the short-term plasticity of N acquisition [Nacry et al., 2013] and involve abovementioned interactions with rhizodeposition along roots, but also regulate the plastic growth of the Root System Architecture (RSA) through sensing and trophic mechanisms. For example, local N availability in contact with a N patch is known to increase lateral branching, i.e. the number of active root tips and root exchange surface in preferential regions of the soil volume, thereby increasing *local* root-soil CN exchanges [Drew and Saker, 1975, Sun et al., 2017, Beckers et al., 2025]. Overall, these elements show that rhizodeposition and N acquisition therefore need to be considered together as *CN root-soil exchanges* when trying to better understand rhizodeposition multiscale regulations and impacts on plant physiology. Despite evidences on the rhizospheric CN intricacy, these interactions are rarely considered in the available literature [Lynch et al., 2024].

Intermediate conclusion: Rhizodeposition, nitrogen and water uptake are not homogeneously distributed along roots. Their spatial variation within the root system architecture appears to be controlled by the local metabolic status of the root, by its anatomy, and by indirect processes occurring locally within the soil. This calls for the integration of these processes at a very fine scale in order to understand how

root-soil exchanges interact and what may result from this interaction at the scale of the whole plant. However, characterizing these interactions at different scales may represent a major methodological challenge.

1.2.3 Experimental challenges associated to the characterization of root-soil C&N exchanges

A wide variety of methods aiming to measure C-N root – soil exchanges have been reported, ranging from whole-plant isotope labeling pulses (e.g., Pausch and Kuzyakov [2018], Fustec et al. [2010], Nacry et al. [2013]) to local membrane, traps and microsensor approaches (e.g., Oburger and Jones [2018], Vranova et al. [2013], McLaughlin et al. [2025]), all applied in a variety of growth medium from hydroponics to soil conditions (Fig. 1.2). **No method appears to be perfect**, knowing that sampling and analysis biases might not apply evenly on each compound, leading to an over- or under-representation of specific types of rhizodeposits in measured fluxes [Oburger and Jones, 2018].

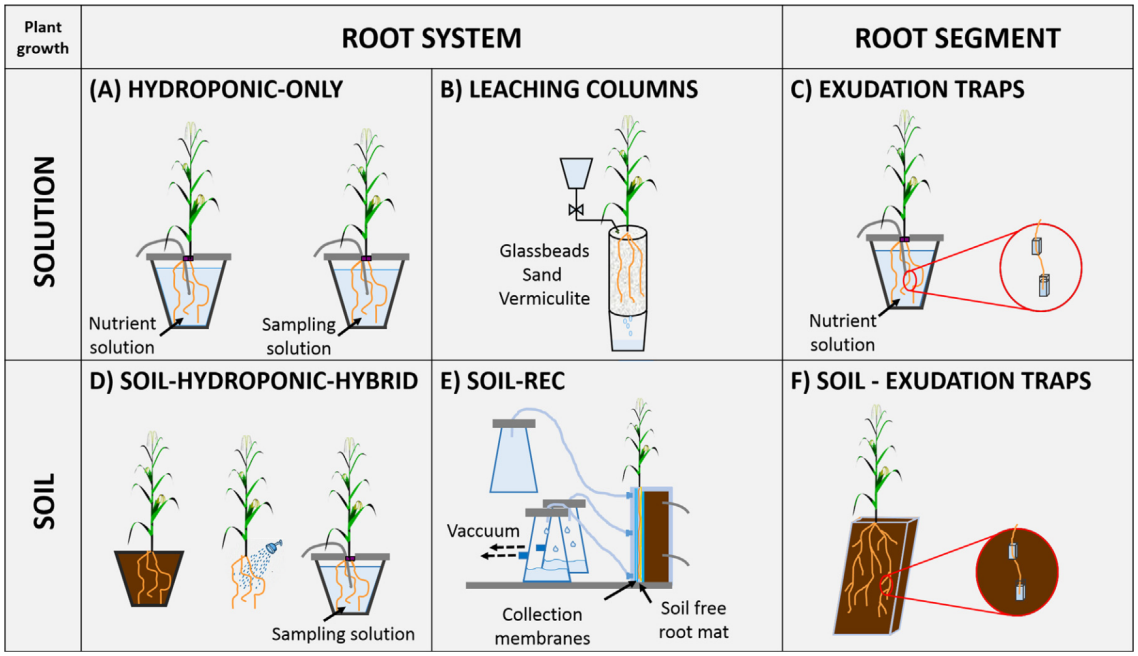

Figure 1.2: Summary of the different approaches for sampling root exudates (i.e. unaltered by soil matrix interactions and microbial decomposition) from either whole root systems or local root segments. Experimental designs are separated based on the plant growth condition, i.e. nutrient solution or soil. (Figure credit Oburger and Jones [2018])

Focusing on approaches that operate under realistic soil conditions is necessary to study root plastic responses, but adds complexity due to the physical inaccessibility of roots and the heterogeneity of soils. However, the most common spatially explicit and quantitative approaches to study root exchanges correspond to hydroponics or semi-hydroponics systems, following either partial [Phillips et al., 2008] or complete excavation [Williams et al., 2021] of the root system, which have certainly introduced biases in the identification of the key determinants and spatial locations of root exchange plasticity. Such simplification of root system environment

enables easy access to the root system, e.g. for ^{15}N short-term labeling followed by immediate segment excision [Lazof et al., 1992], nitrate and ammonium ion-selective micro-electrode measurements [Henriksen et al., 1992, Taylor and Bloom, 1998, Zhong et al., 2014], cuvette [Phillips et al., 2008], or zonal enclosing with local concentrations monitoring [Sorgonà et al., 2011, York et al., 2016]. To reconcile the biological validity of soil-based growth conditions and the accessibility provided by hydroponic systems, adaptations to soil-based growth devices had to be performed [Yee et al., 2021]. Split root devices, with controlled aperture between separated soil volumes, enable to choose only a subset of the root system. It allows for instance to study local N acquisition and translocation for targeted labeling [Ruffel et al., 2008, Veerman et al., 2018]. However, such flux measurement is destructive, and the portion of the root system selected for sampling is not visible and only known afterwards during excavation. To focus on single root axis and follow a segment whose apex position can progress of several cm a day, a visualization of the RSA to guide the choice of sampling location is essential. In soil conditions, common approaches include rhizotrons, buried root windows, and Magnetic Resonance Imaging (MRI).

Most rhizodeposition assessment studies are also based on $^{13}CO_2$, stem-feeding pulse, or continuous labeling strategies, which can only capture the **net** resulting rhizodeposition at sampling date, after soil respiration of these easily assimilated rhizodeposits. So, on top of variable rhizodeposition levels and composition regulated by local soil and root status, adds the variable composition and activity of rhizosphere microbial communities at the time of release, leading to contrasted rhizodeposits persistence in the soil despite similar **gross** rhizodeposition levels [Oburger and Jones, 2018]. Not only does this affect observations, but also the outcomes of rhizodeposition on potential sequestration of rhizodeposits in stable SOC pools and nutrient mineralization through the rhizosphere priming effect[Pausch et al., 2024].

Accessing roots locally in soil

Rhizotrons constrain the root system between two planes within a small volume. Planes use transparent material, e.g. glass or polycarbonate, to enable a visualization over time of the faces along which some root axes are in front of the soil and therefore visible. To maximize the proportion of the RSA that can be visible, imaged, and phenotyped over time, rhizotrons are usually slightly inclined to take advantage of roots gravitropism concentrating most roots on the lower face of the rhizotron [Bontpart et al., 2020]. Some rhizotron setups also use a fiber cloth, e.g. fine mesh nylon, to separate the root system from the soil, enabling the soil solution to go through while ensuring a complete visualization of the RSA [Oburger et al., 2013, Tixier et al., 2025]. The capture of RSA images over time is then used to retrace the age of sampled root segments and their positioning in the root system topology.

Field buried root windows also use a transparent planar materials buried under crop stands to visualize portions of several root systems over time under realistic climatic conditions and plant density, without constraining the RSA, but to the expanse root plant and axis traceability [Vetterlein et al., 2021]. These devices also enable the opening and closure of these transparent faces to non-destructively access targeted root segments and assess their current root-soil exchange levels.

Likewise, MRI can be used in pot experiments to visualize the root system without constraining the soil volume in 2D, guiding the insertion of thin sampling devices such as microdialysis heads [Brackin et al., 2017]. However this constrains the range of *in situ* sampling techniques that can be applied because roots still remain inaccessible for manual operations and no preparation step are possible, such as enclosing the targeted root to prevent an immediate degradation of rhizodeposits by soil microorganisms.

Sampling approaches at root segment scale

Several techniques have been developed to estimate rhizodeposition and uptake fluxes once a targeted portions of a single root axis in contact with soil, a root segment, can be accessed locally. Most soil-based methods aim at characterizing variations in rhizosphere composition and concentrations to estimate flux differences along roots.

A first example for rhizodeposition sampling is the use of absorbing patches placed against targeted root segments and associated soil, non destructively. These patches are left in place for few hours, then removed for chemical analysis, e.g. GC-MS for profiling and possible quantification [Neumann et al., 2014]. Example materials are glass filters, nylon, cellulose nitrate, agar or resins pressed on specific root segments to capture localized exudation [Oburger and Jones, 2018, Akatsuki and Makita, 2020, Tixier et al., 2025, Bohm et al., 2025]. Other methods focus on mapping the gradients along few centimeters of root and in associated soil by the apposition of membranes and Diffusive Gradient Thing films (DGT) subsequently analyzed by laser desorption/ionization and mass spectrometer imaging [Tiziani et al., 2021, Liu et al., 2024, Veličković et al., 2024]. Micro-suction devices have also been used as a targeted location sampling [Dessureault-Rompré et al., 2006], but caution was advised as it was associated with significant soil solution volume removal during sampling [Oburger and Jones, 2018]. To sample N uptake heterogeneity along roots growing in soil, microdialysis probes, ion-selective sensors and rhizons have been used to collect and analyze soil solution surrounding the root region [Dessureault-Rompré et al., 2006, Brackin et al., 2017, Capstaff et al., 2021].

These approaches are useful to compare rhizosphere concentrations and relate observed heterogeneities along roots to potential effects of increased root-shoot exchanges. However, they suffer from quantification limitations. First, they perform a surface sampling capturing only a portion of root segment's exchanges in the case of exudates, without enclosing roots temporary from the soil. Microbial processes, such as exudate degradation or N mineralization, immediately superimpose root fluxes, leading to potential misinterpretations from concentrations evolutions and detected compounds [Kuijken et al., 2015, Shabtai et al., 2024, Williams et al., 2021]. Second, rhizodeposits are sampled in a small spatial and temporal frame (few millimeters of root length and few hours), which corresponds to small amounts which are difficult to quantify precisely with standard method. Third, the complete opening of rhizotron and soil windows are often destructive for soil structure. While these studies followed the dynamic growth of the RSA over time, estimation of root-soil exchanges is performed destructively at the end of the experiment [Oburger and Jones, 2018]. Finally, since comparison to standard samples is necessary to quantify

each rhizodeposited compound precisely, unexpected compounds might suffer from precision biases in untargeted analysis approaches, hampering a reliable quantification of total C-N rhizodeposition of the considered root segment [Ritter et al., 2025, Tsai et al., 2025].

Complementary measurements to elucidate rhizodeposition variability

Complementary destructive measurements are often performed to better understand the determinants of observed root-soil exchanges variability. A first step is normalization of measured fluxes to enable comparison between sampled root segments. Destructive aliquots corresponding to sampled locations are therefore necessary to normalize fluxes per root segment length, surface area, fresh or dry weight. No normalization consensus is currently found in the literature which limits comparison between studies [Oburger and Jones, 2018]. In the case of P uptake and exudation Hu et al. [2014] compared measured fluxes to aerenchyma proportions, obtained sampled from excised and cross sectioned root aliquots. Even though such approach could not be found for the measurement of C or N exchanges, measuring local anatomical properties would provide insights in the role of anatomical root exchange surface and volume. Another determinant suggested in the literature is the root-soil concentration gradient of C-N metabolites that would drive exudation [Nguyen, 2009]. While most above-mentioned approaches focus on non destructive measurement of rhizosphere composition, complementary measurements of CN metabolite concentrations have been performed to estimate root-soil gradients and confirmed it to be a key driver for exudation [Peñaloza et al., 2002]. Example methods are HPLC, GC-MS and LC-MS analyses of root aliquots extracts [Peñaloza et al., 2002, Ćavar Zeljković et al., 2024, Loo et al., 2024]. More recently, cryosections of root and adhering soil were analyzed with laser desorption ionization coupled with mass spectrometer to precisely map the gradient around root segments [Lohse et al., 2021].

Aside RSA imaging over time to reposition sampling points, a precise description of local abiotic conditions perceived by root segments and shoot organs is essential to contextualize sampling events, ensure experiment comparison and replicability. For example, local temperature and soil moisture perceived by organs are critical to estimate root segment thermal age and activity at sampling [Both et al., 2015, Lynch et al., 2021]. Planar optode foils measuring of pH, CO_2 and O_2 dynamics are also relevant to link C-N flux and concentration measurements to consequences on overall soil microbial activity [Blossfeld et al., 2013, Lenzewski et al., 2018, Holz et al., 2020].

Intermediate conclusion: Various experimental approaches have been proposed and tested to characterize the net or gross rhizodeposition rates and N uptake rates. Some are able to estimate C&N root-soil exchanges at the scale of the whole plant, while others have attempted to measure them locally for a restricted portion of the root system. Very few studies have tried to measure both types of flows simultaneously. Each method has its own limitation, and no standardized method currently allows to precisely monitor the rhizodeposition and N uptake rates along the roots in a realistic, non-sterile soil environment. For a better quantification and mechanistic understanding of the interactions between these processes at a local scale, modeling approaches may represent an interesting alternative to experimental approaches.

However, modeling approaches have their own limitations.

1.2.4 Simulating root-soil C&N exchanges at different scales: opportunities and limits

Several types of numeric modeling can be considered for investigating how root-soil C&N exchanges evolve over time or space at different scales, which can be roughly divided into **data-driven statistical models, land surface models, crop models** and **functional-structural plant models**, as detailed below. Given the lack of empirical data required for assessing the precise evolution of rhizodeposition and N uptake, statistical models will not be examined here.

Land surface and crop models approach on root-soil exchanges plasticity

Process-based models of plant – soil functioning now exist along a hierarchy of spatial and organizational scales, from gene and cell to organ, whole plant, field, and regional-to-global land-surface models. At the coarsest scale, land-surface and ecosystem models embedded in Earth system models represent agricultural vegetation as grid cells exchanging water, energy and C – N with the atmosphere and hydrosphere, whereas field-scale crop models focus on stand development, management and yield responses to climate and soil conditions. At finer scales, whole-plant and organ-level structural–functional models explicitly resolve 3D plant architecture and local root – soil interactions. This multiscale model continuum, schematized for crop systems by Peng et al. [2020], motivates a comparison of how different model families represent root C inputs, rhizodeposition, N uptake and root water uptake.

Ecological/land surface models (e.g., *ORCHIDEE-CNP*) mechanistically couple soil CN biogeochemistry with plant nutrient uptake at ecosystem scale but do not resolve where along roots carbon is released, treating belowground C inputs at bulk pool resolution rather than as spatially explicit rhizosphere processes [Sun et al., 2021]. Microbial explicit SOC frameworks typically take root exudates as labile C inputs to grid/pool models to drive microbial activity and SOM transformations, without representing 3D rhizosphere geometry [Chandel et al., 2023]. Field scale crop models (e.g. *DSSAT, APSIM, STICS*), useful for their predictive value of agronomic variables such as yield, compute water uptake per soil layer as a function of root length density and available water, with cross model comparisons showing methodological diversity but a shared 1D layered sink formulation [Camargo and Kemanian, 2016]. In these models, N uptake is generally based on algorithms of potential demand versus available supply, and then depth partitioned by root length density. Explicit rhizodeposition is most often not represented explicitly, the only input of C from roots being root decay [Beaudoin et al., 2023]. Zhu et al. [2017] introduced more mechanistic plant – microbe N competition in land-surface models to simulate the effects of N nutrition on C allocation, but without accounting for 3D root architecture to compute local interaction with soil. Consequently, because this model family lacks a mechanistic representation of CN processes in a 3D RSA and rhizosphere structure, they are not suitable to identify multiscale determinants of CN root – soil exchange plasticity, as highlighted by reviews on fine rhizosphere

processes integration at field and land scale [Schnepf et al., 2022].

Functional-Structural Plant Models mechanistic representation of root-soil fluxes

Functional-Structural Plant Models (FSPM) have been extensively used to study the relationship between plants architecture and local organs resources acquisition, metabolism and growth in an heterogeneous environment [Louarn and Song, 2020, Schäfer et al., 2022]. In particular, RSA growth models coupled with rhizodeposition, nutrient acquisition models are promising tools to integrate C/N interactions and predict CN fluxes along roots.

Across 3D FSPMs that explicitly couple rhizodeposition to an evolving root system architecture, Schnepf et al. [2012] was the first FSPM linking a growing RSA with a prescribed citrate exudation rate per unit of root length to a soil diffusion – reaction model, showing that tip proximal exudation and root segment age shift P uptake at whole root system scale. Landl et al. [2021] then extended this approach by introducing a constant mucilage production term per unit of root length, quantifying hotspot volumes and durations and demonstrating sensitivity to architectural features such as tip density, branching and release location. The *CPlantBox* platform was then published as a coupled and 3D soil-root-shoot framework with explicit water-carbon flows, and included a rhizosphere – soil C model, enabling to simulate the integration of spatially explicit prescribed rates of citrate and mucilage to SOC [Giraud et al., 2023, 2025, Sırcan et al., 2025]. However this approach did not represent the local root metabolism and metabolite concentrations that regulate local growth, rhizodeposition and N uptake, which prevents the study of rhizodeposition plasticity to heterogeneous soil conditions. In parallel, general 3D soil – plant transport frameworks that accept root surface release boundary conditions were developed: Fang et al. [2019] integrated variably saturated flow with multi-component reactive transport and root uptake/release around realistic RSAs. Mai et al. [2019] introduced a continuum multiscale scheme that resolves steep rhizosphere gradients for every root segment while keeping whole domain costs tractable, both directly applicable to exudation scenarios. Recently, the *RhizoDep* model [Rees et al., 2025] was used to simulate carbon allocation to exudates, mucilage and sloughed cells along individual segments of the RSA, as components of a C-driven metabolism and growth in each segment. It reproduced ^{14}C pulse labeling dynamics observed in field, and evidenced that exudation dominates total rhizodeposition with near-tip hotspots modulated by apoplastic barriers and concentration gradients along root axes. Overall, these models represent explicitly the variations rhizodeposition within a 3D root system architecture, with different levels of complexity between prescribed rhizodeposition rates and an explicit regulation by C metabolism and growth. However, all existing rhizodeposition FSPMs are limited to carbon, for both root physiology and SOC dynamics, and to date no root FSPM accounts for C-N multiscale interactions linking local CN rhizodeposition, N uptake and shoot C&N functioning.

Indeed, root FSPMs focusing on the ecophysiological determinants of N acquisition and allocation remain separated from C rhizodeposition models. Early 3D FSPMs introduced explicit 3D RSA mainly to compute soil resource capture, typi-

cally formulating NW uptake as an advection-diffusion problem into a soil-root hydraulic continuum [Dunbabin et al., 2002, Javaux et al., 2008]. The hydraulic-tree water uptake model [Doussan et al., 1998] resolved axial and radial conductances along every segment and inspired subsequent models accounting for water and solute uptake [Bauget et al., 2023]. N uptake models often use root segments cylindrical external surface as the exchange surface, although multicellular FSPMs that make anatomical boundaries explicit now enable to link anatomical traits to transport function [Heymans et al., 2020, Sidhu et al., 2023]. Finally, generic frameworks such as OpenSimRoot couple 3D RSA to soil N&W solvers, and are used to analyze the effects of anatomical and architectural root trait on N uptake heterogeneity and significance in root system balance [Postma et al., 2017, Schäfer et al., 2022, Lynch et al., 2024].

A common challenge for these C- or N-specific root FSPMs is that they rely on complex measurements, i.e. spatial and temporal parametrization and input data [Wang et al., 2020]. Architectural-anatomical traits, heterogeneity of processes kinetic properties along roots, local soil boundary conditions or root-shoot allocations are all examples of challenging, sometimes inaccessible measurements which limit the quantitative validation of these models and restricts the simulation times to avoid unrealistic results [Meunier et al., 2017, Koch et al., 2019, Wang et al., 2020]. Root-shoot CN interactions in particular are thought to strongly interact with local root-soil exchanges and tightly coordinate shoot and root growth, while root FSPMs often rely on input data at the root-shoot junction without any feedback of root system's functioning on the shoot [Rees et al., 2025]. Existing FSPMs such as *CN-Wheat* [Barillot et al., 2016, Gauthier et al., 2020] introduced mechanistic CN interactions between a root compartment and each architectured shoot organs. However it represents roots as a homogeneous compartment, prohibiting its use to study local root plasticity. On the other side, CPlantBox and OpenSimRoot have approached root-shoot coordination with a whole plant explicit representation of C exchanges [Giraud et al., 2025, Punyasu et al., 2025], but without introducing plant N cycle and its impact on both root-shoot and root-soil exchanges. Similarly, recent models of soil biochemistry introduced local interactions between C&N cycles, but they have not been coupled to 3D root FSPMs [Wang et al., 2022, Kyker-Snowman et al., 2020].

Up to now, no model exists that would allow one to simulate, within a single coherent framework, (i) a 3D root system architecture growth driven by (ii) a spatially explicit C&N metabolism and transport especially regulating rhizodeposition variations along roots, and (iii) the C&N allocations linking local root functioning to shoot metabolism and growth across an entire cropping cycle. Building blocks simulating different facets of these C&N interactions already exist, but they have been developed in isolation by specialized communities focusing either on plant or soil processes, on shoot or root ecophysiology, on C or N resources, and on morphological or metabolic traits. As a result, the multiscale regulations linking local rhizodeposition and N uptake plasticity to whole-plant C – N balance and soil C – N dynamics currently remain out of reach. Multidisciplinary initiatives have started to bridge these gaps [Passot et al., 2019, Saint Cast et al., 2022, Schnepf et al., 2023], but they have not yet produced an operational framework that unifies these

components. This missing integrative model is precisely what motivates the model coupling and design strategies of this thesis.

To justify and structure such integrative developments, it is first necessary to examine how model coupling is currently practiced in FSPMs and neighboring communities, and which concepts from crop, land-surface and climate modeling can guide the construction of a multiscale C – N framework.

Model coupling in FSPMs and neighboring communities: current practices to study multiscale regulation patterns

Coupling practices between several models developed and validated independently are contrasted among plant modeling communities. These practices are especially not standardized in the FSPM community which could benefit from well established concepts in crop, land-surface and climate modeling fields.

Within the FSPM community, architectured plants are stored and exchanged as graphs with several intricate scales (local tissue, organ, axis, plant), which de facto creates a common ground for variable exchange between coupled models. Main standardized representations of the plant architecture are the Multiscale Tree Graph (MTG) formalism [Pradal and Godin, 2020], L-systems strings [Boudon et al., 2012, Hemmerling et al., 2008] and the Root System Markup Language (RSML) for root architectures [Lobet et al., 2015], all with available conversion tools between them and cross language bindings. MTG and L-system ecosystems (OpenAlea, vlab/LStudio, GroIMP/XL) are widely used for crop and tree FSPMs, while RSML has become the standard format for exchanging root architectures between phenotyping analysis and simulation tools [Pradal et al., 2015, Hemmerling et al., 2013].

Across several modeling fields, complex systems are represented by an assembly of *components*, as in the OpenAlea FSPM platform, the Crop2ML crop-model framework [Midingoyi et al., 2021] or the Earth System Modeling Framework (ESMF, Keller et al. [2014]). A component encompasses a coherent set of scientific knowledge, processes and equations, that operate on a shared data structure. Each component exposes inputs (parameters, initialization, data forcing), and outputs (simulated variables) that are exchanged on the data structure. Based on components documentation of core principles, validity hypotheses and exchanged variables definition, unit and stoichiometry, several components can be coupled through the shared data structure by linking their inputs and outputs. Under such practices, each FSPM would therefore be composed by coupled components, and such a composite structure would ease cross FSPM coupling, components reusability and intercomparisons. However, the adoption of the principles remains limited in the FSPM community and this exposes several challenges that have restrained the emergence of models accounting for CN multiscale interactions in the soil-root-shoot continuum.

The first challenge is that many FSPMs are not yet structured as components: implementations often superimpose architecture evolution, physiology, numerics and input/output management, which hinders reuse and coupling. Clear guidelines for (re)factoring existing or new FSPMs into components are scarce in the literature [Henke et al., 2016]. Future recommendations could be inspired from crop-model, earth system and atmospheric chemistry communities which have explicitly designed components to be swappable and reusable, with a clear definition of templates to

produce a platform-compliant component [Holzworth et al., 2018, Keller et al., 2014].

Semantic contract definition between inputs and outputs is not straightforward in the FSPM community. Taking the C/N root-shoot coupling example, vocabulary, metabolite discretization, common units and considered time scale differs between shoot and root modeling communities [Du et al., 2018, Freschet et al., 2021]. While crop models use mature variable dictionaries and semantic mapping to couple weather, plant, soil and management components [White et al., 2013, Midingoyi, 2020], straightforward transposition to FSPM is not possible because multiscale states and fluxes coupling require finer semantics than plot scale variables. Still, even if light-shoot, shoot-root, root-soil, and cross-nutrient metabolic coupling require dedicated approaches, these four coupling points are common to all soil-plant-atmosphere FSPM frameworks. Several studies have separately defined clear semantic and variable mapping for each coupling typology [Barillot et al., 2019, Giraud et al., 2025, Lobet et al., 2015], and unifying these practices would contribute to progressively build reusable and community-wide FSPM coupling frameworks.

Mapped component networks then have to be orchestrated by a common language. In the crop modeling community, Crop2ML introduces an orchestration language and automatic model translations to facilitate coupling. However, FSPM platforms are often language specific, for example with OpenAlea using Python as a common glue language for models of computation [Pradal et al., 2015], which simplifies new components prototyping but restricts the coupling with components developed in other languages support, considering the time-consuming task of developing a Python binding for each programming language. Recent generalist tools like yggdrasil [Lang, 2019] have emerged to ease cross language coupling and could be applied to FSPM platforms. Beyond language issues to wire the component network, time integration strategies (continuous vs. iterative, sub-stepping vs. simultaneous resolution) strongly affect results. Collaborative benchmarks of coupled root – soil models have documented divergences that arise solely from exchange timing and coupling tightness, underscoring the need for orchestrators that allow to test alternative run sequences on the same component network [Lang, 2019, Schnepf et al., 2023]. Besides plant-centered coupling, interactions between FSPMs and 3D environment models is a central aspect to study the effect of organ scale CN processes at stand and ecosystem level, where several plants interact via shared 3D soil and atmospheric conditions. Even though successful examples of soil-plant-atmosphere FSPMs exist, such as the *DuMux-CPlantBox-PiafMunch* coupling [Giraud et al., 2025], there is still no standardized way for FSPM graph data structures to exchange variables with 3D environment models, which also encourages the structuration of environment models as components.

Among the FSPMs reviewed above, **the potential, but non-trivial coupling between *CN-Wheat* and *RhizoDep* is particularly noteworthy**, as both models regulate organ processes by local metabolite concentrations while describing complementary parts of the plant.

CN-Wheat and *RhizoDep*: a coupling opportunity for two existing physiological models regulating processes by metabolite concentrations

The *CN-Wheat* model [Barillot et al., 2016, Gauthier et al., 2020] simulates the acquisition and allocation of carbon and nitrogen resources at the plant scale as an emergent property of the interactions between the functioning of each organ and its microclimate. The model was calibrated for wheat and accounts for the 3D architecture of every shoot organs (laminae, sheaths, internodes and leaf growth zones), while the root system is represented by a single non-spatialized compartment. The dynamic representation of the above-ground architecture is based on the *ADEL-Wheat* model [Fournier et al., 2003], and the light distribution within the 3D canopy is calculated with a radiative model using a projective method of [Chelle et al., 1998] (Fig. 1.3).

The main biological processes involved in the primary C and N metabolism are described at the organ level and are governed by local metabolite concentrations and local environmental conditions (light, temperature, CO_2, air humidity, wind speed, soil N content). These biological processes include leaf photosynthesis, respiration and transpiration, root N uptake, the growth of leaves and internodes in mass and dimensions, and the growth of roots in mass, senescence, and C and N fluxes within the plant (transport, synthesis/degradation) and outside the plant (respiration, C-N exudation).

The model considers different groups of state variables for each organ: their dimensions, structural mass (equivalent to the "immobilized" dry mass mainly in cell wall compounds), concentrations of mobile metabolites, i.e. sucrose, nitrates, amino acids, and of storage metabolites (starch, fructans, proteins). The exchange of metabolites between the organs is assumed to occur through a common pool of sucrose and amino acids, which mimics the role of the phloem. Metabolite dynamics are described by differential equations reflecting the physiological activities occurring in the plant. Metabolite concentrations and the physical environment of each organ regulate the rate of these activities. As such, plant and leaf traits are emergent properties resulting from feedbacks between morphogenesis, local environmental factors, and the source-sink activities described at the organ scale.

The model *RhizoDep* [Rees et al., 2025] simulates how roots grow, respire, and emit rhizodeposits into the soil, based on the distribution of available C within a dynamic 3D root architecture (Fig. 1.4). The model operates at fine spatial and temporal scales, typically simulating root segments of 1-mm with an hourly time step. *RhizoDep* incorporates simplified physiological processes that account for major C transfers within the roots and between roots, soil and atmosphere. Aside from soil temperature, which can affect rates in various ways, the main input variable of the model is the net C transferred from the aerial parts of the plant to the root system. This input is represented as sucrose transported through roots' phloem vessels. A portion of this sucrose is then unloaded and converted into hexose, which serves as the substrate driving key metabolic processes. These include: i) the production of root structural mass, associated with the elongation of roots or root hairs and secondary growth, following growth rules derived from the model *ArchiSimple* [Pagès et al., 2014], ii) root maintenance, iii) sugar immobilization in or remobilization from a reserve pool, and iv) rhizodeposition. No priority is

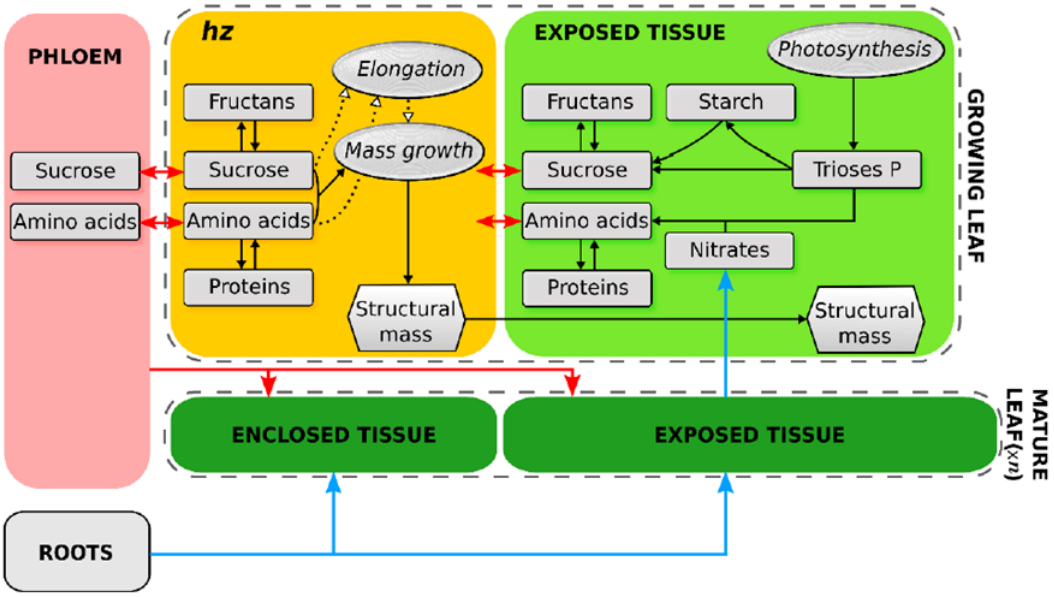

Figure 1.3: Description of the main metabolic pools and botanical compartments of a growing leaf considered in the *CN-Wheat* model. The leaf structural mass is described with hexagons and metabolite concentrations with rectangles. Leaf elongation and mass growth processes (ovals) take place in the hidden growth zone (hz) and are regulated by local metabolite concentrations (dotted arrows). Only exposed tissues are photosynthetic. Fluxes of sucrose and amino acids between compartments, and imports of nitrates and amino acids from the root compartment, are represented by arrows. (Figure credit, Gauthier et al. [2020])

assigned to any of these processes in terms of hexose consumption. Rhizodeposition processes include the net exudation of hexose or sucrose (difference between gross exudation by diffusion from root symplasm and reuptake of sugars from the soil by the roots), the secretion of mucilage at root tips and the release of border cells from root caps. Additionally, a simple representation of the fate of rhizodeposits outside the roots has been implemented, though such processes are expected to be managed by a dedicated soil model in the future. *RhizoDep* focuses on C dynamics within the root-soil system, and as such does not simulate the aerial parts of the plant, C allocation from shoots to roots, or the dynamics of nitrogen and water.

Both *CN-Wheat* and *RhizoDep* are implemented in the *OpenAlea* platform [Pradal et al., 2008, 2015] in the form of a set of sub-models communicating via a central data structure, the Multi-scale Tree Graph (MTG)[Fournier et al., 2010, Albasha et al., 2019, Barillot et al., 2019, Pradal and Godin, 2020, Reyes et al., 2025]. Considering how both models share the same ecophysiological vision by simulating how the dynamics of key metabolites within the plant interact with the evolution of the structure of the plant, and how these models are complementary in their representation of the shoot system and the root system (Table 1.1), coupling *CN-Wheat* and *RhizoDep* models could offer a new opportunity to explore the mechanisms by which plant adapts to its environment, and in particular how it regulates its levels of rhizodeposition. However, **such a coupling would require several adaptations and additions to the two models**, which does not make the coupling straightforward. A first difficulty lies in the current structure of *CN-Wheat*, which gathers

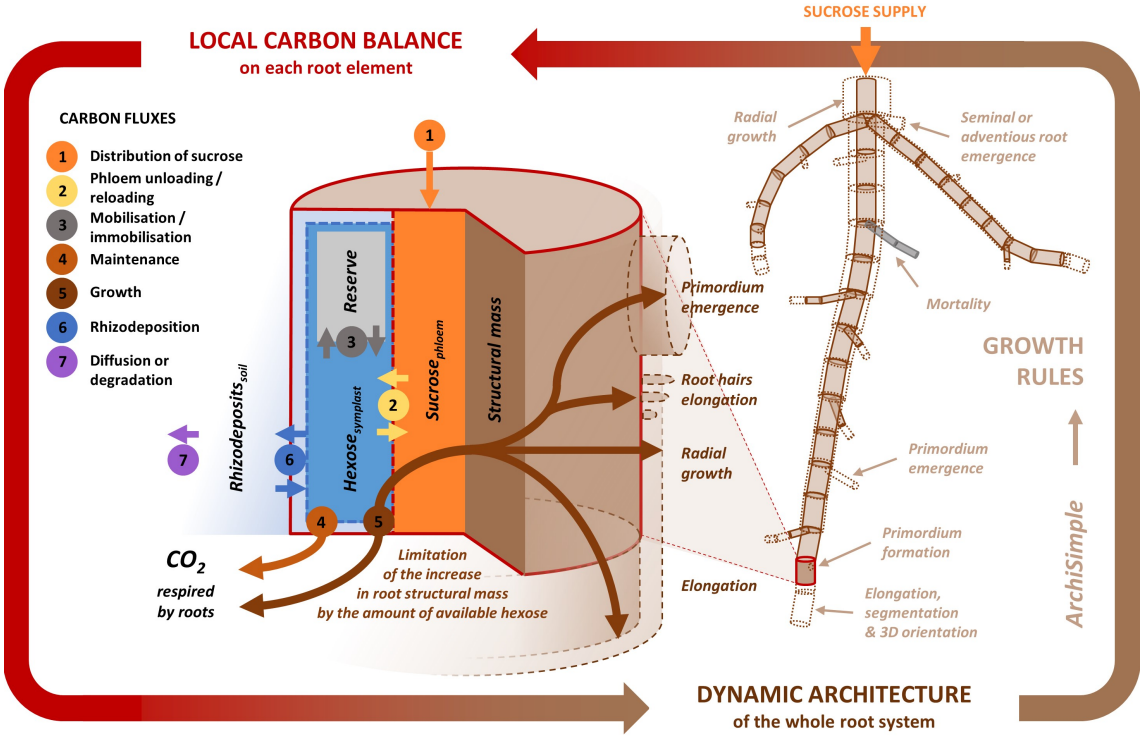

Figure 1.4: Overview of the *RhizoDep* model [Rees et al., 2025]. Photoassimilated C enters the root system as sucrose (model input), which is then distributed among each root element (1) and can be converted into hexose (2). Hexose may be stored in a reserve pool (3), used for maintenance (4), or consumed for growth, contributing to structural mass production - either through longitudinal growth (for an apex) or radial growth (for a segment), or through the emergence of new lateral roots or root hairs (5). Once exuded outside the root, sugars can be reabsorbed by the root (6) or lost from the root-soil interface due to microbial degradation, sorption, or diffusion (7). Similarly, other rhizodeposits (e.g., mucilage, sloughed cells) can accumulate at the root-soil interface or be lost. The local C balance within each root element ultimately constrains potential root architecture development, as defined by growth rules adapted from the *ArchiSimple* model [Pagès et al., 2014]. (Figure credit, Rees et al. [2025])

all plant organs into a single system of differential equations, including a homogeneous root compartment. Replacing this unique compartment with *RhizoDep* would require splitting *CN-Wheat* into distinct shoot and root equation systems, and this refactoring would itself need to be checked to ensure that it does not compromise the original validation of *CN-Wheat* before any coupling with *RhizoDep*. In addition, if the objective is to study the interactions between local rhizodeposition, mineral N uptake and shoot C&N activity, the root model coupled to *CN-Wheat* must simulate mineral N uptake, its regulation by photosynthate allocation from the shoot and the subsequent export of N to the shoot. Since *RhizoDep* currently accounts only for C processes and C balance, the design of a new root N FSPM appears essential to close the loop of plant C – N allocation and to enable such a coupling. Moreover, several authors have suggested a link between tiller or leaf emergence and nodal root emergence [Klepper et al., 1984, NGUYEN, 2023], a synchronization that can only be represented in a fully architectured plant model and therefore calls for further developments in both models. Finally, beyond these conceptual issues and

the additional processes required, the practical methodology for coupling the two models remains unclear: how to exchange variables at the shoot – root junction, how to introduce N processes and metabolites into the existing root carbon model, and in which order shoot and root modules should be executed in the simulation loop. All these developments remain necessary before a coupling between *CN-Wheat* and *RhizoDep* can be made operational.

Table 1.1: Summary of a possible coupling strategy between *CN-Wheat* and *RhizoDep*: opportunities, common characteristics facilitating the coupling task, and remaining challenges to overcome

Model name	Opportunities & objectives of the coupling	Facilitating similarities	Remaining challenges
CN-Wheat	• Improving the representation of heterogeneous root processes and their regulation in a growing root system architecture, including rhizodeposition, N uptake and their footprint in plant C&N balance	• Same vision of processes regulated at organ- and tissue-scale by massic concentrations, easing the definition of a shoot-root concentration gradient for C allocation • Same vision of explicit architecture for both shoot and roots, enabling to account for all environmental heterogeneities to study the plasticity of rhizodeposition • Same discretization of metabolites, e.g. with phloem C represented as sucrose • Same hourly time-step • Same language and MTG data structure	• Splitting *CN-Wheat* equation system into shoot + root systems is the first step to prepare the replacement of *CN-Wheat's* root model with *RhizoDep*. Does the splitting compromise the validation of the original *CN-Wheat*? • Can the shoot-root allocations still be handled by *CN-Wheat* when coupling to an architectured root model?
RhizoDep	• Reducing uncertainties for the complex estimation of C inputs to the root system with realistic variations throughout the cropping cycle • Reposition rhizodeposition heterogeneity and its determinants in whole-plant C&N balance		• No model of N uptake, N cycling in root, or mineral N and amino acids export to the shoot, hampering the coupling as no feedback of C allocation to roots is simulated through N uptake and N export to shoot • No amino acids in root phloem • Coordination rules between the emission of nodal roots and shoot development remain to be introduced

Intermediate conclusion: Although rhizodeposition has often been neglected in widely-used land and crop models, other models, e.g. FSPM, can simulate it, either as a prescribed rate distributed along the roots, or as an emerging property resulting from the evolution of metabolite concentrations. To this date, no model has allowed simulating simultaneously rhizodeposition, N uptake and water uptake along the roots together with shoot and root growth. The coupling of two existing FSPM, CN-Wheat and RhizoDep, has been perceived as a promising starting point, although this coupling is associated with several conceptual and methodological challenges.

1.2.5 Conclusion

Over the past decades, evidence has accumulated that rhizodeposition is highly heterogeneous in space and time. Local rhizodeposition would be mainly regulated by interactions between C&N cycles which impact exuded metabolites root-soil gradient, local tissue anatomy, and day - to - day changes in shoot carbon supply. Yet, the quantitative implications of such conceptual picture are currently unknown and the literature still relies heavily on simplifying assumptions, often treating exudation

as uniform over root system mass, or as a fixed fraction of photoassimilate supply, and on invasive measurements that average over compartments or time windows too coarse to expose the underlying drivers.

Key coupling points between C and N cycles have been suggested in the literature (e.g. local transport and metabolism regulation by C and N availability, C and N acquisition coupling through photosynthesis, co-location of C and N root-soil exchanges by the dynamics of RSA and root tissue anatomy), however their quantitative role in the variability of C&N rhizodeposition and N uptake variability along roots has not yet been proven.

Empirical knowledge about rhizodeposition is limited by its physical inaccessibility in soils. Rhizotrons appear as an interesting tool to image and access a growing RSA non destructively in order to sample rhizodeposits, but current approaches lack quantification value for flux and rather focus on rhizosphere condition sampling.

Root-soil exchanges are part of multiscale interaction loops between C&N cycle, but no existing FSPM model has managed so far to represent C&N flows exchanged within the plant and between plant and soil by taking into account both *local* processes detailed at the scale of the organ or root segment and by integrating them at *plant scale*, while taking into account interactions with a 3D environment. Specific models exist for each of these targeted components but remain isolated. Generic coupling approaches have been developed in others areas of research like crop models but have not yet been fully implemented in the FSPM community.

1.3 Research questions, strategy and organization of this work

My thesis focuses on rhizodeposition and its importance for the functioning of the plant, acknowledging its significant yet variable impact in plant nutritional balance, with limited understanding of its interactions with local root-soil status and shoot-root interactions. **My objective in this thesis is i) to characterize the determinants of spatial and temporal variability of rhizodeposition and N uptake, and ii) to quantify the impact of these local exchanges on plant's carbon and nitrogen balance.**

In this perspective I have considered the following **scientific and methodological questions**:

- What is the variability of rhizodeposition, N uptake, and their sub-processes, along roots and over time?
- How can it be linked to local root metabolic activity, root anatomy, and root architecture?
- What is the impact of these local root C&N processes in plant C&N balance?

On a more methodological point of view, the evaluation of the drivers of rhizodeposition and N uptake variability implies specific strategies:

- How to design a multiscale functional-structural modeling framework of the soil-plant-atmosphere system to investigate the complexity of rhizodeposition determinants? To what extent can it assist researchers in a better understanding of root-soil exchanges plasticity?
- In addition to simulations, are the spatial and temporal variations of rhizodeposition and its drivers measurable experimentally?

These questions were represented in the following conceptual scheme that will be progressively completed throughout this manuscript.

This thesis relies on **five distinct hypotheses**:

- I have assumed that *rhizodeposition it not simply proportional to root system biomass or the allocation of photosynthates from shoot (**H1**).*
- Conversely, when accounting for root-soil exchanges heterogeneity throughout the root system architecture, some studies have suggested that only a small fraction of the root system contributes to the majority of root-soil exchanges, leading to the concept of *active root zones*. I have considered that *such a binary concept is not relevant, as the contribution of a given fraction of the growing root system to rhizodeposition or plant N uptake will significantly vary over time and depending on the environment (**H2**).*
- In such varying conditions, I have also supposed that *the main processes dominating these root-soil exchanges can shift over time, root zones or depending on the soil environment (**H3**)*, e.g. N uptake mediated by water uptake reaching similar levels as transmembranar N uptake.

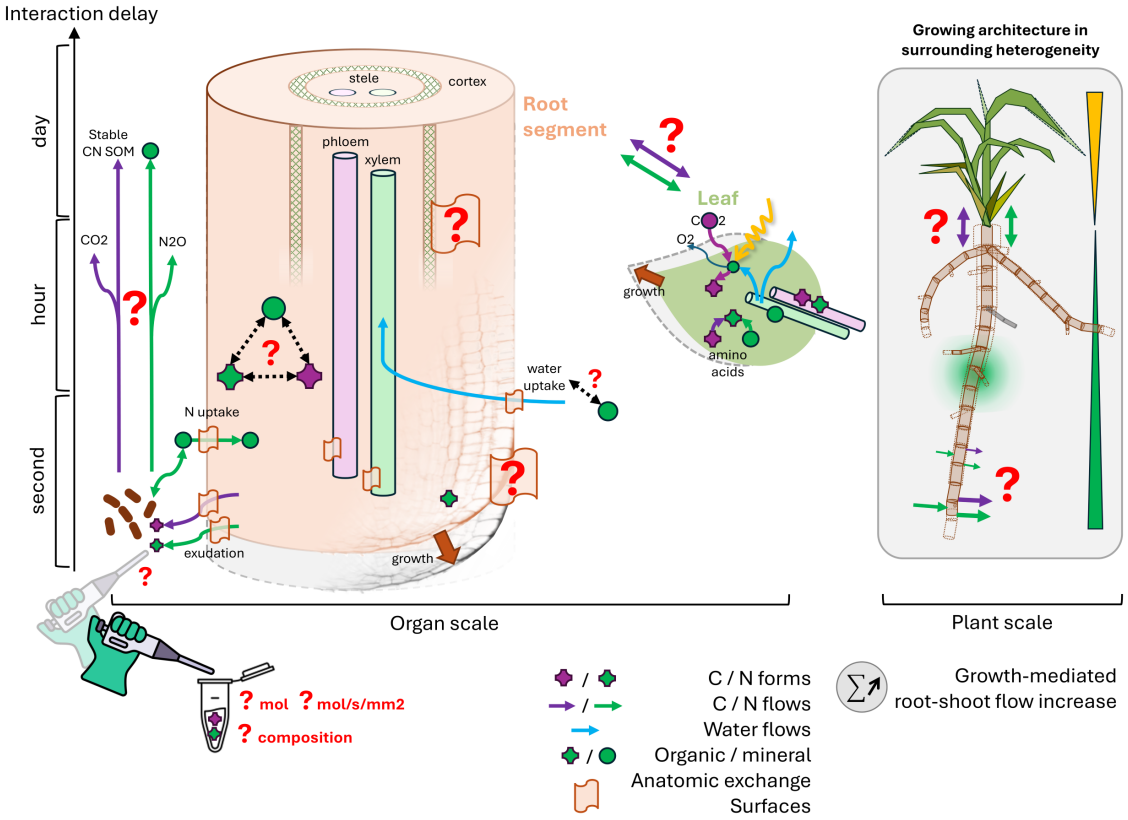

Figure 1.5: Conceptual scheme positioning key unknowns regarding the C&N multiscale interactions from organ to whole plant scale that would impact the variability of rhizodeposition and N uptake along roots, as well as methodological uncertainties regarding the sampling methods to quantify this variability.

- Despite such process diversity, I have also assumed *the heterogeneity of root anatomy and metabolite concentrations in the root system architecture to be a common driver to all root-soil exchanges, co-localizing rhizodeposition and N uptake along roots (**H4**).*
- Alongside these local regulations, I also assumed *plant scale variations in total N uptake and rhizodeposition to be synchronized over time, with photosynthetic activity at the core of their C&N interaction (**H5**).*

During my thesis, I have combined mechanistic modeling and original experiments, using **wheat (*Triticum aestivum*) as a case study**. This species was chosen for its importance in food security as the third annual crop worldwide [FAO, 2025] while being critically impacted by N nutritional stresses, e.g. under climate change, which calls for a better understanding of the physiological bases of N acquisition variability [Martre et al., 2024] . Wheat was also chosen because of the coupling prospects offered by the FSPM *CN-Wheat*, which is specific to this species.

In **Chapter 2**, I introduce the new model *Root-CyNAPS*, a segment-scale N, water and anatomy FSPM. This model was developed to complement the existing FSPM *CN-Wheat* and *RhizoDep*, and aimed at investigating the drivers of heterogeneous N and water uptake along roots and assess the contribution of specific root parts to plant N balance. *Root-CyNAPS* was tested here over short periods on static root system architectures of wheat for different plant ages and environmental conditions to highlight the variability of N uptake and N rhizodeposition.

In **Chapter 3**, I introduce *MetaFSPM*, a toolkit developed to standardize the coupling of existing FSPM, which was necessary to couple the above-mentioned models.

In **Chapter 4**, I introduce *Wheat-BRIDGES*, a new composite model accounting for C, N and water dynamics within a growing plant, in interaction with plant's architecture and anatomy, from organ to stand scale. This model results from the coupling of *CN-Wheat*, *RhizoDep* and *Root-CyNAPS* using the toolkit *MetaFSPM*. *Wheat-BRIDGES* simulations were compared with *CN-Wheat* and used to analyze root-soil exchanges heterogeneity along the roots in the context of the functioning of the whole plant.

In **Chapter 5**, the strategy and the first results from two original wheat growth experiments in rhizotrons are presented. These experiments aimed at providing more accurate parameters to *Wheat-BRIDGES* and at validating some of the assumptions made in the model.

Finaly, **Chapter 6** is dedicated to a general discussion of the results obtained in the different chapters, and presents prospects for using and improving the developed models and methods.

Scientific references are available at the end of this document, followed by additional information and data supporting the different chapters.

Chapter 2

Do specific root zones shape plant net N uptake? Insights from the *Root-CyNAPS* model

2.1 Chapter strategy

This chapter addresses my first thesis objective, i.e. characterizing the spatial variability of net mineral N uptake along roots and over time, its contribution to root system N balance and its key interactions with C cycling and rhizodeposition. It focuses on the following questions:

- *What is the variability of N uptake and its sub-processes along roots and over time?*
- *How can this variability be linked to local root metabolite availability, anatomy and architecture?*

In this context, I focused on the concept of *active root zones* and its relevance with hypotheses **H2**, **H3** and **H4** introduced in Chapter 1:

- **H2**, according to which the contribution of an active fraction of the growing root system to plant N uptake is not constant and pre-determined, but varies over time and with the soil environment;
- **H3** suggesting that the dominant processes underlying net N fluxes (active uptake, water-driven transport, exudation, metabolism) can shift between root zones and scenarios;
- **H4** stating that the heterogeneity of root anatomical features and metabolite concentrations along roots is a common driver of these local exchanges. My approach at these hypotheses during this chapter are repositioned on the conceptual scheme below (Fig. 2.1).

To address these questions, I have developed *Root-CyNAPS*, a segment-scale nitrogen, water and anatomy root FSPM. The model explicitly represents transmembrane N transport, water-driven apoplastic N transport, N metabolism and N exudation in each segment of a 3D root system architecture, with a symplastic compartment and conductive elements whose volumes, exchange surfaces and conductances are provided by an anatomy module. *Root-CyNAPS* was applied to static root system architectures of wheat during short-term hydroponic scenarios, under contrasted plant ages and external nitrate concentrations, in order to quantify how the heterogeneity of net N uptake along roots and its impact on root system N balance respond to various root system development stages and external N availability. This chapter corresponds to the article entitled "*Do specific root zones shape plant net N uptake? Modeling insights from Root-CyNAPS*" , by Tristan Gérault, Christophe Pradal, Romain Barillot, Céline Richard-Molard, Marion Gauthier, Alexandra Jullien, and Frédéric Rees submitted to the *In Silico Plants* journal. The following pages therefore correspond to the submitted PDF file and follow the formatting guidelines of the journal.

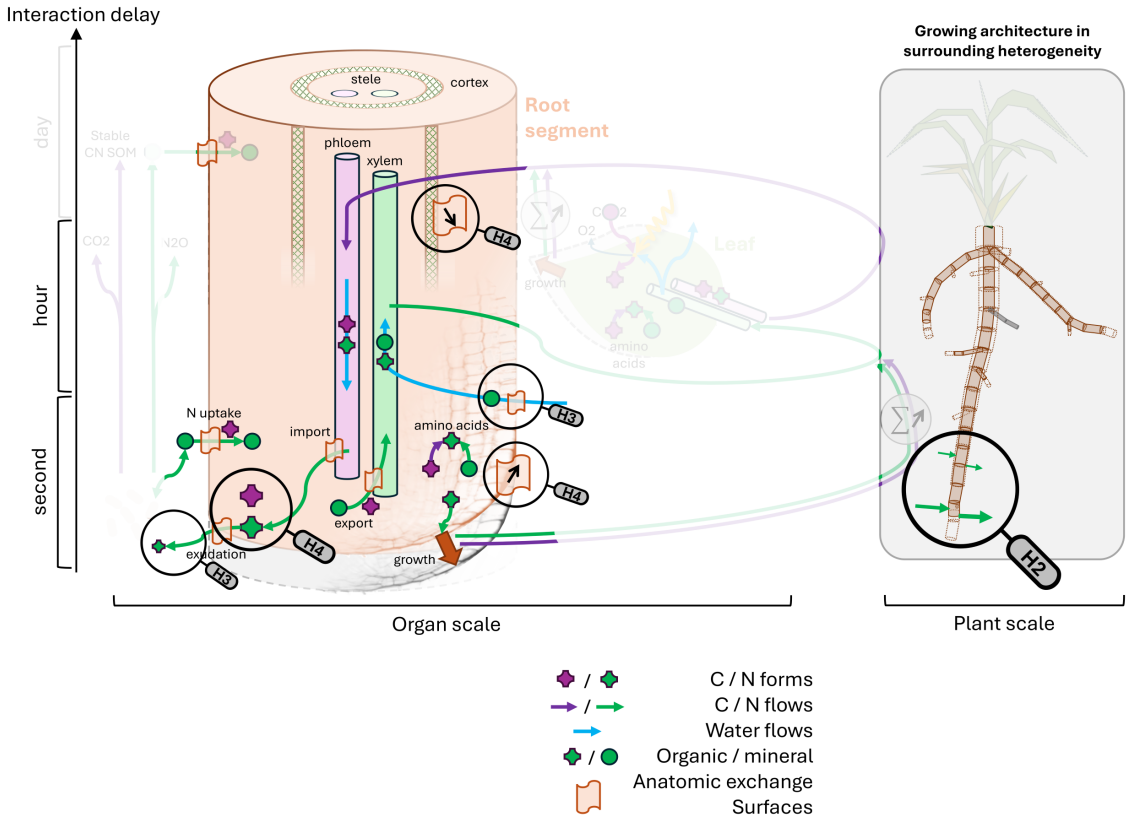

Figure 2.1: Conceptual scheme summarizing the key N processes considered in Chapter 2, with magnifying glasses positioning tested hypotheses.

in silico Plants Vol. , No. , pp. 1–42
doi:

Paper in press

Do specific root zones shape plant net N uptake? Modeling insights from Root-CyNAPS

Tristan Gérault[1,*] Christophe Pradal[2, 3] Romain Barillot[4] Céline Richard-Molard[1] Marion Gauthier[5, 6] Alexandra Jullien[1] Frédéric Rees[1,*]

[1]Université Paris-Saclay, INRAE, AgroParisTech, UMR EcoSys, 91120, Palaiseau, France,[2]CIRAD, UMR AGAP institut and Inria, LIRMM, CNRS, Univ Montpellier, Montpellier, France,[3]AGAP institut, Univ Montpellier,CIRAD, INRAE, Institut Agro, Montpellier, France,[4]INRAE, UR P3F, F-86600, Lusignan, France,[5]IGEPP, INRAE – Institut Agro Rennes-Angers – Université de Rennes, 35650, Le Rheu, France,[6]GEVES, 49370, La Pouëze, France,

*Corresponding authors: frederic.rees@inrae.fr
FOR PUBLISHER ONLY Submitted Date Month Year; Revised Date Month Year; revised version accepted Date Month Year;

ABSTRACT

Net nitrogen (N) uptake results from active and water-mediated N inflows, partly offset by N exudation. These processes exhibit significant variations along root axes, suggesting the existence of specific zones of higher N exchanges. However, the precise location, drivers, and significance of such active root zones in root N budget remain unclear. Here, we identified and characterized *active root zones* using *Root-CyNAPS*, a new functional-structural plant model that simulates the space-time variations in net N uptake, based on the interactions between nitrogen, carbon, and water flows, and root anatomy in each segment of a 3D root system architecture. Our simulations on wheat for various plant ages and external nitrate concentrations revealed two zones of preferential net N uptake: one near the root apices and the other one coinciding with the lateral root initiation zone, both characterized by a net N uptake activity about 10 times higher than adjacent segments. Higher water uptake and N exudation rates were also located next to apices. The contribution of *most active root zones* (defined here by the top 10% of root length) varied between 20% and 80% of plant net N uptake, depending on root environment and age. Our simulations also showed that water-mediated N uptake could represent up to two thirds of gross N uptake, while N losses could offset more than half of it. *Root-CyNAPS* offers coupling opportunities with other functional-structural models to simulate nitrogen, carbon, and water multiscale interactions across the soil-plant-atmosphere continuum.

KEYWORDS: Functional-Structural Plant Model, Water uptake, Root anatomy, Nitrogen exudation, RhizoDep, OpenAlea

© The Author . Published by Oxford University Press. All rights reserved. For permissions, please e-mail: journals.permissions@oup.com

INTRODUCTION

The sustainability of land ecosystem primary production is largely influenced by soil nitrogen (N) availability, water availability, and the ability of the root system to extract these resources. In recent years, research has focused on the identification of architectural and physiological root traits that could sustain and maximize resource uptake from the soil (Holz et al., 2024; Lynch et al., 2024). Rooting depth, root length density, diameter distribution, root-hair abundance, high-affinity N transporters, N-sensing pathways, and symbiotic associations are examples of traits targeted by root breeding research to optimize N acquisition (Odone et al., 2024; Liu et al., 2022; Postma et al., 2014; Saengwilai et al., 2021; Griffiths and York, 2020; Zhu et al., 2016). Yet net root N uptake is multifaceted: it results from the balance between mineral N uptake and N loss. N losses can correspond to the release of organic N (e.g. amino acids, mucilage, and proteins) through rhizodeposition, and the diffusion of mineral N from roots to soil, and have been show to account for 2-71% of plant N budget (Pausch and Kuzyakov, 2018; Wichern et al., 2008; Fustec et al., 2010; Cao et al., 2021). Targeted root traits for improved N acquisition should therefore always be repositioned in the net balance between gross N uptake and N rhizodeposition.

Identifying root traits to sustain levels of net N uptake has become even more critical in the context of climate change, where major crop species face amplified soil resource scarcity and variability over space and time (Zhu et al., 2024; Raij-Hoffman et al., 2024). While facing stiff gradients of nitrogen concentrations and water content in the soil, plants locally adjust the positioning of their roots and the range of resource uptake to thrive in such varying conditions, with significant impacts on root-shoot exchanges and ultimately on the whole-plant budget (Robinson, 1994; Zhou et al., 2022; Ceolin et al., 2025). Mineral N uptake, which involves both active transmembrane transport and passive apoplastic inflow via water uptake, is regulated not only by the local availability of mineral N in the soil but also by the local physiological status of the root, itself linked to the whole-plant nutritional budget. In addition to water uptake from the soil, heterogeneous xylem and phloem sap flows within the root system may interact with symplasmic N concentrations locally and overall root-shoot N allocations (Bollard, 1960; Dodd et al., 2008, 2009; Bauget et al., 2023). This highlights the importance of linking the variability in nitrogen and water flows observed throughout the root system.

The existence of high-activity N uptake zones has been reported, typically near root apices, young lateral or root hair elongation zones (Yoneyama and Kumazawa, 1975; Henriksen et al., 1992; Sorgonà et al., 2011; Zhong et al., 2014). Several overlapping concepts are found in the literature to define preferential exchange zones in the Root System Architecture (RSA) and measure their contribution to plant N budget. It includes *active root length* (Hodge et al., 2009; Bechmann et al., 2014), *active root biomass* (Malagoli and Le Deunff, 2014; Le Deunff et al., 2019), *cortical-senescence-free length* (Schneider et al., 2017), and *hot spots* (Kanno et al., 2016; Canarini et al., 2019). These concepts aim to capture the long-standing observation that a relatively small, physiologically young, or anatomically specialized fraction of the root system performs the majority of root exchanges (Grasmanis and Barley, 1969). We therefore chose to group these concepts under the broader term *most active root zones*. However, each concept uses a different grouping criterion to delineate the *most active root zones*, such as percentages of root mass, length, or flux, as well as categorical variables including root age class, branching order, or tissue integrity. Different root fraction thresholds are also used across studies, and the contribution of these *most active root zones* to total root exchange is often not explicitly reported. According to the review by Hodge et al. (2009), only 10% of total root length would contribute to the *majority* of N uptake, and 30% for water uptake; however, the definition of *majority* remains unclear. In another study, Cruz et al. (1995) found that, in 7 day-old carob seedlings, the first 4 cm from the root tip accounted for approximately 40% of total N uptake. Modeling work by Robinson et al. (1991a) on spring wheat suggests that, for contrasted plant age and soil nitrate concentrations, between 2 to 22% of root length account for the total measured N uptake. Similarly, Le Deunff et al. (2019) estimated that 4 to 7% of the root biomass, mostly fine root apices, was *active* in terms of N uptake in winter oilseed rape, although the contribution of this *active* part over the remaining part of the root system was not specified. Overall, the location, number, and contribution of the *most active root zones*

to plant N budget vary substantially across studies and remain insufficiently quantified. The main reasons for this are that available experimental methods, such as hydroponics, rhizobox, excavation, or *in situ* sampling techniques, are not only labor-intensive with invasive measurement bias, but also provide only partial spatiotemporal snapshots of N uptake variability. (Nguyen et al., 2016; Wacker et al., 2024; Buckley et al., 2020). Both data scarcity and conceptual ambiguity related to root N exchange variability make it difficult to elucidate how and where *most active root zones* arise, and how much these account for in the whole plant N budget.

To address these challenges, modeling offers a suitable integrative approach for gathering existing knowledge on N and water processes, helping to disentangle the determinants of the complex root-soil exchanges responses observed experimentally. Model simulations also inform experimental designs by enabling rapid mechanistic testing of hypotheses through simulation prior to conducting costly experiments aimed at addressing knowledge gaps. Functional-Structural Plant Models (FSPM) have been extensively used to study the local variability of plant growth and functioning in response to local environmental heterogeneity (Louarn and Song, 2020; Schäfer et al., 2022). Early mechanistic modeling work approached root N acquisition as a purely radial soil-to-root diffusion problem (Barber and Cushman, 1981). The first 3D FSPMs added an explicit 3D RSA, which was discretized as root segments for numerical representation, solely to compute soil resource capture, therefore exploring interactions between water and N uptake as a one-dimensional radial problem (Dunbabin et al., 2002). The hydraulic-tree water uptake model (Doussan et al., 1998) resolved axial and radial conductances along every segment and inspired subsequent models accounting for dynamic interactions with soil (Javaux et al., 2008), or accounting for simultaneous water and solute uptake (Bauget et al., 2023). By accounting for the RSA and relationships between root segments, they evidenced that the spatialization of radial and axial exchange flows enables to simulate locations at which water preferentially is taken up, which can shift along the roots depending on external conditions and root system status, and that this dynamic heterogeneity along roots could significantly affect whole-plant uptake balance. To better understand the regulation of these processes at the tissue scale, the model *MECHA* translated complete cross-sectional anatomy into hydraulic maps and emergent conductivities of the root segment (Couvreur et al., 2018). However, the model was designed only for water transport. N uptake models often use root segments cylindrical external surface as the exchange surface, even though models simulating explicitly anatomical boundaries were published (Heymans et al., 2020; Sidhu et al., 2023). Generic frameworks allow 3D RSA to be coupled to soil solvers, such as *OpenSimRoot* (Postma et al., 2017; Schäfer et al., 2022), *CPlantBox* (Schnepf et al., 2018; Giraud et al., 2023, 2025), or models coupling uptake functions with architectural models (Mai et al., 2019; Meunier et al., 2022) . They have been used to map heterogeneous kinetic parameter fields onto roots, e.g. on maize RSA to study N foraging variability (York et al., 2016). However, none of these models include intermediate feedback with local carbon (C) or N metabolism and balance that would regulate N exchanges. The local C and N metabolite concentrations in root tissues, such as sugars, amino acids, nitrate and ammonium, are indeed thought to be critical in modeling approaches for the regulation of local N exchanges (Barillot et al., 2016; Le Deunff et al., 2019). Accounting for feedback loops between local C-N concentrations, N flows and N balance therefore appears necessary to reliably simulate N and water exchanges within an architectured root system, and characterize in particular the nature and importance of *most active root zones*.

In this study, we present *Root-CyNAPS* (Root-Cycling Nitrogen Across Plant Scales), a functional-structural root model that simulates local N uptake, water uptake, and N rhizodeposition, with dynamic interactions between the internal status of the root segment and local soil conditions. To our knowledge, this is the first root FSPM to simultaneously (i) discretize each segment of the RSA into anatomically-defined compartments and exchange surfaces, (ii) simulate a local balance of mineral N and amino acids pools from key N transport and metabolic processes, and (iii) integrate N flows into the whole-plant budget through water-driven flows and axial N advection. After a detailed description of the model, we illustrate a use-case for wheat (*Triticum aestivum*), the third most important annual crop worldwide (FAO, 2025), which is facing critical resource acquisition challenges in the context of climate change, justifying an increased and urgent need to decipher the physiological bases of N acquisition variability (Martre et al.,

2024). The model was parameterized and used on the vegetative phase of spring wheat, by simulating its short-term behavior in a homogeneous nutrient solution. We used these simulations to evaluate the variability in *most active root zones* location and in their actual contribution to the whole plant N uptake. We also hypothesized that depending on plant age or external nitrate concentration, the water-mediated N uptake and/or the exudation of N may approach the magnitude of active transmembrane N uptake into root cells, thereby substantially shaping net N uptake.

ROOT-CYNAPS MODEL DESCRIPTION

The core originality of the model *Root-CyNAPS* is to account for a set of N-related processes regulated by local metabolite concentrations, local soil temperature, local exchange surfaces and local structural mass in a root segment (Fig. 1). The root system architecture is represented by a Multiscale Tree Graph (MTG), where nodes represent root elements of a constant length of few millimeters (segments) or of a shooter length (apices), and edges represent the connection between two nodes, according to root topology.. Hereafter, we define *local* properties as related to this node scale. Variables describing root segments geometry, anatomy, physiological status and processes rates are therefore stored in nodes as node graph properties. We acknowledge that the root segments corresponding to each node do not convey any biological meaning, and are instead used as a way to discretize the root system and compute processes at a local scale. Processes represented within this spatial discretization of the root architecture are N and water uptake, N_2 fixation by nodules and N acquisition by mycorrhiza, N exudation, N local assimilation, and N and water transport along xylem and phloem vessels. The balance of these processes modifies the *local* concentrations of labile N in three distinct compartments of the root segment: 1) parenchyma symplasm, 2) phloem symplasm, and 3) xylem apoplasm. The parenchyma apoplasm is not represented and is supposed to be at equilibrium with the soil solution. The root tissue related to each compartment is not spatialized, but their volume and exchange surface is accounted for in each root element. In each compartment, labile N is divided into a mineral form, accounting for nitrate and ammonium, and an organic form, accounting for total amino acids. Amino acids can in turn contribute to a storage protein pool or to the root segment dry structural mass as structural N.

Processes at the root segment-scale are then scaled up to the entire root system by summing the contribution of individual segments, while also accounting for transport processes between segments to study how N and water root-shoot exchanges build up from these local contributions. *Root-CyNAPS* simulates heterogeneous fluxes across a static 3D root architecture at hourly time-steps, regulated by local root and soil conditions. In *Root-CyNAPS*, root growth is not simulated, but its cost in terms of amino acids consumption is accounted for. Root architecture therefore needs to be provided as an input of the model, along with growth costs and labile hexose concentration profiles in the root system, water potentials and labile N concentrations at the shoot-root interface, and soil N, water, and temperature boundary conditions.

All transport and metabolic processes implemented in *Root-CyNAPS* were selected based on our current understanding of literature. The implementation and underlying hypotheses are detailed below for the main processes considered as critical to N and water exchange variability along roots. The complete set of process rate derivatives and balance equations is provided in Supplementary Tab. S1. In the following, model variables are shown in black, parameters in blue, and input variables (i.e., variables not simulated by our model) in red. All quantities are expressed in SI units and described in Tab. 1 for model variables and Tab. 2 for model parameters. Unless otherwise stated, variables are expressed for a specific segment i at the current time-step t.

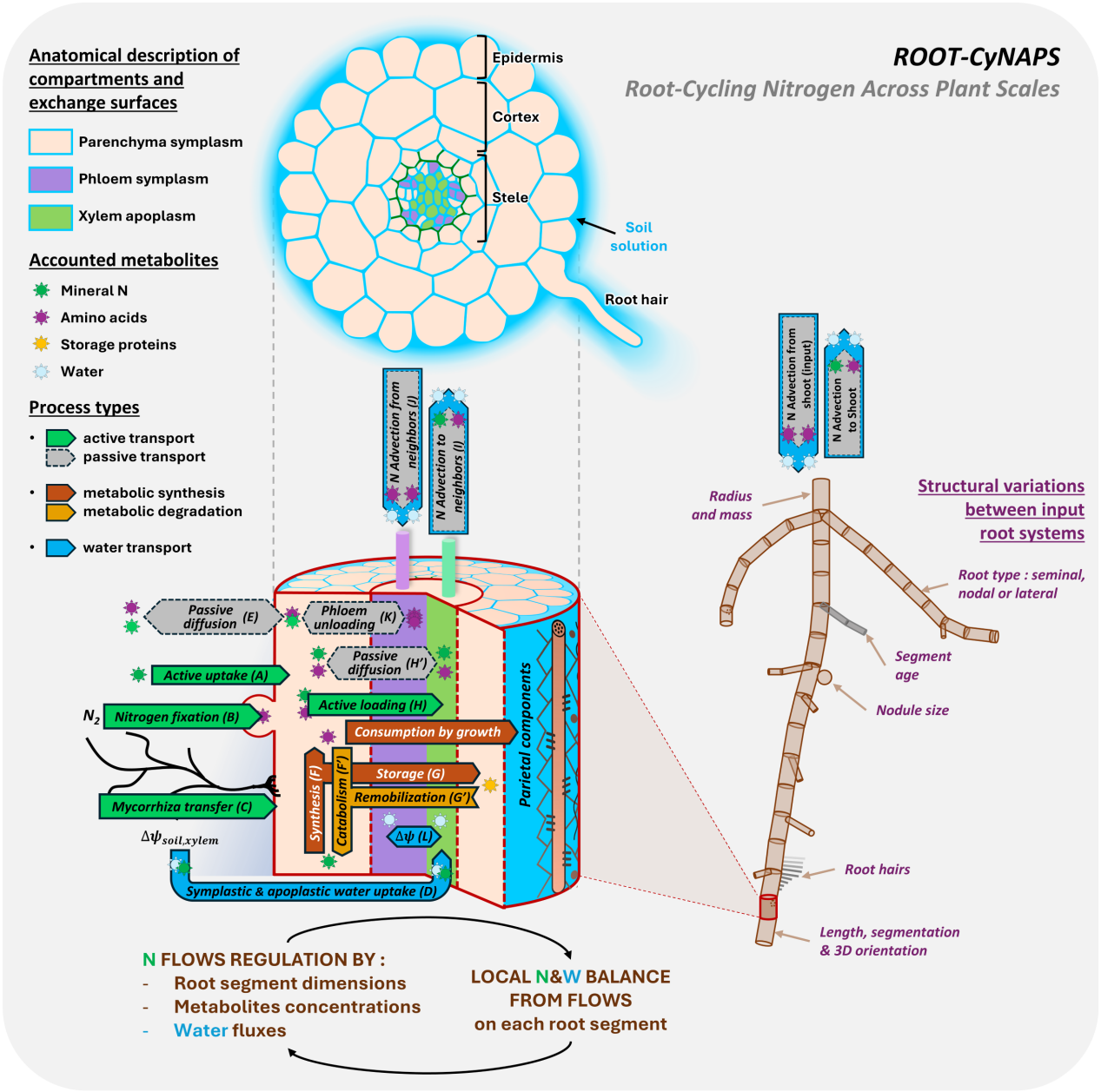

Fig. 1. Conceptual scheme of the *Root-CyNAPS* model. The root system is discretized into segments, each characterized by three distinct compartments: parenchyma symplasm, phloem symplasm, and xylem apoplasm. N is represented in four forms : mineral N (green star), amino acids (purple star), N storage (yellow star), and N contained in structural mass (parietal components). N uptake from the external solution into root cells occurs via active transporters (A), and, in some cases, through N_2 fixation by nodules (B) and mycorrhiza-mediated uptake (C). Roots can also take up N directly into the xylem when absorbing water through the apoplasm (D). Water uptake is driven by a decreasing gradient of water potentials. N can also be lost from root segments to the external solution via passive diffusion of mineral N or exudation of amino acids (E). A part of the mineral N in the root symplasm can be transformed into amino acids (F), which can be used for sustaining growth, be stored (G), or be loaded into the xylem together with mineral N (H) and exported to the shoots (I). Amino acids can also be imported from the shoots into the root system phloem (J) and unloaded in each root segment (K). Finally, a radial water flow between xylem and phloem couples the axial sap flows of the two vessels (L).

Table 1: Description and units of the *Root-CyNAPS* model variables. gDW refers to grams of root segment dry structural mass.

Variable name	Description	Unit (SI)
State variables		
n^{Ni}_{symp}, n^{Ni}_{xylem}	Quantity of mineral nitrogen in parenchyma symplasm and xylem apoplasm, respectively	mol of mineral nitrogen
$[Ni_{symp}]_m$, $[Ni_{xylem}]_m$	Massic concentration of mineral nitrogen in parenchyma symplasm and xylem apoplasm, respectively. m indice is replaced by v for corresponding volumic concentrations	$mol.gDW^{-1}$ and $mol.m^{-3}$ of mineral nitrogen, respectively
n^{AA}_{symp}, n^{AA}_{xylem}, n^{AA}_{phloem}	Quantity of total amino acids in parenchyma symplasm, xylem apoplasm and phloem symplasm, respectively	mol of amino acids
$[AA_{symp}]_m$, $[AA_{xylem}]_m$, $[AA_{phloem}]_m$	Massic concentration of total amino acids in parenchyma symplasm, xylem apoplasm and phloem symplasm, respectively. m indice is replaced by v for corresponding volumic concentrations	$mol.gDW^{-1}$ *and* $mol.m^{-3}$ *of amino acids, respectively*
n^{Prot}_{symp}	Quantity of storage proteins in parenchyma symplasm	mol of storage proteins
$[Prot_{symp}]_m$	Massic concentration of storage proteins in root symplasm	$mol.gDW^{-1}$ of storage proteins
V^{water}_{symp}, V^{water}_{xylem}, V^{water}_{phloem}	Water volume in parenchyma symplasm, xylem and phloem, respectively	m^3 of water
Ψ_{xylem}, Ψ_{phloem}	Water hydrostatic pressure in xylem and phloem, respectively	Pa
$[solute_{xylem}]_v$, $[solute_{phloem}]_v$	Total solute concentration in xylem and phloem, respectively	$mol.gDW^{-1}$ of solutes
Exchange surfaces and conductances based on anatomy		
$S_{soil\|symp}$	Exchange surface between soil and root symplasm	m^2
$S_{symp\|xylem}$	Exchange surface between root symplasm and xylem apoplasm	m^2
$S_{symp\|phloem}$	Exchange surface between root symplasm and phloem vessels	m^2

Table 1: continued from previous page

Variable name	Description	Unit (SI)
K_{Endo}, K_{Exo}	Conductance factor decreasing from 1 to 0 with endodermis and exodermis differentiation, respectively	Dimensionless
$Diff_{protoxylem}$	Differentiation factor increasing from 0 to 1 with protoxylem apoplastic transition	Dimensionless
K_{xylem}, K_{phloem}	Axial water conductance of xylem and phloem, respectively, based on the Hagen-Poiseuille model	$m^3.Pa^{-1}.s^{-1}$
Name of processes differential equation		
$Tf^{Ni}_{soil \Rightarrow symp}$	Mineral nitrogen active uptake by root from soil solution to root symplasm, composed of two active and passive transporter pathways	$mol.s^{-1}$ of mineral nitrogen
$Tf^{Ni}_{symp \rightarrow soil}$	Mineral nitrogen passive diffusion from root symplasm to soil solution	$mol.s^{-1}$ of mineral nitrogen
$Tf^{Ni,\text{Advection}}_{soil \rightarrow xylem}$	Mineral nitrogen apoplastic uptake through water advection from soil solution to xylem apoplasm	$mol.s^{-1}$ of mineral nitrogen
$Tf^{Ni}_{symp \Rightarrow xylem}$	Mineral nitrogen active loading from root symplasm to xylem apoplasm	$mol.s^{-1}$ of mineral nitrogen
$Tf^{Ni}_{xylem \rightarrow symp}$	Mineral nitrogen passive back-diffusion from xylem apoplasm to symplasm	$mol.s^{-1}$ of mineral nitrogen
$Mt^{Ni,hexose \Rightarrow AA}_{symp}$	Amino acids synthesis in root symplasm from locally available mineral nitrogen and hexose	$mol.s^{-1}$ of amino acids
$Mt^{AA \Rightarrow Ni,hexose}_{symp}$	Amino acids catabolism in root symplasm producing mineral nitrogen and hexose	$mol.s^{-1}$ of amino acids
$Tf^{Ni}_{mycorrhiza \Rightarrow symp}$	Mineral nitrogen active transport from mycorrhiza symplasm to root symplasm	$mol.s^{-1}$ of mineral nitrogen
$Tf^{Ni}_{rhizobia \Rightarrow symp}$	N_2 fixation as mineral nitrogen into root nodule symplasm	$mol.s^{-1}$ of mineral nitrogen
$Tf^{AA}_{phloem \rightarrow symp}$	Amino acid passive unloading from phloem symplasm to root symplasm	$mol.s^{-1}$ of amino acids
$Tf^{AA}_{symp \Rightarrow xylem}$	Amino acid active loading from root symplasm to xylem apoplasm	$mol.s^{-1}$ of amino acids
$Tf^{AA}_{symp \rightarrow soil}$	Amino acid passive exudation from root symplasm to soil solution	$mol.s^{-1}$ of amino acids

Table 1: continued from previous page

Variable name	Description	Unit (SI)
$Tf^{AA}_{soil \Rightarrow symp}$	Amino acid active reuptake from the soil solution	$mol.s^{-1}$ of amino acids
$Mt^{AA \Rightarrow storage}_{symp}$	Storage protein synthesis in root symplasm from locally available amino acids	$mol.s^{-1}$ of storage proteins
$Mt^{storage \Rightarrow AA}_{symp}$	Storage protein catabolism in root symplasm remobilizing amino acids	$mol.s^{-1}$ of storage proteins
$Tf^{water}_{soil \rightarrow xylem}$	Radial water import from soil to root xylem's apoplasm driven by a water potential gradient, composed of a transmembrane and an apoplastic pathway	$m^3.s^{-1}$ of water
$Tf^{water}_{phloem(i) \rightarrow xylem(i)}$	Radial transmembrane water exchange between xylem and phloem driven by a water potential gradient	$m^3.s^{-1}$ of water
$Tf^{water}_{xylem(i) \rightarrow (i-1)}$, $Tf^{water}_{phloem(i) \rightarrow (i-1)}$	Axial water flow from root segment i to its parent segment *i-1*, within xylem and phloem respectively. In phloem, sap usually flows downwards and flux value becomes negative	$m^3.s^{-1}$ of water
Kinetic regulators of processes		
$Vmax^{Ni,HATS}_{soil \Rightarrow symp}$	Michaelis-Menten maximal rate for mineral N active surfacic uptake by the High Affinity Transport System (HATS)	$mol.m^{-2}.s^{-1}$ of mineral nitrogen
$Km^{Ni,HATS}_{soil \Rightarrow symp}$	Soil concentration at which the transporter reaches half of the maximal rate for mineral N active uptake by the HATS	$mol.m^{-3}$ of mineral nitrogen
$K^{Ni,LATS}_{soil \Rightarrow symp}$	Linear slope modifier for mineral N active uptake by the Low Affinity Transport System (LATS)	$m.s^{-1}$
f_{hex}	Regulation factor for active transport processes increasing from 0 to 1 with symplastic hexose concentration	Dimensionless
$Vmax^{N^2 \Rightarrow Ni}_{nodule}$	Michaelis-Menten maximal rate for N_2 active massic fixation by a root nodule	$mol.gDW^{-1}.s^{-1}$ of mineral nitrogen
$Process(T_{soil})$	A generic temperature modifier for above differential equations according to soil temperature	Same as modified process

Computing N Metabolites Concentration at Segment Scale

The labile metabolites, i.e. circulating nutrients as opposed to structural and storage molecules, include total mineral nitrogen (nitrate and ammonium) and total amino acids, each expressed as a quantities in moles noted n^{Ni}_{symp} and n^{Ni}_{symp} respectively . These labile metabolites are transported via the xylem and phloem, unlike storage proteins (n^{Prot}_{symp}) and N allocated to structural mass. Each are expressed as concentration relative the segment structural mass (gram of dry weight), noted $[Ni_{symp}]_m$, $[AA_{symp}]_m$ and $[Prot_{symp}]_m$ respectively (m for massic concentration). Additionally, water volumes (V^{water}_{symp}, V^{water}_{xylem} and V^{water}_{phloem}) are defined from local root anatomy to compute volumetric concentrations within each compartment, e.g. $[Ni_{symp}]_v$, which regulates the transport processes detailed below (Eq. 3.7; 3.9; 3.12).

For each pool, the processes affecting N balance are presented in equations 1.1 to 1.4. Notably, process names have been standardized according to the following conventions: Tf stands for transport flow rate, where no reaction occurs, and Mt for metabolic rate, where at least one metabolite is transformed. For Tf, the transported metabolite is represented as an upper indice and the source and destination compartments are separated with an arrow ($\Rightarrow$ for active transport and $\rightarrow$ for passive transport). For Mt, the compartment where the transformation occurs is placed as lower indice, and the reaction equation is denoted as $Mt^{substrates \Rightarrow products}_{compartment}$.

In the example of the symplastic mineral N quantity in a root segment in Eq. 1.1, its derivative is equal to the sum of a net radial transport between soil and symplasm ($Tf^{Ni}_{soil \Rightarrow symp} - Tf^{Ni}_{symp \rightarrow soil}$), a net radial transport between symplasm and xylem ($Tf^{Ni}_{xylem \rightarrow symp} - Tf^{Ni}_{symp \Rightarrow xylem}$), the net synthesis of total amino acids in the root symplasm ($Mt^{AA \Rightarrow Ni,hexose}_{symp} - Mt^{Ni,hexose \Rightarrow AA}_{symp}$), and finally the acquisition of N from mycorrhiza and nitrogen-fixing nodules ($Tf^{Ni}_{mycorrhiza \Rightarrow symp} + Tf^{Ni}_{rhizobia \Rightarrow symp}$). All these processes are expressed in moles of metabolite per second per root segment. Metabolic transformations between two pools require conversion factors, such as the average number of nitrogen atoms per amino acid represented by the parameter $nb_{N:AA}$.

$$\begin{aligned}\frac{d\, n^{Ni}_{symp}}{dt} &= Tf^{Ni}_{soil \Rightarrow symp} + Tf^{Ni}_{xylem \rightarrow symp} + Tf^{Ni}_{mycorrhiza \Rightarrow symp} + Tf^{Ni}_{rhizobia \Rightarrow symp} \\ &\quad - Tf^{Ni}_{symp \rightarrow soil} - Tf^{Ni}_{symp \Rightarrow xylem} + (Mt^{AA \Rightarrow Ni,hexose}_{symp} - Mt^{Ni,hexose \Rightarrow AA}_{symp}) \cdot nb_{N:AA}\end{aligned} \tag{1.1}$$

The change in the mineral N concentration in symplasm ($[Ni_{symp}]_m$) over time is eventually obtained by dividing the change in the quantity of symplastic mineral N by the structural mass of the segment. Similarly, the derivatives of amino acids (AA), storage proteins and xylem water are calculated as follows:

$$\begin{aligned}\frac{d\, n^{AA}_{symp}}{dt} =& Tf^{AA}_{soil \Rightarrow symp} + Tf^{AA}_{phloem \rightarrow symp} - Tf^{AA}_{symp \Rightarrow xylem} - Tf^{AA}_{symp \rightarrow soil} + Mt^{Ni,hexose \Rightarrow AA}_{symp} + Mt^{storage \Rightarrow AA}_{symp} \\ &- Mt^{AA \Rightarrow Ni,hex}_{symp} - Mt^{AA,hexose \Rightarrow struct}_{symp} \cdot nb_{AA:struct} - Mt^{AA \Rightarrow storage}_{symp} \cdot nb_{AA:stor}\end{aligned} \tag{1.2}$$

$$\frac{d\, n^{Prot}_{symp}}{dt} = Mt^{AA \Rightarrow storage}_{symp} - \frac{Mt^{storage \Rightarrow AA}_{symp}}{nb_{AA:stor}} \tag{1.3}$$

And during a short time step, for a given state of the root system architecture, we assume water mass conservation and no difference in density:

$$\frac{d\, V^{water}_{symp}}{dt} = \frac{d\, V^{water}_{xylem}}{dt} = \frac{d\, V^{water}_{phloem}}{dt} = 0 \tag{1.4}$$

Computing Root Exchange Surfaces from Anatomical Properties of a Root Segment

The structural mass of a root segment is computed from its cylindrical volume and a homogeneous tissue density. However, the exchange surface with the soil is not assumed to be cylindrical, as recent studies suggest that variations in

histological surfaces play a major role in root exchange variability (Couvreur et al., 2018; Le Deunff et al., 2019). In this perspective, *Root-CyNAPS* integrates a local anatomy module accounting for 5 different interfaces: 1) soil-epidermis (including root hairs), 2) soil-symplasm for cortex, 3) soil-symplasm for stele, 4) symplasm-xylem and 5) symplasm-phloem (Fig. 1). The maximal soil-symplasm exchange surface corresponds to the total surface of root hairs, epidermis, cortex, and stele cell (Eq. 2.1). The surfacic ratio of epidermis, cortex and stele surface over the cylindrical surface of the root segment are parametrized. Root hairs surface and mass, introduced in Eq. 2.1, are an input of the model. Additionally, we introduce the progressive differentiation of two boundary layers, endodermis and exodermis, which increasingly restrict access to these exchange surfaces due to a gradual decrease in their conductance as root ages (Eq. 2.3). This approach accounts for the restriction of free soil solution movement through the apoplasm, caused by the progressive suberization and lignification during root segment aging (Clarkson et al., 1971; Hose et al., 2001; Enstone et al., 2002; Wu et al., 2019).

$$S_{soil|symp} = 2 \cdot \pi \cdot R \cdot L.(\frac{S_{epidermis}}{S_{cylinder}} + \frac{S_{cortex}}{S_{cylinder}} \cdot K_{Exo} + \frac{S_{stele}}{S_{cylinder}} \cdot K_{Endo}) + S_{RootHairs} \tag{2.1}$$

The conductivity of the endodermis of a given root segment is calculated from its thermal age since tissue formation to account for the distinct aging dynamics between different root types and orders (Eq. 2.2). This age is noted $age(T_{ref})$ and expressed in seconds equivalent at a reference temperature T_{ref} (°C) selected to match parametrization. We introduced a decreasing Gompertz formalism chosen to account for the progressive transition between maximal and minimal conductivity.

$$K_{endo,age} = 1 - L_{Endo}^{Diff} \cdot \exp[\ln(0.01) \cdot \exp(r_{Endo}^{Diff}(s_{Endo}^{Diff} - age(T_{ref})))] \tag{2.2}$$

The age of each root segment $age(T_{ref})$ has to be provided as an input of the model. The r_{Endo}^{Diff} parameter represents the rate (s^{-1}) at which the differentiation occur, s_{Endo}^{Diff} is a delay parameter (s) representing the thermal age at which the differentiation starts, and L_{Endo}^{Diff} (adim) is a limit parameter, representing the maximal possible reduction of conductance. This last parameter was introduced to account for tissues remaining permeable when fully differentiated, such as exodermis (Schreiber et al., 2005; Ouyang et al., 2020). $K_{exo,age}$ decreases with root age in a similar manner, though more gradually due to its specific parametrization (Eq. S7 Table S1). Additionally, a disruption of endodermis and exodermis barriers occurs when a ramification primordium emerges from the parent root, which increases the conductance of the supporting root segment. This disruption lasts for a period of time ($\Delta t_{endo,max}^{disrupt}$) and conductance decreases linearly with the time since primordium started to emerge ($\Delta t_{endo}^{disrupt}$). The overall conductance of the root segment (K_{endo}) is therefore modeled as the maximal conductance value between age-related differentiation ($K_{endo,age}$) and disruption-related differentiation (Eq. 2.3). K_{exo} is represented with the same combined relationship (Eq. S6 Table S1).

$$K_{endo} = \max(K_{endo,age} \quad , \quad 1 - \frac{\Delta t_{endo}^{disrupt}}{\Delta t_{endo,max}^{disrupt}}) \tag{2.3}$$

Exchange surfaces between the root symplasm and transport vessels are also considered using a surfacic fraction parameter relative to the segment's external cylindrical surface. We assume that the xylem is in equilibrium with the stele apoplasm as soon as its cells lose their membrane through apoptose (Clarkson, 1993). Consequently, a differentiation factor ($Diff_{protoxylem}$, from 0 to 1) is introduced to account for protoxylem functionalization through apoptose (Eq. 2.4).

$$S_{symp|xylem} = 2.\pi.R.L.\frac{S_{stele}}{S_{cylinder}}.Diff_{protoxylem} \tag{2.4}$$

with

$$Diff_{protoxylem} = \exp[\ln(0.01) \cdot \exp(r_{xylem}^{Diff}(s_{xylem}^{Diff} - age(T_{ref})))] \tag{2.5}$$

The parameters s_{xylem}^{Diff} (s) and r_{xylem}^{Diff} (s^{-1}) define the starting thermal age and rate of xylem differentiation along the root axis, respectively. In turn, the exchange surface between the symplasm and phloem is described as a stable surfacic fraction of the segment's cylindrical surface (Eq. S8 Table S1).

When defining these exchange surfaces, *Root-CyNAPS* does not distinguish between different root types and assumes that similar differentiation processes over time occur across different root orders.

Key Exchange Processes with Environment

In *Root-CyNAPS*, the net N uptake of each root segment is decomposed into i) two transporter-mediated active N uptake flows, ii) a bidirectional diffusive exchange of mineral N and amino acids with the soil, iii) a N uptake mediated by water uptake through advection, and iv) a possible additional N uptake from mycorrhiza and *Rhizobium* symbiosis.

Net Mineral Nitrogen Uptake from Soil to Root Symplasm

We decompose the active mineral nitrogen uptake between two distinct High and Low Affinity Transporter Systems (HATS/LATS) (Pace and McClure, 1986; Nacry et al., 2013). As in the CN-Wheat model (Barillot et al., 2016), we model HATS uptake with the commonly used Michaelis-Menten (MM) formalism (Eq. 3.2), and the LATS uptake with a linear non-saturating formalism (Siddiqi et al. (1989); Eq. 3.5).

$$Tf_{soil\Rightarrow symp}^{Ni} = Tf_{soil\Rightarrow symp}^{Ni,HATS} + Tf_{soil\Rightarrow symp}^{Ni,LATS} \tag{3.1}$$

For HATS, we use a Michaelis-Menten formalism while recognizing its limitations when scaling from individual transporter studies to the root segment tissue scale we consider here. We adapted the model to account for the reported uptake variability resulting from phosphorylation (Liu and Tsay, 2003), transporter availability, transition between diffusion limitations, transporter limitations regimes (Le Deunff et al., 2019) or balance between symplastic and apoplastic ways. We therefore introduced a lognormal modulation of the kinetic parameters $Vmax_{soil\Rightarrow symp}^{Ni}$ and $Km_{soil\Rightarrow symp}^{Ni}$ with the concentration of mineral N in the symplasm (Siddiqi et al., 1989), to account for such local regulations of N uptake (Eq. 3.2). Mineral nitrogen uptake being an active process regulated by the availability of labile carbon (Lejay et al., 2003; Barillot et al., 2016), a modulation according to the availability of labile hexose (f_{hex}) is also considered:

$$Tf_{soil\Rightarrow symp}^{Ni,HATS} = \frac{[Ni_{soil}]_v \cdot Vmax_{soil\Rightarrow symp}^{Ni,HATS}}{[Ni_{soil}]_v + Km_{soil\Rightarrow symp}^{Ni,HATS}} \cdot S_{soil|symp} . f_{hex} \tag{3.2}$$

with

$$f_{hex} = \frac{[hex_{symp}]_m}{[hex_{symp}]_m + Km_{root}^{hex}} \tag{3.3}$$

The dependency of $Vmax_{soil\Rightarrow symp}^{Ni,HATS}$ to symplasmic mineral N concentration is expressed by:

$$Vmax_{soil\Rightarrow symp}^{Ni,HATS} = \frac{A_{Vmax}^{Ni,HATS}}{[Ni_{symp}]_m \cdot \sigma_{Vmax}^{Ni,HATS} \cdot \sqrt{2\pi}} \cdot exp\left(-\frac{(\ln [Ni_{symp}]_m - \mu_{Vmax}^{Ni,HATS})^2}{2\sigma_{Vmax}^{Ni,HATS 2}} \right) \tag{3.4}$$

$A_{Vmax}^{Ni,HATS}$ is the amplitude of the variation, $\mu_{Vmax}^{Ni,HATS}$ the natural logarithm of the mineral N massic concentration in symplasm at which the value is maximal, and $\sigma_{Vmax}^{Ni,HATS}$ is the standard variation according to the mineral N massic concentration in symplasm. The dependency of $Km_{soil\Rightarrow symp}^{Ni,HATS}$ to symplasmic mineral N concentration is expressed the same way with different parameter values.

For LATS, we introduced linear dependency to external mineral N to match the uptake profiles observed experimentally at high concentrations (Siddiqi, 1990; Rao et al., 1997).

$$Tf_{soil\Rightarrow symp}^{Ni,LATS} = K_{soil\Rightarrow symp}^{Ni,LATS} \cdot [Ni_{soil}]_v \cdot S_{soil|symp}.f_{hex} \tag{3.5}$$

With a decrease of the slope when mineral N increases in roots as introduced by the CN-Wheat model (Barillot et al., 2016) :

$$K_{soil\Rightarrow symp}^{Ni,LATS} = -K_{LATS}^{slope} \cdot [Ni_{symp}]_m + K_{LATS}^{origin} \tag{3.6}$$

Finally, we account for a passive and diffusion flow (Eq. 3.7), reflecting a loss of mineral N impacting the balance of net mineral N uptake when the concentration of mineral N in root symplasm is higher than that in the soil (Lazof et al., 1992; Henriksen et al., 1992). A reverse gradient resulting in an inflow can in turn reflect transitions between mostly diffusive or active uptake regimes (Epstein, 1960; Hopmans and Bristow, 2002).

$$Tf_{symp\rightarrow soil}^{Ni} = D_{symp\rightarrow soil}^{Ni} \cdot ([Ni_{symp}]_v - [Ni_{soil}]_v) \cdot S_{soil|symp} \tag{3.7}$$

In the symplasm compartment, volumic concentrations are calculated from mineral N quantities and symplasm volume (Eq. 3.8).

$$[Ni_{symp}]_v = \frac{n_{symp}^{Ni}}{\pi \cdot R^2 \cdot r_{S_{symp}}^{CrossSection} \cdot L \cdot (1 - f_{symp}^{CellLine})} \tag{3.8}$$

with $r_{S_{symp}}^{CrossSection}$ the ratio of symplasmic cell cross sectional surface to root discus surface, and $f_{symp}^{CellLine}$ a longitudinal cell line frequency factor.

Amino Acid Exudation

Amino-acids are lost by passive diffusion and selectively reabsorbed by active import (Jones and Darrah, 1994; Phillips et al., 2004; Lesuffleur et al., 2007). Total amino acid rhizodeposition is modeled through a diffusion equation driven by the soil-symplasm concentration gradient, similar to Eq. 3.7 :

$$Tf_{symp\rightarrow soil}^{AA} = D_{symp\rightarrow soil}^{AA} \cdot ([AA_{symp}]_v - [AA_{soil}^{inorg}]_v) \cdot S_{soil|symp} \tag{3.9}$$

Active reuptake of amino acid is in turn modeled with MM formalism (Eq. S10 Table S1), including the down-regulation by symplasmic mineral N accumulation, to account for the observed preferential uptake of mineral forms under non-limiting mineral N availability in the soil (El-Naggar et al., 2009).

Radial Water Uptake and Co-transportation of N Towards Xylem

The variability in the rate of nitrogen uptake and transport between root segments has been related to the variable intensity of the advective water flow in the xylem (Bollard, 1960; Bauget et al., 2023). Thus, we introduced a water balance module in *Root-CyNAPS* to account for the heterogeneity of radial (Eq. 3.10) and axial water flow (Eq. 4.1, see below) in the xylem and phloem vessels. As suggested by Couvreur et al. (2018), we account for the apoplastic and symplastic water uptake pathways separately (Eq. 3.10) to avoid biases of the composite water flow model (Fiscus and Kramer, 1975).

$$Tf_{soil\rightarrow xylem}^{water} = Tf_{soil\rightarrow apop\rightarrow xylem}^{water} + Tf_{soil\rightarrow symp\rightarrow xylem}^{water} \tag{3.10}$$

We assume the apoplastic water pathway from soil to xylem apoplasm ($Tf^{water}_{soil\to apop\to xylem}$) to be mainly driven by the gradient of hydrostatic pressure between the soil and the xylem, but we also account for the gradient of osmotic potential, which can become significant under dry soil conditions (Eq. 3.11).

$$Tf^{water}_{soil\to apop\to xylem} = k^{apop}_{water}\cdot\Big(\Psi_{soil} - \Psi_{xylem} - \sigma R T_{soil}\big([solutes_{soil}]_v - [solutes_{xylem}]_v\big)\Big)\cdot K_{endo} \tag{3.11}$$

Ψ_{soil} and Ψ_{xylem} are the hydrostatic water potential of soil solution and xylem respectively (Pa), σ is a reflection coefficient, R the gas constant, T_{soil} soil temperature, $[solute_{soil}]_v$ and $[solute_{xylem}]_v$ the total concentrations of solute in the soil and the xylem, respectively. k^{apop}_{water} is the radial hydraulic conductance of the apoplasm ($m.s^{-1}.Pa^{-1}$). K_{Endo} from Eq. 2.3 accounts for the closure of the apoplastic pathway during endodermis differentiation. The apoplastic water uptake flowing into the xylem without crossing any selective barrier, it also transports mineral N and amino acids through advection. In particular, the advective transport of mineral N between soil and xylem is expressed as:

$$Tf^{Ni,\text{Advection}}_{soil\to xylem} = \begin{cases} Tf^{water}_{soil\to apop\to xylem}\cdot[Ni_{soil}]_v & \text{if} \quad Tf^{water}_{soil\to apop\to xylem} > 0 \\ Tf^{water}_{soil\to apop\to xylem}\cdot[Ni_{xylem}]_v & \text{if} \quad Tf^{water}_{soil\to apop\to xylem} < 0 \end{cases} \tag{3.12}$$

The symplastic water pathway is represented in a similar way, depending on the radial hydraulic conductance of the symplasm k^{symp}_{water}, the same gradients of hydrostatic pressure and concentrations, and the area of the interface between the soil solution and the symplasm (Eq. S14 Table S1).

Analogous to the MECHA model (Couvreur et al., 2018), k^{apop}_{water} and k^{symp}_{water} are intermediate segment-scale parameters, which can be obtained from parameters of cell wall, transmembrane, aquaporin and plasmodesmata conductances applied on actual cross sectional images.

Mycorrhizal Uptake and Translocation to Roots

For some species, a significant proportion of root N uptake has been reported to be taken up by mycorrhiza mediated pathways (Hawkins et al., 2000; De Souza Campos et al., 2021). Active transporters have been identified as main drivers of the N transfer from mycorrhiza into the roots (Hui et al., 2022), suggesting a regulation by mycorrhiza symplasmic N concentration. In order to include this possible additional N uptake, *Root-CyNAPS* introduces a simple Michaelis-Menten formalism to account for mycorrhizal N uptake (Eq. 3.13).

$$Tf^{Ni}_{mycorrhiza\Rightarrow symp} = \frac{Vmax^{Ni}_{mycorrhiza\Rightarrow symp}\cdot[N^{inorg}_{mycorrhiza}]_m}{Km^{Ni}_{mycorrhiza\Rightarrow symp} + [N^{inorg}_{mycorrhiza}]_m}\cdot L^{myccorhiza}_{infection}\cdot f_{hex} \tag{3.13}$$

$L^{myccorhiza}_{infection}$ is the length of infection by mycorrhiza in the considered segment, which needs to be provided by a mycorrhiza growth model as an input (Schnepf et al., 2016). f_{hex} from Eq. 3.3 introduces the regulation of symbiotic exchanges by hexose availability in root symplasm and their subsequent export to mycorrhiza (Douds et al., 2000). Considering the paucity of studies reporting how the transfer from the fungi to the root may be regulated by the N status of the root segment, we did not introduce such a regulation here.

N_2 Nodule Fixation

In legume species, biological nitrogen fixation within nodules can sustain root segments N consumption under limiting mineral N availability (Xia et al., 2017; Lyu et al., 2020). A complex set of transformations is involved in this symbiotic relationship between N_2 fixation and transfer to the root. We account for its reported dependency on carbohydrate local availability and consumption by the nodule (Udvardi and Day, 1997; Day* et al., 2001) (Eq. 3.14):

$$Tf_{nodule}^{N^2 \Rightarrow Ni} = \frac{m_{nodule}^{struct}.Vmax_{nodule}^{N^2 \Rightarrow Ni}.[hex_{symp}]_m}{[hex_{symp}]_m + Km_{nodule}^{N^2 \Rightarrow Ni}} \tag{3.14}$$

with

$$Vmax_{nodule}^{N^2 \Rightarrow Ni} = \frac{[Ni_{symp}]_m \cdot Vmax_{nodule}^{N^2 \Rightarrow Ni}}{[Ni_{symp}]_m + Km_{inibition}^{N^2 \Rightarrow Ni}} \tag{3.15}$$

$Vmax_{nodule}^{N^2 \Rightarrow Ni}$ introduces a non linear inhibition by local mineral N availability in the root symplasm observed experimentally.

Key Internal Transport Processes

Radial N Flows Between Symplasm and Vessels

All axial flows between segments are occurring through the vessels of symplasmic phloem and apoplastic xylem. Amino acids are assumed to be unloaded from phloem vessels through symplastic diffusion only (Eq. S21 Table S1), as no active amino acid transporters have been reported in phloem unloading zone (Tegeder and Hammes, 2018; Deinum et al., 2019). Morphological variations of the parenchyma surrounding the phloem vessels have been reported to alter the plasmodesmata connections, and therefore the rate of phloem unloading (Spicer, 2014). We accounted for these variations by explicitly modeling the exchange surface between symplasm and phloem (Eq. S8 Table S1). The export of mineral N and amino acid from symplasm to xylem apoplasm has been described as an active transport (Devienne et al., 1994; Pitman, 2008) , which would involve the same LATS transporter family found on the soil-symplasm exchange surface (Duan et al., 2018). This active export is represented in our model by a Michaelis-Menten kinetics, depending on the concentration of either form of N in the root symplasm (Eq. S18 and S19 Table S1). The net export to xylem for both N forms also includes a transmembrane diffusion flow from xylem to symplasm (Eq. S20 and S21 Table S1). As xylem cells can be in contact with the soil solution when Casparian strips are not limiting the apoplastic continuum, we also introduced diffusive and water advected flows of mineral N and amino acids that can occur directly between those two compartments only in root tip and lateral primordium emergence regions where the endodermis is not fully differentiated (Eq. S22 and S23 Table S1).

Coupled Axial Water Flow in Xylem and Phloem

We model the heterogeneity of axial water transport in xylem and phloem along roots, as well as the radial water exchanges linking the two vessels according to the Münch model (Nakad et al., 2022). Adapting from the *HydroRoot* model (Bauget et al., 2023), we describe the axial water flux between considered segment (i) and its parent $(i-1)$ using the Hagen-Poiseuille law in a similar way for xylem (Eq. 4.1) and phloem (Eq. 4.2).

$$Tf_{xylem(i)\rightarrow(i-1)}^{water} = K_{xylem(i)} \cdot (\Psi_{xylem(i)} - \Psi_{xylem(i-1)} + \rho_{xylem} \cdot g \cdot (z_{(i)} - z_{(i-1)})) \tag{4.1}$$

$$Tf_{phloem(i)\rightarrow(i-1)}^{water} = K_{phloem(i)} \cdot (\Psi_{phloem(i)} - \Psi_{phloem(i-1)} + \rho_{phloem} \cdot g \cdot (z_{(i)} - z_{(i-1)})) \tag{4.2}$$

Taking the example of xylem, $\Psi_{xylem(i)}$ represents the hydrostatic water potential and $\rho_{xylem} \cdot g \cdot z_{(i)}$ the gravitational potential of segment i, with ρ_{xylem} the volumic mass of xylem content, g the gravitational constant, and $z_{(i)}$ the height of segment i from input architecture. Osmotic potential was not accounted for axial water transport as it is considered to mainly affect radial water transport (See Eq. 3.10), and matric potential gradients were assumed negligible for axial transport in open conductive elements (Jensen, 2018; De Swaef et al., 2022). Segment axial conductance $K_{xylem,(i)}$ (Eq. 4.3) is estimated from the length of the segment, the viscosity of sap $\eta_{xylem}(i)$ at current soil temperature and solute

concentration (Andrade, 1930; Telis et al., 2007), and the sum of individual xylem vessels conductance, whose radii r are parametrized. $Diff_{protoxylem}$ from Eq. 2.5 accounts for the progressive functionalization of xylem when becoming apoplastic. Phloem axial conductance is represented with the same formalism (Eq. S24 Table S1).

$$K_{xylem(i)} = Diff_{protoxylem} \sum_{\text{r}}^{\text{vessels}} \frac{\pi \cdot r^4}{8 \cdot \eta_{xylem}(i) \cdot L} \tag{4.3}$$

The radial water flow between xylem and phloem is then represented similarly to Eq. 3.11 according to the gradients of hydrostatic and osmotic potentials (Eq. 4.4). The total solute concentrations in xylem and phloem are estimated from the sum of simulated metabolites concentrations, which are then multiplied by a scaling factor S1 to account for the osmotic contribution of ions not represented in the model but with high reported concentrations, such as potassium (Munns and Passioura, 1984; Dinant et al., 2010).

$$Tf^{water}_{phloem(i)\to xylem(i)} = k^{phloem(i)}_{water}.\Big(\Psi_{phloem(i)} - \Psi_{xylem(i)} - \sigma R T_{soil(i)}\big([solutes_{phloem(i)}]_v - [solutes_{xylem(i)}]_v\big)\Big) \tag{4.4}$$

According to water mass conservation in the segment (Eq. 1.4), we write the flows compensation for each vessel, Eq. 4.5 and 4.6. Using a matrix representation of the whole root system, we then solve for the xylem and phloem water potentials at which the system is at equilibrium simultaneously for all root segments. To do so we use a Newton-Raphson approach which is an iterative method to identify the water potential profiles along roots at which the system converges. Once the water potentials of xylem and phloem have been stabilized, the axial water flows of the time step are deduced from Eq. 4.1 and 4.2.

$$Tf^{water}_{xylem(i)\to xylem(i-1)} = Tf^{water}_{soil(i)\to apop\to xylem(i)} + Tf^{water}_{phloem(i)\to xylem(i)} + \sum_{j}^{children} Tf^{water}_{xylem(j)\to xylem(i)} \tag{4.5}$$

$$Tf^{water}_{phloem(i)\to phloem(i-1)} = \sum_{j}^{children} Tf^{water}_{phloem(j)\to phloem(i)} - Tf^{water}_{phloem(i)\to xylem(i)} \tag{4.6}$$

Axial N Flows Through the Xylem and Phloem Sap Advection

Axial transport of N in the xylem and phloem is modeled based on advection-driven redistribution of sap solutes for both mineral N and amino acids. Considering a segment i and the example of mineral N in xylem, it sends part of its original N content towards its parent $i-1$ if the water flux to parent is positive, and conversely receives an inflow from its parent if the flux reverses (Eq. 4.7). N mass conservation is ensured as all segments follow the same logic.

$$Tf^{Ni}_{xylem(i)\to xylem(i-1)} = \begin{cases} Tf^{water}_{xylem(i)\to xylem(i-1)} \cdot [Ni_{xylem}]_v(i) & , Tf^{water}_{xylem(i)\to xylem(i-1)} > 0 \\ Tf^{water}_{xylem(i)\to xylem(i-1)} \cdot [Ni_{xylem}]_v(i-1) & , Tf^{water}_{xylem(i)\to xylem(i-1)} < 0 \end{cases} \tag{4.7}$$

When the parent $i-1$ is the shoot-root junction, $[Ni_{xylem}]_v(i-1) = [Ni_{xylem}]_v(shoot)$, a constant concentration provided as input of the model to compute the input flux from the shoot in case of downward sap advection.

We compute the derivative of xylem mineral N content for segment i (Eq. 4.8, also including the radial mineral N exchanges with symplasm and soil presented above. We solved the resulting concentration profiles in xylem using an implicit Euler scheme which introduces an adaptive subdivision of the time step for numerical stability when the axial sap flow increases.

$$\frac{d\, n^{Ni}_{xylem(i)}}{dt} = \sum_{k}^{children} Tf^{Ni}_{xylem(k)\Rightarrow xylem(i)} - Tf^{Ni}_{xylem(i)\Rightarrow xylem(i-1)} + Tf^{Ni}_{symp(i)\Rightarrow xylem(i)} + Tf^{Ni,\text{Advection}}_{soil(i)\rightarrow xylem(i)} - Tf^{Ni}_{xylem(i)\rightarrow symp(i)} - Tf^{Ni}_{xylem(i)\rightarrow soil(i)} \quad (4.8)$$

After convergence of the concentration profiles along the roots, we compute the resulting mineral N flow at the root-shoot junction from the mineral N content variation and the sum of radial flows for the whole root system between t and $t + \Delta t$ (Eq. 4.9).

$$Tf^{Ni}_{xylem\rightarrow shoot} = \sum_i n^{Ni}_{xylem(i,t)} - \sum_i n^{Ni}_{xylem(i,t+\Delta t)} + \sum_i (Tf^{Ni}_{symp(i,t)\Rightarrow xylem(i,t)} + Tf^{Ni,\text{Advection}}_{soil(i,t)\rightarrow xylem(i,t)} - Tf^{Ni}_{xylem(i,t)\rightarrow symp(i,t)}) \cdot \Delta t \quad (4.9)$$

The same equations are applied for the axial transport of mineral N and amino-acids in both xylem and phloem (Eq. S1, S2, S27 and S28 Table S1).

Amino Acids Metabolism within Segment

Along with transport processes, we also account for metabolic synthesis and degradation processes in root symplasm between mineral N, amino acids, storage proteins and N integrated to the structural mass. We represent the synthesis of amino acids in the roots, which may account for up to 40% of total amino acids synthesized in the plants with an important variability related to plant species and soil environment (ANDREWS et al., 1992; Scheurwater et al., 2002). We consider its regulation by the concentration of mineral N and labile hexose (Eq. 5.1).

$$Mt^{Ni,hexose\Rightarrow AA}_{symp} = \frac{Vmax^{Ni,hexose\Rightarrow AA}_{symp}}{\frac{1+Km^{Ni\Rightarrow AA}_{symp}}{[Ni_{symp}]_m} \cdot \frac{1+Km^{hexose\Rightarrow AA}_{symp}}{[hex_{symp}]_m}} . m^{struct}_{root} \quad (5.1)$$

A reverse catabolic flow is introduced in Eq. S29 of Table S1 , in line with experimental evidences of amino acid remobilization in case of hexose deprivation, also suggesting a significant flow of mineral N remobilization from amino acids (Robinson et al., 1991b; Millard, 1988; Dubois et al., 2003; Forde and Lea, 2007). Similarly, the reversible transformation between amino acids and storage proteins is represented by two active processes (Eq. S30 and S31, Table S1). Amino acid consumption by growth processes to build structural N is considered in the N balance of each root segment (Eq. 1.2). *Root-CyNAPS* does not simulate this flow since it does not simulate root carbon metabolism; a profile of consumption rates of amino acids for growth along the roots has therefore to be provided as an input of the model.

Regulation of Processes by Soil Temperature

A regulation of all the above-mentioned processes by soil temperature T_{soil} has been implemented in *Root-CyNAPS* (Eq. 11). We reused the versatile equation from the *RhizoDep* model (Rees et al., 2025), where four contrasted behaviors can be expected, depending on the values of the coefficients A, B and C :

$$Process(T_{soil}) = Process(T_{ref})(A(T_{soil} - T_{ref}) + B)^{1-C} \cdot (A(T_{soil} - T_{ref}) + B)^{\frac{C(T_{soil}-T_{ref})}{10}} \quad (6.1)$$

$Process(T_{ref})$ is the process reference value from literature measured at T_{ref}. If $C = 0$, $A = 0$ and $B = 1$ the process does not depend on soil temperature. If $C = 0$ and $A > 0$: the relationship is equivalent to a linear increase of the process value with temperature, on which the calculation of growing degree days is usually based. If $C = 1$, $A = 0$ and $B > 0$ the relationship is equivalent to the commonly-used *Q10* function, which predicts an exponential growth of the process value with temperature. In this case B represents the *Q10* value, i.e. the relative increase of the process rate for each 10-degree increase in temperature. Finally, based on the observation of temperature optimality of enzymatic processes from Tjoelker et al. (2001) and Parent et al. (2010), when $C = 1$, $A < 0$ and $B > 0$ the relationship is equivalent to a bell-shaped curve that is similar to the *Q10* function at low temperature but reaches a maximum at intermediate temperature and then decreases at higher temperature. For the specific case of axial water transport in xylem and phloem, we model the dependence of sap viscosity to soil temperature and solute concentration according to empirical relationships of Andrade (1930) and Telis et al. (2007) (Eq. S32 and S33). Finally, the thermal age $age(T_{ref})$ introduced to account for anatomical differentiations (Eq. 2.2) is linearly dependent to the difference between T_{soil} and chosen T_{ref}.

Numerical Strategy for Solving Differential Equation System

Root-CyNAPS implements distinct modules for anatomy, water and nitrogen that are solved sequentially (Fig. S1). For each module, the differential equation system is solved in each element of the root system architecture represented as a Multiscale Tree Graph (MTG) using an explicit Euler scheme, i.e. using a small discrete time step ($\Delta t = 1h$) and finite differences for the studied variables. It is solved globally at each time-step, without preferential order between processes. In each module, all the rates are computed first, then the states are updated at the end of the time step. Only water flows in xylem and phloem are solved differently, i.e. using the Newton-Raphson method on the water mass conservation equations in each root segment (4.5, 4.6). An implicit Euler resolution is then used to solve the N concentration profiles resulting from water advection equations (Eq. 4.8).

Table 2: Description and units of the *Root-CyNAPS* model parameters

Parameter name	Description	Unit	Eq. n°
Stoichiometry parameters			
$nb_{N:AA}$	Number of nitrogen moles per mol of amino acids	Dimensionless	1.1
$nb_{AA:stor}$	Number of amino acid moles per mol of storage proteins	Dimensionless	1.2, 1.3
$nb_{AA:struct}$	Number of amino acid moles per gram of structural mass	Dimensionless	1.2
Anatomical parameters			
$\frac{Sepidermis}{Scylinder}$	Ratio of the actual exchange surface of the epidermis cells with the outer cylindrical surface of the root segment	$m^2 \cdot m^{-2}$	2.1
$\frac{Scortex}{Scylinder}$	Ratio of the actual exchange surface of the cortex cells with the outer cylindrical surface of the root segment	$m^2 \cdot m^{-2}$	2.1

Table 2: continued from previous page

Parameter name	Description	Unit	Eq. n°
$\frac{Sstele}{Scylinder}$	Ratio of the actual exchange surface of the stele cells with the outer cylindrical surface of the root segment	$m^2 \cdot m^{-2}$	2.1, 2.4
r_{Endo}^{Diff}, r_{Exo}^{Diff}	Rate of endodermis and exodermis differentiation with tissue aging, respectively	s^{-1}	2.2
s_{Endo}^{Diff}, s_{Exo}^{Diff}	Delay after tissue formation before endodermis and exodermis differentiation starts, respectively	s	2.2
L_{Endo}^{Diff}, L_{Exo}^{Diff}	Maximal possible reduction of endodermis and exodermis conductance, respectively	Dimensionless	2.2
r_{xylem}^{Diff}	Rate of xylem apoplastic differentiation with tissue aging	s^{-1}	2.5
s_{xylem}^{Diff}	Delay after tissue formation before xylem differentiation starts	s	2.5
$r_{S_{symp}}^{CrossSection}$	Ratio of symplasmic cells cross sectional surface area to root cross section area	$m^2 \cdot m^{-2}$	3.8
$f_{symp}^{CellLine}$	A longitudinal cell line frequency factor	Dimensionless	3.8
Active processes kinetic parameters			
Km_{root}^{hex}	Hexose symplastic concentration at which regulation of active transport processes equals 0.5	$mol.gDW^{-1}$ of hexose	3.3
$A_{Vmax}^{Ni,HATS}$	Amplitude of $Vmax_{soil \Rightarrow symp}^{Ni,HATS}$ log-normal variation with mineral N concentration in the root symplasm	$\frac{Parameter\ unit}{mol.gDW^{-1}}$	3.4
$\mu_{Vmax}^{Ni,HATS}$	Natural logarithm of the mineral N massic concentration in root symplasm at which $Vmax_{soil \Rightarrow symp}^{Ni,HATS}$ is maximal	Dimensionless	3.4
$\sigma_{Vmax}^{Ni,HATS}$	Standard deviation of $Vmax_{soil \Rightarrow symp}^{Ni,HATS}$ according to the mineral N concentration in symplasm	Dimensionless	3.4
A_{LATS}	Maximal value of the Low Affinity Transport System (LATS) slope parameter when mineral N concentration in symplasm approaches 0	$m.s^{-1}$	3.6
λ_{LATS}	Rate of exponential decay with the increase of mineral N concentration in symplasm for the LATS slope parameter	$gDW.mol^{-1}$ of mineral N	3.6
$Vmax_{mycorrhiza \Rightarrow symp}^{Ni}$	Rate of mineral N transfer per unit root length from the mycorrhiza to the root symplasm	$mol.m^{-1}.s^{-1}$	3.13

Table 2: continued from previous page

Parameter name	Description	Unit	Eq. n°
$Km^{Ni}_{mycorrhiza \Rightarrow symp}$	Mineral N concentration in mycorrhiza at which the transfer to root symplasm is half its maximum	mol of mineral N $.gDW^{-1}$ of mycorrhiza	3.13
$Vmax^{N^2 \Rightarrow Ni}_{nodule}$	Maximal massic N_2 fixation rate into mineral N in root nodule symplasm	$mol.gDW^{-1}.s^{-1}$ of mineral N	3.15
$Km^{N^2 \Rightarrow Ni}_{nodule}$	Hexose concentration in nodule symplasm at which the fixation rate is half its maximum	$mol.gDW^{-1}$ of hexose	3.14
$Km^{N^2 \Rightarrow Ni}_{inibition}$	Mineral N concentration in nodule symplasm at which maximal the fixation rate reduced by half	$mol.gDW^{-1}$ of mineral N	3.15
$Vmax^{Ni,hexose \Rightarrow AA}_{symp}$	Maximal massic amino acid synthesis rate in root symplasm	$mol.gDW^{-1}.s^{-1}$	5.1
$Km^{Ni \Rightarrow AA}_{symp}$	Affinity coefficient for mineral N fueling amino acid synthesis in root symplasm	$mol.gDW^{-1}$ of mineral N	5.1
$Km^{hexose \Rightarrow AA}_{symp}$	Affinity coefficient for hexose fueling amino acid synthesis in root symplasm	$mol.gDW^{-1}$ of hexose	5.1
$Process(T_{ref})$	Process reference value from literature measured at T_{ref}	same as regulated process	6.1
A, B, C	Parameters related to the temperature regulation to switch between i) temperature-independent process, ii) linear dependency, iii) *Q10* function exponential dependency and iv) bell-shaped dependency with an optimum.	Dimensionless	6.1
Passive processes conductance parameters			
$D^{Ni}_{symp \rightarrow soil}$	Surfacic diffusion parameter of mineral N between root symplasm and soil	$m.s^{-1}$	3.7
$D^{AA}_{symp \rightarrow soil}$	Surfacic diffusion parameter of mineral N between root symplasm and soil	$m.s^{-1}$	3.9
k^{apop}_{water}, k^{symp}_{water}	radial hydraulic conductance of the symplastic and apoplastic water uptake pathways, respectively	$m.s^{-1}.Pa^{-1}$	3.11
k^{phloem}_{water}	radial hydraulic conductance of the water exchange between xylem and phloem	$m.s^{-1}.Pa^{-1}$	4.4
σ	A reflection coefficient of the osmotic component of radial water transport	Dimensionless	3.11

Table 2: continued from previous page

Parameter name	Description	Unit	Eq. n°
r	radius of individual xylem vessels, used to estimate root segment axial water conductance	m	4.3
ρ_{xylem}, ρ_{phloem}	Volumic mass of xylem and phloem solution, respectively	$g\ m^{-3}$	4.1, 4.2

USE CASE: SIMULATION OF WHEAT N UPTAKE

Simulation Scenarios

The aim of this use-case was to illustrate the use of *Root-CyNAPS* to localize and characterize the *most active root zones* in terms of N uptake, and to quantify their contributions to the overall N uptake of the plant. To do so, the simulations reproduced root functioning of wheat grown in hydroponic conditions at 20°C, and simulated the metabolic status of a static root system, starting from a predetermined wheat root system architecture composed of seminal (seed-born), nodal (leaf-born) and lateral (branching) roots (Fig. S3), and a set of initial conditions estimated from literature data. We ran simulations for 24 h using a 1-h time step to ensure that N flows and concentrations would reach an equilibrium for a given set of initial conditions (Fig. S5). We also compared this approach with 1-min time steps during 24h simulations and confirmed similar model convergence (Fig. S6). We therefore assumed the 1-h time step to be a good approximation and used it for all simulation scenarios to lower computation time. We also restrained to 24h simulations as higher simulation periods may have led to unrealistic results given the use of a static architecture and the absence of feedback of N balance on carbon and growth cycles. We compared the physiological state of the root system after 24h between 18 different scenarios, which corresponded to a combination of 6 plant ages with contrasted root architectures from 10 to 60 days after sowing and 5 external concentrations of nitrate from 5 µM to 50 mM (Table 3), as explained below.

Table 3. Simulation scenarios presented in the core text of the article, varying in plant age from 10 to 60 days after sowing, and external nitrate concentrations from 5 µM to 50 mM. The parametrization of the model is identical for all scenarios. A more complete exploration of the plant age and external nitrate concentrations ranges presented below is available in Fig. S14

Scenario name	Plant age (days)	External nitrate concentration (mM)
1, 2	10	0.5, 50
3, 4	20	0.5, 50
5, 6	30	0.5, 50
7, 8, 9, 10, 11	40	0.005, 0.05, 0.5, 5, 50
12, 13, 14, 15, 16	50	0.005, 0.05, 0.5, 5, 50
17, 18	60	0.5, 50

Table 4. Inputs and initial conditions estimated from literature for root system architecture, carbon content heterogeneity, exchanges at the shoot-root interface, soil status and initial N concentrations in tissues. Values presented here illustrate the example of a 50 day-old spring wheat and 0.5 mM N availability (Scenario 14)

Model inputs		
Variable name	**Value**	**References**
Root system architecture	See Fig. 2	(Rees et al., 2025), *RhizoDep*
$[hex_{symp}]_m$	0.01 to 0.4 mmol gDW^{-1}	(Rees et al., 2025), *RhizoDep*
Amino acid consumption by growth	0 to 0.25 µmol h^{-1}	(Rees et al., 2025), *RhizoDep*
$[Ni_{soil}]_v$	0.5 mM	(Devienne et al., 1994)
Ψ_{soil}	0 MPa	Hydroponics scenario to match homogeneous soil concentrations
$\Psi_{xylem(shoot)}$	-0.5 MPa	(McGowan and Tzimas, 1985)
$\Psi_{phloem(shoot)}$	+2.0 MPa	(Dinant et al., 2010)
$[Ni_{xylem}]_v(shoot)$	6 mM	(Kirkman and Miflin, 1979)
$[AA_{xylem}]_v(shoot)$	10 mM	(Kirkman and Miflin, 1979)
$[AA_{phloem}]_v(shoot)$	260 mM	(Winter et al., 1992; Dinant et al., 2010)
T_{soil}	20°C	(Devienne et al., 1994)
Initial concentrations		
Variable name	**Value**	**References**
$[Ni_{symp}]_m$	100 $\mu mol\ gDW^{-1}$	(Devienne et al., 1994)
$[AA_{symp}]_m$	26 $\mu mol\ gDW^{-1}$	(Annunziata et al., 2017)
$[Ni_{xylem}]_m$	100 $\mu mol\ gDW^{-1}$	No initial gradient with symplasm
$[AA_{xylem}]_m$	26 $\mu mol\ gDW^{-1}$	No initial gradient with symplasm
$[AA_{phloem}]_m$	26 $\mu mol\ gDW^{-1}$	No initial gradient with symplasm

Root-CyNAPS Inputs and Adaptation to Simulated Growth Stage

To run the model, input variables and initial conditions were either estimated from experimental data derived from the literature or retrieved using existing FSPMs (Fig. S1). Table 4 presents the complete list of model inputs and initial concentrations for the example of a 50 day-old root system with 0.5 mM of external nitrate (scenario 14). Initial, homogeneous concentrations in the whole root-system were identical for all scenarios. The inputs that varied between scenarios, i.e. root system architecture, hexose concentration profiles, amino acid consumption by growth varying with plant age, and homogeneous external nitrate concentration, are summarized in Table 3 and Fig. S2.

Several key inputs required by *Root-CyNAPS* are not easily available from literature, e.g. the complete acquisition of a growing root system architecture, hexose concentration profiles along roots, or gradients of amino acid consumption

by growth processes. These inputs were therefore specifically estimated using the RhizoDep model, a segment-scale root FSPM simulating root growth, respiration, and rhizodeposition into the soil, based on the distribution of available C within a dynamic 3D root architecture (Rees et al. (2025), see Supplementary Note C). The static 3D root architectures from this use case corresponded to the root architectures simulated by the *RhizoDep* model in a reference scenario validated for spring wheat (scenario Sc1, Rees et al. (2025)). We selected different growth stages to assess the effect of contrasted root system ages on the heterogeneity of N exchanges with the soil (Fig. 2, S2 and S3). Among the continuous range of RSAs simulated by *RhizoDep* over wheat growth from March to August under field conditions, we selected RSAs whose thermal age corresponded to 10, 20, 30, 40, 50 and 60 days-old at constant 20°C for an easier comparison with literature data related to N uptake. In *Root-CyNAPS* root hexose concentration locally regulates active transport, metabolic and symbiotic N processes of the root segment (Eq. 3.2; 3.13 and 5.1). As hexose concentrations are not simulated by *Root-CyNAPS*, we used the hexose concentration profiles already simulated by *RhizoDep* for the 6 RSA described above. Similarly, the consumption rate of amino acids to sustain growth, which needs to be included in the balance of N, was assumed to be proportional to the rate of hexose consumption by growth simulated by *RhizoDep* in these 6 RSA, using a C:N stoichiometry corresponding to a final N content in structural mass of 2% (Barillot et al., 2016). Note that the initial characteristics of the root systems simulated by *RhizoDep* were averaged over 7 hours for each of the 6 targeted plant ages to smoothen the input data provided to *Root-CyNAPS*.

The root-shoot junction water potential for xylem and phloem were set constant across all scenarios to simulate axial water transport (Eq. 4.1), based on average potentials reported by McGowan and Tzimas (1985) and Dinant et al. (2010). Axial N transport from shoot to root in xylem and phloem is possible through advection when the simulated sap flow is oriented downwards (Eq. 4.7), which occurred only for phloem here given the water potentials set at the interface with the shoot. We therefore set constant concentrations of amino acids and mineral N for xylem and phloem at the shoot-root interface based on average concentrations reported by Kirkman and Miflin (1979) and Winter et al. (1992). We also set homogeneous concentrations of external nitrate to compare our simulations with hydroponic experimental results, e.g. Devienne et al. (1994).

Parametrization of Root-CyNAPS for Wheat

The same set of parameters was used for each of the 18 scenarios. All parameters for wheat were taken or recalculated from the literature and, in the case of tissue-specific parameters, completed by our own measurements on cross sections at different distances along wheat roots (Fig. S15). Given the limited number of physiological studies on the spatialization of N processes along the roots and the physiological similarities among cereals, we extended data sourcing to wheat, barley, and maize. Given that wheat does not develop nodules on its root system, the N_2 fixation module (Eq. 3.14) was not used here. A complete list of the 85 model parameters with their meaning, estimated values and their associated reference is provided in Supporting Table S2.

RESULTS

Using *Root-CyNAPS*, we simulated N flows throughout a 3D root system of wheat over a 24h period for a range of plant age and external nitrate concentrations. We then compared the simulation outputs with reference data from the literature, investigated the spatial and temporal variations of net N uptake along the roots, and their possible drivers. We confirmed the existence of *most active root zones* and studied the significance of their net N uptake on the whole root system N balance, while decomposing all underlying processes.

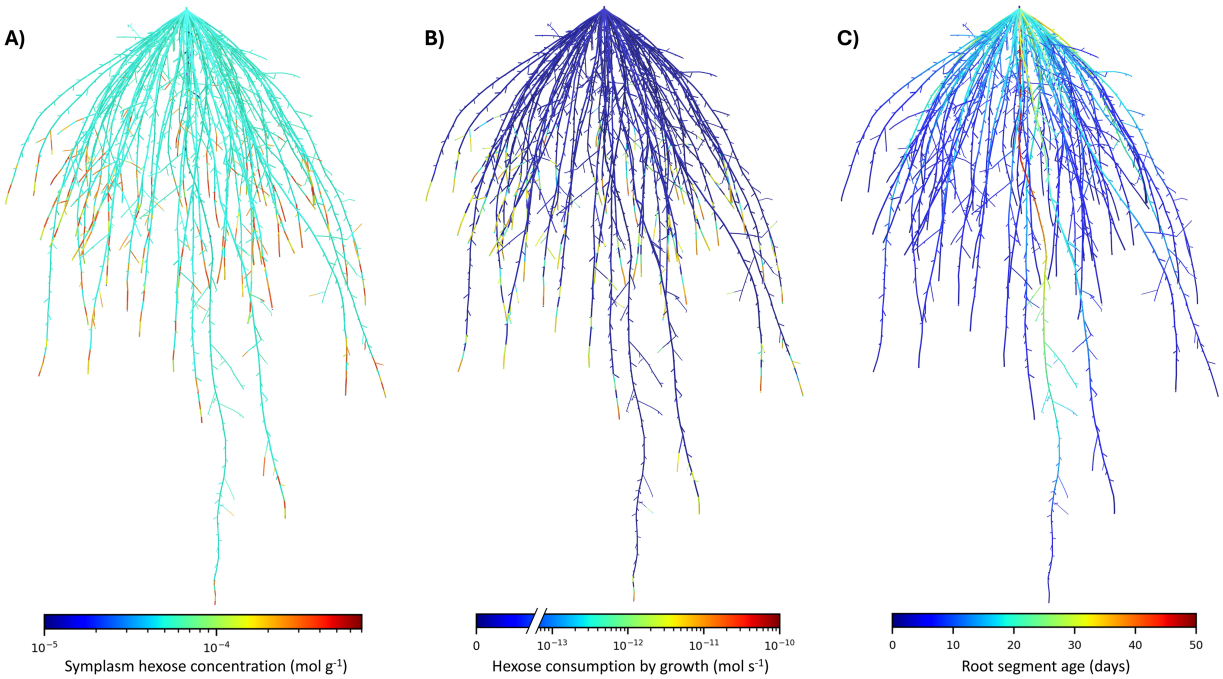

Fig. 2. 3D static root system architecture displaying (A) hexose concentrations heterogeneity, (B) hexose consumption by growth and (C) age of each root segment, computed by the RhizoDep model (Rees et al., 2025) and provided as input to the *Root-CyNAPS* model (50 day-old spring wheat example)

Root-CyNAPS Simulations Showed Realistic Orders of Magnitude

In order to evaluate *Root-CyNAPS*, we compared the range of values of some key variables simulated for wheat plants grown under 0.5 mM nitrate solution with experimental values from the literature obtained for similar concentration conditions (Table 5). Compared scenario was chosen to match the thermal age of the plants at sampling in the experiment. Model outputs were averaged at the scale of the root system and normalized by root dry weight to match the scale of measured data. Note that the experimental variability reported in the literature relates mostly to sampling uncertainty and differences between plant replicates, while the variability of the simulated results arises from the heterogeneity of flow rates and concentrations between individual root segments at the final stage of a specific simulation scenario.

Table 5. Net N uptake, amino acids net exudation, water uptake, mineral N and amino acids symplastic concentration in symplasm simulated by *Root-CyNAPS* after 24h on a static root system of wheat under 0.5 mM nitrate, as compared with values reported in the literature under similar concentrations. Compared scenario was chosen to match the thermal age of the plants at sampling (see Table 3). All variables were normalized by root system dry biomass weight (gDW). Simulated and measured values are indicated as Mean ± Standard Error.

Variable name	unit	*Root-CyNAPS* simulated range	Reference	Scenario number (plant age)	Measured range
Net N uptake	nmol gDW^{-1} s^{-1}	2.9 ± 0.2	Devienne et al. (1994)	5 (30 days)	5.4 ± 3.4
Net N uptake	nmol gDW^{-1} s^{-1}	1.4 ± 0.2	Pang et al. (2015)	3 (20 days)	4.8 ± 0.4
Total amino acids net exudation	nmol gDW^{-1} s^{-1}	0.29 ± 0.10	Phillips et al. (2004)	1 (10 days)	0.31 ± 0.06
Water uptake	µL gDW^{-1} s^{-1}	4.6 ± 0.3	Shi et al. (2013)	5 (30 days)	0.7 ± 0.36
Mineral N root concentration	µmol gDW^{-1}	315 ± 5.4	Devienne et al. (1994)	5 (30 days)	396 ± 66
Amino acids root concentration	µmol gDW^{-1}	71.0 ± 11.9	Annunziata et al. (2017)	3 (20 days)	52.1 ± 2.8

We simulated a net N uptake rate of 2.9 ± 0.2 nmol gDW^{-1} s^{-1} (mean ± SE) for a 30 days-old root system in 0.5 mM nitrate, which intersects with ranges of 5.4 ± 3.4 nmol gDW^{-1} s^{-1} reported by Devienne et al. (1994). For amino acids exudation, water uptake, mineral N concentration and amino acids concentration in symplasm, simulated values were also consistent with the orders of magnitude reported in the literature. Among the 5 different variables compared, only scenario 3 showed an underestimation of simulated net N uptake as compared with the data from Pang et al. (2015).

High Spatial Heterogeneity of Net N Uptake Along the Roots

Our simulation results revealed a high spatial variation of net mineral N uptake along the roots of wheat. As seen in the case of a 50 days-old wheat plant grown in a 0.5 mM nitrate medium (Scenario 14), the net N uptake rate (expressed per length of root segment) showed a 12-fold variation throughout the 3D root system architecture (from 0.5 to 6 nmol cm^{-1} h^{-1}, Fig. 3). When looking more closely at any seminal root, two distinct *most active root zones* for N uptake were simulated along the first 3 cm from the root tip, one near the root apex and the other about 1 cm away, after the first lateral root of the axis (Fig. 3 - Zoom B). Amino acid exudation, a negative component of net N uptake, peaked at the apical root segment and at the same second zone after first lateral root (Fig. 3 - Zoom C). Water uptake was also maximal in the first centimeter near root apex, and decreased gradually with distance from tip without showing a second peak (Fig. 3 - Zoom D).

To test the robustness of this simulated pattern across all types of roots, we ordered root segments of seminal, nodal and lateral roots according to their distance from the tip of the same axis (Fig. 4). One or two regions of maximal net N uptake could again be distinguished, depending on the root type. The first peak between 0.5 to 2 cm distance from root tip reached about 6 nmol cm^{-1} h^{-1} for seminal, nodal and lateral roots. This first peak coincided with the root elongation zone, as simulated by the *RhizoDep* model used here for generating the root structure and hexose concentration profiles (Rees et al., 2025). The second peak was simulated for seminal and nodal roots only between 1.8 to 3 cm distance from tip, reaching up to 6 nmol cm^{-1} h^{-1}, which also coincided with an increase in hexose concentrations (Fig. 2). This second

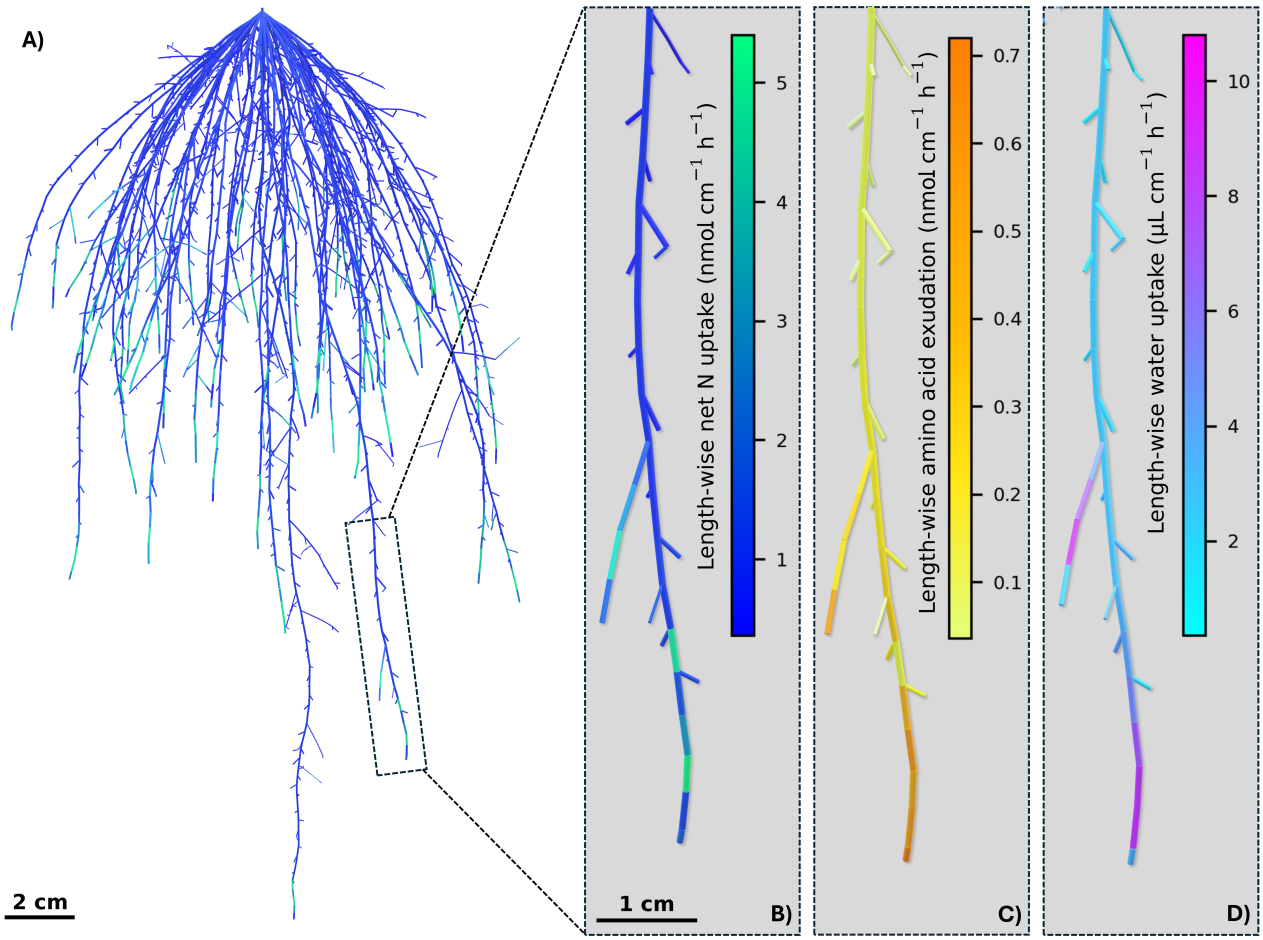

Fig. 3. Visualization of the spatial heterogeneity of net N uptake within the 3D root system of wheat under Scenario 14 (50 days-old, 0.5 mM nitrate), as simulated by *Root-CyNAPS*. The uptake rate of each root segment was normalized by its corresponding length (A). The zoomed views focus on active exchange zones for (B) net N uptake, (C) amino acid exudation and (D) water uptake over the first 10 cm of a seminal root. All variables were normalized by root segment length.

zone corresponded with an increase in sucrose unloading and a disturbance in transport barriers associated with the emergence of the lateral root closest to root tip (Rees et al. 2025).. This second zone coincided with the emergence of the lateral root closest to root tip which disturbed transport barriers. This second peak was not observed on lateral roots, which usually did not support second-order laterals primordium (Fig. 2). The variable position of these two regions among individual roots was correlated to differences in elongation rate between root axes, as less variability of net N uptake was observed when plotting it with root segment's age (Fig. S7). Similar regions of maximal net N uptake were observed when normalizing flows by root segment structural mass (Fig. S8). Interestingly, we simulated negative rates of net N uptake for some nodal and lateral roots between 0 to 1 cm distance from root tip, meaning that losses of mineral N and amino acids exceeded mineral N uptake in the apical zone of these roots.

When decomposing net N uptake between gross N uptake and N loss through diffusion, and looking at the best explanatory variables for the simulated spatial heterogeneity (Fig. S10, S11 and S12), we observed that for some axis types gross N uptake could be correlated with root exchange surface, water uptake, hexose concentrations, mineral N concentrations, and N export to xylem (r = 0.66, 0.65, 0.94, 0.98 and 0.77, respectively) while it was poorly correlated

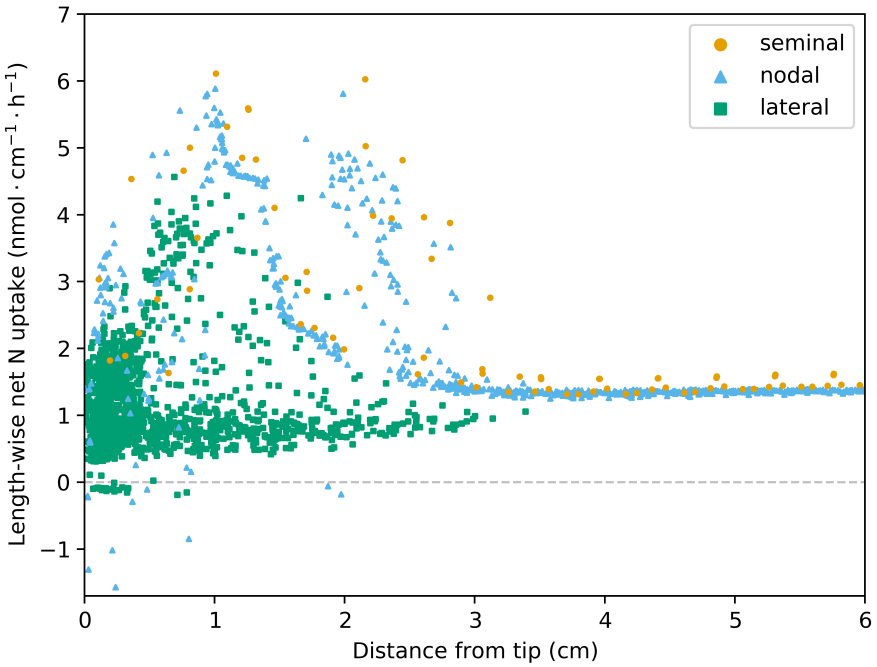

Fig. 4. Evolution of net N uptake per unit root length with the distance from root tip, as simulated by *Root-CyNAPS* for wheat under Scenario 14 (50 days-old, 0.5 mM nitrate). Each individual point corresponds to one root segment. Colors indicates root types: seminal (orange circles), nodal (blue triangles), and lateral (green squares). For each root type 6, 51 and 1784 axes are represented on the figure, respectively.

to amino acid concentrations in the symplasm. N loss through diffusion was in turn mainly correlated to concentrations of amino acids in the symplasm ($r = 0.76$, Fig. S12).

A Variable Contribution of Most Active Root Zones to Plant N Uptake

To capture the contribution of any *most active root zones* in the total mineral N uptake, we reordered the root segments according to their net N uptake rate per root length, and calculated their cumulative contribution to both the total length and total N uptake by the root system (Fig. 5). Both cumulative variables were then converted into the proportions of root system total uptake and total length, respectively, and plotted for root-system ages from 10 to 60 days-old and culture solution nitrate concentrations from 0.005 to 50 mM. We illustrated a 10% of root length threshold on the figure. The scenarios presented here were selected from a larger exploration (see Fig. S14).

According to our simulations, the top 10% of the most active root parts contributed between 20% and 80% to the total N uptake of the root system, depending on plant age and on the external nitrate concentration (Fig. 5). This top 10% most active root length accounted for about 12% of root system structural mass for all plant ages (Fig. S13). In general, the contribution of root segments to the total N uptake of the root system did not follow their contribution to total root length, as the cumulative N uptake did not evolve linearly with the cumulative root length. On one hand, the sensitivity of this relationship to plant age differed according to the external nitrate concentration, as illustrated here with 0.5 mM (Fig. 5A) and 50 mM (Fig. 5B). At 0.5 mM nitrate, root system age had little influence, with an average contribution of 30% of total N uptake by the top 10% of root length. At 50 mM nitrate, this contribution ranged from 40 to 80% of total N uptake. On the other hand, the response to N concentration varied across plant ages. At 20 days, an increase in external nitrate concentration from 0.005 mM to 50 mM had little influence, with an average contribution

to N uptake of 45% (Fig. 5C). In contrast at 50 days, the external concentration of nitrate exerted a large effect on the spatial distribution of mineral N uptake, with contributions between 30 and 60% of total N uptake (Fig. 5D). Another way to analyze these outputs is to consider the percentage of active root length accounting for 50% of plant's net N uptake (black dotted line Fig. 5). At 50 mM, despite important variations in the fraction of plant's N uptake corresponding to the top 10% root length, the percentage of root length grouping 50% of N uptake was restrained to 5-15% of root length (Fig. 5B). In contrast, under varying nitrate concentrations at 50 days, an increased variability of the length associated with 50% of N uptake was reported, ranging between 8 and 32% of total root length (Fig. 5D).

When looking for scenarios where 10% of root length would account for the *majority* of net N uptake (i.e. more than 50%, top left dial), we observed no straightforward relationship with plant age or external nitrate concentration. For an external nitrate concentration of 50 mM (Fig. 5B), the 50% threshold is reached for root system older than 50 days-old, but also at 20 days. For a plant age of 50 days (Fig. 5D), the 50% threshold occurs both at 0.005 and 50 mM, with no intermediate scenarios reaching the threshold.

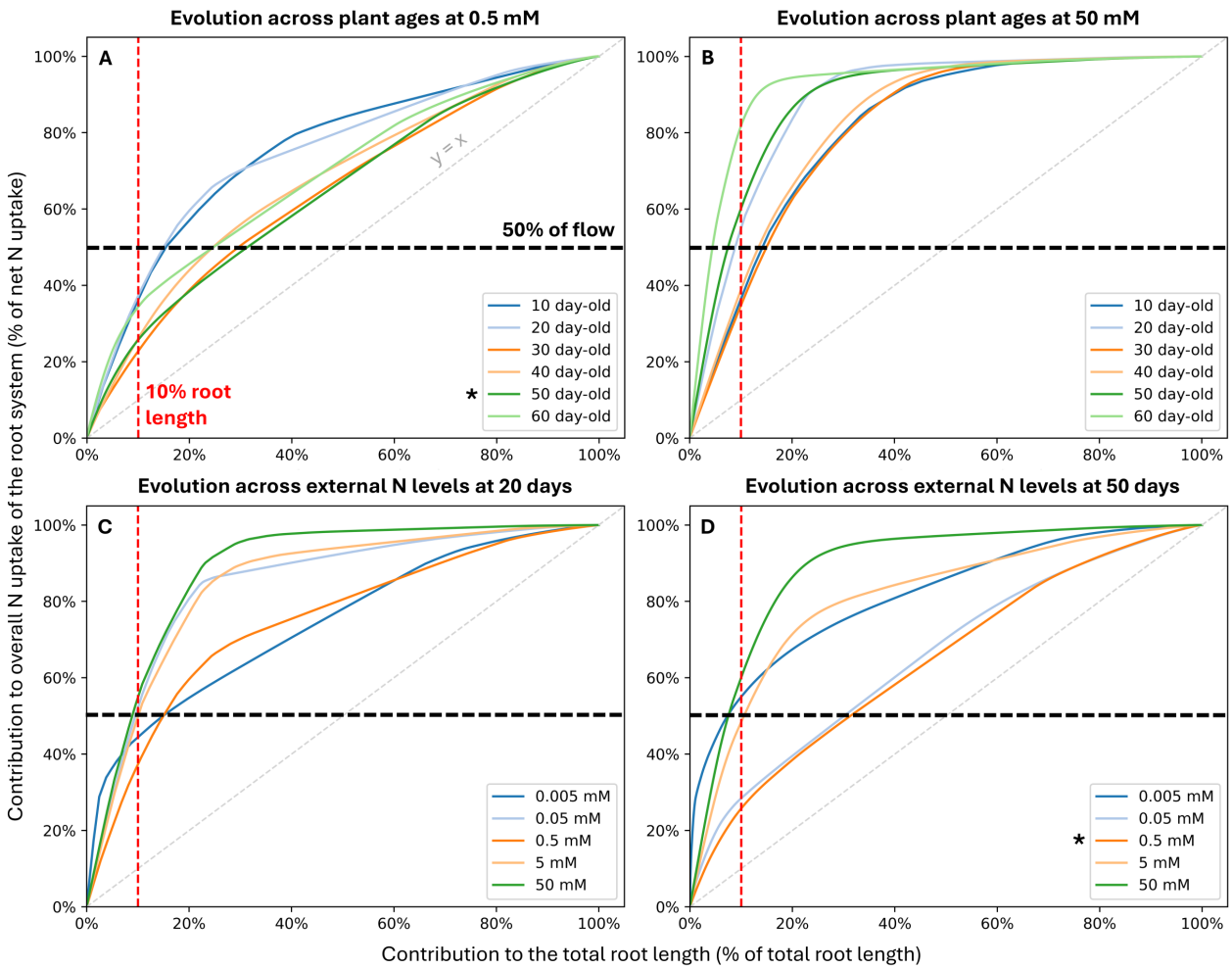

Fig. 5. Evolution of the cumulative contribution of roots to the net N uptake of the root system with their cumulative contribution to total root length, as simulated by *Root-CyNAPS*. Root segments were first ranked in descending order according to their rate of net N uptake normalized by length. The cumulative values are plotted for distinct root system ages in 0.5 mM (A) and 50 mM (B) nitrate solution, and for various external concentrations for 40 and 50 day-old root systems (C and D respectively). The vertical red dotted line corresponds to an arbitrary threshold of 10% of root system length, and the horizontal black dotted line corresponds to a threshold above which more than 50% of total net N uptake flow is cumulated

. The diagonal grey dotted line represents the theoretical curve expected if the contribution of root segments to N uptake followed exactly their contribution to root length. Scenario 14 is positioned on the graphs with a star (*).

Importance of Water-Mediated N Uptake and N Exudation in Net N Uptake

In Fig 6, we represented the simulated inflows and outflows of the root system at both root-soil and root-shoot interfaces. Root-soil exchanges resulted from active transmembrane N uptake into root symplasm, water-mediated N uptake, amino acids exudation and mineral N diffusive loss from root to soil. For all scenarios, the mineral N export to the shoot through the transpiration stream followed the mineral N uptake from soil minus mineral N diffusion to soil, showing that few retention of mineral N occurred in the root system.

When increasing external N concentration from 0.05 to 5 mM on a 50-day old root system (Fig. 6A), an increase in total mineral N uptake was simulated from 5.7 to 25 µmol gDW^{-1} h^{-1}, respectively. A progressive shift in the contribution

of distinct processes to mineral N uptake was also observed with increased nitrate concentrations. At 0.05 and 0.5 mM, water-mediated N uptake was mostly negligible compared to mineral N active uptake (< 10%). In contrast, at 5 mM, water-mediated N uptake accounted for about 65% of the total flux.

When considering variations over plant age at 0.5 mM nitrate concentration (Fig. 6B), we observed that net N uptake relative to dry mass was maximal for the 30 days-old root system. This coincided with the maximal hexose concentrations in the root system at 30 days (Fig. S4). Interestingly, the N uptake rate through water transport remained stable (2 to 3 µmol gDW^{-1} h^{-1}) across all root system ages. The simulated variation in net N uptake across plant ages was therefore mainly related to the variation in active N uptake and total N loss through diffusion. The latter had a large impact on net N uptake, subtracting from a third to half of N inflows in all age scenarios at 0.5 mM. In contrast at 50 days old despite variations in external nitrate levels (Fig. 6A), total N loss through diffusion remained stable at about 3 µmol gDW^{-1} h^{-1}.

DISCUSSION

We designed a new model of N and water uptake combining (i) local anatomical features of a root segment, (ii) N balance over a set of N transport and metabolic processes regulated by local concentrations and anatomy, and (iii) the co-transportation of metabolites by radial water uptake and axial water transport between root segments through the coupled sap flows of xylem and phloem. *Root-CyNAPS* has been designed to simulate a wide range of species, including *Fabaceae* species able to fix atmospheric nitrogen, or species with tuberized pivot root as in the *Brassica* genus. In this study, *Root-CyNAPS* was used to simulate the heterogeneity of N uptake and exudation rates throughout a 3D root system architecture of wheat in hydropony, to locate *most active root zones* for the different components of net N uptake, and to study their contribution to root system N balance. Our simulations showed that *most active root zones* contribution to roots N balance is so variable that this concept appears of little practical use. We also confirmed that water-mediated N uptake and N exudation can substantially influence net N uptake.

Determinants of Root N Uptake Most Active Root Zones

On a range of plant age and external N availability, we located two *most active root zones* for net N uptake per unit root length, one near the apex of all root types, the other one - for seminal and nodal roots only - at the emergence of a lateral primordium. The existence of these two zones mainly resulted from variations in root exchange surface, hexose symplastic concentration and water uptake along the roots (see details in supplementary note B). Interestingly, a similar *most active root zone* located next to the apex was observed for net N uptake, water uptake and N exudation (Fig. 3), suggesting that root tips represent general *hotspots* of root-soil exchange. However, detailed studies focusing on this co-location could not be found in the literature, given the complexity of measuring several root-soil fluxes simultaneously along roots. Evidences of maximal exchange rates near apices were reported independently for N uptake and N exudation (Zhong et al., 2014; Canarini et al., 2019). In this context, FSPMs as *Root-CyNAPS* appear as valuable tools to bridge between studies, to fill experimental gaps (Louarn and Song, 2020), and to quantify the relevance of theoretical concepts.

Most Active Root Zones : a Fluctuating Concept

Our simulations showed that the contribution of active root zones to the overall N uptake by the plant dramatically changed according to plant age and external nitrate concentration (Fig. 5). In particular, our model simulated that the top 10% of roots that were most active contributed between 20% and 80% of total net N uptake. The contribution of the top 10% was minimal in 30 days-old plants compared to other ages, which coincided with an overall higher accumulation of hexose in the root system at nodal roots emergence, resulting in a higher homogeneity of N uptake rates throughout

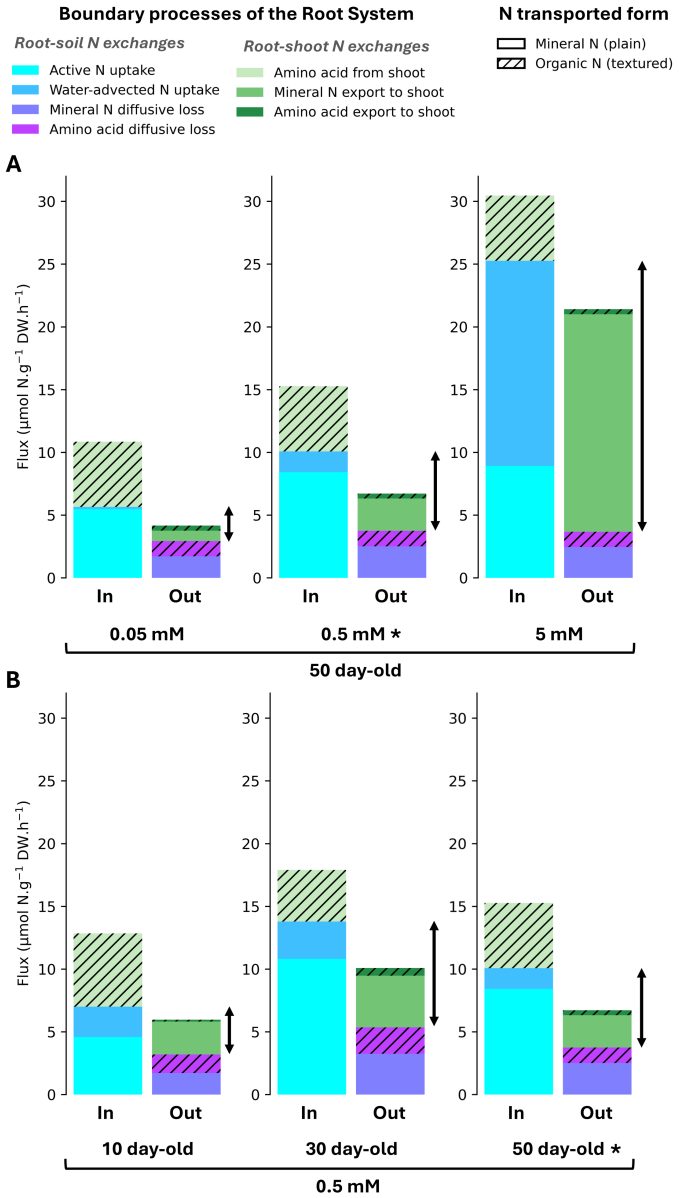

Fig. 6. Decomposition of total root N balance into N inflows and outflows simulated by *RootCyNAPS* for contrasted nitrate concentrations (A) and root system ages (B). N input flows include active uptake through membrane transporters, direct uptake through water advection towards the xylem, and amino acids inputs from the shoots through the phloem. N output flows include N export to the shoots through the xylem, as well as the exudation of amino acids and diffusive loss of mineral N towards the soil. All flows are normalized by root system dry weight ($\mu mol\ gDW^{-1}\ h^{-1}$). Mineral N transport is shown with plain colors and amino acid transport with hashed colors. The length of vertical arrows indicate net root N uptake, resulting from the difference between root N uptake and root N losses. Scenario 14 is positioned on the graphs with a star (*).

the root system (Fig. S2 & S4). Young root systems also presented the least variations in the contribution of 10% active root length (Fig. 5C). In contrast, older root systems ($\geq$ 50 days-old) showed a higher spatial heterogeneity of N uptake rate and were more sensitive to a change in external nitrate concentrations. The wider diversity of root types, growth

dynamics, hexose concentrations, and tissue aging profiles in older root systems would indeed amplify the heterogeneity of N uptake along the roots (Wells and Eissenstat, 2002; Vetterlein and Doussan, 2016).

Complementary to the 10% active root length viewpoint, Fig. 5 also allows estimating the fraction of root length required to cumulate a given share of net N uptake (e.g. 50%). In our simulations, the fraction of total root length generating 50% of total flow varied substantially with nitrate availability, especially at 50 days (Fig. 5D): extreme concentrations led to more polarized N uptake (a small fraction of root length was sufficient to reach 50% of total net N uptake), whereas intermediate concentrations produced a near-linear cumulative relationship, indicating a more even distribution of N uptake across a larger fraction of the root system. Such shifts are consistent with strong age-dependent changes in root function, with nutrient uptake capacity declining rapidly with tissue aging and differentiation (Volder et al., 2005; Lynch et al., 2024). While our simulations suggest that aging increases functional contrasts in the root system, they also show that, under some intermediate soil nitrate concentration, older root regions can contribute to N uptake as much as younger parts of the root system. Importantly, a low direct contribution of most of the root system to net N uptake under extreme nitrate concentrations does not imply that this "non-active" root length is non-functional. Older root portions contribute to water and metabolite transport, storage and anchorage, and they condition where new absorptive roots can be deployed (Lynch, 2022). In heterogeneous environments, architectural deployment remains critical to encounter and exploit nutrient-rich patches, with plant plasticity relying on the ability of the plant to dynamically position young roots in favorable locations (Hodge, 2004; Liu et al., 2020). Conversely, understanding under which conditions older regions can regain activity (e.g. via shifting N uptake activity, lateral emergence, altered barrier development, or changes in carbon/nitrogen status) is also key to explore adaptive foraging strategies and root plasticity.

Hodge et al. (2009) proposed that 10% of total root length would account for the majority (i.e. $> 50\%$) of N uptake. Our scenario exploration, from 10 to 60 days-old and from 0.005 to 50 mM external nitrate, suggests that this is the exception rather than the norm, as only 10 out of 99 tested scenarios led to this situation (Fig. S14). Our results are however comparable with a previous estimation done by Robinson et al. (1991a), who calculated that between 2% and 22% of wheat's root length would explain the totality of N uptake. Despite their model was dramatically different, considering diffusive-only and non-saturating N uptake, we simulated that 22% of root length could indeed explain almost all of plant N uptake under specific conditions (22% of root length contributed to 90% of net N uptake in Fig. S14, scenario 18). In contrast, the lower reported value, 2% of root length, could never gather all of root system flow in our simulations and represented at most 10% of plant N uptake.

Overall, this work confirmed the existence of *most active root zones*, whose locations are defined by root tips dynamic growth and root tissue (de)differentiation. However, the substantial variability in the contribution of these zones to total N uptake, depending on plant age and external N concentration, highlights that mature parts of the root system cannot be neglected when simulating N and water uptake in a 3D root system architecture. Consequently, simple approaches - such as assuming uniform uptake rates along the roots or assuming that a constant fraction of the root system is exclusively responsible for the uptake - are useful to study average N kinetic properties of the root system, but may prove insufficient to explore the local variations in uptake rates along roots over soil depth and over time. By integrating histological and physiological processes at the root segment scale, the *Root-CyNAPS* model is a first step to overcome these limitations, simulating gradients of N and water uptake along the roots as an emergent outcome of localized processes. It opens new avenues for conducting numerical experiments to explore how these gradients adapt to plant and environmental variations, and assess their broader impacts on root system net N balance.

Deciphering Root Net N Balance

Simulation results indicate that water-driven N uptake, which may occur when endodermis does not fully block the apoplastic pathway, can be negligible compared to the transmembrane active N uptake at 0.05 mM, but can account for

up to 51% of total mineral N uptake at 5 mM (Fig. 6). We did not find any measurements of the specific contribution of water advection through the apoplasm to the overall N uptake in the available literature. Hydroponics experiments on wheat (Lu and Fricke, 2023) and rice (Faiyue et al., 2010) grown in 50 mM of external sodium showed an apoplastic "bypass flow" of sodium representing 6.6 ± 2.3 % and 26.0 ± 1.2 % of total plant Na^+ uptake, respectively. Although these results cannot be directly transposed to mineral N uptake, our simulations nonetheless intersected this 6 to 26% range, e.g. for scenario 14 (50 days-old, 0.5 mM external nitrate) where the apoplastic N uptake accounted for 16% of the total. In turn, the 65% value simulated by *Root-CyNAPS* at 5 mM external nitrate appears as a possible overestimate, which could relate to the parametrization uncertainties of endodermis differentiation rates along the roots. However, both previously-published measurements and our new simulations confirm that this apoplastic pathway is non negligible in plant N balance, and would deserve further investigations.

Another highlighted component of net N uptake was the passive loss of mineral N and amino acids through diffusion from roots to soil, representing more than a third of gross mineral N uptake in most scenarios. N exudation range is often compared to plant net N acquisition (i.e. N content) in labeling studies to illustrate its significance in plant N budget. In our simulations from 10 to 60 days-old and 0.05 to 5 mM external nitrate, N exudation ranged between 14% and 52% of gross N uptake (Fig. 6). This corroborate with the ranges reported for C3 cereals by Wichern et al. (2008), 14% median and 4 to 56% extrema across 11 studies, as well as the review of Jones et al. (2009) reporting a 10% median and 1 to 56% extrema from 33 studies on non legume species. It is however worth noting that we performed a uniform initialization of amino acids symplastic concentrations at 25 $\mu mol\ \ gDW^{-1}$ in the whole root system and for all scenarios, a value transposed from Annunziata et al. (2017) since we could not find measured profiles of amino acid concentrations along the roots of cereals in the available literature. This assumption led to scenarios where the amino acid levels and consequently the related N exudation rates did not align with the external N availability. For example, in scenario 13 (50 days-old, 0.05 mM), net N uptake was strongly lowered by total N exudation, which would not be sustainable over the long run. This mainly relates to the absence of root-shoot interactions in *Root-CyNAPS*, which are expected to lower amino acids allocation to the root system at low external nitrate availability to ensure a positive N balance (Wang and Ruan, 2015). Note also that labeling studies mentioned earlier all measured total N release from the root, including all types of N rhizodeposition pathways and mineral N loss. Our model accounts solely for amino acids and mineral N exudation, while less-studied pathways such as protein release, cell cap sloughing or senescence may contribute substantially and modulate the N balance simulated here.

Root-CyNAPS Use Cases, Limitations and Coupling Perspectives

To date, the model is restricted to short term simulations on static 3D root systems because it does not simulate root growth and its regulation by local N balance. It could for example be used to explore root traits and ideotypes in contact with vertical gradients of N and water availability reported in soils (Dathe et al., 2016; Hayat et al., 2019; Rangarajan et al., 2022), or for the analysis of knockout experiments results by shutting down a process or an anatomical feature of the root system, e.g. root hairs (Lippold et al., 2021).

One of the main challenges to adapt Root-CyNAPS to other species is to estimate parameter values, either through estimations from the literature (Table S2) or dedicated experiments (Fig. S15). To limit the parametrization effort needed for further uses of the model, a complete sensitivity analysis would help to identify the key measurable parameters that should be targeted by experiments and literature review (Blanc et al., 2021). This approach would in particular highlight the sensitivity of the model to the discretization parameters, i.e. the 1 h time-step and 4.5 mm segment dimension, which have been selected in this work as a compromise between the realism of root architecture, the time-scale of physiological processes, and the performance of the model. Here model exploration was also limited by the availability and reliability of input data needed by *Root-CyNAPS* (Table 4). First, the precision of the root system architecture provided to the model is critical to study the influence of root segments topology and positioning. For this reason, we eventually decided

to use simulated 3D root architectures rather than experimental ones, which suffered from segmentation errors (data not shown). Second, *Root-CyNAPS* expects profiles of hexose concentrations and amino acids consumption rates for growth along the roots as an input, and we showed these input gradients to be influential in the outputs of the model (Fig. S11). Since such spatial and age dependent measurements are scarce in the literature (Ogawa, 2005), we used outputs of the *RhizoDep* model at different plant ages as a first estimate, carrying their own uncertainties. Third, we assumed the boundary water potentials and N concentrations at the root-shoot junction to be identical for all scenarios and constant over time, due to a lack of literature data.

Despite these limitations, *Root-CyNAPS* first simulations showed realistic orders of magnitude for N-water uptake, N exudation, and symplastic N concentrations at root system scale (Table 5). For some metabolic and internal transport processes described in the model, we could not find suitable validation data in the literature. Nonetheless we assume their inclusion in the balance of the model provide useful access to intermediate physiological indicators during *in silico* explorations, unveiling patterns that would have stayed hidden behind experimental uncertainties. Validation methods based on relative variations between treatments have been proposed as an alternative to quantitative comparison with experiments (Vos et al., 2010; Wang et al., 2018, 2020). These methods should be targeted for FSPMs as *Root-CyNAPS* that inherently suffer from data scarcity because of their costly requirements for spatial and temporal parametrization, initialization and validation.

The coupling root-focused FSPMs with other 3D functional-structural plant and soil models has also been suggested as a strategy to account for the interdependence of C-N-water cycles at various scales of the soil-plant-atmosphere system (Passot et al., 2019). Such modeling framework would overcome the need for complex input data when using *Root-CyNAPS* alone, as it would explicitly simulate the spatial and temporal variations of C-N-water interactions within the growing root system, at the root-soil interface and at the root-shoot junction. Consequently, we foresee the coupling of *Root-CyNAPS* with 3D C budget and root growth models to better account for the variability of amino acids consumption by growth in a dynamic architecture, but also the feedback of local root N availability on growth rates and branching processes (Hodge et al., 1999; Cambui et al., 2011). A coupling with a shoot FSPM would allow to account for interactions between resource uptake from the soil and shoot activity (Wang and Ruan, 2015; Gloser et al., 2020). Finally, coupling *Root-CyNAPS* with a 3D soil model would enable to address quantitatively key concepts of the literature on C-N nutrient cycling in the rhizosphere (Moreau et al., 2019; Carminati et al., 2016; Dijkstra et al., 2013). Studying such dynamic interactions would unveil critical determinants of nutrient acquisition strategies adopted by plants under heterogeneous field conditions.

CONCLUSION

Root-CyNAPS is a mechanistic root model simulating the heterogeneity of net N uptake throughout a 3D root system architecture, as an emerging property of regulations by local C & N metabolite concentrations, N & water transport, N transformations, and local root anatomy. Our simulations on wheat grown in hydroponics highlighted zones of highest N uptake, located at root apices and at the site of lateral roots emergence, whose contribution to plant N balance was highly variable across plant ages and external N concentrations. This challenges the concept of *active root zones* and demonstrates that less active, older and more differentiated parts of the root system should not be neglected, as they can represent a significant proportion of the uptake. These results also highlight the importance of accounting for water transport and N exudation along roots in plant net N uptake. Overall, *Root-CyNAPS* is a generic open-source root model that can be used on several species to study the physiological determinants of N and water exchanges along roots. Coupling *Root-CyNAPS* with existing root, shoot and soil mechanistic models will enable further exploration of these determinants in the soil-plant-atmosphere continuum, considering multiscale interactions among C, N and water cycles.

MODEL IMPLEMENTATION AND ACCESSIBILITY

Root-CyNAPS was implemented in Python, leveraging the Multiscale Tree Graph (MTG, Pradal and Godin (2020)) from the *OpenAlea* platform (Pradal et al., 2008, 2015). *Root-CyNAPS* is publicly available under an open-source license at https://github.com/openalea/Root-CyNAPS.

COMPETING INTERESTS

No competing interest is declared.

AUTHOR CONTRIBUTIONS STATEMENT

Writing, review and editing: T.G., C.P., R.B., C.R-M., M.G., A.J., F.R.; conceptualization: T.G., C.P., R.B., A.J., F.R. ; software: T.G., C.P., F.R.

ACKNOWLEDGMENTS

The authors thank F. Bauget for his help on the adaptation of the *Hydroroot* model. This work benefited from the support of the project MIXROOT-C (2021-2024) funded by the European Union's Horizon 2020 research and innovation program under grant agreement No. 862695 EJP SOIL. The PhD of T.G. was funded by the French doctoral school ABIES. C.P. received support from CIRAD's MaCS4Plants network, initiated by the AGAP Institute and AMAP joint research units, and from the EU's Horizon research and innovation program (IntercropValues project No. 101081973).

The authors thank the anonymous reviewers for their constructive comments.

SUPPLEMENTARY MATERIAL

Additional information is available in the Supplementary Material file for more details about the *Root-CyNAPS* model. A complete list of model equations and parametrization in the case of wheat is detailed. We also present model inputs, parametrization, simulated heterogeneous N flows along roots and their physiological determinants, as well as the contribution of most active N exchange zones to plant balance.

REFERENCES

E. N. D. C. Andrade. The Viscosity of Liquids. *Nature*, 125(3148):309–310, Mar. 1930. ISSN 1476-4687. doi: 10.1038/125309b0. URL `https://www.nature.com/articles/125309b0`. Publisher: Nature Publishing Group.

M. ANDREWS, J. D. MORTON, M. LIEFFERING, and L. BISSET. The Partitioning of Nitrate Assimilation Between Root and Shoot of a Range of Temperate Cereals and Pasture Grasses. *Annals of Botany*, 70(3):271–276, Sept. 1992. ISSN 0305-7364. doi: 10.1093/oxfordjournals.aob.a088469. URL `https://doi.org/10.1093/oxfordjournals.aob.a088469`.

Anjana, S. Umar, Y. P. Abrol, and M. Iqbal. Modulation of Nitrogen-Utilization Efficiency in Wheat Genotypes Differing in Nitrate Reductase Activity. *Journal of Plant Nutrition*, 34(6):920–933, Feb. 2011. ISSN 0190-4167. doi: 10.1080/01904167.2011.544529. URL `https://doi.org/10.1080/01904167.2011.544529`. Publisher: Taylor & Francis _eprint: https://doi.org/10.1080/01904167.2011.544529.

M. G. Annunziata, L. F. Ciarmiello, P. Woodrow, E. Maximova, A. Fuggi, and P. Carillo. Durum Wheat Roots Adapt to Salinity Remodeling the Cellular Content of Nitrogen Metabolites and Sucrose. *Frontiers in Plant Science*, 7, Jan. 2017. ISSN 1664-462X. doi: 10.3389/fpls.2016.02035. URL `http://journal.frontiersin.org/article/10.3389/fpls.2016.02035/full`.

S. Barber and J. Cushman. Nitrogen uptake model for agronomic crops. *Modeling Waste Water Renovation- Land Treatment*, 1981.

R. Barillot, C. Chambon, and B. Andrieu. CN-Wheat, a functional–structural model of carbon and nitrogen metabolism in wheat culms after anthesis. I. Model description. *Annals of Botany*, 118(5):997–1013, Oct. 2016. ISSN 0305-7364. doi: 10.1093/aob/mcw143. URL https://doi.org/10.1093/aob/mcw143.

F. Bauget, V. Protto, C. Pradal, Y. Boursiac, and C. Maurel. A root functional-structural model allows to assess effects of water deficit on water and solute transport parameters. *Journal of Experimental Botany*, page erac471, 2023. ISSN 0022-0957. doi: 10.1093/jxb/erac471. URL https://doi.org/10.1093/jxb/erac471.

M. Bechmann, C. Schneider, A. Carminati, D. Vetterlein, S. Attinger, and A. Hildebrandt. Parameterizing complex root water uptake models – the arrangement of root hydraulic properties within the root architecture affects dynamics and efficiency of root water uptake, Jan. 2014. URL https://hess.copernicus.org/articles/18/4189/2014/hess-18-4189-2014-discussion.html.

E. Blanc, J. Enjalbert, and P. Barbillon. Automatic calibration of a functional-structural wheat model using an adaptive design and a metamodelling approach, July 2021. URL https://www.biorxiv.org/content/10.1101/2021.07.29.454328v1. Pages: 2021.07.29.454328 Section: New Results.

E. G. Bollard. Transport in the Xylem. 1960.

S. Buckley, R. Brackin, S. Jämtgård, T. Näsholm, and S. Schmidt. Microdialysis in soil environments: Current practice and future perspectives. *Soil Biology and Biochemistry*, 143:107743, Apr. 2020. ISSN 0038-0717. doi: 10.1016/j.soilbio.2020.107743. URL https://www.sciencedirect.com/science/article/pii/S0038071720300407.

C. A. Cambui, H. Svennerstam, L. Gruffman, A. Nordin, U. Ganeteg, and T. Näsholm. Patterns of Plant Biomass Partitioning Depend on Nitrogen Source. *PLOS ONE*, 6(4):e19211, 2011. ISSN 1932-6203. doi: 10.1371/journal.pone.0019211. URL https://journals.plos.org/plosone/article?id=10.1371/journal.pone.0019211. Publisher: Public Library of Science.

A. Canarini, C. Kaiser, A. Merchant, A. Richter, and W. Wanek. Root Exudation of Primary Metabolites: Mechanisms and Their Roles in Plant Responses to Environmental Stimuli. *Frontiers in Plant Science*, 10, Feb. 2019. ISSN 1664-462X. doi: 10.3389/fpls.2019.00157. URL https://www.frontiersin.org/journals/plant-science/articles/10.3389/fpls.2019.00157/full. Publisher: Frontiers.

Y. Cao, X. Sun, Y. Shi, C. Lu, Y. Miao, Z. Chen, and S. Han. Quantitative evidence of underestimated nitrogen rhizodeposition using 15N split-root labeling during spring wheat developmental period. *CATENA*, 207:105618, Dec. 2021. ISSN 0341-8162. doi: 10.1016/j.catena.2021.105618. URL https://www.sciencedirect.com/science/article/pii/S0341816221004768.

A. Carminati, M. Zarebanadkouki, E. Kroener, M. A. Ahmed, and M. Holz. Biophysical rhizosphere processes affecting root water uptake. *Annals of Botany*, 118(4):561–571, Oct. 2016. ISSN 0305-7364. doi: 10.1093/aob/mcw113. URL https://www.ncbi.nlm.nih.gov/pmc/articles/PMC5055629/.

S. Ceolin, S. J. Schymanski, D. Van Dusschoten, R. Koller, and J. Klaus. Root growth dynamics and allocation as a response to rapid and local changes in soil moisture. *Biogeosciences*, 22(3):691–703, Feb. 2025. ISSN 1726-4189. doi: 10.5194/bg-22-691-2025. URL https://bg.copernicus.org/articles/22/691/2025/.

D. T. Clarkson. Roots and the delivery of solutes to the xylem. 1993.

D. T. Clarkson, A. W. Robards, and J. Sanderson. The tertiary endodermis in barley roots: Fine structure in relation to radial transport of ions and water. *Planta*, 96(4):292–305, Dec. 1971. ISSN 1432-2048. doi: 10.1007/BF00386944. URL https://doi.org/10.1007/BF00386944.

V. Couvreur, M. Faget, G. Lobet, M. Javaux, F. Chaumont, and X. Draye. Going with the Flow: Multiscale Insights into the Composite Nature of Water Transport in Roots. *Plant Physiology*, 178(4):1689–1703, Dec. 2018. ISSN 0032-0889. doi: 10.1104/pp.18.01006. URL https://doi.org/10.1104/pp.18.01006. Number: 4.

C. Cruz, S. H. Lips, and M. A. Martins-Loução. Uptake regions of inorganic nitrogen in roots of carob seedlings. *Physiologia Plantarum*, 95(2):167–175, Feb. 1995. ISSN 0031-9317, 1399-3054. doi: 10.1111/j.1399-3054.1995.tb00824.x. URL https://onlinelibrary.wiley.com/doi/10.1111/j.1399-3054.1995.tb00824.x.

A. Dathe, J. A. Postma, M. B. Postma-Blaauw, and J. P. Lynch. Impact of axial root growth angles on nitrogen acquisition in maize depends on environmental conditions. *Annals of Botany*, 118(3):401–414, Sept. 2016. ISSN 0305-7364. doi: 10.1093/aob/mcw112. URL https://doi.org/10.1093/aob/mcw112.

D. A. Day*, P. S. Poole, S. D. Tyerman, and L. Rosendahl. Ammonia and amino acid transport across symbiotic membranes in nitrogen-fixing legume nodules. *Cellular and Molecular Life Sciences CMLS*, 58(1):61–71, Jan. 2001. ISSN 1420-9071. doi: 10.1007/PL00000778. URL https://doi.org/10.1007/PL00000778.

P. M. De Souza Campos, F. Borie, P. Cornejo, S. Meier, J. A. López-Ráez, López-Garcia, and A. Seguel. Wheat root trait plasticity, nutrient acquisition and growth responses are dependent on specific arbuscular mycorrhizal fungus and plant genotype interactions. *Journal of Plant Physiology*, 256:153297, Jan. 2021. ISSN 01761617. doi: 10.1016/j.jplph.2020.153297. URL https://linkinghub.elsevier.com/retrieve/pii/S0176161720301875.

T. De Swaef, O. Pieters, S. Appeltans, I. Borra-Serrano, W. Coudron, V. Couvreur, S. Garré, P. Lootens, B. Nicolaï, L. Pols, C. Saint Cast, J. Šalagovič, M. Van Haeverbeke, M. Stock, and F. Wyffels. On the pivotal role of water potential to model plant physiological processes. *in silico Plants*, 4(1), Jan. 2022. doi: 10.1093/insilicoplants/diab038. URL https://dx.doi.org/10.1093/insilicoplants/diab038.

E. E. Deinum, B. M. Mulder, and Y. Benitez-Alfonso. From plasmodesma geometry to effective symplasmic permeability through biophysical modelling. *eLife*, 8:e49000, Nov. 2019. ISSN 2050-084X. doi: 10.7554/eLife.49000. URL https://doi.org/10.7554/eLife.49000. C.

F. Devienne, B. Mary, and T. Lamaze. Nitrate transport in intact wheat roots: I. Estimation of cellular fluxes and NO_3 distribution using compartmental analysis from data of^{15} NO_3 efflux. *Journal of Experimental Botany*, 45 (5):667–676, 1994. ISSN 0022-0957, 1460-2431. doi: 10.1093/jxb/45.5.667. URL https://academic.oup.com/jxb/article-lookup/doi/10.1093/jxb/45.5.667.

F. A. Dijkstra, Y. Carrillo, E. Pendall, and J. A. Morgan. Rhizosphere priming: a nutrient perspective. *Frontiers in Microbiology*, 4, July 2013. ISSN 1664-302X. doi: 10.3389/fmicb.2013.00216. URL https://www.frontiersin.org/journals/microbiology/articles/10.3389/fmicb.2013.00216/full. Publisher: Frontiers.

S. Dinant, J.-L. Bonnemain, C. Girousse, and J. Kehr. Phloem sap intricacy and interplay with aphid feeding. *Comptes Rendus Biologies*, 333(6):504–515, June 2010. ISSN 1631-0691. doi: 10.1016/j.crvi.2010.03.008. URL https://www.sciencedirect.com/science/article/pii/S1631069110001137.

I. Dodd, W. Davies, and G. Egea. MEASURING SAP FLOW IN "TWO ROOT-ONE SHOOT" GRAFTED PLANTS TO MODEL SHOOT XYLEM ABA CONCENTRATION DURING PARTIAL ROOTZONE DRYING. *Acta Horticulturae*, (846):277–284, Nov. 2009. ISSN 0567-7572, 2406-6168. doi: 10.17660/ActaHortic.2009.846.31. URL https://www.actahort.org/books/846/846_31.htm.

I. C. Dodd, G. Egea, and W. J. Davies. Accounting for sap flow from different parts of the root system improves the prediction of xylem ABA concentration in plants grown with heterogeneous soil moisture. *Journal of Experimental Botany*, 59(15):4083–4093, Nov. 2008. ISSN 0022-0957. doi: 10.1093/jxb/ern246. URL https://doi.org/10.1093/jxb/ern246.

D. D. Douds, P. E. Pfeffer, and Y. Shachar-Hill. Carbon Partitioning, Cost, and Metabolism of Arbuscular Mycorrhizas. In Y. Kapulnik and D. D. Douds, editors, *Arbuscular Mycorrhizas: Physiology and Function*, pages 107–129. Springer Netherlands, Dordrecht, 2000. ISBN 978-90-481-5515-6 978-94-017-0776-3. doi: 10.1007/978-94-017-0776-3_6. URL http://link.springer.com/10.1007/978-94-017-0776-3_6.

C. Doussan, L. Pagès, and G. Vercambre. Modelling of the Hydraulic Architecture of Root Systems: An Integrated Approach to Water Absorption—Model Description. *Annals of Botany*, 81(2):213–223, Feb. 1998. ISSN 0305-7364. doi: 10.1006/anbo.1997.0540. URL https://www.sciencedirect.com/science/article/pii/S0305736497905400.

F. Duan, R. F. H. Giehl, N. Geldner, D. E. Salt, and N. v. Wirén. Root zone–specific localization of AMTs determines ammonium transport pathways and nitrogen allocation to shoots. *PLOS Biology*, 16(10):e2006024, Oct. 2018. ISSN 1545-7885. doi: 10.1371/journal.pbio.2006024. URL https://journals.plos.org/plosbiology/article?id=10.

1371/journal.pbio.2006024. Number: 10 Publisher: Public Library of Science.

F. Dubois, T. Tercé-Laforgue, M.-B. Gonzalez-Moro, J.-M. Estavillo, R. Sangwan, A. Gallais, and B. Hirel. Glutamate dehydrogenase in plants: is there a new story for an old enzyme? *Plant Physiology and Biochemistry*, 41(6):565–576, June 2003. ISSN 0981-9428. doi: 10.1016/S0981-9428(03)00075-5. URL https://www.sciencedirect.com/science/article/pii/S0981942803000755.

V. M. Dunbabin, A. J. Diggle, Z. Rengel, and R. van Hugten. Modelling the interactions between water and nutrient uptake and root growth. *Plant and Soil*, 239(1):19–38, Feb. 2002. ISSN 1573-5036. doi: 10.1023/A:1014939512104. URL https://doi.org/10.1023/A:1014939512104.

A. El-Naggar, A. De Neergaard, A. El-Araby, and H. Hgh-Jensen. Simultaneous Uptake of Multiple Amino Acids by Wheat. *Journal of Plant Nutrition*, 32(5):725–740, Apr. 2009. ISSN 0190-4167, 1532-4087. doi: 10.1080/01904160902787842. URL http://www.tandfonline.com/doi/abs/10.1080/01904160902787842.

D. E. Enstone, C. A. Peterson, and F. Ma. Root Endodermis and Exodermis: Structure, Function, and Responses to the Environment. *Journal of Plant Growth Regulation*, 21(4):335–351, Dec. 2002. ISSN 0721-7595, 1435-8107. doi: 10.1007/s00344-003-0002-2. URL http://link.springer.com/10.1007/s00344-003-0002-2.

E. Epstein. SPACES, BARRIERS, AND ION CARRIERS: ION ABSORPTION BY PLANTS. *American Journal of Botany*, 47(5):393–400, May 1960. ISSN 0002-9122, 1537-2197. doi: 10.1002/j.1537-2197.1960.tb07142.x. URL https://bsapubs.onlinelibrary.wiley.com/doi/10.1002/j.1537-2197.1960.tb07142.x.

B. Faiyue, M. J. Al-Azzawi, and T. J. Flowers. The role of lateral roots in bypass flow in rice (Oryza sativa L.). *Plant, Cell & Environment*, 33(5):702–716, 2010. ISSN 1365-3040. doi: 10.1111/j.1365-3040.2009.02078.x. URL https://onlinelibrary.wiley.com/doi/abs/10.1111/j.1365-3040.2009.02078.x. _eprint: https://onlinelibrary.wiley.com/doi/pdf/10.1111/j.1365-3040.2009.02078.x.

FAO. Cereal Supply and Demand Brief – World Food Situation. Technical report, Food and Agriculture Organization of the United Nations, Rome, June 2025. URL https://www.fao.org/worldfoodsituation/csdb/en.

E. L. Fiscus and P. J. Kramer. General model for osmotic and pressure-induced flow in plant roots. *Proceedings of the National Academy of Sciences*, 72(8):3114–3118, Aug. 1975. doi: 10.1073/pnas.72.8.3114. URL https://www.pnas.org/doi/abs/10.1073/pnas.72.8.3114. Publisher: Proceedings of the National Academy of Sciences.

B. G. Forde and P. J. Lea. Glutamate in plants: metabolism, regulation, and signalling. *Journal of Experimental Botany*, 58(9):2339–2358, July 2007. ISSN 0022-0957. doi: 10.1093/jxb/erm121. URL https://doi.org/10.1093/jxb/erm121.

J. Fustec, F. Lesuffleur, S. Mahieu, and J.-B. Cliquet. Nitrogen rhizodeposition of legumes. A review. *Agronomy for Sustainable Development*, 30(1):57–66, Mar. 2010. ISSN 1773-0155. doi: 10.1051/agro/2009003. URL https://doi.org/10.1051/agro/2009003.

Giraud, S. L. Gall, M. Harings, M. Javaux, D. Leitner, F. Meunier, Y. Rothfuss, D. van Dusschoten, J. Vanderborght, H. Vereecken, G. Lobet, and A. Schnepf. CPlantBox: a fully coupled modelling platform for the water and carbon fluxes in the soil–plant–atmosphere continuum. *in silico Plants*, 5(2):diad009, July 2023. ISSN 2517-5025. doi: 10.1093/insilicoplants/diad009. URL https://doi.org/10.1093/insilicoplants/diad009.

Giraud, A. K. Sırcan, T. Streck, D. Leitner, G. Lobet, H. Pagel, and A. Schnepf. In silico analysis of carbon stabilisation by plant and soil microbes for different weather scenarios. *EGUsphere*, pages 1–76, Mar. 2025. doi: 10.5194/egusphere-2025-572. URL https://egusphere.copernicus.org/preprints/2025/egusphere-2025-572/. Publisher: Copernicus GmbH.

V. Gloser, M. Dvorackova, D. H. Mota, B. Petrovic, P. Gonzalez, and C. M. Geilfus. Early Changes in Nitrate Uptake and Assimilation Under Drought in Relation to Transpiration. *Frontiers in Plant Science*, 11, Dec. 2020. ISSN 1664-462X. doi: 10.3389/fpls.2020.602065. URL https://www.frontiersin.org/journals/plant-science/articles/10.3389/fpls.2020.602065/full. Publisher: Frontiers.

V. O. Grasmanis and K. P. Barley. The Uptake of Nitrate and Ammonium by Suceessive Zones of the Pea Radicle. *Australian Journal of Biological Sciences*, 22(6):1313–1320, 1969. doi: 10.1071/bi9691313. URL https://www.

publish.csiro.au/bi/bi9691313. Publisher: CSIRO PUBLISHING.

M. Griffiths and L. M. York. Targeting Root Ion Uptake Kinetics to Increase Plant Productivity and Nutrient Use Efficiency1[OPEN]. *Plant Physiology*, 182(4):1854–1868, Apr. 2020. ISSN 0032-0889. doi: 10.1104/pp.19.01496. URL https://doi.org/10.1104/pp.19.01496.

H.-J. Hawkins and E. George. Effect of plant nitrogen status on the contribution of arbuscular mycorrhizal hyphae to plant nitrogen uptake. *Physiologia Plantarum*, 105(4):694–700, 1999. ISSN 1399-3054. doi: 10.1034/j.1399-3054.1999.105414.x. URL https://onlinelibrary.wiley.com/doi/abs/10.1034/j.1399-3054.1999.105414.x. _eprint: https://onlinelibrary.wiley.com/doi/pdf/10.1034/j.1399-3054.1999.105414.x.

H.-J. Hawkins, A. Johansen, and E. George. Uptake and transport of organic and inorganic nitrogen by arbuscular mycorrhizal fungi. *Plant and Soil*, 226(2):275–285, Nov. 2000. ISSN 1573-5036. doi: 10.1023/A:1026500810385. URL https://doi.org/10.1023/A:1026500810385.

F. Hayat, M. A. Ahmed, M. Zarebanadkouki, G. Cai, and A. Carminati. Measurements and simulation of leaf xylem water potential and root water uptake in heterogeneous soil water contents. *Advances in Water Resources*, 124: 96–105, Feb. 2019. ISSN 03091708. doi: 10.1016/j.advwatres.2018.12.009. URL https://linkinghub.elsevier.com/retrieve/pii/S0309170818302823.

G. H. Henriksen, D. R. Raman, L. P. Walker, and R. M. Spanswick. Measurement of Net Fluxes of Ammonium and Nitrate at the Surface of Barley Roots Using Ion-Selective Microelectrodes: II. Patterns of Uptake along the Root Axis and Evaluation of the Microelectrode Flux Estimation Technique. *Plant Physiology*, 99(2):734–747, 1992. URL http://www.jstor.org/stable/4274411.

A. Heymans, V. Couvreur, T. LaRue, A. Paez-Garcia, and G. Lobet. GRANAR, a Computational Tool to Better Understand the Functional Importance of Monocotyledon Root Anatomy1 [OPEN]. *Plant Physiology*, 182(2):707–720, Feb. 2020. ISSN 0032-0889. doi: 10.1104/pp.19.00617. URL https://doi.org/10.1104/pp.19.00617.

A. Heymans, V. Couvreur, and G. Lobet. Combining cross-section images and modeling tools to create high-resolution root system hydraulic atlases in. *Plant Direct*, 5(7):e00290, 2021. ISSN 2475-4455. doi: 10.1002/pld3.334. URL https://onlinelibrary.wiley.com/doi/abs/10.1002/pld3.334. _eprint: https://onlinelibrary.wiley.com/doi/pdf/10.1002/pld3.334.

Hodge, G. Berta, C. Doussan, F. Merchan, and M. Crespi. Plant root growth, architecture and function. *Plant and Soil*, 321(1):153–187, Aug. 2009. ISSN 1573-5036. doi: 10.1007/s11104-009-9929-9. URL https://doi.org/10.1007/s11104-009-9929-9. Number: 1 R.

A. Hodge. The plastic plant: root responses to heterogeneous supplies of nutrients. *New Phytologist*, 162(1):9–24, 2004. ISSN 1469-8137. doi: 10.1111/j.1469-8137.2004.01015.x. URL https://onlinelibrary.wiley.com/doi/abs/10.1111/j.1469-8137.2004.01015.x. _eprint: https://onlinelibrary.wiley.com/doi/pdf/10.1111/j.1469-8137.2004.01015.x.

A. Hodge, D. Robinson, B. S. Griffiths, and A. H. Fitter. Why plants bother: root proliferation results in increased nitrogen capture from an organic patch when two grasses compete. *Plant, Cell & Environment*, 22(7):811–820, 1999. ISSN 1365-3040. doi: 10.1046/j.1365-3040.1999.00454.x. URL https://onlinelibrary.wiley.com/doi/abs/10.1046/j.1365-3040.1999.00454.x. _eprint: https://onlinelibrary.wiley.com/doi/pdf/10.1046/j.1365-3040.1999.00454.x.

M. Holz, M. Zarebanadkouki, P. Benard, M. Hoffmann, and M. Dubbert. Root and rhizosphere traits for enhanced water and nutrients uptake efficiency in dynamic environments. *Frontiers in Plant Science*, 15, July 2024. ISSN 1664-462X. doi: 10.3389/fpls.2024.1383373. URL https://www.frontiersin.org/journals/plant-science/articles/10.3389/fpls.2024.1383373/full. Publisher: Frontiers.

J. W. Hopmans and K. L. Bristow. Current Capabilities and Future Needs of Root Water and Nutrient Uptake Modeling. In *Advances in Agronomy*, volume 77, pages 103–183. Elsevier, 2002. ISBN 978-0-12-000795-0. doi: 10.1016/S0065-2113(02)77014-4. URL https://linkinghub.elsevier.com/retrieve/pii/S0065211302770144.

E. Hose, D. Clarkson, E. Steudle, L. Schreiber, and W. Hartung. The exodermis: a variable apoplastic barrier. *Journal of Experimental Botany*, 52(365):2245–2264, Dec. 2001. ISSN 0022-0957. doi: 10.1093/jexbot/52.365.2245. URL https://doi.org/10.1093/jexbot/52.365.2245.

J. Hui, X. An, Z. Li, B. Neuhäuser, U. Ludewig, X. Wu, W. X. Schulze, F. Chen, G. Feng, H. Lambers, F. Zhang, and L. Yuan. The mycorrhiza-specific ammonium transporter ZmAMT3;1 mediates mycorrhiza-dependent nitrogen uptake in maize roots. *The Plant Cell*, 34(10):4066–4087, Oct. 2022. ISSN 1040-4651. doi: 10.1093/plcell/koac225. URL https://doi.org/10.1093/plcell/koac225.

M. Javaux, T. Schröder, J. Vanderborght, and H. Vereecken. Use of a Three-Dimensional Detailed Modeling Approach for Predicting Root Water Uptake. *Vadose Zone Journal*, 7(3):1079–1088, 2008. ISSN 1539-1663. doi: 10.2136/vzj2007.0115. URL https://onlinelibrary.wiley.com/doi/abs/10.2136/vzj2007.0115. _eprint: https://onlinelibrary.wiley.com/doi/pdf/10.2136/vzj2007.0115.

K. H. Jensen. Phloem physics: mechanisms, constraints, and perspectives. *Current Opinion in Plant Biology*, 43:96–100, June 2018. ISSN 1369-5266. doi: 10.1016/j.pbi.2018.03.005. URL https://www.sciencedirect.com/science/article/pii/S1369526617302066.

D. L. Jones and P. R. Darrah. Amino-acid influx at the soil-root interface of Zea mays L. and its implications in the rhizosphere. *Plant and Soil*, 163(1):1–12, June 1994. ISSN 0032-079X, 1573-5036. doi: 10.1007/BF00033935. URL http://link.springer.com/10.1007/BF00033935.

D. L. Jones, C. Nguyen, and R. D. Finlay. Carbon flow in the rhizosphere: carbon trading at the soil–root interface. *Plant and Soil*, 321(1-2):5–33, Aug. 2009. ISSN 0032-079X, 1573-5036. doi: 10.1007/s11104-009-9925-0. URL http://link.springer.com/10.1007/s11104-009-9925-0. Number: 1-2.

S. Jämtgård, T. Näsholm, and K. Huss-Danell. Characteristics of amino acid uptake in barley. *Plant and Soil*, 302(1-2):221–231, Jan. 2008. ISSN 0032-079X, 1573-5036. doi: 10.1007/s11104-007-9473-4. URL http://link.springer.com/10.1007/s11104-007-9473-4.

S. Kanno, J.-F. Arrighi, S. Chiarenza, V. Bayle, R. Berthomé, B. Péret, H. Javot, E. Delannoy, E. Marin, T. M. Nakanishi, M.-C. Thibaud, and L. Nussaume. A novel role for the root cap in phosphate uptake and homeostasis. *eLife*, 5:e14577, Apr. 2016. ISSN 2050-084X. doi: 10.7554/eLife.14577. URL https://doi.org/10.7554/eLife.14577. Publisher: eLife Sciences Publications, Ltd.

M. A. Kirkman and B. J. Miflin. The nitrate content and amino acid composition of the xylem fluid of spring wheat throughout the growing season. *Journal of the Science of Food and Agriculture*, 30(7):653–660, July 1979. ISSN 0022-5142, 1097-0010. doi: 10.1002/jsfa.2740300703. URL https://onlinelibrary.wiley.com/doi/10.1002/jsfa.2740300703.

D. B. Lazof, T. W. Rufty, and M. G. Redinbaugh. Localization of Nitrate Absorption and Translocation within Morphological Regions of the Corn Root. *Plant Physiology*, 100(3):1251–1258, Nov. 1992. ISSN 0032-0889, 1532-2548. doi: 10.1104/pp.100.3.1251. URL https://academic.oup.com/plphys/article/100/3/1251-1258/6085991.

E. Le Deunff, P. Malagoli, and M.-L. Decau. Modelling Nitrogen Uptake in Plants and Phytoplankton: Advantages of Integrating Flexibility into the Spatial and Temporal Dynamics of Nitrate Absorption. *Agronomy*, 9(3):116, Mar. 2019. ISSN 2073-4395. doi: 10.3390/agronomy9030116. URL https://www.mdpi.com/2073-4395/9/3/116. Number: 3 Publisher: Multidisciplinary Digital Publishing Institute.

L. Lejay, X. Gansel, M. Cerezo, P. Tillard, C. Müller, A. Krapp, N. Von Wirén, F. Daniel-Vedele, and A. Gojon. Regulation of Root Ion Transporters by Photosynthesis: Functional Importance and Relation with Hexokinase. *The Plant Cell*, 15(9):2218–2232, Sept. 2003. ISSN 1040-4651, 1532-298X. doi: 10.1105/tpc.013516. URL https://academic.oup.com/plcell/article/15/9/2218-2232/6010119.

F. Lesuffleur, F. Paynel, M.-P. Bataillé, E. Le Deunff, and J.-B. Cliquet. Root amino acid exudation: measurement of high efflux rates of glycine and serine from six different plant species. *Plant and Soil*, 294(1):235–246, May 2007. ISSN 1573-5036. doi: 10.1007/s11104-007-9249-x. URL https://doi.org/10.1007/s11104-007-9249-x.

E. Lippold, M. Phalempin, S. Schlüter, and D. Vetterlein. Does the lack of root hairs alter root system architecture of Zea mays? *Plant and Soil*, 467(1):267–286, Oct. 2021. ISSN 1573-5036. doi: 10.1007/s11104-021-05084-8. URL https://doi.org/10.1007/s11104-021-05084-8.

B. Liu, J. Wu, S. Yang, J. Schiefelbein, and Y. Gan. Nitrate regulation of lateral root and root hair development in plants. *Journal of Experimental Botany*, 71(15):4405–4414, July 2020. ISSN 0022-0957. doi: 10.1093/jxb/erz536. URL https://doi.org/10.1093/jxb/erz536.

H. Liu, T. Colombi, O. Jäck, A. Westerbergh, and M. Weih. Linking wheat nitrogen use to root traits: Shallow and thin embryonic roots enhance uptake but reduce conversion efficiency of nitrogen. *Field Crops Research*, 285:108603, Sept. 2022. ISSN 0378-4290. doi: 10.1016/j.fcr.2022.108603. URL https://www.sciencedirect.com/science/article/pii/S0378429022001745.

K.-H. Liu and Y.-F. Tsay. Switching between the two action modes of the dual-affinity nitrate transporter CHL1 by phosphorylation. *The EMBO Journal*, 22(5):1005–1013, Mar. 2003. ISSN 0261-4189. doi: 10.1093/emboj/cdg118. URL https://www.embopress.org/doi/full/10.1093/emboj/cdg118. Number: 5 Publisher: John Wiley & Sons, Ltd.

G. Louarn and Y. Song. Two decades of functional–structural plant modelling: now addressing fundamental questions in systems biology and predictive ecology. *Annals of Botany*, 126(4):501–509, Sept. 2020. ISSN 0305-7364. doi: 10.1093/aob/mcaa143. URL https://doi.org/10.1093/aob/mcaa143.

Y. Lu and W. Fricke. Diurnal changes in apoplast bypass flow of water and ions in salt-stressed wheat (Triticum aestivum L.) and barley (Hordeum vulgare L.). *Physiologia Plantarum*, 175(4):e13955, 2023. ISSN 1399-3054. doi: 10.1111/ppl.13955. URL https://onlinelibrary.wiley.com/doi/abs/10.1111/ppl.13955. _eprint: https://onlinelibrary.wiley.com/doi/pdf/10.1111/ppl.13955.

K. Lucas. D. S. Viswanath, G. Natarajan: Data Book on the Viscositiy of Liquids, Hemisphere Publishing Corporation, New York, Washington, Philadelphia, London 1989. 990 Seiten, Preis: £ 125,-. *Berichte der Bunsengesellschaft für physikalische Chemie*, 93(10):1149–1150, 1989. ISSN 0005-9021. doi: 10.1002/bbpc.19890931023. URL https://onlinelibrary.wiley.com/doi/abs/10.1002/bbpc.19890931023. _eprint: https://onlinelibrary.wiley.com/doi/pdf/10.1002/bbpc.19890931023.

J. P. Lynch. Harnessing root architecture to address global challenges. *The Plant Journal*, 109(2):415–431, Jan. 2022. ISSN 0960-7412. doi: 10.1111/tpj.15560. URL https://pmc.ncbi.nlm.nih.gov/articles/PMC9299910/.

J. P. Lynch, T. Galindo-Castañeda, H. M. Schneider, J. S. Sidhu, H. Rangarajan, and L. M. York. Root phenotypes for improved nitrogen capture. *Plant and Soil*, 502(1):31–85, Sept. 2024. ISSN 1573-5036. doi: 10.1007/s11104-023-06301-2. URL https://doi.org/10.1007/s11104-023-06301-2.

X. Lyu, M. Li, X. Li, S. Li, C. Yan, C. Ma, and Z. Gong. Assessing the Systematic Effects of the Concentration of Nitrogen Supplied to Dual-Root Systems of Soybean Plants on Nodulation and Nitrogen Fixation. *Agronomy*, 10(6):763, June 2020. ISSN 2073-4395. doi: 10.3390/agronomy10060763. URL https://www.mdpi.com/2073-4395/10/6/763. Number: 6 Publisher: Multidisciplinary Digital Publishing Institute.

T. H. Mai, A. Schnepf, H. Vereecken, and J. Vanderborght. Continuum multiscale model of root water and nutrient uptake from soil with explicit consideration of the 3D root architecture and the rhizosphere gradients. *Plant and Soil*, 439(1-2):273–292, June 2019. ISSN 0032-079X, 1573-5036. doi: 10.1007/s11104-018-3890-4. URL http://link.springer.com/10.1007/s11104-018-3890-4.

P. Malagoli and E. Le Deunff. An updated model for nitrate uptake modelling in plants. II. Assessment of active root involvement in nitrate uptake based on integrated root system age: measured versus modelled outputs. *Annals of Botany*, 113(6):1007–1019, May 2014. ISSN 0305-7364. doi: 10.1093/aob/mcu022. URL https://doi.org/10.1093/aob/mcu022.

P. Martre, S. Dueri, J. R. Guarin, F. Ewert, H. Webber, D. Calderini, G. Molero, M. Reynolds, D. Miralles, G. Garcia, H. Brown, M. George, R. Craigie, J.-P. Cohan, J.-C. Deswarte, G. Slafer, F. Giunta, D. Cammarano, R. Ferrise,

T. Gaiser, Y. Gao, Z. Hochman, G. Hoogenboom, L. A. Hunt, K. C. Kersebaum, C. Nendel, G. Padovan, A. C. Ruane, A. K. Srivastava, T. Stella, I. Supit, P. Thorburn, E. Wang, J. Wolf, C. Zhao, Z. Zhao, and S. Asseng. Global needs for nitrogen fertilizer to improve wheat yield under climate change. *Nature Plants*, 10(7):1081–1090, July 2024. ISSN 2055-0278. doi: 10.1038/s41477-024-01739-3. URL https://www.nature.com/articles/s41477-024-01739-3. Publisher: Nature Publishing Group.

M. McGowan and E. Tzimas. Water Relations of Winter Wheat: the Root System, Petiolar Resistance and Development of a Root Abstraction Equation. *Experimental Agriculture*, 21(4):377–388, Oct. 1985. ISSN 0014-4797, 1469-4441. doi: 10.1017/S001447970001320X. URL https://www.cambridge.org/core/product/identifier/S001447970001320X/type/journal_article.

F. Meunier, V. Couvreur, X. Draye, G. Lobet, K. Huber, N. Schroeder, H. Jorda, A. Koch, M. Landl, A. Schnepf, J. Vanderborght, H. Vereecken, and M. Javaux. Investigating Soil–Root Interactions with the Numerical Model R-SWMS. In M. Lucas, editor, *Plant Systems Biology: Methods and Protocols*, pages 259–283. Springer, New York, NY, 2022. ISBN 978-1-0716-1816-5. doi: 10.1007/978-1-0716-1816-5_13. URL https://doi.org/10.1007/978-1-0716-1816-5_13.

P. Millard. The accumulation and storage of nitrogen by herbaceous plants. *Plant, Cell and Environment*, 11(1):1–8, Jan. 1988. ISSN 0140-7791, 1365-3040. doi: 10.1111/j.1365-3040.1988.tb01769.x. URL https://onlinelibrary.wiley.com/doi/10.1111/j.1365-3040.1988.tb01769.x. Number: 1.

D. Moreau, R. D. Bardgett, R. D. Finlay, D. L. Jones, and L. Philippot. A plant perspective on nitrogen cycling in the rhizosphere. *Functional Ecology*, 33(4):540–552, 2019. ISSN 1365-2435. doi: 10.1111/1365-2435.13303. URL https://onlinelibrary.wiley.com/doi/abs/10.1111/1365-2435.13303. _eprint: https://onlinelibrary.wiley.com/doi/pdf/10.1111/1365-2435.13303.

R. Munns and J. B. Passioura. Effect of Prolonged Exposure to Nacl on the Osmotic Pressure of Leaf Xylem Sap From Intact, Transpiring Barley Plants. *Functional Plant Biology*, 11(6):497–507, 1984. ISSN 1445-4416. doi: 10.1071/pp9840497. URL https://www.publish.csiro.au/fp/pp9840497. Publisher: CSIRO PUBLISHING.

P. Nacry, E. Bouguyon, and A. Gojon. Nitrogen acquisition by roots: physiological and developmental mechanisms ensuring plant adaptation to a fluctuating resource. *Plant and Soil*, 370(1):1–29, Sept. 2013. ISSN 1573-5036. doi: 10.1007/s11104-013-1645-9. URL https://doi.org/10.1007/s11104-013-1645-9.

M. Nakad, J.-C. Domec, S. Sevanto, and G. Katul. Radial–axial transport coordination enhances sugar translocation in the phloem vasculature of plants. *Plant Physiology*, 189(4):2061–2071, Aug. 2022. ISSN 0032-0889. doi: 10.1093/plphys/kiac231. URL https://doi.org/10.1093/plphys/kiac231.

N. T. Nguyen, S. A. McInturf, and D. G. Mendoza-Cózatl. Hydroponics: A Versatile System to Study Nutrient Allocation and Plant Responses to Nutrient Availability and Exposure to Toxic Elements. *Journal of Visualized Experiments : JoVE*, (113):54317, July 2016. ISSN 1940-087X. doi: 10.3791/54317. URL https://www.ncbi.nlm.nih.gov/pmc/articles/PMC5091364/.

A. Odone, O. Popovic, and K. Thorup-Kristensen. Deep roots: implications for nitrogen uptake and drought tolerance among winter wheat cultivars. *Plant and Soil*, 500(1):13–32, July 2024. ISSN 1573-5036. doi: 10.1007/s11104-023-06255-5. URL https://doi.org/10.1007/s11104-023-06255-5.

A. Ogawa. Sugar Accumulation along the Seminal Root Axis, as Affected by Osmotic Stress in Maize: A Possible Physiological Basis for Plastic Lateral Root Development: Plant Production Science: Vol 8, No 2, 2005. URL https://www.tandfonline.com/doi/abs/10.1626/pps.8.173.

W. Ouyang, X. Yin, J. Yang, and P. C. Struik. Comparisons with wheat reveal root anatomical and histochemical constraints of rice under water-deficit stress. *Plant and Soil*, 452(1):547–568, July 2020. ISSN 1573-5036. doi: 10.1007/s11104-020-04581-6. URL https://doi.org/10.1007/s11104-020-04581-6.

Pace and McClure. Comparison of nitrate uptake kinetic parameters across maize inbred lines: Journal of Plant Nutrition: Vol 9, No 8, 1986. URL https://www.tandfonline.com/doi/abs/10.1080/01904168609363512.

L. Pagès, C. Bécel, H. Boukcim, D. Moreau, C. Nguyen, and A.-S. Voisin. Calibration and evaluation of ArchiSimple, a simple model of root system architecture. *Ecological Modelling*, 290:76–84, Oct. 2014. ISSN 03043800. doi: 10.1016/j.ecolmodel.2013.11.014. URL https://linkinghub.elsevier.com/retrieve/pii/S0304380013005619.

J. Pang, S. P. Milroy, G. J. Rebetzke, and J. A. Palta. The influence of shoot and root size on nitrogen uptake in wheat is affected by nitrate affinity in the roots during early growth. *Functional Plant Biology*, 42(12):1179, 2015. ISSN 1445-4408. doi: 10.1071/FP15215. URL http://www.publish.csiro.au/?paper=FP15215.

B. Parent, O. Turc, Y. Gibon, M. Stitt, and F. Tardieu. Modelling temperature-compensated physiological rates, based on the co-ordination of responses to temperature of developmental processes. *Journal of Experimental Botany*, 61(8): 2057–2069, May 2010. ISSN 1460-2431, 0022-0957. doi: 10.1093/jxb/erq003. URL https://academic.oup.com/jxb/article-lookup/doi/10.1093/jxb/erq003. Number: 8.

S. Passot, V. Couvreur, F. Meunier, X. Draye, M. Javaux, D. Leitner, L. Pagès, A. Schnepf, J. Vanderborght, and G. Lobet. Connecting the dots between computational tools to analyse soil–root water relations. *Journal of Experimental Botany*, 70(9):2345–2357, Apr. 2019. ISSN 0022-0957. doi: 10.1093/jxb/ery361. URL https://doi.org/10.1093/jxb/ery361.

J. Pausch and Y. Kuzyakov. Carbon input by roots into the soil: Quantification of rhizodeposition from root to ecosystem scale. *Global Change Biology*, 24(1):1–12, Jan. 2018. ISSN 13541013. doi: 10.1111/gcb.13850. URL https://onlinelibrary.wiley.com/doi/10.1111/gcb.13850. Number: 1.

C. A. Peterson and G. J. Moon. The Effect of Lateral Root Outgrowth on the Structure and Permeability of the Onion Root Exodermis. *Botanica Acta*, 106(5):411–418, 1993. ISSN 1438-8677. doi: 10.1111/j.1438-8677.1993.tb00768.x. URL https://onlinelibrary.wiley.com/doi/abs/10.1111/j.1438-8677.1993.tb00768.x. _eprint: https://onlinelibrary.wiley.com/doi/pdf/10.1111/j.1438-8677.1993.tb00768.x.

A. D. Peuke. Correlations in concentrations, xylem and phloem flows, and partitioning of elements and ions in intact plants. A summary and statistical re-evaluation of modelling experiments in Ricinus communis. *Journal of Experimental Botany*, 61(3):635–655, Mar. 2010. ISSN 1460-2431, 0022-0957. doi: 10.1093/jxb/erp352. URL https://academic.oup.com/jxb/article-lookup/doi/10.1093/jxb/erp352.

D. A. Phillips, T. C. Fox, M. D. King, T. Bhuvaneswari, and L. R. Teuber. Microbial Products Trigger Amino Acid Exudation from Plant Roots. *Plant Physiology*, 136(1):2887–2894, Sept. 2004. ISSN 0032-0889. doi: 10.1104/pp.104.044222. URL https://www.ncbi.nlm.nih.gov/pmc/articles/PMC523350/.

Pitman. Ion transport to the xylem. 2008. R.

J. A. Postma, A. Dathe, and J. P. Lynch. The Optimal Lateral Root Branching Density for Maize Depends on Nitrogen and Phosphorus Availability. *Plant Physiology*, 166(2):590–602, Oct. 2014. ISSN 0032-0889. doi: 10.1104/pp.113.233916. URL https://doi.org/10.1104/pp.113.233916.

J. A. Postma, C. Kuppe, M. R. Owen, N. Mellor, M. Griffiths, M. J. Bennett, J. P. Lynch, and M. Watt. OpenSimRoot : widening the scope and application of root architectural models. *New Phytologist*, 215(3):1274–1286, Aug. 2017. ISSN 0028-646X, 1469-8137. doi: 10.1111/nph.14641. URL https://onlinelibrary.wiley.com/doi/10.1111/nph.14641.

P. Pouliquin, J.-C. Boyer, J.-P. Grouzis, and R. Gibrat. Passive Nitrate Transport by Root Plasma Membrane Vesicles Exhibits an Acidic Optimal pH Like the H+-ATPase1 | Plant Physiology | Oxford Academic, 2000. URL https://academic.oup.com/plphys/article/122/1/265/6091935.

C. Pradal and C. Godin. MTG as a standard representation of plants in FSPMs. *FSPM2020*, 2020.

C. Pradal, S. Dufour-Kowalski, F. Boudon, C. Fournier, and C. Godin. OpenAlea: a visual programming and component-based software platform for plant modelling. *Functional Plant Biology*, 35(10):751–760, Nov. 2008. ISSN 1445-4416. doi: 10.1071/FP08084. URL https://www.publish.csiro.au/fp/FP08084. Publisher: CSIRO PUBLISHING.

C. Pradal, C. Fournier, P. Valduriez, and S. Cohen-Boulakia. OpenAlea: scientific workflows combining data analysis and simulation. In *Proceedings of the 27th International Conference on Scientific and Statistical Database Management*, SSDBM '15, pages 1–6, New York, NY, USA, 2015. Association for Computing Machinery. ISBN 978-1-4503-3709-0.

doi: 10.1145/2791347.2791365. URL https://doi.org/10.1145/2791347.2791365.

I. Raij-Hoffman, O. Dahan, H. E. Dahlke, T. Harter, and I. Kisekka. Assessing Nitrate Leaching During Drought and Extreme Precipitation: Exploring Deep Vadose-Zone Monitoring, Groundwater Observations, and Field Mass Balance. *Water Resources Research*, 60(11):e2024WR037973, Nov. 2024. ISSN 1944-7973. doi: 10.1029/2024WR037973. URL https://agupubs.onlinelibrary.wiley.com/doi/10.1029/2024WR037973. Publisher: John Wiley & Sons, Ltd.

H. Rangarajan, D. Hadka, P. Reed, and J. P. Lynch. Multi-objective optimization of root phenotypes for nutrient capture using evolutionary algorithms. *The Plant Journal*, 111(1):38–53, 2022. ISSN 1365-313X. doi: 10.1111/tpj.15774. URL https://onlinelibrary.wiley.com/doi/abs/10.1111/tpj.15774. _eprint: https://onlinelibrary.wiley.com/doi/pdf/10.1111/tpj.15774.

T. P. Rao, I. , Osamu, M. , Ryoichi, , and T. Yoneyama. Kinetics of 15N-labelled nitrate uptake by maize (Zea mays L.) root segments. *Soil Science and Plant Nutrition*, 43(3):491–498, Sept. 1997. ISSN 0038-0768. doi: 10.1080/00380768.1997.10414776. URL https://doi.org/10.1080/00380768.1997.10414776. Publisher: Taylor & Francis _eprint: https://doi.org/10.1080/00380768.1997.10414776.

F. Rees, T. Gérault, M. Gauthier, R. Barillot, C. Richard-Molard, A. Jullien, C. Chenu, C. Pradal, and B. Andrieu. Deciphering spatiotemporal patterns of rhizodeposition with a functional-structural root model: RhizoDep. *Plant and Soil*, Aug. 2025. ISSN 1573-5036. doi: 10.1007/s11104-025-07766-z. URL https://doi.org/10.1007/s11104-025-07766-z.

D. Robinson. The responses of plants to non-uniform supplies of nutrients. *New Phytologist*, 127(4):635–674, Aug. 1994. ISSN 0028-646X, 1469-8137. doi: 10.1111/j.1469-8137.1994.tb02969.x. URL https://nph.onlinelibrary.wiley.com/doi/10.1111/j.1469-8137.1994.tb02969.x.

D. Robinson, D. J. Linehan, and S. Caul. What limits nitrate uptake from soil? *Plant, Cell & Environment*, 14(1):77–85, Jan. 1991a. ISSN 0140-7791, 1365-3040. doi: 10.1111/j.1365-3040.1991.tb01373.x. URL https://onlinelibrary.wiley.com/doi/10.1111/j.1365-3040.1991.tb01373.x.

S. A. Robinson, A. P. Slade, G. G. Fox, R. Phillips, R. G. Ratcliffe, and G. R. Stewart. The Role of Glutamate Dehydrogenase in Plant Nitrogen Metabolism 12. *Plant Physiology*, 95(2):509–516, Feb. 1991b. ISSN 0032-0889. URL https://www.ncbi.nlm.nih.gov/pmc/articles/PMC1077561/. Number: 2.

L. Rossato, C. L. Dantec, P. Laine, and A. Ourry. Nitrogen storage and remobilization in Brassica napus L. during the growth cycle: identification, characterization and immunolocalization of a putative taproot storage glycoprotein. *Journal of Experimental Botany*, 53(367):265–275, Feb. 2002. ISSN 0022-0957. doi: 10.1093/jexbot/53.367.265. URL https://doi.org/10.1093/jexbot/53.367.265.

P. Saengwilai, C. Strock, H. Rangarajan, J. Chimungu, J. Salungyu, and J. P. Lynch. Root hair phenotypes influence nitrogen acquisition in maize. *Annals of Botany*, 128(7):849–858, Aug. 2021. ISSN 0305-7364. doi: 10.1093/aob/mcab104. URL https://www.ncbi.nlm.nih.gov/pmc/articles/PMC8577201/.

I. Scheurwater, M. Koren, H. Lambers, and O. K. Atkin. The contribution of roots and shoots to whole plant nitrate reduction in fast- and slow-growing grass species. *Journal of Experimental Botany*, 53(374):1635–1642, July 2002. ISSN 0022-0957. doi: 10.1093/jxb/erf008. Number: 374.

H. M. Schneider, T. Wojciechowski, J. A. Postma, K. M. Brown, A. Lücke, V. Zeisler, L. Schreiber, and J. P. Lynch. Root cortical senescence decreases root respiration, nutrient content and radial water and nutrient transport in barley. *Plant, Cell & Environment*, 40(8):1392–1408, 2017. ISSN 1365-3040. doi: 10.1111/pce.12933. URL https://onlinelibrary.wiley.com/doi/abs/10.1111/pce.12933. _eprint: https://onlinelibrary.wiley.com/doi/pdf/10.1111/pce.12933.

A. Schnepf, D. Leitner, P. F. Schweiger, P. Scholl, and J. Jansa. L-System model for the growth of arbuscular mycorrhizal fungi, both within and outside of their host roots. *Journal of The Royal Society Interface*, 13(117):20160129, Apr. 2016. doi: 10.1098/rsif.2016.0129. URL https://royalsocietypublishing.org/doi/full/10.1098/rsif.2016.0129. Publisher: Royal Society.

A. Schnepf, D. Leitner, M. Landl, G. Lobet, T. H. Mai, S. Morandage, C. Sheng, M. Zörner, J. Vanderborght, and H. Vereecken. CRootBox: a structural–functional modelling framework for root systems. *Annals of Botany*, 121(5): 1033–1053, Apr. 2018. ISSN 0305-7364, 1095-8290. doi: 10.1093/aob/mcx221. URL https://academic.oup.com/aob/article/121/5/1033/4844040.

L. Schreiber, R. Franke, K.-D. Hartmann, K. Ranathunge, and E. Steudle. The chemical composition of suberin in apoplastic barriers affects radial hydraulic conductivity differently in the roots of rice (Oryza sativa L. cv. IR64) and corn (Zea mays L. cv. Helix). *Journal of Experimental Botany*, 56(415):1427–1436, May 2005. ISSN 0022-0957. doi: 10.1093/jxb/eri144. URL https://doi.org/10.1093/jxb/eri144.

E. D. Schäfer, M. R. Owen, J. A. Postma, C. Kuppe, C. K. Black, and J. P. Lynch. Simulating Crop RootRootsSystems Using OpenSimRoot. In M. Lucas, editor, *Plant Systems Biology: Methods and Protocols*, pages 293–323. Springer, New York, NY, 2022. ISBN 978-1-0716-1816-5. doi: 10.1007/978-1-0716-1816-5_15. URL https://doi.org/10.1007/978-1-0716-1816-5_15.

J. Shi, A. Ben-Gal, U. Yermiyahu, L. Wang, and Q. Zuo. Characterizing root nitrogen uptake of wheat to simulate soil nitrogen dynamics. *Plant and Soil*, 363(1):139–155, Feb. 2013. ISSN 1573-5036. doi: 10.1007/s11104-012-1299-z. URL https://doi.org/10.1007/s11104-012-1299-z.

M. Y. Siddiqi. Studies of the Regulation of Nitrate Influx by Barley Seedlings Using 3N03'. 1990.

M. Y. Siddiqi, A. D. M. Glass, T. J. Ruth, and M. Fernando. Studies of the Regulation of Nitrate Influx by Barley Seedlings Using 13NO31. *Plant Physiology*, 90(3):806–813, July 1989. ISSN 0032-0889. doi: 10.1104/pp.90.3.806. URL https://doi.org/10.1104/pp.90.3.806.

J. S. Sidhu, I. Ajmera, S. Arya, and J. P. Lynch. RootSlice—A novel functional-structural model for root anatomical phenotypes. *Plant, Cell & Environment*, 46(5):1671–1690, 2023. ISSN 1365-3040. doi: 10.1111/pce.14552. URL https://onlinelibrary.wiley.com/doi/abs/10.1111/pce.14552. _eprint: https://onlinelibrary.wiley.com/doi/pdf/10.1111/pce.14552.

A. G. Smith, E. Han, J. Petersen, N. A. F. Olsen, C. Giese, M. Athmann, D. B. Dresbøll, and K. Thorup-Kristensen. RootPainter: deep learning segmentation of biological images with corrective annotation. *New Phytologist*, 236(2): 774–791, 2022. ISSN 1469-8137. doi: 10.1111/nph.18387. URL https://onlinelibrary.wiley.com/doi/abs/10.1111/nph.18387. _eprint: https://onlinelibrary.wiley.com/doi/pdf/10.1111/nph.18387.

F. M. Soper, C. Simon, and V. Jauss. Measuring nitrogen fixation by the acetylene reduction assay (ARA): is 3 the magic ratio? *Biogeochemistry*, 152(2):345–351, Feb. 2021. ISSN 1573-515X. doi: 10.1007/s10533-021-00761-3. URL https://doi.org/10.1007/s10533-021-00761-3.

A. Sorgonà, A. Lupini, F. Mercati, L. Di Dio, F. Sunseri, and M. R. Abenavoli. Nitrate uptake along the maize primary root: an integrated physiological and molecular approach. *Plant, Cell & Environment*, 34(7):1127–1140, 2011. ISSN 1365-3040. doi: 10.1111/j.1365-3040.2011.02311.x. URL https://onlinelibrary.wiley.com/doi/abs/10.1111/j.1365-3040.2011.02311.x. _eprint: https://onlinelibrary.wiley.com/doi/pdf/10.1111/j.1365-3040.2011.02311.x.

R. Spicer. Symplasmic networks in secondary vascular tissues: parenchyma distribution and activity supporting long-distance transport. *Journal of Experimental Botany*, 65(7):1829–1848, Apr. 2014. ISSN 0022-0957. doi: 10.1093/jxb/ert459. URL https://doi.org/10.1093/jxb/ert459. Number: 7 R.

M. Tegeder and U. Z. Hammes. The way out and in: phloem loading and unloading of amino acids. *Current Opinion in Plant Biology*, 43:16–21, June 2018. ISSN 1369-5266. doi: 10.1016/j.pbi.2017.12.002. URL https://www.sciencedirect.com/science/article/pii/S1369526617301450. R.

V. Telis, J. Telis-Romero, H. Mazzotti, and A. Gabas. Viscosity of Aqueous Carbohydrate Solutions at Different Temperatures and Concentrations. *International Journal of Food Properties*, 10(1):185–195, Jan. 2007. ISSN 1094-2912, 1532-2386. doi: 10.1080/10942910600673636. URL http://www.tandfonline.com/doi/abs/10.1080/10942910600673636.

2.7 Chapter Contribution to Thesis Strategy

In the framework of the thesis, the *Root-CyNAPS* simulations clarify how plant-scale N balance emerges from heterogeneous local N processes along the roots. The simulations show that net N uptake is organized around zones of increased exchange activity near root tips and lateral emergence, but that the contribution of these zones to total N uptake strongly depends on plant age and external nitrate availability. These simulation results support hypothesis **H2** by suggesting that total N uptake cannot be inferred from a fixed fraction of the root system, and hypothesis **H3** by revealing shifts in the dominant processes controlling net N uptake (active N uptake, water-driven passive N uptake, N exudation offset) across locations in the root system architecture zones and age-nitrate scenarios. By explicitly accounting for anatomical compartments and local metabolite pools, *Root-CyNAPS* also provides a first quantitative illustration of hypothesis **H4**, where anatomical and metabolic heterogeneity tend to up-regulate mineral N uptake and N rhizodeposition at similar locations along roots.

Beyond these specific conclusions, this chapter supplies a mechanistic FSPM of root N, water and anatomy for the rest of the thesis. The regulations of local N processes and water flows by sugars availability, growth costs and shoot-root exchanges were implemented as flexible inputs, so that *Root-CyNAPS* can later be coupled to *RhizoDep* and *CN-Wheat*, two models simulating the inputs expected by *Root-CyNAPS* with similar discretization of the system. This alignment prepares the multiscale coupling work presented in Chapter 3 with the *MetaFSPM* toolkit and its application in Chapter 4 to the *Wheat-BRIDGES* model, where root-soil exchange heterogeneity is integrated into whole-plant C&N balance to study multiscale regulations of rhizodeposition. The identification of active root zones in *Root-CyNAPS* also motivated methodological developments to contribute to model validation in Chapter 5, where localized anatomical measurements and $^{15}NO_3^-$ labeling tests on soil-grown root segments of wheat were initiated to quantify the heterogeneity of root exchange surface and net N uptake along roots, respectively.

Chapter 3

MetaFSPM, a new toolkit for FSPM modularization and coupling enabling the study of multiscale C&N regulations in wheat

3.1 Chapter Strategy

This chapter addresses the methodological objective of my thesis related to the construction of a multiscale FSPM framework for the soil – root – shoot – atmosphere system, in particular to decipher the key regulations and functions behind rhizodeposition heterogeneity. It responds in particular to the methodological question formulated in Chapter 1:

- *How to design a multiscale functional-structural modeling framework of the soil– plant– atmosphere system to investigate the complexity of rhizodeposition determinants*

- *To what extent can such a framework assist researchers in a better understanding of root– soil exchanges plasticity?*

Indirectly, it prepares the test of hypotheses **H2-H5** in Chapter 4, by providing the modeling infrastructure and abstractions needed to link local root – soil exchanges with whole-plant C&N balance.

To meet this objective, I developed *MetaFSPM*, a coupling toolkit that makes independently developed FSPMs modular and interoperable within the *OpenAlea* platform. The strategy followed in this chapter is to (i) formalize a common component architecture for process modules acting on shared data structures, (ii) define explicit coupling schemes and scheduling rules in a composite FSPM builder, and (iii) apply this framework to reorganize existing models used in the thesis (*CN-Wheat*, *RhizoDep*, *Root-CyNAPS* from Chapter 2 and associated environment models) into components and reuse them into composite models, such as the *Wheat-BRIDGES* use case developed in Chapter 4.

3.2 Introduction

In Chapter 1, I reviewed current practices for coupling process-based models in FSPM and related communities, and highlighted three main requirements for studying multiscale C&N regulation patterns in the soil – root – shoot continuum: (i) a clear component architecture separating scientific formalisms from numerical resolution and input/output handling, (ii) explicit semantic contracts between components, and (iii) flexible orchestration of coupled models, allowing alternative coupling hypotheses to be tested on the same network of processes. I also identified *CN-Wheat* and *RhizoDep* as two complementary architectured FSPMs regulating local processes by metabolite concentrations and representing, respectively, the C&N functioning of shoot organs and the C-dependent functioning of root segments (Section 1.2.4), and argued that coupling such models—together with the root N and water model *Root-CyNAPS* (Chapter 2)—would be a promising way to investigate the determinants of rhizodeposition and N uptake variability.

Translating these conceptual recommendations into an operational coupling for this thesis raises several practical difficulties. First, *CN-Wheat*, *RhizoDep*, and *Root-CyNAPS* were developed independently, with different internal code structures and

numerical solvers. Moreover, despite the fact they share the same principle of regulating local processes by metabolite concentrations in organs, the exact discretizations of C-N metabolites and processes are only partially overlapping between each model, with necessary unit conversions to exchange variables. Second, even though all three models are implemented on the *OpenAlea* platform and rely on the same multiscale tree graph (MTG) representation for plant architecture, their current implementations mixes architecture evolution, physiology, numerical resolution, and input/output management in ways that hinder reuse and coupling, as already noted for other FSPMs[Henke et al., 2016]. Third, coupling these models implies exchanging a large number of variables (e.g. local metabolite concentrations and flows, water flows, ages, anatomical features, flows and potentials at the shoot-root junction) at different spatial and temporal scales that may have different names, semantics, units. In this context, tailored scripts or purely visual workflows quickly become difficult to maintain and to document when hundreds of variables have to be managed.

In Crop and Earth system modeling, similar issues have motivated the development of frameworks. Crop2ML [Midingoyi et al., 2021] formalizes model components, their metadata, and their coupling contracts independently of implementation language. Modular toolkits such as xarray-simlab and its ODE extension XSO[Benoit Bovy et al., 2021, Post et al., 2024] assemble models from reusable "processes" with explicit dependencies and scheduling. For FSPMs, Jupyter-based virtual modeling environments have been proposed to make complex models more modular, reproducible and easier to orchestrate, including for OpenAlea-based models[Vaillant et al., 2022]. However, these frameworks remain generic by design, and do not directly address the specific constraints of coupling architectured plant models and 3D environment processes within OpenAlea, where many FSPMs already exist but are not all structured as swappable components [Pradal et al., 2015].

In this context, the objective of this chapter is to provide a concrete coupling solution tailored to the OpenAlea platform and to the models used in this thesis. Rather than proposing another general modeling framework, I introduce *MetaFSPM*, a lightweight Python toolkit that builds on the existing OpenAlea component concept and MTG data structures to make FSPM modularization and coupling more systematic. *MetaFSPM* is based on two main ideas. First, it defines a common *component* structure that separates ecophysiological equations from execution utilities, and homogenizes the declaration of inputs, outputs, internal formalisms, and access to central data structures (plant MTGs, soil voxel grids). Second, it provides a composite FSPM builder that assembles such components into coupled models, centralizing their coupling contracts (variable mappings, unit conversions, aggregations), and resolution schemes (time-stepping and scheduling of component execution). Based on these functionalities, targeted models for this thesis, i.e. *RhizoDep*, *Root-CyNAPS*, *CN-Wheat*, and associated soil and light models, were refactored into *MetaFSPM* components and assembled into composite models such as *Root-CyNAPS* and *Wheat-BRIDGES*. The Results section illustrates these use cases, before discussing the benefits and limitations of this approach for multiscale C&N regulation studies and proposing perspectives for extending *MetaFSPM* to other FSPMs and modeling contexts.

3.3 Material & Methods

3.3.1 *MetaFSPM* - a generic coupling toolkit

In response to these requirements and practical constraints, a generic and modular coupling toolkit for FSPMs, called *MetaFSPM*, was designed. The goal of *MetaFSPM* is to make the targeted coupling strategy for this thesis operational: coupling independently developed models such as *CN-Wheat*, *RhizoDep* and *RootCyNAPS*, which must share a large number of state variables while operating at different time scales, spatial resolutions and units. To do so, the toolkit provides a consensus coupling method that reconciles the different modeling scales, hypotheses and code structures adopted by each model and research team. Beyond the specific objectives of this work, this coupling toolkit was also designed to foster future collaborations between different research fields and teams. It was therefore made publicly available on the OpenAlea platform at `https://github.com/openalea/metafspm` and is written in pure Python.

The *MetaFSPM* toolkit is presented bellow and is divided into (i) a modularization utility to structure coherent sets of mechanistic processes as *components*, and (ii) a composite FSPM builder coupling using individual *components* to produce a functional model.

Homogenizing *component* structure, scheduling and resolution in OpenAlea

A *component* is the basic building block of a complex system which encompasses a coherent set of scientific knowledge, processes and equations. In the OpenAlea platform, coupled networks of *components* are named scientific workflows and their execution is demand-driven, i.e. a provider component is triggered by the request for inputs of a receiver component [Pradal et al., 2008, 2015]. Edition of workflows is done using a visual programming application (i.e. VisuAlea), that allows to drag and drop reusable components and intuitively connect the output of a component with the input of another one. This has allowed to build complex simulation model, like apple tree FSPM (Boudon et al. [2012]) or plant-pathogen FSPM (Garin et al. [2014]). However, the visual approach does not scale well when models have large number of variables and when the scheduling of the composition is complex. This makes the component wrapping and coupling of complex FSPMs both time consuming and rigid for alternative hypotheses exploration. Here we formalized a common structure for all components in OpenAlea, generalizing (i) the declaration of inputs (parameters, initialization and forcing data) and simulated outputs, (ii) the centralization of formalisms (either differential equation systems or custom functions) to have control and flexibility on the solving strategy, (iii) the generation of component's documentation to make inputs, outputs and formalisms readable for a user to perform coupling choices, (iv) the read/write access to shared data structures that allows indirect communication between components, variables conversion and coupling (Fig. 3.1). These four steps are automated and hidden to the user, so that the scientific sections of the code are kept separated from execution aspects, making component/model code more readable and faster to implement. Briefly, we

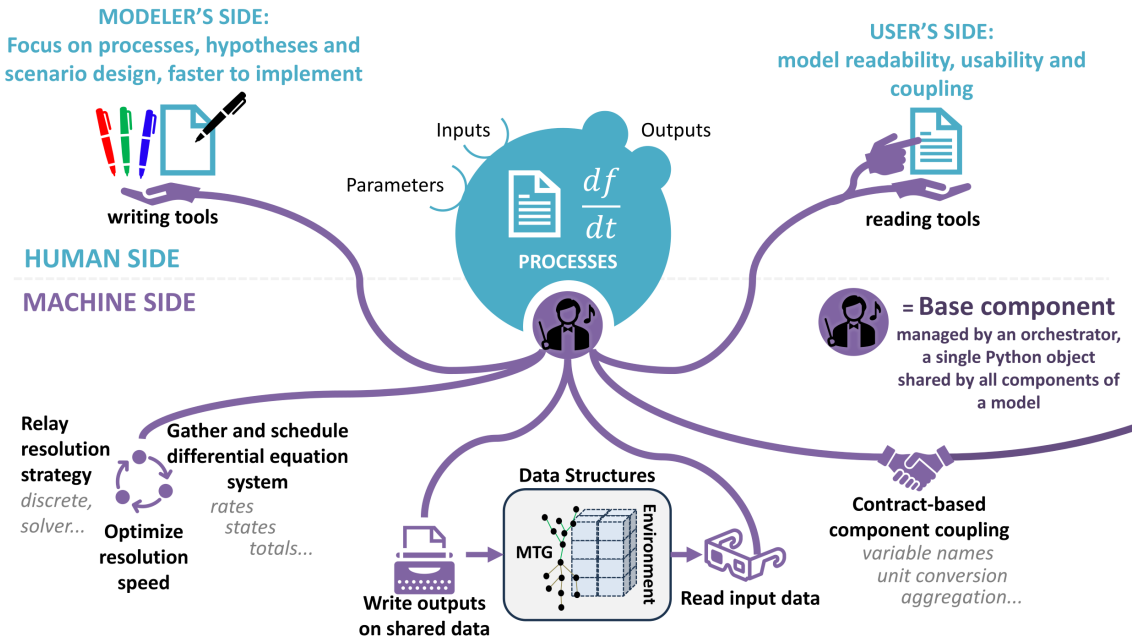

Figure 3.1: Functionality of the *component* structure introduced by *MetaFSPM*. "Ecophysiological" parts of the code are represented in blue, while hidden utilities are in purple.

defined a *base component* Python class that can be imported by the user, exposing all utilities to efficiently write a complex yet readable component, while structuring it automatically for a straightforward coupling in a larger FSPM framework. Example components structured with *MetaFSPM* in the perspective of the *Wheat-BRIDGES* coupling are presented in Figure 3.1.

Model assembly from components

Based on this common elementary structure, another *MetaFSPM* utility, a composite FSPM maker, was developed to build a model from the coupling of individual components. This tool brings together a network of components to compose a plant model according to the following principles:

- It declares the **central data structures** on which components will communicate and exchange variables. In OpenAlea, plant architectures are represented with the Multiscale Tree Graph (MTG) and all plant components rely on it. For the soil model, 3D voxel grids are a common approach.

- It establishes a **coupling contract between components**, a mapping summarizing explicitly for each pair of components (i) corresponding variable names, (ii) unit conversions, and (iii) possible aggregations, e.g. if the metabolite discretization is not the same between models. As long as this contract is preserved or adapted, several modelers can continue to mutualize their work, update and compare components to stay in line with their current understanding of system's functioning.

- It then allows the user to easily modify the internal **time-stepping of each component** and the **scheduling of the composite model's resolution loop**, i.e. whether components should run in parallel or sequentially during a time step. This is a critical aspect to enable testing hypotheses about processes priority when designing a model's resolution loop. Please note that this is distinct from a single component's internal resolution loop, which can be more consensual and standardized (Fig. 3.1).

- It **manages** how the **parameters, input time-series** are read and provided to components, and how **output results** are written on disk, using scenario builders and data loggers of the OpenAlea platform.

- It enables to **simulate an isolated plant or a stand** of several composite FSPMs interacting through the environment models. Identical composite model instances can be planted into a stand, differing only by random effects, but the main novelty of this *MetaFSPM* tool is to enable several independent plant MTGs with very different structures to interact within the same shared environment. This feature is particularly relevant when different models for different species need to be planted together to study intercropping or weed management scenarios.

3.4 Results

Refactor existing models into reusable components for coupling

To couple existing models, I refactor them as independent and reusable component using the MetaFSPM framework. The RhizoDep model was split into three thematic components; a C transport and metabolism component, a C-driven growth component, and an anatomy component. The *Root-CyNAPS* was split into i) a N transport and metabolism component, ii) a water transport component, and reuse the anatomy component of *RhizoDep*. *CN-Wheat*, which already holds a custom component structure, was wrapped into a single shoot component to interface with root models. Only the *CARIBU* light model was separated as a standalone component compared to the original version of *CN-Wheat* to keep plant components separated from environment components. A soil model was also designed and implemented from i) a water-solute transport component wrapping the *CMF* model as is [Kraft et al., 2011] and, ii) a CN-biochemistry component wrapping the *MIMICS-CN* model [Kyker-Snowman et al., 2020].

In this work, we therefore produced the 9 first *MetaFSPM* components of the *OpenAlea* platform whose main processes are summarized in Fig. 3.1. This number is anticipated to grow with other models from my research teams, or the *OpenAlea* community scheduled to be structured as components, e.g. the SIMBAL model [Perthame et al., 2023].

Table 3.1: Example of components structured with the *MetaFSPM* toolkit. For each component, its source model before being included to modularized for *MetaFSPM* is indicated, a synthetic descriptions of accounted processes and regulation is provided, and the composite FSPMs models in which these components are used are also summarized. A complementary representation exchanged variables during the coupling of these individual components in the use case of *Wheat-BRIDGES* is presented in Figure 3.2. A star * in component description indicates a process or regulation that was introduced only for models coupling C&N processes in roots, i.e. *Root-BRIDGES* and *Wheat-BRIDGES*. Published model references: [1] Rees et al. [2025], [2] See Chapter 2, [3] Barillot et al. [2016], Gauthier et al. [2020], [4] Chelle et al. [1998], [5] Kyker-Snowman et al. [2020], [6] Kraft et al. [2011]

	Component name	From	Simulated processes and outputs	Used by
C	**Root Carbon**	*RhizoDep* [1]	Transport of sucrose in phloem, transport of hexoses at phloem-symplasm and soil-symplasm interfaces, symplastic hexose vacuolar (un)storage, transformation and consumption by growth	*RhizoDep, Root-BRIDGES, Wheat-BRIDGES*
GROWTH	**Root Growth**	*RhizoDep*	3D growth of root segments in a MTG (elongation, thickening, branching, root hairs formation), based the *ArchiSimple* model and the introduction of growth processes regulations by available C (and N*) metabolites	*RhizoDep, Root-BRIDGES, Wheat-BRIDGES*
ANATOMY	**Root Anatomy**	*RhizoDep*	Anatomical properties of a root segment (symplasmic and conductive elements exchange surfaces, volumes, conductances, differentiation of endodermis and exodermis) based on its cylindrical dimensions, its thermal age since formation and possible disruption by a root lateral emergence	*RhizoDep, Root-CyNAPS, Root-BRIDGES, Wheat-BRIDGES*
N	**Root Nitrogen**	*Root-CyNAPS* [2]	Spatialized transport of N in xylem and phloem, radial active and passive transport of mineral N and amino acids between soil, symplasm and conductive elements, symplastic N transformations and consumption by growth	*Root-CyNAPS, Root-BRIDGES, Wheat-BRIDGES*
W	**Root Water**	*Root-CyNAPS*	Water uptake from soil to xylem, axial water transport in xylem and phloem with a radial flow coupling according to the Münch hypothesis, all including an osmotic term function of N (and C*) metabolite concentrations	*Root-CyNAPS, Root-BRIDGES, Wheat-BRIDGES*
SHOOT CN	**Shoot C,N, Growth, Photosynthesis & Senescence**	*CN-Wheat* [3]	Leaf and stem photosynthesis, C&N metabolism in green organs and hidden-zone, 3D growth and senescence, transport in of sucrose and amino acids in phloem towards sink organs, including roots, mineral N and amino acids import from the roots	*CN-Wheat, Wheat-BRIDGES*
LIGHT	**Light Interception**	*Caribu* [4]	Light interception by a 3D canopy from incident PAR using a nested radiosity approach	*CN-Wheat, Wheat-BRIDGES*
SOIL CN	**Soil C&N**	*MIMICS-CN*[5]	C&N transformations between dissolved and stabilized pools of Soil Organic Matter driven by microbial activity of r and K strategists, interacting with available mineral N	*Root-BRIDGES, Wheat-BRIDGES*
SOIL W & TRANSPORT	**Soil Solute & Water Transport**	*CMF* [6]	Water transport in a 3D soil grid according the Richard's equations and solutes advection-diffusion transport	*Root-BRIDGES, Wheat-BRIDGES*

Applying the FSPM composition tool to design *Root-CyNAPS* and *Wheat-BRIDGES* models

This composite FSPM framework was first used on each abovementioned models after they were split as a set of specialist components, e.g. on *Root-CyNAPS* which is the name of the composite FSPM coupling a root nitrogen, water, and anatomy component. This framework was then applied to all 9 targeted components to develop *Wheat-BRIDGES*, the targeted plant scale model accounting for C, N, W, anatomy, growth, and architecture interactions, from organ to stand scale (Fig. 3.2).

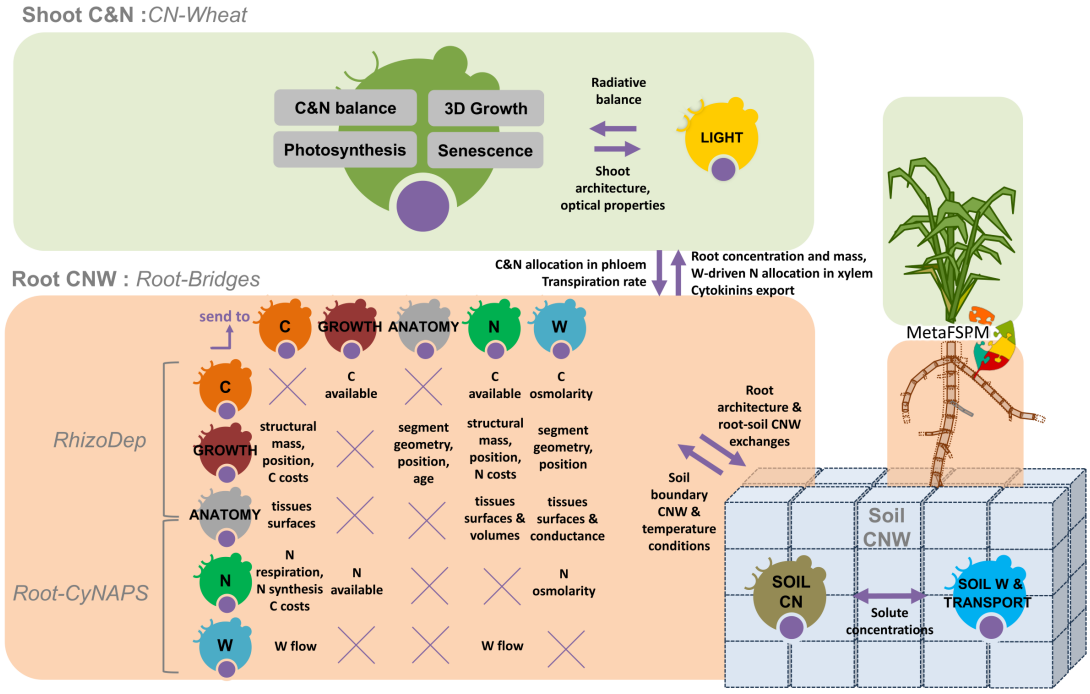

Figure 3.2: Components coupling scheme for the *Wheat-BRIDGES* model. Purple arrows represent the variables exchanged from a component's output to an other's input. For the *Root-BRIDGES* model, a matrix representation was proposed for better readability, with rows representing the source component and columns the receiver. In the representation of unitary components, the purple circle refers to the Base component utility of *MetaFSPM* introduced in Figure 3.1. Colors, corresponding component description and source model are have been listed in Figure 3.1. C stands for Carbon, N for Nitrogen, and W for Water -related processes simulated by the component.

Yet, each component used in *Wheat-BRIDGES* was not originally developed to study shoot-root, root-root and root-soil CN interactions. Adaptations to these models were therefore necessary and are presented in next chapter.

3.5 Discussion

3.5.1 Positioning *MetaFSPM* among existing FSPM platforms and coupling approaches

Functional–structural plant models were explicitly designed as modular representations of plant architectures and processes, in which elementary units and their associated state variables can be combined into more complex models[Sievänen et al., 2014]. Several platforms and formalisms now support the assembly of such models, notably *OpenAlea* and its visual programming environment *VisuAlea* [Pradal et al., 2008, 2015], L-Studio [Cieslak et al., 2011], GroIMP and XL [Hemmerling et al., 2008], or Jupyter-based "virtual modeling environments" [Vaillant et al., 2022]. These frameworks already facilitate the reuse of model components and the construction of heterogeneous workflows. *OpenAlea* use a central data-structure, the MTG, to ease the communication between components. Shared variable are accessed through a graph property. And the components are scheduled using a model of computation, orchestrating the execution of the components. While this approach have been used with success to reuse light models or full FSPM like *Adel*, it does not scale well with fine grain processes and complex scheduling strategies. Moreover, it is cumbersome to implement specific solvers inside the visual programming environment *VisuAlea*. L-Studio and GroIMP have in turn designed powerful formalisms, but they are restricted to their rewriting formalism where the central data-structure (L-string or XL graph) is implicit. Moreover, these approaches provide limited guidance on how to couple independently developed FSPMs that differ in spatial discretization, time step, internal solvers, and metabolite or process representations, especially when many variables have to be exchanged at each time step.

MetaFSPM addresses this methodological gap for models developed on the *OpenAlea* platform by introducing an explicit component abstraction and a composite-model builder on top of existing workflows. At the component level, the *base component* class enforces a homogeneous structure for inputs, outputs, internal formalisms and reading/writing access to central data structures (e.g. MTG for plant architecture, voxel grids for soils). At the composite-model level, *MetaFSPM* formalizes a coupling contract that makes explicit (i) which variables are exchanged between components, (ii) how units and metabolite pools are converted, and (iii) how variables are aggregated or disaggregated when models use different spatial or biochemical resolutions. In contrast to more generic middleware designed to integrate FSPMs across platforms [Long et al., 2018], *MetaFSPM* focuses on within-platform couplings in *OpenAlea*, where components already share central data structures and can therefore be wired together with minimal geometric or topological transformations.

Finally, *MetaFSPM* keeps the demand-driven execution logic of *VisuAlea* workflows, but moves the description of scheduling and solvers to a textual, Python-based scriptable layer. This choice follows the more general trend towards notebook- or script-based environments for model development and experimentation, [Vaillant et al., 2022, Benoit Bovy et al., 2021], while preserving compatibility with existing

OpenAlea components. In practice, this makes it easier to track the provenance of variables, and modify coupling hypotheses (e.g. alternative variable mappings or resolution orders) as part of the scientific code rather than as a visual workflow that becomes difficult to maintain when dozens of components and hundreds of exchanged variables are involved.

3.5.2 Component-based coupling to foster the exploration of multiscale C – N regulations

Applied to nitrogen, carbon, water, growth and anatomical processes in wheat, *MetaFSPM* provided a practical way to decompose complex models into thematic components and to recombine them into composite FSPMs. The coupling of a limited set of components produced *Root-CyNAPS*, a root-scale model of N, water and anatomy (Chapter 2), while the coupling of nine components produced *Wheat-BRIDGES*, a full soil – plant – atmosphere model of wheat. In both cases, the same component interfaces and coupling mechanisms were reused, so that model complexity could be increased progressively without rewriting existing code.

For the scientific questions addressed in this thesis, an important benefit of this approach is the ability to test alternative coupling hypotheses while preserving each component' s internal consistency. For example, the same nitrogen component can be coupled either to a simple homogeneous root carbon supply, or to detailed carbon and growth components, without changing its internal equations. Conversely, the same root architecture and anatomy components can be coupled to different soil hydrology or CN biogeochemistry models to explore how environmental formalisms affect plant – soil feedbacks. This type of "plug-and-play" reconfiguration, which is often cited as a promise of FSPMs but remains difficult to implement in practice [Sievänen et al., 2014, Soualiou et al., 2021], is made more accessible by the explicit coupling contracts and shared data structures implemented in *MetaFSPM*. Moreover, component edition was also made straightforward through inheritance, facilitating targeted equation modifications, e.g. during the coupling of C&N cycles in roots, without compromising the original versions of components that are still in use in other models. This versioning scheme through object-oriented paradigm allows also to improve reproducibility and robustness.

A second benefit is the separation between scientific formalisms and numerical resolution strategies, making the implementation of new components easier by focusing only on physiological parts of the code, while allowing flexibility and control over resolution strategies. In *MetaFSPM*, components can either be executed as black boxes (using their original solvers) or delegated to the toolkit' s own resolution utilities when their equation systems have been declared. This was exploited in *Wheat-BRIDGES*, where different solvers (e.g. explicit Euler for root symplastic CN balance, Newton – Raphson methods for xylem and phloem water flow, implicit Euler scheme for solute advection in sap, ODE solvers for shoot CN balance) were combined within a single resolution loop while ensuring mass conservation and consistent variable passing between components. Such flexibility is critical when coupling models with very different time scales and stiffness properties, and is increasingly emphasized in other modular modeling frameworks beyond plant science

[Post et al., 2024].

3.5.3 Limitations and future developments

At this stage, *MetaFSPM* is tightly coupled to the *OpenAlea* ecosystem and to an MTG-based representation of plant architecture. This choice offers a strong advantage for the present work, since it allows direct reuse of existing *OpenAlea* components and tools,[Pradal et al., 2008, 2015] but it limits interoperability with FSPMs implemented on alternative platforms such as *GroIMP/XL*, *L-Py* outside *OpenAlea*, or *CPlantBox*. One strategy would be to bridge these platforms by adding an additional layers similar to the middleware proposed by Long et al. [2018] for *GroIMP–OpenAlea* integration, or the adoption of more generic exchange standards for architectures and fluxes. In this sense, *MetaFSPM* should be viewed as a contribution to within-platform modularity and coupling practices, rather than as a universal FSPM coupling solution. Another strategy would be to depends on shared, multi-scale, multi-language central data-structure, similar to RSML [Lobet et al., 2015], with an efficient implementation.

Another limitation is that *MetaFSPM* currently focuses on deterministic, mechanistic models. Stochastic processes (e.g. trait-based variability within stands) or data-driven components (e.g. machine-learning surrogates) can technically be wrapped as components, but their systematic integration raises questions about uncertainty propagation, parameter readability and reproducibility that are beyond the scope of this chapter. Yet, recent developments around agricultural digital twins and hybrid modeling frameworks highlight the need to integrate FSPMs into broader modeling infrastructures [Mitsanis et al., 2024], which will further increase the importance of clear component interfaces, coupling contracts and scenario builders of the type implemented in *MetaFSPM*.

Finally, *MetaFSPM* requires to transform boilerplate code into independent, documented, curated components. This require a significant amount of work and may limit its adoption. A solution would be to use agentic LLM to extract all semantic information and build component specification and documentation from existing code base. This strategy is currently tested in *Crop2ML* [Raihauti et al., 2026].

Beyond the use case of this thesis, the core principles included in the *MetaFSPM* framework have therefore been designed to encompass a large variety of models, which opens several prospects. First, extending the library of *MetaFSPM* components to other models developed within the *Openalea* platform or the FSPM community (e.g. SIMBAL Perthame et al. [2023] and other root- or soil-focused models) would broaden the range of processes and scales that can be combined in composite FSPMs for mechanistic exploration and facilitate cross-comparisons of alternative formalisms within a single coupling framework. Second, coupling *MetaFSPM*-based models to utilities for scenario design and standardized downstream analyses will ease the deployment, repeatability and readability of complex FSPM simulations. Third, integrating explicit tools for model calibration, sensitivity analysis and pattern-oriented validation at the level of composite models would help to systematically constrain the growing space of possible couplings and to quan-

tify the added value of refined soil – plant – atmosphere representations for predicting rhizodeposition and N uptake variability.

3.6 Conclusion

In this chapter, we introduced *MetaFSPM*, a generic toolkit for modularizing and coupling Functional-Structural Plant Models on the OpenAlea platform. By formalizing a common *component* structure and separating ecophysiological formalisms from execution utilities, *MetaFSPM* standardizes how inputs, outputs, and equation systems are declared and documented. This homogenization simplifies the integration of independently developed models, reduces the effort required to build and maintain complex workflows, and improves the readability and reusability of component code.

Building on this elementary structure, the composite FSPM builder of *MetaFSPM* allows modelers to assemble networks of components into operational plant or soil-plant-atmosphere models, define explicit coupling contracts, and flexibly configure scheduling and time-stepping strategies. The first applications to *RhizoDep*, *Root-CyNAPS*, *CN-Wheat*, and associated environment models demonstrate that existing FSPMs can be reorganized into interoperable components and recombined into complex models such as *Root-BRIDGES* and *Wheat-BRIDGES*. These use cases illustrate that *MetaFSPM* can progressively accommodate additional components and alternative formalisms, offering a scalable framework for future developments in mechanistic soil-plant-atmosphere modeling.

3.7 Chapter Contribution to Thesis Strategy

Within the overall thesis, this chapter provides the methodological infrastructure required to link local root–soil exchanges to whole-plant C&N balance. By modularizing existing models into standardized components and assembling them with the *MetaFSPM* toolkit, I show that independently-developed FSPMs of roots and shoots, soil models, and light interception models can be combined into a single, coherent framework. This directly answers the methodological question on how to design a multiscale FSPM framework for the soil-plant-atmosphere system (Chapter 1), and prepares the quantitative assessment of how explicit root–soil exchange heterogeneity affects plant C&N balance. Although *MetaFSPM* does not answer to hypotheses **H2-H5** on its own, it makes them testable by the construction of composite models such as *Root-BRIDGES* and *Wheat-BRIDGES* that integrate (i) heterogeneous root N uptake and rhizodeposition (central to **H2-H4**) with (ii) shoot photosynthesis and C allocation controlling N acquisition and rhizodeposition dynamics (**H5**). The outcomes of this chapter are used directly in Chapter 4, where *Wheat-BRIDGES* is built from *MetaFSPM* components to quantify the impact of explicit root-soil exchange heterogeneity on plant C&N balance.

Chapter 4

Wheat-BRIDGES, a whole-plant model to study the multiscale determinants of C&N exchanges between roots and soil

4.1 Chapter strategy

This chapter addresses the second modeling step of my thesis: propagating the local heterogeneity of root – soil exchanges described in Chapter 2 to whole-plant C&N balance using the tools of Chapter 3. It directly contributes to the first thesis objective of quantifying the impact of spatially-variable rhizodeposition and N uptake on plant C&N balance, and addresses more specifically the following questions:

- *What is the impact of local root C&N processes on plant-scale C&N balance?*
- *To what extent can explicit root – soil exchange heterogeneity alter the dynamics predicted by an existing whole-plant model with a homogeneous root compartment?*

Here, I have used the composite model *Wheat-BRIDGES* to test, from organ to plant scale, several hypotheses introduced in Chapter 1. In particular:

- **H1**, stating that rhizodeposition is not simply proportional to root system biomass or photosynthate allocation;
- **H2** and **H3**, stating that the contribution of a active regions of the root system and the dominant processes underlying N uptake and rhizodeposition can shift over time and between root zones;
- **H4**, stating that heterogeneity in anatomy and metabolite concentrations tends to co-localize C and N exchanges along roots;
- **H5**, stating that plant-scale variations in rhizodeposition and N uptake are synchronized over time by photosynthetic activity. These assumptions are summarized in the conceptual scheme below (Fig. 4.1).

To address these questions, I have used the *MetaFSPM* framework (Chapter 3) in order to (i) integrate root C, N, and water dynamics with dynamic root architecture and anatomy within the *Root-BRIDGES* model (derived from *Root-CyNAPS* and *RhizoDep*), (ii) replace the homogeneous root submodel of *CN-Wheat* and create a new plant model with the same level of architecture and process discretization between shoot and root compartments, and finally (iii) couple this plant model to existing 3D light and soil components. The resulting composite FSPM, *Wheat-BRIDGES*, has been applied to winter wheat growth under a realistic field scenario previously used to validate *CN-Wheat*, in order to check the coherence of the new coupled model against the reference outputs of *CN-Wheat*, and then leverage the integration of the root system architecture in *Wheat-BRIDGES* to analyze C&N balance and root – soil exchange patterns across scales, from root segments to plant scale.

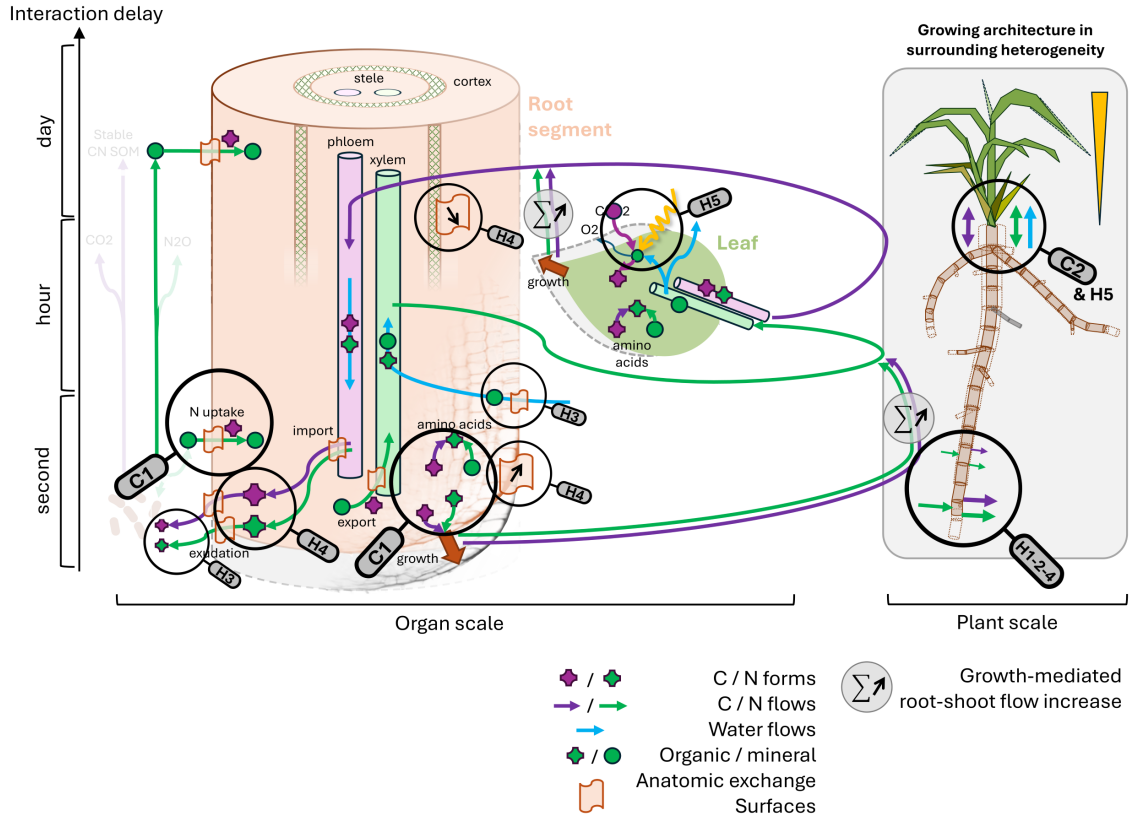

Figure 4.1: Conceptual scheme summarizing the key processes and scales considered in Chapter 4, with magnifying glasses positioning C&N cycles coupling points and tested hypotheses. **C1** stands for C&N coupling at local scale with the regulation of active N transport by hexose and co-regulation of metabolic and growth processes by hexose and amino-acids, and **C2** for shoot-root C&N allocations. Hypotheses **H1** to **H5** are also positioned on the scheme.

4.2 Introduction

In previous chapters, I developed the building blocks needed to couple existing FSPMs of wheat into a whole plant architectured model that represents local root – soil exchanges and integrate them in plant C&N balance. In Chapter 2, *Root-CyNAPS* was used to simulate heterogeneous N process, water flow and anatomy features on static root system architectures, soil conditions and shoot-root junction boundary conditions. These static boundaries however restrained the use of the model to short term simulations, with important uncertainties in the estimation of model inputs. In parallel, *RhizoDep* simulates carbon allocation and metabolism within the root system and the resulting rhizodeposition processes (exudation, mucilage, sloughed cells) as functions of local hexose availability [Rees et al., 2025]. At plant scale, *CN-Wheat* simulates shoot architecture, light interception and C&N metabolism in each shoot organ, with a homogeneous, non-architectured root compartment [Barillot et al., 2016, Gauthier et al., 2020]. These three models share a common representation, local processes regulated by metabolite concentrations, and would complement each other by mechanistically simulating the complex inputs expected by other components (e.g. metabolite concentration profiles along roots or shoot-root C&N allocations). However, these models differ in structure, solving strategy and spatial resolution, and could not be naively merged.

Chapter 3 introduced *MetaFSPM*, a coupling toolkit for OpenAlea that reorganizes such models into standardized components and assembles them into composite FSPMs via explicit coupling contracts. Using this framework, *RhizoDep* and *Root-CyNAPS* were first combined into *Root-BRIDGES*, a generic root module that jointly simulates C, N and water processes in a growing, architectured root system. However, as long as *Root-BRIDGES* is driven by prescribed shoot – root boundary conditions, its simulation of total rhizodeposition and N uptake remains dependent on predetermined inputs at the root – shoot junction. Conversely, *CN-Wheat* describes the feedbacks between organ-scale C&N status and leaf growth and photosynthesis, but it aggregates root processes into a single compartment and cannot represent the spatial heterogeneity of root – soil exchanges. To understand how local root processes shape plant-scale C&N balance, and to test the hypotheses formulated in Chapter 1, it was therefore necessary to close the C&N cycles of the plant by coupling *CN-Wheat* and *Root-BRIDGES* using *MetaFSPM*, yielding the *Wheat-BRIDGES* plant scale model.

This C&N coupling process required (i) replacing the homogeneous root compartment of *CN-Wheat* with *Root-BRIDGES*, (ii) ensuring that shoot – root allocation and xylem/phloem transport remain numerically stable when moving from homogeneous to spatialized compartments, and (iii) coupling the resulting plant model with 3D soil and light models, so that realistic gradients of resource availability and soil C/N dynamics are simulated along the root and shoot exchange surfaces. In this chapter, I detail the targeted adaptations made to each component, the simulation loop of the model and numerical resolution choices used to maintain mass conservation, and the parametrization of *Wheat-BRIDGES* under the field scenario of Ljutovac [2002]. I then compare simulations from *Wheat-BRIDGES* and *CN-Wheat* to assess the impact of introducing an architectured root system on plant C&N

balance, before analyzing C rhizodeposition, N uptake and water uptake patterns across scales, from plant totals to localized *active root zones* to address hypotheses **H1** to **H5**.

4.3 Material & Methods

4.3.1 Adaptation of existing FSPM components for the *Wheat-BRIDGES* model

This section details how the composite *Wheat-BRIDGES* model was designed and used to couple local root – soil exchange heterogeneity to whole-plant C&N balance. I first recall the structure of *Wheat-BRIDGES*, obtained by coupling *RhizoDep*, *CN-Wheat* and *Root-CyNAPS*, and then present a first field simulation scenario.

Root-BRIDGES: modeling the dynamics of C&N rhizodeposition with *RhizoDep* and *Root-CyNAPS*

Root-BRIDGES is an intermediate root-scale FSPM built by coupling the carbon processes of *RhizoDep* with the nitrogen and water processes of *Root-CyNAPS*. Its purpose is to simulate, along a growing root system architecture, the joint dynamics of C, N and water, together with root growth and anatomy, in order to mechanistically simulate and identify the determinants of rhizodeposition and N uptake heterogeneity along roots. Both parent models adopt the same root-segment-scale description, rely on the same root system architecture and anatomical component, and use consistent units. This shared representation makes *Root-BRIDGES* a natural extension of *RhizoDep* and *Root-CyNAPS* towards a coupled C – N – water framework. The coupling between *RhizoDep* and *Root-CyNAPS* was therefore introduced at three levels: (i) between C and N components for local C&N metabolism and transport, (ii) between N and root growth components for co-regulation of root growth by local hexose and amino acids concentrations, and (iii) between water and C components for spatialized transport of sucrose.

In *Root-CyNAPS*, a dependency of N active transport and amino acid synthesis on symplastic hexose concentrations had already been implemented, with concentration gradients along roots provided by RhizoDep C component as inputs. In addition, Root-BRIDGES introduced a **respiration cost associated to the exchange of N** in the C balance component, i.e. C costs for N active transport and amino acids synthesis, storage proteins synthesis and related energetic costs (Fig. 3.2). In line with Thornley and Cannell [2000], Robinson [2001], Barillot et al. [2016], respiratory costs are considered as proportional to N transport and synthesis costs with dedicated parameters.

Then, a N dependency for the growth component was introduced by co-regulating root tip elongation by the symplastic concentrations of not only hexoses but also amino acids, based on expected C&N content in structural mass [Heinemann et al., 2023, Fradgley et al., 2021]. As for hexose in RhizoDep, we defined the amount amino acids available for root tip elongation based on the volume of the elongation zone, itself driven by root tip diameter (Eq. S7; Rees et al. [2025]). The corresponding

massic concentrations are noted $[hex_{symp}^{available}]_m$ and $[AA_{symp}^{available}]_m$ $(mol.s^{-1})$. The same formalism as in RhizoDep (Eq. S6) was then kept for root tip elongation rate in Eq. 1.1 :

$$elongation = elongation_{max} \cdot R \cdot (1 - friction) \cdot elongation_{reg}^{CN} \tag{1.1}$$

where $elongation_{max}$ is the maximal rate of root elongation per unit of root radius (s^{-1}), R is the root radius (m), $friction$ is a coefficient related to soil mechanical impedance (dimensionless), and $elongation_{reg}^{CN}$ is a Michaelis-Menten function accounting for the availability of metabolites consumed by growth in the root zone (dimensionless). The main adaptation from RhizoDep is the introduction of a co-regulation by hexose and amino acids in this function (Eq. 1.2).

$$\begin{aligned} elongation_{reg}^{CN} = (1 - p_{struct}^{CfromAA}) \cdot \frac{[hex_{symp}^{available}]_m}{K_{elongation}^{hexose} + [hex_{symp}^{available}]_m} \\ + p_{struct}^{CfromAA} \cdot \frac{[AA_{symp}^{available}]_m}{K_{elongation}^{AA} + [AA_{symp}^{available}]_m} \end{aligned} \tag{1.2}$$

where $K_{elongation}^{hexose}$ and $K_{elongation}^{AA}$ represents the concentrations of hexose and amino acids for which half of the maximal rate is reached, respectively, and $p_{struct}^{CfromAA}$ is the proportion of carbon consumed by growth that is sourced from amino acids, estimated as follows:

$$p_{struct}^{CfromAA} = \frac{nb_{C:AA} \cdot p_{struct}^{N}}{nb_{N:AA} \cdot p_{struct}^{C}} \tag{1.3}$$

where $nb_{C:AA}$ and $nb_{N:AA}$ are the average C and N numbers per amino acid, respectively, while p_{struct}^{N} and p_{struct}^{C} are the N and C molar proportions in structural mass, respectively. A similar C-N co-regulation was introduced for root thickening processes with dedicated $K_{thickening}^{hexose}$ and $K_{thickening}^{AA}$ parameters.

Finally, the **spatialized transport of sucrose in phloem** was introduced as in *Root-CyNAPS* in addition to the transport of amino acids driven by the phloem sap flux (Eq. 4.7; Gerault et al.). Sap flow was therefore introduced as input of the carbon component. To align with Root-CyNAPS, volumic concentrations of sugars were introduced to drive the diffusive flows between phloem, symplasm and soil, which contrasts with gradients of massic concentrations used in RhizoDep. Since the water transport in xylem and phloem accounts for an osmotic component in addition to advection, the variable sucrose volumic concentration in phloem was also provided to the water component. Indeed, this solute is considered to be the major contributor of osmotic potential variations in phloem, impacting local water flows [Dinant et al., 2010].

RhizoDep and *Root-CyNAPS* were designed to be generic to any species. Before further coupling these with a wheat-specific shoot model for the objective of this thesis, this root C, N, W, growth and anatomy intermediate coupling was structured as the *Root-BRIDGES* model (Root Biogeochemical Integration by Development and Growth of Environmental Signals), which offers the possibility to be coupled with a wide variety of FSPM shoot models.

Targeted components modifications for *Root-BRIDGES* were made clearly readable in the code by *component inheritance* and are available at https://github.com/GeraultTr/Root_BRIDGES. Inheritance is a coding practice, made possible the usage of MetaFSPM's *base component*, that enabled to reuse the whole structure and functionality of a component and make precise processes editions, while keeping the base models functional. This means modifications introduced for *Root-BRIDGES* are not specific to a version of *RhizoDep* or *Root-CyNAPS*, which is a critical aspect for a multidisciplinary coupling framework where unitary components keep evolving.

Wheat-BRIDGES: a plant scale C&N model coupling *Root-BRIDGES* and *CN-Wheat*

The published version of *CN-Wheat* is already a whole plant model, and includes a homogeneous and non-architectured root compartment (Barillot et al. [2016], Gauthier et al. [2020], see State of the Art chapter). Moreover, all metabolite flows and concentrations balance in *CN-Wheat* are solved simultaneously by a single solver. Before replacing the root model by *Root-BRIDGES*, we first verified that splitting the differential equation system of *CN-Wheat* into shoot and roots subsystems, did not significantly change the simulated results compared to the published original version. By resolving the differential equations system sequentially, with first a shoot solver and then a root solver, no significant deviation from the reference version of the model was observed.

Four coupling adaptations were made to allow *Root-BRIDGES* to interact with *CN-Wheat* shoot organs:

1. First, we kept the same formalism as *CN-Wheat* for sucrose and amino acids allocation to the roots as a diffusive process driven by a shoot-root gradient of mass concentrations. However, the CN-Wheat model does not originally split the phloem compartment between roots and shoot; phloem is defined as a homogeneous, plant-scale compartment. Thus, the concentration gradient driving allocation between shoots and roots in CN-Wheat is defined between a plant-scale phloem and a root compartment that encompasses all root tissues except phloem. However, *Root-BRIDGES* introduced a dedicated root phloem compartment. *CN-Wheat* was therefore modified by redefining, for any metabolite, the phloem concentration to which every shoot organ is connected as the amount of metabolite divided by the shoot structural mass, therefore excluding root structural mass. This enabled the definition of a mass concentration gradient between an average shoot phloem and root phloem at root-shoot junction, without overlap between the two models, to drive shoot-root exchanges. This diffusion formalism was then transferred to the root water-solute transport solver, in order to ensure numerical stability in the computation of high sucrose and amino acids flows to roots through very tiny phloem volumes. To do so, a *hard wiring* of the two models reusing CN-Wheat conductance parameter was not possible, as it was to high and created bouncing concentrations and reverting flows compromising the numerical stability of the model. Instead, we initialized the model at a far lower conductance (10^{-9} factor) and exponentially increased the conductance over the first 3 mg

of root growth towards the desired parameter value. This ensured a stable initialization of the model while allowing high root-shoot allocation fluxes.

2. Second, a key modification is the explicit modeling of solute advection through the transpiration stream in root xylem, compared to *CN-Wheat* for xylem root-to-shoot allocation. Leaf transpiration simulated by *CN-Wheat* has therefore directly been applied to the root-shoot junction as an input of the water component, assuming a low capacitance of shoot tissues [Orieux et al., 2018, Khare et al., 2022]. As a consequence, the allocation of mineral N and amino acids towards the shoot is simulated by *Root-BRIDGES* as the sum of advection flows reaching the shoot-root junction (Eq. 4.7; Gerault et al.).

3. Third, we introduced a synchronization of nodal roots emergence with leaves emergence, a phenological observation reported by several authors that would be key to balance roots C costs for soil resource acquisition and the development of leaf area [Woodruff, 1980, Klepper et al., 1984, York et al., 2018, NGUYEN, 2023]. All adaptations in this regard were performed on the growth component of *Root-BRIDGES*, receiving the leaf initiation status from *CN-Wheat* as input to initiate the emergence of nodal primordium. In RhizoDep, all nodal primordium are initiated at germination and their emergence is delayed by a thermal duration defined from input data. Here we adapted the growth component so that following each leaf emergence, 2 to 4 nodals primordia can emerge after a constant thermal time delay parametrized at 180°C day. Following results from Klepper et al. [1984], this phenological rule was introduced for all leaves emergence, whether carried by the main stem or tillers. Exception was made for leaves whose insertion nodes are positioned aboveground by internode elongation, since nodal roots primordium are carried by these nodes and cannot emerge in the air compartment.

4. Finally, a total cytokinin synthesis and balance of the root system was replicated from *CN-Wheat* to link shoot protein degradation to root system CN availability [Criado et al., 2009, Barillot et al., 2016]. Compared to *CN-Wheat*, which expresses C&N pools as root system totals, here cytokinin synthesis was co-regulated by root system average hexose and mineral N *symplastic* concentrations. Otherwise the same pools and parameters were used, and the export of cytokinins to the shoot was calculated by *CN-wheat* and passed to the roots as in the original model.

These four adaptations of the *CN-Wheat* and *Root-BRIDGES* components enabled the coupling of root-shoot CN allocation and growth/decay phenology. The resulting plant-scale component network was called *Wheat-BRIDGES*, available at github.com/GeraultTr/Wheat-BRIDGES, and was also coupled to existing soil models to study the spatial and temporal CNW interactions between roots and soil.

Coupling root uptake and rhizodeposition to soil in *Wheat-BRIDGES*

Exchanged variables between roots and soil relate to the processes associated with net mineral N uptake, net rhizodeposition and water uptake. Conversely, *Wheat-*

BRIDGES requires indications of soil mineral N, organic solutes, and water availability as well as soil temperature perceived for each root segment. In its current state, two soil model options were introduced in *Wheat-BRIDGES*.

First, the original version of *CN-Wheat* already introduced a homogeneous soil N model to simulate the evolution of the average mineral N concentration over time [Barillot et al., 2016], which was transposed to Wheat-BRIDGES.

Second, we designed a new 3D CNW soil model, *RhizoSoil*, to study the local CN interactions between root and soil. This model was developed from the coupling of two existing soil models in the *MetaFSPM* framework: (i) the *CMF* model (Catchment Modeling Framework, Kraft et al. [2011]) was selected to introduce water-solute transport in a 3D voxel grid using Richard's equations and advection-diffusion for solute transport, (ii) the *MIMICS-CN* model (MIcrobial-MIneral Carbon Stabilization, C&N version of Kyker-Snowman et al. [2020]) was used in each soil voxel to introduce the microbial-mediated biochemistry of stable, particulate and labile C&N pools of soil organic matter. Other relevant C-N soil models were also reviewed [Zhang et al., 2021, Wang et al., 2022], but *MIMICS-CN* was selected for convenient coupling since it was already implemented in Python by Brunmayr et al. [2024]. No modification was introduced from the published versions of these two models, except for the 3D transport of labile pools (mineral N and dissolved organic matter) by *CMF*, compared to the published version of *MIMICS-CN* which was not spatialized. To parametrize the model for a use-case, one should provide soil texture and bulk density, as well as the meteorological time series for soil temperature and rainfall. This soil model was effectively coupled to *Wheat-BRIDGES* and made available at github.com/geraultTr/rhizosoil, but was not used in the presented use case to focus first simulations on plant physiology and avoid confusion with the overlap of heterogeneous soil processes.

4.3.2 *Wheat-BRIDGES* simulation loop

The *Wheat-BRIDGES* model was used with an hourly time-step for all components, and plant components were ordered as follows.

1. The root growth component is executed based on the availability of C&N metabolites computed at the previous time step, and updates root architecture and the related C&N costs. It runs three discrete resolutions during the time-step: (i) it computes the maximal potential growth of each elements regulated by hexose and amino acids concentrations in the growing zone, (ii) it solves the actual metabolite consumption rates by growth and related respiration from available amounts in the growing zones, and (iii) runs the architectural model to segment new root segments when growing zones have reached a threshold length.

2. The root anatomy component updates the exchange surfaces, volumes and conductances of the new root architecture. The root anatomy component therefore also runs at a discrete hourly time-step with no priority between the simulated state variables, which are all used by following components.

3. The root water component simulates water radial and axial flows based on the current state of the root system, and the shoot transpiration and the pressure and osmotic components of the water potential computed at the previous time step. To do so it uses a Newton-Raphson approach which is an iterative method to identify the water potential profiles along roots at which the system converges.

4. Using a *MetaFSPM* capability, the root C and N components were merged to run simultaneously, thus implying no priority between C and N processes. This merged component runs in 3 steps: (i) it runs a discrete resolution on all metabolic and radial C-N processes, (ii) the axial transport in xylem and phloem is then solved from input water flows, previous time-step concentrations and just computed radial flows with the symplasm using an implicit Euler scheme. In particular, this resolution solves the export rate of mineral N and amino acids export to shoot model through xylem and the import rate of sucrose and amino acids from the shoot through phloem. This resolution also recomputes the radial xylem-symplasm and phloem-symplasm exchange rates to finally (iii) update cytosolic concentrations using a discrete approach.

5. Finally, the CN-Wheat shoot component sequentially simulates shoot senescence, photosynthesis, architectured growth using discrete resolutions, and CN metabolism, transport and concentration balance balance is computed by a solver of ordinary differential equations.

When simulating a stand, all *Wheat-BRIDGES* plants in the stand are first run in parallel, and then all environment models (light and soil) are run in parallel based on the updated plant variables.

4.3.3 First *Wheat-BRIDGES* parametrization and simulation scenario under variables environmental conditions

To build a simulation scenario, *Wheat-BRIDGES* is more autonomous than isolated root models in terms of input data and only requires meteorological time series. However, its initialization requires specific adaptations to align the initialization of its shoot and root components. Indeed, the original *CN-Wheat* model is initialized at the 3-leaf stage, which corresponds to 51 days after sowing according to measurements by Ljutovac [2002], whereas *Root-BRIDGES* starts from seed germination. In order to compensate for this discrepancy, *Root-BRIDGES* had to be provided with sucrose and amino acid allocations to the roots, as well as leaf transpiration data for the first 51 days. Unfortunately, no realistic experimental data for these values could be found in the literature under such variable weather conditions. We therefore used the results of a new version of CN-Wheat (Barillot comm. pers.) from germination onward to provide plausible C&N allocation and transpiration data to *Root-BRIDGES* during the first 51 days of growth and, ultimately, to initialize the root system state for all *Wheat-BRIDGES* simulation scenarios.

A first *Wheat-BRIDGES* simulation scenario was built from the same field experiment used by *CN-Wheat* for its validation on winter wheat vegetative stage, i.e. the meteorological series and shoot measurements of Ljutovac [2002] (Fig. 4.2).

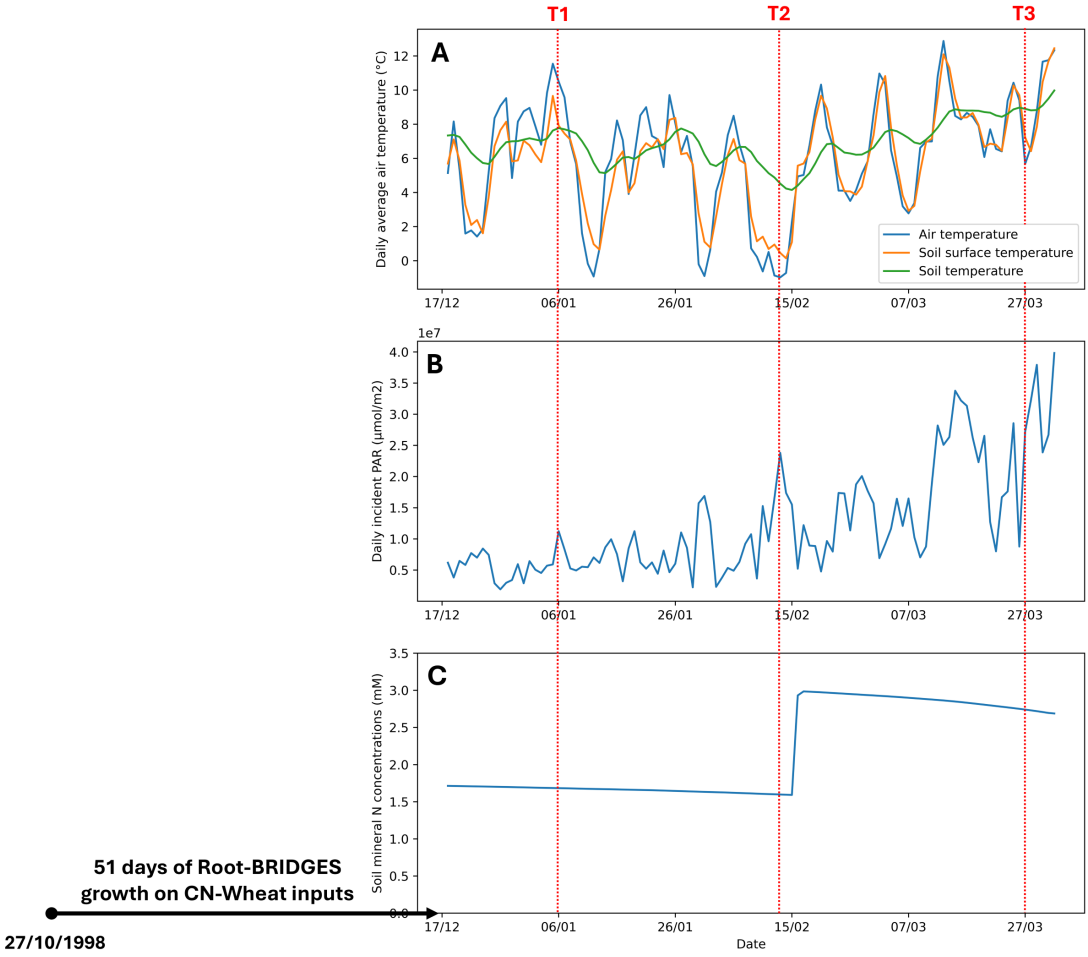

Figure 4.2: Environmental conditions at the boundary of *Wheat-BRIDGES* organs, after 51 days of root system growth since germination to match the 3-leaf stage initialization of CN-Wheat. **A)** Evolution of air temperature perceived by shoot aboveground organs, soil-surface temperature perceived by shoot nodes, and soil temperature perceived by the root system. **B)** Evolution of daily incident PAR, and of **C)** mineral N concentration in soil, with a 50 $kg\ N\ \ ha^{-1}$ fertilization event at 60 days. **T1**, **T2** and **T3** correspond to specific times studied in this Chapter.

We chose to reuse this scenario for *Wheat-BRIDGES* to avoid introducing differences in experienced environments that would confuse the identification of differences between the two models related to different plant modeling choices, i.e. the introduction of an architectured root system. In this perspective, the homogeneous soil option was also selected in Wheat-BRIDGES to ease the direct comparison with *CN-Wheat*. Starting from the 3-leaf initialization presented above, both *Wheat-BRIDGES* and *CN-Wheat* were run to simulate 104 days of wheat growth under the same climatic series, with plants in stand (250 plant/m^2) interacting through the homogeneous soil N model of *CN-Wheat*.

Default wheat parameter values were kept for all components of Wheat-BRIDGES to enable a direct comparison of simulated patterns with reference simulations of CN-Wheat, RhizoDep, Root-CyNAPS and HydroRoot. Only one exception was made for the parameter of surfacic permeability between local root phloem and root symplasm, which is critical to the unloading rate of hexose and amino acids to

growing root zones and ultimately the extent of root system development. This parameter was **calibrated manually** under one objective, aligning *Wheat-BRIDGES* results with the evolution of leaf length simulated by the reference simulation of *CN-Wheat*. Leaf length measurements from Ljutovac [2002] were indeed a key validation focus of *CN-Wheat* and we ensured *Wheat-BRIDGES* did not diverged from these reference trends. However, early tests showed that the phloem permeability value introduced by *RhizoDep*, converted when switching from massic to volumic concentration gradients in *Wheat-BRIDGES*, was too low to sustain sufficient root growth, resulting in low N uptake levels and a significant downregulation of leaf growth by low N concentrations in shoot compared to CN-Wheat simulations. Acknowledging the impacts of spatializing phloem sap transport, discussed below, compared to homogeneous phloem compartments of RhizoDep and CN-Wheat, we therefore iteratively increased this phloem permeability parameter so that root growth and its interactions with shoot growth could sustain the evolution of leaf length reported experimentally.

4.4 Results

The analyses of the first *Wheat-BRIDGES* simulation results are presented below to evaluate the coherence of model's outputs and also confront our hypotheses. **First**, we compared the simulation outputs from *Wheat-BRIDGES* with those of the original *CN-Wheat* model to evaluate the impact of the new allocation formalisms and the introduced leaf-nodal emergence synchronization on root and shoot development (H5). **Second**, we looked at plant's C & N balance to assess the share of rhizodeposition in this balance and compare it with estimates from the literature. **Third**, we tested the hypothesis of a correlation between rhizodeposition and net N uptake at the plant scale over time (H4). **Fourth**, we addressed the same issue at a finer spatial scale, looking at the co-location of distinct root-soil exchange processes along roots. **Finally**, we re-evaluated the contribution to N absorption of *most active root zones* identified in Chapter 2.

4.4.1 Comparison of simulation outputs between *CN-Wheat* and *Wheat-BRIDGES*

We observe a good consistency between the *CN-Wheat* and *Wheat-BRIDGES* models on most blade lengths and emergence dates (Fig. 4.3). Slight overestimations were simulated by Wheat-BRIDGES before 500°C day. In contrast, blades of metamers 8 and 9 were significantly shorter than in *CN-Wheat* outputs past 500°C day. These small discrepancies were mainly related to differences in root N uptake and allocation between the two models, resulting in more variable shoot N content in *Wheat-BRIDGES* than in *CN-Wheat* simulations (Fig. S6.15). At the end of the simulation, the reached Leaf Area Index (LAI) was 3.8 and 3.3 for *CN-Wheat* and *Wheat-BRIDGES*, respectively.

The evolution of shoot and root structural mass was compared between the original *CN-Wheat* model and *Wheat-BRIDGES* in order to investigate how accounting for an explicit root system architecture and specific shoot-root coordination rules

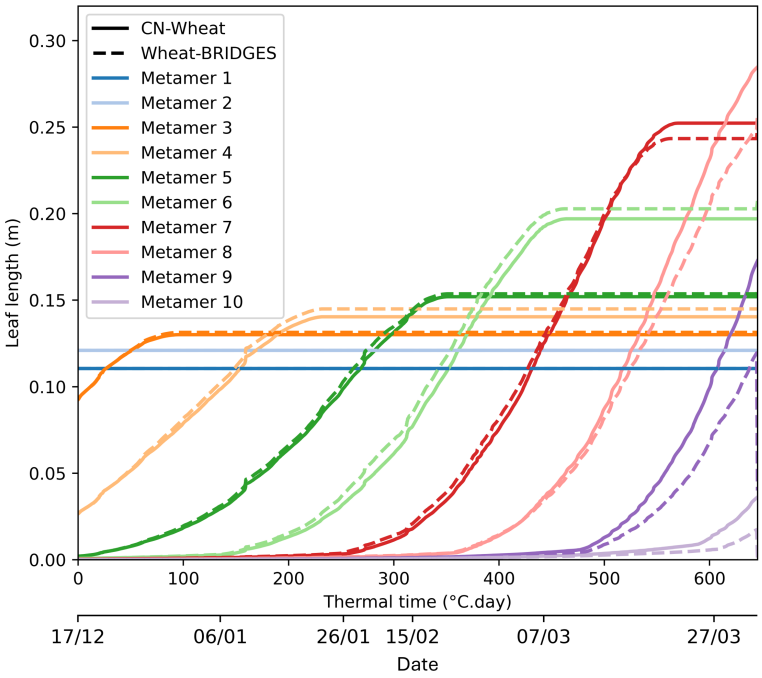

Figure 4.3: Evolution of the length of individual leaves on the main stem over time, simulated by *CN-Wheat* (solid lines) and *Wheat-BRIDGES* (dashed). Each color corresponds to an individual blade.

can alter shoot-root resource allocation (Fig. 4.4). The shoot structural mass simulated by *Wheat-BRIDGES* matched well that simulated by *CN-Wheat* until 200 growing degree days and then increased faster than in the reference simulation. The production of root structural mass was however faster in *Wheat-BRIDGES* since the beginning of the simulation, with local accelerations in root growth compared to *CN-Wheat* related to the emergence of sets of nodal roots synchronized with leaf emergence. As root biomass was not measured in the experiment of Ljutovac [2002], this evolution remains theoretical for either model. Consequently, the shoot:root mass ratio simulated by *Wheat-BRIDGES* was lower compared to that simulated by *CN-Wheat* simulations at the start of the simulation, before reaching similar levels at the end of the simulation (Fig. 4.5).

4.4.2 Cumulated C&N plant balance over time

We first verified that despite its complexity, the *Wheat-BRIDGES* model respects the conservation of C & N mass at the whole plant scale (Fig. 4.6), with the sum of resource allocations being equal to the corresponding input into the system by photosynthesis or net N uptake. For both C and N allocations, we simulated an exponential increase of cumulative of flows over time, mirroring the production of plant biomass, which was composed at 66% of structural mass and remaining 34% under labile form for carbon, and only 16% of nitrogen in root biomass ended up in structural mass.

Then, we simulated that C rhizodeposition represented in average 6% of C fix-

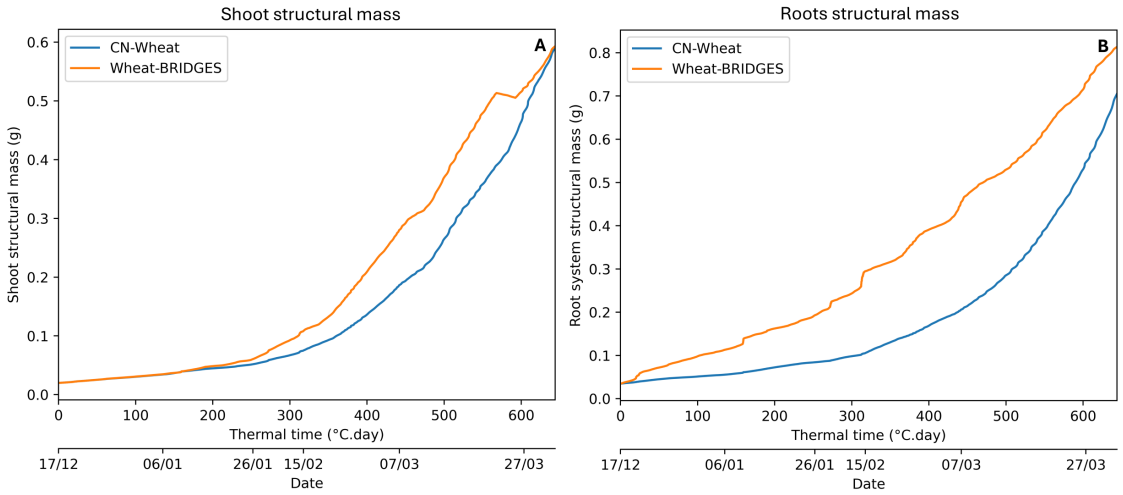

Figure 4.4: Evolution of structural mass over thermal time for both shoot (A) and roots (B), comparing simulations of CN-Wheat (blue) and Wheat-BRIDGES (orange) models

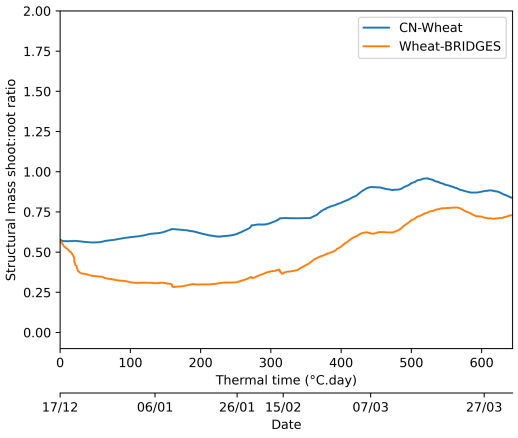

Figure 4.5: Evolution of the structural mass shoot:root ratio of winter wheat over time, as simulated by CN-Wheat (blue) and by Wheat-BRIDGES (orange) models

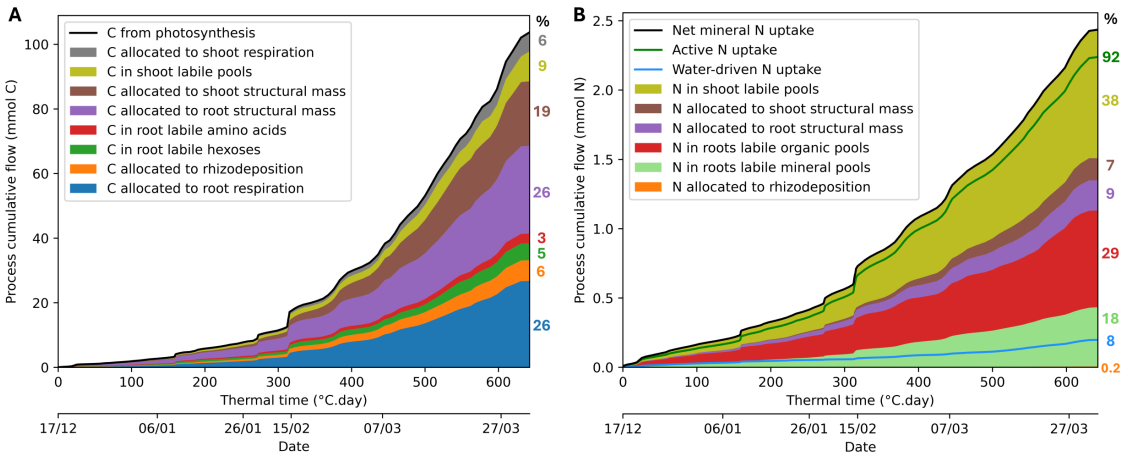

Figure 4.6: Evolution of the cumulative amounts of carbon (A) and nitrogen (B) taken by the plant and allocated to different plant compartments or lost by the plant though respiration and rhizodeposition. The simulation corresponds to the vegetative growth of winter wheat from mid-December to end of March. Three types of C&N allocations are represented: (i) cumulative allocation to shoot or root structural mass production, (ii) the size of the shoot or root labile pools at corresponding time on X axis, which is not cumulative, and (iii) the cumulative allocation to outflows from the plant (respiration and rhizodeposition). Final percentage of each process and pool in plant balance is indicated by a number at the right of the graph.

ation by photosynthesis throughout the simulated vegetative stage. Comparatively, N rhizodeposition was much lower (0.2%) than N uptake (Fig. 4.6B). Moreover, root respiration was 5 times higher than shoot respiration (Fig. 4.6A). Active N uptake represented 92% of total N uptake against 8% for water-driven, apoplastic N uptake. The relative allocation of C & N within the plant, expressed in percentage of photosynthesis and N uptake respectively, remained very stable over time, except for the first day where C & N accumulated in labile pools (Fig. 4.7). In particular, the relative proportion between active N uptake, water-driven N uptake and N rhizodeposition did not vary significantly throughout the simulation, challenging hypothesis **H3** about the shift in dominant exchange processes over time.

4.4.3 Correlations between C & N flow rates over time at the scale of the plant

Hypothesis **H5** assumes a correlation between total C rhizodeposition and net N uptake. In Fig. 4.8A, a positive correlation between the two flows appeared when expressed in absolute values (mol per day per plant), suggesting that C rhizodeposition and N uptake respond to the extension of the root system in a similar way. However, when normalizing by the structural mass of the root system, no consistent trend was observed, as both positive and negative correlations could be observed between C rhizodeposition and net N uptake, depending on the period (Fig. 4.8B).

Total C rhizodeposition and net N uptake were also plotted against shoot photosynthetic activity to evidence whether the two massic flows differed in their response to photosynthetic activity and/or their influence on it (Fig. 4.9 and Fig. 4.10). The

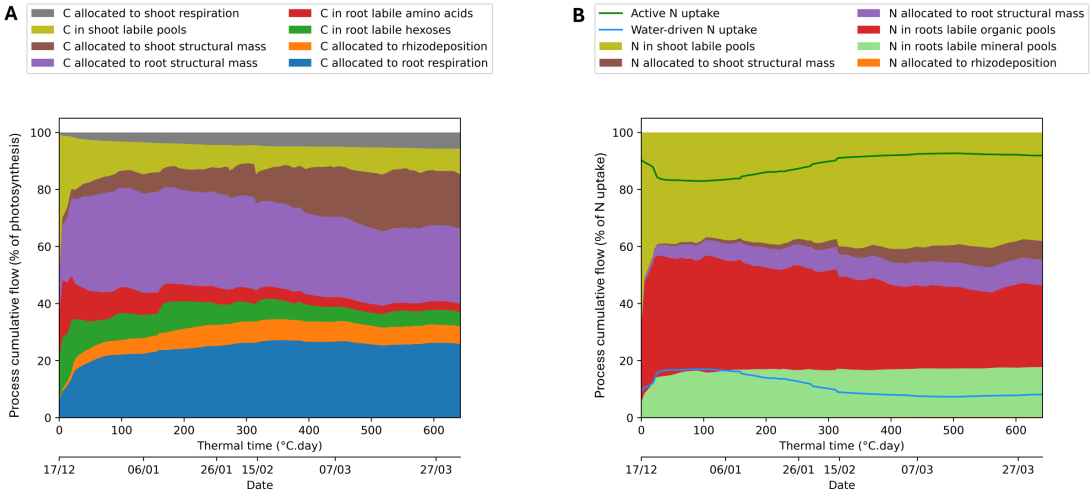

Figure 4.7: Evolution of cumulative allocation and loss flows of the plant represented as percentage of A) photosynthesis C input and B) net N uptake input. Flows are represented in a stack, where the height of the corresponding color is the the flux percentage of input C or N flow.

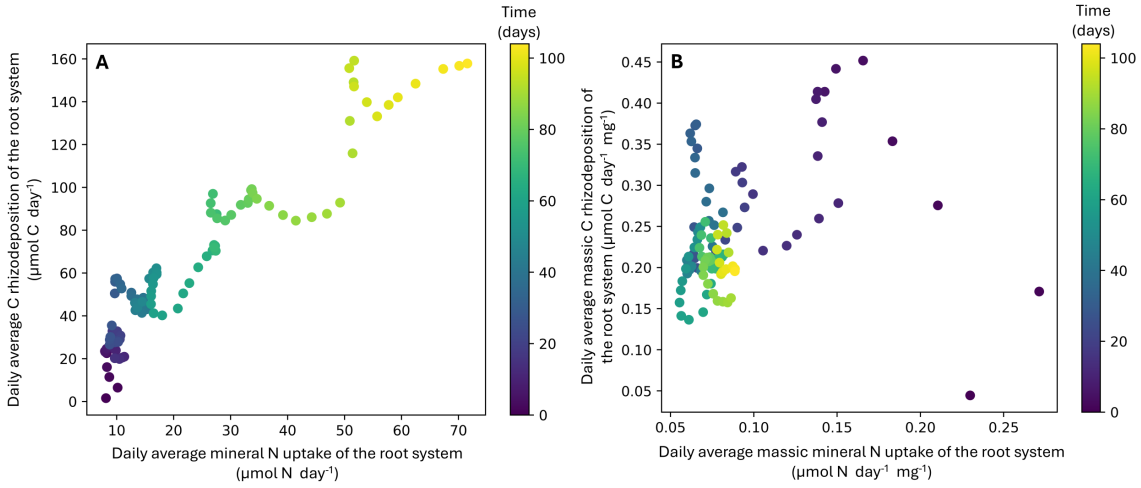

Figure 4.8: Daily average total C rhizodeposition as a function of net N uptake over time **A)** for absolute flows and **B)** normalized by root system's structural mass. The colors represent the time in days since the simulation started.

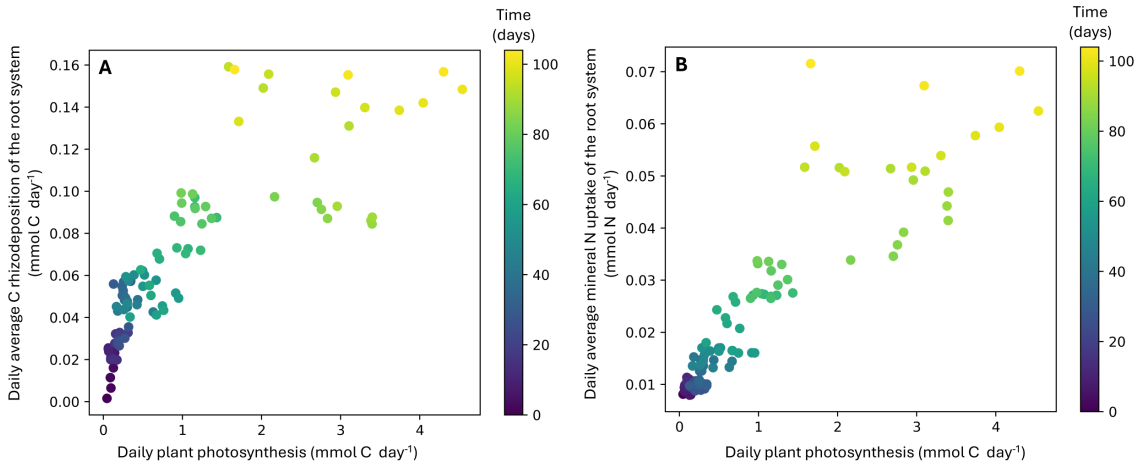

Figure 4.9: Daily average root system total C rhizodeposition (A) and net mineral N uptake (B) as a function of daily plant photosynthesis. The colors represent days since the simulation started.

absolute flows are first plotted in Fig. 4.9. We observed an increase of both variables with daily photosynthesis and over time. Until day 80, both C rhizodeposition and N uptake showed a linear relationship to daily photosynthesis, with a higher increase in rhizodeposition compared to that in N uptake. Then, the response of C rhizodeposition and N uptake to daily photosynthesis tended to saturate. In contrast, the correlation of rhizodeposition and N uptake with C allocation from the shoot was lower than for photosynthesis (Fig. S6.16). When plotting the same variables but normalized by root system structural mass, no clear relationship between massic root-soil exchanges and massic photosynthesis was observed (Fig. 4.10). Normalization by root system root exchange surface did not highlight a straightforward relationship either (Fig. S6.17). Similarly, no clear relationship was observed between rhizodeposition or N uptake and C or N allocation from shoots to roots (Fig. S6.18). A first stage before 20 days of growth showed a high variability of both massic C rhizodeposition and massic mineral N uptake, with no significant correlation to the photosynthesis variations of that period. In contrast, after 40 days of growth the variability of both massic flows was lower despite important variations in photosynthetic activity. Furthermore, time color-coding clearly evidences sequential evolution, with specific plant ages related to specific plateau values despite photosynthesis heterogeneity. Note that the points represented on the graphs are not independent, as the flows simulated at a given time result from a cumulative ontogenic regulation over previous time steps.

In summary, a first simulation of winter wheat growth by *Wheat-BRIDGES* confirmed that massic C rhizodeposition and massic N uptake are neither constant nor proportional to shoot photosynthetic activity (hypothesis **H1**). These results also question hypothesis **H5**, which assumes a synchronization between plant-scale rhizodeposition and N uptake partly due to their interactions with photosynthetic activity. The simulation results here do not reveal any simple determinism between the two variables, and invite to get a closer look at the spatial variability of root-soil exchanges within the root system architecture to understand the conditions and

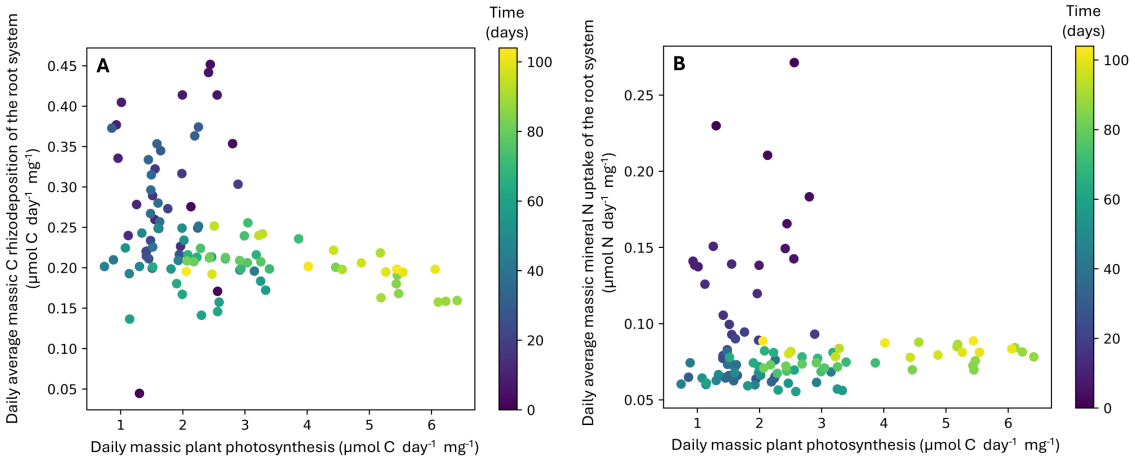

Figure 4.10: Daily average root system massic C rhizodeposition (A) and net massic mineral N uptake (B) as a function of daily massic plant photosynthesis. All three massic flows were normalized by root system structural mass. The colors represent days since the simulation started.

scales under which these two flows might co-locate and interact.

4.4.4 Spatial variability of C&N exchanges along roots

To investigate the spatial variability of root-soil exchanges along the root system and its possible evolution over time, three specific moments were selected at 4-, 12- and 22-leaf stages on main stem, corresponding to 8, 20 and 38 nodal roots respectively (January 6, February 13 and March 27; Fig. 4.2). For each date, two distinct active zones for C rhizodeposition were visible along nodal and seminal roots (Fig. 4.11). The first zone was located near the root tip, and the second zone was around at the point where lateral root emerge from the parent root. The zoomed view at T3 illustrates this spatial distribution on a fast growing nodal root growth, where the two zones are clearly separated. At cold temperatures, a slower growth rate of long seminal roots was also observed, causing these two zones to overlap. In the root tip and lateral emergence active zones, C rhizodeposition rate peaked at $5 \cdot 10^{-10}$ $mol\ s^{-1}\ m^{-1}$, while it was about ten times smaller in neighboring segments of the same axis. In older seminal roots also visible on the zoomed view, C rhizodeposition rate was about 100 times lower in neighboring zones than in active zones. The laterals they carried had stopped growing and negligible C rhizodeposition activity was observed in these lateral roots. Similar location and relative flow values were reported for net mineral N uptake (Fig. S6.19), confirming a spatial co-location of C and N root-soil exchanges (**H4**). For N rhizodeposition, a wider zone of increased rates starting from root tip was simulated, with a less stiff transition to older root regions (Fig. S6.20). This zone still encompassed the root tip and lateral emergence point but also the root segments in between, making a collocation with C rhizodeposition or mineral N uptake less straightforward. Finally, water uptake was minimal at root tips and near the root shoot junction, and maximal at the insertion of young laterals, with important oscillations of the span of these zones along roots with the daily variations of transpiration (Fig. S6.21). This confirms that water

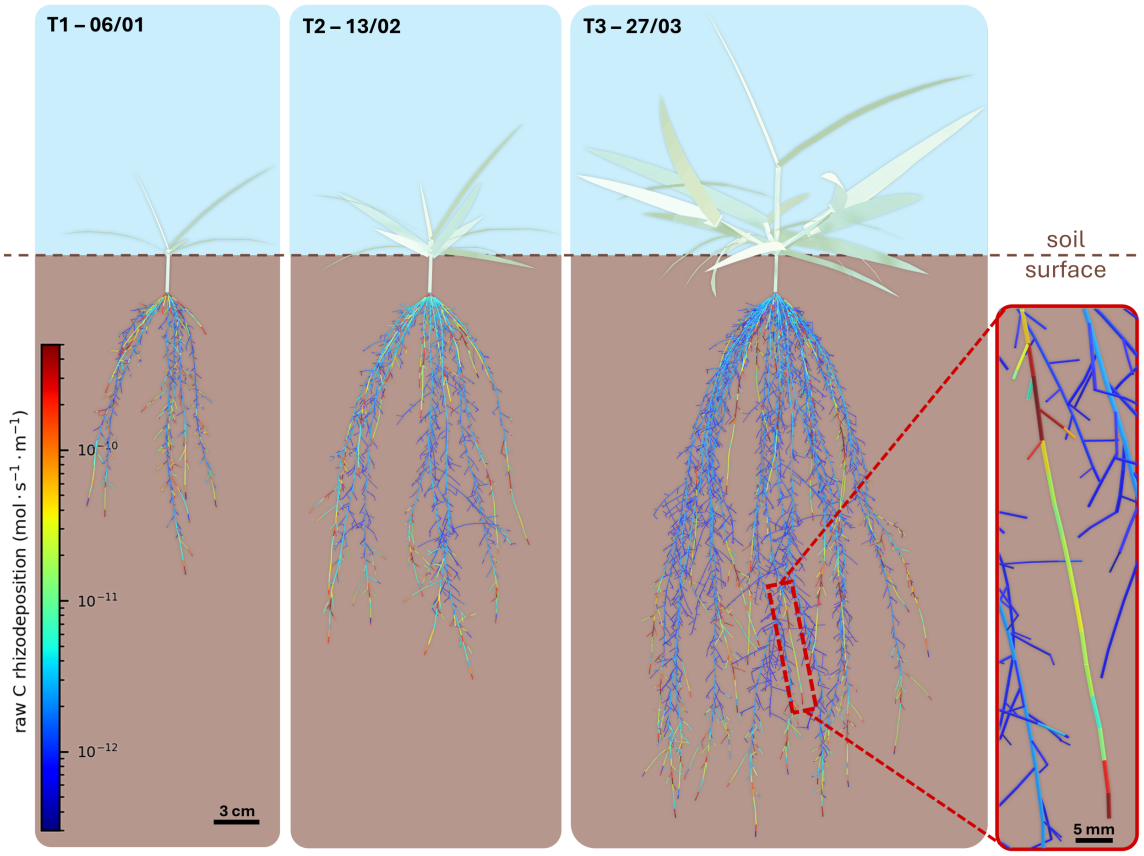

Figure 4.11: Spatial distribution of net C rhizodeposition per unit of root length throughout the root system architecture of winter wheat as simulated by Wheat-BRIDGES, shown at 20, 57 and 100 days after simulation started (T1, T2 & T3 respectively). For an interactive video, see geraulttr.github.io/AR_glb_viewer

uptake co-locates with mineral N uptake and C rhizodeposition only where a lateral root emerges. The complete interactive time series for these four variables are available at geraulttr.github.io/AR_glb_viewer to complement static figures and illustrate daily variations.

The spatial and temporal heterogeneity of flows in these active root regions was further investigated to decipher the complexity observed at plant scale. In Fig. 4.12, C rhizodeposition rate has been plotted against net mineral N uptake rate for each root segment, normalized by its length. A high variability of those rates was observed between root segments, with no general relationship between C rhizodeposition and mineral N uptake for each root type. For each date, the maximum flow rate values were higher for nodal and lateral roots than for seminals. On Feb. 2 and March 27, C rhizodeposition and mineral N uptake appeared to be clearly independent, with a large variability of one flow rate within a narrow range of the other flow rate, and vice versa. This suggests that in zones of increased root-soil exchanges, some would be more active for C rhizodeposition and others for mineral N uptake. However the attribution of this specialization for C rhizodeposition or mineral N uptake to either the root tip zone or the lateral emergence zone is not possible when looking at all root segments simultaneously.

In order to disentangle the complexity of spatial patterns across the root system,

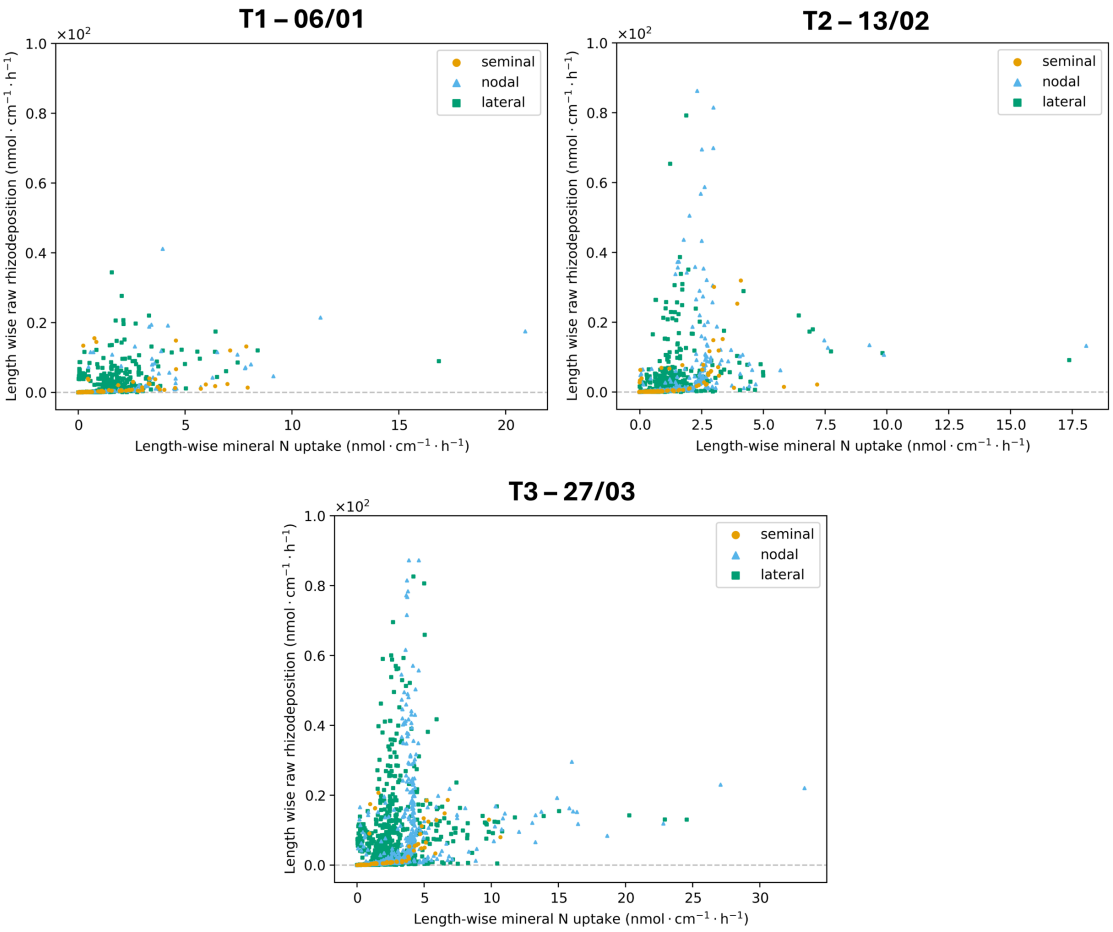

Figure 4.12: C rhizodeposition against mineral N uptake, both normalized by root segment length, for the whole root system at specific dates (Fig. 4.2). Colors represent root types, orange circles for seminals, blue triangles for nodals, and green squares for laterals.

a focus was made on individual roots. One representative example of a seminal, nodal, and lateral root was selected, and rates of C rhizodeposition and net mineral N uptake were studied over the first 10 cm from root tip, for several growth stages (Fig. 4.13). Increased rates at root tips were confirmed for each root type, followed by one or more active zones related to the emergence of lateral roots at higher distances from root tip in the case of the seminal and nodal roots. A co-location of C rhizodeposition and mineral N uptake in these two zones was therefore confirmed quantitatively on these isolated roots. However the relative contribution of these two zones could vary over considered root type, time and exchange process.

First, for the **seminal root** in Figure 4.13A&D, the contribution of the apical zone and the zone of lateral root emergence to C rhizodeposition were shown to be similar, except on January 6 as no lateral had emerged yet. When considering mineral N uptake, the peak of activity progressively shifted from the apical zone to the zone of lateral root emergence from the January 6 to March 27. For both variables, the position of the lateral emergence zone shifted over time due to variations in root growth rate. Second, for the **nodal root** in Figure 4.13B&E, different trends were simulated, with C rhizodeposition rate being maximal in the zone of lateral root emergence and mineral N uptake rate being similar in root tip and lateral emergence zones. The distance between the two zones was also more important for the nodal than the seminal root, probably because of a higher growth rate of nodal roots. Third, the **lateral root** in Figure 4.13C&F also showed the two active zones on January 6, with C rhizodeposition being similar between the two zones, and mineral N uptake higher at root tip, but the rates collapsed on February 13 and March 27 after the root had stopped growing. A more complete investigation of space-time variations along roots and over time was performed in Fig. S6.22 and confirmed the consistency of the spatial distribution of C rhizodeposition and N uptake described above for each root type throughout the simulation.

Overall, for a single root at a given stage, C rhizodeposition and mineral N uptake were co-localized in the root tip region and at the site of emergence of a lateral root, supporting H4. However the zone exhibiting maximal exchange activity shifted between root types, the type of flow, and time (Fig. 4.13), explaining previous observations about the absence of straightforward correlations between C rhizodeposition and mineral N uptake when considering all roots contributions at plant scale.

To study the quantitative implications of such variable active root zones to the whole plant balance, the same cumulative contribution representations as with *Root-CyNAPS* (Chapter 2) was used on C rhizodeposition, mineral N uptake, N rhizodeposition and water uptake processes. For each flow of interest, we reordered the root segments according to the considered flow rate per root length, and calculated their cumulative contribution to both the total length and the total flow by the root system (Fig. 4.14). Simulations with *Wheat-BRIDGES* showed that, regardless of the investigated date, the 10% most active root length accounted for about 90% of C rhizodeposition, 50% of mineral N uptake, 45% of organic N exudation, and 25% of water uptake. This consistency across times is surprising given the variable contribution of the different root types to root system length over time (Fig. 4.11 and 4.13) that were reported above. C rhizodeposition was therefore mainly con-

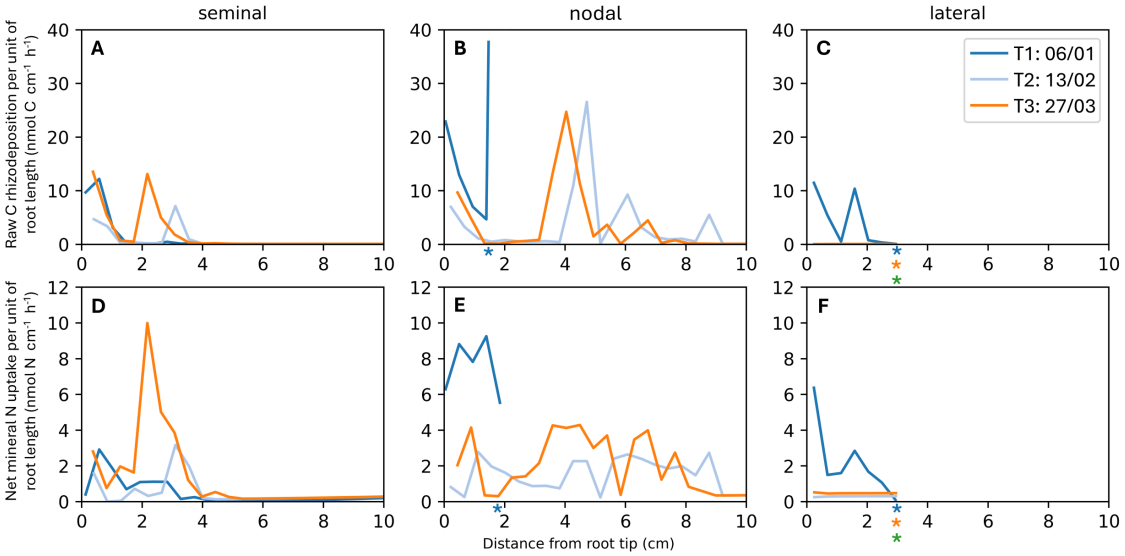

Figure 4.13: Spatial distribution of the rates of C rhizodeposition (A, B, C) and net mineral N uptake (D, E, F) simulated by the Wheat-BRIDGES model in the first 10 cm from root tip, for one seminal (A, D), nodal (B, E) and lateral root (C, F) of winter wheat, at three different dates. Rates for each segment have been normalized by root segment length. Colors represent three dates focused in Fig. 4.2. When roots were shorter than 10 cm, a star indicate the distance from tip at which this root inserts either on the root-shoot junction for seminals and nodals or its parent root for laterals. Flow rates have been averaged between 10 AM and 2 PM to ensure that the spatial distribution observed here is not biased by oscillations from one hour step to another.

centrated at root tip and at the site of lateral root emergence, while the remaining zones of the root system also significantly contributed to mineral N uptake. Reading the figure with a different approach, 90% of total flow was concentrated in only 10% of root length for C rhizodeposition, while 90% of mineral N uptake involved over 70% of total root length.

4.5 Discussion

Here I presented *Wheat-BRIDGES*, a new FSPM accounting for C&N metabolism, transport, growth, and tissue anatomy in 3D organs within an explicit plant architecture (leaves, hidden zones, stems and root segments). *Wheat-BRIDGES* was assembled from the coupling of existing FSPM components and biophysics components, i.e. *CN-Wheat*, *RhizoDep*, *Root-CyNAPS*, *Caribu*, and a soil model. The coupling was facilitated using the *MetaFSPM* framework presented in chapter 3. *Wheat-BRIDGES* is the first FSPM to account for multidimensional and bidirectional C-N interactions in a whole-plant architecture where the functioning and balance of each vegetative tissue is represented explicitly :

1. It describes local C&N co-regulation of metabolic processes and common regulations for C&N transport flows as a function of local metabolite concentrations and accessible exchange surfaces.

2. Instead of using prescribed allocation rules at the scale of the plant, it inter-

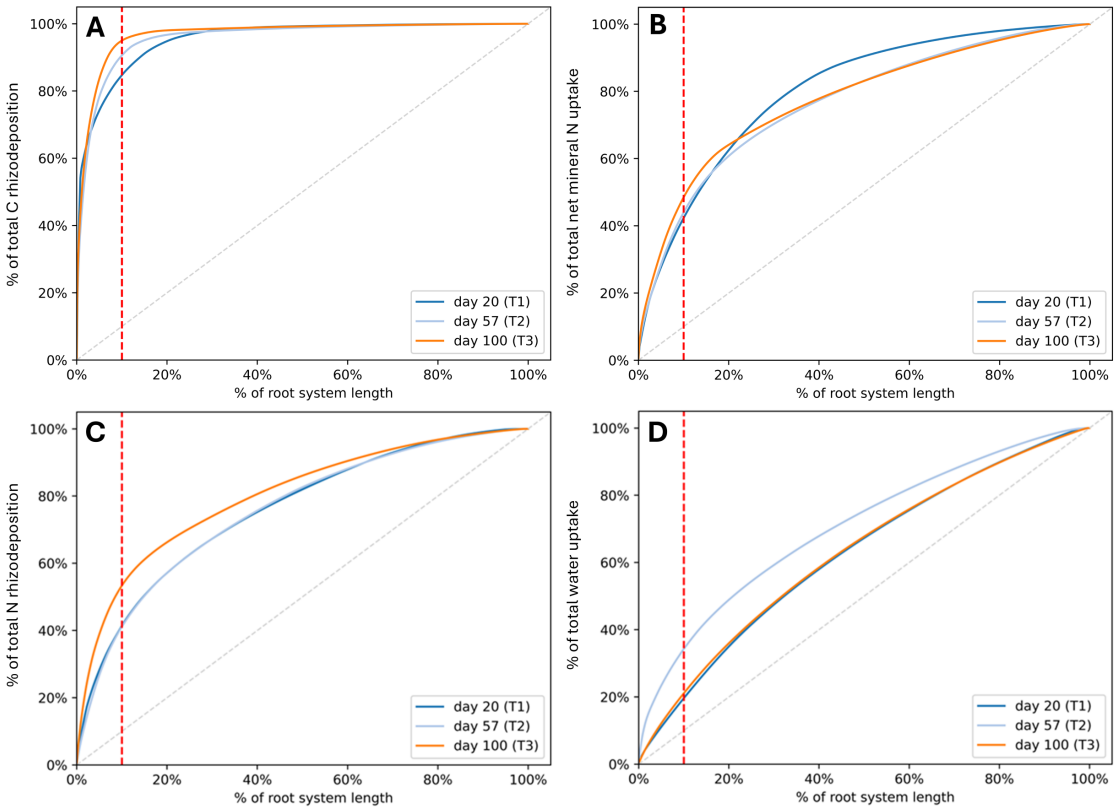

Figure 4.14: Evolution of the cumulative contribution of active root length to the total root-soil exchange of the root system for C rhizodeposition (A), net mineral N uptake (B), N rhizodeposition (C) and water uptake (D). Root segments were first ranked in descending order according to their rate of root-soil exchange normalized by length. The cumulative values are plotted for distinct environmental conditions and root system ages (time T1, T2 and T3 from Figure 4.2). The vertical red dotted line corresponds to an arbitrary threshold of 10% of root system length. The diagonal grey dotted line represents the theoretical curve expected if the contribution of root segments to the root-soil exchange followed exactly their contribution to root length.

faces distant organs' local activities through transport in spatialized xylem and phloem conductive elements, making plant functions an emerging property of each organ activity rather than a constrain by model design.

3. The two previous interactions occur at short term but also accumulate over time with plant growth, i.e. with cumulative impacts on local morphogenesis and resulting plant architecture.

These properties of the model make it relevant to study the multiscale regulations behind C rhizodeposition and N uptake heterogeneity along roots, and to assess the impact of this heterogeneity on plant C&N balance. To illustrate this, a simulation of *Wheat-BRIDGES* was performed under a realistic environment to reproduce the vegetative growth of winter wheat.

In this section, I **first** discuss the realism of cumulative plant budget simulated by *Wheat-BRIDGES*, which was calibrated as for *CN-Wheat* based on leaf length measurements of Ljutovac [2002]. **Second**, I discuss the importance of introducing root system architecture and local C&N physiology in FSPMs to decipher complex spatial patterns and dynamics of C rhizodeposition and N uptake. Two active root zones were identified, similarly to observations made in chapter 2 for C rhizodeposition and N uptake, but the positioning of these zones and their relative contribution to total exchanges could vary significantly with root type and root age. I advocate that the identification of these active zones and hot moments would not have been possible with a homogeneous root compartment, uniform root-soil exchange along roots or focus on a fixed proportion of the root system. **Third**, this first model exploration enabled to identify exploration axes regarding the determinants of rhizodeposition patterns along roots, but its complexity with hundreds of parameters calls for further calibration and validation techniques to ensure model's robustness. **Fourth**, the model was tested in this study in homogeneous soil conditions with no local impact on soil functioning and feedback on root activity, calling for supplementary simulation scenarios using the *RhizoSoil* model introduced in *Wheat-BRIDGES* to fully embed rhizodeposition in the soil-plant-atmosphere regulation continuum. **Finally**, I also emphasize on the need for further data exploration tools for complex FSPM model outputs and their alignment with experimental data, since varying, overlapping flows on growing plant architectures are challenging to study with simple visualization and statistical tools.

4.5.1 *Wheat-BRIDGES* outputs coherence

Wheat-BRIDGES complemented the approaches of *Root-CyNAPS* (chapter 2) and *RhizoDep* by closing the whole C&N cycling of the plant. This made plant activity an emerging property of each organs activity rather than a constrain by model design, and reduced the uncertainty of estimating complex inputs at the root-shoot junction. To calibrate this model, I adjusted the parameter for phloem unloading into root symplasm compared to *RhizoDep* so that the leaf length profile remained similar to those simulated by *CN-Wheat* (see 4.4.1). This was a central validation point of the *CN-Wheat* model that I aimed at preserving for *Wheat-BRIDGES* calibration. Shoot and root mass could nonetheless deviate between the two mod-

els, since root growth and shoot variables such as blade width and root growth were not targeted during model calibration. Simulated shoot structural mass was slightly higher *Wheat-BRIDGES* compared to *CN-Wheat*, and root structural mass markedly increased faster in *Wheat-BRIDGES* than in *CN-Wheat*, with localized root growth accelerations at the emergence of nodal roots. No measurements were available from Ljutovac [2002] to assess the performance of the two models in this regard. In such field experiments, the measurement of root mass profiles for individual plants in soil through excavation is challenging and often subjected to underestimations [York et al., 2018]. *Wheat-BRIDGES* could therefore be used as a proxy for inaccessible root traits, accounting explicitly for root distribution profiles compared to non architectured plant models, and being plastic to environmental conditions compared to a parametric root architecture model.

The flows competing with structural mass production in terms of resource consumption were then investigated by decomposing the C&N balance of the model. In particular, gross C rhizodeposition was simulated at 6% of shoot gross photosynthesis, which is in line with ranges quantified in the literature with labeling experiments on wheat [Swinnen et al., 1994, Dilkes et al., 2004]. However, some inconsistencies regarding root respiration and the low proportion of N exudation call for further calibration. For example, the temperature response of root respiration was calibrated from experiments of Gifford [1995] in controlled conditions between 15 and 30 °C. In contrast, the scenario of winter wheat growth used for the present simulation corresponded to meteorological temperature series oscillating between 4 and 10°C. This suggests that a finer parametrization based on a calibration in this temperature range could improve the response of root respiration to temperature and alleviate the overestimation of root respiration suggested by the simulation. Furthermore, diffusion parameters describing root exudation were homogenized between *RhizoDep* and *Root-CyNAPS* for consistency, assuming a similar exudation response of all metabolites to a given gradient intensity. We therefore expected a difference in the importance of N exudation in plant N balance compared to the results previously obtained in Chapter 2 using *Root-CyNAPS* , but here we simulated N exudation rates that appear very low compared to ranges up to 56% of mineral N uptake reported in the literature [Wichern et al., 2008, Jones et al., 2009] . This suggest that parameters values for hexose exudation and amino acid exudation should be kept distinct in future simulations.

Despite its quantitative uncertainties, this complex model enabled us to further investigate the relative contribution and interactions between different processes, different times and different parts of the root system, following the conclusion that FSPMs can be used for mechanistic exploration despite their limited validation due to data scarcity on the scale they consider [Wang et al., 2020].

4.5.2 Do we need an explicit root system architecture to understand root-soil exchanges?

Approaching rhizodeposition and N uptake regulations at plant scale

In available literature, the measured footprint of rhizodeposition on plant C balance is highly variable across a limited number of studies, which correspond to differ-

ent growth conditions, sampling techniques and/or indirect quantification methods. This heterogeneity limits the identification of rhizodeposition key determinants with statistical approaches. Reference reviews on C allocation to rhizodeposition [Nguyen, 2009, Pausch and Kuzyakov, 2018] have supported the view that *rhizodeposition is not simply proportional to root system biomass or the allocation of photosynthates from shoot* (**Hypothesis 1**). Indeed, rhizodeposition rate relative to root mass varied significantly over time in the present simulation, and absolute rhizodeposition rate was not proportional to C allocation from shoot (Fig. S6.16). Similarly, no straightforward determinant was identified for root system N uptake. Environmental variations in temperature, PAR and soil mineral N concentrations reproducing the actual growth conditions on the site of Grignon (France) in this simulation scenario were also expected to contribute to this plant scale complexity. Nonetheless, no clear correlation between these environmental variables and rhizodeposition or N uptake could be observed in the simulation. **Hypothesis 5**, suggesting that *variations in total N uptake and rhizodeposition to be synchronized over time, with photosynthetic activity at the core of their C&N interaction*, was only partially validated, since absolute C rhizodeposition, mineral N uptake and photosynthesis all increased over time only due to the extension of the root system, but no clear relationship does appear when functionally normalized by a plant pool or flow. Such plant scale complexity would therefore arise from the sum of local mechanistic regulations on metabolism and transport applying differently to each organ of the growing plant architecture, but also from the interaction of C&N cycles at various plant scales.

Wheat-BRIDGES shows that investigating which processes and root zones are driving total flows is necessary to understand plant scale variations, and provides a method to do so. This mechanistic decomposition would not have been possible using crop models, which do not represent root system architecture and approximate rhizodeposition as root decay or as a fixed proportion of plant C allocation [Beaudoin et al., 2023, Zhang et al., 2021, Raynaud, 2010]. Existing FSPMs have tried different strategies to study the spatialization of root-soil exchanges; (i) assuming root system architecture as the only driver of spatialization in soil with a constant rhizodeposition rate [Landl et al., 2021], (ii) forcing the gradients along roots by restricting exchanges to root tips [Giraud et al., 2023, 2025], (iii) spatializing single N uptake functions without regulation by internal plant status [Postma et al., 2017, Schäfer et al., 2022], or (iv) accounting for local regulations of root exchanges but forcing shoot-root allocations (Rees et al. [2025]; *Root-CyNAPS* in chapter 2). Here *Wheat-BRIDGES* builds on these foundational studies and provides a way to simulate and investigate realistic C&N exchange gradients along roots as an emergent property of model's multiscale mechanistic regulations, as presented below.

Simulating spatial and temporal heterogeneity in the root system

I first confirmed the presence of two active root exchange zones identical to those identified in chapter 2 for C rhizodeposition and N uptake, i.e. at root tip and lateral root emergence zone, for all root types and ages. These two locations for the two processes relate to common regulations by i) increased root exchange surface, ii) increased phloem unloading in growing regions, and iii) increased hexose and

amino acid symplastic concentrations, as introduced in the formalisms of *RhizoDep* and *Root-CyNAPS*. However the exact distance from tip of the lateral emergence zone varied among individual axes, with a higher heterogeneity of apex growth rate in *Wheat-BRIDGES* as compared with *RhizoDep*, resulting from the introduction of spatialized phloem transport. When focusing on a given root axis, a co-location of C rhizodeposition and mineral N uptake was evidenced, supporting **Hypothesis H4**. However, this hypothesis can hardly be generalized to other flows, e.g. for water uptake that co-localized with rhizodeposition and N uptake only in the lateral emergence zone. Water uptake was minimal at root tips compared to other flows, which relates to the higher radial cell wall conductance between xylem and phloem in these regions compared to older root parts. This causes the high pressure in the phloem to increase the pressure of the xylem through radial water flow, effectively lowering water uptake, especially at night when transpiration stops and allows xylem pressure to rise. This co-location of N uptake and water uptake occurring only at lateral root emergence supports **Hypothesis 3** on the shifting dominance of composite N uptake processes. As reported in section 4.4.3, net mineral N uptake is composed of about 20% of water-driven N uptake. Increased rates of water uptake and N uptake only in this region therefore suggest that the contribution of this pathway strongly increases at lateral emergence and becomes negligible compared to active N uptake in other zones. Further model exploration will allow to expose these relative proportions of N uptake flows along roots more precisely, and assess how these can be modified in realistic soil conditions where N and water uptake spatialization does not respond the same way to resource availability [Javaux et al., 2008, Dathe et al., 2016].

Moreover, a third active root zone was simulated for C rhizodeposition and mineral N uptake at the shoot-root junction only at times of young nodals emergence (see geraulttr.github.io/AR_glb_viewer). This relates to the distribution of growth costs sustaining the new root emergence on first root segment, which increases the unloading of metabolites and the subsequent rhizodeposition and N uptake rates in this region. Furthermore, this effect is amplified by the simultaneous emergence of several nodal roots, resulting from the simultaneous emergence of leaves on different shoot axes in *CN-Wheat*, and a fixed thermal time nodal emergence delay estimated from Klepper et al. [1984] . This causes hexose and amino acids concentrations to increase in this region. No mention of this temporary hot spot of rhizodeposition and N uptake at the base of the root system could be found in the investigated literature. Studies reporting measurements of spatial heterogeneity of these flows did not investigate the the shoot-root junction, which is considered as a less active region. Despite the expectation of a dryer soil with less available mineral N near the surface in experimental conditions compared to the homogeneous soil of this simulation, adding this location to the sampling procedure developed in chapter 5 might enable to evaluate the relevance of this result.

The discretization of the root system can confuse the identification of co-locations

The simulation showed that the relative contribution of root tip and lateral root emergence zone to different root-soil exchanges vary depending on the processes (N

and water uptake, rhizodeposition). There are only a few specific frames in space and time where maximal C&N flows are co-located, therefore challenging **Hypothesis 4**, which states that *the heterogeneity of root anatomy and metabolite concentrations in the root system architecture to be a common driver to all root-soil exchanges, co-localizing rhizodeposition and N uptake along roots.* For a young root system mostly composed of seminal roots, C rhizodeposition and N uptake activities are balanced between the two active zones, with an actual **in-axis co-location** of both C&N exchanges at the same root segments. Nodal roots multiplication however tend to quickly dominate root length during plant growth, and I showed the two flows to be uncoupled for this root type, as C rhizodeposition occurs mainly at lateral emergence and N uptake mainly at root tips (Fig. S6.22). This causes a transition to an **inter-axes co-location** because lateral roots emerging from nodal segments with high C rhizodeposition expose high N uptake rates at lateral root tip despite their small diameter. Lateral roots remaining active only during a few days, this effectively co-locates rhizodeposition in the nodal mother root's segment and N uptake at the lateral root tip in a relatively small spatial and temporal frame. Similarly, nodal roots were characterized by high rates of N uptake and C rhizodeposition at root tip during their emergence, apparently co-locating with the increased exchanges at shoot-root junction described above. This inter-axes co-location during root emergence amplified with root system age as the number of root tips increase, explaining why representations focusing on single root segments along distance from tip or single root axes can be misleading (Fig. 4.4.4). This result suggests that the analysis of co-locations in the root system should rather be focused on how they are integrated in the environment to account for overlapping influences between axes [Schnepf et al., 2022]. This also connects to the wide variety of discretization methods for environment models, from environment-centered static or adaptive voxel grids [Postma et al., 2017] to root-centered radial approaches [Giraud et al., 2025].

One plausible functional implication for these two successive zones along root growth in soil would be that active seminal or nodal root tips could act as a first rhizodeposition priming signal to soil during apex crossing, followed by a few days delay to increase soil organic mineralization [Mastný et al., 2021, Nannipieri et al., 2023, Wiesenbauer et al., 2024] which could benefit lateral roots N uptake at the time of their emergence. More complex situations however occur, as several roots can superimpose in the same soil volume, and call for further simulation scenarios in heterogeneous soil conditions with *Wheat-BRIDGES* to test such hypotheses and complement experiments where such spatial and temporal patterns are difficult to capture in realistic soil conditions. Moreover, this co-location over time can also occur during roots proliferation in localized nitrate patches. Following the experimental conditions of Drew and Saker [1975], another simulation scenario was set up with *Root-BRIDGES* and showed an immediate increase in N uptake in the nitrate patch, followed by a colonization of the patch by lateral root proliferation, increasing the number of both active root zones in this location for sustained N uptake and increased C rhizodeposition. These results are not detailed here, but were presented at the International Society of Root Research 2024 conference. Details can be found in Supplementary note 6.14.

Quantitative importance of active root zones in total root length and plant C&N balance

To study the contribution of the active root zones presented above, I first compared *Wheat-BRIDGES* outputs with *Root-CyNAPS* results from chapter 2 regarding the cumulative contribution of most active root zones to total N uptake and total length. Results were consistent between the two models considering an external nitrate concentration of about 0.5 mM: for all plant ages and despite important temperature variations, 10% of root length contributed to about 50% of total N uptake. When extending this cumulative representation to other root-soil exchanges, we simulated that C rhizodeposition was very polarized in active regions with stiffer gradients (90% of flow in 10% of root length). This can relate to the model formalism increasing hexose unloading from phloem upon root growth to ensure model stability. This formalism can potentially overestimate the local hexose concentration and resulting rhizodeposition when a lot of growth costs cumulate, such as in the shoot-root junction. In all simulations presented here, low concentrations of hexose were kept constant in the homogeneous soil, which might have increased this polarization. N rhizodeposition showed a contribution of active root zones similar to N uptake, and did not compared to the high polarization of C rhizodeposition in part because of a too low parametrization of the permeability for amino acid exudation. Water uptake was the most homogeneous variable along roots, which relates to much faster homogenization of pressure waves in conductive elements [Doussan et al., 1998, Bauget et al., 2023] and the absence of the symplastic buffer in our model contrary to metabolites.

To our knowledge, this is the first time that the spatialization of C&N rhizodeposition, mineral N uptake, and water uptake can be determined simultaneously, while assessing the quantitative impact of gradients along roots in plant balance. Considering the difficulty to sample spatial and temporal evolution of any flow along roots, FSPMs like *Wheat-BRIDGES* resulting from the coupling of distinct specialized models could provide researchers valuable information about non-measurable flow variations.

4.5.3 Methodological contribution to FSPM coupling

Several resolution strategies have been included in *Wheat-BRIDGES* to tackle key attention points to ensure the numerical stability of the model. These could be useful for future modeling initiatives and are detailed below.

Wheat-BRIDGES first simulations used an hourly time-step for all its components, which, if not handled properly, can lead to instability and mass conservation issues when important fluxes cross tiny organ compartments. This may be especially the case for **(i) tiny root tip elements** with high metabolite consumption by growth, **(ii) for small conductive xylem and phloem volumes** which are crossed by important sap flows with any imbalance between inputs and outputs being regulated much faster that the chosen hourly time-step, and **(iii) for shoot-root allocation stability** when the phloem concentration gradient driving organic C&N allocation to roots switches from an average shoot / average root gradient, to a gradient between an average shoot and the first tiny element of a spatialized root

system.

- **To handle tiny root elements (i)**, *RhizoDep* introduced a repartition of hexose growth costs in a growing zone length, depending on apex diameter, which is independent of root system discretization. This enabled to keep the hourly discretization while ensuring growth costs do not apply solely on a small root tip element but are instead distributed over the whole elongation zone to avoid a completely depletion of metabolite content in the first apical root element over a time step. In *Root-BRIDGES* this rule was also generalized to amino acids consumption by growth.

- **For avoiding issues with small xylem and phloem volumes(ii)**, stability of solute concentrations in xylem and phloem vessels was ensured with an implicit Euler time integration of solute advection by sap flows over the time-step. To avoid constant vessel loading or unloading flows over the time step that would overshoot concentrations or lead to negative values, I included radial diffusive flows in the solver along with axial flows resolution. Along with the Patankar decomposition [Patankar, 1980] of source and sink terms in such linear radial-axial advection-diffusion system, this ensured the converged concentration profiles along roots to be in positive, realistic concentration ranges, which yielded realistic exchange flows with symplastic compartments. Similarly, I selected the Newton-Raphson approach from the *HydroRoot* model [Bauget et al., 2023] to ensure that the water flow underlying solute advection is conservative and stable despite small xylem and phloem volumes in root segments.

- **For shoot-to-root allocation in phloem (iii)**, *CN-Wheat* diffusion formalism could not be directly applied to the discretized root system in *Wheat-BRIDGES*. When using a high diffusion parameter value as in *CN-Wheat* in order to sustain the growth requirements of the root system, unrealistic, high concentrations appeared in the first element of the root system, with repeated gradient inversion with the shoot, ultimately leading to oscillating, high, and non conservative shoot-root allocations. Mechanistically, I rather expected the average shoot concentration and the concentration at shoot-root junction to be equal, not to be the driver of shoot-root allocation. To solve this instability related to root system discretization, I therefore used a progressive initialization technique for the shoot-root diffusion parameter. Starting from a very low parameter value to avoid the initial instability, I then exponentially increased the diffusion parameter over the first milligrams of root growth until average shoot concentrations and the shoot-root concentrations were equal, ensuring a progressive and stable initialization of phloem concentrations along the way. A realistic allocation from shoot to roots was then emerged from the summed unloading dynamics of each root segment within the root system architecture rather than a regulation by a single process at the shoot-root junction. N and C allocation from roots to shoot in xylem was not impacted by this issue, since it was not computed from a root-shoot concentration gradient but rather emerged from the transpiration stream imposed by the shoot to the root.

4.5.4 Model limitations and targeted improvements

Several limits of the model as well as their resolution strategies have been identified. **First**, the organ and tissue scale chosen to represent processes in the model inherently makes it difficult to calibrate and validate due to data scarcity in the available literature regarding rhizodeposition and N uptake gradients along roots, but also regarding the heterogeneity of internal flows (e.g. metabolite transport within the roots) accessible only destructively. This impossibility of quantitative validation for every variable of interest simulated in each organ of the plant therefore calls for specific calibration strategies presented below. Performing a sensitivity analysis of all or specific parameters of *Wheat-BRIDGES* would also enable to identify the key measurable traits to focus in future experiments to reach a more complete validation of the model. **Second**, we still aim at designing simulation scenarios using *Wheat-BRIDGES* in heterogeneous soil conditions to study root exchange plasticity in contact with realistic soil variations and to integrate the footprint of C&N rhizodeposition, N uptake and water uptake in soil balance. This would allow to identify possible conditions for increased C storage in stable soil pools and increased local C&N cycling in soil that would be mediated by rhizodeposition. **Third**, as *CN-Wheat* is initialized at 3-leaf stage or later, *Root-BRIDGES* needs to be initialized at that stage too, with a fully operating root system. This has required a pre-simulation with *Root-BRIDGES* only, for a period at the end of which the root structural mass simulated by *Root-BRIDGES* corresponds to the root structural mass targeted for *CN-Wheat* initialization. This process is still prone to error since it uses data inputs for shoot-root allocations rather than bidirectional interactions with the shoot. The coupling with a new version of *CN-Wheat* currently in development which starts from seed germination is expected to solve this issue in a near future.

Wheat-BRIDGES sensitivity analysis, calibration and validation

Calibration and validation of *Wheat-BRIDGES* *Wheat-BRIDGES* parameter calibration was performed from a wide variety of heterogeneous experimental studies, with different growth conditions, genotypes, or sampling practices. Such a wide reach was necessary to gather the data necessary to parametrize the different physiological processes of our integrative model, but this introduced uncertainties in model outputs, and several assumptions were formulated when the parameters were not directly measured. To complement this manual approach at complex models calibration in a context of data scarcity, Wang et al. [2020] suggested a pattern-oriented calibration approach to identify only plausible parameter sets to match an ensemble of output patterns *simultaneously*. This simultaneous constraint is a key advantage for FSPMs where a wide variety of scales need to be tested to ensure the reliability of the outputs of the model during a single simulation (for example: cumulative plant biomass and C-N balance, instantaneous flow or anatomy profiles along plant axes, local activity responses to environmental shifts, divergence between observed and simulated architectures). As with sensitivity analysis, the parameter space for our model remains impossible to fully explore, but the sequential filtering makes this approach realistic by rapidly discarding implausible parameter regions to lower

the number of required simulations.

After this calibration step, validating the patterns of rhizodeposition and N uptake along roots simulated by *Wheat-BRIDGES* is challenging, data scarcity is also a strong limitation here considering the difficulties of sampling local root-soil exchanges in realistic soil conditions. However, for such local scale specific measurements, it is often difficult to separate calibration from validation datasets when comparing FSPMs to available data, calling to design further experiments specifically to test hypotheses formulated with *Wheat-BRIDGES* outputs.

Sensitivity analysis strategies for complex FSPMs Sensitivity analysis techniques are approaches assessing the impact of model's input parameters on its outputs variance. Given the hundreds of parameters grouped by the different components of *Wheat-BRIDGES*, a uniform sampling of values between plausible bounds, as used in Sobol global sensitivity analyses, would yield more than trillions of simulations to perform to explore the parameter space, which is highly unrealistic given the average 3 hours execution time of the model for the whole vegetative cycle. Moreover, sensitivity analyses are often performed on plant-scale aggregated variables, such as yield or biomass, but the focus of this thesis on local processes variations along roots and over time questions the relevance of such approaches. Reducing the parameter space to only measurable traits or traits thought to be critically influencing local concentrations, root exchange surface and ultimately root-soil exchanges would be a first reduction approach, as suggested by Blanc and Barbillon [2021]. However this approach would be valid if each organ's functioning could be almost considered independent, as in *Root-CyNAPS*' short simulations for example. A more pragmatic method would be a screening method such as that proposed by Morris, which tests parameter one-at-a-time with a randomized design [Morris, 1991], but at the expanse of ignoring interaction effects between parameters. In practice, a combination of an initial screening followed by a global sensitivity analysis is advised [Bergman et al., 2024]. However, *Wheat-BRIDGES*' numerous outputs cannot be screened with dedicated sensitivity analyses for each one of them, and the multiscale and temporal dynamics of outputs' sensitivity have not been introduced in existing approaches. The sensitivity analysis should therefore be narrowed down to a few key outputs for each research question. For this thesis, cumulative C rhizodeposition and N uptake flows expressed as a fraction of C or N input could be set as objective plant-scale outputs for the end of the simulation, and the contribution of active root zones of the root system in total root-soil exchanges at fixed plant ages could be used to assess the sensibility of spatial variations of the root system to input parameters.

Key sensitive parameters identified with such approaches will then be explored numerically to identify trait combinations and ideotypes with contrasted flow heterogeneity in the root system and plant performance. Functional implications simulated for such parameter values will then guide experimental design to test these hypotheses and assess the genotypic variations and plasticity for those parameters.

Coupling heterogeneous root-soil exchanges with soil biogeochemical processes

Coupling root-soil exchanges along roots with a soil model able to simulate local C, N and water dynamics would allow to understand how local root and soil balance are interconnected and to quantify the impact of rhizodeposition on SOM dynamics and mineral N availability to roots. Such scenario will also expose the root system to heterogeneous solute concentrations and water potential along roots, affecting the spatialization of flows compared to a use of *Wheat-BRIDGES* in homogeneous soil conditions. As a first step, I used two existing soil models, *MIMICS-CN* a dimensionless model of C&N biochemistry which was spatialized in a 3D voxel grid and coupled to the water-solute transport model *CMF*. The resulting model, *RhizoSoil*, has been readily coupled with *Wheat-BRIDGES* and shows realistic pool sizes for stabilized organic matter, particulate organic matter and dissolved C&N pools (data not shown). A complete validation of this model remains to be performed to verify the coherence of simulated microbial activities compared to the original version of *MIMICS-CN,* which was originally not tested with rhizodeposit inputs but only with plant residues. Variations in soil temperature also significantly impact the relative allocations in *Wheat-BRIDGES* plant balance. A spatialized soil temperature model from a recent benchmark performed in the OpenAlea platform could be used to simulate a realistic soil temperature profile between variable surface temperatures and buffered temperatures at depth. At short term, comparative simulation scenarios between root system locations, between climatic scenarios or between management practices could nonetheless use this soil model to evidence preferential conditions for local C&N cycling.

Understanding processes heterogeneity and regulation pattern exploration for complex FSPM outputs

FSPM outputs cannot be easily understood by modelers with current data analysis techniques. Indeed, FSPMs simulate multidimensional time-series in each organs which are interconnected in time by a growing graph structure and environmental grids. Such data structures are not easily represented in a human readable way, which hinders our understanding of FSPM emergent patterns and alignment with experimental data, despite a good understanding of each introduced formalism and assumptions introduced in the model. For example, during the exploration of presented simulation results, I faced the challenge of choosing the right representation scale to study co-location, which mobilized complex representations that include a very small subset of simulated and interacting variables (Fig. S6.22).

Here I foresee an opportunity for FSPM models to use data analysis techniques from other fields of research that have been dedicated to multivariate growing graphs. In this context, we used the *MetaFSPM* framework to exploit the shared component structure of *Wheat-BRIDGES* and implement a single output manager: all components write to one dataset that collects every simulated time, variable, and spatial scale in the plant architecture, which greatly simplifies downstream data analysis (see Chapter 3). In this thesis, I have therefore tested an adaption of the method of Ali et al. [2019] to these unified FSPM outputs, taking each plant organ multivariate

time series at the same level and clustering their *physiological state* to decipher the determinants contrasted organs activity throughout the plant (See supplementary note 6.14). This preliminary approach showed an agreement with simpler representation modes, such as the location of increase N uptake when looking at a color-coded root system architecture snapshot. However, these first tests revealed that dimensionality-reduction strategies alone cannot address a deeper question that is central to FSPM interpretation: why do certain organ groups diverge in their simulated trajectories? The tested clustering approach identifies recurrent physiological states, but they do not expose the dependencies between these states, nor can they reveal which past organ activities produced the divergence observed at a given time. In other words, such projections summarize *what* patterns exist, but not *how* they emerged.

To overcome this limitation, recent developments in **unified spatio-temporal graph attention networks** offer a more suitable framework [Tang et al., 2023]. Briefly, attention is a learning mechanism that lets a neural network determine which inputs of the data structure matters most for a given output. These models jointly learn spatial, temporal and variable-wise dependencies within multivariate growing graphs, allowing each organ – time – variable triplet to attend to relevant organs at earlier times and across other physiological variables. Once trained in a self-supervised manner (e.g. with masked reconstruction), the resulting attention maps can be analyzed to extract mechanistic patterns directly from the simulation outputs. This makes it possible to identify, for example, *consistent groups of organs that diverge metabolically at time t*, and to link this divergence to *the past activity of specific root zones* or to *the evolution of specific C – N indicators* at earlier time steps. Such unified attention models would therefore act as explainable intermediaries between the raw multidimensional output of FSPMs and a human-interpretable representation of regulatory interactions, enabling the identification of multiscale emergent patterns that are otherwise inaccessible through classical clustering or hand-crafted indicators.

4.6 Chapter conclusion and perspectives

In this chapter, I assembled and explored the composite whole-plant FSPM *Wheat-BRIDGES*, which couples the architectured root module *Root-BRIDGES* with the shoot model *CN-Wheat* and environment components. The resulting model closes plant C&N cycles while resolving local C and N processes in each organ of the plant architecture, while preserving the main shoot-scale validation targets of *CN-Wheat* for leaf length dynamics under the Ljutovac [2002] field scenario. The first simulation showed that plant-scale C and N budgets are conserved and that the simulated magnitude of C rhizodeposition (around 6% of gross photosynthesis) is consistent with published ranges, even though root respiration and N exudation still require dedicated calibration. At the scale of the root system, the explicit representation of root architecture and local C – N – water physiology revealed persistent active zones of C rhizodeposition and mineral N uptake at root tips and lateral emergence sites across root types and stages, while water uptake displayed more homogeneous patterns along roots. Quantitatively, about 10% of root length accounted for roughly

90% of C rhizodeposition but only about half of mineral N uptake, illustrating that different processes do not share the same degree of spatial concentration and that a homogeneous root compartment would miss a large part of this internal heterogeneity.

Wheat-BRIDGES now calls for targeted quantitative calibration (e.g. root respiration, N exudation parameters), and for structured sensitivity and pattern-oriented calibration to identify the key traits controlling both cumulative C&N balances and the contribution of active zones to total exchanges. Beyond homogeneous soil scenarios, the coupling with existing C-N-water 3D soil models will enable to explore how simulated active root zones of rhizodeposition and N uptake interact with heterogeneous soil C&N dynamics, while the unified output management implemented via *MetaFSPM* will support more systematic data-analysis pipelines to provide a better readability of complex FSPMs outputs, unveil hidden ecophysiological patterns inaccessible experimentally and relate them to measurable traits to facilitate interactions between mechanistic models and experimental data.

4.7 Chapter Contribution to Thesis Strategy

Within the overall thesis, this chapter presents the first whole-plant exploration of how explicitly representing root – soil exchange heterogeneity affects wheat C&N balance. By assembling *Root-BRIDGES*, *CN-Wheat* and environment components into the composite FSPM *Wheat-BRIDGES*, we show that local C, N, water processes and local anatomy in an architectured root system can be coupled consistently with shoot photosynthesis, growth and senescence, while preserving the main validation targets of *CN-Wheat* at shoot scale. This closes the C&N cycles of the plant in a mechanistic way and makes plant resource uptake, root growth and root – soil exchanges emergent properties of local organ activities rather than prescribed flows.

The simulation analysis carried out in this chapter clarifies the status of the hypotheses introduced in Chapter 1. At plant scale, *Wheat-BRIDGES* supports hypothesis **H1** by showing that rhizodeposition is neither constant nor simply proportional to root biomass or photosynthetic activity, and challenges hypothesis **H5**, since temporal variations of total rhizodeposition and N uptake are not trivially synchronized with photosynthesis when expressed per unit root mass or surface. At root-system scale, the model confirms that a limited fraction of root length contributes disproportionately to total exchanges, thus refining hypothesis **H2**, and shows that the relative contribution of different processes and zones (root tips, lateral emergence, root base) changes with root type and ontogeny, in line with hypothesis **H3**. Finally, the co-location of C rhizodeposition and mineral N uptake in apical and lateral emergence zones along individual roots provides mechanistic support to hypothesis **H4**, while highlighting that such co-locations could also be defined and studied from the soil perspective rather than with root centric approaches.

These results motivate the need for experimental data on localized rhizodeposition and N uptake along roots and over time to further calibrate and evaluate the simulated patterns obtained with *Wheat-BRIDGES*. Chapter 5 directly contributes to this gap and our hypotheses, presenting a new a soil-filled windowed rhizotron method tested on winter wheat to quantify C&N rhizodeposition heterogeneity along

growing roots, decompose its underlying processes, and identify its key determinants.

Chapter 5

Experimental characterization of wheat root architecture, root anatomy, and rhizodeposition over space and time

5.1 Introduction and chapter strategy

This chapter provides the experimental counterpart to the modeling work developed in Chapters 2, 3 and 4. In particular, this chapter aims to generate experimental data that can be used to confront the modeling hypotheses introduced in Chapter 1 and explored in Chapters 2 and 4, i.e. that rhizodeposition is not simply proportional to root biomass or C allocation (**H1**), that only a subset of root length accounts for most root – soil exchanges but that this contribution is sensitive to plant age and environmental conditions (**H2**), and that increased rhizodeposition rates can co-locate with increased N uptake rates in specific *active root zones* (**H4**).

To this end, I conducted two complementary rhizotron experiments with winter wheat (*Triticum aestivum* L., cv. Soissons). A preliminary experiment (Exp. 1) was used to quantify root growth under controlled conditions and to characterize radial and longitudinal anatomical traits along seminal roots, using histological cross-sections, apex transparization and an adaptation of the GRANAR anatomical reconstruction model. These data were intended to refine the calibration of wheat parameters for the anatomy component used by *RhizoDep*, *Root-CyNAPS* and *Wheat-BRIDGES* (See Chapters 2 and 4). A second experiment (Exp. 2) was then dedicated to testing a non-destructive sand-patch trapping method for repeated sampling of rhizodeposits on targeted root segments, while simultaneously monitoring root and shoot development by time-lapse imaging and complementary measurements. This experiment aimed to (i) assess the feasibility and sensitivity of localized rhizodeposition measurements in soil-filled rhizotrons, (ii) obtain first-order estimates of C rhizodeposition rates along different root types and distances from the apex, and (iii) evaluate to what extent the experimental patterns support or challenge the modeling-derived hypotheses on rhizodeposition heterogeneity and active root zones. These methodological developments and tested hypotheses during Chapter 5 are summarized in the following conceptual scheme (Fig. 5.1).

In the following, I first describe the common rhizotron design, soil preparation and growth conditions used in both experiments, and then detail the specific sampling and imaging protocols for root anatomy, rhizodeposition and shoot/root phenotyping. I finally present the main experimental results, focusing on (i) the apparent invariance of seminal root anatomy along distance from the tip, and (ii) the limitations and partial successes of the sand-patch method to quantify C rhizodeposition at high spatial resolution.

5.2 Material & Methods

Two separate experiments were conducted in phytotronic growth chambers to study the anatomy of root tissue and the dynamics of root growth and rhizodeposition of winter wheat (*Triticum aestivum* L., cv. Soissons) over time, using soil - filled rhizotrons. A first experiment (Exp. 1) was conducted in order to i) evaluate the growth rate of wheat roots in rhizotrons in a given set of environmental conditions, and ii) determine the evolution of root anatomy along roots. Based on the results of Exp. 1, a second experiment (Exp. 2) was conducted in adapted environmental conditions and aimed to i) optimize the collection of rhizodeposits along roots over time,

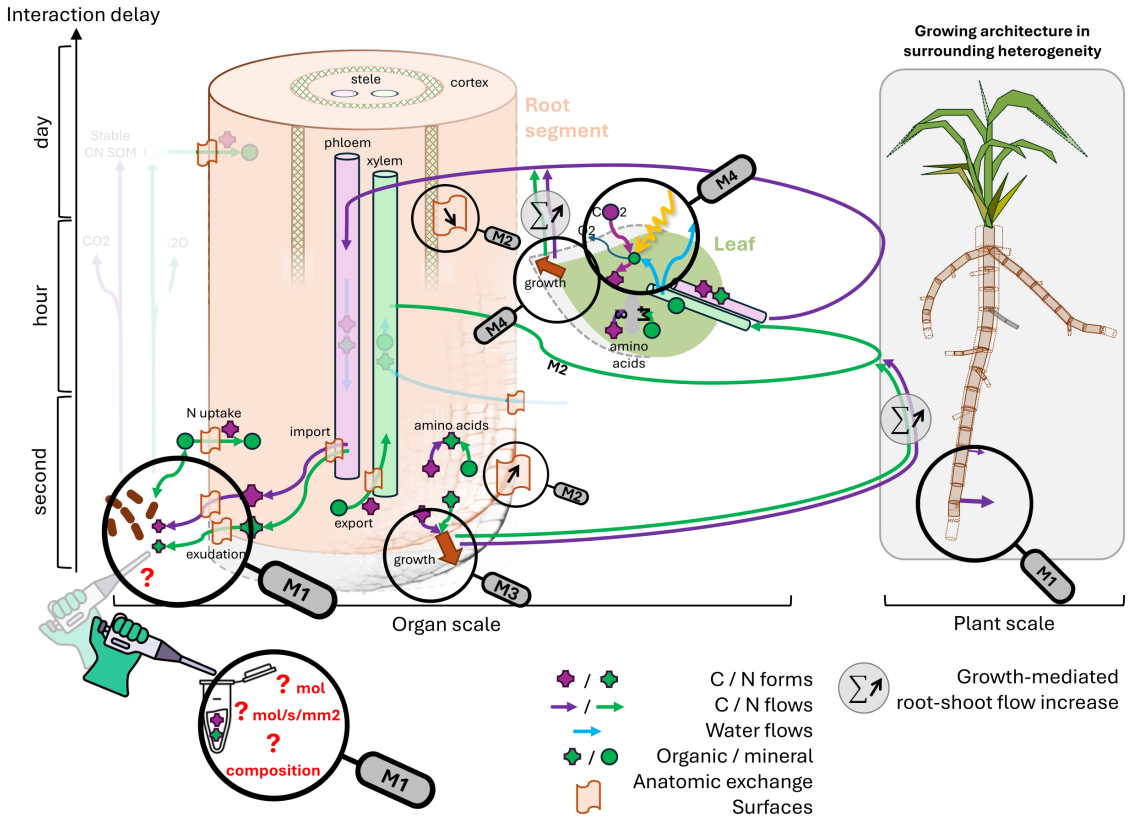

Figure 5.1: Conceptual scheme summarizing the scales considered in Chapter 5, with magnifying glasses positioning experimental methods and underlying hypotheses. **Methods 1 (M1)** aims at quantifying rhizodeposition rates, composition along wheat roots and root-soil metabolite concentration gradients using soil-filled windowed rhizotrons (**H2-H3**). **M2** aims at quantifying the heterogeneity of anatomical features and their role in rhizodeposition variability along wheat roots to test **H4**. **M3** aims at repositioning local sampling points in a growing root system architecture through imaging and contribute to the measurement of anatomical traits for FSPM calibration. Expecting a regulation of total rhizodeposition range by photosynthetic activity, **M4** aims at estimating leaf area over time as photosynthesis rate to test hypothesis **H5**.

and ii) to link the corresponding rhizodeposition rate with the local characteristics of the root (e.g. root anatomy, root metabolites' concentrations) .

5.2.1 Experimental design

For both experiments, custom-made rhizotrons with several movable windows (Fig. 5.3) were used to repeatedly access specific zones of the root system while minimizing disturbances for collecting rhizodeposits with traps (i.e., absorbing patches) one to two times a week. Each face of the rhizotron was also imaged three times a week using a photographic bench (Fig. 5.5) in order to monitor the evolution of root system architecture over time and to determine the age of each root segment at any time.

In Exp. 1, seven rhizotrons were used for monitoring non-destructively shoot and root growth over 7 weeks in a first set of environmental conditions (see below). One destructive sampling of root and soil aliquots was performed at the end of this period in order to measure metabolites concentrations and the corresponding root-soil gradients, and to determine the evolution of root tissue anatomy. Two rhizotrons of this experiment were also selected to test and improve the non-destructive weekly collection of rhizodeposits along the growing roots, which was then set up in Exp. 2 at a larger scale.

In Exp 2., three groups (G1, G2, G3) of four rhizotrons each were used to allow a destructive sampling of specific root and soil aliquots at various growth stages, in addition to the non-destructive collection of rhizodeposits over time. A new set of environmental conditions was used compared to Exp. 1, with in particular a lower temperature to slow down root growth (see below). G1 was destructively sampled 28 days after sowing (5 leaves on main stem, tiller 3 emergence), G2 at 35 days after sowing (6 leaves on main stem, tiller 4 emergence), and G3 at 47 days after sowing (7 leaves on main stem, tiller 8 emergence). Two wheat plants were grown in each rhizotron, resulting in 24 monitored plants in total. Rhizodeposit traps were applied every Wednesday to the group scheduled for the next destructive harvest: from week 3 to week 5 for G1, from week 5 to week 6 for G2, and from week 6 to week 8 for G3. The sampling planning of Exp. 2 is presented in Figure 5.2 bellow. In addition to the twelve rhizotrons used for collecting rhizodeposits, two additional rhizotrons were used as control without patch application, one of them being equipped with Campbell thermocouples for monitoring the evolution of soil temperature at different depth.

Unless otherwise stated, all steps described below apply to both experiments.

5.2.2 Preparation steps

Soil collection and preparation

The growth substrate in the rhizotrons was an agricultural loamy soil collected from the Plateau de Saclay near Paris (France), mixed with 30% volume of sand. Main soil properties are summarized in Tab. 5.1. 300 kg of soil was air - dried in a greenhouse for one week at around 25°C, and homogenized by repeatedly raking it to break clods and avoid moisture gradients. The air-dried soil was then sieved at 5

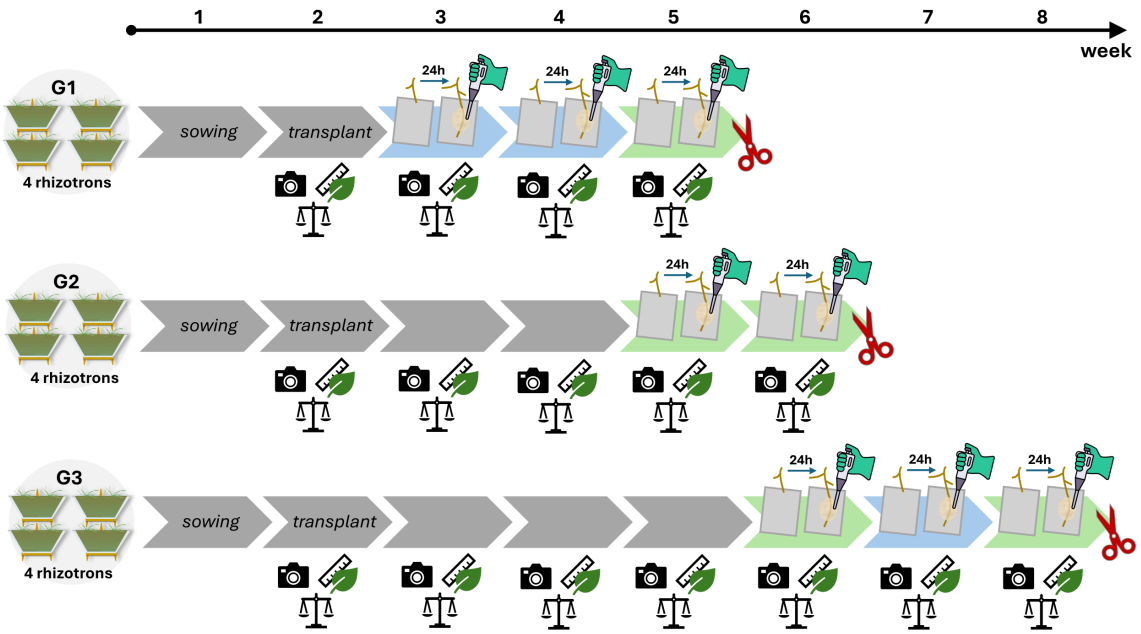

Figure 5.2: Sampling planning of Experiment 2, divided in 3 groups of 4 rhizotrons for a total duration of 8 weeks. Sowing on week 1 occurred on Friday, followed by a transplanting of 2 seedlings per rhizotron on Wednesday of week 2. Grey arrows indicate no sampling was conducted on this group for considered week. Blue arrows indicate groups undergoing bolting cloth application at targeted root tips on Tuesday, with a subsequent sand absorbing patch application on Wednesday for all root locations with a bolting cloth $\leq$20 cm from root tip (See 5.2.3). Green arrows indicate an additional sampling on Thursday on all bolting cloth of a seminal axis, which occurs at the same time for two consecutive groups. The red scissors indicate the destructive sampling following this whole axis sampling. Camera and scale icons indicate rhizotron imaging and weighting for irrigation adjustment 3 times a week. The ruler and leaf icon indicates measurements of leaf elongation every Tuesday.

Table 5.1: Average properties of a soil collected from the *Plateau de Saclay*, mixed with 30% volume of sand, and used in Exp. 1 and 2. All soil properties were measured after drying and sieving

Measurement	Unit	Value
Clay	% (g/100g)	11.2
Loam	% (g/100g)	57.2
Sand	% (g/100g)	29.5
pH (water)	-	8.12
Organic carbon	% (gC/100g)	0.59
Inorganic carbon	% (gC/100g)	0.12
Total nitrogen	% (gN/100g)	0.069
Total phosphorous	% (gP/100g)	0.021
Extractible phosphorous (P_2O_5 Olsen)	mg/g	11.8
Bulk density	kg dry soil / L	1.38 - 1.46
Residual water content	% (g water/100g dry soil)	4.3
Field capacity	% (g water/100g dry soil)	23.9

mm. Three 1 kg sub-samples were taken to determine residual water content by oven drying at 105°C for 24h and to determine field capacity. For the latter, soil columns (2 L perforated tubes) were filled with dry soil, saturated by slow water infiltration, and then allowed to drain for 24 h and 48 h. Field capacity was approximated as the gravimetric water content of the drained soil (after 48 h), calculated from the difference between the mass of the drained columns and their oven-dried mass. The same soil was used for Exp. 1 and Exp. 2.

Rhizotron design and assembly

Each rhizotron was fabricated from transparent polycarbonate and measured 100 × 50 × 1.5 cm externally (Fig. 5.3). The internal soil compartment measured 90 × 45 × 0.5 cm (2.025 L). A series of twelve windows (25 × 15 cm each, 6 rows, 2 columns) were cut into the front panel; a 1-mm gap between window frames prevented them from touching and bending. The back panel comprised a large polycarbonate sheet. For each of the six 20-cm horizons of the rhizotron, a layer of FEP film was introduced between the polycarbonate window and the soil to avoid soil loss when opening the windows and to prevent the roots from growing outside the rhizotron. Rhizotron were assembled using screws traversing holes pierced in each part. Prior to filling, each empty rhizotron weighed 6.3 kg. The same rhizotron design was used for Exp. 1 and Exp 2., except for Group 3 of Exp. 2 where 3 additional horizons (6 windows) were added to extend the maximal depth of the rhizotron up to 135 cm.

Soil filling and water addition

Each empty rhizotrons was filled horizontally with 5-mm sieved soil to reach a target bulk density of 1.1 g cm^{-3}, i.e. about 2.2 kg of dry soil per 90-cm high rhizotron. Soil was added in small batches using a hand shovel and the soil surface was progressively leveled thanks to a flat piece of PVC. Following soil addition, deionized water was

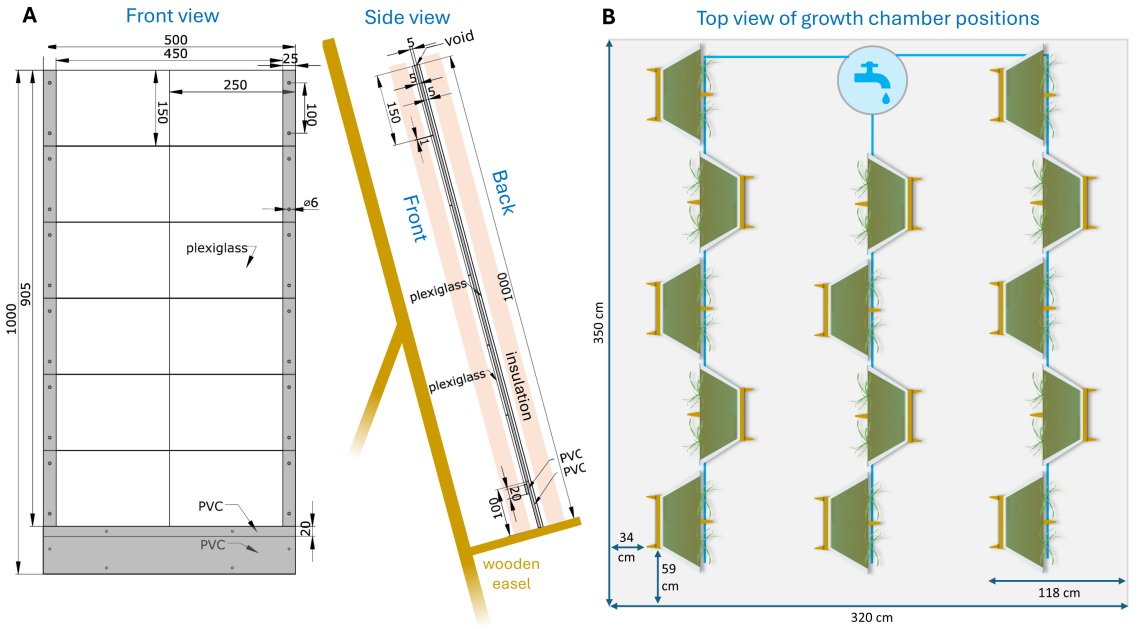

Figure 5.3: Schematic representation of A) rhizotron setup dimensions in mm, materials and assembly, and B) positioning in the growth chamber in cm. Insulation in the growth chamber was not represented for clarity.

applied with a sprinkler to reach 80 % of field capacity. For a given experiment, all rhizotrons were filled and positioned in the growth chamber the same day in random order. Rhizotrons were checked one day later for soil subsidence; if any, voids visible through the windows were filled with dry soil and rewetted at 80 % of added soil field capacity.

Installation in the growth chamber

Rhizotrons were placed on wooden easels in the phytotron at an inclination angle of 15° from the vertical, so that most of the root system is visible and accessible from the opening face of the rhizotron because of root gravitropism. Each rhizotron rested on two insulating foam boards to darken the root compartment and provide thermal insulation. In Exp. 2, aluminum sheets were also added on rhizotron vertical edges to protect them from light transmission through the plexiglass. This was also intended to avoid any negative phototropism of lit apices that would force them into the soil and prevent their observation. A plastic gutter was positioned below each rhizotron to collect any drained water, even though none was observed at the watering regulation at 80 % field - capacity. The rhizotrons were initially randomly assigned to positions within three lines of 5 rhizotrons each (Fig. 5.3B). Rhizotrons positions were rotated 3 times a week, at each imaging event, to mitigate positional effects.

Plant material, sowing and rhizotron transplanting

Seeds were not surface - sterilized to allow a realistic rhizosphere microbial community to develop, and they were not vernalized considering the growth period re-

stricted to the developmental stage. 60 seeds were pre - soaked for 1 h in deionized water and placed in a germination petri dish on moist Kimtech wipes in darkness at 20 °C for 48 h. 26 seedlings with homogeneous dimensions were then selected for transplanting, i.e. with three radicles $\geq$ 5 mm and a coleoptile $>$ 2 mm criteria. Two seedlings per rhizotron were then positioned at 11.25 cm from each side to avoid the central window junctions, and at a 2.5 cm depth representing ten times the seed width. Twelve rhizotrons and one planted control therefore receive a pair of seedlings. Plants were monitored for damage for the first two days after transplanting and replacements were made if necessary. Given the position of each rhizotron within the phytotron and the large spacing between the three lines, the competition for light between plants was low, and plants could therefore be considered as isolated.

Growth conditions

A programmable LED array with 4 independent green, blue red, and far red channels (Pandora, Colasse SA) was used to provide a 600 $\mu mol\ m^{-2}\ s^{-1}$ photon flux density (PPFD) at canopy height and a red:far-red ratio of 1.2 to ensure a realistic tillering behavior. We measured incident PPFD at plant height (140 cm from ground) before the experiment to confirm homogeneous lighting conditions between the different rhizotron positions within the phytotron. The same lighting intensity and composition was used in both experiments. In Exp. 1, the photoperiod was 9 h day with day / night temperature of 20 / 15 °C and a transition rate of 0.1 °C min^{-1}. Relative humidity (RH) was set at 70 % during day and night, corresponding to a vapor pressure deficit (VPD) of 0.7 and 0.5 kPa, respectively. In Exp. 2, the photoperiod was adjusted to 13 h of day length, while lower day / night temperatures (14 °C and 10 °C, respectively) were set. This was intended to decrease root growth rate in order to make the sampling protocol presented below feasible. RH was set to 70 % during the day and 60% at night to maintain a constant 0.5 kPa VPD throughout the day. In Exp. 2, organ temperatures were monitored to relate their growth speed to thermal time. Shoot temperatures were monitored before each destructive event of G1, G2 and G3 with a thermal camera (FLIR E60), and soil temperature in contact with roots was estimated with thermocouples inserted into each horizons of a control rhizotron connected to a Campbell acquisition card (See Fig. S6.26). Ambient CO_2 concentration was not actively controlled and was assumed to be close to 450 ppm thanks to the regular ventilation of the phytotron.

Ultrapure water (ELGA Veolia, $<$ 18 MΩ) was delivered daily via a 36 - channel peristaltic pump. No fertilizer was supplied, as the initial nutrient content of the soil was considered sufficient for the eight - week growth period. Each rhizotron was equipped with two nozzles inserted in the soil surface at 1 cm of each plant's emergence point. The pump ran at 2 rpm, delivering 0.5 $mL\ min^{-1}$ per nozzle. Water volumes were progressively adjusted from 10 $mL\ rhizotron^{-1}\ day^{-1}$ immediately after transplanting to 15 $mL\ rhizotron^{-1}\ day^{-1}$ to maintain soil moisture at 80 % of field capacity (estimated from weighting the rhizotrons 3 times a week). Additional beakers connected to spare pump lines were weighted weekly to check pump precision. Irrigation lines were removed and repositioned at each root sampling and imaging event.

5.2.3 Repeated bolting cloth installation and rhizodeposit sampling with sand patches

Here is presented a non-destructive rhizodeposit trap sampling method that occurs in two steps. **First**, 24h prior the sampling, a bolting cloth is placed between the soil surface and a targeted root tip, so that the root axis continues to grow on the cloth, separated from adhering soil particles but still exchanging with the soil solution. **Second**, on sampling day the root tip has grown few centimeters on the bolting cloth, enabling to access a root segment free of soil particles that would have contaminated the sample. The segment is then enclosed between two aluminum sheets along with a sand absorbing patch left in place for 4 hours within the phytotron chamber. The aluminum sheets are finally reopened, the sand patch collected and frozen, and the root is non-destructively replaced in contact with the bolting cloth. Note that after collection, bolting cloths are left in place so that in subsequent weeks the same root location can be sampled. However the root tip is only temporarily separated from the soil: few hours after sampling, it finally grows out of the bolting cloth so that a majority of root system length is always in direct contact with soil.

Sampling location choice and bolting cloth installation

Three root types were distinguished and targeted for rhizodeposition sampling; seminals, nodals, and laterals. When present, 2 seminal apices, 1 nodal apex, and 1 lateral apex per plant were targeted for each sampling. At each sampling event of Exp. 2, for the current target group of 4 rhizotrons replicates, this corresponded to 16 spatial repetitions collected on seminal root segments with similar distance from apices and, when present, 8 on nodals and 8 on laterals. The rhizodeposit sampling protocol presented below being non destructive, the corresponding apices continued growing in the subsequent weeks, and as long as the apex was visible in front of the soil, sampling along the same root axis across sampling events was prioritized. If the apex was no longer accessible, it was replaced by an apex of similar root type and depth in order to maintain the number of spatial repetition per plant. The first accessible root apices were seminal roots 1 week after transplanting the seedlings into the rhizotrons (Fig. 5.2).

To sample rhizodeposits at specific positions along roots, bolting cloths (SEFAR Nitex nylon with 37 μm mesh, cut at 4 $\times$ 3 cm) were inserted between the soil and a targeted root apex, preventing soil particles from adhering to the corresponding future root segment. After opening the corresponding window and the Teflon film, a small section of cloth was carefully slid under the root apex. This apposition was performed the day before a rhizodeposition collection so that apex growth makes the whole bolting cloth length occupied by the root the next day, while still including the apex. After collection, bolting cloths were left in place. It enabled the sampling of rhizodeposits on old root segments during the subsequent collection weeks. The application of 4 new bolting cloth per plant before each sampling event was therefore additive; it progressively increased the number of possible sampling location from 4 per rhizotron to at most 18 per rhizotron for G3 of Exp. 2. However, the sampling protocol detailed below being time consuming, the targeted locations were restricted

to bolting cloths at locations $\leq$ 20 cm from root tip, where most of the variations in rhizodeposition levels are thought to occur. Exception was made in Exp. 2 at the junction between the destructive sampling of a group and the start of the next group (See green arrows, Fig. 5.2), during which all cloth locations of one seminal axis per plant were targeted for sampling in the two groups.

Rhizodeposition sampling with sand patches

Prior rhizodeposit sampling, dry quartz sand patches (Fontainebleau sand, 0.3 mm) were prepared. 1 kg of sand was first pretreated to remove traces of organic matter that would overlap with the rhizodeposits' signal. The batch was burnt at 500°C during 24 h, then rotated in a 1 mM HCl suspension during 24 h to remove carbonates. Sand was rinsed and agitated 4 times with ultrapure water, with a resulting pH of 6.5. After removing the supernatant, sand was finally dried in an aluminum container at 105 °C for 24 hours and stored in a glass bottle for further use.

For each rhizodeposit sampling on a prepared cloth location, we applied the following procedure to apply an sand absorbing patch in contact with the root. All steps were performed using washed aluminum tools and wearing nitrile gloves, a mask and a hair protection cap to avoid any contamination of the patch. In the morning, rhizotrons were imaged prior sampling, sand patches were applied on target root locations, rest for exactly 4 h in contact with the roots within the growth chamber, and then collected in the afternoon in the same order as in the morning (Fig. 5.4).

For patch application, we laid flat the rhizotron outside the growth chamber and accessed to the target location by opening the window and the corresponding Teflon film. Using round edged pliers, the root was first gently unsticked from the bolting cloth as root hairs have developed inside the mesh. A 3 x 6 cm aluminum foil was then placed in between the cloth and the root to ensure soil solution will not contaminate the sand patch during application. An Eppendorf tube containing 140 mg of cleaned sand was then evenly spilled on the root length lying on the aluminum foil. 150 μL of ultrapure water was applied on the patch to prevent root drying, and immediately a 3 x 3 cm portion of the aluminum foil was then folded up so that the sand patch and the root were enclosed between two aluminum layers. The two layers were cramped together by pushing on the edges with a pointy plier so that the soil solution cannot penetrate the patch from the edges. The Teflon film and the window were finally put back once all the sand patches of a specific horizon were applied. Each rhizotron also included a control sand patch which underwent the exact same protocol inside the rhizotron but without being in contact with roots.

After 4 h exposure, the patch was gently unfolded, a drop of ultrapure water was spilled on the root to detach sand particles and slide the aluminum foil and the sand off the root. The aluminum foil was then folded in a V-shaped gutter to transfer the sand containing rhizodeposits into a 1.5 mL Eppendorf tube by spilling drops of water on the gutter to flush all sand in the Eppendorf tube. The total rinse water volume was at most 0.5 mL. Extra care must be taken during this step not to touch the Eppendorf tube with the gutter, because the reverse side of the aluminum foil is contaminated with soil. During collection of sand patches, Eppendorf tubes were progressively kept on ice during handling and then stored

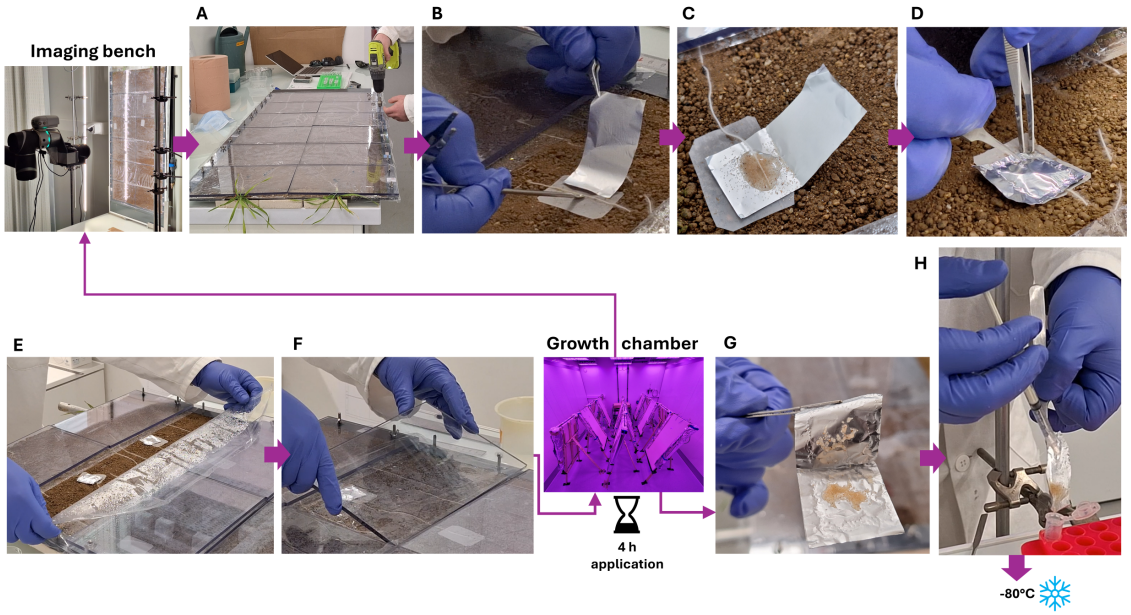

Figure 5.4: Key steps of the protocol to apply absorbing sand patch in contact with roots for rhizodeposits collection, repeated for each rhizotron of the current sampled group. A) Laying flat and opening rhizotron out of the growth chamber after imaging, B) gently lifting the root from the bolting cloth to slide a 3 x 6 cm aluminum sheet, C) spill sand on intercepted root length and moisturizing with ultrapure water, D) closing and clamping the sand patch with the root between two aluminum sheet, E) closing the Teflon film and F) the windows before putting back the rhizotron in the growth chamber. After 4 h of application, rhizotron is again opened out of the growth chamber, G) the aluminum sheet is opened, slid away from the root while ensuring the retrieval of all sand, and H) the aluminum is folded in a V-shaped gutter to transfer the sand into a 1.5 mL Eppendorf tube by spilling drops of ultrapure water on it. Collected patches are then stored at -80 °C.

at – 80°C until lyophilization. Sampling start and freezing times were recorded to calculate the exact exposure time, and normalize the amount measured in the patch to estimate the rhizodeposition flux.

This protocol required extra care to avoid any damage to the sampled root segment and any contamination of the sand patch until freezing. Specific gestures developed during this experiment were therefore recorded on video to ensure the repeatability of this protocol.

5.2.4 Repeated root and shoot phenotyping

Time - lapse imaging

Root growth was monitored non - destructively by taking images of the whole root profile 3 times a week using an semi-automated imaging bench (Fig. 3). An Omron TM5 - 900 six - axis robotic arm was mounted with a Nikon D5300 camera equipped with a macro lens. This setup was used to take 65 overlapping closeup images by moving the camera in a plane perpendicular to the rhizotron, yielding 1150 DPI images enabling a clear delineation of root axes for further analysis. Rhizotrons were manually transported from the growth chamber to a dark root where they were clamped on a fixed jig during imaging to ensure consistent positioning in front of the robot, and lit with fixed vertical LED arrays. After each movement of the robot arm, camera capture commands were sent through Omron TM - Flow using a Python script that waited for robot commands and triggered image capture using the software DigiCamControl. Camera settings were kept constant (ISO 400, 1/20 s, f/5.6, auto-focus every 10 images) to facilitate downstream stitching using the Hugin software. A complete capture of one rhizotron took approximately 6 min. A second camera also captured images of the aerial parts while the root system was imaged.

Shoot phenotyping and gas exchange

Leaf appearance and development were recorded weekly by measuring non ligulated leaf length and internode length on main axis and tillers. A decimal leaf stage was reconstructed to estimate phyllochron and leaf area dynamics assuming a constant leaf width:length ratio.

A Li - COR 6400 equipped with a transparent chamber was used to measure net photosynthesis on the oldest and youngest ligulated leaves of the main axis during the week of destructive harvest. This was intended to study the relationship between rhizodeposition levels and photosynthetic activity. Measurements were performed near early afternoon under chamber conditions (flow rate 250 $\mu mol\ s^{-1}$, CO_2 level 420 ppm, average PAR in transparent chamber 480 $\mu mol\ m^{-2}\ s^{-1}$ and leaf temperature regulation 16°C). Leaf width at the clamp was recorded to calculate the actual exchange area. Data were collected after 5 min stabilization. Leaf temperature was set based on average canopy temperature using a thermal camera (FLIR E60).

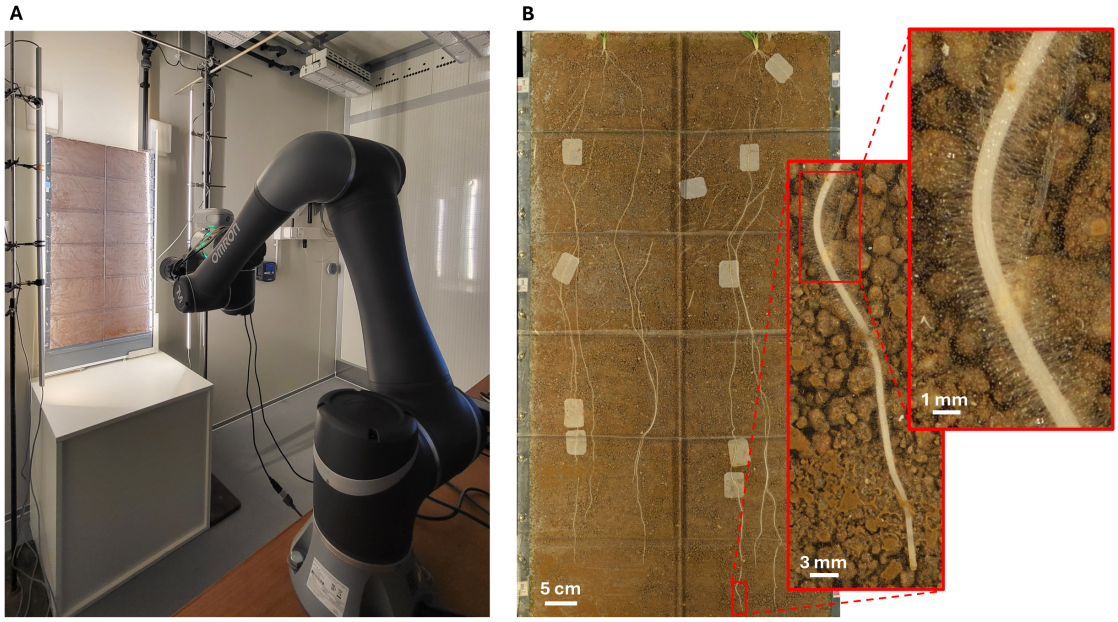

Figure 5.5: A) Rhizotron photographic bench during capture in the growth chamber. B) Example output image for a rhizotron of Experimentation 2, group 2, 31 days after sowing

5.2.5 Destructive sampling protocols

Root and shoot tissue sampling

At defined harvest weeks, plants from one group of rhizotrons were destructively sampled. Root segments corresponding to bolting cloth positions were excised (2.5 cm segments), weighed fresh and frozen at -80 °C for later lyophilization and analysis. These samples were collected to analyze metabolic concentrations and study their relationship with rhizodeposition fluxes measurements. Additional 2.5 cm root segments from adjacent zones not disturbed by rhizodeposition sampling were collected as controls, together with rhizospheric soil adherent to the root segment, to similarly estimate the gradient of metabolites' concentrations between the two compartments in an undisturbed location.

The entire shoots were harvested after cutting all roots. Leaves were separated by rank and fresh mass recorded. Root-system fresh biomass was determined after washing roots carefully to remove soil and absorbing excess water with a dense sponge prior weighting. All samples were frozen at – 80 °C for later lyophilization, assessment of per-compartment dry biomass and metabolic analyses.

Microscopy and histology

After 35 days of growth in Exp. 1, we performed cross sectional and axial observations on paraffin included root segments and transparized apices to estimate the heterogeneity of several anatomical features, such as root exchange surface, endodermis and exodermis differentiation, thought to regulate rhizodeposition levels along seminal roots. 2 cm root aliquots were sampled from the 5 rhizotrons not sampled for rhizodeposition, at apex, 3, 15, 40 cm from seminal root apex and 1

cm bellow root-shoot junction. Root apices were fixed in formaldehyde, produced from 4 % paraformaldehyde in phosphate buffered saline, during 1 h under vacuum at 20°C and one night at 4°C. Apices were then transparized using ClearSee, and stained with Auramine O (lignin/suberin) and Calcofluor White (cellulose) [Ursache et al., 2018]. Samples were imaged on a Zeiss LSM 710 confocal microscope to get stitched images of the first centimeter from apex in the central plane of the root, in order to capture the elongation of cells in the first mm impacting root exchange surface. Aliquots from other locations were fixed as described above, dehydrated in increasing concentrations of ethanol in aqueous solution, and then cleared with increasing proportion of HistoClear in ethanol. Once in 100 % HistoClear, the root segments were included in paraffin, stored at 4°C and progressively cross sectioned at 10 μM width using a Leica HistoCore AUTOCUT microtome mounted with Sec. 35 blades. Cross sections were then directly stained for 10 minutes in toluidine blue and observed using optical microscopy at x40. Cross sections were kept in paraffin for microscope observations, as pre-tests showed that removing paraffin caused heavy damages to the cortical tissue. For a given root section, several images were taken and reassembled using ImageJ Pairwise stitching [Preibisch et al., 2009].

5.2.6 Analytical protocols

Quantification of rhizodeposition using total C&N elementary and isotopic analysis

After 24h lyophilization, the absorbing sand patches and controls collected at week 2, 4 and 6 were analyzed for total C&N content using a Vario ISOTOPE Elementar analyzer coupled to an isotopic analyzer (isoprime precisION Elementar). Additional 140-mg control sand patches, spiked with either a standard mix of sucrose, glucose, glutamine, and citric acid, or known amounts of potassium phtalate, were also analyzed (8 replicates each). Prior to analysis, sand patches were first transferred inside tin capsules, weighted before analysis and pressed into a small cobblestone-shape to fit in the analyzer.

Root cross sections image analysis

Cross sections obtained from the destructive collection of root aliquots at 0.4, 0.8, 3, 10, 15 and 40 cm from the tip (Exp. 1, See 5.2.5) were observed with a x40 magnification to ensure sufficient image resolution, but seminal roots diameter often exceeded the field of view of the acquisition camera. Several overlapping images were therefore captured and stitched using the imageJ pairwise stitching plugin [Preibisch et al., 2009] before further analysis.

For a given root aliquot corresponding to a distance from tip, two ribbons of paraffin were produced at 3 and 7 mm from an extremity of the included root segment, avoiding the edges to exclude damages related to aliquots excision. With up to 20 cross sections per ribbon, this ensured to obtain several good quality cross sections, but many were also damaged causing cortex and stele dislocation or blurred observation, preventing the measurement of targeted anatomical features. A first preselection step then guaranteed the feasibility of the analytical steps presented

below. Selection criteria were the presence of an undamaged cortex, a balance in the sharpness of both cortex and stele cell walls to ensure a proper delineation, and finally avoid over-saturated toluidine blue staining that would hamper cross section's readability and overestimate cell wall thickness measurements. Epidermis and root hairs were not consistently visible on these cross sections so it was not included in this image quality control.

To assess the heterogeneity of anatomical features along the seminal roots of wheat, targeted traits on cross sectional images were the following for each tissue type. A complete manual annotation of all cells of a cross section was not possible, given the incompleteness of most root sections and the presence of reflection artifacts caused by paraffin. The microscope images were not used to directly measure the exchange surface from different tissues, but were instead annotated using ImageJ in order to determine specific anatomical parameters and to simulate virtual root sections. The following features were determined on the whole root section or on a subset of it (measurements made on 6 to 20 cells of each tissue):

- number of xylem and phloem poles
- number of cell layers in the stele and in the cortex
- diameter of tissue layers (e.g. pericycle, endodermis, exodermis and epidermis)
- position of the xylem and phloem poles relative to the root center
- average cell diameter and cell wall thickness for each tissue (central xylem pole, metaxylem poles, protoxylem cells, phloem pole, phloem companion cells, pericycle, endodermis, inner cortical cells, outer cortical cells, exodermis, epidermis).

In addition, an estimation of cell height for xylem poles, stele cells and cortex cells was made by measuring the evolution of cell height with the distance from root tip in the first 7 mm of transparized apices. A set of longitudinal images of one of these transparized apex was also used to reconstitute the root sections at 0.4 and 0.8 mm from root tip.

From these anatomical features, virtual root sections were simulated using the GRANAR model [Heymans et al., 2020], after adapting and improving the model to generate specific features observed in the wheat root sections. Specifically, the vascular features were modified to include a central xylem pole in addition to radial metaxylem poles, and to allow for the creation of phloem companion cells close to the phloem poles. In addition, two additional functions were added for shrinking cells to allow a dedicated space for cell walls and for smoothing the edges of cells to allow for more intercellular space in the cortex. The new version of the model is available on https://github.com/frees86/granar/tree/bridges

From the virtual root sections generated by the new version of GRANAR, the total external cell surface in each tissue was computed, accounting for cell walls interruptions in the cell file, as well as the cumulative volume inside and outside cells, assumed to represent the volume of symplasm and apoplasm, respectively.

Rhizotron time lapse image processing and root segmentation

In order to reference the locations at which rhizodeposit traps were applied to the roots, a method was developed to digitalize the growing root system architecture from the recto/verso high resolution scans captured throughout the experiment, as summarized in Fig. 5.6.

First, segmentation of roots from the heterogeneous soil background was performed using *RootPainter* [Smith et al., 2022]. A training dataset was created by extracting 1000 image tiles from the mosaics. Initially, two tiles containing root and soil were manually annotated; after training, four more annotated tiles were added. Corrective annotation was then used iteratively, correctively annotating 150 additional tiles until the model reliably detected roots. The final model was used to segment rhizotron images into binary masks delineating visible roots for root architectural analysis. Both recto and verso time series were segmented.

Second, the SIFT algorithm [Lowe, 1999] was used in ImageJ was used to align the binary masks for the whole recto and verso time series, starting from the oldest state of the root system to ensure a feature-rich registration of all images. Using a custom ImageJ macro, the registered time series was then color-coded and stacked into a single time-map image summarizing all capture times and recto-verso information (Fig. 5.6). This provided a lightweight handling of the whole temporal information of the rhizotron compared to full time-series stack, while enabling subsequent analyses in root system annotation tools which only support static images.

Third, the semi-automated annotation software *SmartRoot* [Lobet et al., 2011] was used to leverage the automatic annotation of well-segmented, continuous root axes, while remaining flexible with manual annotations for situations where root axes were temporarily not visible on both rhizotron faces. Additionally, original images were opened and synchronized with the *SmartRoot* view in order to regularly check the measurements of root diameter in performed on segmented images. Aside root system skeleton, branching and diameter, the successive root tip locations where also annotated using the color code of the time map, as well as the location of bolting cloth on which rhizodeposit traps were positioned. When a visible root system was fully annotated, it was saved in the standard RSML format [Lobet et al., 2015] for further analyses.

Fourth, an adaptation of the RSML parser of Schnepf et al. [2023] was used to translate *SmartRoot* RSML outputs to MTG format and also convert diameter, age and rhizodeposit traps location measurements into properties of the MTG. **Fifth**, the saved MTG was used to test automatic measurement of *ArchiSimple* parameters, and compute simple indicators on these experimental root system architectures (Fig. 5.6) to test the feasibility of applying FSPMs directly to experimental architectures that would be able to integrate punctual measurements of rhizodeposition along roots and over time into whole plant functioning.

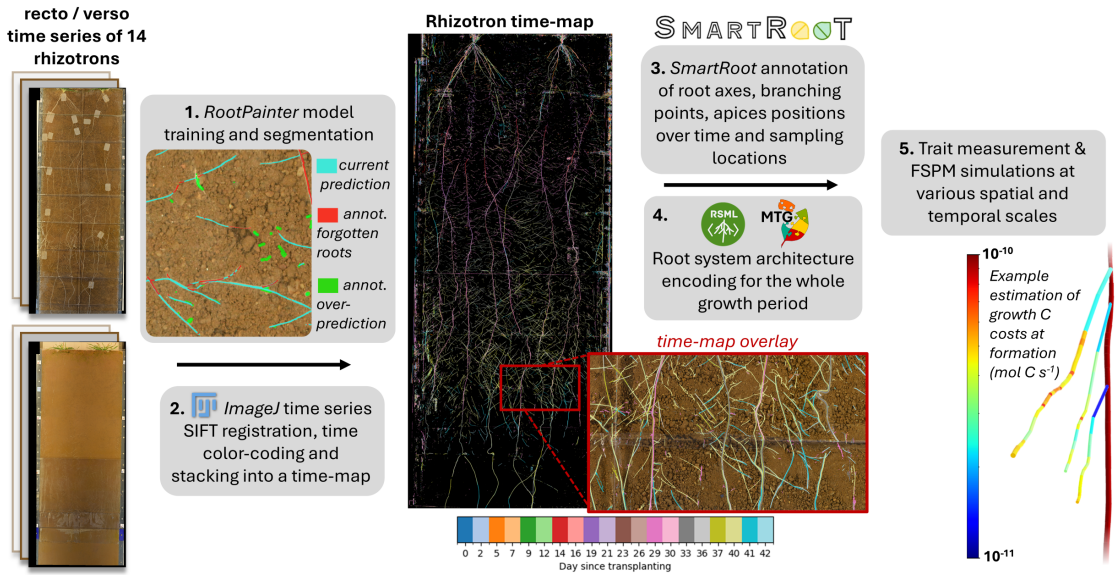

Figure 5.6: Processing pipeline for the high resolution rhizotron images dataset

5.3 Experimental results

5.3.1 Root cross sections image analysis

The observation of root sections at 0.4, 0.8, 3, 10, 15 and 40 cm from the tip of a seminal root of wheat prepared in Exp. 1 revealed that the root anatomy barely changes with the distance from root tip (Fig. 5.7). A similar cell organization occurred whatever the distance from the tip up to 40 cm, with one central xylem pole and six metaxylem poles nearby the pericycle layer, interspersed with six phloem poles. The stele is made by three to four layers of cells surrounding the central xylem, while the cortex has three larger cell layers, ending with one layer corresponding to the exodermis and one layer of epidermis. Very few exceptions were observed to this rule, and the root section that was analyzed below for each distance from root tip was selected based on its representativity compared to other root sections prepared at the same distance. A higher anatomical variability was however observed near the base of the root system, as root sections often lacked epidermis and exodermis cell layers, and sometimes displayed a different pattern of vascular tissue within the stele (e.g. an absence of central xylem, the presence of a few large metaxylem poles, or a multiplication of small xylem and/or phloem poles).

The analysis of a 6-mm long transparized apex enabled to show a linear increase in cell height with the distance from the root tip (Fig 5.8). The height of the central xylem doubled every 2 mm, while the rate of cell height increase for stele or cortex parenchyma cells was three time lower. Using these linear relationships, the cell height for each targeted tissue was estimated for the root sections at 3, 10, 15, 40 cm from the root tip and at the base of the root system by assuming that the root elongation zone ended at 0.86 cm from root tip [Watt et al., 2003] and that cell height remained constant afterwards. For the root sections located at 0.04 and 0.08 cm from root tip, the cell height was actually measured directly from the longitudinal microscope images. By combining cell height, cell wall thickness and

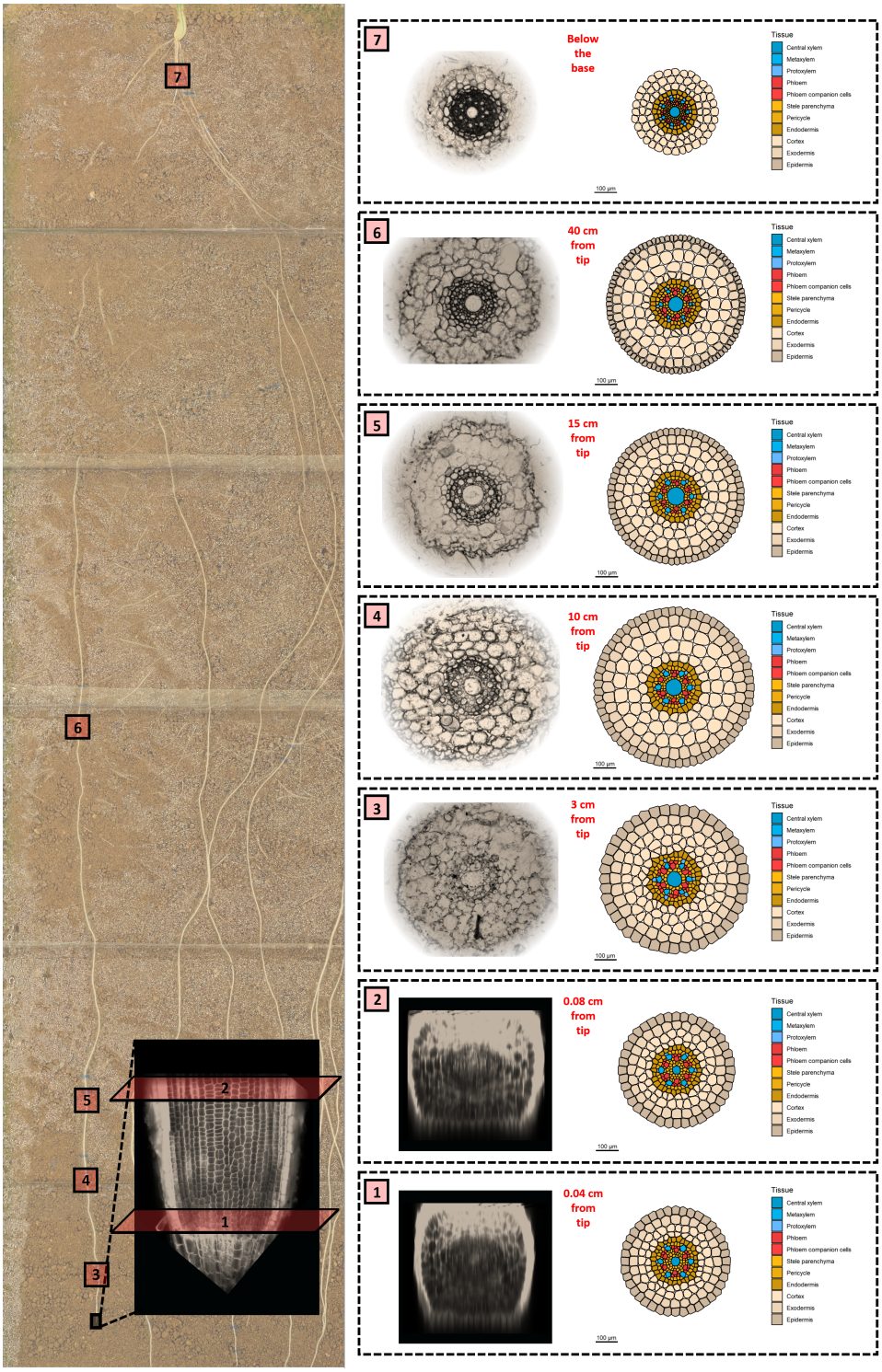

Figure 5.7: Illustration of the root sections observed under microscope at 0.04, 0.08, 3, 10, 15 and 40 cm from the tip of a seminal root of a 576 degree day wheat, and the corresponding virtual root sections generated by a modified version of the GRANAR model. The two sections closest to the root tip were generated from a stack of longitudinal images observed under confocal microscope fluorescence after calcofluor white staining, while the five other root sections were observed after root impregnation in paraffin, slicing with microtome and toluidine blue staining. As the root sections may have originated from different seminal roots, variations in the diameter of root sections does not necessarily reflect an actual evolution of root diameter with the distance from root tip.

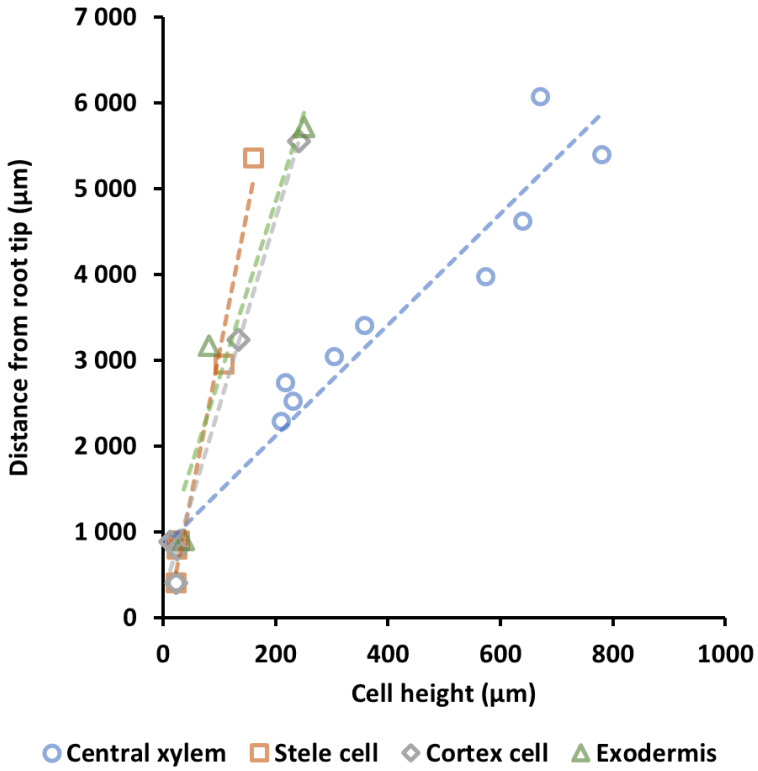

Figure 5.8: Evolution of cell height along the first 6 mm of a seminal root of wheat for different tissues, as measured from longitudinal images from transparized apices.

the radial dimensions of each cell obtained from the simulated root sections, the total external surface of cells in each tissue per length of root was computed for the seven distances from tip. As seen from Table 5.2, the total external surface developed by cells and normalized by the radius of the actual analyzed root section did not significantly vary along the root, leading to the development of a total root cells' external surface of about 103 $\pm$ 10 mm^2 per mm of root length and per mm of root radius. When normalized by the radius of the stele, the exchange surface of xylem, phloem or stele parenchyma cells was also remarkably stable across the distance from root tip. The cortical cells, including exodermis and epidermis but excluding endodermis, represented about 75 % of the total root cells' exchange surface, except in the case of the root section observed near the base of the root system, where only 3 cell layers could be observed around the stele, instead of 4-5 for the other root sections.

5.3.2 C&N rhizodeposition rates estimated from rhizodeposit traps

In the absence of a reliable method for analyzing low amounts of root metabolites and exudates with GC-MS-MS (currently being developed at UMR EcoSys, INRAE), samples of sand collected in rhizodeposit traps were analyzed for total C & N only. As total N analysis was not accurate enough and led to major inconsistency among the samples, only the results obtained for C are presented below.

Table 5.2: Stele and root radius measured on root sections obtained at 7 distinct locations from the tip of a seminal root of wheat, and total cell external surface of distinct root tissue for each section computed using a modified version of the *GRANAR* model. The total cell external surface is either expressed relative to the root length only, to root length and root radius, or to root length and stele radius. SD : Standard deviation.

	Actual tissue radius measured (mm from root section's center)		Computed total cell external surface (mm^2 per mm of root length)				
Distance from root tip (cm)	Stele radius	Root external radius	Xylem	Phloem	Stellar parenchyma*	Cortex and epidermis**	TOTAL
0.04	0.107	0.219	1.03	1.17	6.21	18.8	27.2
0.08	0.105	0.257	1.04	1.22	6.25	20.3	28.8
3	0.107	0.294	1.09	1.28	5.96	23.9	32.2
10	0.115	0.348	1.05	1.07	5.98	27.0	35.1
15	0.112	0.278	0.99	0.97	5.79	23.1	30.9
40	0.101	0.280	0.85	1.04	5.42	23.0	30.3
Base	0.092	0.171	0.85	0.79	4.70	8.5	14.9
MEAN	0.105	0.274	1.0	1.0	5.6	21.1	28.7
SD	0.01	0.06	0.11	0.18	0.54	7.22	7.94
	Actual tissue radius measured (mm from root section's center)		Computed total cell external surface per root radius (mm^2 per mm of root length per mm of root radius)				
Distance from root tip (cm)	Stele radius	Root external radius	Xylem	Phloem	Stellar parenchyma*	Cortex and epidermis**	TOTAL
0.04	0.107	0.219	4.69	5.34	28.37	86.0	124.4
0.08	0.105	0.257	4.04	4.77	24.38	79.2	112.4
3	0.107	0.294	3.71	4.35	20.28	81.3	109.7
10	0.115	0.348	3.02	3.07	17.17	77.6	100.8
15	0.112	0.278	3.56	3.49	20.85	83.3	111.1
40	0.101	0.280	3.02	3.72	19.37	82.3	108.4
Base	0.092	0.171	4.95	4.64	27.49	49.9	87.0
MEAN	0.105	0.274	3.7	3.9	21.0	74.9	103.4
SD	0.01	0.06	0.79	0.64	3.87	14.11	10.00
	Actual tissue radius measured (mm from root section's center)		Computed tissue external surface per stele radius (mm^2 per mm of root length per mm of stele radius)				
Distance from root tip (cm)	Stele radius	Root external radius	Xylem	Phloem	Stellar parenchyma*	Cortex and epidermis**	TOTAL Stele
0.04	0.107	0.219	9.57	10.89	57.88	175.4	78.34
0.08	0.105	0.257	9.86	11.66	59.54	193.5	81.05
3	0.107	0.294	10.23	12.00	55.92	224.2	78.15
10	0.115	0.348	9.10	9.25	51.79	234.1	70.14
15	0.112	0.278	8.85	8.67	51.86	207.1	69.39
40	0.101	0.280	8.37	10.29	53.62	227.9	72.28
Base	0.092	0.171	9.15	8.58	50.81	92.3	68.53
MEAN	0.105	0.274	9.1	9.8	52.8	197.1	71.7
SD	0.01	0.06	0.68	1.43	2.02	59.45	3.86

Very low amounts of C were detected in rhizodeposit traps, ranging from 2 to 69 μgC after 4 hours of contact with roots. Moreover, the concentration of C in the traps at the contact of a root barely differed from the concentration of C measured in the control traps without contact with roots. The average C concentration in blank controls was 99 ± 50 μgC per gram of dry sand, while it was 135 ± 105 μgC per gram of dry sand in rhizodeposit traps. The analysis of control sand samples, where known amounts of C (i.e. 0.8, 3, 15 or 78 μgC) were injected by adding a specific volume of either a mixture of glucose, citric acid and glutamine or a solution of sodium phtalate, showed that, when the sand samples were oven-dried at 80°C for 48h, the amount of C measured matched the expected levels, with an average C recovery of 93% (Fig. 5.9A&B). However, when the sand samples had been lyophilized similarly to the samples from rhizodeposit traps, the recovery rate dropped to 75% with the mixture of metabolites and to 68% with the phtalate solution (Fig. 5.9C to F). This suggests that lyophilization induced a loss of organic material from the sand samples, regardless of the biodegradability. The analysis of oven-dried samples also suggests that the quantification of C in the sand significantly lost accuracy below 3 μgC per sample (Fig. 5.9B).

Among the 77 rhizodeposit trap samples that were analyzed for total C, only 46 of them had a C concentration higher than the average concentration in the blank control samples, and only 11 of them had a concentration significantly higher than that of control samples, i.e. higher than the upper limit of their 95% confidence interval (196 μgC per gram of dry sand). Among these 11 samples, 8 of them corresponded to the apex of a seminal or nodal root, and 3 of them to a more mature zone from such root. The average rhizodeposition rate corresponded to **25 ± 74 μgC per cm of root per day** when all rhizodeposit traps were included, 62 ± 79 μgC per cm of root per day when only the 46 samples with C concentration higher than in the blank controls were included, and 165 ± 106 μgC per cm of root per day when only the 11 samples whose C concentration was significantly higher than in the blank controls were included. Given the high variability of C rhizodeposition rates calculated from those samples, it was not possible to give an accurate estimation of the evolution of C rhizodeposition rate along different types of roots.

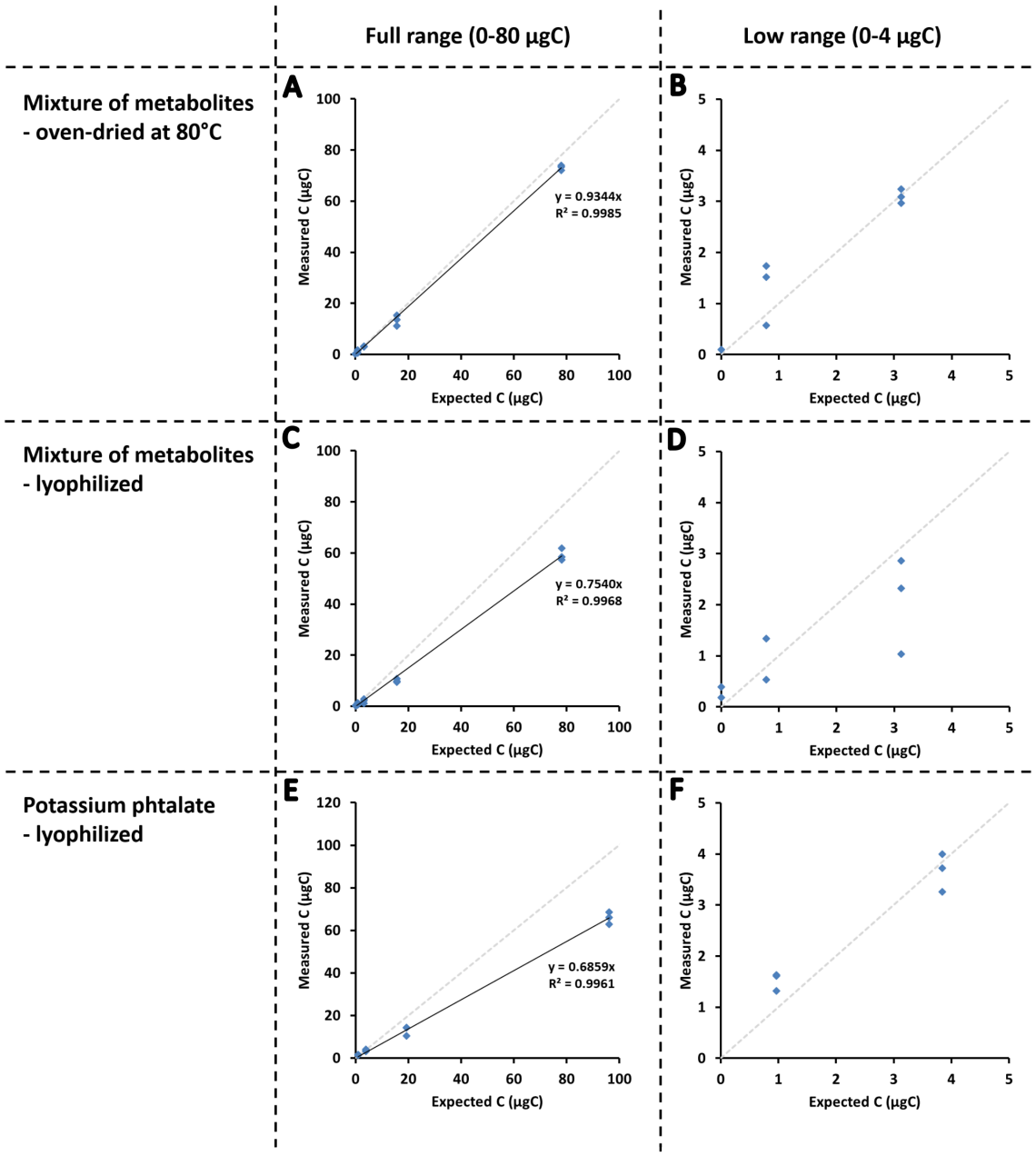

Figure 5.9: Comparison between the amount of C expected in control sand samples and the amount of C actually measured in the sand collected in rhizodeposit traps, after injecting 200 μL of either a mixture of glucose, citric acid and glutamine or a solution of sodium phtalate at four distinct concentrations. Phtalate was assumed to be less biodegradable than the mixture of metabolites. After injecting the solution, sand samples were either oven-dried at 80°C for 48h, or lyophilized.

5.4 Discussion

A new experimental setup was developed to get as much information as possible about the spatial evolution of rhizodeposition rates along roots and its relationship with root architecture and the spatial evolution of root metabolite concentrations and root tissue anatomy. The data gathered so far has allowed calculating the evolution of the exchange surface between root cells and the soil solution and estimating an average, length-related rhizodeposition rate of wheat, although a complete, accurate exploration of the evolution of rhizodeposition rates along different types of roots and over time could not be achieved with total C&N analysis only. The main achievements obtained by this experimental approach, its limitations and the perspectives of improvement are discussed below.

5.4.1 Anatomy of wheat roots and its possible influence on root-soil exchanges

Root anatomy plays a significant role in controlling how matter is exchanged between roots and soil and transported along roots. In particular, root tissue organization determines the surface of exchange between various types of root cells and the apoplast in contact with root surrounding environment, and controls the apparent radial conductivity for water transport. Consequently, any variation in root anatomy may directly impact root exudation and root N and water uptake. Experiment 1 was therefore conducted with the main objective of assessing the variability of root anatomy along roots, by observing histological sections of roots and deriving anatomical root traits from these observations.

Observations made here along wheat seminal roots revealed that the anatomical structure is remarkably constant along of the root. The results suggest that, when related to root diameter, the total external surface of wheat root cells does not evolve with the distance from root tip. Only wheat roots were observed and analyzed here, which makes it difficult to generalize this result to other species. Given that monocotyledons do not experience root secondary growth, this invariance of the ratio of root cells exchange surface with root diameter along roots may at least stand for all cereals, but additional observations on other species will be needed to confirm this. In practical terms, this invariance allows to estimate the root exchange surface from root diameter only, using a simple proportionality coefficient, which in the case of the seminal roots observed here correspond to about 100 mm^2 per mm of root length and per mm of root radius. The only exception to this general rule was observed at the base of the root system, where a significant fraction of epidermis and cortex appeared to have been lost from the sections, effectively lowering both the total exchange surface between root cells and the surrounding environment and the proportionality coefficient. Whether this loss corresponds to an actual loss of cortical cells caused by senescence or to an artifact during root sections' preparation remains uncertain. Root cortical senescence in cereals, as assessed by the presence of a functional cell nucleus, has been shown to start after only a few days after root emergence, corresponding to a so-called cell programmed death [Liljeroth, 1995, Schneider et al., 2017]. Henry and Deacon [1981] reported that seminal roots of field-

grown wheat showed an advanced state of cortical senescence 7 weeks after sowing, which would correspond to the state of the wheat root system as sampled here in the rhizotron. Monitoring root cortical senescence requires special observations techniques or staining, and was not attempted in the present work. Additional observations and alternative histological sections preparation would be necessary to evaluate the extent by which cortical senescence can affect root exchange surface and therefore root-soil exchanges during early vegetative wheat growth.

Besides cortical senescence, another anatomical feature may significantly affect root-soil exchanges along roots despite the invariance of root cells exchange surface, i.e. the formation of apoplasmic barriers at the endodermis and possibly at the exodermis which limit or impair the apoplastic transport of water and solutes along cell walls and condition the actual fraction of the root cells in effective contact with the soil solution around the root. Although patterns of Casparian strips could often be inferred from the observation of endodermis above 3 cm from root tip and were not detected around the endodermis at any distance from root tip (data not shown), it was not possible to precisely quantify the evolution of both these barriers along roots, nor their level of water impermeability. As recent works suggest that the integrity of endodermis apoplastic barrier is a strong determinant of root exudation [Tsai et al., 2025] and as the models developed in this thesis support this assumption, a precise quantification of the evolution of both endodermis and exodermis along roots should be attempted in a near future to better take these physical limitations of transport into account.

Quantifying rhizodeposition rate along roots - Mission impossible?

Collecting and analyzing rhizodeposits, and in particular root exudates, remains a major challenge, whatever the method. This led Oburger and Jones (2018) to question whether sampling root exudates is indeed "Mission impossible". The present work aimed at quantifying rhizodeposition rates along roots and over different growth stages, using rhizodeposit traps associated to root growth in soil-filled rhizotrons. Some may consider this as the most difficult method for characterizing rhizodeposition, given i) the low amounts/volumes of samples taken over a given root segment, ii) the risk of fast alteration of the rhizodeposits by rhizospheric microorganisms, iii) the risk of root damage or disturbance during the installation of the trap, iv) the difficulty in interpolating the results for estimating rhizodeposition rates at the level of the whole plant (Oburger and Jones, 2018). This approach was used here in order to quantify the actual rhizodeposition rates along roots and link them to the local properties of roots (e.g. root anatomical features, root metabolites concentrations). Despite all the precautions taken here to minimize contamination from the soil - by using a combination of blotting cloth and aluminum foil to easily isolate roots from soil - or from the silica sand itself used in the trap - by removing any trace of organic or inorganic carbon from it, the amount of C measured in the rhizodeposit samples was highly variable and could be distinguished from the amount of C measured in control samples only in a few cases. Consequently, no clear conclusions could be drawn about the evolution of C rhizodeposition rates along roots and over time, although the results suggest that root tips could correspond to a rhizodeposition hotspot compared to older root zones, as three quarters of the samples that had a C concentration significantly higher than in control sam-

ples corresponded to root tips. The range of rhizodeposition rates calculated in this work (1-100 μgC per cm of root per day) is in line with previously reported rates. In the case of wheat, the exudate rate of malate - a major carboxylate in root exudates - was shown to reach up to 8 μgC per cm per day at root tip in standard environmental conditions [Ryan et al., 1995]. In terms of total organic C exudation, [Nielsen et al., 1994] also reported C exudation rates of 15-25 μgC over the first 6 cm of the primary root of common bean, which is line with the C rhizodeposition rates calculated in the present work on wheat roots. This suggests that the protocol of rhizodeposit collection along roots developed here can lead to realistic estimations of rhizodeposition rates, but fails to capture the temporal and spatial variations along roots.

The rhizodeposit traps used here - sand patches - have rarely been used and tested for a similar purpose. Several studies have used rhizodeposit traps made of glass fibers, cellulose or nylon [Haase et al., 2007, Shi et al., 2011, Akatsuki and Makita, 2020, Tixier et al., 2023, Bohm et al., 2025]; however only a few of them used these to investigate the spatial distribution of rhizodeposition rates. Among these, only one study attempted to quantify total C & N from rhizodeposit traps, after applying glass fiber filters at the contact of root apices from conifer trees for two hours [Akatsuki and Makita, 2020]. These authors also reported a wide range of rhizodeposition rates variation as observed in the present work, and indicated that several samples had C concentrations below the detection limits of the C&N elemental analyzer. This suggests that the direct measurement of total C&N in rhizodeposits collected in C-free traps still needs further optimization. Care was taken here to calibrate the analyzer for very low amounts of C, and to account for the traces of C both in the sand samples and in the tin foil used for wrapping the sample before its introduction into the analyzer. The analysis of control samples, in which a known amount of different compounds was added to mimic root exudates, suggests that the analysis can be accurate and reproducible above 3 μg of C in the sample, which would correspond to a minimal rhizodeposition rate of about 18 μgC per cm and per day when assuming that one rhizodeposit sample would be collected on 1 cm of root over 4 hours. This lower limit is similar to the mean average rhizodeposition rate calculated when including all the rhizodeposit samples, i.e. 25 μgC per cm of root per day. Given this rate, protocol conditions that would favor a higher amount of C collected in the trap could allow reducing the variability due to analyzer's detection limits. For example, the collection duration could be extended to collect more rhizodeposits; however, this would increase the risk of microbial degradation of rhizodeposits in the sample or favor the re-uptake of exudates by the root itself, leading to an underestimation of the actual rhizodeposition rate. Increasing the length of root over which rhizodeposits are trapped could also allow collecting more rhizodeposits within a given sample, but this would lower the spatial resolution along the roots and increase the volume of sample, knowing that the typical volume of one solid sample for a C&N analyzer is below 1 ml.

The observed variability in C rhizodeposition rates measured along roots may also result from factors other than the analyzer limitations. Despite all precautions taken, a contamination by the soil solution possibly diffusing within the sand sample inside the folded aluminum foil used to isolate the sample from the soil cannot

be completely excluded, which would induce a high source of variability in the results. To validate this assumption, the quality control could be improved in the protocol by injecting known amounts of metabolites in a new type of control samples, which would be directly installed within the rhizotrons using the same isolation with aluminum foil. The comparison between control samples that were either dried by oven at 80°C or dried by lyophilization also suggests that lyophilization, which was used for the treatment of all rhizodeposit traps, may have led to a loss of metabolites of at least 25% of the initial content, possibly because of the volatilization of small molecules.

Although the C&N analysis of the samples obtained from the rhizodeposits traps did not lead to robust results, half of the samples have been preserved for a later analysis of specific metabolites (e.g. carbohydrates, carboxylates and amino acids), in conjugation with the corresponding analysis of labile metabolites from the root segments. The methodology for extracting and quantifying these compounds by gas chromatography coupled to mass spectrometry (GC-MS-MS) is currently being tested at UMR EcoSys. If proved successful on these types of samples, this new analysis could significantly improve our understanding of the spatial distribution of root exudation along roots and its link with the concentration of labile metabolites inside these roots.

Towards an automated analysis of root system architecture monitored in rhizotrons

The experimental setup used in this work allowed capturing very detailed pictures of the root system over time, which can be used to derive root architectural traits, investigate specific events (e.g. the emergence of nodal roots in link with the development of the aerial parts of the plant), and determine parameters used in *ArchiSimple* / *Root-BRIDGES* that cannot be easily estimated from single root scans, such as the elongation rate normalized by the diameter of the root tip or the delay of lateral root emergence. This unique dataset could also be further used to give a more statistically-accurate description of the root system architecture and its evolution over time, provided that root segmentation (i.e., the recognition of roots from the soil background) and root annotation can be automated. This strategy was initiated by supervising a student for a few months for the annotation of two complete rhizotron time series from Experiment 2. Although the resulting workflow produced reliable segment detection and precise diameter measurements, it was ultimately constrained by the time required to fully annotate a single rhizotron, which prevented its application to the entire dataset generated in this thesis. In parallel, I initiated a collaboration with the team of Fernandez et al. [2022] to develop automated annotation procedures for rhizotron image time series that can handle the interruptions in root-axis visibility inherent to root growth in soil.

5.5 Conclusions

This chapter provided a first experimental exploration of wheat root growth, anatomy and rhizodeposition along roots in soil-filled rhizotrons, with the explicit aim of confronting and informing the *Root-CyNAPS* and *Wheat-BRIDGES* models developed in the previous chapters.

From the anatomical viewpoint, observations and *GRANAR*-based reconstructions of seminal root cross sections indicated that, up to at least 40 cm from the tip, wheat seminal roots exhibit a remarkably stable radial organization. When normalized by root radius, the total external cell surface per unit root length was approximately constant along the root, with cortical tissues contributing the majority of the exchange surface, and only the most basal sections showing a marked reduction consistent with cortex loss. This supports the modeling choice made in *RhizoDep*, *Root-CyNAPS* and *Wheat-BRIDGES* to treat exchange surface as proportional to local root radius for most of the root length, and suggests that longitudinal variations in root – soil exchanges are more likely to stem from changes in apoplastic barriers (endodermis, exodermis), metabolite gradients or growth status than from large changes in geometrical exchange surface. At the same time, the possible presence of cortical senescence and evolving apoplastic barriers near the root base, which could not be quantified precisely here, highlights specific anatomical processes that should be measured more explicitly in future experiments and be represented more explicitly in the models.

From the rhizodeposition viewpoint, the sand-patch trap method tested in Exp. 2 proved technically feasible but close to the detection limits of elemental C&N analysis under the sampled root length and patch exposure time. After careful calibration and control of background C in sand and tin capsules, only a subset of samples had C contents significantly above that of blank controls, and these were predominantly associated with root apices. This is consistent with the idea of apices as rhizodeposition hotspots, in line with model predictions, but the large variability and low signal-to-noise ratio prevented the reconstruction of robust rhizodeposition profiles along different root types and distances. Practically, the experiment revealed stringent constraints for future measurements: either higher sensitivity analytical methods (e.g. targeted/untargeted GC – MS applied to sand extracts), longer exposure times balanced against microbial degradation, or alternative trap designs will be required to obtain quantitative rhizodeposition gradients comparable in resolution and quality to model outputs. The preliminary ^{15}N patch-labeling test presented in the Supplementary Material also illustrates a promising route to quantify localized N uptake along roots, which could directly complement the modeling hypotheses on N uptake heterogeneity (H2 and H4).

Beyond these partial quantitative limits, the windowed rhizotron setup and time-lapse imaging protocol developed here produced a rich dataset on root system architectures developing under controlled conditions (root emergence timing, seminal and nodal root number, growth rates, depth distribution), together with shoot phenology and leaf-level photosynthesis. These data can be used to constrain and evaluate the architectural and phenological aspects of *RhizoDep*, *Root-BRIDGES* and *Wheat-BRIDGES* under conditions where belowground structure is visible, and to refine the representation of nodal root emergence rules and elongation rates that proved critical in Chapter 4.

5.6 Chapter contribution to Thesis Strategy

Within the overall thesis strategy, this chapter therefore contributes three key elements. **First**, it supports the modeling assumption that longitudinal variations in root – soil exchanges cannot be explained simply by a simple proportion of root system mass or length. Instead, a first analytical approaches on the produced samples (cross – section images, rhizodeposition traps and time – lapse of root system architectures) point to dynamic anatomical and physiological regulations acting within a changing root system architecture over time, which reinforces the mechanistic perspectives developed in Chapters 2 and 4. **Second**, it demonstrates that localized rhizodeposition measurement in soil-filled rhizotrons is technically possible but currently sits at the edge of analytical sensitivity, which explains the scarcity and uncertainty of available data and motivates the use of models as exploratory tools. **Third**, it identifies concrete experimental and analytical improvements (better quantification of apoplastic barriers and cortical senescence, more sensitive rhizodeposition quantification, localized ^{15}N pulse labeling and systematic use of time-lapse imaging) that will be discussed in the general discussion as priorities for future work aimed at fully testing and calibrating the multiscale rhizodeposition and N uptake patterns predicted by *Wheat-BRIDGES*.

Chapter 6

General Discussion

6.1 Reminder of thesis objectives and strategy

In the context of climate change, a better understanding of the potential of root C&N inputs to the soil for increasing the resilience of plant nutrition and mitigating greenhouse gas emissions is necessary. In this thesis, I focused on the role of rhizodeposition, acknowledging its quantitative yet variable impact on plant nutritional balance, with limited understanding of its C&N interactions with local root-soil status and shoot-root interactions. The variability of rhizodeposition reported between studies would relate to genotypic, growth conditions and methodological differences, but also to the heterogeneity of rhizodeposition rates and composition throughout the root system architecture, e.g. with hotspots of rhizodeposition reported at root tips. However, the magnitude of these rhizodeposition gradients along roots, their possible regulations by plant status, their response to the environment as part of root plasticity, and their significance in plant C&N balance are still poorly understood. This essentially relates to the methodological limitations of reliably measuring local rhizodeposition flows in realistic soil conditions, and non-destructively repeating the process at various locations and ages of the root system. Suggested determinants of local rhizodeposition magnitude would be the local metabolite concentrations in root tissues, the anatomical exchange surface between roots and soil, as well as the multiscale interactions between mineral N uptake, organic C&N cycling, and rhizodeposition. Measuring the variations of these flows along roots and over time is very challenging. Functional-structural root models have proven to be relevant mechanistic tools to estimate non-measurable variables within a realistic root system architecture [Dunbabin et al., 2013, Postma et al., 2017]. They would enable to simulate the variability of rhizodeposition and its determinants along roots while integrating the effects of this heterogeneity in root system C&N balance. Yet, no existing FSPM simultaneously represents carbon, nitrogen, growth, and anatomical processes at root segment-scale within a plant growing in heterogeneous soil conditions, while including a C&N shoot FSPM to model the interactions between these local C&N processes and shoot-root allocations. Some of these processes have been implemented separately in distinct models, exposing the need to couple these and complement them with new modules to leverage existing knowledge in the FSPM community.

To contribute to these knowledge gaps, the *CN-Wheat*, *RhizoDep* and *RootCyNAPS* models were targeted as complementary FSPMs to couple C&N cycles from root segment scale to whole plant scale to study the regulations of rhizodeposition and N uptake along roots, as well as their integration in plant C&N balance. In parallel, a windowed rhizotron experimental approach was developed to identify the determinants of spatial and temporal variability of rhizodeposition along roots and relate this heterogeneity with local root anatomy and local metabolite concentrations in roots.

6.1.1 Validity of initial hypotheses

The thesis I defend is that **a functional-structural model that integrates the quantitatively influential processes of C&N metabolism, growth, trans-**

port, and anatomical transformations in every vegetative tissue of the wheat architecture, while constraining them in the full C&N cycling of the plant, substantially improves our understanding of the multiscale determinants of rhizodeposition and mineral N uptake plasticity under heterogeneous soil and atmospheric conditions. By explicitly linking the local responses of *active* root exchange zones to environmental heterogeneity with their consequences for plant C&N balance, this mechanistic framework allows the scarce, punctual and uncertain measurements of rhizodeposition to be interpreted and upscaled by re-contextualizing them in reported sampling conditions. This approach is expected to help reaching a better understanding of existing rhizodeposition datasets on *Poaceae* species and ultimately identify conditions for improved soil C storage, local N cycling and plant nutritional balance mediated by rhizodeposition. Underlying this view, several hypotheses have been formulated and tested to illustrate the capabilities of this model, named *Wheat-BRIDGES*.

From a modeling standpoint, the acceptance and interpretation of the simulation results discussed below are conditional on the acceptance of the validity of *Wheat-BRIDGES* for the questions addressed here. Chapters 2 and 4 provide a partial evaluation of the model, by confronting simulated dynamics of water and N uptake, rhizodeposition and C&N allocation against patterns o. **Second**, the main qualitative and quantitative patterns emerging from the simulations are consistent with experimental observations that point in the same direction, which suggests that the behaviors described here are not purely artifacts of model structure, but arise from a realistic representation of the underlying processes. Together, these elements justify using *Wheat-BRIDGES* as a mechanistic framework to revisit the initial hypotheses, while keeping in mind that the conclusions remain conditional on these validation steps.

First, the assumption that *rhizodeposition is not simply proportional to root system biomass or the allocation of photosynthates from shoot* (**H1**) was supported by simulations of *Wheat-BRIDGES* showing significant variations of plant scale rhizodeposition compared to simple proportion approaches. Similarly, **hypothesis 5** assuming that *plant scale variations in total N uptake and rhizodeposition are synchronized over time, with photosynthetic activity at the core of their C&N interaction* appeared to be valid as *Wheat-BRIDGES* simulations showed that total rhizodeposition and mineral N uptake were positively correlated to photosynthetic activity over time. However, this correlation was mainly due to the increase in plant size over time. When normalizing these flows by root structural mass, no proportionality was observed anymore, which suggests that additional drivers of root-soil C&N exchanges should be explored

Second, I nuanced the theory of *active root zones* under which only a stable small fraction of the root system would contribute to the majority of root-soil exchanges (i.e., rhizodeposition and N uptake), assuming that such constant fractions are not relevant given the shifting properties of the root system architecture during its development and its plasticity to environmental conditions. *Root-CyNAPS* simulations on root system architectures supported this view, showing that a fixed proportion of most active regions of the root system did not systematically account for the majority mineral N uptake depending on plant age and external nitrate concentrations.

I further explored the consistency of these results with the *Wheat-BRIDGES* model and showed that the contribution of *active root zones* to total rhizodeposition, mineral N uptake or water uptake remained similarly variable when introducing root growth, C&N interactions, and variable soil temperatures. This invariant results despite varying temperature and light conditions suggest that external mineral N levels remain the key regulator of local exchange plasticity.

Third, simulations are consistent with the hypothesis that the main processes dominating root-soil exchanges in *active root zones* could shift along roots and over time, with the example of water-mediated mineral N uptake simulated by *Root-CyNAPS*, which could represent up to 50% of net mineral N uptake under high transpiration and high external nitrate levels in mature root systems. I also showed that within the dual HATS/LATS active N uptake system, only the high affinity transporters contributed significantly to total N uptake, questioning the relevance of separating these two processes. Theses patterns in the composition of mineral N uptake remained consistent between *Root-CyNAPS* and *Wheat-BRIDGES*, and the addition of the C cycle from *RhizoDep* in *Wheat-BRIDGES* led to the conclusion that C exudation was systematically dominant over other rhizodeposition processes, making the determinants of such diffusive processes a central focus of this work.

Indeed, the **fourth** hypothesis stating that local metabolite concentrations and root anatomy regulate both rhizodeposition and N uptake in a similar way was verified using *Wheat-BRIDGES*, which showed a co-location of these two flows at root tip and lateral emergence zones due to increased hexose concentrations in actively growing root zones, and maximal exchange surfaces with low differentiation in newly formed tissues. However, the uniformity of root exchange surfaces, volumes, and stele dimensions measured on seminal roots of wheat grown in rhizotron suggested that the absence of endodermal differentiation in newly formed root segments is the main anatomical driver of increased root-soil exchanges near root tips. An important point emerging from Chapter 2 is that the interpretation of simulated C and N fluxes cannot be fully dissociated from the intermediate structural outputs generated by the architectural and anatomical modules. In practice, the location, intensity and persistence of net N uptake or rhizodeposition hotspots depend on the simulated distribution of root segment ages, branching patterns, diameters, exchange surfaces and barrier differentiation states. A more explicit exploration of these architectural and anatomical traits variations among wheat varieties and a comparison with the sensitivity of the model to related parameter variations therefore appears necessary to strengthen the discussion of the mechanisms underlying flux heterogeneity and provid a more direct basis for comparison with *in planta* phenotypic diversity.

Testing these hypotheses led to a better understanding of the impact of multiscale C&N interactions affecting the local distribution of rhizodeposition and mineral N uptake, which are summarized in the full conceptual scheme of the thesis in Figure 6.1 and further discussed in the following section.

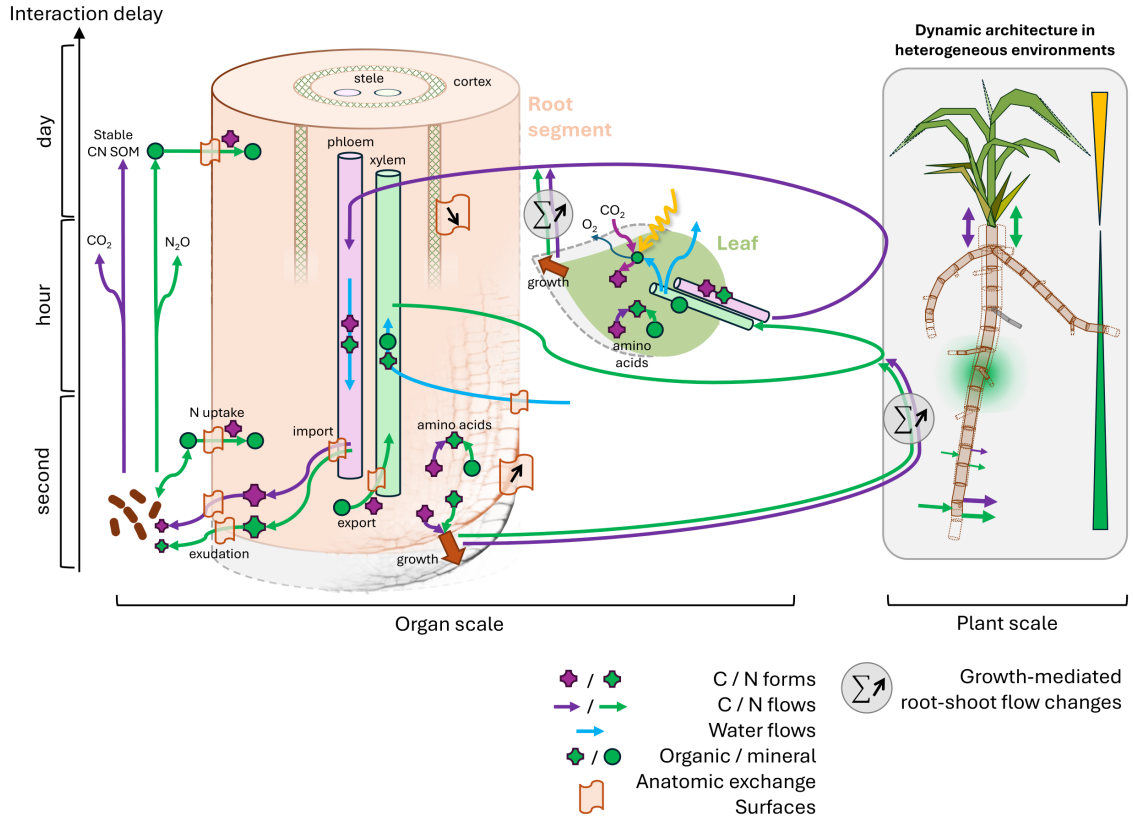

Figure 6.1: Final conceptual scheme summarizing key coupling points between C&N cycles considered in the multiscale regulations of rhizodeposition and N uptake. At short term and root segment scale, rhizodeposition is regulated by local anatomical exchange surfaces and the local concentration of hexose in root symplasm. N uptake is similarly regulated by the local C and N availability and exchange surfaces. Conversely, co-regulations by and co-consumption of available metabolites during amino acid synthesis and growth shape the C-N balance of the root segment, affecting root-soil exchanges. N acquisition, rhizodeposition and C-N transport in xylem and phloem are also influenced by the heterogeneity of water uptake and transport along roots. As introduced in the model *Wheat-BRIDGES*, these transport processes along each organ of the plant connect source and sink organs for C or N, in particular connecting roots C&N activity with photosynthesis and other shoot processes. Plant architecture integrates these local interactions and shoot-root allocations over time. This integration is also oriented by soil and aboveground environment heterogeneities as part of plant plasticity. In turn, plant rhizodeposition and N uptake interact with local soil C&N balance.

6.2 Main scientific findings

6.2.1 Carbon rhizodeposition is more than a simple fraction of the carbon fixed by the plant and allocated to the roots

In the objective of quantifying the impact of rhizodeposition in plant C balance, I used the new *Wheat-BRIDGES* whole plant FSPM. In Chapter 4 I showed no consistent relationship over time between rhizodeposition and root system biomass, photosynthetic activity, photosynthate allocation from shoot or mineral N uptake, despite observing a clear dependency between time points due to cumulative ontogenic effects. This supported **my first hypothesis**, under which no simple correlation of rhizodeposition to a total plant pool or flow was expected. Similarly, rhizodeposition levels could not be simply correlated to the variations of environmental variables such as soil temperature or nitrate concentration even though the root component include several regulations to each of these variables (see chapter 2). This plant scale complexity contrasted with existing models describing rhizodeposition as a fixed proportion of a total plant pool or flow, and emerged from the explicit simulation of multiscale C&N regulations applying to each organ of the growing plant architecture. This intrinsic variability of rhizodeposition at individual scale would contribute to the variable ranges reported in the literature related to heterogeneous genotypes, environmental conditions, or measurement uncertainties between each experiment [Nguyen, 2009, Pausch and Kuzyakov, 2018], overall confusing the identification of rhizodeposition key determinants. Whole plant FSPMs as *Wheat-BRIDGES* are therefore relevant tools to focus on a single scenario and estimate the role of rhizodeposition heterogeneity along roots in the functional plasticity of simulated total root system exchanges.

6.2.2 Active root zones: an oversimplified concept

Subsequently, I aimed at studying the spatial and temporal heterogeneity of local C&N rhizodeposition rates composing this plant scale variability, jointly with local mineral N uptake which is thought to interact with rhizodeposition through local C&N metabolism and the regulation of shoot photosynthesis. In particular, several authors suggest that root-soil exchanges heterogeneity can be summarized by a small proportion of the root system that would be more active and gather the majority of total root system uptake [Hodge et al., 2009, Bechmann et al., 2014, Le Deunff et al., 2019, Canarini et al., 2019]. However, the location and contribution to total flows of such *active root zones* are rarely quantified due to experimental limitations. Here, I proposed to evaluate this notion with *Root-CyNAPS* and *Wheat-BRIDGES* simulations. The two model's outputs were consistent despite the limitations of *Root-CyNAPS* to static root system architecture and static boundary conditions at the shoot-root junction. Both evidenced two *active root zones*: one near the root tip and the other at the emergence of lateral roots. I confirmed **my second hypothesis** with the example of mineral N uptake, showing that the contribution of these two zones to total N uptake could significantly vary with plant age and external nitrate

concentrations. Therefore, constant fractions of the root system are not relevant indicators of its total activity (see Chapter 2). The *Wheat-BRIDGES* simulation also mitigated this statement, showing that under high nitrate concentration, this plasticity could be much more restricted for C&N rhizodeposition, mineral N uptake, and water uptake, despite important environmental variations during the whole vegetative stage (see Chapter 4).

In these *active root zones*, the relative contribution of the distinct processes composing total N uptake also shifted with plant age and environmental conditions, water-driven N uptake reaching about 50% of total flow for older root systems and high external nitrate concentrations. This supported **my third hypothesis** while being in line with the "bypass uptake flows" that have been reported in the literature for other solutes [Faiyue et al., 2010, Lu and Fricke, 2023], calling for the design of further experiments to challenge the importance of this apoplastic uptake pathway for nitrate. In contrast, mucilage production, cell sloughing, and amino-acids exudation remained consistently low compared to hexose exudation. Even though further calibration of those processes is still needed- using for example the analysis of rhizodeposit traps (See chapter 5) - this suggests that the main drivers of exudation, i.e. processes sustaining high symplastic concentrations locally and high exchange surfaces with the soil, would also be key determinants of total C rhizodeposition. More precisely, the local growth processes would be a crossroad for these regulations, and would determine the location of the active root zones identified by model simulations. Indeed, local root growth would increase the local metabolite concentrations with the sink strength exerted by local growth C&N costs on the locally accessible root phloem resources and ultimately on shoot phloem. Local growth processes of elongation, thickening, branching, and root hair formation are also key events that extend the exchange surface locally before apoplastic barriers differentiation start decreasing it. In the root growth component of *RhizoDep* and *Wheat-BRIDGES*, these growth processes occur only near root tip and at lateral emergence points in the case of wheat, which matches increased root-soil exchanges in those locations. Beyond direct regulations of exudation and N uptake processes, the plasticity of the C&N regulations of growth and differentiation processes should also be investigated to understand the variable contribution of *active root zones* in plant C&N balance. The coordination rule between leaves and nodal roots emergence introduced in *Wheat-BRIDGES* also illustrates the role of plant discrete developmental events which significantly reorient growth cost and affect the timing of emergence of most active root zones. Overall, *Wheat-BRIDGES* opens prospects for such exploration on wheat, as these local growth regulations accumulate over time in the resulting plant architecture, and the complete looping of C&N allocation in the model enables to perform more reliable long-term simulations compared to existing root FSPMs relying on complex and hardly measured model inputs.

Here we showed that no constant threshold could be chosen to consistently delineate *active* and *less active* root zones. This absence of binary criteria therefore questions the relevance of the two presented *active root zones* which were essentially reported from visual criteria on simple model outputs. In practice, these two zones grouped a wide range of variations between individual roots and considered location, and this heterogeneity differed between processes, questioning if these zones

were actually common to the different root-soil exchanges and actually lead to a co-location of C, N and water flows along roots.

6.2.3 Studying the co-location of rhizodeposition and resource uptake hotspots

A functional co-location of rhizodeposition and mineral N uptake related to soil mineralization activity can be hypothesized from recent the literature [Bilyera et al., 2021, Liu et al., 2022, Pausch et al., 2024]. However, given the experimental complexity of measuring only one of these flows locally and in soil conditions, these processes are often studied separately. In *Wheat-BRIDGES*, this co-location in root tip and lateral emergence zones emerged from the shared regulation of simulated processes by local C&N metabolite concentrations and available exchange surfaces. This generally corresponded to the expected pattern formulated in **my fourth hypothesis**. However, this hypothesis was also challenged by the observation that zones of maximal rhizodeposition rates and maximal N uptake rates did not always match. The simulations of *Wheat-BRIDGES* showed different locations for peak activity between individual roots. For a single root axis, preferential exchange location between root tip and lateral emergence zones did not always match between rhizodeposition and N uptake. These results connect with the absence of simple rhizodeposition or N uptake determinants reported at plant scale. This shows that each root axis has its own polarization in *active root zones*, depending on its current growth stage, resource allocation, and environmental conditions. This confuses approaches at root system scale where the superimposition of this heterogeneity hides co-location patterns, suggesting to focus on single root axes to evidence the conditions for rhizodeposition and N uptake co-location to emerge. However, single roots always need to be repositioned in root system architecture, as shown by the example of a lateral root emerging from a nodal root on which no apparent co-location between rhizodeposition and N uptake was reported. Even if N uptake was low on the nodal root at the insertion of the lateral, the high N uptake activity of the lateral itself actually co-located in a few millimeters range with the high rhizodeposition rates of the nodal at the branching point (See Chapter 4). This evidences the limits of studying co-location only at root segment scale, which depends on the discretization of the root system. More generally, studying a population of heterogeneous roots and identifying representative roots for investigating how specific flows such as nutrient uptake evolve over time and space has been pointed as a major challenge in root ecology [Wells and Eissenstat, 2002]. *Wheat-BRIDGES* simulations suggest that co-location could also be studied from soil's perspective, with a soil grid and transport processes that determine if rhizodeposition and N uptake activities of a set of neighboring root segments will eventually impact the same soil volume at the same time. For example, an exploration scenario tested with *Root-BRIDGES* for a communication showed that within a soil nitrate patch, both immediate regulation of fluxes and long term effects with lateral proliferation in the patch zone led to a co-location of N-uptake and rhizodeposition within that soil volume (See Supplementary Note 6.14).

To complement this modeling exploration on the co-location of rhizodeposition

and N uptake along roots, additional experiments could be conducted to measure these two local flows simultaneously. I conducted tests where sand patches spiked with 10 mM $^{15}NO3^{-}$ were applied at various locations along wheat seminal roots grown in soil-filled rhizotrons, in order to quantify the heterogeneity of mineral N uptake in the same experimental setup used to apply rhizodeposit traps (See Supplementary Note 6.14).

6.2.4 Importance of the spatial heterogeneity of root-soil exchange and consequences on the functioning of the plant

A central question of this thesis was whether the strong spatial heterogeneity of root–soil exchanges has a significant impact on whole-plant C and N balance, and how it contributes to plant plasticity under variable environments. **Hypothesis 5** assumed that plant-scale variations in mineral N uptake and rhizodeposition would be synchronized over time with photosynthetic activity, as a direct consequence of their tight C – N coupling at local scale and during shoot – root allocations. Simulations with *Root-CyNAPS* and *Wheat-BRIDGES* showed that a small fraction of root length (about 10%) accounts for a disproportionate share of exchanges (around half of total mineral N uptake and up to 90% of C rhizodeposition), with hotspots systematically located near root tips and lateral emergence zones and shifting with root type and age. Rhizodeposition and C allocation from shoot remained correlated over the vegetative phase but no robust relationship emerged between massic C rhizodeposition or massic N uptake and photosynthetic activity once normalized by root structural mass or exchange surface, which further emphasizes on the polarization of root soil exchanges in a restrained but variable proposition of the root system mass.

Hypothesis 5 is therefore only partially supported: total fluxes co-vary loosely with plant growth and photosynthesis through the extension of shoot and root exchange surfaces, but not via a direct synchronization by shoot photosynthesis. This suggest that plasticity simulated in the tested scenario arise less from global shifts in C&N allocation with the shoot than from changes in the location, duration, and intensity of active root zones. This points towards traits and processes affecting nodal and lateral emergence, or regulation of apoplastic barriers as promising targets for future exploration with *Wheat-BRIDGES*. Moreover, as previously discussed in Chapter 4, the range of temperature and nitrate concentrations variations in the tested scenario was limited. To further explore with *Wheat-BRIDGES* the plastic patterns of shoot-root allocation that modulate rhizodeposition, additional contrasted scenarios should be tested.

6.3 Methodological achievements and remaining challenges

6.3.1 *MetaFSPM*, a new coupling framework for complex FSPMs

Beyond the specific case study developed in this thesis, the *MetaFSPM* toolkit represents a methodological contribution on its own. It was designed to address a recurrent difficulty in multiscale plant modeling: how to couple existing FSPMs, soil, and atmosphere models with strong code heterogeneity, in a modular framework, rather than into a monolithic code base. By enforcing a common *component* structure, explicit scheduling rules, and a clear separation between ecophysiological equations and simulation utilities, *MetaFSPM* provides a generic framework to assemble composite FSPMs while preserving the internal logic of each sub-model (Chapter 3). Doing so, it translates conceptual plant – soil – atmosphere hypotheses into explicit coupling contracts and data flows, making them easier to inspect, revise and compare. The development of the *Wheat-BRIDGES* model in Chapter 4 has served as a demanding test case for this approach, and illustrates how components representing plant, soil, and light processes can be orchestrated within a single framework. Methodologically, *MetaFSPM* also contributes to improving transparency and reproducibility of complex FSPMs. By construction, every component declares the variables it reads and writes, the parameters it uses, and the order in which its computations are executed. This explicit declaration facilitates automatic checking of unit consistency, input completeness and schedule coherence. It provides a structured documentation of model architecture. Each models can be tested separately before being assembled. In addition, the unified output management system developed on top of *MetaFSPM* for *Wheat-BRIDGES* will greatly ease further explorations such as sensitivity analysis, pattern-oriented evaluation, metamodel construction, and dedicated analyses of spatio-temporal patterns.

Despite these advantages, several challenges remain before such a coupling framework can be broadly reusable across FSPM platforms. First, generality and modularity still come with a cost: when the number of components and exchanged variables increases, the time necessary to manage schedules, data routing, and diagnostics is still non-negligible, even though it already constitutes a major improvement compared to purely ad hoc or visual coupling approaches. Scaling *MetaFSPM* to larger model ensembles or finer spatial resolutions will therefore require additional work on performance and on profiling tools that help modelers identify bottlenecks. Second, while *MetaFSPM* enforces structural conventions, it does not yet impose a shared semantic vocabulary. Harmonizing variable names, units, and metadata across components, or connecting *MetaFSPM* to emerging ontologies for plant and soil processes, would greatly facilitate model reuse and interoperability between teams [Saint Cast et al., 2022]. In the longer term, I envision *MetaFSPM* evolving from a project-specific toolkit into a shared platform where plant modelers can deposit, document and reuse components developed for different species, organs, or environmental processes. In that sense, the work carried out in this thesis should be seen as a first demonstration that a component-based coupling framework can

support the construction of a highly detailed whole-plant FSPM, while still leaving room for future extensions towards additional soil processes, atmosphere modules, and multi-species interactions discussed in the next subsection.

6.3.2 *Root-CyNAPS*, a new root FSPM to study the heterogeneity of mineral N uptake along roots

To contribute to the overall objective of this thesis and couple shoot and root C&N physiology, we designed a new model of N and water uptake combining (i) local anatomical features of a root segment, (ii) N balance over a set of N transport and metabolic processes regulated by local concentrations and anatomy, and (iii) the co-transportation of metabolites by radial water uptake and axial water transport between root segments through the coupled sap flows of xylem and phloem. *Root-CyNAPS* has been designed to simulate a wide range of species, including cereals the illustrated wheat use case, *Fabaceae* species able to fix atmospheric nitrogen, or species with tuberized pivot root as in the *Brassica* genus. In this study, *Root-CyNAPS* was used to simulate the heterogeneity of N uptake and exudation rates throughout a 3D root system architecture of wheat in hydropony, to locate *most active root zones* for the different components of net N uptake, and to study their contribution to root system N balance. Our simulations showed that *most active root zones* contribution to roots N balance is so variable that this concept appears of little practical use. We also confirmed that water-mediated N uptake and N exudation can substantially influence net N uptake. Root-CyNAPS was then coupled to the *RhizoDep* and *CN-Wheat* FSPMs to yield the *Wheat-BRIDGES* model.

6.3.3 *Wheat-BRIDGES*, a new whole-plant FSPM to explore the heterogeneity and plasticity of root-soil exchanges

The construction of *Wheat-BRIDGES* was motivated by gaps in existing FSPMs which prevented the representation of multiscale regulations of rhizodeposition and mineral N uptake from organ C&N processes to plant C&N trophic allocations, the central question of this thesis. *RhizoDep* and *CN-Wheat* provided complementary views of the mechanistic description of processes driving metabolite concentrations at tissue scale. However, the lack of N components in rhizodeposition, N regulations on the C cycle, and uncertain shoot-root allocations in *RhizoDep*, as well as the simplification of roots as a single homogeneous compartment in *CN-Wheat*, prevented the coupling of root segment C&N exchanges to shoot functioning. *Root-CyNAPS* and *Root-BRIDGES* were designed to contribute to this gap, coupling C&N transport, metabolism and growth locally in an explicit root anatomy, and enabling a coupling of shoot and root functioning and architectures by representing C&N allocations at the shoot-root junction in xylem and phloem. *Wheat-BRIDGES* was therefore designed as an integrated FSPM that combines the mechanistic descriptions of *Root-BRIDGES* and *CN-Wheat*, so that rhizodeposition and N uptake emerge consistently from local processes while remaining constrained by realistic a

plant-budgets and a realistic response to varying environmental conditions along the whole-plant architecture.

In its current form, *Wheat-BRIDGES* has met its initial objective by enabling a decomposition of rhizodeposition and N uptake among root types, ages and positions, and by relating these contributions to plant C&N status and environmental drivers. Nonetheless, various aspects of the model can still be improved. This first aspect is the limited range of plasticity scenarios that can be explored with the current homogeneous soil model. This soil model was first used to compare *Wheat-BRIDGES* to *CN-Wheat* reference simulation. Later on, a new 3D C-N-water soil model coupling the *MIMICS-CN* and *CMF* was developed to study the plastic response of rhizodeposition and N uptake in *Wheat-BRIDGES* to a dynamic soil heterogeneity, but not used for the simulations. This root-soil coupling would allow on short-term to assess how local rhizodeposition impacts the cycling of soil organic matter, and which conditions can lead to a net increase in soil carbon storage or an increase in soil organic N mineralization that could sustain root N uptake. Nonetheless, even though Wheat-BRIDGES was designed to study the plastic response of the plant to a changing environment, most of its components have been evaluated under non-stressed conditions. One should be aware that using current version of the model to study N-, water-, or heat-stress conditions would call for a revision of its calibration and assumptions. Still, the model still offers a great adaptability to various environmental scenarios, from controlled conditions to field conditions to contribute to the connection of experimental scales. Moreover, the *Wheat-BRIDGES* and *MetaFSPM* modeling framework have been designed to be extensible and easily modified to answer to those limitations, provided sufficient calibration data is available for the targeted simulation scenarios. This opens to a series of perspective to further extend the multiscale representation of plant and environment processes affecting the regulation root-soil exchanges, which are presented in the last section of this discussion.

6.3.4 Exploring the spatial and temporal variations of root-soil exchanges with innovative experimental approaches

To contribute to produced FSPMs validation, I also approached the variability of rhizodeposition along roots experimentally with soil-filled windowed rhizotrons which were used to access non-destructively specific locations along growing wheat roots for rhizodeposition sampling, while referencing sampled zones position in the root system architecture with high resolution imaging. I evidenced that **enclosing local root segments repeatedly for sampling did not compromise the survival and growth of the root axis**, demonstrating the relevance and feasibility of this technique to study *local* root-soil variability over time. This approach builds on a growing body of work that has used solid supports to capture exudates in situ while preserving soil structure. In forests, Akatsuki and Makita [2020] developed a clamping method using glass fiber to quantify mass-based exudation rates directly in the field. In controlled RhizoTube systems, Tixier et al. [2023] used paper traps applied against pea roots to quantify total soluble sugars and amino acids exuded along the day – night cycle. More recently, the EcoRoot method proposed by Bohm

et al. [2025] evaluated different sorption discs placed on roots in rhizotrons for untargeted GC – HRMS metabolomics. These studies illustrate both the potential and the limitations of trap-based strategies: they offer local, non-destructive sampling, but are constrained by detection limits, the restricted set of chemical families targeted and strong material-specific biases in compound recovery. This aligns with our results showing that the small amounts of rhizodeposits that are collected on such small spatial and temporal frames cannot be reliably quantified with total C&N elementary analyses. This advocated for more precise quantification protocols for *local* rhizodeposition trap approaches, such as GC-MS-MS [Fiehn, 2016], while raising challenges to quantify total rhizodeposition and unknown compounds with such approaches which are usually quantitatively reliable only for targeted molecules with precise standards. Alongside these quantification limitations which also prevents us to also quantify the bias of our approach, several improvements have been targeted. First, we compared rhizodeposit traps to spiked sand controls prepared independently from the experimentation, and blank sand controls that were placed in the rhizotron without being in contact with roots. Including additional controls, spiked with known quantities of compound and placed in the rhizotron without roots would enable to study if the aluminum foil used to enclose the root was tight enough to ensure they were no leak of rhizodeposits into the soil or contamination from the soil solution. Then, even if this method builds on previous rhizodeposit trap approaches as it allows repeated measurements at the same root location to assess the evolution of rhizodeposition gradients, measurements were systematically performed during the day, which might restrict our understanding of daily variations of rhizodeposition along roots, calling for further experiments performed at night, which is technically achievable using phytotronic chambers. Finally, this experiment was restricted to 12 large rhizotron replicates due to the long manual handling time to position and retrieve sand traps, statistically restricting the exploration to one tested modality per experiment. This illustrates a drawback of multiplying sampling points, and future improvements can be made either by lowering the number of patch per rhizotron to focus on a single root region, or using longer-term successive experimental plans, where each individual experiment can be compared provided the same genotype, soil and controlled conditions in phytotron are used.

I additionally performed sets of measurements in the same experimental setup to link local rhizodeposition measurements to its determinants. **First**, I measured anatomical exchange surfaces and volumes along wheat roots, one of the key anticipated determinants of root-soil exchanges heterogeneity. I showed remarkable homogeneity of these anatomical features per root length and root diameter along seminal wheat roots, suggesting that root diameter distribution, with differences among root types, as well as the dynamics of endodermis and exodermis differentiation, would be the key anatomical drivers of N uptake and rhizodeposition heterogeneity in the root system. Our adaptation of the GRANAR model to the context of wheat nonetheless estimates precisely key anatomical parameters for the designed FSPMs, that could only be roughly estimated from literature data beforehand. **Second**, I also performed $^{15}NO_3^-$ pulse labeling tests to develop a method quantifying the gradients of nitrate uptake along roots and compare it with rhizodeposition measurements (see Supplementary Note 6.14). **Third**, I produced a high resolu-

tion dataset of recto/verso root system architecture time-series that will be used to reposition measured local root-soil flows at sampling time. I also demonstrated the potential usage of this dataset for complex trait measurement, the delineation of roots being precise to digitalize visible parts of the root system to RSML and MTG formats, making the automated trait measurement and their variations along roots straightforward. Such digitization also opens opportunities to apply developed FSPMs directly on experimental architectures as digital twins, either enforcing root system growth or using model inversion techniques to assess plausible local activities that would lead to such architecture.

In the objective of quantifying rhizodeposition at plant scale, I also contributed to side experiments in my research team aiming at measuring plant scale net rhizodeposition through $^{13}CO_2$ pulse labeling on oilseed rape, another technique providing insights on net rhizodeposition footprint in photosynthesis C fixation at the end of the cropping cycle. Such labeling experiment would however be difficult to apply on rhizotrons whose windows' edges are not completely air-tight, introducing contamination that would superimpose with C fixed by photosynthesis. This emphasize the necessary complementarity between experimental scales to access to different scales of quantification, and position mechanistic FSPMs as good interpolation tools between experimental knowledge, since direct translation of regulation patterns between scales is not always valid and should be approached with a mechanistic up-scaling [Huber, 2011, Schnepf et al., 2022].

6.3.5 Towards a better understanding of plant-soil interactions

On the longer term, I anticipate an extension of the *Wheat-BRIDGES* simulation framework to further connect soil-plant-atmosphere description scales, and serve as a hub for different ecophysiological research directions.

- *Wheat-BRIDGES* simulations restricts to a stand of a few plants with infinite boundaries. To apply *Wheat-BRIDGES* simulations at field scale, and include variations of soil properties in field or edge effects, metamodeling strategies would enable to simplify model's to key parameters and abstract processes' explicit description while keeping emergent patterns in model's outputs, with a better runtime to enable this up-scaling. From Gaussian process statistical approaches to machine learning approaches or simplifications of plant architecture [Pagès et al., 2020, Blanc et al., 2023, Gawinowski et al., 2024], a wide variety of metamodeling choices are available. The selection of a strategy will ultimately be based on the identification of key parameters from the sensitivity analysis and key patterns identified by an in-depth analysis of *Wheat-BRIDGES* output data that should be preserved in the metamodel.

- To perform simulations in realistic field complexity, scenarios of intra-specific mixtures, intercropping, and competition with adventitious species would be a critical step to study the ecophysiological determinants of *local* competition and cooperation. Such simulations would be relevant exploration tools to guide

sustainable and extensive diversification and management practices. *Root-BRIDGES* was designed to be specie-agnostic. A possible use case to value the coupling experience acquired during this thesis would be to couple *Root-BRIDGES* with the *SIMBAL* oilseed rape and faba bean intercropping FSPM Perthame et al. [2023].

- Regarding environment models, the structural-functional hypothesis has also been applied to soil models in the last decade. Switching to an explicit representation of soil dynamic structure would enhance the realism of solute concentrations, water potential or gas composition profiles along roots, C&N microbial dynamics, and physical resistance to root growth [Daly et al., 2016, Rötzer et al., 2025]. For the interaction with the air compartment, introducing processes of Volatile Organic Compounds into the model would enable to connect with research axes on plant stress signaling and air quality [Guenther et al., 2012]. The modularity of the MetaFSPM framework also enables to easily change the light model used in Wheat-BRIDGES. For example I tested the replacement of the *Caribu* model with the *Virtual Plant Laboratory Raytracer* [Morales et al., 2025] to enable the simulation of growth chamber environments and multiple wavelengths. This work was not presented in current results because still preliminary, but it opens promising prospects to perform *Wheat-BRIDGES* simulations in conditions matching the exact environmental conditions in the growth chamber where rhizotrons were installed.

- In *Wheat-BRIDGES*, some metabolite families were introduced to represent average C&N flows and interactions. However, taking the example of amino acids, dominant amino acid species are thought to differ between organs, with specific kinetics and regulations for each specie. In such context, the parametrization of *Wheat-BRIDGES* to represent averaged amino acids dynamics was challenging because most physiological studies focus on specific amino acids which often expose distinct dynamics. Similarly, *RhizoDep* focused on a representation of C metabolites as hexoses, but other forms such as organic acids could be considered. In line with our modeling approach where accounting for spatialized processes in an explicit root system architecture enabled to identify emergent patterns and reduce uncertainty compared to root system aggregations, I advocate that an explicit representation of symplastic metabolic networks with dedicated pools for each chemical species would provide more accurate local regulations for rhizodeposition and N uptake. Existing models have been identified, such as models of Shaw and Cheung [2018] on whole *A. thaliana* plants or Hunt et al. [2023] in a maize root anatomical FSPM, which are grounded in metabolomic data for parametrization and propose a more straightforward link to quantitative trait loci and genotypic variations [Rao and Liu, 2025]. Given the optimizations that have been performed to efficiently parallelize the computation of transport and metabolism flows in each root segment, such simulations are numerically plausible in a context where GPU massive parallelization becomes more and more common.

6.4 Conclusion

The conceptual scheme in Figure 6.1 summarizes how the work carried out in this thesis connects local C&N processes in roots to whole-plant functioning and soil dynamics. Starting from the initial objective of understanding how spatially heterogeneous rhizodeposition and mineral N uptake emerge along a growing wheat root system and feed back on plant C&N balance, I combined new FSPMs (*Root-CyNAPS*, *Root-BRIDGES*, *Wheat-BRIDGES*) with rhizotron experiments to explore five main hypotheses. Together, the simulations and measurements show that (i) rhizodeposition cannot be represented as a fixed fraction of root biomass or photosynthate allocation, (ii) the notion of '*active root zones*' can be misleading, as the relative contribution of tips and lateral-emergence regions depends strongly on plant age and external nitrate, (iii) water-driven N uptake can become as high as active transport systems depending on shoot transpiration and soil water availability, (iv) rhizodeposition and N uptake share common local regulators and often co-locate, but their peaks do not consistently coincide along a given root, and (v) plant-scale flows are only loosely synchronized with photosynthesis, so that plasticity arises mainly from shifts in the location, duration and intensity of root zones of high activity rather than from plant-scale changes in C&N allocation.

Methodologically, the thesis delivers a coupled modeling-experimental framework that can now be reused and extended. The *MetaFSPM* toolkit formalizes a component-based strategy to assemble complex FSPMs, and its application to build *Wheat-BRIDGES* demonstrates that detailed organ-scale C&N processes, realistic root architectures and soil biogeochemistry can be integrated into a coherent whole-plant model with traceable data flows and a unified output structure. The *RhizoSoil* model complements this by providing a reduced soil description driven by *Wheat-BRIDGES* outputs, opening a first route for up-scaling to larger spatial and temporal scales. On the experimental side, the rhizotron-based trap methodology, anatomical measurements and $^{15}NO_3^-$ pulse-labeling tests provide proof-of-concept tools to quantify local root – soil exchanges and their determinants, and to generate the type of spatially resolved data required to constrain such models.

These results directly point to several perspectives. Short-term extensions include exploring a wider range of environmental scenarios (e.g. contrasted nitrate, light, temperature and water regimes) and genotypes within the current *Wheat-BRIDGES* framework, and exploiting *RhizoSoil* and metamodels derived from *Wheat-BRIDGES* outputs to project rhizodeposition and N uptake patterns to field scale. In parallel, refining the representation of metabolites, anatomy and coupling to more detailed soil-structure and microbial models would make it possible to address questions at the interface with root microbiome assembly and soil C cycling. Finally, the species-agnostic design of *Root-BRIDGES* and the modularity of *MetaFSPM* open perspectives towards multi-species simulations where contrasting architectures and root-soil exchange patterns interact in shared soil volumes. Overall, the framework developed in this thesis lays the foundation for a multiscale, mechanistic exploration of plant – soil interactions, where local exchange processes, whole-plant C&N balance, and soil functioning can be analyzed jointly rather than in isolation.

References

D. Abalos, S. Recous, K. Butterbach-Bahl, C. De Notaris, T. F. Rittl, C. F. Topp, S. O. Petersen, S. Hansen, M. A. Bleken, R. M. Rees, and J. E. Olesen. A review and meta-analysis of mitigation measures for nitrous oxide emissions from crop residues. *Science of The Total Environment*, 828:154388, July 2022. ISSN 00489697. doi: 10.1016/j.scitotenv.2022.154388. URL https://linkinghub.elsevier.com/retrieve/pii/S0048969722014814.

C. Ai, M. Zhang, Y. Sun, L. Zhang, L. Zeng, Y. Liu, X. Wang, Y. Chai, P. He, G. Liang, and W. Zhou. Wheat rhizodeposition stimulates soil nitrous oxide emission and denitrifiers harboring the *nosZ* clade I gene. *Soil Biology and Biochemistry*, 143:107738, Apr. 2020. ISSN 0038-0717. doi: 10.1016/j.soilbio.2020.107738. URL https://www.sciencedirect.com/science/article/pii/S0038071720300353.

M. Akatsuki and N. Makita. Influence of fine root traits on in situ exudation rates in four conifers from different mycorrhizal associations. *Tree Physiology*, 40(8):1071–1079, July 2020. ISSN 1758-4469. doi: 10.1093/treephys/tpaa051. URL https://doi.org/10.1093/treephys/tpaa051.

R. Albasha, C. Fournier, C. Pradal, M. Chelle, J. A. Prieto, G. Louarn, T. Simonneau, and E. Lebon. HydroShoot: a functional-structural plant model for simulating hydraulic structure, gas and energy exchange dynamics of complex plant canopies under water deficit—application to grapevine (Vitis vinifera). *in silico Plants*, 1(1):diz007, Jan. 2019. ISSN 2517-5025. doi: 10.1093/insilicoplants/diz007. URL https://doi.org/10.1093/insilicoplants/diz007.

M. Ali, M. W. Jones, X. Xie, and M. Williams. TimeCluster: dimension reduction applied to temporal data for visual analytics. *The Visual Computer*, 35(6):1013–1026, June 2019. ISSN 1432-2315. doi: 10.1007/s00371-019-01673-y. URL https://doi.org/10.1007/s00371-019-01673-y.

M. A. Altieri. The ecological role of biodiversity in agroecosystems. In M. G. Paoletti, editor, *Invertebrate Biodiversity as Bioindicators of Sustainable Landscapes*, pages 19–31. Elsevier, Amsterdam, Jan. 1999. ISBN 978-0-444-50019-9. doi: 10.1016/B978-0-444-50019-9.50005-4. URL https://www.sciencedirect.com/science/article/pii/B9780444500199500054.

M. A. Altieri. *Agroecology: The Science Of Sustainable Agriculture, Second Edition*. CRC Press, Feb. 2018. ISBN 978-0-429-96401-5. Google-Books-ID: vwTFDwAAQBAJ.

J. N. Amoah, C. Keitel, and B. N. Kaiser. Nitrogen deficiency identifies carbon metabolism pathways and root adaptation in maize. *Physiology and Molecular Biology of Plants*, 31(7):1089–1103, July 2025. ISSN 0974-0430. doi: 10.1007/s12298-025-01631-0. URL https://doi.org/10.1007/s12298-025-01631-0.

M. Andrews and J. A. Raven. Root or shoot nitrate assimilation in terrestrial vascular plants – does it matter? *Plant and Soil*, 476(1):31–62, July 2022. ISSN 1573-5036. doi: 10.1007/s11104-021-05164-9. URL https://link.springer.com/article/10.1007/s11104-021-05164-9. Company: Springer Distributor: Springer Institution: Springer Label: Springer Number: 1 Publisher: Springer International Publishing.

S. Asseng, F. Ewert, P. Martre, R. P. Rötter, D. B. Lobell, D. Cammarano, B. A. Kimball, M. J. Ottman, G. W. Wall, J. W. White, M. P. Reynolds, P. D. Alderman, P. V. V. Prasad, P. K. Aggarwal, J. Anothai, B. Basso, C. Biernath, A. J. Challinor, G. De Sanctis, J. Doltra, E. Fereres, M. Garcia-Vila, S. Gayler, G. Hoogenboom, L. A. Hunt, R. C. Izaurralde, M. Jabloun, C. D. Jones, K. C. Kersebaum, A.-K. Koehler, C. Müller, S. Naresh Kumar, C. Nendel, G. O' Leary, J. E. Olesen, T. Palosuo, E. Priesack, E. Eyshi Rezaei, A. C. Ruane, M. A. Semenov, I. Shcherbak, C. Stöckle, P. Stratonovitch, T. Streck, I. Supit, F. Tao, P. J. Thorburn, K. Waha, E. Wang, D. Wallach, J. Wolf, Z. Zhao, and Y. Zhu. Rising temperatures reduce global wheat production. *Nature Climate Change*, 5(2):143–147, Feb. 2015. ISSN 1758-6798. doi: 10.1038/nclimate2470. URL https://www.nature.com/articles/nclimate2470. Publisher: Nature Publishing Group.

D. V. Badri and J. M. Vivanco. Regulation and function of root exudates. *Plant, Cell & Environment*, 32(6):666–681, 2009. ISSN 1365-3040. doi: 10.1111/j.1365-3040.2009.01926.x. URL https://onlinelibrary.wiley.com/doi/abs/10.1111/j.1365-3040.2009.01926.x. _eprint: https://onlinelibrary.wiley.com/doi/pdf/10.1111/j.1365-3040.2009.01926.x.

References

J. Baffes and X. Etienne. Yield growth patterns of food commodities: Insights and challenges. *PLOS ONE*, 19(11): e0313088, Nov. 2024. ISSN 1932-6203. doi: 10.1371/journal.pone.0313088. URL https://journals.plos.org/plosone/article?id=10.1371/journal.pone.0313088. Publisher: Public Library of Science.

S. Bakhshandeh, P. E. Corneo, L. Yin, and F. A. Dijkstra. Drought and heat stress reduce yield and alter carbon rhizodeposition of different wheat genotypes. *Journal of Agronomy and Crop Science*, 205(2):157–167, Apr. 2019. ISSN 1439-037X. doi: 10.1111/jac.12314. URL https://onlinelibrary.wiley.com/doi/10.1111/jac.12314. Publisher: John Wiley & Sons, Ltd.

R. Barillot, C. Chambon, and B. Andrieu. CN-Wheat, a functional – structural model of carbon and nitrogen metabolism in wheat culms after anthesis. I. Model description. *Annals of Botany*, 118(5):997–1013, Oct. 2016. ISSN 0305-7364. doi: 10.1093/aob/mcw143. URL https://doi.org/10.1093/aob/mcw143.

R. Barillot, C. Chambon, C. Fournier, D. Combes, C. Pradal, and B. Andrieu. Investigation of complex canopies with a functional – structural plant model as exemplified by leaf inclination effect on the functioning of pure and mixed stands of wheat during grain filling. *Annals of Botany*, 123(4):727–742, Mar. 2019. ISSN 0305-7364. doi: 10.1093/aob/mcy208. URL https://www.ncbi.nlm.nih.gov/pmc/articles/PMC6417479/.

F. Bauget, V. Protto, C. Pradal, Y. Boursiac, and C. Maurel. A root functional-structural model allows to assess effects of water deficit on water and solute transport parameters. *Journal of Experimental Botany*, page erac471, 2023. ISSN 0022-0957. doi: 10.1093/jxb/erac471. URL https://doi.org/10.1093/jxb/erac471.

N. Beaudoin, P. Lecharpentier, D. Ripoche-Wachter, L. Strullu, B. Mary, J. Léonard, M. Launay, and E. Justes, editors. *STICS soil-crop model: Conceptual framework, equations and uses*. éditions Quae, 2023. doi: 10.35690/978-2-7592-3679-4. URL https://library.oapen.org/handle/20.500.12657/85111. Accepted: 2023-11-14T12:18:30Z.

M. Bechmann, C. Schneider, A. Carminati, D. Vetterlein, S. Attinger, and A. Hildebrandt. Parameterizing complex root water uptake models – the arrangement of root hydraulic properties within the root architecture affects dynamics and efficiency of root water uptake, Jan. 2014. URL https://hess.copernicus.org/articles/18/4189/2014/hess-18-4189-2014-discussion.html.

A. Beckers, A. Mamiya, M. Furutani, M. J. Bennett, H. Fukaki, S. Sawa, P. Gantet, L. Laplaze, and S. Guyomarc'h. Multiple layers of regulators emerge in the network controlling lateral root organogenesis. *Trends in Plant Science*, 30(5):499–514, May 2025. ISSN 1360-1385. doi: 10.1016/j.tplants.2024.09.018. URL https://www.cell.com/trends/plant-science/abstract/S1360-1385(24)00268-1. Publisher: Elsevier.

Benoit Bovy, G. D. McBain, B. Gailleton, and R. Lange. benbovy/xarray-simlab: 0.5.0, Jan. 2021. URL https://zenodo.org/record/4469813.

D. R. Bergman, T. Jackson, H. V. Jain, and K.-A. Norton. SMoRe GloS: An efficient and flexible framework for inferring global sensitivity of agent-based model parameters. *bioRxiv*, page 2024.09.18.613723, Sept. 2024. ISSN 2692-8205. doi: 10.1101/2024.09.18.613723. URL https://pmc.ncbi.nlm.nih.gov/articles/PMC11429786/.

B. Bicharanloo, M. Bagheri Shirvan, T. R. Cavagnaro, C. Keitel, and F. A. Dijkstra. Nitrogen addition and defoliation alter belowground carbon allocation with consequences for plant nitrogen uptake and soil organic carbon decomposition. *Science of The Total Environment*, 846:157430, Nov. 2022. ISSN 0048-9697. doi: 10.1016/j.scitotenv.2022.157430. URL https://www.sciencedirect.com/science/article/pii/S0048969722045284.

N. Bilyera, X. Zhang, P. Duddek, L. Fan, C. C. Banfield, S. Schlüter, A. Carminati, A. Kaestner, M. A. Ahmed, Y. Kuzyakov, M. A. Dippold, S. Spielvogel, and B. S. Razavi. Maize genotype-specific exudation strategies: An adaptive mechanism to increase microbial activity in the rhizosphere. *Soil Biology and Biochemistry*, 162:108426, Nov. 2021. ISSN 0038-0717. doi: 10.1016/j.soilbio.2021.108426. URL https://www.sciencedirect.com/science/article/pii/S003807172100300X.

E. Blanc and P. Barbillon. Modélisation des conséquences évolutives de la compétition pour la lumière dans des populations composites de blé. 2021.

E. Blanc, J. Enjalbert, T. Flutre, and P. Barbillon. Efficient Bayesian automatic calibration of a functional – structural wheat model using an adaptive design and a metamodelling approach. *Journal of Experimental Botany*, 74(21):6722–6734, Nov. 2023. ISSN 0022-0957, 1460-2431. doi: 10.1093/jxb/erad339. URL https://academic.oup.com/jxb/article/74/21/6722/7252026.

S. Blossfeld, C. M. Schreiber, G. Liebsch, A. J. Kuhn, and P. Hinsinger. Quantitative imaging of rhizosphere pH and CO2 dynamics with planar optodes. *Annals of Botany*, 112(2):267–276, July 2013. ISSN 1095-8290. doi: 10.1093/aob/mct047.

V. Bohm, E. Forey, M. Chauvat, P. Cardinael, and V. Peulon-Agasse. Evaluation of trap discs for root exudate eco-friendly sampling using rhizoboxes: Application to untargeted screening of organic compounds by gas chromatography hyphenated with high resolution mass spectrometry. *Journal of Chromatography Open*, 7:100205, May 2025. ISSN 2772-3917. doi: 10.1016/j.jcoa.2025.100205. URL https://www.sciencedirect.com/science/article/pii/S2772391725000039.

E. G. Bollard. Transport in the Xylem. 1960.

T. Bontpart, C. Concha, M. V. Giuffrida, I. Robertson, K. Admkie, T. Degefu, N. Girma, K. Tesfaye, T. Haileselassie, A. Fikre, M. Fetene, S. A. Tsaftaris, and P. Doerner. Affordable and robust phenotyping framework to analyse root system architecture of soil-grown plants. *The Plant Journal*, 103(6):2330–2343, 2020. ISSN 1365-313X. doi: 10.1111/tpj.14877. URL https://onlinelibrary.wiley.com/doi/abs/10.1111/tpj.14877. _eprint: https://onlinelibrary.wiley.com/doi/pdf/10.1111/tpj.14877.

A. J. Both, L. Benjamin, J. Franklin, G. Holroyd, L. D. Incoll, M. G. Lefsrud, and G. Pitkin. Guidelines for measuring and reporting environmental parameters for experiments in greenhouses. *Plant Methods*, 11(1):43, Sept. 2015. ISSN 1746-4811. doi: 10.1186/s13007-015-0083-5. URL https://doi.org/10.1186/s13007-015-0083-5.

F. Boudon, C. Pradal, T. Cokelaer, P. Prusinkiewicz, and C. Godin. L-Py: An L-System Simulation Framework for Modeling Plant Architecture Development Based on a Dynamic Language. *Frontiers in Plant Science*, 3, May 2012. ISSN 1664-462X. doi: 10.3389/fpls.2012.00076. URL https://www.frontiersin.org/journals/plant-science/articles/10.3389/fpls.2012.00076/full. Publisher: Frontiers.

R. Brackin, B. S. Atkinson, C. J. Sturrock, and A. Rasmussen. Roots-eye view: Using microdialysis and microCT to non-destructively map root nutrient depletion and accumulation zones. *Plant, Cell & Environment*, 40(12): 3135–3142, 2017. ISSN 1365-3040. doi: 10.1111/pce.13072. URL https://onlinelibrary.wiley.com/doi/abs/10.1111/pce.13072. _eprint: https://onlinelibrary.wiley.com/doi/pdf/10.1111/pce.13072.

J. Brun, M.-H. Jeuffroy, C. Pénicaud, M. Cerf, and J.-M. Meynard. Designing a research agenda for coupled innovation towards sustainable agrifood systems. *Agricultural Systems*, 191:103143, June 2021. ISSN 0308-521X. doi: 10.1016/j.agsy.2021.103143. URL https://www.sciencedirect.com/science/article/pii/S0308521X21000962.

A. S. Brunmayr, F. Hagedorn, M. Moreno Duborgel, L. I. Minich, and H. D. Graven. Radiocarbon analysis reveals underestimation of soil organic carbon persistence in new-generation soil models. *Geoscientific Model Development*, 17(15):5961–5985, Aug. 2024. ISSN 1991-959X. doi: 10.5194/gmd-17-5961-2024. URL https://gmd.copernicus.org/articles/17/5961/2024/. Publisher: Copernicus GmbH.

S. Buckley, R. Brackin, S. Jämtgård, T. Näsholm, and S. Schmidt. Microdialysis in soil environments: Current practice and future perspectives. *Soil Biology and Biochemistry*, 143:107743, Apr. 2020. ISSN 0038-0717. doi: 10.1016/j.soilbio.2020.107743. URL https://www.sciencedirect.com/science/article/pii/S0038071720300407.

M. Calvo - Polanco, Z. Ribeyre, M. Dauzat, G. Reyt, C. Hidalgo - Shrestha, P. Diehl, M. Frenger, T. Simonneau, B. Muller, D. E. Salt, R. B. Franke, C. Maurel, and Y. Boursiac. Physiological roles of Casparian strips and suberin in the transport of water and solutes. *New Phytologist*, 232(6):2295–2307, Dec. 2021. ISSN 0028-646X, 1469-8137. doi: 10.1111/nph.17765. URL https://nph.onlinelibrary.wiley.com/doi/10.1111/nph.17765.

G. G. T. Camargo and A. R. Kemanian. Six crop models differ in their simulation of water uptake. *Agricultural and Forest Meteorology*, 220:116–129, Apr. 2016. ISSN 0168-1923. doi: 10.1016/j.agrformet.2016.01.013. URL https://www.sciencedirect.com/science/article/pii/S0168192316300156.

A. Canarini, A. Merchant, and F. A. Dijkstra. Drought effects on *Helianthus annuus* and *Glycine max* metabolites: from phloem to root exudates. *Rhizosphere*, 2:85–97, Dec. 2016. ISSN 2452-2198. doi: 10.1016/j.rhisph.2016.06.003. URL https://www.sciencedirect.com/science/article/pii/S2452219816300647.

A. Canarini, C. Kaiser, A. Merchant, A. Richter, and W. Wanek. Root Exudation of Primary Metabolites: Mechanisms and Their Roles in Plant Responses to Environmental Stimuli. *Frontiers in Plant Science*, 10:157, Feb. 2019. ISSN 1664-462X. doi: 10.3389/fpls.2019.00157. URL https://www.frontiersin.org/article/10.3389/fpls.2019.00157/full.

N. M. Capstaff, C. Domoney, and A. J. Miller. Real-time monitoring of rhizosphere nitrate fluctuations under crops following defoliation. *Plant Methods*, 17(1):11, Jan. 2021. ISSN 1746-4811. doi: 10.1186/s13007-021-00713-w. URL https://doi.org/10.1186/s13007-021-00713-w.

A. Carminati, M. Zarebanadkouki, E. Kroener, M. A. Ahmed, and M. Holz. Biophysical rhizosphere processes affecting root water uptake. *Annals of Botany*, 118(4):561–571, Oct. 2016. ISSN 0305-7364. doi: 10.1093/aob/mcw113. URL https://www.ncbi.nlm.nih.gov/pmc/articles/PMC5055629/.

References

P. Cellier, S. Génermont, A. Pierart, S. Agasse, J.-L. Drouet, N. Edouard, T. Eglin, L. Galsomiès, N. Guingand, B. Loubet, and I. Roussel. Reducing the Impacts of Agriculture on Air Quality. In C. Bedos, S. Génermont, J.-F. Castell, and P. Cellier, editors, *Agriculture and Air Quality: Investigating, Assessing and Managing*, pages 245–282. Springer Netherlands, Dordrecht, 2020. ISBN 978-94-024-2058-6. doi: 10.1007/978-94-024-2058-6_9. URL https://doi.org/10.1007/978-94-024-2058-6_9.

A. K. Chandel, L. Jiang, and Y. Luo. Microbial Models for Simulating Soil Carbon Dynamics: A Review. *Journal of Geophysical Research: Biogeosciences*, 128(8):e2023JG007436, Aug. 2023. ISSN 2169-8961. doi: 10.1029/2023JG007436. URL https://agupubs.onlinelibrary.wiley.com/doi/10.1029/2023JG007436. Publisher: John Wiley & Sons, Ltd.

M. Chelle, B. Andrieu, and K. Bouatouch. Nested radiosity for plant canopies. *The Visual Computer*, 14(3):109–125, 1998.

M. Cieslak, A. N. Seleznyova, P. Prusinkiewicz, and J. Hanan. Towards aspect-oriented functional – structural plant modelling. *Annals of Botany*, 108(6):1025–1041, Oct. 2011. ISSN 0305-7364. doi: 10.1093/aob/mcr121. URL https://doi.org/10.1093/aob/mcr121.

D. T. Clarkson, A. W. Robards, and J. Sanderson. The tertiary endodermis in barley roots: Fine structure in relation to radial transport of ions and water. *Planta*, 96(4):292–305, Dec. 1971. ISSN 1432-2048. doi: 10.1007/BF00386944. URL https://doi.org/10.1007/BF00386944.

T. Colombi, A. Chakrawal, and A. M. Herrmann. Carbon supply – consumption balance in plant roots: effects of carbon use efficiency and root anatomical plasticity. *New Phytologist*, 233(4):1542–1547, 2022. ISSN 1469-8137. doi: 10.1111/nph.17598. URL https://onlinelibrary.wiley.com/doi/abs/10.1111/nph.17598. _eprint: https://nph.onlinelibrary.wiley.com/doi/pdf/10.1111/nph.17598.

S. Cornu, S. Keesstra, A. Bispo, M. Fantappie, F. van Egmond, B. Smreczak, R. Wawer, L. Pavlů, J. Sobocká, Z. Bakacsi, K. Farkas-Iványi, S. Molnár, A. B. Møller, S. Madenoglu, D. Feiziene, K. Oorts, F. Schneider, M. da Conceição Gonçalves, R. Mano, G. Garland, R. Skalský, L. O'Sullivan, R. Kasparinskis, and C. Chenu. National soil data in EU countries, where do we stand? *European Journal of Soil Science*, 74(4):e13398, 2023. ISSN 1365-2389. doi: 10.1111/ejss.13398. URL https://onlinelibrary.wiley.com/doi/abs/10.1111/ejss.13398. _eprint: https://onlinelibrary.wiley.com/doi/pdf/10.1111/ejss.13398.

D. Coumou and S. Rahmstorf. A decade of weather extremes. *Nature Climate Change*, 2(7):491–496, July 2012. ISSN 1758-6798. doi: 10.1038/nclimate1452. URL https://www.nature.com/articles/nclimate1452. Publisher: Nature Publishing Group.

V. Couvreur, M. Faget, G. Lobet, M. Javaux, F. Chaumont, and X. Draye. Going with the Flow: Multiscale Insights into the Composite Nature of Water Transport in Roots. *Plant Physiology*, 178(4):1689–1703, Dec. 2018. ISSN 0032-0889. doi: 10.1104/pp.18.01006. URL https://doi.org/10.1104/pp.18.01006. Number: 4.

M. V. Criado, C. Caputo, I. N. Roberts, M. A. Castro, and A. J. Barneix. Cytokinin-induced changes of nitrogen remobilization and chloroplast ultrastructure in wheat (*Triticum aestivum*). *Journal of Plant Physiology*, 166(16):1775–1785, Nov. 2009. ISSN 0176-1617. doi: 10.1016/j.jplph.2009.05.007. URL https://www.sciencedirect.com/science/article/pii/S0176161709002181.

C. Cruz, S. H. Lips, and M. A. Martins - Loução. Uptake regions of inorganic nitrogen in roots of carob seedlings. *Physiologia Plantarum*, 95(2):167–175, Feb. 1995. ISSN 0031-9317, 1399-3054. doi: 10.1111/j.1399-3054.1995.tb00824.x. URL https://onlinelibrary.wiley.com/doi/10.1111/j.1399-3054.1995.tb00824.x.

K. R. Daly, S. D. Keyes, S. Masum, and T. Roose. Image-based modelling of nutrient movement in and around the rhizosphere. *Journal of Experimental Botany*, 67(4):1059–1070, Feb. 2016. ISSN 0022-0957, 1460-2431. doi: 10.1093/jxb/erv544. URL https://academic.oup.com/jxb/article-lookup/doi/10.1093/jxb/erv544.

A. Dathe, J. A. Postma, M. B. Postma-Blaauw, and J. P. Lynch. Impact of axial root growth angles on nitrogen acquisition in maize depends on environmental conditions. *Annals of Botany*, 118(3):401–414, Sept. 2016. ISSN 0305-7364. doi: 10.1093/aob/mcw112. URL https://doi.org/10.1093/aob/mcw112.

J. Dessureault-Rompré, B. Nowack, R. Schulin, and J. Luster. Modified micro suction cup/rhizobox approach for the in-situ detection of organic acids in rhizosphere soil solution. *Plant and Soil*, 286(1):99–107, Aug. 2006. ISSN 1573-5036. doi: 10.1007/s11104-006-9029-z. URL https://doi.org/10.1007/s11104-006-9029-z.

F. A. Dijkstra, Y. Carrillo, E. Pendall, and J. A. Morgan. Rhizosphere priming: a nutrient perspective. *Frontiers in Microbiology*, 4, July 2013. ISSN 1664-302X. doi: 10.3389/fmicb.2013.00216. URL https://www.frontiersin.org/journals/microbiology/articles/10.3389/fmicb.2013.00216/full. Publisher: Frontiers.

N. B. Dilkes, D. L. Jones, and J. Farrar. Temporal Dynamics of Carbon Partitioning and Rhizodeposition in Wheat. *Plant Physiology*, 134(2):706–715, Feb. 2004. ISSN 0032-0889. doi: 10.1104/pp.103.032045. URL https://doi.org/10.1104/pp.103.032045.

S. Dinant, J.-L. Bonnemain, C. Girousse, and J. Kehr. Phloem sap intricacy and interplay with aphid feeding. *Comptes Rendus Biologies*, 333(6):504–515, June 2010. ISSN 1631-0691. doi: 10.1016/j.crvi.2010.03.008. URL https://www.sciencedirect.com/science/article/pii/S1631069110001137.

I. Dodd, W. Davies, and G. Egea. MEASURING SAP FLOW IN "TWO ROOT-ONE SHOOT" GRAFTED PLANTS TO MODEL SHOOT XYLEM ABA CONCENTRATION DURING PARTIAL ROOTZONE DRYING. *Acta Horticulturae*, (846):277–284, Nov. 2009. ISSN 0567-7572, 2406-6168. doi: 10.17660/ActaHortic.2009.846.31. URL https://www.actahort.org/books/846/846_31.htm.

I. C. Dodd, G. Egea, and W. J. Davies. Accounting for sap flow from different parts of the root system improves the prediction of xylem ABA concentration in plants grown with heterogeneous soil moisture. *Journal of Experimental Botany*, 59(15):4083–4093, Nov. 2008. ISSN 0022-0957. doi: 10.1093/jxb/ern246. URL https://doi.org/10.1093/jxb/ern246.

A. Don, F. Seidel, J. Leifeld, T. Kätterer, M. Martin, S. Pellerin, D. Emde, D. Seitz, and C. Chenu. Carbon sequestration in soils and climate change mitigation—Definitions and pitfalls. *Global Change Biology*, 30(1): e16983, 2024. ISSN 1365-2486. doi: 10.1111/gcb.16983. URL https://onlinelibrary.wiley.com/doi/abs/10.1111/gcb.16983. _eprint: https://onlinelibrary.wiley.com/doi/pdf/10.1111/gcb.16983.

C. Doussan, L. Pagès, and G. Vercambre. Modelling of the Hydraulic Architecture of Root Systems: An Integrated Approach to Water Absorption—Model Description. *Annals of Botany*, 81(2):213–223, Feb. 1998. ISSN 0305-7364. doi: 10.1006/anbo.1997.0540. URL https://www.sciencedirect.com/science/article/pii/S0305736497905400.

M. C. Drew and L. R. Saker. Nutrient Supply and the Growth of the Seminal Root System in Barley: II. LOCALIZED, COMPENSATORY INCREASES IN LATERAL ROOT GROWTH AND RATES OP NITRATE UPTAKE WHEN NITRATE SUPPLY IS RESTRICTED TO ONLY PART OF THE ROOT SYSTEM. *Journal of Experimental Botany*, 26(1):79–90, Feb. 1975. ISSN 0022-0957. doi: 10.1093/jxb/26.1.79. URL https://doi.org/10.1093/jxb/26.1.79.

L. E. Drinkwater and S. S. Snapp. Nutrients in Agroecosystems: Rethinking the Management Paradigm. In D. L. Sparks, editor, *Advances in Agronomy*, volume 92, pages 163–186. Academic Press, Jan. 2007. doi: 10.1016/S0065-2113(04)92003-2. URL https://www.sciencedirect.com/science/article/pii/S0065211304920032.

Z. Du, E. Weng, L. Jiang, Y. Luo, J. Xia, and X. Zhou. Carbon – nitrogen coupling under three schemes of model representation: a traceability analysis. *Geoscientific Model Development*, 11(11):4399–4416, Nov. 2018. ISSN 1991-959X. doi: 10.5194/gmd-11-4399-2018. URL https://gmd.copernicus.org/articles/11/4399/2018/. Publisher: Copernicus GmbH.

V. M. Dunbabin, A. J. Diggle, Z. Rengel, and R. van Hugten. Modelling the interactions between water and nutrient uptake and root growth. *Plant and Soil*, 239(1):19–38, Feb. 2002. ISSN 1573-5036. doi: 10.1023/A:1014939512104. URL https://doi.org/10.1023/A:1014939512104.

V. M. Dunbabin, J. A. Postma, A. Schnepf, L. Pagès, M. Javaux, L. Wu, D. Leitner, Y. L. Chen, Z. Rengel, and A. J. Diggle. Modelling root – soil interactions using three – dimensional models of root growth, architecture and function. *Plant and Soil*, 372(1-2):93–124, Nov. 2013. ISSN 0032-079X, 1573-5036. doi: 10.1007/s11104-013-1769-y. URL http://link.springer.com/10.1007/s11104-013-1769-y.

M. Duru, O. Therond, and M. Fares. Designing agroecological transitions; A review. *Agronomy for Sustainable Development*, 35(4):0, Oct. 2015. doi: 10.1007/s13593-015-0318-x. URL https://hal.science/hal-01340332. Publisher: Springer Verlag/EDP Sciences/INRA.

D. E. Enstone, C. A. Peterson, and F. Ma. Root Endodermis and Exodermis: Structure, Function, and Responses to the Environment. *Journal of Plant Growth Regulation*, 21(4):335–351, Dec. 2002. ISSN 0721-7595, 1435-8107. doi: 10.1007/s00344-003-0002-2. URL http://link.springer.com/10.1007/s00344-003-0002-2.

R. E. Evenson and D. Gollin. Assessing the Impact of the Green Revolution, 1960 to 2000. *Science*, 300(5620): 758–762, May 2003. doi: 10.1126/science.1078710. URL https://www.science.org/doi/full/10.1126/science.1078710. Publisher: American Association for the Advancement of Science.

B. Faiyue, M. J. Al-Azzawi, and T. J. Flowers. The role of lateral roots in bypass flow in rice (Oryza sativa L.). *Plant, Cell & Environment*, 33(5):702–716, 2010. ISSN 1365-3040. doi: 10.1111/j.1365-3040.2009.02078.x. URL https://onlinelibrary.wiley.com/doi/abs/10.1111/j.1365-3040.2009.02078.x. _eprint: https://onlinelibrary.wiley.com/doi/pdf/10.1111/j.1365-3040.2009.02078.x.

Y. Fang, S. B. Yabusaki, A. H. Ahkami, X. Chen, and T. D. Scheibe. An efficient three-dimensional rhizosphere modeling capability to study the effect of root system architecture on soil water and reactive transport. *Plant and Soil*, 441(1):33–48, Aug. 2019. ISSN 1573-5036. doi: 10.1007/s11104-019-04068-z. URL https://doi.org/10.1007/s11104-019-04068-z.

References

FAO. Cereal Supply and Demand Brief – World Food Situation. Technical report, Food and Agriculture Organization of the United Nations, Rome, June 2025. URL https://www.fao.org/worldfoodsituation/csdb/en.

G. D. Farquhar, S. von Caemmerer, and J. A. Berry. A biochemical model of photosynthetic CO2 assimilation in leaves of C3 species. *Planta*, 149(1):78–90, June 1980. ISSN 1432-2048. doi: 10.1007/BF00386231. URL https://doi.org/10.1007/BF00386231.

R. Fernandez, A. Crabos, M. Maillard, P. Nacry, and C. Pradal. High-throughput and automatic structural and developmental root phenotyping on Arabidopsis seedlings. *Plant Methods*, 18(1):127, Dec. 2022. ISSN 1746-4811. doi: 10.1186/s13007-022-00960-5. URL https://doi.org/10.1186/s13007-022-00960-5.

A. Fernández González, Z. T. Fang, D. Sen, B. Henrich, Y. Nagashima, A. V. Sokolov, S. Okumoto, and A. J. Verhoef. In-vivo Raman microspectroscopy reveals differential nitrate concentration in different developmental zones in Arabidopsis roots. *Plant Methods*, 20(1):185, Dec. 2024. ISSN 1746-4811. doi: 10.1186/s13007-024-01302-3. URL https://doi.org/10.1186/s13007-024-01302-3.

O. Fiehn. Metabolomics by Gas Chromatography – Mass Spectrometry: Combined Targeted and Untargeted Profiling. *Current Protocols in Molecular Biology*, 114(1), Apr. 2016. ISSN 1934-3639, 1934-3647. doi: 10.1002/0471142727.mb3004s114. URL https://currentprotocols.onlinelibrary.wiley.com/doi/10.1002/0471142727.mb3004s114.

C. Fournier, B. Andrieu, S. Ljutovac, and S. Saint-Jean. ADEL-Wheat: a 3D Architectural Model of wheat development. In Hu, B.-G., Jaeger, and M., editors, *Plant Growth Modeling and Applications*, pages 54–63. Springer Verlag, 2003. URL https://hal.science/hal-00909184.

C. Fournier, C. Pradal, G. Louarn, D. Combes, J.-C. Soulié, D. Luquet, F. Boudon, and M. Chelle. Building modular FSPM under OpenAlea: concepts and applications. page 109. University of California, 2010. URL https://inria.hal.science/hal-01192232.

N. S. Fradgley, A. R. Bentley, and S. M. Swarbreck. Defining the physiological determinants of low nitrogen requirement in wheat. *Biochemical Society Transactions*, 49(2):609–616, Mar. 2021. ISSN 0300-5127. doi: 10.1042/BST20200282. URL https://doi.org/10.1042/BST20200282.

C. Francis, G. Lieblein, S. Gliessman, T. A. Breland, N. Creamer, R. Harwood, L. Salomonsson, J. Helenius, D. Rickerl, R. Salvador, M. Wiedenhoeft, S. Simmons, P. Allen, M. Altieri, C. Flora, and R. Poincelot. Agroecology: The ecology of food systems. *Journal of Sustainable Agriculture*, 22(3):99–118, 2003. ISSN 1044-0046. doi: 10.1300/J064v22n03_10. URL https://www.scopus.com/pages/publications/10744230232.

G. T. Freschet, L. Pagès, C. M. Iversen, L. H. Comas, B. Rewald, C. Roumet, J. Klimešová, M. Zadworny, H. Poorter, J. A. Postma, T. S. Adams, A. Bagniewska ‐ Zadworna, A. G. Bengough, E. B. Blancaflor, I. Brunner, J. H. C. Cornelissen, E. Garnier, A. Gessler, S. E. Hobbie, I. C. Meier, L. Mommer, C. Picon ‐ Cochard, L. Rose, P. Ryser, M. Scherer ‐ Lorenzen, N. A. Soudzilovskaia, A. Stokes, T. Sun, O. J. Valverde ‐ Barrantes, M. Weemstra, A. Weigelt, N. Wurzburger, L. M. York, S. A. Batterman, M. Gomes de Moraes, ☒ Janeček, H. Lambers, V. Salmon, N. Tharayil, and M. L. McCormack. A starting guide to root ecology: strengthening ecological concepts and standardising root classification, sampling, processing and trait measurements. *The New Phytologist*, 232(3):973–1122, Nov. 2021. ISSN 0028-646X. doi: 10.1111/nph.17572. URL https://www.ncbi.nlm.nih.gov/pmc/articles/PMC8518129/.

J. Fustec, F. Lesuffleur, S. Mahieu, and J.-B. Cliquet. Nitrogen rhizodeposition of legumes. A review. *Agronomy for Sustainable Development*, 30(1):57–66, Mar. 2010. ISSN 1773-0155. doi: 10.1051/agro/2009003. URL https://doi.org/10.1051/agro/2009003.

T. Galindo-Castañeda, M. Hartmann, and J. P. Lynch. Location: root architecture structures rhizosphere microbial associations. *Journal of Experimental Botany*, 75(2):594–604, Jan. 2024. ISSN 0022-0957, 1460-2431. doi: 10.1093/jxb/erad421. URL https://academic.oup.com/jxb/article/75/2/594/7330382.

D. Gan, H. Zeng, and B. Zhu. The rhizosphere effect on soil gross nitrogen mineralization: A meta-analysis. *Soil Ecology Letters*, 4(2):144–154, June 2022. ISSN 2662-2297. doi: 10.1007/s42832-021-0098-y. URL https://doi.org/10.1007/s42832-021-0098-y.

G. Garin, C. Fournier, B. Andrieu, V. Houlès, C. Robert, and C. Pradal. A modelling framework to simulate foliar fungal epidemics using functional–structural plant models. *Annals of botany*, 114(4):795–812, 2014.

M. Gauthier, R. Barillot, A. Schneider, C. Chambon, C. Fournier, C. Pradal, C. Robert, and B. Andrieu. A functional structural model of grass development based on metabolic regulation and coordination rules. *Journal of Experimental Botany*, 71(18):5454–5468, Sept. 2020. ISSN 0022-0957, 1460-2431. doi: 10.1093/jxb/eraa276. URL https://academic.oup.com/jxb/article/71/18/5454/5851451. Number: 18.

M. Gawinowski, L. Perthame, F. Rees, C. Richard-Molard, P. Barbillon, and A. Jullien. Meta-modelling of FSPMs to study plant-plant interactions in rapeseed and fababean mixtures: from plant to plot scale. 2024.

T. Gerault, C. Pradal, R. Barillot, C. Richard-Molard, M. Gauthier, A. Jullien, and F. Rees. Do specific root zones shape plant net N uptake? Modeling insights from Root-CyNAPS.

R. M. Gifford. Whole plant respiration and photosynthesis of wheat under increased CO2 concentration and temperature: long-term vs. short-term distinctions for modelling. *Global Change Biology*, 1(6):385–396, 1995. ISSN 1365-2486. doi: 10.1111/j.1365-2486.1995.tb00037.x. URL https://onlinelibrary.wiley.com/doi/abs/10.1111/j.1365-2486.1995.tb00037.x. _eprint: https://onlinelibrary.wiley.com/doi/pdf/10.1111/j.1365-2486.1995.tb00037.x.

Giraud, S. L. Gall, M. Harings, M. Javaux, D. Leitner, F. Meunier, Y. Rothfuss, D. van Dusschoten, J. Vanderborght, H. Vereecken, G. Lobet, and A. Schnepf. CPlantBox: a fully coupled modelling platform for the water and carbon fluxes in the soil – plant – atmosphere continuum. *in silico Plants*, 5(2):diad009, July 2023. ISSN 2517-5025. doi: 10.1093/insilicoplants/diad009. URL https://doi.org/10.1093/insilicoplants/diad009.

Giraud, A. K. Sırcan, T. Streck, D. Leitner, G. Lobet, H. Pagel, and A. Schnepf. In silico analysis of carbon stabilisation by plant and soil microbes for different weather scenarios. *EGUsphere*, pages 1–76, Mar. 2025. doi: 10.5194/egusphere-2025-572. URL https://egusphere.copernicus.org/preprints/2025/egusphere-2025-572/. Publisher: Copernicus GmbH.

S. Gliessman. Agroecology and Social Transformation. *Agroecology and Sustainable Food Systems*, 38(10):1125–1126, Nov. 2014. ISSN 2168-3565. doi: 10.1080/21683565.2014.951904. URL https://doi.org/10.1080/21683565.2014.951904. Publisher: Taylor & Francis _eprint: https://doi.org/10.1080/21683565.2014.951904.

T. Gomiero. Soil Degradation, Land Scarcity and Food Security: Reviewing a Complex Challenge. *Sustainability*, 8 (3):281, Mar. 2016. ISSN 2071-1050. doi: 10.3390/su8030281. URL https://www.mdpi.com/2071-1050/8/3/281.

V. O. Grasmanis and K. P. Barley. The Uptake of Nitrate and Ammonium by Suceessive Zones of the Pea Radicle. *Australian Journal of Biological Sciences*, 22(6):1313–1320, 1969. doi: 10.1071/bi9691313. URL https://www.publish.csiro.au/bi/bi9691313. Publisher: CSIRO PUBLISHING.

L. Gratani. Plant Phenotypic Plasticity in Response to Environmental Factors. *Advances in Botany*, 2014(1): 208747, 2014. ISSN 2314-7857. doi: 10.1155/2014/208747. URL https://onlinelibrary.wiley.com/doi/abs/10.1155/2014/208747. _eprint: https://onlinelibrary.wiley.com/doi/pdf/10.1155/2014/208747.

P. J. Gregory. RUSSELL REVIEW Are plant roots only "in" soil or are they "of" it? Roots, soil formation and function. *European Journal of Soil Science*, 73(1):e13219, 2022. ISSN 1365-2389. doi: 10.1111/ejss.13219. URL https://onlinelibrary.wiley.com/doi/abs/10.1111/ejss.13219. _eprint: https://onlinelibrary.wiley.com/doi/pdf/10.1111/ejss.13219.

M. Griffiths and L. M. York. Targeting Root Ion Uptake Kinetics to Increase Plant Productivity and Nutrient Use Efficiency1[OPEN]. *Plant Physiology*, 182(4):1854–1868, Apr. 2020. ISSN 0032-0889. doi: 10.1104/pp.19.01496. URL https://doi.org/10.1104/pp.19.01496. Number: 4.

B. Guenet, B. Gabrielle, C. Chenu, D. Arrouays, J. Balesdent, M. Bernoux, E. Bruni, J.-P. Caliman, R. Cardinael, S. Chen, P. Ciais, D. Desbois, J. Fouche, S. Frank, C. Henault, E. Lugato, V. Naipal, T. Nesme, M. Obersteiner, S. Pellerin, D. S. Powlson, D. P. Rasse, F. Rees, J.-F. Soussana, Y. Su, H. Tian, H. Valin, and F. Zhou. Can N2O emissions offset the benefits from soil organic carbon storage? *Global Change Biology*, 27(2):237–256, 2021. ISSN 1365-2486. doi: 10.1111/gcb.15342. URL https://onlinelibrary.wiley.com/doi/abs/10.1111/gcb.15342. _eprint: https://onlinelibrary.wiley.com/doi/pdf/10.1111/gcb.15342.

A. B. Guenther, X. Jiang, C. L. Heald, T. Sakulyanontvittaya, T. Duhl, L. K. Emmons, and X. Wang. The Model of Emissions of Gases and Aerosols from Nature version 2.1 (MEGAN2.1): an extended and updated framework for modeling biogenic emissions. *Geoscientific Model Development*, 5(6):1471–1492, Nov. 2012. ISSN 1991-959X. doi: 10.5194/gmd-5-1471-2012. URL https://gmd.copernicus.org/articles/5/1471/2012/. Publisher: Copernicus GmbH.

S. Haase, G. Neumann, A. Kania, Y. Kuzyakov, V. Römheld, and E. Kandeler. Elevation of atmospheric CO2 and N-nutritional status modify nodulation, nodule-carbon supply, and root exudation of Phaseolus vulgaris L. *Soil Biology and Biochemistry*, 39(9):2208–2221, Sept. 2007. ISSN 00380717. doi: 10.1016/j.soilbio.2007.03.014. URL https://linkinghub.elsevier.com/retrieve/pii/S0038071707001186.

S. Hatt, S. Artru, D. Brédart, L. Lassois, F. Francis, ☒ Haubruge, S. Garré, P. M. Stassart, M. Dufrêne, A. Monty, and F. Boeraeve. Towards sustainable food systems: the concept of agroecology and how it questions current research practices. A review. *BASE*, pages 215–224, 2016. ISSN 1780-4507, 1370-6233. doi: 10.25518/1780-4507.12997. URL https://popups.uliege.be/1780-4507/index.php?id=12997.

H. Heinemann, J. Hirte, F. Seidel, and A. Don. Increasing root biomass derived carbon input to agricultural soils by genotype selection – a review. *Plant and Soil*, 490(1):19–30, Sept. 2023. ISSN 1573-5036. doi: 10.1007/s11104-023-06068-6. URL https://doi.org/10.1007/s11104-023-06068-6.

References

R. Hemmerling, O. Kniemeyer, D. Lanwert, W. Kurth, and G. Buck-Sorlin. The rule-based language XL and the modelling environment GroIMP illustrated with simulated tree competition. *Functional Plant Biology*, 35(10): 739–750, Nov. 2008. ISSN 1445-4416. doi: 10.1071/FP08052. URL https://www.publish.csiro.au/fp/FP08052. Publisher: CSIRO PUBLISHING.

R. Hemmerling, J. B. Evers, K. Smoleňová, G. Buck-Sorlin, and W. Kurth. Extension of the GroIMP modelling platform to allow easy specification of differential equations describing biological processes within plant models. *Computers and Electronics in Agriculture*, 92:1–8, Mar. 2013. ISSN 0168-1699. doi: 10.1016/j.compag.2012.12.007. URL https://www.sciencedirect.com/science/article/pii/S016816991200292X.

M. Henke, W. Kurth, and G. H. Buck-Sorlin. Fspm-p: towards a general functional-structural plant model for robust and comprehensive model development. *Frontiers of computer science*, 10(6):1103–1117, 2016.

G. H. Henriksen, D. R. Raman, L. P. Walker, and R. M. Spanswick. Measurement of Net Fluxes of Ammonium and Nitrate at the Surface of Barley Roots Using Ion-Selective Microelectrodes: II. Patterns of Uptake along the Root Axis and Evaluation of the Microelectrode Flux Estimation Technique. *Plant Physiology*, 99(2):734–747, 1992. URL http://www.jstor.org/stable/4274411.

C. M. Henry and J. W. Deacon. Natural (non-pathogenic) death of the cortex of wheat and barley seminal roots, as evidenced by nuclear staining with acridine orange. *Plant and Soil*, 60(2):255–274, June 1981. ISSN 1573-5036. doi: 10.1007/BF02374110. URL https://doi.org/10.1007/BF02374110.

A. Heymans, V. Couvreur, T. LaRue, A. Paez-Garcia, and G. Lobet. GRANAR, a Computational Tool to Better Understand the Functional Importance of Monocotyledon Root Anatomy1 [OPEN]. *Plant Physiology*, 182(2): 707–720, Feb. 2020. ISSN 0032-0889. doi: 10.1104/pp.19.00617. URL https://doi.org/10.1104/pp.19.00617.

Hodge, G. Berta, C. Doussan, F. Merchan, and M. Crespi. Plant root growth, architecture and function. *Plant and Soil*, 321(1):153–187, Aug. 2009. ISSN 1573-5036. doi: 10.1007/s11104-009-9929-9. URL https://doi.org/10.1007/s11104-009-9929-9. Number: 1 R.

M. Holz, M. Zarebanadkouki, Y. Kuzyakov, J. Pausch, and A. Carminati. Root hairs increase rhizosphere extension and carbon input to soil. *Annals of Botany*, 121(1):61–69, Jan. 2018. ISSN 0305-7364. doi: 10.1093/aob/mcx127. URL https://www.ncbi.nlm.nih.gov/pmc/articles/PMC5786240/.

M. Holz, J. N. Becker, G. Daudin, and E. Oburger. Application of planar optodes to measure CO2 gradients in the rhizosphere of unsaturated soils. *Rhizosphere*, 16:100266, Dec. 2020. ISSN 2452-2198. doi: 10.1016/j.rhisph.2020.100266. URL https://www.sciencedirect.com/science/article/pii/S2452219820301786.

M. Holz, M. Zarebanadkouki, P. Benard, M. Hoffmann, and M. Dubbert. Root and rhizosphere traits for enhanced water and nutrients uptake efficiency in dynamic environments. *Frontiers in Plant Science*, 15, July 2024. ISSN 1664-462X. doi: 10.3389/fpls.2024.1383373. URL https://www.frontiersin.org/journals/plant-science/articles/10.3389/fpls.2024.1383373/full.

D. Holzworth, N. I. Huth, J. Fainges, H. Brown, E. Zurcher, R. Cichota, S. Verrall, N. I. Herrmann, B. Zheng, and V. Snow. APSIM Next Generation: Overcoming challenges in modernising a farming systems model. *Environmental Modelling & Software*, 103:43–51, May 2018. ISSN 1364-8152. doi: 10.1016/j.envsoft.2018.02.002. URL https://www.sciencedirect.com/science/article/pii/S1364815217311921.

E. Hose, D. Clarkson, E. Steudle, L. Schreiber, and W. Hartung. The exodermis: a variable apoplastic barrier. *Journal of Experimental Botany*, 52(365):2245–2264, Dec. 2001. ISSN 0022-0957. doi: 10.1093/jexbot/52.365.2245. URL https://doi.org/10.1093/jexbot/52.365.2245.

B. Hu, A. Henry, K. M. Brown, and J. P. Lynch. Root cortical aerenchyma inhibits radial nutrient transport in maize (Zea mays). *Annals of Botany*, 113(1):181–189, Jan. 2014. ISSN 0305-7364. doi: 10.1093/aob/mct259. URL https://www.ncbi.nlm.nih.gov/pmc/articles/PMC3864730/.

S. Huber. Grand Challenges in Plant Physiology: The Underpinning of Translational Research. *Frontiers in Plant Science*, 2, Sept. 2011. ISSN 1664-462X. doi: 10.3389/fpls.2011.00048. URL https://www.frontiersin.org/journals/plant-science/articles/10.3389/fpls.2011.00048/full. Publisher: Frontiers.

H. Hunt, S. Leape, J. S. Sidhu, I. Ajmera, J. P. Lynch, R. G. Ratcliffe, and L. J. Sweetlove. A role for fermentation in aerobic conditions as revealed by computational analysis of maize root metabolism during growth by cell elongation. *The Plant Journal*, 116(6):1553–1570, 2023. ISSN 1365-313X. doi: 10.1111/tpj.16478. URL https://onlinelibrary.wiley.com/doi/abs/10.1111/tpj.16478. _eprint: https://onlinelibrary.wiley.com/doi/pdf/10.1111/tpj.16478.

R. B. Jackson, K. Lajtha, S. E. Crow, G. Hugelius, M. G. Kramer, and G. Piñeiro. The Ecology of Soil Carbon: Pools, Vulnerabilities, and Biotic and Abiotic Controls. *Annual Review of Ecology, Evolution, and Systematics*, 48(Volume 48, 2017):419–445, Nov. 2017. ISSN 1543-592X, 1545-2069. doi: 10.1146/annurev-ecolsys-112414-054234. URL https://www.annualreviews.org/content/journals/10.1146/annurev-ecolsys-112414-054234. Publisher: Annual Reviews.

M. Javaux, T. Schröder, J. Vanderborght, and H. Vereecken. Use of a Three-Dimensional Detailed Modeling Approach for Predicting Root Water Uptake. *Vadose Zone Journal*, 7(3):1079–1088, 2008. ISSN 1539-1663. doi: 10.2136/vzj2007.0115. URL https://onlinelibrary.wiley.com/doi/abs/10.2136/vzj2007.0115. _eprint: https://onlinelibrary.wiley.com/doi/pdf/10.2136/vzj2007.0115.

D. L. Jones and P. R. Darrah. Re-sorption of organic compounds by roots of Zea mays L. and its consequences in the rhizosphere. *Plant and Soil*, 153(1):47–59, June 1993. ISSN 1573-5036. doi: 10.1007/BF00010543. URL https://doi.org/10.1007/BF00010543.

D. L. Jones, C. Nguyen, and R. D. Finlay. Carbon flow in the rhizosphere: carbon trading at the soil – root interface. *Plant and Soil*, 321(1-2):5–33, Aug. 2009. ISSN 0032-079X, 1573-5036. doi: 10.1007/s11104-009-9925-0. URL http://link.springer.com/10.1007/s11104-009-9925-0. Number: 1-2.

H. Kahiluoto, J. Kaseva, J. Balek, J. E. Olesen, M. Ruiz-Ramos, A. Gobin, K. C. Kersebaum, J. Takáč, F. Ruget, R. Ferrise, P. Bezak, G. Capellades, C. Dibari, H. Mäkinen, C. Nendel, D. Ventrella, A. Rodríguez, M. Bindi, and M. Trnka. Decline in climate resilience of European wheat. *Proceedings of the National Academy of Sciences*, 116(1):123–128, Jan. 2019. doi: 10.1073/pnas.1804387115. URL https://www.pnas.org/doi/abs/10.1073/pnas.1804387115. Publisher: Proceedings of the National Academy of Sciences.

S. Kanno, J.-F. Arrighi, S. Chiarenza, V. Bayle, R. Berthomé, B. Péret, H. Javot, E. Delannoy, E. Marin, T. M. Nakanishi, M.-C. Thibaud, and L. Nussaume. A novel role for the root cap in phosphate uptake and homeostasis. *eLife*, 5:e14577, Apr. 2016. ISSN 2050-084X. doi: 10.7554/eLife.14577. URL https://doi.org/10.7554/eLife.14577. Publisher: eLife Sciences Publications, Ltd.

S. D. Keesstra, C. Chenu, L. J. Munkholm, S. Cornu, P. J. Kuikman, M. H. Thorsøe, A. Besse-Lototskaya, and S. M. Visser. European agricultural soil management: Towards climate-smart and sustainability, knowledge needs and research approaches. *European Journal of Soil Science*, 75(1):e13437, 2024. ISSN 1365-2389. doi: 10.1111/ejss.13437. URL https://onlinelibrary.wiley.com/doi/abs/10.1111/ejss.13437. _eprint: https://onlinelibrary.wiley.com/doi/pdf/10.1111/ejss.13437.

C. A. Keller, M. S. Long, R. M. Yantosca, A. M. Da Silva, S. Pawson, and D. J. Jacob. HEMCO v1.0: a versatile, ESMF-compliant component for calculating emissions in atmospheric models. *Geoscientific Model Development*, 7(4):1409–1417, July 2014. ISSN 1991-9603. doi: 10.5194/gmd-7-1409-2014. URL https://gmd.copernicus.org/articles/7/1409/2014/.

D. Khare, T. Selzner, D. Leitner, J. Vanderborght, H. Vereecken, and A. Schnepf. Root System Scale Models Significantly Overestimate Root Water Uptake at Drying Soil Conditions. *Frontiers in Plant Science*, 13:798741, Feb. 2022. ISSN 1664-462X. doi: 10.3389/fpls.2022.798741. URL https://www.frontiersin.org/articles/10.3389/fpls.2022.798741/full.

B. Klepper, R. K. Belford, and R. W. Rickman. Root and Shoot Development in Winter Wheat[1]. *Agronomy Journal*, 76(1):117–122, Jan. 1984. ISSN 0002-1962, 1435-0645. doi: 10.2134/agronj1984.00021962007600010029x. URL https://acsess.onlinelibrary.wiley.com/doi/10.2134/agronj1984.00021962007600010029x.

A. Koch, F. Meunier, J. Vanderborght, S. Garré, A. Pohlmeier, and M. Javaux. Functional – structural root-system model validation using a soil MRI experiment. *Journal of Experimental Botany*, 70(10):2797–2809, May 2019. ISSN 0022-0957. doi: 10.1093/jxb/erz060. URL https://doi.org/10.1093/jxb/erz060.

K. Kornhuber, C. Lesk, C. F. Schleussner, J. Jägermeyr, P. Pfleiderer, and R. M. Horton. Risks of synchronized low yields are underestimated in climate and crop model projections. *Nature Communications*, 14(1):3528, July 2023. ISSN 2041-1723. doi: 10.1038/s41467-023-38906-7. URL https://www.nature.com/articles/s41467-023-38906-7. Publisher: Nature Publishing Group.

P. Kraft, K. B. Vaché, H.-G. Frede, and L. Breuer. CMF: A Hydrological Programming Language Extension For Integrated Catchment Models. *Environmental Modelling & Software*, 26(6):828–830, June 2011. ISSN 1364-8152. doi: 10.1016/j.envsoft.2010.12.009. URL https://www.sciencedirect.com/science/article/pii/S1364815210003439.

R. C. P. Kuijken, J. F. H. Snel, M. M. Heddes, H. J. Bouwmeester, and L. F. M. Marcelis. The importance of a sterile rhizosphere when phenotyping for root exudation. *Plant and Soil*, 387(1):131–142, Feb. 2015. ISSN 1573-5036. doi: 10.1007/s11104-014-2283-6. URL https://doi.org/10.1007/s11104-014-2283-6.

E. Kyker-Snowman, W. R. Wieder, S. D. Frey, and A. S. Grandy. Stoichiometrically coupled carbon and nitrogen cycling in the MIcrobial-MIneral Carbon Stabilization model version 1.0 (MIMICS-CN v1.0). *Geoscientific Model Development*, 13(9):4413–4434, Sept. 2020. ISSN 1991-9603. doi: 10.5194/gmd-13-4413-2020. URL https://gmd.copernicus.org/articles/13/4413/2020/.

A. Lacointe and P. E. H. Minchin. Modelling phloem and xylem transport within a complex architecture. *Functional Plant Biology*, 35(10):772–780, Nov. 2008. ISSN 1445-4408. doi: 10.1071/FP08085. URL https://doi.org/10.1071/FP08085.

References

M. Landl, A. Haupenthal, D. Leitner, E. Kroener, D. Vetterlein, R. Bol, H. Vereecken, J. Vanderborght, and A. Schnepf. Simulating rhizodeposition patterns around growing and exuding root systems. *in silico Plants*, 3 (2):diab028, July 2021. ISSN 2517-5025. doi: 10.1093/insilicoplants/diab028. URL https://doi.org/10.1093/insilicoplants/diab028.

M. Lang. yggdrasil: a Python package for integrating computational models across languages and scales. *in silico Plants*, 1(1):diz001, Jan. 2019. ISSN 2517-5025. doi: 10.1093/insilicoplants/diz001. URL https://doi.org/10.1093/insilicoplants/diz001.

D. B. Lazof, T. W. Rufty, and M. G. Redinbaugh. Localization of Nitrate Absorption and Translocation within Morphological Regions of the Corn Root. *Plant Physiology*, 100(3):1251–1258, Nov. 1992. ISSN 0032-0889, 1532-2548. doi: 10.1104/pp.100.3.1251. URL https://academic.oup.com/plphys/article/100/3/1251-1258/6085991.

E. Le Deunff, P. Malagoli, and M.-L. Decau. Modelling Nitrogen Uptake in Plants and Phytoplankton: Advantages of Integrating Flexibility into the Spatial and Temporal Dynamics of Nitrate Absorption. *Agronomy*, 9(3):116, Mar. 2019. ISSN 2073-4395. doi: 10.3390/agronomy9030116. URL https://www.mdpi.com/2073-4395/9/3/116. Number: 3 Publisher: Multidisciplinary Digital Publishing Institute.

L. Lejay, X. Gansel, M. Cerezo, P. Tillard, C. Müller, A. Krapp, N. Von Wirén, F. Daniel-Vedele, and A. Gojon. Regulation of Root Ion Transporters by Photosynthesis: Functional Importance and Relation with Hexokinase. *The Plant Cell*, 15(9):2218–2232, Sept. 2003. ISSN 1040-4651, 1532-298X. doi: 10.1105/tpc.013516. URL https://academic.oup.com/plcell/article/15/9/2218-2232/6010119.

N. Lenzewski, P. Mueller, R. J. Meier, G. Liebsch, K. Jensen, and K. Koop-Jakobsen. Dynamics of oxygen and carbon dioxide in rhizospheres of Lobelia dortmanna – a planar optode study of belowground gas exchange between plants and sediment. *New Phytologist*, 218(1):131–141, Apr. 2018. ISSN 1469-8137. doi: 10.1111/nph.14973. URL https://nph.onlinelibrary.wiley.com/doi/10.1111/nph.14973. Publisher: John Wiley & Sons, Ltd.

N. R. Lersten. Morphology and Anatomy of the Wheat Plant. In *Agronomy Monographs*, pages 33–75. American Society of Agronomy, Crop Science Society of America, Soil Science Society of America, Madison, WI, USA, 1987. ISBN 978-0-89118-208-5 978-0-89118-091-3. doi: 10.2134/agronmonogr13.2ed.c2. URL http://doi.wiley.com/10.2134/agronmonogr13.2ed.c2.

E. Liljeroth. Comparisons of early root cortical senescence between barley cultivars, Triticum species and other cereals. *New Phytologist*, 130(4):495–501, 1995. ISSN 1469-8137. doi: 10.1111/j.1469-8137.1995.tb04326.x. URL https://onlinelibrary.wiley.com/doi/abs/10.1111/j.1469-8137.1995.tb04326.x. _eprint: https://nph.onlinelibrary.wiley.com/doi/pdf/10.1111/j.1469-8137.1995.tb04326.x.

E. Liljeroth, J. A. Van Veen, and H. J. Miller. Assimilate translocation to the rhizosphere of two wheat lines and subsequent utilization by rhizosphere microorganisms at two soil nitrogen concentrations. *Soil Biology and Biochemistry*, 22(8):1015–1021, Jan. 1990. ISSN 0038-0717. doi: 10.1016/0038-0717(90)90026-V. URL https://www.sciencedirect.com/science/article/pii/003807179090026V.

E. Lippold, M. Phalempin, S. Schlüter, and D. Vetterlein. Does the lack of root hairs alter root system architecture of Zea mays? *Plant and Soil*, 467(1):267–286, Oct. 2021. ISSN 1573-5036. doi: 10.1007/s11104-021-05084-8. URL https://doi.org/10.1007/s11104-021-05084-8.

C. Liu, T.-X. Ding, A. van der Ent, C. Liu, J. L. Morel, C. Sirguey, W.-S. Liu, Y.-T. Tang, and R.-L. Qiu. A novel method for in situ imaging of root exudates and labile elements reveals phosphorus deficiency-induced mobilization of rare earth elements in the rhizosphere of Phytolacca americana. *Plant and Soil*, 495(1):13–26, Feb. 2024. ISSN 1573-5036. doi: 10.1007/s11104-023-06146-9. URL https://doi.org/10.1007/s11104-023-06146-9.

K.-H. Liu and Y.-F. Tsay. Switching between the two action modes of the dual-affinity nitrate transporter CHL1 by phosphorylation. *The EMBO Journal*, 22(5):1005–1013, Mar. 2003. ISSN 0261-4189. doi: 10.1093/emboj/cdg118. URL https://www.embopress.org/doi/full/10.1093/emboj/cdg118. Number: 5 Publisher: John Wiley & Sons, Ltd.

Y. Liu, S. E. Evans, M. L. Friesen, and L. K. Tiemann. Root exudates shift how N mineralization and N fixation contribute to the plant-available N supply in low fertility soils. *Soil Biology and Biochemistry*, 165:108541, Feb. 2022. ISSN 0038-0717. doi: 10.1016/j.soilbio.2021.108541. URL https://www.sciencedirect.com/science/article/pii/S0038071721004156.

S. Ljutovac. *Coordination dans l'extension des organes aériens et conséquence pour les relations entre les dimensions finales des organes chez le blé.* These de doctorat, Institut national agronomique Paris-Grignon (1971-2006), Jan. 2002. URL https://theses.fr/2002INAP0011.

G. Lobet, L. Pagès, and X. Draye. A Novel Image-Analysis Toolbox Enabling Quantitative Analysis of Root System Architecture. *Plant Physiology*, 157(1):29–39, Sept. 2011. ISSN 1532-2548. doi: 10.1104/pp.111.179895. URL https://academic.oup.com/plphys/article/157/1/29/6108704.

G. Lobet, M. P. Pound, J. Diener, C. Pradal, X. Draye, C. Godin, M. Javaux, D. Leitner, F. Meunier, P. Nacry, T. P. Pridmore, and A. Schnepf. Root System Markup Language: Toward a Unified Root Architecture Description Language. *Plant Physiology*, 167(3):617–627, Mar. 2015. ISSN 0032-0889. doi: 10.1104/pp.114.253625. URL https://doi.org/10.1104/pp.114.253625.

M. Lohse, R. Haag, E. Lippold, D. Vetterlein, T. Reemtsma, and O. J. Lechtenfeld. Direct Imaging of Plant Metabolites in the Rhizosphere Using Laser Desorption Ionization Ultra-High Resolution Mass Spectrometry. *Frontiers in Plant Science*, 12, Dec. 2021. ISSN 1664-462X. doi: 10.3389/fpls.2021.753812. URL https://www.frontiersin.org/journals/plant-science/articles/10.3389/fpls.2021.753812/full. Publisher: Frontiers.

Q. Long, W. Kurth, C. Pradal, V. Migault, and B. Pallas. An Architecture for the Integration of Different Functional and Structural Plant Models. In *Proceedings of the 7th International Conference on Informatics, Environment, Energy and Applications*, IEEA '18, pages 107–113, New York, NY, USA, Mar. 2018. Association for Computing Machinery. ISBN 978-1-4503-6362-4. doi: 10.1145/3208854.3208875. URL https://dl.acm.org/doi/10.1145/3208854.3208875.

E. P.-I. Loo, P. Durán, T. Y. Pang, P. Westhoff, C. Deng, C. Durán, M. Lercher, R. Garrido-Oter, and W. B. Frommer. Sugar transporters spatially organize microbiota colonization along the longitudinal root axis of Arabidopsis. *Cell Host & Microbe*, 32(4):543–556.e6, Apr. 2024. ISSN 19313128. doi: 10.1016/j.chom.2024.02.014. URL https://linkinghub.elsevier.com/retrieve/pii/S193131282400057X.

G. Louarn and Y. Song. Two decades of functional – structural plant modelling: now addressing fundamental questions in systems biology and predictive ecology. *Annals of Botany*, 126(4):501–509, Sept. 2020. ISSN 0305-7364. doi: 10.1093/aob/mcaa143. URL https://doi.org/10.1093/aob/mcaa143.

D. Lowe. Object recognition from local scale-invariant features. In *Proceedings of the Seventh IEEE International Conference on Computer Vision*, volume 2, pages 1150–1157 vol.2, Sept. 1999. doi: 10.1109/ICCV.1999.790410. URL https://ieeexplore.ieee.org/abstract/document/790410.

Y. Lu and W. Fricke. Diurnal changes in apoplast bypass flow of water and ions in salt-stressed wheat (Triticum aestivum L.) and barley (Hordeum vulgare L.). *Physiologia Plantarum*, 175(4):e13955, 2023. ISSN 1399-3054. doi: 10.1111/ppl.13955. URL https://onlinelibrary.wiley.com/doi/abs/10.1111/ppl.13955. _eprint: https://onlinelibrary.wiley.com/doi/pdf/10.1111/ppl.13955.

J. P. Lynch, C. F. Strock, H. M. Schneider, J. S. Sidhu, I. Ajmera, T. Galindo-Castañeda, S. P. Klein, and M. T. Hanlon. Root anatomy and soil resource capture. *Plant and Soil*, 466(1):21–63, Sept. 2021. ISSN 1573-5036. doi: 10.1007/s11104-021-05010-y. URL https://doi.org/10.1007/s11104-021-05010-y.

J. P. Lynch, T. Galindo-Castañeda, H. M. Schneider, J. S. Sidhu, H. Rangarajan, and L. M. York. Root phenotypes for improved nitrogen capture. *Plant and Soil*, 502(1):31–85, Sept. 2024. ISSN 1573-5036. doi: 10.1007/s11104-023-06301-2. URL https://doi.org/10.1007/s11104-023-06301-2.

M. M. Tahat, K. M. Alananbeh, Y. A. Othman, and D. I. Leskovar. Soil Health and Sustainable Agriculture. *Sustainability*, 12(12):4859, Jan. 2020. ISSN 2071-1050. doi: 10.3390/su12124859. URL https://www.mdpi.com/2071-1050/12/12/4859. Number: 12 Publisher: Multidisciplinary Digital Publishing Institute.

T. M. Maaz, T. B. Sapkota, A. J. Eagle, M. B. Kantar, T. W. Bruulsema, and K. Majumdar. Meta-analysis of yield and nitrous oxide outcomes for nitrogen management in agriculture. *Global Change Biology*, 27(11):2343–2360, 2021. ISSN 1365-2486. doi: 10.1111/gcb.15588. URL https://onlinelibrary.wiley.com/doi/abs/10.1111/gcb.15588. _eprint: https://onlinelibrary.wiley.com/doi/pdf/10.1111/gcb.15588.

T. H. Mai, A. Schnepf, H. Vereecken, and J. Vanderborght. Continuum multiscale model of root water and nutrient uptake from soil with explicit consideration of the 3D root architecture and the rhizosphere gradients. *Plant and Soil*, 439(1):273–292, June 2019. ISSN 1573-5036. doi: 10.1007/s11104-018-3890-4. URL https://doi.org/10.1007/s11104-018-3890-4.

P. Malagoli and E. Le Deunff. An updated model for nitrate uptake modelling in plants. II. Assessment of active root involvement in nitrate uptake based on integrated root system age: measured versus modelled outputs. *Annals of Botany*, 113(6):1007–1019, May 2014. ISSN 0305-7364. doi: 10.1093/aob/mcu022. URL https://doi.org/10.1093/aob/mcu022.

E. Malézieux. Designing cropping systems from nature. *Agronomy for Sustainable Development*, 32(1):15–29, Jan. 2012. ISSN 1773-0155. doi: 10.1007/s13593-011-0027-z. URL https://doi.org/10.1007/s13593-011-0027-z.

P. Martre, S. Dueri, J. R. Guarin, F. Ewert, H. Webber, D. Calderini, G. Molero, M. Reynolds, D. Miralles, G. Garcia, H. Brown, M. George, R. Craigie, J.-P. Cohan, J.-C. Deswarte, G. Slafer, F. Giunta, D. Cammarano, R. Ferrise, T. Gaiser, Y. Gao, Z. Hochman, G. Hoogenboom, L. A. Hunt, K. C. Kersebaum, C. Nendel, G. Padovan, A. C. Ruane, A. K. Srivastava, T. Stella, I. Supit, P. Thorburn, E. Wang, J. Wolf, C. Zhao, Z. Zhao, and S. Asseng. Global needs for nitrogen fertilizer to improve wheat yield under climate change. *Nature Plants*, 10(7):1081–1090, July 2024. ISSN 2055-0278. doi: 10.1038/s41477-024-01739-3. URL https://www.nature.com/articles/s41477-024-01739-3. Publisher: Nature Publishing Group.

References

J. Mastný, J. Bárta, E. Kaštovská, and T. Picek. Decomposition of peatland DOC affected by root exudates is driven by specific r and K strategic bacterial taxa. *Scientific Reports*, 11(1):18677, Sept. 2021. ISSN 2045-2322. doi: 10.1038/s41598-021-97698-2. URL https://www.nature.com/articles/s41598-021-97698-2. Publisher: Nature Publishing Group.

D. Maurer, F. Malique, S. Alfarraj, G. Albasher, M. A. Horn, K. Butterbach-Bahl, M. Dannenmann, and H. Rennenberg. Interactive regulation of root exudation and rhizosphere denitrification by plant metabolite content and soil properties. *Plant and Soil*, 467(1):107–127, Oct. 2021. ISSN 1573-5036. doi: 10.1007/s11104-021-05069-7. URL https://doi.org/10.1007/s11104-021-05069-7.

S. McLaughlin, P. Himmighofen, S. A. Khan, A. Siffert, C. A. M. Robert, and J. Sasse. Root Exudation: An In-Depth Experimental Guide. *Plant, Cell & Environment*, 48(5):3052–3065, 2025. ISSN 1365-3040. doi: 10.1111/pce.15311. URL https://onlinelibrary.wiley.com/doi/abs/10.1111/pce.15311. _eprint: https://onlinelibrary.wiley.com/doi/pdf/10.1111/pce.15311.

F. Meunier, V. Couvreur, X. Draye, J. Vanderborght, and M. Javaux. Towards quantitative root hydraulic phenotyping: novel mathematical functions to calculate plant-scale hydraulic parameters from root system functional and structural traits. *Journal of Mathematical Biology*, 75(5):1133–1170, 2017. ISSN 0303-6812. doi: 10.1007/s00285-017-1111-z. URL https://www.ncbi.nlm.nih.gov/pmc/articles/PMC5591877/.

J.-M. Meynard, F. Charrier, M. Fares, M. Le Bail, M.-B. Magrini, A. Charlier, and A. Messéan. Socio-technical lock-in hinders crop diversification in France. *Agronomy for Sustainable Development*, 38(5):54, Oct. 2018. ISSN 1773-0155. doi: 10.1007/s13593-018-0535-1. URL https://doi.org/10.1007/s13593-018-0535-1.

C. A. Midingoyi. *Semantic and modular representation of crop models using a declarative metalanguage*. phdthesis, Institut national d'enseignement supérieur pour l'agriculture, l'alimentation et l'environnement, Dec. 2020. URL https://theses.hal.science/tel-04076267.

C. A. Midingoyi, C. Pradal, A. Enders, D. Fumagalli, H. Raynal, M. Donatelli, I. N. Athanasiadis, C. Porter, G. Hoogenboom, D. Holzworth, F. Garcia, P. Thorburn, and P. Martre. Crop2ML: An open-source multi-language modeling framework for the exchange and reuse of crop model components. *Environmental Modelling & Software*, 142:105055, Aug. 2021. ISSN 1364-8152. doi: 10.1016/j.envsoft.2021.105055. URL https://www.sciencedirect.com/science/article/pii/S1364815221000980.

B. Minasny, B. P. Malone, A. B. McBratney, D. A. Angers, D. Arrouays, A. Chambers, V. Chaplot, Z.-S. Chen, K. Cheng, B. S. Das, D. J. Field, A. Gimona, C. B. Hedley, S. Y. Hong, B. Mandal, B. P. Marchant, M. Martin, B. G. McConkey, V. L. Mulder, S. O'Rourke, A. C. Richer-de Forges, I. Odeh, J. Padarian, K. Paustian, G. Pan, L. Poggio, I. Savin, V. Stolbovoy, U. Stockmann, Y. Sulaeman, C.-C. Tsui, T.-G. Vågen, B. van Wesemael, and L. Winowiecki. Soil carbon 4 per mille. *Geoderma*, 292:59–86, Apr. 2017. ISSN 0016-7061. doi: 10.1016/j.geoderma.2017.01.002. URL https://www.sciencedirect.com/science/article/pii/S0016706117300095.

C. Mitsanis, W. Hurst, and B. Tekinerdogan. A 3D functional plant modelling framework for agricultural digital twins. *Computers and Electronics in Agriculture*, 218:108733, Mar. 2024. ISSN 0168-1699. doi: 10.1016/j.compag.2024.108733. URL https://www.sciencedirect.com/science/article/pii/S0168169924001248.

A. Morales, D. B. Kottelenberg, A. Ernst, R. Vezy, and J. B. Evers. The Virtual Plant Laboratory: a modern plant modelling framework in Julia. *in silico Plants*, 7(1):diaf005, Jan. 2025. ISSN 2517-5025. doi: 10.1093/insilicoplants/diaf005. URL https://doi.org/10.1093/insilicoplants/diaf005.

M. D. Morris. Factorial Sampling Plans for Preliminary Computational Experiments. *Technometrics*, 33(2):161–174, May 1991. ISSN 0040-1706. doi: 10.1080/00401706.1991.10484804. URL https://www.tandfonline.com/doi/abs/10.1080/00401706.1991.10484804. Publisher: ASA Website _eprint: https://www.tandfonline.com/doi/pdf/10.1080/00401706.1991.10484804.

C. W. Mueller, V. Baumert, A. Carminati, A. Germon, M. Holz, I. Kögel-Knabner, S. Peth, S. Schlüter, D. Uteau, D. Vetterlein, P. Teixeira, and A. Vidal. From rhizosphere to detritusphere – Soil structure formation driven by plant roots and the interactions with soil biota. *Soil Biology and Biochemistry*, 193:109396, June 2024. ISSN 00380717. doi: 10.1016/j.soilbio.2024.109396. URL https://linkinghub.elsevier.com/retrieve/pii/S0038071724000853.

G.-J. Nabuurs, R. Mrabet, A. Abu Hatab, M. Bustamante, H. Clark, P. Havlík, J. House, C. Mbow, K. N. Ninan, A. Popp, S. Roe, B. Sohngen, and S. Towprayoon. Agriculture, Forestry and Other Land Uses (Chapter 7). In A. R. Shukla, J. Skea, R. Slade, A. Al Khourdajie, R. van Diemen, D. McCollum, M. Pathak, S. Some, P. Vyas, R. Fradera, M. Belkacemi, A. Hasija, G. Lisboa, S. Luz, and J. Malley, editors, *IPCC 2022: Climate Change 2022: Mitigation of Climate Change. Contribution of Working Group III to the Sixth Assessment Report of the Intergovernmental Panel on Climate Change*, pages 747–860. Cambridge University Press, Cambridge, UK and New York, NY, USA, Sept. 2023. ISBN 978-1-009-15792-6. URL https://www.ipcc.ch/report/ar6/wg3/.

P. Nacry, E. Bouguyon, and A. Gojon. Nitrogen acquisition by roots: physiological and developmental mechanisms ensuring plant adaptation to a fluctuating resource. *Plant and Soil*, 370(1):1–29, Sept. 2013. ISSN 1573-5036. doi: 10.1007/s11104-013-1645-9. URL https://doi.org/10.1007/s11104-013-1645-9.

M. Nakad, J.-C. Domec, S. Sevanto, and G. Katul. Radial – axial transport coordination enhances sugar translocation in the phloem vasculature of plants. *Plant Physiology*, 189(4):2061–2071, Aug. 2022. ISSN 0032-0889. doi: 10.1093/plphys/kiac231. URL https://doi.org/10.1093/plphys/kiac231.

J. Namyslov, Z. Bauriedlová, J. Janoušková, A. Soukup, and E. Tylová. Exodermis and Endodermis Respond to Nutrient Deficiency in Nutrient-Specific and Localized Manner. *Plants*, 9(2):201, Feb. 2020. ISSN 2223-7747. doi: 10.3390/plants9020201. URL https://www.ncbi.nlm.nih.gov/pmc/articles/PMC7076471/.

P. Nannipieri, S. E. Hannula, G. Pietramellara, M. Schloter, T. Sizmur, and S. I. Pathan. Legacy effects of rhizodeposits on soil microbiomes: A perspective. *Soil Biology and Biochemistry*, 184:109107, Sept. 2023. ISSN 00380717. doi: 10.1016/j.soilbio.2023.109107. URL https://linkinghub.elsevier.com/retrieve/pii/S0038071723001694.

G. Neumann, S. Bott, M. Ohler, H.-P. Mock, R. Lippmann, R. Grosch, and K. Smalla. Root exudation and root development of lettuce (Lactuca sativa L. cv. Tizian) as affected by different soils. *Frontiers in Microbiology*, 5, Jan. 2014. ISSN 1664-302X. doi: 10.3389/fmicb.2014.00002. URL https://www.frontiersin.org/journals/microbiology/articles/10.3389/fmicb.2014.00002/full. Publisher: Frontiers.

C. Nguyen. Rhizodeposition of Organic C by Plant: Mechanisms and Controls. In E. Lichtfouse, M. Navarrete, P. Debaeke, S. Véronique, and C. Alberola, editors, *Sustainable Agriculture*, pages 97–123. Springer Netherlands, Dordrecht, 2009. ISBN 978-90-481-2666-8. doi: 10.1007/978-90-481-2666-8_9. URL https://doi.org/10.1007/978-90-481-2666-8_9.

H. A. NGUYEN. *RELIER LES MODÈLES DE CROISSANCE DES CULTURES, LES MODÈLES ARCHITECTURAUX RACINAIRES ET LES PLATEFORMES DE PHÉNOTYPAGE RACINAIRE À HAUT DEBIT*. PhD thesis, 2023.

N. T. Nguyen, S. A. McInturf, and D. G. Mendoza-Cózatl. Hydroponics: A Versatile System to Study Nutrient Allocation and Plant Responses to Nutrient Availability and Exposure to Toxic Elements. *Journal of Visualized Experiments : JoVE*, (113):54317, July 2016. ISSN 1940-087X. doi: 10.3791/54317. URL https://www.ncbi.nlm.nih.gov/pmc/articles/PMC5091364/.

K. L. Nielsen, J. P. Lynch, A. G. Jablokow, and P. S. Curtis. Carbon cost of root systems: an architectural approach. *Plant and Soil*, 165(1):161–169, Mar. 1994. ISSN 1573-5036. doi: 10.1007/BF00009972. URL https://doi.org/10.1007/BF00009972.

A. Nouri, S. Lukas, S. Singh, S. Singh, and S. Machado. When do cover crops reduce nitrate leaching? A global meta-analysis. *Global Change Biology*, 28(15):4736–4749, 2022. ISSN 1365-2486. doi: 10.1111/gcb.16269. URL https://onlinelibrary.wiley.com/doi/abs/10.1111/gcb.16269. _eprint: https://onlinelibrary.wiley.com/doi/pdf/10.1111/gcb.16269.

E. Oburger and D. L. Jones. Sampling root exudates – Mission impossible? *Rhizosphere*, 6:116–133, June 2018. ISSN 2452-2198. doi: 10.1016/j.rhisph.2018.06.004. URL https://www.sciencedirect.com/science/article/pii/S2452219818300661.

E. Oburger, M. Dell 'mour, S. Hann, G. Wieshammer, M. Puschenreiter, and W. W. Wenzel. Evaluation of a novel tool for sampling root exudates from soil-grown plants compared to conventional techniques. *Environmental and Experimental Botany*, 87:235–247, Mar. 2013. ISSN 0098-8472. doi: 10.1016/j.envexpbot.2012.11.007. URL https://www.sciencedirect.com/science/article/pii/S0098847212002328.

A. Ogawa. Sugar Accumulation along the Seminal Root Axis, as Affected by Osmotic Stress in Maize: A Possible Physiological Basis for Plastic Lateral Root Development: Plant Production Science: Vol 8, No 2, 2005. URL https://www.tandfonline.com/doi/abs/10.1626/pps.8.173.

C. Orieux, G. Demarest, M.-L. Decau, P. Beauclair, M.-P. Bataillé, and E. Le Deunff. Changes in 15NO3- Availability and Transpiration Rate Are Associated With a Rapid Diurnal Adjustment of Anion Contents as Well as 15N and Water Fluxes Between the Roots and Shoots. *Frontiers in Plant Science*, 9, Dec. 2018. ISSN 1664-462X. doi: 10.3389/fpls.2018.01751. URL https://www.frontiersin.org/journals/plant-science/articles/10.3389/fpls.2018.01751/full. Publisher: Frontiers.

W. Ouyang, X. Yin, J. Yang, and P. C. Struik. Comparisons with wheat reveal root anatomical and histochemical constraints of rice under water-deficit stress. *Plant and Soil*, 452(1):547–568, July 2020. ISSN 1573-5036. doi: 10.1007/s11104-020-04581-6. URL https://doi.org/10.1007/s11104-020-04581-6.

L. Pagès, C. Bécel, H. Boukcim, D. Moreau, C. Nguyen, and A.-S. Voisin. Calibration and evaluation of ArchiSimple, a simple model of root system architecture. *Ecological Modelling*, 290:76–84, Oct. 2014. ISSN 03043800. doi: 10.1016/j.ecolmodel.2013.11.014. URL https://linkinghub.elsevier.com/retrieve/pii/S0304380013005619.

L. Pagès, O. Pointurier, D. Moreau, A.-S. Voisin, and N. Colbach. Metamodelling a 3D architectural root-system model to provide a simple model based on key processes and species functional groups. *Plant and Soil*, 448 (1-2):231–251, Mar. 2020. ISSN 0032-079X, 1573-5036. doi: 10.1007/s11104-019-04416-z. URL http://link.springer.com/10.1007/s11104-019-04416-z. Number: 1-2.

References

S. Passot, V. Couvreur, F. Meunier, X. Draye, M. Javaux, D. Leitner, L. Pagès, A. Schnepf, J. Vanderborght, and G. Lobet. Connecting the dots between computational tools to analyse soil – root water relations. *Journal of Experimental Botany*, 70(9):2345–2357, Apr. 2019. ISSN 0022-0957. doi: 10.1093/jxb/ery361. URL https://doi.org/10.1093/jxb/ery361.

S. V. Patankar. *Numerical heat transfer and fluid flow*. Jan. 1980. URL https://ui.adsabs.harvard.edu/abs/1980wdch.book.....P. Publication Title: Washington ADS Bibcode: 1980wdch.book.....P.

J. Pausch and Y. Kuzyakov. Carbon input by roots into the soil: Quantification of rhizodeposition from root to ecosystem scale. *Global Change Biology*, 24(1):1–12, 2018. ISSN 1365-2486. doi: 10.1111/gcb.13850. URL https://onlinelibrary.wiley.com/doi/abs/10.1111/gcb.13850. _eprint: https://onlinelibrary.wiley.com/doi/pdf/10.1111/gcb.13850.

J. Pausch, M. Holz, B. Zhu, and W. Cheng. Rhizosphere priming promotes plant nitrogen acquisition by microbial necromass recycling. *Plant, Cell & Environment*, 47(6):1987–1996, 2024. ISSN 1365-3040. doi: 10.1111/pce.14858. URL https://onlinelibrary.wiley.com/doi/abs/10.1111/pce.14858. _eprint: https://onlinelibrary.wiley.com/doi/pdf/10.1111/pce.14858.

K. Paustian, J. Lehmann, S. Ogle, D. Reay, G. P. Robertson, and P. Smith. Climate-smart soils. *Nature*, 532 (7597):49–57, Apr. 2016. ISSN 1476-4687. doi: 10.1038/nature17174. URL https://www.nature.com/articles/nature17174. Publisher: Nature Publishing Group.

B. Peng, K. Guan, J. Tang, E. A. Ainsworth, S. Asseng, C. J. Bernacchi, M. Cooper, E. H. Delucia, J. W. Elliott, F. Ewert, R. F. Grant, D. I. Gustafson, G. L. Hammer, Z. Jin, J. W. Jones, H. Kimm, D. M. Lawrence, Y. Li, D. L. Lombardozzi, A. Marshall-Colon, C. D. Messina, D. R. Ort, J. C. Schnable, C. E. Vallejos, A. Wu, X. Yin, and W. Zhou. Towards a multiscale crop modelling framework for climate change adaptation assessment. *Nature Plants*, 6(4):338–348, Apr. 2020. ISSN 2055-0278. doi: 10.1038/s41477-020-0625-3. URL https://www.nature.com/articles/s41477-020-0625-3. Publisher: Nature Publishing Group.

Y. Peng, E. L. Rieke, I. Chahal, C. E. Norris, K. Janovicek, J. P. Mitchell, K. L. Roozeboom, Z. D. Hayden, J. S. Strock, S. Machado, V. R. Sykes, B. Deen, O. B. Tavarez, A. V. Gamble, K. M. Scow, D. C. Brainard, N. Millar, G. A. Johnson, R. R. Schindelbeck, K. S. M. Kurtz, H. van Es, S. Kumar, and L. L. Van Eerd. Maximizing soil organic carbon stocks under cover cropping: insights from long-term agricultural experiments in North America. *Agriculture, Ecosystems & Environment*, 356:108599, Oct. 2023. ISSN 0167-8809. doi: 10.1016/j.agee.2023.108599. URL https://www.sciencedirect.com/science/article/pii/S016788092300258X.

E. Personeni, C. Nguyen, P. Marchal, and L. Pagès. Experimental evaluation of an efflux – influx model of C exudation by individual apical root segments. *Journal of Experimental Botany*, 58(8):2091–2099, June 2007. ISSN 0022-0957. doi: 10.1093/jxb/erm065. URL https://doi.org/10.1093/jxb/erm065.

L. Perthame, F. Rees, X. Cornilleau, C. Richard-Molard, C. Pradal, and A. Jullien. SIMBAL: A structural-functional plant model to simulate C and N dynamics and shoot-root architecture of winter oilseed rape associated with legumes. Mar. 2023. URL https://hal.inrae.fr/hal-04262992.

E. Peñaloza, L. J. Corcuera, and J. Martinez. Spatial and temporal variation in citrate and malate exudation and tissue concentration as affected by P stress in roots of white lupin. *Plant and Soil*, 241(2):209–221, Apr. 2002. ISSN 1573-5036. doi: 10.1023/A:1016148222687. URL https://doi.org/10.1023/A:1016148222687.

R. P. Phillips, Y. Erlitz, R. Bier, and E. S. Bernhardt. New approach for capturing soluble root exudates in forest soils. *Functional Ecology*, 22(6):990–999, 2008. ISSN 1365-2435. doi: 10.1111/j.1365-2435.2008.01495.x. URL https://onlinelibrary.wiley.com/doi/abs/10.1111/j.1365-2435.2008.01495.x. _eprint: https://onlinelibrary.wiley.com/doi/pdf/10.1111/j.1365-2435.2008.01495.x.

D. C. Plett, K. Ranathunge, V. J. Melino, N. Kuya, Y. Uga, and H. J. Kronzucker. The intersection of nitrogen nutrition and water use in plants: new paths toward improved crop productivity. *Journal of Experimental Botany*, 71(15):4452–4468, July 2020. ISSN 0022-0957. doi: 10.1093/jxb/eraa049. URL https://www.ncbi.nlm.nih.gov/pmc/articles/PMC7382376/.

B. Post, E. Acevedo-Trejos, A. D. Barton, and A. Merico. The XSO framework (v0.1) and Phydra library (v0.1) for a flexible, reproducible, and integrated plankton community modeling environment in Python. *Geoscientific Model Development*, 17(3):1175–1195, Feb. 2024. ISSN 1991-9603. doi: 10.5194/gmd-17-1175-2024. URL https://gmd.copernicus.org/articles/17/1175/2024/.

J. A. Postma, C. Kuppe, M. R. Owen, N. Mellor, M. Griffiths, M. J. Bennett, J. P. Lynch, and M. Watt. OpenSimRoot: widening the scope and application of root architectural models. *New Phytologist*, 215(3):1274–1286, 2017. ISSN 1469-8137. doi: 10.1111/nph.14641. URL https://onlinelibrary.wiley.com/doi/abs/10.1111/nph.14641. _eprint: https://onlinelibrary.wiley.com/doi/pdf/10.1111/nph.14641.

C. Pradal and C. Godin. MTG as a standard representation of plants in FSPMs. *FSPM2020*, 2020.

C. Pradal, S. Dufour-Kowalski, F. Boudon, C. Fournier, and C. Godin. OpenAlea: a visual programming and component-based software platform for plant modelling. *Functional Plant Biology*, 35(10):751–760, Nov. 2008. ISSN 1445-4416. doi: 10.1071/FP08084. URL https://www.publish.csiro.au/fp/FP08084. Publisher: CSIRO PUBLISHING.

C. Pradal, C. Fournier, P. Valduriez, and S. Cohen-Boulakia. OpenAlea: scientific workflows combining data analysis and simulation. In *Proceedings of the 27th International Conference on Scientific and Statistical Database Management*, SSDBM '15, pages 1–6, New York, NY, USA, 2015. Association for Computing Machinery. ISBN 978-1-4503-3709-0. doi: 10.1145/2791347.2791365. URL https://doi.org/10.1145/2791347.2791365.

S. Preibisch, S. Saalfeld, and P. Tomancak. Globally optimal stitching of tiled 3D microscopic image acquisitions. *Bioinformatics*, 25(11):1463–1465, June 2009. ISSN 1367-4803. doi: 10.1093/bioinformatics/btp184. URL https://doi.org/10.1093/bioinformatics/btp184.

C. Proctor and Y. He. Quantifying root extracts and exudates of sedge and shrub in relation to root morphology. *Soil Biology and Biochemistry*, 114:168–180, Nov. 2017. ISSN 0038-0717. doi: 10.1016/j.soilbio.2017.07.006. URL https://www.sciencedirect.com/science/article/pii/S0038071716302711.

N. Punyasu, J. Thaiprasit, S. Kalapanulak, T. Saithong, and J. A. Postma. Modeling cassava root system architecture and the underlying dynamics in shoot – root carbon allocation during the early storage root bulking stage. *Plant and Soil*, 507(1):863–880, Feb. 2025. ISSN 1573-5036. doi: 10.1007/s11104-024-06771-y. URL https://doi.org/10.1007/s11104-024-06771-y.

T. Raihauti, C. Pradal, M. Adam, C. A. Midingoyi, M. Berg-Mohnicke, H. Brown, R. Cichota, A. Enders, T. B. Ferreira, D. Fumagalli, D. Holzworth, G. Hoogenboom, F. A. Oliveira, and P. Martre. Llm-assisted workflow for crop model components generation towards interoperable agricultural platforms. In *Proceedings of the iCROPM 2026 Conference*, 2026. Submitted.

X. Rao and W. Liu. A Guide to Metabolic Network Modeling for Plant Biology. *Plants*, 14(3):484, Jan. 2025. ISSN 2223-7747. doi: 10.3390/plants14030484. URL https://www.mdpi.com/2223-7747/14/3/484. Publisher: Multidisciplinary Digital Publishing Institute.

D. P. Rasse, C. Rumpel, and M.-F. Dignac. Is soil carbon mostly root carbon? Mechanisms for a specific stabilisation. *Plant and Soil*, 269(1):341–356, Feb. 2005. ISSN 1573-5036. doi: 10.1007/s11104-004-0907-y. URL https://doi.org/10.1007/s11104-004-0907-y.

X. Raynaud. Soil properties are key determinants for the development of exudate gradients in a rhizosphere simulation model. *Soil Biology and Biochemistry*, 42(2):210–219, Feb. 2010. ISSN 0038-0717. doi: 10.1016/j.soilbio.2009.10.019. URL https://www.sciencedirect.com/science/article/pii/S0038071709003964.

F. Rees, T. Gérault, M. Gauthier, R. Barillot, C. Richard-Molard, A. Jullien, C. Chenu, C. Pradal, and B. Andrieu. Deciphering spatiotemporal patterns of rhizodeposition with a functional-structural root model: RhizoDep. *Plant and Soil*, Aug. 2025. ISSN 1573-5036. doi: 10.1007/s11104-025-07766-z. URL https://doi.org/10.1007/s11104-025-07766-z.

F. Reyes, B. Pitchers, C. Pradal, and P.-☒ Lauri. Young apple tree development under agroforestry radiative conditions: a multi-scale morphological and architectural dataset. *AoB PLANTS*, 17(4):plaf029, Aug. 2025. ISSN 2041-2851. doi: 10.1093/aobpla/plaf029. URL https://doi.org/10.1093/aobpla/plaf029.

A. Ritter, P. J. Becker, K. Möller, D. Granse, K. Jensen, I. C. Meier, and H. J. Subrahmaniam. Targeting the untargeted: Uncovering the chemical complexity of root exudates. *Plant and Soil*, Aug. 2025. ISSN 1573-5036. doi: 10.1007/s11104-025-07757-0. URL https://doi.org/10.1007/s11104-025-07757-0.

C. A. M. Robert, P. Himmighofen, S. McLaughlin, T. M. Cofer, S. A. Khan, A. Siffert, and J. Sasse. Environmental and Biological Drivers of Root Exudation. *Annual Review of Plant Biology*, 76(Volume 76, 2025): 317–339, May 2025. ISSN 1543-5008, 1545-2123. doi: 10.1146/annurev-arplant-083123-082752. URL https://www.annualreviews.org/content/journals/10.1146/annurev-arplant-083123-082752. Publisher: Annual Reviews.

D. Robinson. Root proliferation, nitrate inflow and their carbon costs during nitrogen capture by competing plants in patchy soil. *Plant and Soil*, 232(1):41–50, May 2001. ISSN 1573-5036. doi: 10.1023/A:1010377818094. URL https://doi.org/10.1023/A:1010377818094.

S. A. Robinson, A. P. Slade, G. G. Fox, R. Phillips, R. G. Ratcliffe, and G. R. Stewart. The Role of Glutamate Dehydrogenase in Plant Nitrogen Metabolism 12. *Plant Physiology*, 95(2):509–516, Feb. 1991. ISSN 0032-0889. URL https://www.ncbi.nlm.nih.gov/pmc/articles/PMC1077561/. Number: 2.

References

T. J. Ross-Elliott, K. H. Jensen, K. S. Haaning, B. M. Wager, J. Knoblauch, A. H. Howell, D. L. Mullendore, A. G. Monteith, D. Paultre, D. Yan, S. Otero, M. Bourdon, R. Sager, J.-Y. Lee, Y. Helariutta, M. Knoblauch, and K. J. Oparka. Phloem unloading in Arabidopsis roots is convective and regulated by the phloem-pole pericycle. *eLife*, 6:e24125, Feb. 2017. ISSN 2050-084X. doi: 10.7554/eLife.24125. URL https://elifesciences.org/articles/24125.

S. Ruffel, S. Freixes, S. Balzergue, P. Tillard, C. Jeudy, M. L. Martin-Magniette, M. J. van der Merwe, K. Kakar, J. Gouzy, A. R. Fernie, M. Udvardi, C. Salon, A. Gojon, and M. Lepetit. Systemic Signaling of the Plant Nitrogen Status Triggers Specific Transcriptome Responses Depending on the Nitrogen Source in Medicago truncatula. *Plant Physiology*, 146(4):2020–2035, Apr. 2008. ISSN 0032-0889. doi: 10.1104/pp.107.115667. URL https://www.ncbi.nlm.nih.gov/pmc/articles/PMC2287368/.

P. R. Ryan, E. Delhaize, and P. J. Randall. Characterisation of Al-stimulated efflux of malate from the apices of Al-tolerant wheat roots. *Planta*, 196(1):103–110, Mar. 1995. ISSN 1432-2048. doi: 10.1007/BF00193223. URL https://doi.org/10.1007/BF00193223.

M. Rötzer, H. Braunmiller, E. Lehndorff, N. Ray, A. Scheibe, and A. Prechtel. Coupled C and N turnover in a dynamic pore scale model reveal the impact of exudate quality on microbial necromass formation. *EGUsphere*, pages 1–33, Oct. 2025. doi: 10.5194/egusphere-2025-4717. URL https://egusphere.copernicus.org/preprints/2025/egusphere-2025-4717/. Publisher: Copernicus GmbH.

C. Saint Cast, G. Lobet, L. Cabrera-Bosquet, V. Couvreur, C. Pradal, F. Tardieu, and X. Draye. Connecting plant phenotyping and modelling communities: lessons from science mapping and operational perspectives. *in silico Plants*, 4(1):diac005, Jan. 2022. ISSN 2517-5025. doi: 10.1093/insilicoplants/diac005. URL https://doi.org/10.1093/insilicoplants/diac005.

J. Sasse, E. Martinoia, and T. Northen. Feed Your Friends: Do Plant Exudates Shape the Root Microbiome? *Trends in Plant Science*, 23(1):25–41, Jan. 2018. ISSN 13601385. doi: 10.1016/j.tplants.2017.09.003. URL https://linkinghub.elsevier.com/retrieve/pii/S1360138517301991.

I. Scheurwater, M. Koren, H. Lambers, and O. K. Atkin. The contribution of roots and shoots to whole plant nitrate reduction in fast- and slow-growing grass species. *Journal of Experimental Botany*, 53(374):1635–1642, July 2002. ISSN 0022-0957. doi: 10.1093/jxb/erf008. Number: 374.

H. M. Schneider, T. Wojciechowski, J. A. Postma, K. M. Brown, A. Lücke, V. Zeisler, L. Schreiber, and J. P. Lynch. Root cortical senescence decreases root respiration, nutrient content and radial water and nutrient transport in barley. *Plant, Cell & Environment*, 40(8):1392–1408, 2017. ISSN 1365-3040. doi: 10.1111/pce.12933. URL https://onlinelibrary.wiley.com/doi/abs/10.1111/pce.12933. _eprint: https://onlinelibrary.wiley.com/doi/pdf/10.1111/pce.12933.

A. Schnepf, D. Leitner, and S. Klepsch. Modeling Phosphorus Uptake by a Growing and Exuding Root System. *Vadose Zone Journal*, 11(3):vzj2012.0001, Aug. 2012. ISSN 1539-1663. doi: 10.2136/vzj2012.0001. URL https://acsess.onlinelibrary.wiley.com/doi/10.2136/vzj2012.0001. Publisher: John Wiley & Sons, Ltd.

A. Schnepf, D. Leitner, M. Landl, G. Lobet, T. H. Mai, S. Morandage, C. Sheng, M. Zörner, J. Vanderborght, and H. Vereecken. CRootBox: a structural – functional modelling framework for root systems. *Annals of Botany*, 121 (5):1033–1053, Apr. 2018. ISSN 0305-7364, 1095-8290. doi: 10.1093/aob/mcx221. URL https://academic.oup.com/aob/article/121/5/1033/4844040.

A. Schnepf, A. Carminati, M. A. Ahmed, M. Ani, P. Benard, J. Bentz, M. Bonkowski, M. Knott, D. Diehl, P. Duddek, E. Kröner, M. Javaux, M. Landl, E. Lehndorff, E. Lippold, A. Lieu, C. W. Mueller, E. Oburger, W. Otten, X. Portell, M. Phalempin, A. Prechtel, R. Schulz, J. Vanderborght, and D. Vetterlein. Linking rhizosphere processes across scales: Opinion. *Plant and Soil*, 478(1):5–42, Sept. 2022. ISSN 1573-5036. doi: 10.1007/s11104-022-05306-7. URL https://doi.org/10.1007/s11104-022-05306-7.

A. Schnepf, C. K. Black, V. Couvreur, B. M. Delory, C. Doussan, A. Heymans, M. Javaux, D. Khare, A. Koch, T. Koch, C. W. Kuppe, M. Landl, D. Leitner, G. Lobet, F. Meunier, J. A. Postma, E. D. Schäfer, T. Selzner, J. Vanderborght, and H. Vereecken. Collaborative benchmarking of functional-structural root architecture models: Quantitative comparison of simulated root water uptake. *in silico Plants*, 5(1):diad005, Jan. 2023. ISSN 2517-5025. doi: 10.1093/insilicoplants/diad005. URL https://doi.org/10.1093/insilicoplants/diad005.

L. Schreiber, R. Franke, K.-D. Hartmann, K. Ranathunge, and E. Steudle. The chemical composition of suberin in apoplastic barriers affects radial hydraulic conductivity differently in the roots of rice (Oryza sativa L. cv. IR64) and corn (Zea mays L. cv. Helix). *Journal of Experimental Botany*, 56(415):1427–1436, May 2005. ISSN 0022-0957. doi: 10.1093/jxb/eri144. URL https://doi.org/10.1093/jxb/eri144.

S. R. Schultes, L. Rüger, D. Niedeggen, J. Freudenthal, K. Frindte, M. F. Becker, R. Metzner, D. Pflugfelder, A. Chlubek, C. Hinz, D. van Dusschoten, S. L. Bauke, M. Bonkowski, M. Watt, R. Koller, and C. Knief. Photosynthate distribution determines spatial patterns in the rhizosphere microbiota of the maize root system. *Nature Communications*, 16(1):7286, Aug. 2025. ISSN 2041-1723. doi: 10.1038/s41467-025-62550-y. URL https://www.nature.com/articles/s41467-025-62550-y. Publisher: Nature Publishing Group.

E. D. Schäfer, M. R. Owen, J. A. Postma, C. Kuppe, C. K. Black, and J. P. Lynch. Simulating Crop Root-RootsSystems Using OpenSimRoot. In M. Lucas, editor, *Plant Systems Biology: Methods and Protocols*, pages 293–323. Springer, New York, NY, 2022. ISBN 978-1-0716-1816-5. doi: 10.1007/978-1-0716-1816-5_15. URL https://doi.org/10.1007/978-1-0716-1816-5_15.

T. Semeraro, A. Scarano, A. Leggieri, A. Calisi, and M. De Caroli. Impact of Climate Change on Agroecosystems and Potential Adaptation Strategies. *Land*, 12(6):1117, June 2023. ISSN 2073-445X. doi: 10.3390/land12061117. URL https://www.mdpi.com/2073-445X/12/6/1117. Number: 6 Publisher: Multidisciplinary Digital Publishing Institute.

S. Sevanto. Phloem transport and drought. *Journal of Experimental Botany*, 65(7):1751–1759, Apr. 2014. ISSN 0022-0957. doi: 10.1093/jxb/ert467. URL https://doi.org/10.1093/jxb/ert467.

I. A. Shabtai, B. D. Hafner, S. A. Schweizer, C. Höschen, A. Possinger, J. Lehmann, and T. Bauerle. Root exudates simultaneously form and disrupt soil organo-mineral associations. *Communications Earth & Environment*, 5(1): 1–12, Nov. 2024. ISSN 2662-4435. doi: 10.1038/s43247-024-01879-6. URL https://www.nature.com/articles/s43247-024-01879-6. Publisher: Nature Publishing Group.

R. Shaw and C. Y. M. Cheung. A Dynamic Multi-Tissue Flux Balance Model Captures Carbon and Nitrogen Metabolism and Optimal Resource Partitioning During Arabidopsis Growth. *Frontiers in Plant Science*, 9, June 2018. ISSN 1664-462X. doi: 10.3389/fpls.2018.00884. URL https://www.frontiersin.org/journals/plant-science/articles/10.3389/fpls.2018.00884/full. Publisher: Frontiers.

S. Shi, L. Condron, S. Larsen, A. E. Richardson, E. Jones, J. Jiao, M. O' Callaghan, and A. Stewart. In situ sampling of low molecular weight organic anions from rhizosphere of radiata pine (Pinus radiata) grown in a rhizotron system. *Environmental and Experimental Botany*, 70(2-3):131–142, Feb. 2011. ISSN 00988472. doi: 10.1016/j.envexpbot.2010.08.010. URL https://linkinghub.elsevier.com/retrieve/pii/S0098847210001620.

M. Y. Siddiqi, A. D. M. Glass, T. J. Ruth, and M. Fernando. Studies of the Regulation of Nitrate Influx by Barley Seedlings Using 13NO3 − 1. *Plant Physiology*, 90(3):806–813, July 1989. ISSN 0032-0889. doi: 10.1104/pp.90.3.806. URL https://doi.org/10.1104/pp.90.3.806.

J. S. Sidhu, I. Ajmera, S. Arya, and J. P. Lynch. RootSlice—A novel functional-structural model for root anatomical phenotypes. *Plant, Cell & Environment*, 46(5):1671–1690, 2023. ISSN 1365-3040. doi: 10.1111/pce.14552. URL https://onlinelibrary.wiley.com/doi/abs/10.1111/pce.14552. _eprint: https://onlinelibrary.wiley.com/doi/pdf/10.1111/pce.14552.

R. Sievänen, C. Godin, T. M. DeJong, and E. Nikinmaa. Functional – structural plant models: a growing paradigm for plant studies. *Annals of Botany*, 114(4):599–603, Sept. 2014. ISSN 0305-7364. doi: 10.1093/aob/mcu175. URL https://doi.org/10.1093/aob/mcu175.

A. G. Smith, E. Han, J. Petersen, N. A. F. Olsen, C. Giese, M. Athmann, D. B. Dresbøll, and K. Thorup-Kristensen. RootPainter: deep learning segmentation of biological images with corrective annotation. *New Phytologist*, 236 (2):774–791, 2022. ISSN 1469-8137. doi: 10.1111/nph.18387. URL https://onlinelibrary.wiley.com/doi/abs/10.1111/nph.18387. _eprint: https://onlinelibrary.wiley.com/doi/pdf/10.1111/nph.18387.

A. Sorgonà, A. Lupini, F. Mercati, L. Di Dio, F. Sunseri, and M. R. Abenavoli. Nitrate uptake along the maize primary root: an integrated physiological and molecular approach. *Plant, Cell & Environment*, 34(7):1127–1140, 2011. ISSN 1365-3040. doi: 10.1111/j.1365-3040.2011.02311.x. URL https://onlinelibrary.wiley.com/doi/abs/10.1111/j.1365-3040.2011.02311.x. _eprint: https://onlinelibrary.wiley.com/doi/pdf/10.1111/j.1365-3040.2011.02311.x.

S. Soualiou, Z. Wang, W. Sun, P. de Reffye, B. Collins, G. Louarn, and Y. Song. Functional – Structural Plant Models Mission in Advancing Crop Science: Opportunities and Prospects. *Frontiers in Plant Science*, 12, Dec. 2021. ISSN 1664-462X. doi: 10.3389/fpls.2021.747142. URL https://www.frontiersin.org/journals/plant-science/articles/10.3389/fpls.2021.747142/full. Publisher: Frontiers.

C.-H. Sun, J.-Q. Yu, and D.-G. Hu. Nitrate: A Crucial Signal during Lateral Roots Development. *Frontiers in Plant Science*, 8, Apr. 2017. ISSN 1664-462X. doi: 10.3389/fpls.2017.00485. URL https://www.frontiersin.org/journals/plant-science/articles/10.3389/fpls.2017.00485/full. Publisher: Frontiers.

Y. Sun, D. S. Goll, J. Chang, P. Ciais, B. Guenet, J. Helfenstein, Y. Huang, R. Lauerwald, F. Maignan, V. Naipal, Y. Wang, H. Yang, and H. Zhang. Global evaluation of the nutrient-enabled version of the land surface model ORCHIDEE-CNP v1.2 (r5986). *Geoscientific Model Development*, 14(4):1987–2010, Apr. 2021. ISSN 1991-959X. doi: 10.5194/gmd-14-1987-2021. URL https://gmd.copernicus.org/articles/14/1987/2021/. Publisher: Copernicus GmbH.

J. Swinnen, J. Van Veen, and R. Merckx. Rhizosphere carbon fluxes in field-grown spring wheat: Model calculations based on 14C partitioning after pulse-labelling. *Soil Biology and Biochemistry*, 26(2):171–182, Feb. 1994. ISSN 00380717. doi: 10.1016/0038-0717(94)90160-0. URL https://linkinghub.elsevier.com/retrieve/pii/0038071794901600.

References

A. K. Sırcan, T. Streck, A. Schnepf, M. Giraud, A. Lattacher, E. Kandeler, C. Poll, and H. Pagel. Trait-based modeling of microbial interactions and carbon turnover in the rhizosphere. *Soil Biology and Biochemistry*, 202: 109698, Mar. 2025. ISSN 0038-0717. doi: 10.1016/j.soilbio.2024.109698. URL https://www.sciencedirect.com/science/article/pii/S0038071724003900.

J. Tang, L. Xia, and C. Huang. Explainable Spatio-Temporal Graph Neural Networks. In *Proceedings of the 32nd ACM International Conference on Information and Knowledge Management*, CIKM '23, pages 2432–2441, New York, NY, USA, Oct. 2023. Association for Computing Machinery. ISBN 979-8-4007-0124-5. doi: 10.1145/3583780.3614871. URL https://dl.acm.org/doi/10.1145/3583780.3614871.

A. R. Taylor and A. J. Bloom. Ammonium, nitrate, and proton fluxes along the maize root. *Plant, Cell & Environment*, 21(12):1255–1263, 1998. ISSN 1365-3040. doi: 10.1046/j.1365-3040.1998.00357.x. URL https://onlinelibrary.wiley.com/doi/abs/10.1046/j.1365-3040.1998.00357.x. _eprint: https://onlinelibrary.wiley.com/doi/pdf/10.1046/j.1365-3040.1998.00357.x.

M. Tegeder and U. Z. Hammes. The way out and in: phloem loading and unloading of amino acids. *Current Opinion in Plant Biology*, 43:16–21, June 2018. ISSN 1369-5266. doi: 10.1016/j.pbi.2017.12.002. URL https://www.sciencedirect.com/science/article/pii/S1369526617301450. R.

J. H. M. Thornley and M. G. R. Cannell. Modelling the Components of Plant Respiration: Representation and Realism. *Annals of Botany*, 85(1):55–67, Jan. 2000. ISSN 0305-7364. doi: 10.1006/anbo.1999.0997. URL https://www.sciencedirect.com/science/article/pii/S0305736499909976.

D. Tilman, C. Balzer, J. Hill, and B. L. Befort. Global food demand and the sustainable intensification of agriculture. *Proceedings of the National Academy of Sciences*, 108(50):20260–20264, Dec. 2011. doi: 10.1073/pnas.1116437108. URL https://www.pnas.org/doi/abs/10.1073/pnas.1116437108. Publisher: Proceedings of the National Academy of Sciences.

A. Tixier, M. Forest, M. Prudent, V. Durey, M. Zwieniecki, and R. L. Barnard. Root exudation of carbon and nitrogen compounds varies over the day – night cycle in pea: The role of diurnal changes in internal pools. *Plant, Cell & Environment*, 46(3):962–974, 2023. ISSN 1365-3040. doi: 10.1111/pce.14523. URL https://onlinelibrary.wiley.com/doi/abs/10.1111/pce.14523. _eprint: https://onlinelibrary.wiley.com/doi/pdf/10.1111/pce.14523.

A. Tixier, R. L. Barnard, C. Jeudy, and M. Prudent. Sugar and amino acid exhibit different spatial patterns of root exudation in response to water stress and n limitation in pea. *Plant and Soil*, 512(1):1261–1277, July 2025. ISSN 1573-5036. doi: 10.1007/s11104-024-07139-y. URL https://doi.org/10.1007/s11104-024-07139-y.

R. Tiziani, M. Puschenreiter, E. Smolders, T. Mimmo, J. C. Herrera, S. Cesco, and J. Santner. Millimetre-resolution mapping of citrate exuded from soil-grown roots using a novel, low-invasive sampling technique. *Journal of Experimental Botany*, 72(10):3513–3525, May 2021. ISSN 0022-0957. doi: 10.1093/jxb/erab123. URL https://doi.org/10.1093/jxb/erab123.

H.-H. Tsai, Y. Tang, L. Jiang, X. Xu, V. Dénervaud Tendon, J. Pang, Y. Jia, K. Wippel, J. Vacheron, C. Keel, T. G. Andersen, N. Geldner, and F. Zhou. Localized glutamine leakage drives the spatial structure of root microbial colonization. *Science*, 390(6768):eadu4235, Oct. 2025. ISSN 0036-8075, 1095-9203. doi: 10.1126/science.adu4235. URL https://www.science.org/doi/10.1126/science.adu4235.

F. N. Tubiello, K. Karl, A. Flammini, J. Gütschow, G. Obli-Laryea, G. Conchedda, X. Pan, S. Y. Qi, H. Halldórudóttir Heiðarsdóttir, N. Wanner, R. Quadrelli, L. Rocha Souza, P. Benoit, M. Hayek, D. Sandalow, E. Mencos Contreras, C. Rosenzweig, J. Rosero Moncayo, P. Conforti, and M. Torero. Pre- and post-production processes increasingly dominate greenhouse gas emissions from agri-food systems. *Earth System Science Data*, 14(4): 1795–1809, Apr. 2022. ISSN 1866-3508. doi: 10.5194/essd-14-1795-2022. URL https://essd.copernicus.org/articles/14/1795/2022/. Publisher: Copernicus GmbH.

R. Ursache, T. G. Andersen, P. Marhavý, and N. Geldner. A protocol for combining fluorescent proteins with histological stains for diverse cell wall components. *The Plant Journal*, 93(2):399–412, Jan. 2018. ISSN 0960-7412, 1365-313X. doi: 10.1111/tpj.13784. URL https://onlinelibrary.wiley.com/doi/10.1111/tpj.13784.

A. Usyskin-Tonne, Y. Hadar, U. Yermiyahu, and D. Minz. Elevated CO2 and nitrate levels increase wheat root-associated bacterial abundance and impact rhizosphere microbial community composition and function. *The ISME Journal*, 15(4):1073–1084, Apr. 2021. ISSN 1751-7370. doi: 10.1038/s41396-020-00831-8. URL https://www.nature.com/articles/s41396-020-00831-8. Publisher: Nature Publishing Group.

J. Vaillant, I. Grechi, F. Normand, and F. Boudon. Towards virtual modelling environments for functional – structural plant models based on Jupyter notebooks: application to the modelling of mango tree growth and development. *in silico Plants*, 4(1):diab040, Jan. 2022. ISSN 2517-5025. doi: 10.1093/insilicoplants/diab040. URL https://academic.oup.com/insilicoplants/article/doi/10.1093/insilicoplants/diab040/6461084.

M. Van de Broek, S. Ghiasi, C. Decock, A. Hund, S. Abiven, C. Friedli, R. A. Werner, and J. Six. The soil organic carbon stabilization potential of old and new wheat cultivars: a $^{13}CO_2$-labeling study. *Biogeosciences*, 17(11): 2971–2986, June 2020. ISSN 1726-4170. doi: 10.5194/bg-17-2971-2020. URL https://bg.copernicus.org/articles/17/2971/2020/. Publisher: Copernicus GmbH.

L. Veerman, K. Kalbitz, J. C. Schoorl, and A. Tietema. Split-root labelling to investigate 15N rhizodeposition by Pinus sylvestris and Picea abies*. *Isotopes in Environmental and Health Studies*, 54(1):16–27, Jan. 2018. ISSN 1025-6016. doi: 10.1080/10256016.2017.1352586. URL https://doi.org/10.1080/10256016.2017.1352586. Publisher: Taylor & Francis _eprint: https://doi.org/10.1080/10256016.2017.1352586.

D. Veličković, T. Winkler, V. Balasubramanian, T. Wietsma, C. R. Anderton, A. H. Ahkami, and K. Zemaitis. RhizoMAP: a comprehensive, nondestructive, and sensitive platform for metabolic imaging of the rhizosphere. *Plant Methods*, 20:117, Aug. 2024. ISSN 1746-4811. doi: 10.1186/s13007-024-01249-5. URL https://www.ncbi.nlm.nih.gov/pmc/articles/PMC11297713/.

D. Vetterlein, E. Lippold, S. Schreiter, M. Phalempin, T. Fahrenkampf, F. Hochholdinger, C. Marcon, M. Tarkka, E. Oburger, M. Ahmed, M. Javaux, and S. Schlüter. Experimental platforms for the investigation of spatiotemporal patterns in the rhizosphere—Laboratory and field scale. *Journal of Plant Nutrition and Soil Science*, 184 (1):35–50, 2021. ISSN 1522-2624. doi: 10.1002/jpln.202000079. URL https://onlinelibrary.wiley.com/doi/abs/10.1002/jpln.202000079. _eprint: https://onlinelibrary.wiley.com/doi/pdf/10.1002/jpln.202000079.

P. Voothuluru, D. M. Braun, and J. S. Boyer. An in Vivo Imaging Assay Detects Spatial Variability in Glucose Release from Plant Roots. *Plant Physiology*, 178(3):1002–1010, Nov. 2018. ISSN 0032-0889. doi: 10.1104/pp.18.00614. URL https://doi.org/10.1104/pp.18.00614.

V. Vranova, K. Rejsek, K. R. Skene, D. Janous, and P. Formanek. Methods of collection of plant root exudates in relation to plant metabolism and purpose: A review. *Journal of Plant Nutrition and Soil Science*, 176(2): 175–199, Apr. 2013. ISSN 1436-8730, 1522-2624. doi: 10.1002/jpln.201000360. URL https://onlinelibrary.wiley.com/doi/10.1002/jpln.201000360.

T. S. Wacker, F. van der Bom, B. M. Delory, D. Vetterlein, J. A. Postma, K. A. Nagel, A. Schnepf, and D. B. Dresbøll. Back to the roots: standardizing root length density terminology. *Plant and Soil*, Nov. 2024. ISSN 1573-5036. doi: 10.1007/s11104-024-07075-x. URL https://doi.org/10.1007/s11104-024-07075-x.

C. Wang and Y. Kuzyakov. Mechanisms and implications of bacterial – fungal competition for soil resources. *The ISME Journal*, 18(1):wrae073, Jan. 2024. ISSN 1751-7362. doi: 10.1093/ismejo/wrae073. URL https://doi.org/10.1093/ismejo/wrae073.

G. Wang, Q. Gao, Y. Yang, S. E. Hobbie, P. B. Reich, and J. Zhou. Soil enzymes as indicators of soil function: A step toward greater realism in microbial ecological modeling. *Global Change Biology*, 28(5):1935–1950, 2022. ISSN 1365-2486. doi: 10.1111/gcb.16036. URL https://onlinelibrary.wiley.com/doi/abs/10.1111/gcb.16036. _eprint: https://onlinelibrary.wiley.com/doi/pdf/10.1111/gcb.16036.

M. Wang, N. White, J. Hanan, D. He, E. Wang, B. Cribb, D. J. Kriticos, D. Paini, and V. Grimm. Parameter estimation for functional – structural plant models when data are scarce: using multiple patterns for rejecting unsuitable parameter sets. *Annals of Botany*, 126(4):559–570, Sept. 2020. ISSN 0305-7364. doi: 10.1093/aob/mcaa016. URL https://doi.org/10.1093/aob/mcaa016.

M. Watt, M. E. McCully, and J. A. Kirkegaard. Soil strength and rate of root elongation alter the accumulation of Pseudomonas spp. and other bacteria in the rhizosphere of wheat. *Functional Plant Biology*, 30(5):483–491, June 2003. ISSN 1445-4408. doi: 10.1071/FP03045. URL https://doi.org/10.1071/FP03045.

C. E. Wells and D. M. Eissenstat. Beyond the Roots of Young Seedlings: The Influence of Age and Order on Fine Root Physiology. *Journal of Plant Growth Regulation*, 21(4):324–334, Dec. 2002. ISSN 1435-8107. doi: 10.1007/s00344-003-0011-1. URL https://doi.org/10.1007/s00344-003-0011-1.

A. Wezel, S. Bellon, T. Doré, C. Francis, D. Vallod, and C. David. Agroecology as a Science, a Movement and a Practice: A Review. *Department of Agronomy and Horticulture: Faculty Publications*, Jan. 2009. URL https://digitalcommons.unl.edu/agronomyfacpub/927.

E. D. Whalen, A. S. Grandy, N. W. Sokol, M. Keiluweit, J. Ernakovich, R. G. Smith, and S. D. Frey. Clarifying the evidence for microbial- and plant-derived soil organic matter, and the path toward a more quantitative understanding. *Global Change Biology*, 28(24):7167–7185, 2022. ISSN 1365-2486. doi: 10.1111/gcb.16413. URL https://onlinelibrary.wiley.com/doi/abs/10.1111/gcb.16413. _eprint: https://onlinelibrary.wiley.com/doi/pdf/10.1111/gcb.16413.

J. W. White, L. A. Hunt, K. J. Boote, J. W. Jones, J. Koo, S. Kim, C. H. Porter, P. W. Wilkens, and G. Hoogenboom. Integrated description of agricultural field experiments and production: The ICASA Version 2.0 data standards. *Computers and Electronics in Agriculture*, 96:1–12, Aug. 2013. ISSN 0168-1699. doi: 10.1016/j.compag.2013.04.003. URL https://www.sciencedirect.com/science/article/pii/S016816991300077X.

References

F. Wichern, E. Eberhardt, J. Mayer, R. G. Joergensen, and T. Müller. Nitrogen rhizodeposition in agricultural crops: Methods, estimates and future prospects. *Soil Biology and Biochemistry*, 40(1):30–48, Jan. 2008. ISSN 0038-0717. doi: 10.1016/j.soilbio.2007.08.010. URL https://www.sciencedirect.com/science/article/pii/S0038071707003434.

J. Wiesenbauer, A. König, S. Gorka, L. Marchand, N. Nunan, B. Kitzler, E. Inselsbacher, and C. Kaiser. A pulse of simulated root exudation alters the composition and temporal dynamics of microbial metabolites in its immediate vicinity. *Soil Biology and Biochemistry*, 189:109259, Feb. 2024. ISSN 0038-0717. doi: 10.1016/j.soilbio.2023.109259. URL https://www.sciencedirect.com/science/article/pii/S0038071723003218.

A. Williams, H. Langridge, A. L. Straathof, G. Fox, H. Muhammadali, K. A. Hollywood, Y. Xu, R. Goodacre, and F. T. De Vries. Comparing root exudate collection techniques: An improved hybrid method. *Soil Biology and Biochemistry*, 161:108391, Oct. 2021. ISSN 00380717. doi: 10.1016/j.soilbio.2021.108391. URL https://linkinghub.elsevier.com/retrieve/pii/S0038071721002650.

D. R. Woodruff. Influence of nodal root production on wheat yields under conditions of limited soil water and phosphorus supply. *Queensland Journal of Agricultural and Animal Sciences*, 37(1):53–62, 1980. URL https://era.dpi.qld.gov.au/id/eprint/11388/. Number: 1.

M. O. Yee, P. Kim, Y. Li, A. K. Singh, T. R. Northen, and R. Chakraborty. Specialized Plant Growth Chamber Designs to Study Complex Rhizosphere Interactions. *Frontiers in Microbiology*, 12:625752, Mar. 2021. ISSN 1664-302X. doi: 10.3389/fmicb.2021.625752. URL https://www.ncbi.nlm.nih.gov/pmc/articles/PMC8032546/.

T. Yoneyama, K. , Kenzo, , and K. Kumazawa. Nitrogen transport in intact corn roots. *Soil Science and Plant Nutrition*, 21(4):371–377, Dec. 1975. ISSN 0038-0768. doi: 10.1080/00380768.1975.10432652. URL https://doi.org/10.1080/00380768.1975.10432652. Publisher: Taylor & Francis _eprint: https://doi.org/10.1080/00380768.1975.10432652.

L. M. York, M. Silberbush, and J. P. Lynch. Spatiotemporal variation of nitrate uptake kinetics within the maize (Zea mays L.) root system is associated with greater nitrate uptake and interactions with architectural phenes. *Journal of Experimental Botany*, 67(12):3763–3775, June 2016. ISSN 0022-0957. doi: 10.1093/jxb/erw133. URL https://doi.org/10.1093/jxb/erw133.

L. M. York, S. Slack, M. J. Bennett, and M. J. Foulkes. Wheat shovelomics I: A field phenotyping approach for characterising the structure and function of root systems in tillering species, Mar. 2018. URL http://biorxiv.org/lookup/doi/10.1101/280875.

Y. Zhang, J. M. Lavallee, A. D. Robertson, R. Even, S. M. Ogle, K. Paustian, and M. F. Cotrufo. Simulating measurable ecosystem carbon and nitrogen dynamics with the mechanistically defined MEMS 2.0 model. *Biogeosciences*, 18(10):3147–3171, May 2021. ISSN 1726-4170. doi: 10.5194/bg-18-3147-2021. URL https://bg.copernicus.org/articles/18/3147/2021/. Publisher: Copernicus GmbH.

Y. Zhong, W. Yan, J. Chen, and Z. Shangguan. Net ammonium and nitrate fluxes in wheat roots under different environmental conditions as assessed by scanning ion-selective electrode technique. *Scientific Reports*, 4(1):7223, Nov. 2014. ISSN 2045-2322. doi: 10.1038/srep07223. URL https://www.nature.com/articles/srep07223. Publisher: Nature Publishing Group.

Q. Zhu, W. J. Riley, and J. Tang. A new theory of plant – microbe nutrient competition resolves inconsistencies between observations and model predictions. *Ecological Applications*, 27(3):875–886, Apr. 2017. ISSN 1939-5582. doi: 10.1002/eap.1490. URL https://esajournals.onlinelibrary.wiley.com/doi/10.1002/eap.1490. Publisher: John Wiley & Sons, Ltd.

S. Ćavar Zeljković, N. De Diego, L. Drašar, J. Nisler, L. Havlíček, L. Spíchal, and P. Tarkowski. Comprehensive LC-MS/MS analysis of nitrogen-related plant metabolites. *Journal of Experimental Botany*, 75(17):5390–5411, Sept. 2024. ISSN 0022-0957. doi: 10.1093/jxb/erae129. URL https://doi.org/10.1093/jxb/erae129.

Supplementary Material

Hereafter are listed the supplementary figures, tables and notes of the manuscript, grouped by chapter (Ch. 2 to 5). As a complementary view, the following table of content summarizes the complete list of supplementary figures and tables with hyperlinks.

- Chapter 2

List of Supplementary Figures

6.1 Final conceptual scheme of the thesis 167

6.2 Inputs provided to Root-CyNAPS and resolution loop 224

6.3 Evolution of input root system architecture over plant age 225

6.4 3D static root system architecture displaying the root type . . . 226

6.5 Evolution of the hexose concentration in the root system symplasm with plant age simulated by RhizoDep 227

6.6 Temporal variations of Root-CyNAPS outputs over 24 hours of simulations 228

6.7 Evolution of length-wise net mineral N uptake with the thermal time since root tissue formation 229

6.8 Evolution of massic net mineral N uptake with the distance from tip 230

6.9 Decomposition of net N uptake between gross N uptake and N losses through diffusion with distance from root tip 231

6.10 Evolution of length-wise net N uptake with various state variables of the Root-CyNAPS model 232

6.11 Evolution of length-wise gross N uptake with various state variables of the Root-CyNAPS model 233

6.12 Evolution of length-wise N loss through diffusion with various state variables of the Root-CyNAPS model 234

6.13 Percentage of root system structural mass as a function of the percentage of root system length for plant ages from 10 to 60 days-old 235

6.14 Contribution of the 10% most active root length in whole-plant N budget, as a function of root system age and nitrate concentration in culture solution 236

6.15 Simulated shoot N content by *CN-Wheat* and *Wheat-BRIDGES* 243
6.16 Simulated C rhizodeposition and N uptake as a function of C allocation to roots . . . 243
6.17 Simulated C rhizodeposition and N uptake as a function of massic photosynthesis . . . 244
6.18 Simulated C rhizodeposition and N uptake as a function of massic C & N allocation to roots . . . 244
6.19 Simulated spatial distribution of length-related net mineral N uptake along roots . . . 245
6.20 Simulated spatial distribution of length-related N rhizodeposition along roots . . . 246
6.21 Simulated spatial distribution of length-related water uptake along roots . . . 247
6.22 Simulated spatial distribution of length-related C rhizodeposition and N uptake along a single root . . . 248
6.23 Simulation scenario applied to *Root-BRIDGES* . . . 249
6.24 Nitrate patch scenario applied to *Root-BRIDGES* . . . 250
6.25 Data analysis workflow for FSPM time-series outputs . . . 251
6.26 Rhizotrons' temperature profile over soil depth . . . 252

List of Supplementary Tables

6.1 Complete list of equations, description and units of the Root-CyNAPS model . . . 203
6.2 Description and units of the Root-CyNAPS model parameters . . . 214

Chapter 2 Supplementary Material

This corresponds to the manuscript entitled "Do specific root zones shape plant net N uptake? Modeling insights from Root-CyNAPS", by Tristan Gérault, Christophe Pradal, Romain Barillot, Céline Richard-Molard, Marion Gauthier, Alexandra Jullien, and Frédéric Rees submited to *in silico Plants*.

SUPPLEMENTARY MATERIAL

Additional information is available in the Supplementary Material file for more details about the *Root-CyNAPS* model. A complete list of model equations and parametrization in the case of wheat is detailed. We also present model inputs, parametrization, simulated heterogeneous N flows along roots and their physiological determinants, as well as the contribution of most active N exchange zones to plant balance. The document is structured as follows :

- Table S1: Complete list of Root-CyNAPS equations
- Table S2: Complete list of Root-CyNAPS parameters
- Detailed information on inputs provided to *Root-CyNAPS* for the presented use cases on wheat : Figure S1, S2, S3 and S4
- Figure S5: Stabilization of the model's outputs over the 24h of simulation in a static root system architecture
- Figure S6: Comparison of the evolution of mineral N concentration between 1-h and 1-min time-steps during a 24h simulation of Root-CyNAPS.
- Net N uptake representation along thermal age of the root segments (S7), alternative normalization by segment structural mass (Fig. S8), and decomposition between gross uptake and N exudation (Fig. S9) for scenario 14.
- Correlation plots showing the possible determinants of *most active root zones* : Figures S10, S11 and S12:
- Figure S13: Percentage of root-system structural mass with the percentage of root system length between 10 and 60 days-old plants.
- Figure S14: Contribution of the 10% most active root length in whole-plant N budget, as a function of root system age and nitrate concentration in culture solution.
- Supplementary note A and Figure S15: Methodological note on the acquisition of anatomical parameters for Root-CyNAPS
- Supplementary note B: Further discussion on the determinants of simulated *most active root zones*.
- Supplementary note C: Further presentation details of the *RhizoDep* model used for *Root-CyNAPS* input estimation.

Model Equations

Table S1: Complete list of equations, description and units of the Root-CyNAPS model. Model variables are shown in black, parameters in blue, and input variables in red. All quantities are expressed in SI units. Unless otherwise stated, variables are expressed for a specific segment i at the current time-step t. *adim* stands for *Dimensionless* variable for concision. Unless included in the core text of the article, supplementary equations are numbered with a *S* prefix. gDW refers to grams of root segment dry structural mass.

Equation	Description	Unit (SI)	Eq. n°
Metabolites balance			
$\frac{d\, n^{Ni}_{symp}}{dt} = Tf^{Ni}_{soil\Rightarrow symp} + Tf^{Ni}_{xylem\rightarrow symp} + Tf^{Ni}_{mycorrhiza\Rightarrow symp} + Tf^{Ni}_{rhizobia\Rightarrow symp} - Tf^{Ni}_{symp\rightarrow soil} - Tf^{Ni}_{symp\Rightarrow xylem} + (Mt^{AA\Rightarrow Ni,hexose}_{symp} - Mt^{Ni,hexose\Rightarrow AA}_{symp}) \cdot nb_{N:AA}$	Quantity derivative for mineral nitrogen in parenchyma symplasm	$mol{\cdot}s^{-1}$ of mineral nitrogen	??
$\frac{d\, n^{Ni}_{xylem(i)}}{dt} = \sum_k^{children} Tf^{Ni}_{xylem(k)\rightarrow xylem(i)} - Tf^{Ni}_{xylem(i)\rightarrow xylem(i-1)} + Tf^{Ni}_{symp(i)\Rightarrow xylem(i)} + Tf^{Ni,\text{Advection}}_{soil(i)\rightarrow xylem(i)} - Tf^{Ni}_{xylem(i)\rightarrow symp(i)} - Tf^{Ni}_{xylem(i)\rightarrow soil(i)}$	Quantity derivative for mineral nitrogen in xylem apoplasm of segment i	$mol{\cdot}s^{-1}$ of mineral nitrogen	??
$\frac{d\, n^{AA}_{symp}}{dt} = Tf^{AA}_{soil\Rightarrow symp} + Tf^{AA}_{phloem\rightarrow symp} - Tf^{AA}_{symp\Rightarrow xylem} - Tf^{AA}_{symp\rightarrow soil} + Mt^{Ni,hexose\Rightarrow AA}_{symp} + Mt^{storage\Rightarrow AA}_{symp} - Mt^{AA\Rightarrow Ni,hexose}_{symp} - Mt^{AA,hexose\Rightarrow struct}_{symp} \cdot nb_{AA:struct} - Mt^{AA\Rightarrow storage}_{symp} \cdot nb_{AA:stor}$	Quantity derivative for amino acids in parenchyma symplasm	$mol{\cdot}s^{-1}$ of amino acids	??
$\frac{d\, n^{AA}_{xylem(i)}}{dt} = \sum_k^{children} Tf^{AA}_{xylem(k)\rightarrow xylem(i)} - Tf^{AA}_{xylem(i)\rightarrow xylem(i-1)} + Tf^{AA}_{symp(i)\Rightarrow xylem(i)} + Tf^{AA,\text{Advection}}_{soil(i)\rightarrow xylem(i)} - Tf^{AA}_{xylem(i)\rightarrow symp(i)} - Tf^{AA}_{xylem(i)\rightarrow soil(i)}$	Quantity derivative for amino acids in xylem apoplasm of segment i	$mol{\cdot}s^{-1}$ of amino acids	S 1
$\frac{d\, n^{AA}_{phloem(i)}}{dt} = \sum_k^{children} Tf^{AA}_{phloem(k)\rightarrow phloem(i)} - Tf^{AA}_{phloem(i)\rightarrow phloem(i-1)} - Tf^{AA}_{phloem(i)\rightarrow symp(i)}$	Quantity derivative for amino acids in phloem symplasm of segment i	$mol{\cdot}s^{-1}$ of amino acids	S 2
$\frac{d\, n^{Prot}_{symp}}{dt} = Mt^{AA\Rightarrow storage}_{symp} - \frac{Mt^{storage\Rightarrow AA}_{symp}}{nb_{AA:stor}}$	Quantity of storage proteins in parenchyma symplasm	$mol{\cdot}s^{-1}$ of storage proteins	??

Table S1: continued from previous page

Equation	Description	Unit (SI)	Eq. n°
$\frac{d\ V_{symp}^{water}}{dt} = \frac{d\ V_{xylem}^{water}}{dt} = \frac{d\ V_{phloem}^{water}}{dt} = 0$	Conservation equation (null derivative) for water volume and mass at constant water density.	$m^3 \cdot s^{-1}$ of water	??
Massic and volumic concentrations			
$[Ni_{symp}]_m = \frac{n_{symp}^{Ni}}{m_{root}^{struct}}$	Mineral N massic concentration in symplasm. Amino acids and storage proteins massic concentrations in parenchyma symplasm are expressed the same way.	$mol \cdot gDW^{-1}$ of mineral N	S 3
$[Ni_{symp}]_v = \frac{n_{symp}^{Ni}}{\pi \cdot R^2 \cdot r_{S_{symp}}^{CrossSection} \cdot L \cdot (1 - f_{symp}^{CellLine})}$	Mineral N volumic concentration in symplasm. Amino acids and storage proteins volumic concentrations in parenchyma symplasm are expressed the same way.	$mol \cdot m^{-3}$ of mineral N	??
$[Ni_{xylem}]_v = \frac{n_{xylem}^{Ni}}{\pi \cdot R^2 \cdot r_{S_{xylem}}^{CrossSection} \cdot L \cdot (1 - f_{xylem}^{CellLine})}$	Mineral N volumic concentration in xylem apoplasm. Amino acids volumic concentration in xylem apoplasm is expressed the same way.	$mol \cdot m^{-3}$ of mineral N	S 4
$[AA_{phloem}]_v = \frac{n_{phloem}^{AA}}{\pi \cdot R^2 \cdot r_{S_{phloem}}^{CrossSection} \cdot L \cdot (1 - f_{phloem}^{CellLine})}$	Amino acids volumic concentration in phloem symplasm.	$mol \cdot m^{-3}$ of amino acids	S 5
Exchange surfaces and differentiation processes			

Table S1: continued from previous page

Equation	Description	Unit (SI)	Eq. n°
$S_{soil\|symp} = 2 \cdot \pi \cdot R \cdot L.(\frac{Sepidermis}{Scylinder} + \frac{Scortex}{Scylinder} \cdot K_{Exo} + \frac{Sstele}{Scylinder} \cdot K_{Endo}) + S_{RootHairs}$	Exchange surface between soil solution and all accessible parenchyma of the root segment	m^2	??
$K_{endo} = \max(K_{endo,age} \quad , \quad 1 - \frac{\Delta t_{endo}^{disrupt}}{\Delta t_{endo,max}^{disrupt}})$	Differentiation factor for endodermis related to root segment aging and lateral primordium emergence (1 to 0)	*adim*	??
$K_{endo,age} = 1 - L_{Endo}^{Diff} \cdot \exp[\ln(0.01) \cdot \exp(r_{Endo}^{Diff}(s_{Endo}^{Diff} - age(T_{ref})))]$	Differentiation factor for endodermis related to root segment aging (1 to 0)	*adim*	??
$K_{exo} = \max(K_{exo,age} \quad , \quad 1 - \frac{\Delta t_{exo}^{disrupt}}{\Delta t_{exo,max}^{disrupt}})$	Differentiation factor for exodermis related to root segment aging and lateral primordium emergence (1 to 0)	*adim*	S 6
$K_{exo,age} = 1 - L_{Exo}^{Diff} \cdot \exp[\ln(0.01) \cdot \exp(r_{Exo}^{Diff}(s_{Exo}^{Diff} - age(T_{ref})))]$	Differentiation factor for exodermis related to root segment aging (1 to 0)	*adim*	S 7
$S_{symp\|xylem} = 2.\pi.R.L.\frac{S_{stele}}{S_{cylinder}}.Diff_{protoxylem}$	Exchange surface between parenchyma symplasm and xylem apoplasm	m^2	??
$Diff_{protoxylem} = \exp[\ln(0.01) \cdot \exp(r_{xylem}^{Diff}(s_{xylem}^{Diff} - age(T_{ref})))]$	Differentiation factor for protoxylem opening through apoptose with root segment aging (0 to 1)	*adim*	??

Table S1: continued from previous page

Equation	Description	Unit (SI)	Eq. n°
$S_{symp\|phloem} = 2.\pi.R.L.\frac{S_{phloem}}{S_{cylinder}}$	Exchange surface between parenchyma symplasm and phloem symplasm	m^2	S 8
Key N exchanges with environment			
$Tf^{Ni}_{soil\Rightarrow symp} = Tf^{Ni,HATS}_{soil\Rightarrow symp} + Tf^{Ni,LATS}_{soil\Rightarrow symp}$	Decomposition of active mineral N uptake from soil into symplasm between High Affinity and Low Affinity Transport Systems (HATS and LATS, respectively)	$mol\cdot s^{-1}$ of mineral N	??
$Tf^{Ni,HATS}_{soil\Rightarrow symp} = \frac{[Ni_{soil}]_v \cdot Vmax^{Ni,HATS}_{soil\Rightarrow symp}}{[Ni_{soil}]_v + Km^{Ni,HATS}_{soil\Rightarrow symp}} \cdot S_{soil\|symp} \cdot f_{hex}$	Michaelis-Menten active mineral N uptake by HATS from soil into symplasm	$mol\cdot s^{-1}$ of mineral N	??
$Vmax^{Ni,HATS}_{soil\Rightarrow symp} = \frac{A^{Ni,HATS}_{Vmax}}{[Ni_{symp}]_m \cdot \sigma^{Ni,HATS}_{Vmax} \cdot \sqrt{2\pi}} \cdot exp\left(-\frac{(\ln[Ni_{symp}]_m - \mu^{Ni,HATS}_{Vmax})^2}{2\sigma^{Ni,HATS}_{Vmax}{}^2}\right)$	Dependency to symplastic mineral N concentration of the maximal rate of mineral N uptake by HATS from soil into symplasm	$mol \cdot m^{-2}\ s^{-1}$ of mineral N	??
$Km^{Ni,HATS}_{soil\Rightarrow symp} = \frac{A^{Ni,HATS}_{Km}}{[Ni_{symp}]_m \cdot \sigma^{Ni,HATS}_{Km} \cdot \sqrt{2\pi}} \cdot exp\left(-\frac{(\ln[Ni_{symp}]_m - \mu^{Ni,HATS}_{Km})^2}{2\sigma^{Ni,HATS}_{Km}{}^2}\right)$	Dependency to symplastic mineral N concentration of the HATS affinity for external mineral N, for mineral N uptake from soil into symplasm	$mol \cdot m^{-3}$ of mineral N	S 9
$f_{hex} = \frac{[hex_{symp}]_m}{[hex_{symp}]_m + Km^{hex}_{root}}$	Regulation of transport by the concentration of hexose in symplasm to reflect the energetic costs of active processes	*adim* of mineral N	??

Table S1: continued from previous page

Equation	Description	Unit (SI)	Eq. n°
$Tf_{soil\Rightarrow symp}^{Ni,LATS} = K_{soil\Rightarrow symp}^{Ni,LATS} \cdot [Ni_{soil}]_v \cdot S_{soil\|symp} . f_{hex}$	Active mineral N uptake by LATS from soil into symplasm as a linear dependency to external mineral N concentration	$mol . s^{-1}$ of mineral N	??
$K_{soil\Rightarrow symp}^{Ni,LATS} = A_{LATS} \cdot exp(-\lambda_{LATS} \cdot [Ni_{symp}]_m)$	Dependency to symplastic mineral N concentration of the linear slope of LATS mineral N uptake from soil to symplasm	$m \cdot s^{-1}$	??
$Tf_{soil\Rightarrow symp}^{AA} = \frac{[AA_{soil}]_v \cdot Vmax_{soil\Rightarrow symp}^{AA}}{[AA_{soil}]_v + Km_{soil\Rightarrow symp}^{AA}} \cdot S_{soil\|symp} . f_{hex}$	Michaelis-Menten active amino acids uptake from soil into symplasm	$mol . s^{-1}$ of amino acids	S 10
$Vmax_{soil\Rightarrow symp}^{AA} = \frac{A_{Vmax}^{AA}}{[Ni_{symp}]_m \cdot \sigma_{Vmax}^{AA} \cdot \sqrt{2\pi}} \cdot exp\left(-\frac{(\ln [Ni_{symp}]_m - \mu_{Vmax}^{AA})^2}{2{\sigma_{Vmax}^{AA}}^2}\right)$	Dependency to symplastic mineral N concentration of the maximal rate of amino acids active uptake from soil into symplasm	$mol \cdot m^{-2} \, s^{-1}$ of amino acids N	S 11
$Km_{soil\Rightarrow symp}^{AA} = \frac{A_{Km}^{AA}}{[Ni_{symp}]_m \cdot \sigma_{Km}^{AA} \cdot \sqrt{2\pi}} \cdot exp\left(-\frac{(\ln [Ni_{symp}]_m - \mu_{Km}^{AA})^2}{2{\sigma_{Km}^{AA}}^2}\right)$	Dependency to symplastic mineral N concentration of the Michaelis-Menten affinity for external amino acids, for amino acids active uptake from soil into symplasm	$mol \cdot m^{-3}$ of mineral N	S 12
$Tf_{symp\rightarrow soil}^{Ni} = D_{symp\rightarrow soil}^{Ni} \cdot ([Ni_{symp}]_v - [Ni_{soil}]_v) \cdot S_{soil\|symp}$	Passive diffusion of mineral N from root symplasm to soil	$mol . s^{-1}$ of mineral N	??

Table S1: continued from previous page

Equation	Description	Unit (SI)	Eq. n°
$Tf^{AA}_{symp\to soil} = D^{AA}_{symp\to soil}\cdot([AA_{symp}]_v - [AA^{inorg}_{soil}]_v)\cdot S_{soil\|symp}$	Passive diffusion of amino acids from root symplasm to soil	$mol\cdot s^{-1}$ of amino acids	??
Radial water transport			
$Tf^{water}_{soil\to xylem} = Tf^{water}_{soil\to apop\to xylem} + Tf^{water}_{soil\to symp\to xylem}$	Decomposition of radial water uptake between symplastic and apoplastic pathways from soil to xylem apoplasm	$m^3\cdot s^{-1}$ of water	??
$Tf^{water}_{soil\to apop\to xylem} = k^{apop}_{water}\cdot\Big(\Psi_{soil} - \Psi_{xylem} - \sigma RT_{soil}\big([solutes_{soil}]_v - [solutes_{xylem}]_v\big)\Big)\cdot K_{endo}$	Apoplastic pathway of radial water uptake from soil to xylem apoplasm	$m^3\cdot s^{-1}$ of water	??
$Tf^{Ni,\text{Advection}}_{soil\to xylem} = \begin{cases} Tf^{water}_{soil\to apop\to xylem}\cdot[Ni_{soil}]_v & \text{if } Tf^{water}_{soil\to apop\to xylem} > 0 \\ Tf^{water}_{soil\to apop\to xylem}\cdot[Ni_{xylem}]_v & \text{if } Tf^{water}_{soil\to apop\to xylem} < 0 \end{cases}$	Mineral N advection by radial apoplastic water uptake from soil to xylem apoplasm	$mol\cdot s^{-1}$ of mineral N	??
$Tf^{AA,\text{Advection}}_{soil\to xylem} = \begin{cases} Tf^{water}_{soil\to apop\to xylem}\cdot[AA_{soil}]_v & \text{if } Tf^{water}_{soil\to apop\to xylem} > 0 \\ Tf^{water}_{soil\to apop\to xylem}\cdot[AA_{xylem}]_v & \text{if } Tf^{water}_{soil\to apop\to xylem} < 0 \end{cases}$	Amino acids advection by radial apoplastic water uptake from soil to xylem apoplasm	$mol\cdot s^{-1}$ of amino acids	S 13
$Tf^{water}_{soil\to symp\to xylem} = k^{symp}_{water}\cdot\Big(\Psi_{soil} - \Psi_{xylem} - \sigma RT_{soil}\big([solutes_{soil}]_v - [solutes_{xylem}]_v\big)\Big)$	Symplastic pathway of radial water uptake from soil to xylem apoplasm	$m^3\cdot s^{-1}$ of water	S 14

Table S1: continued from previous page

Equation	Description	Unit (SI)	Eq. n°
$Tf^{water}_{phloem \to xylem} = k^{phloem}_{water} \cdot \Big(\Psi_{phloem} - \Psi_{xylem} - \sigma R T_{soil} \big([solutes_{phloem}]_v - [solutes_{xylem}]_v\big)\Big)$	Radial transmembrane water transport from phloem symplasm to xylem apoplasm	$m^3 \cdot s^{-1}$ of water	??
$[solutes_{xylem}]_v = ([Ni_{xylem}]_v + [AA_{xylem}]_v) \ / \ (1 - p^{NotModeled}_{xylem})$	Total solute concentration in the xylem estimated from modeled metabolites	$mol \cdot m^{-3}$ of solutes	S 15
$[solutes_{phloem}]_v = ([Sucrose_{phloem}]_v + [AA_{phloem}]_v) \ / \ (1 - p^{NotModeled}_{phloem})$	Total solute concentration in the phloem estimated from modeled metabolites	$mol \cdot m^{-3}$ of solutes	S 16
Symbiotic processes			
$Tf^{Ni}_{mycorrhiza \Rightarrow symp} = \frac{Vmax^{Ni}_{mycorrhiza \Rightarrow symp} \cdot [N^{inorg}_{mycorrhiza}]_m}{Km^{Ni}_{mycorrhiza \Rightarrow symp} + [N^{inorg}_{mycorrhiza}]_m} \cdot L^{myccorhiza}_{infection} \cdot f_{hex}$	Mineral N active transport from mycorrhiza to root symplasm	$mol \cdot s^{-1}$ of mineral N	??
$Tf^{N^2 \Rightarrow Ni}_{nodule} = \frac{m^{struct}_{nodule} \cdot Vmax^{N^2 \Rightarrow Ni}_{nodule} \cdot [hex_{symp}]_m}{[hex_{symp}]_m + Km^{N^2 \Rightarrow Ni}_{nodule}}$	Biological N_2 fixation in root nodules symplasm	$mol \cdot s^{-1}$ of mineral N	??
$Vmax^{N^2 \Rightarrow Ni}_{nodule} = \frac{[Ni_{symp}]_m \cdot Vmax^{N^2 \Rightarrow Ni}_{nodule}}{[Ni_{symp}]_m + Km^{N^2 \Rightarrow Ni}_{inibition}}$	Inhibition of the maximal rate of biological N_2 fixation with mineral N concentration in symplasm	$mol \cdot s^{-1}$ of mineral N	??
Radial N flows between symplasm and conductive elements			
$Tf^{AA}_{phloem \to symp} = D^{AA}_{phloem \to symp} \cdot ([AA_{phloem}]_v - [AA_{symp}]_v) \cdot S_{symp \mid phloem}$	Passive unloading of amino acids from phloem symplasm to parenchyma symplasm	$mol \cdot s^{-1}$ of amino acids	S 17

Table S1: continued from previous page

Equation	Description	Unit (SI)	Eq. n°
$Tf^{Ni}_{symp\Rightarrow xylem} = \frac{[Ni_{symp}]_m \cdot Vmax^{Ni}_{symp\Rightarrow xylem}}{[Ni_{symp}]_m + Km^{Ni}_{symp\Rightarrow xylem}} \cdot S_{symp\|xylem} \cdot f_{hex}$	Michaelis-Menten active mineral N transport from parenchyma symplasm to xylem apoplasm	$mol \cdot s^{-1}$ of mineral N	S 18
$Tf^{AA}_{symp\Rightarrow xylem} = \frac{[AA_{symp}]_v \cdot Vmax^{AA}_{symp\Rightarrow xylem}}{[AA_{symp}]_v + Km^{AA}_{symp\Rightarrow xylem}} \cdot S_{symp\|xylem} \cdot f_{hex}$	Michaelis-Menten active amino acids transport from parenchyma symplasm to xylem apoplasm	$mol \cdot s^{-1}$ of mineral N	S 19
$Tf^{Ni}_{xylem\rightarrow symp} = D^{Ni}_{xylem\rightarrow symp} \cdot ([Ni_{xylem}]_v - [Ni_{symp}]_v) \cdot S_{symp\|xylem}$	Passive unloading of amino acids from phloem symplasm to parenchyma symplasm	$mol \cdot s^{-1}$ of amino acids	S 20
$Tf^{AA}_{xylem\rightarrow symp} = D^{AA}_{xylem\rightarrow symp} \cdot ([AA_{xylem}]_v - [AA_{symp}]_v) \cdot S_{xylem\|phloem}$	Passive unloading of amino acids from phloem symplasm to parenchyma symplasm	$mol \cdot s^{-1}$ of amino acids	S 21
$Tf^{Ni}_{xylem\rightarrow soil} = D^{Ni}_{xylem\rightarrow soil} \cdot ([Ni_{xylem}]_v - [Ni_{soil}]_v) \cdot 2\pi RL \cdot K_{endo} \cdot Diff_{protoxylem}$	Passive diffusion of mineral N from xylem apoplasm to soil	$mol \cdot s^{-1}$ of mineral N	S 22
$Tf^{AA}_{xylem\rightarrow soil} = D^{AA}_{xylem\rightarrow soil} \cdot ([AA_{xylem}]_v - [AA_{soil}]_v) \cdot 2\pi RL \cdot K_{endo} \cdot Diff_{protoxylem}$	Passive diffusion of amino acids from xylem apoplasm to soil	$mol \cdot s^{-1}$ of amino acids	S 23
Coupled axial water flows in xylem and phloem			
$Tf^{water}_{xylem(i)\rightarrow(i-1)} = K_{xylem(i)} \cdot (\Psi_{xylem(i)} - \Psi_{xylem(i-1)} + \rho_{xylem} \cdot g \cdot (z_{(i)} - z_{(i-1)}))$	Axial water transport in xylem of segment i	$m^3 \cdot s^{-1}$ of water	??
$Tf^{water}_{phloem(i)\rightarrow(i-1)} = K_{phloem(i)} \cdot (\Psi_{phloem(i)} - \Psi_{phloem(i-1)} + \rho_{phloem} \cdot g \cdot (z_{(i)} - z_{(i-1)}))$	Axial water transport in phloem of segment i	$m^3 \cdot s^{-1}$ of water	??

Table S1: continued from previous page

Equation	Description	Unit (SI)	Eq. n°
$K_{xylem(i)} = Diff_{protoxylem} \sum_{\mathrm{r}}^{\mathrm{vessels}} \frac{\pi \cdot r^4}{8 \cdot \eta_{xylem}(i) \cdot L}$	Axial water conductance of all xylem vessels according to the Hagen-Poiseuille model in segment i	$m^3 \cdot Pa^{-1}\ s^{-1}$	??
$K_{phloem(i)} = \sum_{\mathrm{r}}^{\mathrm{vessels}} \frac{\pi \cdot r^4}{8 \cdot \eta_{phloem}(i) \cdot L}$	Axial water conductance of all phloem vessels according to the Hagen-Poiseuille model in segment i	$m^3 \cdot Pa^{-1}\ s^{-1}$	S 24
$Tf^{water}_{xylem(i)\rightarrow xylem(i-1)} = Tf^{water}_{soil(i)\rightarrow apop\rightarrow xylem(i)} + Tf^{water}_{phloem(i)\rightarrow xylem(i)} + \sum_j^{children} Tf^{water}_{xylem(j)\rightarrow xylem(i)}$	Water conservation equation in xylem of water	$m3 \cdot s^{-1}$	??
$Tf^{water}_{phloem(i)\rightarrow phloem(i-1)} = \sum_j^{children} Tf^{water}_{phloem(j)\rightarrow phloem(i)} - Tf^{water}_{phloem(i)\rightarrow xylem(i)}$	Water conservation equation in phloem of water	$m3 \cdot s^{-1}$	??
Axial N flows through the xylem and phloem sap advection			
$Tf^{Ni}_{xylem(i)\rightarrow xylem(i-1)} = \begin{cases} Tf^{water}_{xylem(i)\rightarrow xylem(i-1)} \cdot [Ni_{xylem}]_v(i) & , Tf^{water}_{xylem(i)\rightarrow xylem(i-1)} > 0 \\ Tf^{water}_{xylem(i)\rightarrow xylem(i-1)} \cdot [Ni_{xylem}]_v(i-1) & , Tf^{water}_{xylem(i)\rightarrow xylem(i-1)} < 0 \end{cases}$	Water-driven advection of mineral N in xylem apoplasm from segment i to its parent *i-1*	$mol \cdot s^{-1}$ of mineral N	??
$Tf^{AA}_{xylem(i)\rightarrow xylem(i-1)} = \begin{cases} Tf^{water}_{xylem(i)\rightarrow xylem(i-1)} \cdot [AA_{xylem}]_v(i) & , Tf^{water}_{xylem(i)\rightarrow xylem(i-1)} > 0 \\ Tf^{water}_{xylem(i)\rightarrow xylem(i-1)} \cdot [AA_{xylem}]_v(i-1) & , Tf^{water}_{xylem(i)\rightarrow xylem(i-1)} < 0 \end{cases}$	Water-driven advection of amino acids in xylem apoplasm from segment i to its parent *i-1*	$mol \cdot s^{-1}$ of amino acids	S 25
$Tf^{AA}_{phloem(i)\rightarrow phloem(i-1)} = \begin{cases} Tf^{water}_{phloem(i)\rightarrow phloem(i-1)} \cdot [AA_{phloem}]_v(i) & , Tf^{water}_{phloem(i)\rightarrow phloem(i-1)} > 0 \\ Tf^{water}_{phloem(i)\rightarrow phloem(i-1)} \cdot [AA_{phloem}]_v(i-1) & , Tf^{water}_{phloem(i)\rightarrow phloem(i-1)} < 0 \end{cases}$	Water-driven advection of amino acids in xylem apoplasm from segment i to its parent *i-1*	$mol \cdot s^{-1}$ of amino acids	S 26

Table S1: continued from previous page

Equation	Description	Unit (SI)	Eq. n°
$Tf^{Ni}_{xylem\rightarrow shoot} = \sum_i n^{Ni}_{xylem(i,t)} - \sum_i n^{Ni}_{xylem(i,t+\Delta t)} + \sum_i (Tf^{Ni}_{symp(i,t)\Rightarrow xylem(i,t)} + Tf^{Ni,\text{Advection}}_{soil(i,t)\rightarrow xylem(i,t)} - Tf^{Ni}_{xylem(i,t)\rightarrow symp(i,t)} - Tf^{Ni}_{xylem(i,t)\rightarrow soil(i,t)}) \cdot \Delta t$	Mineral N allocation to shoot from xylem based on mass conservation	$mol \cdot s^{-1}$ of mineral N	??
$Tf^{AA}_{xylem\rightarrow shoot} = \sum_i n^{AA}_{xylem(i,t)} - \sum_i n^{AA}_{xylem(i,t+\Delta t)} + \sum_i (Tf^{AA}_{symp(i,t)\Rightarrow xylem(i,t)} + Tf^{AA,\text{Advection}}_{soil(i,t)\rightarrow xylem(i,t)} - Tf^{AA}_{xylem(i,t)\rightarrow symp(i,t)} - Tf^{AA}_{xylem(i,t)\rightarrow soil(i,t)}) \cdot \Delta t$	Amino acids allocation to shoot from xylem based on mass conservation	$mol \cdot s^{-1}$ of amino acids	S 27
$Tf^{AA}_{phloem\rightarrow shoot} = \sum_i n^{AA}_{phloem(i,t)} - \sum_i n^{AA}_{phloem(i,t+\Delta t)} + \sum_i (-Tf^{AA}_{phloem(i,t)\rightarrow symp(i,t)}) \cdot \Delta t$	Amino acids allocation to shoot from phloem based on mass conservation (generally negative)	$mol \cdot s^{-1}$ of amino acids	S 28
Key metabolic processes within segment			
$Mt^{Ni,hexose\Rightarrow AA}_{symp} = \frac{Vmax^{Ni,hexose\Rightarrow AA}_{symp}}{\frac{1+Km^{Ni\Rightarrow AA}_{symp}}{[Ni_{symp}]_m} \cdot \frac{1+Km^{hexose\Rightarrow AA}_{symp}}{[hex_{symp}]_m}} \cdot m^{struct}_{root}$	Bi-substrate Michaelis-Menten amino acid synthesis in symplasm	$mol \cdot s^{-1}$ of amino acids	??
$Mt^{AA\Rightarrow Ni,hexose}_{symp} = \frac{[AA_{symp}]_m \cdot Vmax^{AA\Rightarrow Ni,hexose}_{symp}}{[AA_{symp}]_m + Km^{AA\Rightarrow Ni,hexose}_{symp} exp(k^{AA,catab}_{Creg} \cdot [hex_{symp}]_m)} \cdot m^{struct}_{root}$	Michaelis-Menten amino acid degradation in symplasm	$mol \cdot s^{-1}$ of amino acids	S 29
$Mt^{AA\Rightarrow storage}_{symp} = \frac{[AA_{symp}]_m \cdot Vmax^{AA\Rightarrow storage}_{symp}}{[AA_{symp}]_m + Km^{AA\Rightarrow storage}_{symp}} \cdot m^{struct}_{root}$	Michaelis-Menten storage protein synthesis in symplasm	$mol \cdot s^{-1}$ of amino acids	S 30
$Mt^{storage\Rightarrow AA}_{symp} = \frac{[storage_{symp}]_m \cdot Vmax^{storage\Rightarrow AA}_{symp}}{[storage_{symp}]_m + Km^{storage\Rightarrow AA}_{symp} exp(k^{storage,catab}_{Creg} \cdot [hex_{symp}]_m)} \cdot m^{struct}_{root}$	Michaelis-Menten storage protein remobilisation in symplasm	$mol \cdot s^{-1}$ of amino acids	S 31
Regulations by soil temperature			

Table S1: continued from previous page

Equation	Description	Unit (SI)	Eq. n°
$Process(T_{soil}) = Process(T_{ref})(A(T_{soil} - T_{ref}) + B)^{1-C} \cdot (A(T_{soil} - T_{ref}) + B)^{\frac{C(T_{soil}-T_{ref})}{10}}$	A generic temperature modifier for above rate equations according to soil temperature	Same as modified processes	??
$\eta_{xylem}(i) = A_{Kxylem} \cdot \exp(B_{Kxylem}/T_{soil}(i) + C_{Kxylem}T_{soil}(i) + D_{Kxylem}T_{soil}(i)^2)$	Xylem sap viscosity with soil temperature in segment i	$Pa\ s$	S 32
$\eta_{phloem}(i) = \eta_{phloem,ref}(i) \cdot \exp(\frac{Ea_{phloem}(i)}{R}(\frac{1}{T_{soil}(i)} - \frac{1}{T_{ref,phloem}}))$	Phloem sap viscosity with soil temperature and solute concentration in segment i	$Pa\ s$	S 33
$\eta_{phloem,ref}(i) = \exp((A_{phloem,\eta ref}\Phi_{phloem}(i)^2) + B_{phloem,\eta ref}\Phi_{phloem}(i) + C_{phloem,\eta ref})$	Phloem sap reference viscosity at the reference temperature depending on solute volumetric fraction in segment i	$Pa\ s$	S 34
$Ea_{phloem}(i) = Ea_{phloem,ref}\frac{1+0.5\Phi_{phloem}(i)}{1-\Phi_{phloem}(i)}$	Phloem sap activation energy depending on solute volumetric fraction in segment i	$J \cdot mol^{-1}$	S 35
$\Phi_{phloem}(i) = [solutes_{phloem}]_v(i) \cdot \bar{V}_{solutes}$	Solute volumetric fraction in phloem sap of segment i	$adim$	S 36

Model Parameters

Table S2: Description and units of the *Root-CyNAPS* model parameters

Parameter name	Description (unit)	Estimated value for wheat	Reference
Stoichiometry parameters			
$nb_{N:AA}$	Number of nitrogen moles per mol of amino acids ($mol\ mol^{-1}$)	1.4	**?**
$nb_{AA:stor}$	Number of amino acid moles per mol of storage proteins ($mol\ mol^{-1}$)	210	*B. napus* example (**?**), not in wheat
$nb_{AA:struct}$	Number of amino acid moles pet gram of structural mass ($mol\ g^{-1}$)	0.014	**?**
Anatomical parameters			
$r_{S_{symp}}^{CrossSection}$	Ratio of cells cross-sectional surface relative to cross section discus surface for symplasm ($m^2\ m^2$)	0.72	See Fig. S15
$r_{S_{xylem}}^{CrossSection}$	Ratio of cells cross-sectional surface relative to cross section discus surface xylem ($m^2\ m^2$)	0.02	See Fig. S15
$r_{S_{phloem}}^{CrossSection}$	Ratio of cells cross-sectional surface relative to cross section discus surface for phloem ($m^2\ m^2$)	0.008	See Fig. S15
$f_{symp}^{CellLine}$	Frequency of cell lines for symplasm (m^{-1})	4390	See Fig. S15
$f_{xylem}^{CellLine}$	Frequency of cell lines for xylem (m^{-1})	1370	See Fig. S15
$f_{phloem}^{CellLine}$	Frequency of cell lines for phloem (m^{-1})	2310	See Fig. S15
$\frac{Sepidermis}{Scylinder}$	Ratio of the actual exchange surface of the epidermis cells with the outer cylindrical surface of the root segment ($m^2\ m^{-2}$)	2.8	See Fig. S15
$\frac{Scortex}{Scylinder}$	Ratio of the actual exchange surface of the cortex cells with the outer cylindrical surface of the root segment ($m^2\ m^{-2}$)	62	See Fig. S15

Table S2: continued from previous page

Parameter name	Description (unit)	Estimated value for wheat	Reference
$\frac{Sstele}{Scylinder}$	Ratio of the actual exchange surface of the stele cells with the outer cylindrical surface of the root segment ($m^2\ m^{-2}$)	17	See Fig. S15
$\Delta t^{disrupt}_{endo,max}$	Maximal time of endodermis disruption since lateral primordium emergence (s)	21600	**?**
r^{Diff}_{Endo}	Rate of endodermis differentiation with tissue aging (s^{-1})	$1.16 \cdot 10^{-5}$	**?**
s^{Diff}_{Endo}	Delay after tissue formation before endodermis differentiation starts (s)	86400	**?**
L^{Diff}_{Endo}	Maximal possible reduction of endodermis conductance (%)	100	**?**
$\Delta t^{disrupt}_{exo,max}$	Maximal time of exodermis disruption since lateral primordium emergence (s)	172800	**?**
r^{Diff}_{Exo}	Rate of exodermis differentiation with tissue aging (s^{-1})	$0.58 \cdot 10^{-5}$	**?**
s^{Diff}_{Exo}	Delay after tissue formation before exodermis differentiation starts (s)	43200	**?**
L^{Diff}_{Exo}	Maximal possible reduction of exodermis conductance (%)	50	**?**
r^{Diff}_{xylem}	Rate of xylem apoplastic differentiation with tissue aging ((s^{-1})	1.28 $1.28 \cdot 10^{-5}$	**?**
s^{Diff}_{xylem}	Delay after tissue formation before xylem differentiation starts (s)	86400	**?**
Active processes kinetic parameters			
$A^{Ni,HATS}_{Vmax}$	Amplitude of $Vmax^{Ni,HATS}_{soil \Rightarrow symp}$ log-normal variation with mineral N concentration in the root symplasm ($gDW\ m^{-2}\ s^{-1}$)	$3.38 \cdot 10^{-11}$	**?**

Table S2: continued from previous page

Parameter name	Description (unit)	Estimated value for wheat	Reference
$\mu_{Vmax}^{Ni,HATS}$	Natural logarithm of the mineral N massic concentration in root symplasm at which $Vmax_{soil\Rightarrow symp}^{Ni,HATS}$ is maximal (dimensionless)	-8.16	?
$\sigma_{Vmax}^{Ni,HATS}$	Standard deviation of $Vmax_{soil\Rightarrow symp}^{Ni,HATS}$ according to the mineral N concentration in symplasm (dimensionless)	0.99	?
$A_{Km}^{Ni,HATS}$	Amplitude of $Km_{soil\Rightarrow symp}^{Ni,HATS}$ log-normal variation with mineral N concentration in the root symplasm ($m\ s^{-1}$)	$1.31 \cdot 10^{-4}$	?
$\mu_{Km}^{Ni,HATS}$	Natural logarithm of the mineral N massic concentration in root symplasm at which $Km_{soil\Rightarrow symp}^{Ni,HATS}$ is maximal (dimensionless)	-6.23	?
$\sigma_{Km}^{Ni,HATS}$	Standard deviation of $Km_{soil\Rightarrow symp}^{Ni,HATS}$ according to the mineral N concentration in symplasm (dimensionless)	1.75	?
Km_{root}^{hex}	Hexose symplastic concentration at which regulation of active transport processes equals 0.5 ($mol.gDW^{-1}$ of hexose)	0.007	?
K_{LATS}^{slope}	Linear decrease slope with mineral N concentration in symplasm of the Low Affinity Transport System (LATS) slope parameter ($m\ gDW\ mol^{-1}\ s^{-1}$)	$5.62 \cdot 10^{-7}$	?
K_{LATS}^{origin}	Origin of the linear dependency to mineral N concentration in symplasm for the LATS slope parameter (ms^{-1} of mineral N)	$6.50 \cdot 10^{-10}$	?

Table S2: continued from previous page

Parameter name	Description (unit)	Estimated value for wheat	Reference
A^{AA}_{Vmax}	Amplitude of $Vmax^{AA}_{soil \Rightarrow symp}$ log-normal variation with mineral N concentration in the root symplasm ($m\ s^{-1}$)	$3.84 \cdot 10^{-12}$	**?**
μ^{AA}_{Vmax}	Natural logarithm of the mineral N massic concentration in root symplasm at which $Vmax^{AA}_{soil \Rightarrow symp}$ is maximal (dimensionless)	-8.16	Transposed from mineral N uptake regulation
σ^{AA}_{Vmax}	Standard deviation of $Vmax^{AA}_{soil \Rightarrow symp}$ according to the mineral N concentration in symplasm (dimensionless)	0.99	Transposed from mineral N uptake regulation
A^{AA}_{Km}	Amplitude of $Km^{AA}_{soil \Rightarrow symp}$ log-normal variation with mineral N concentration in the root symplasm ($m\ s^{-1}$)	$6.11 \cdot 10^{-5}$	
μ^{AA}_{Km}	Natural logarithm of the mineral N massic concentration in root symplasm at which $Km^{AA}_{soil \Rightarrow symp}$ is maximal (dimensionless)	-6.23	Transposed from mineral N uptake regulation
σ^{AA}_{Km}	Standard deviation of $Km^{AA}_{soil \Rightarrow symp}$ according to the mineral N concentration in symplasm (dimensionless)	1.75	Transposed from mineral N uptake regulation
$Vmax^{Ni}_{mycorrhiza \Rightarrow symp}$	Maximal rate of mineral N transfer from the mycorrhiza to the root symplasm per unit root length ($mol.m^{-1}.s^{-1}$)	$7.1 \cdot 10^{-13}$	**??**
$Km^{Ni}_{mycorrhiza \Rightarrow symp}$	Mineral N concentration in mycorrhiza at which the transfer to root symplasm is half its maximum (mol of mineral N $.gDW^{-1}$ of mycorrhiza)	$1.7 \cdot 10^{-5}$	**?**

Table S2: continued from previous page

Parameter name	Description (unit)	Estimated value for wheat	Reference
$Vmax_{nodule}^{N^2 \Rightarrow Ni}$	Maximal massic N_2 fixation rate into mineral N in root nodule symplasm ($mol.gDW^{-1}.s^{-1}$ of mineral N)	$1.72 \cdot 10^{-8}$	**??**
$Km_{nodule}^{N^2 \Rightarrow Ni}$	Hexose concentration in nodule symplasm at which the fixation rate is half its maximum ($mol.gDW^{-1}$ of hexose)	$1.3 \cdot 10^{-5}$	**??**
$Km_{inibition}^{N^2 \Rightarrow Ni}$	Mineral N concentration in nodule symplasm at which maximal the fixation rate reduced by half ($mol.gDW^{-1}$ of mineral N)	$1.0 \cdot 10^{-4}$	**?**
$Vmax_{symp \Rightarrow xylem}^{Ni}$	Maximal surfacic rate of mineral N active export from root symplasm to xylem apoplasm ($mol.m^{-2}.s^{-1}$)	$1.7 \cdot 10^{-5}$	**?**
$Km_{symp \Rightarrow xylem}^{Ni}$	Mineral N concentration in mycorrhiza at which the transfer to root symplasm is half its maximum (mol of mineral N $.gDW^{-1}$ of mycorrhiza)	0.02	**?**
$Vmax_{symp \Rightarrow xylem}^{AA}$	Maximal surfacic rate of amino acids active export from root symplasm to xylem apoplasm ($mol.m^{-2}.s^{-1}$)	$1.3 \cdot 10^{-7}$	Estimated from mineral N export to xylem
$Km_{symp \Rightarrow xylem}^{AA}$	Amino acids concentration in mycorrhiza at which the transfer to root symplasm is half its maximum (mol of amino acids $.gDW^{-1}$ of mycorrhiza)	0.1	Estimated from mineral N export to xylem
$Vmax_{symp}^{Ni,hexose \Rightarrow AA}$	Maximal massic amino acid synthesis rate in root symplasm ($mol.gDW^{-1}.s^{-1}$)	$5.0 \cdot 10^{-6}$	**??**
$Km_{symp}^{Ni \Rightarrow AA}$	Affinity coefficient for mineral N fueling amino acid synthesis in root symplasm ($mol.gDW^{-1}$ of mineral N)	$2.9 \cdot 10^{-4}$	**?**

Table S2: continued from previous page

Parameter name	Description (unit)	Estimated value for wheat	Reference
$Km_{symp}^{hexose \Rightarrow AA}$	Affinity coefficient for hexose fueling amino acid synthesis in root symplasm ($mol.gDW^{-1}$ of hexose)	$3.5 \cdot 10^{-6}$	**?**
$Vmax_{symp}^{AA \Rightarrow Ni,hexose}$	Maximal massic amino acid degradation rate in root symplasm ($mol.gDW^{-1}.s^{-1}$)	$1.0 \cdot 10^{-9}$	**??**
$Km_{symp}^{AA \Rightarrow Ni,hexose}$	Affinity coefficient for amino acids degradation in root symplasm ($mol.gDW^{-1}$ of mineral N)	$2.4 \cdot 10^{-3}$	**??**
$k_{Creg}^{AA,catab}$	Parameter decreasing exponentially amino acid degradation in root symplasm with hexose availability ($gDW.mol^{-1}$)	30	**??**
$Vmax_{symp}^{AA \Rightarrow storage}$	Maximal massic storage proteins synthesis rate in root symplasm ($mol.gDW^{-1}.s^{-1}$)	$1.1 \cdot 10^{-7}$	**?**, not used for wheat
$Km_{symp}^{AA \Rightarrow storage}$	Affinity coefficient for storage proteins synthesis in root symplasm ($mol.gDW^{-1}$ of mineral N)	$2.5 \cdot 10^{-4}$	**?**
$Vmax_{symp}^{storage \Rightarrow AA}$	Maximal massic storage proteins degradation rate in root symplasm ($mol.gDW^{-1}.s^{-1}$)	$1.1 \cdot 10^{-7}$	Same as storage synthesis, assuming no priority between storage and remobilization, unless when catabolism is down-regulated by hexose concentrations
$Km_{symp}^{storage \Rightarrow AA}$	Affinity coefficient for storage proteins degradation in root symplasm ($mol.gDW^{-1}$ of mineral N)	$2.5 \cdot 10^{-4}$	Same as storage synthesis, assuming no priority between storage and remobilization, unless when catabolism is down-regulated by hexose concentrations

Table S2: continued from previous page

Parameter name	Description (unit)	Estimated value for wheat	Reference
$k_{Creg}^{storage,catab}$	Parameter decreasing exponentially storage protein degradation in root symplasm with hexose availability ($gDW.mol^{-1}$)	30	**??**
Passive processes conductance parameters			
$D_{symp\rightarrow soil}^{Ni}$	Surfacic diffusion parameter of mineral N between root symplasm and soil ($m.s^{-1}$)	$2.5 \cdot 10^{-11}$	**?**
$D_{symp\rightarrow soil}^{AA}$	Surfacic diffusion parameter of amino acids between root symplasm and soil ($m.s^{-1}$)	$2.5 \cdot 10^{-12}$	Set equal to mineral N diffusion parameter
k_{water}^{apop}	radial hydraulic conductance of the apoplastic water uptake pathways ($m.s^{-1}.Pa^{-1}$)	$1.53.3 \cdot 10^{-19}$	See Fig. S15
k_{water}^{symp}	radial hydraulic conductance of the symplastic water uptake pathways ($m.s^{-1}.Pa^{-1}$)	$2.51.4 \cdot 10^{-18}$	See Fig. S15
σ	Reflection coefficient of the osmotic of radial water transport (dimensionless)	0.85	**?**
$p_{xylem}^{NotModeled}$	Proportion of xylem solutes not modeled in *Root-CyNAPS*, e.g. to account to the osmotic contribution of potassium (dimensionless)	0.5	**?**
$p_{phloem}^{NotModeled}$	Proportion of phloem solutes not modeled in *Root-CyNAPS*, e.g. to account to the osmotic contribution of potassium (dimensionless)	0.4	**?**
k_{water}^{phloem}	radial hydraulic conductance of the water exchange between xylem and phloem ($m.s^{-1}.Pa^{-1}$)	$1.40.8 \cdot 10^{-18}$	See Fig. S15
$D_{phloem\rightarrow symp}^{AA}$	Surfacic diffusion parameter of amino acids unloading from phloem symplasm to root symplasm ($m.s^{-1}$)	$1.0 \cdot 10^{-10}$	**?**

Table S2: continued from previous page

Parameter name	Description (unit)	Estimated value for wheat	Reference
$D^{Ni}_{xylem \to symp}$	Surfacic diffusion parameter of mineral N diffusion from xylem apoplasm to root symplasm ($m.s^{-1}$)	$2.5 \cdot 10^{-12}$	Adapted from *symp* → *soil* as also transmembrane
$D^{AA}_{xylem \to symp}$	Surfacic diffusion parameter of amino acids diffusion from xylem apoplasm to root symplasm ($m.s^{-1}$)	$2.5 \cdot 10^{-12}$	Adapted from *symp* → *soil* as also transmembrane
$D^{Ni}_{xylem \to soil}$	Surfacic diffusion parameter of mineral N diffusion from xylem apoplasm to soil solution ($m.s^{-1}$)	$1.0 \cdot 10^{-13}$	-
$D^{AA}_{xylem \to soil}$	Surfacic diffusion parameter of amino acids diffusion from xylem apoplasm to soil solution ($m.s^{-1}$)	$1.0 \cdot 10^{-13}$	-
vessels	Sets of radii for individual xylem or phloem vessels, used to estimate root segment axial water conductance (m)	e.g.$(2.8 ; 1.1 ; 0.4) \cdot 10^{-5}$ for central metaxylem, peripheral metaxylem and protoxylem, respectively	See Fig. S15
Regulations by soil temperature			
T_{ref}	Temperature at which the reference rate of a process has been measured experimentally (°C)	20	Most experiments in controlled environment with standard laboratory conditions
A	With this combination of parameter values, parameter affecting the temperature at which the process rate is maximal (dimensionless)	-0.04	**?**
B	Equivalent to the Q10 value with this combination of parameters values (dimensionless)	1.55	**?**

Table S2: continued from previous page

Parameter name	Description (unit)	Estimated value for wheat	Reference
C	Toggle parameter to switch off the linear increase of the process with temperature, to switch to Q10 or bell-shaped functions (dimensionless)	1	**?**
A_{Kxylem}	Amplitude parameter for xylem sap viscosity dependence to soil temperature ($Pa\ s$)	$1.86 \cdot 10^{-14}$	**?**
B_{Kxylem}	Polynomial parameter for xylem sap viscosity dependence to soil temperature (K)	4209	**?**
C_{Kxylem}	Polynomial parameter for xylem sap viscosity dependence to soil temperature (K^{-1})	0.045	**?**
D_{Kxylem}	Polynomial parameter for xylem sap viscosity dependence to soil temperature (K^{-2})	$-3.38 \cdot 10^{-15}$	**?**
$T_{ref,phloem}$	Reference temperature at which viscosity has been measured for phloem sap viscosity dependence to solute concentration and soil temperature (K)	318.15	**?**
$A_{phloem,\eta ref}$	Polynomial parameter for phloem sap viscosity dependence to solute concentration at $T_{ref,phloem}$ (dimensionless)	$9.65 \cdot 10^{-14}$	**?**
$B_{phloem,\eta ref}$	Polynomial parameter for phloem sap viscosity dependence to solute concentration at $T_{ref,phloem}$ (dimensionless)	0.97	**?**
$C_{phloem,\eta ref}$	Polynomial parameter for phloem sap viscosity dependence to solute concentration at $T_{ref,phloem}$ (dimensionless)	-7.29	**?**

Table S2: continued from previous page

Parameter name	Description (unit)	Estimated value for wheat	Reference
$Ea_{phloem,ref}$	Reference activation energy for for phloem sap viscosity dependence to soil temperature and solute concentration ($J \cdot mol^{-1}$)	15080	**?**
$\bar{V}_{solutes}$	Average molar volume of phloem sap ($m^3\ mol^{-1}$)	$1.6 \cdot 10^{-4}$	**?**

Supplementary Figures

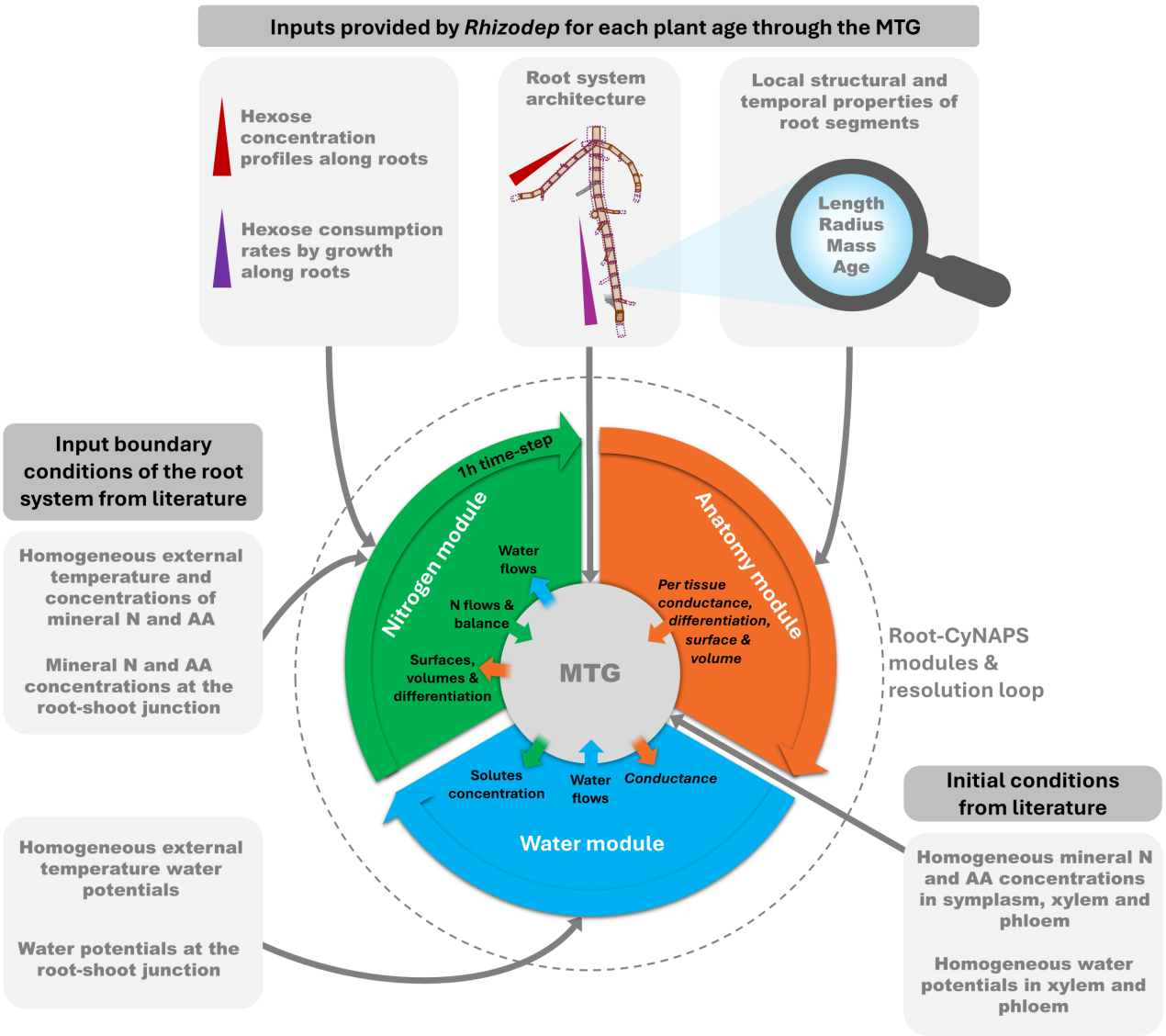

Fig. S1. Inputs provided to Root-CyNAPS for the presented use case and resolution loop between anatomy, water and nitrogen modules. All data, inputs of the model and exchanges between modules, are passed through the Multiscale Tree Graph (MTG). The MTG caries data in each node of the root system architecture and is itself provided by *RhizoDep*. Anatomy, water and nitrogen modules are solved sequentially during an hourly time step, retrieve their input data from the MTG and update the MTG with their outputs. AA stands for Amino Acids.

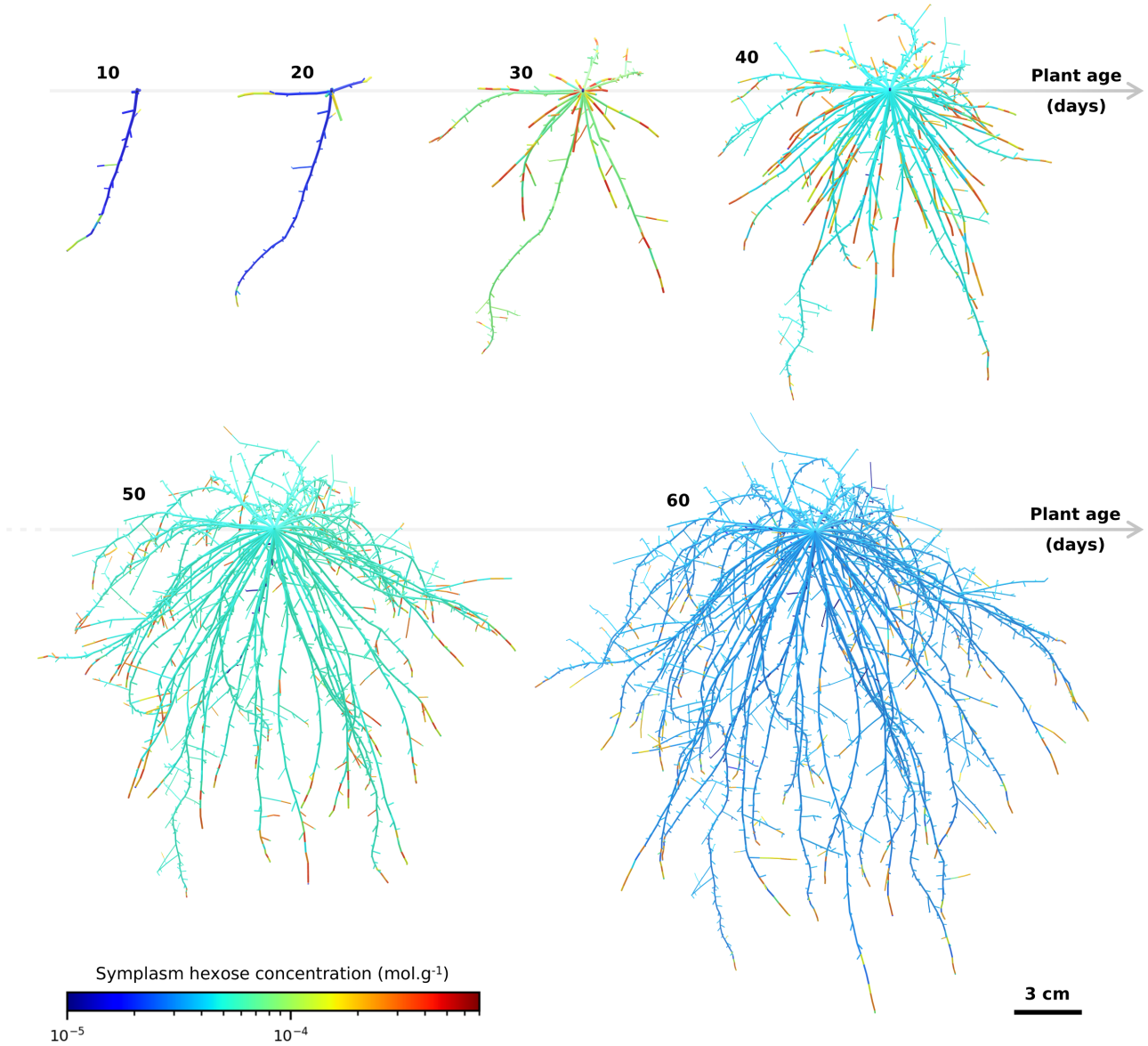

Fig. S2. Evolution of input root system architecture over plant age. Colors correspond to hexose massic concentrations in symplasm of each root segment. Both are provided as input to *RootCyNAPS* by the *RhizoDep* model. The visualization was rendered with a camera oriented at a -70° elevation angle, corresponding to an oblique top-down view.

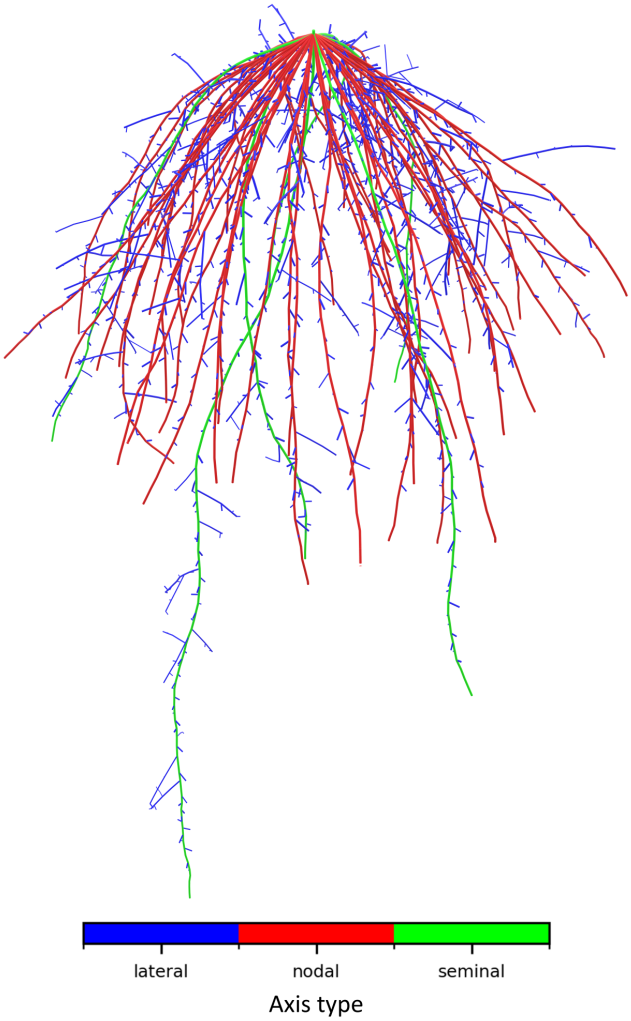

Fig. S3. 3D static root system architecture displaying the root type on each root segment, provided as input to the *Root-CyNAPS* model (50 day-old spring wheat example)

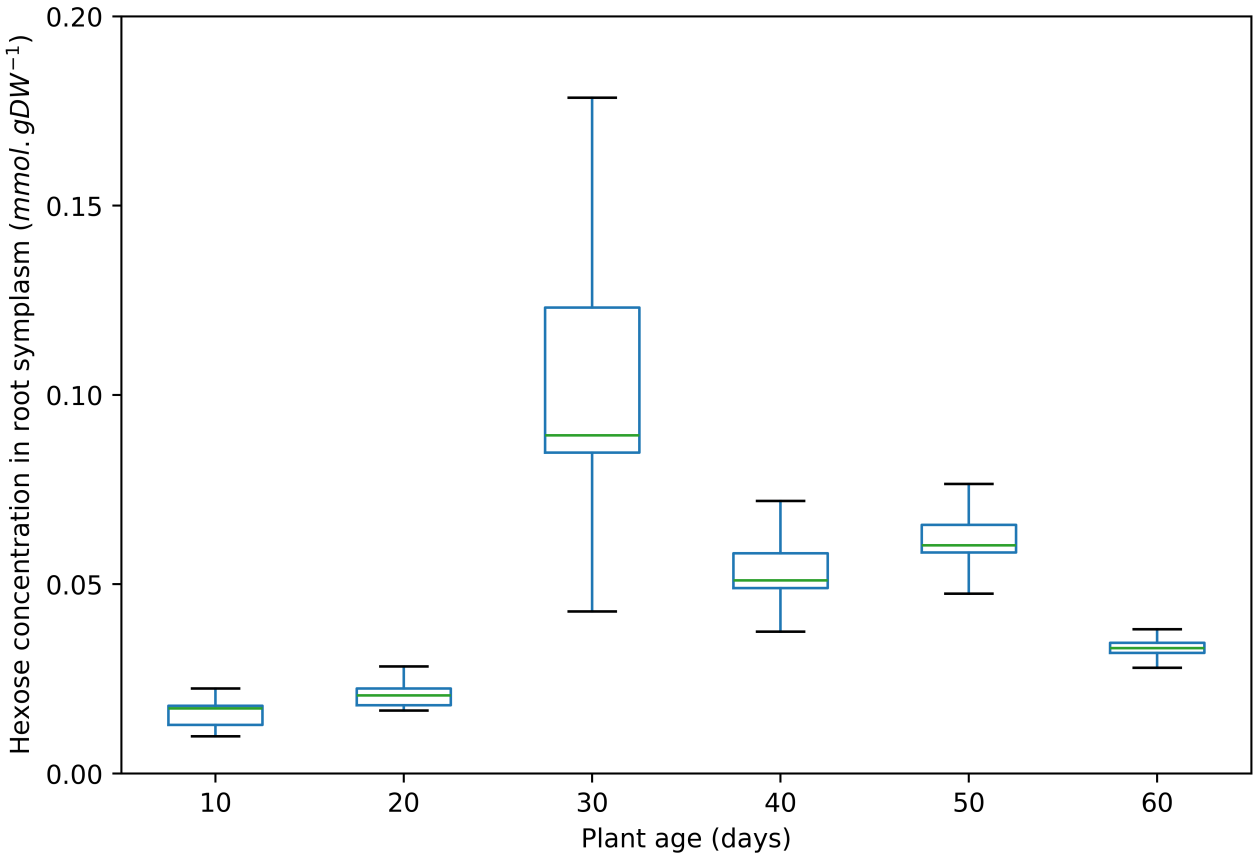

Fig. S4. Evolution of the hexose concentration in the root system symplasm with plant age, as simulated on wheat by the *RhizoDep* model (input data).

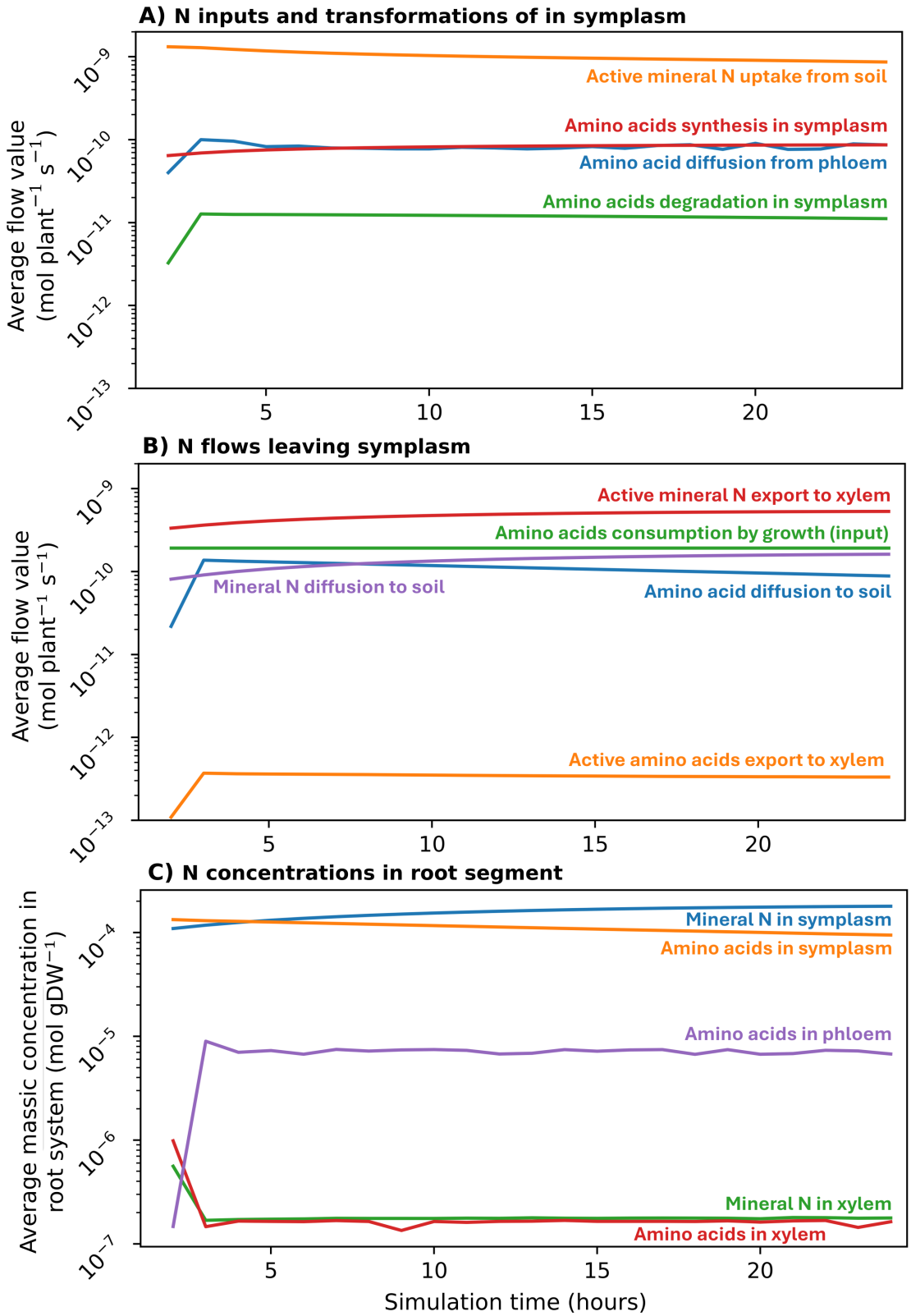

Fig. S5. Temporal variations of *Root-CyNAPS* outputs over 24 hours of simulations, averaged for the whole root-system in the case of a 50 days-old wheat in 0.5 mM nutrient solution (scenario 14). N flows entering root symplasm and N metabolic transformations in root symplasm are represented (A), as well as N flows leaving root symplasm (B), and finally the mineral N and amino acids massic concentrations in the simulated compartments (C). Flows and concentrations are represented with a log scale for figure readability. Note that massic concentration gradients between symplasm and conductive elements do not reflect the volumic concentrations gradients driving diffusion flows in the model.

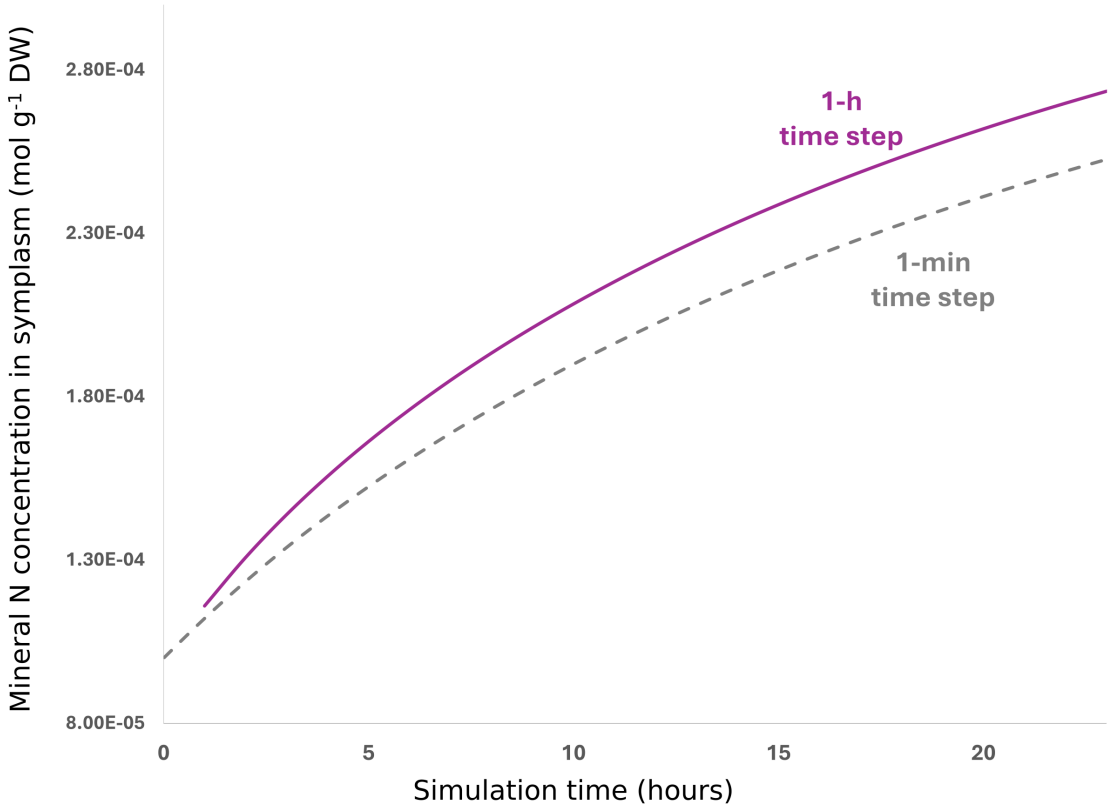

Fig. S6. Temporal variations of mineral N concentration in symplasm as simulated by the *RootCyNAPS* model over 24 hours of simulations, averaged for the whole root-system in the case of a 50 days-old wheat in 0.5 mM nutrient solution (scenario 14). The plain purple line represents simulation outputs using a 1-h time step while the grey dotted line corresponds to the usage of a 1-min time step.

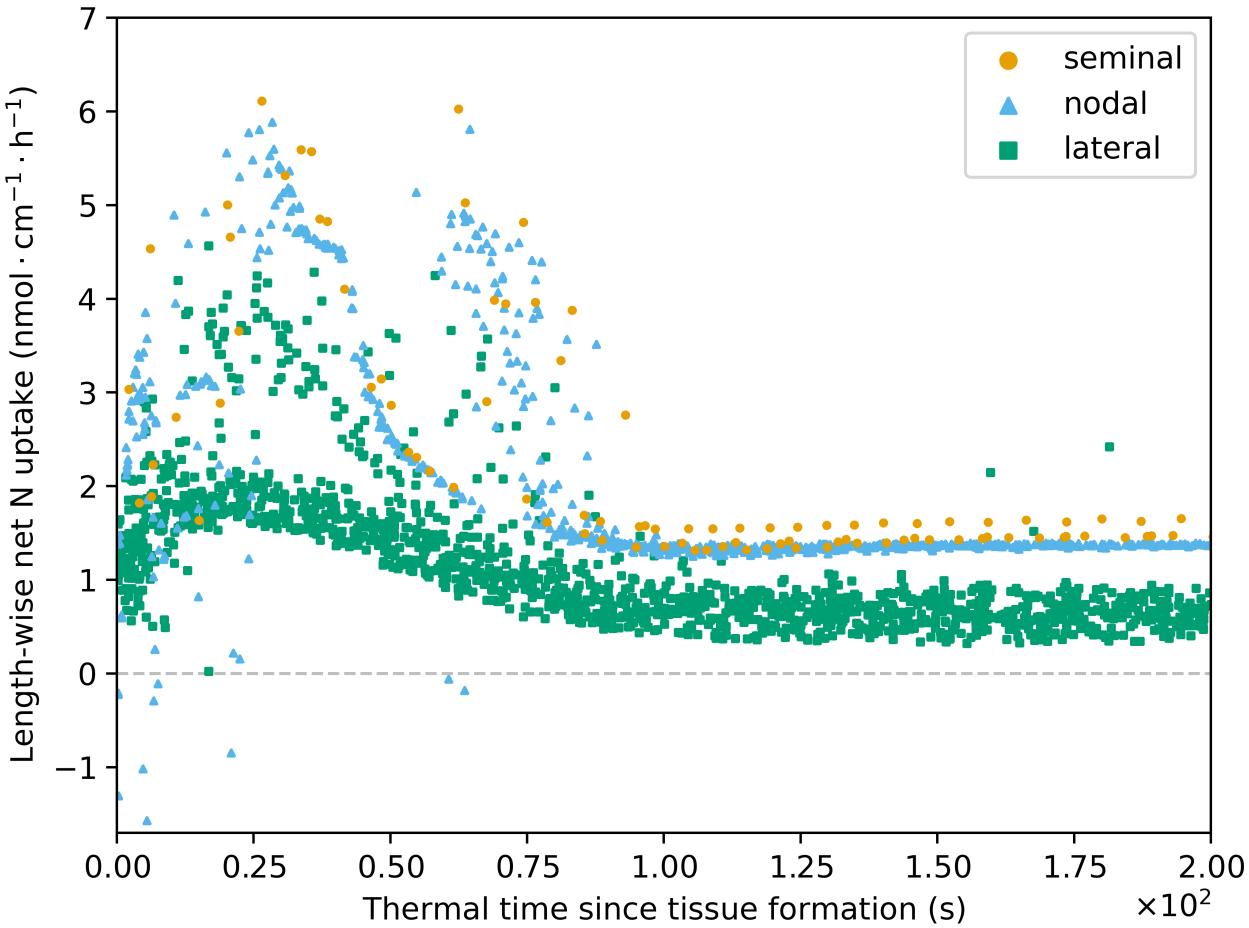

Fig. S7. Evolution of net mineral N uptake per unit root length with the thermal time since root tissue formation, as simulated by *Root-CyNAPS* on wheat under Scenario 14 (50 days-old, 0.5 mM external nitrate). Each individual point corresponds to one root segment. Colors represent different root types (i.e. seminal for orange circles, nodal in blue triangles, and lateral in green squares)

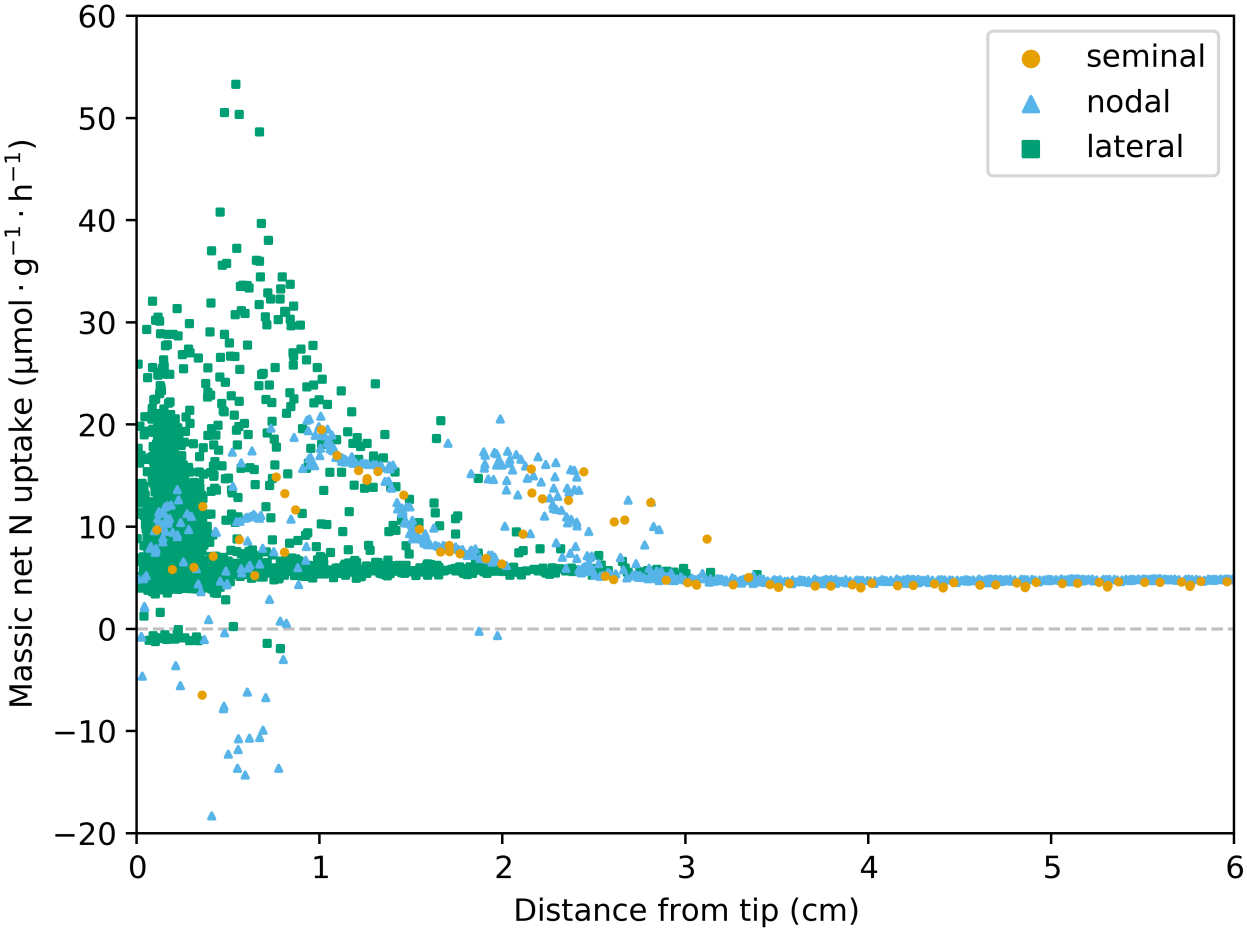

Fig. S8. Evolution of massic net mineral N uptake with the distance from tip, as simulated by *RootCyNAPS* on wheat under Scenario 14 (50 days-old, 0.5 mM external nitrate). Each individual point corresponds to one root segment. Colors represent different root types (i.e. seminal for orange circles, nodal in blue triangles, and lateral in green squares)

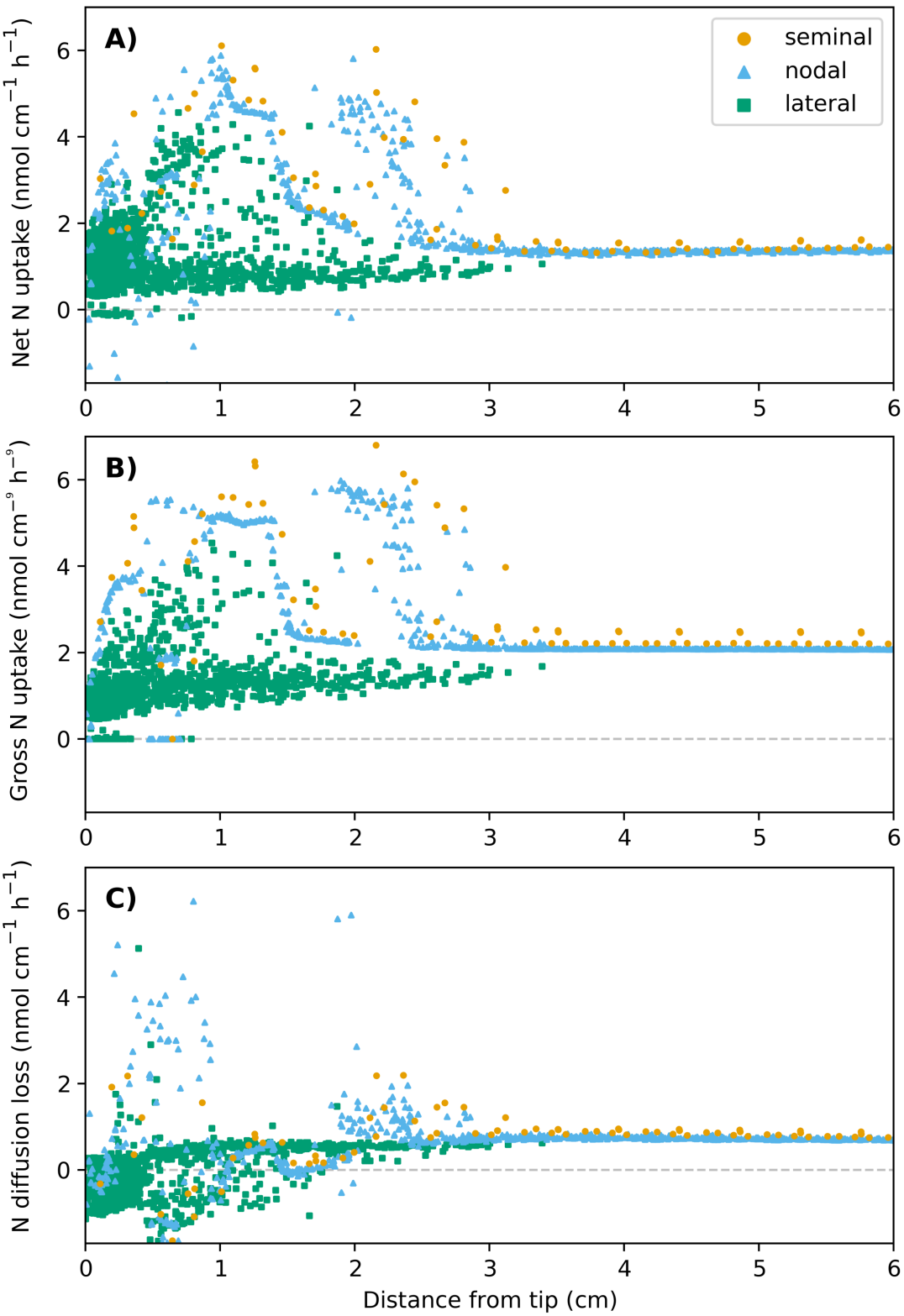

Fig. S9. Decomposition of net N uptake (A) between gross N uptake (B) and N losses through diffusion (C) with distance from root tip, as simulated by *Root-CyNAPS* on wheat under Scenario 14 (50 days-old, 0.5 mM external nitrate). Colors represent different root types (i.e. seminal for orange circles, nodal in blue triangles, and lateral in green squares)

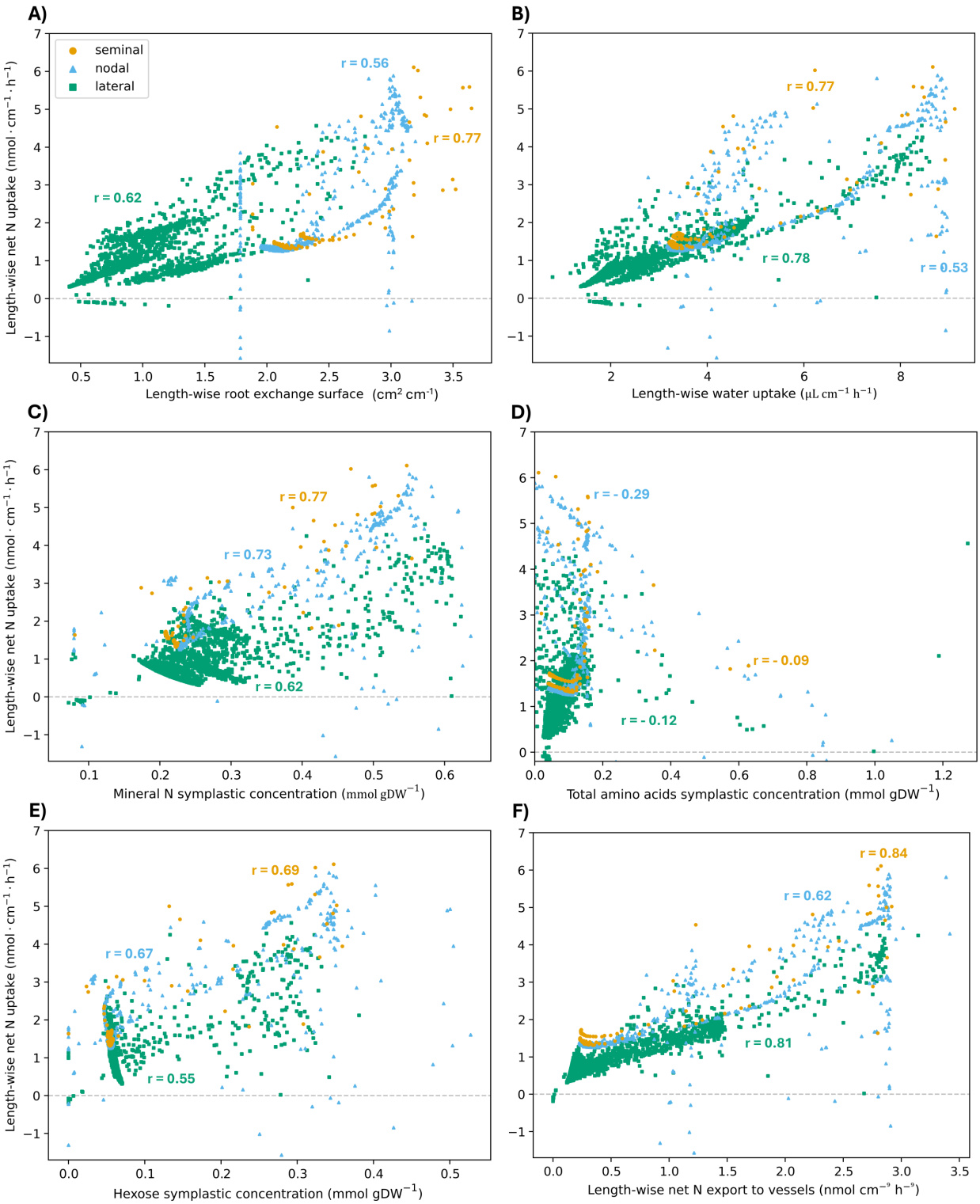

Fig. S10. Evolution of net N uptake per unit root length with (A) root exchange surface normalized by root segment length, (B) water uptake per unit root length, (C) mineral N concentration, (D) total amino acids concentration and (E) hexose concentration in the root segment symplasm, and (F) net N export to vessels between import from phloem and export to xylem per unit root length, as simulated by *Root-CyNAPS* on wheat under Scenario 14 (50 days-old, 0.5 mM external nitrate). Each individual point corresponds to one root segment. Colors represent different root types (i.e. seminal for orange circles, nodal in blue triangles, and lateral in green squares). Pearson correlation r index is shown on graphs with the corresponding colors.



Fig. S11. Evolution of gross N uptake per unit root length with (A) root exchange surface normalized by root segment length, (B) water uptake per unit root length, (C) mineral N concentration, (D) total amino acids concentration and (E) hexose concentration in the root segment symplasm, and (F) net N export to vessels between import from phloem and export to xylem per unit root length, as simulated by *Root-CyNAPS* on wheat under Scenario 14 (50 days-old, 0.5 mM external nitrate). Each individual point corresponds to one root segment. Colors represent different root types (i.e. seminal for orange circles, nodal in blue triangles, and lateral in green squares). Pearson correlation r index is shown on graphs with the corresponding colors.

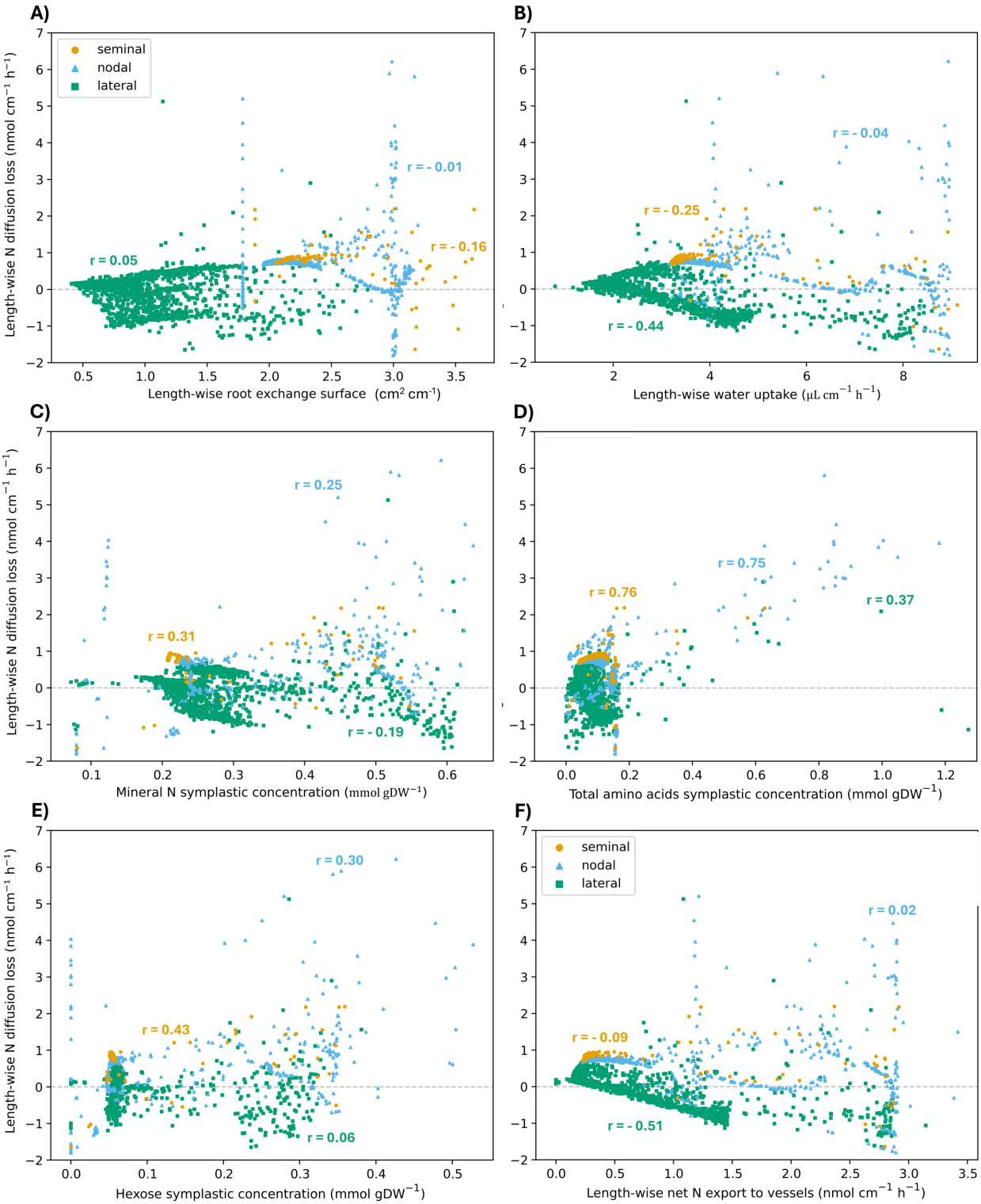

Fig. S12. Evolution of N loss through diffusion per unit root length with (A) root exchange surface normalized by root segment length, (B) water uptake per unit root length, (C) mineral N concentration, (D) total amino acids concentration and (E) hexose concentration in the root segment symplasm, and (F) net N export to vessels between import from phloem and export to xylem per unit root length, as simulated by *Root-CyNAPS* on wheat under Scenario 14 (50 days-old, 0.5 mM external nitrate). Each individual point corresponds to one root segment. Colors represent different root types (i.e. seminal for orange circles, nodal in blue triangles, and lateral in green squares). Pearson correlation r index is shown on graphs with the corresponding colors.

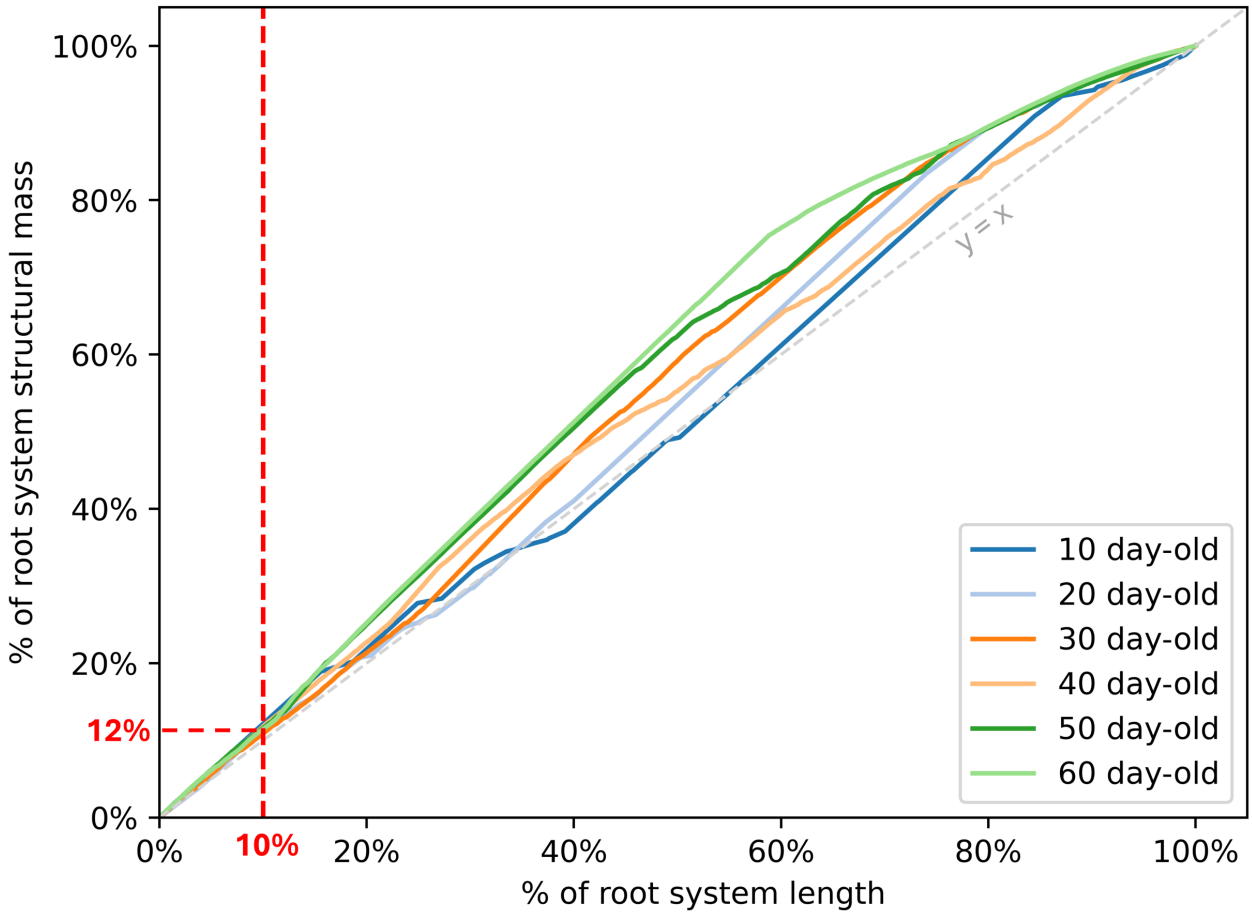

Fig. S13. Percentage of root system structural mass as a function of the percentage of root system length for plant ages from 10 to 60 days-old. The dataset has been ordered by net N uptake per unit root length to compute these cumulative variables.

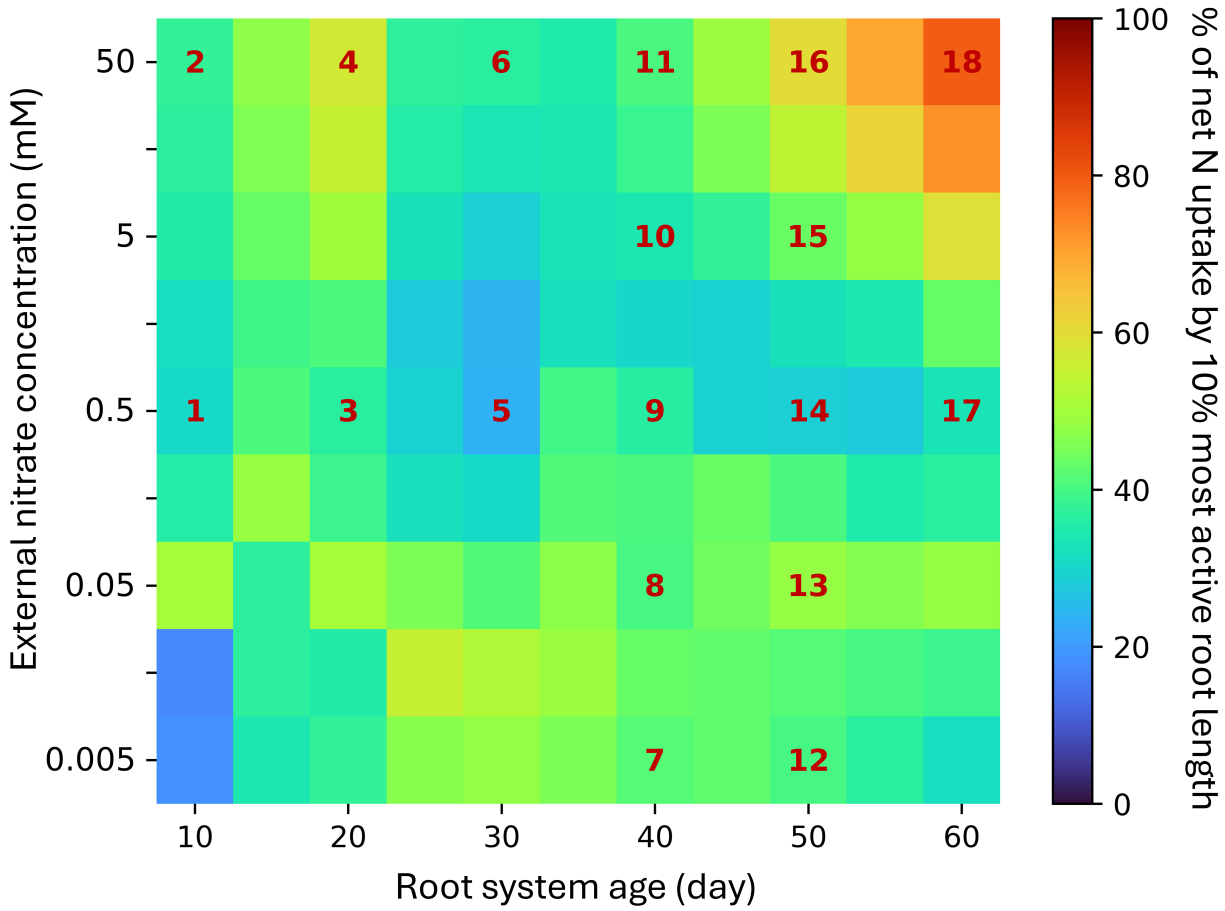

Fig. S14. Contribution of the 10% most active root length in whole-plant N budget, as a function of root system age and nitrate concentration in culture solution. Ages and concentrations investigated in the article main corpus are indicated with corresponding scenario numbers in red

Supplementary Note A: Experimental acquisition of anatomical parameters for Root-CyNAPS

Anatomical features of winter wheat *Soissons* were obtained from controlled condition phytotron experiments. 14 plants were grown for 35 days in rhizotrons filled with agricultural soil under a 15 : 20°C day/night cycle, with a 13 h day length under 600 $\mu mol\ m^{-2}\ s^{-1}$, a red/far-red ratio of 1.2, and 70 : 60% relative humidity. At the end of the experiment, rhizotrons were opened non destructively and 1.5 cm long root segments were sampled at 0, 3, 10, 15, 40 cm from root tip and 1 cm below the root-shoot junction, on seminal, nodal and lateral roots when these regions were accessible. These locations were chosen with respect to expected differentiation transitions for endodermis, exodermis and conductive elements. All samples were immediately fixed in paraformaldehyde. Apical locations were then transparized using ClearSee for longitudinal confocal imaging, and other locations were dehydrated, included in paraffin, and cross sectioned at 10 µm with a microtome. Transparized apices were stained with calcofluor white for confocal imaging, and cross sections were stained with toluidine blue for optical microscopy. (Gérault et al. *in prep*).

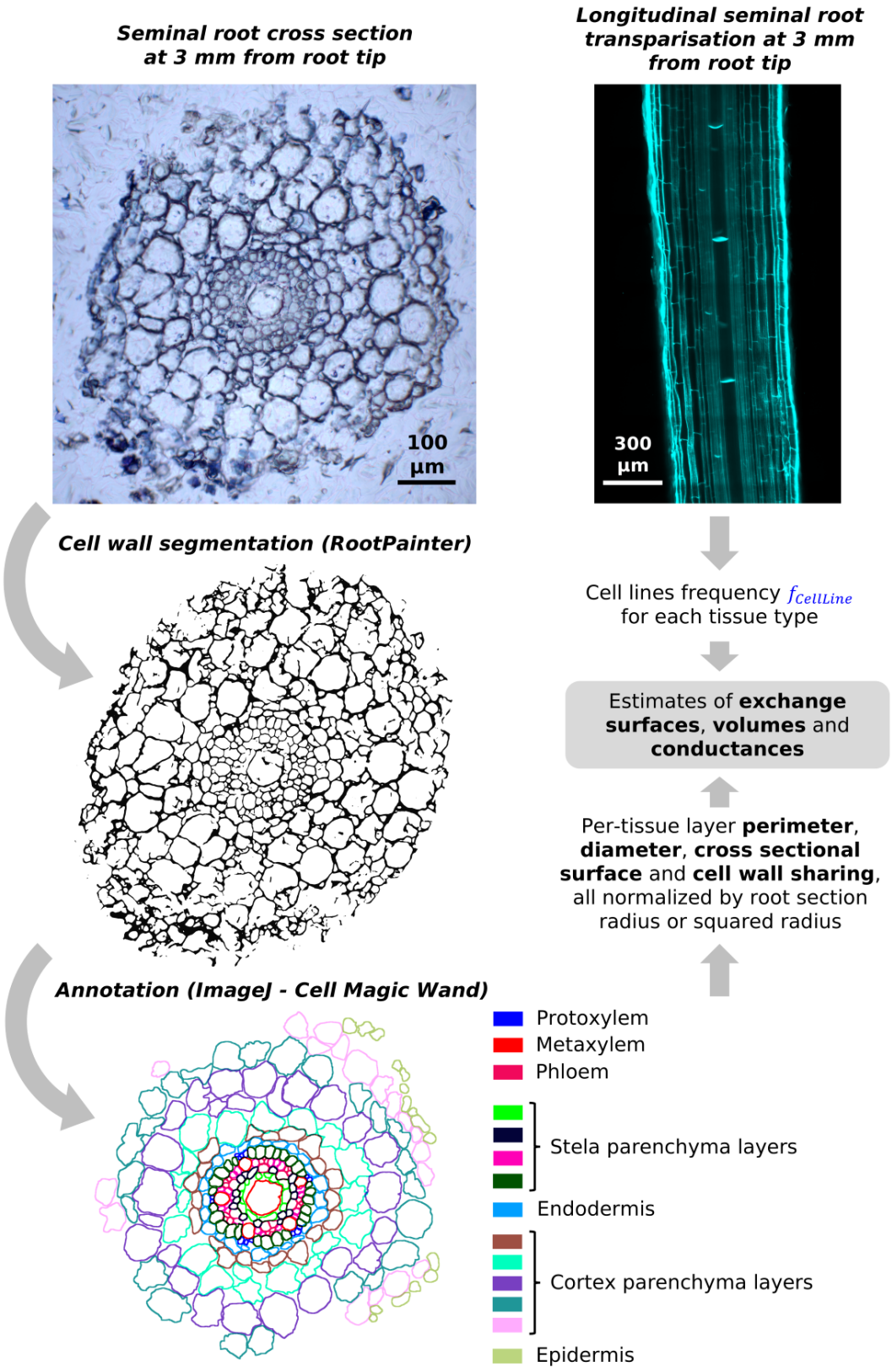

Fig. S15. Methodology summary of parameter measurement for the anatomical features simulated by *Root-CyNAPS*. (A) optical cross-sectional image and (B) a longitudinal confocal image at 3 mm from root tip of a seminal root of a winter wheat, after 35 days of growth in the experimental conditions described below. Image analysis was conducted using *RootPainter* for semi-automated segmentation of cell walls (?) and *ImageJ* with the *Cell Magic Wand* plugin for cell delineations and per tissue measurements (https://github.com/fitzlab/CellMagicWand, accessed on 2024/03/16).

Supplementary Note B: Determinants of most active root zones locations

Root-CyNAPS simulations on wheat in hydroponics revealed two *most active root zones* for net N uptake per unit root length, one near the apex of all root types, the other one - for seminal and nodal roots only - at the emergence of a lateral primordium. The main determinants of these two zones were root exchange surface, hexose symplastic concentration and water uptake.

Regulation by Root Exchange Surface

As most of the fluxes contributing to net N uptake were transmembrane root-soil exchanges, root exchange surface and its variability among root segments were a key determinant of the observed locations (S11). In our simulations, root segments presented a minimal differentiation of both endodermis and exodermis near root apices, with endodermis dedifferentiation also occurring upon lateral primordium emergence (Eq. **??**). This had a critical impact on the spatial distribution of N uptake, which highlights the necessity for reliable experimental data for parameterizing *Root-CyNAPS*. In this study, the parametrization of exchange surfaces was performed on a limited number of replicates in our own experiment (S15), and the tissues differentiation rates were estimated from four distinct anatomical of studies on wheat (Table S2). This should be further investigated through subsequent experiments to improve confidence in the model's representation of anatomical heterogeneity along the roots.

Regulation by Hexose Concentrations in Symplasm

The spatial variations in N uptake along seminal and nodal roots also coincided with variations in root symplastic hexose concentration, as the active N uptake is regulated by hexose availability to reflect the energetic cost associated to the transmembrane transport of N (Eq.**??**). These hexose profiles corresponded to an input of the Root-CyNAPS model, and originated from simulations by *RhizoDep* (**?**), where hexose is preferentially unloaded from phloem into root segments contributing to root growth, i.e. apical regions and support segments for lateral primordium emergence. These hexose concentration profiles were also determined by hexose consumption by growth, which is restricted to the elongation zone, i.e. all root segments between an axis root tip and a distance from tip depending on root apex diameter. In the case of lateral primordium emergence, these hexose costs also propagate to the supporting root segment on the parent root. Since wheat roots do not undergo thickening, there was no cost associated with secondary growth in these scenarios. These modeling principles of *RhizoDep* caused accessible exchange surface and hexose concentrations should be maximal in the same root zones when up-regulating N uptake. The correlation between net N uptake per unit root length and hexose symplastic concentrations was however weaker for lateral roots than for seminal or nodal roots (Fig S11E), as lateral roots usually stopped growing much earlier. The unloading of hexose from the phloem was limited in the apical region of lateral roots once they stopped elongating, which led to a higher homogeneity of hexose symplastic concentrations along these roots.

Advection of N Through Water Uptake

Finally, the increase in N uptake with water uptake relates to the apoplastic N inflow through water uptake. This N uptake pathway is opened near root apices during a short differentiation phase, i.e. when xylem has been functionalized through apoptose (Eq. **??**) and endodermis differentiation does not yet block the apoplastic pathway (**?**). At these locations the soil-xylem water potential gradient enabled a water uptake at root tips as it was observed in figure **??**, this allows a significant proportion of net N uptake to be linearly correlated to water uptake and the external N concentration (Eq. **??**).

Supplementary Note C: Introduction to the RhizoDep model

The model *RhizoDep* (**?**) simulates how roots grow, respire, and emit rhizodeposits into the soil, based on the distribution of available C within a dynamic 3D root architecture (Fig. S16). The model operates at fine spatial and temporal scales, typically simulating root segments of 1-mm with an hourly time step. *RhizoDep* incorporates simplified physiological processes that account for major C transfers within the roots and between roots, soil and atmosphere. Aside from soil temperature, which can affect rates in various ways, the main input variable of the model is the net C transferred from the aerial parts of the plant to the root system. This input is represented as sucrose transported through roots' phloem vessels. A portion of this sucrose is then unloaded and converted into hexose, which serves as the substrate driving key metabolic processes. These include: i) the production of root structural mass, associated with the elongation of roots or root hairs and secondary growth, following growth rules derived from the model *ArchiSimple* (**?**), ii) root maintenance, iii) sugar immobilization in or remobilization from a reserve pool, and iv) rhizodeposition. No priority is assigned to any of these processes in terms of hexose consumption. Rhizodeposition processes include the net exudation of hexose or sucrose (difference between gross exudation by diffusion from root symplasm and reuptake of sugars from the soil by the roots), the secretion of mucilage at root tips and the release of border cells from root caps. Additionally, a simple representation of the fate of rhizodeposits outside the roots has been implemented, though such processes are expected to be managed by a dedicated soil model in the future. *RhizoDep* focuses on C dynamics within the root-soil system, and as such does not simulate the aerial parts of the plant, C allocation from shoots to roots, or the dynamics of nitrogen and water.

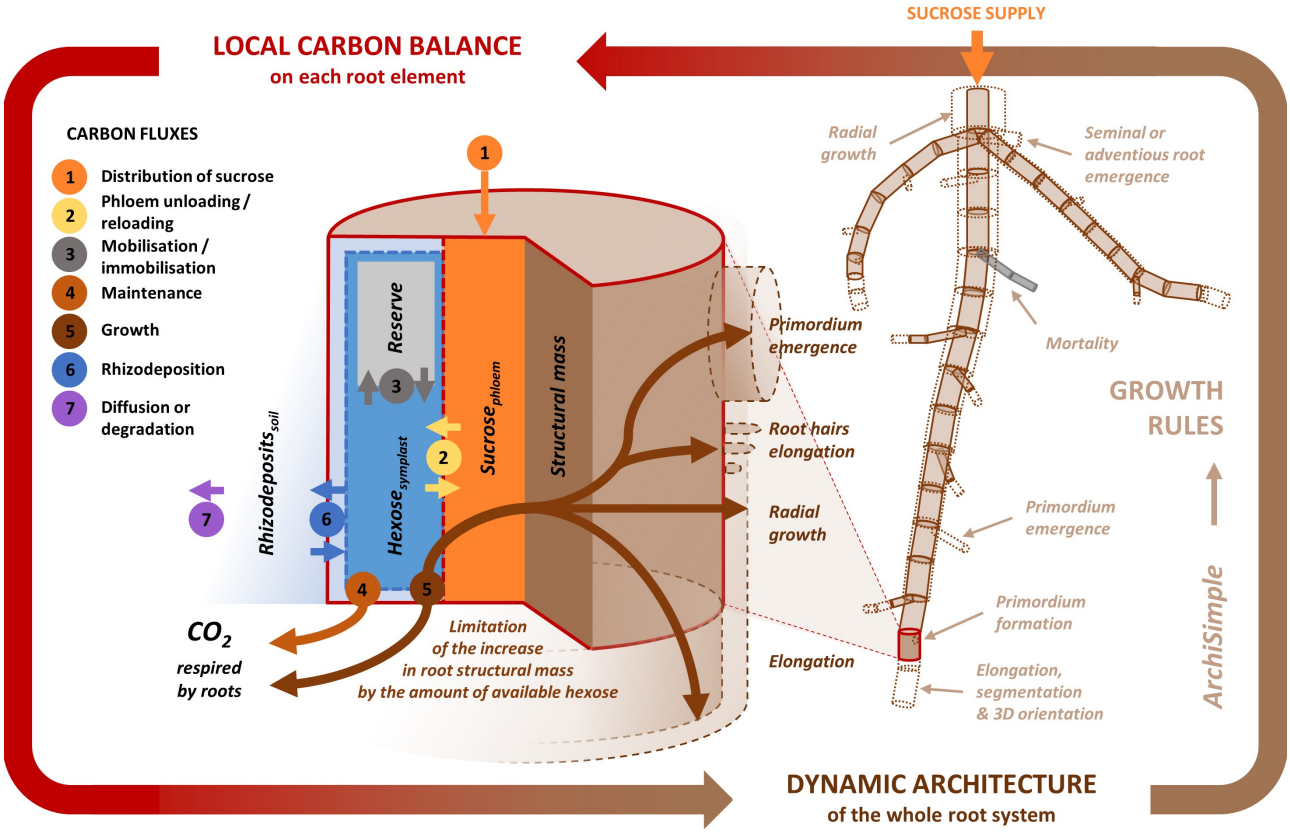

Fig. S16. Overview of the *RhizoDep* model (?). Photoassimilated C enters the root system as sucrose (model input), which is then distributed among each root element (1) and can be converted into hexose (2). Hexose may be stored in a reserve pool (3), used for maintenance (4), or consumed for growth, contributing to structural mass production - either through longitudinal growth (for an apex) or radial growth (for a segment), or through the emergence of new lateral roots or root hairs (5). Once exuded outside the root, sugars can be reabsorbed by the root (6) or lost from the root-soil interface due to microbial degradation, sorption, or diffusion (7). Similarly, other rhizodeposits (e.g., mucilage, sloughed cells) can accumulate at the root-soil interface or be lost. The local C balance within each root element ultimately constrains potential root architecture development, as defined by growth rules adapted from the *ArchiSimple* model (?). (Figure credit, ?)

Chapter 4 Supplementary Material

Supplementary Figures

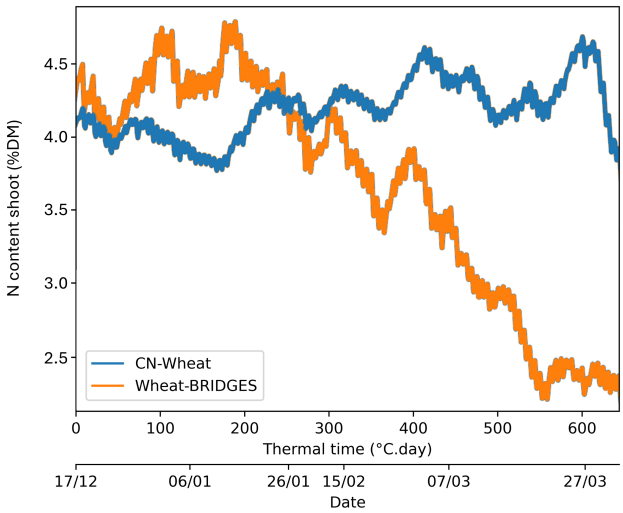

Figure 6.15: Shoot N content in percentage of shoot dry mass over time as simulated by the *CN-Wheat* model (blue) and the *Wheat-BRIDGES* model (orange). The secondary X axis aligns thermal time with corresponding dates.

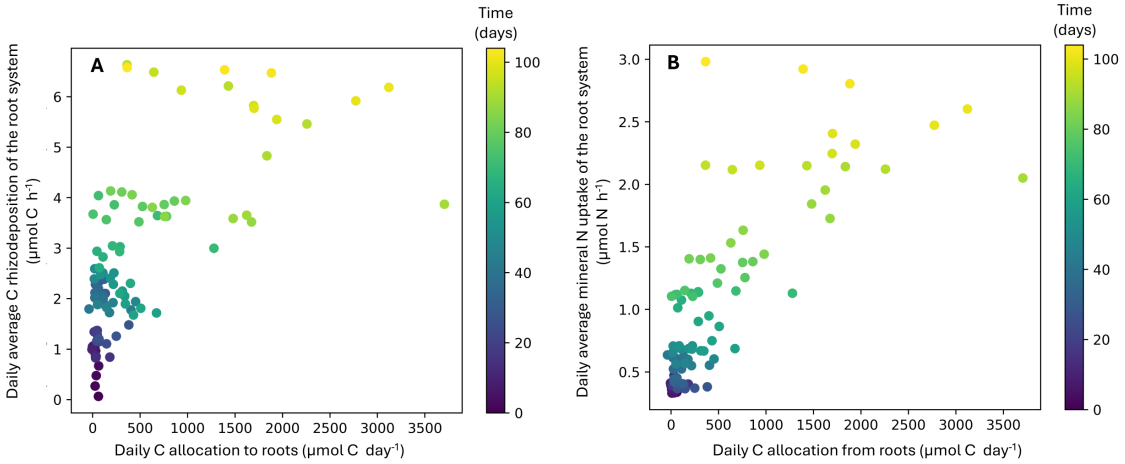

Figure 6.16: Daily average root system total C rhizodeposition (A) and net mineral N uptake (B) as a function of daily C allocation from shoot to roots. The colors represent days since the simulation started.

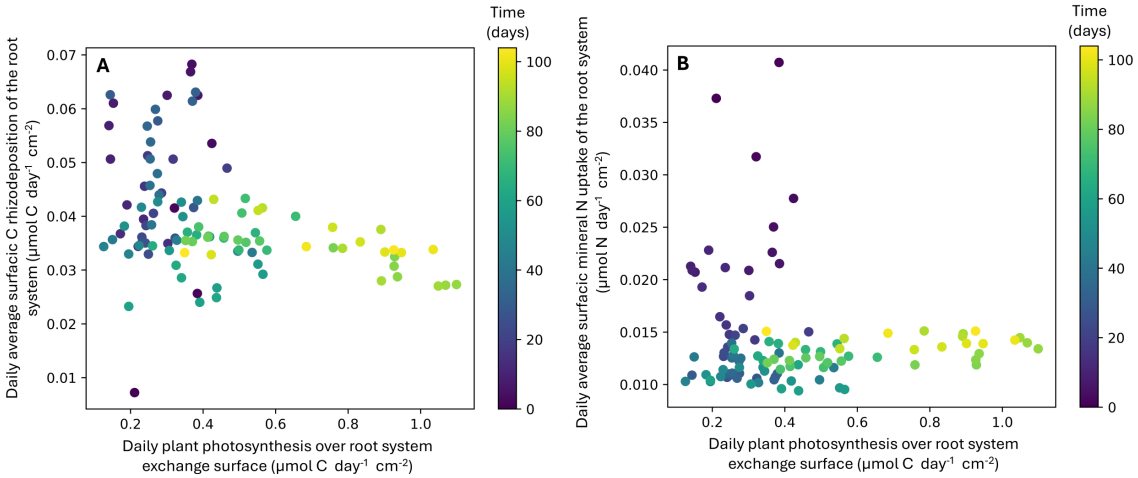

Figure 6.17: Daily average root system surfacic C rhizodeposition (A) and net surfacic mineral N uptake (B) as a function of daily massic plant photosynthesis. All three massic flows were normalized by root system total exchange surface. The colors represent days since the simulation started.

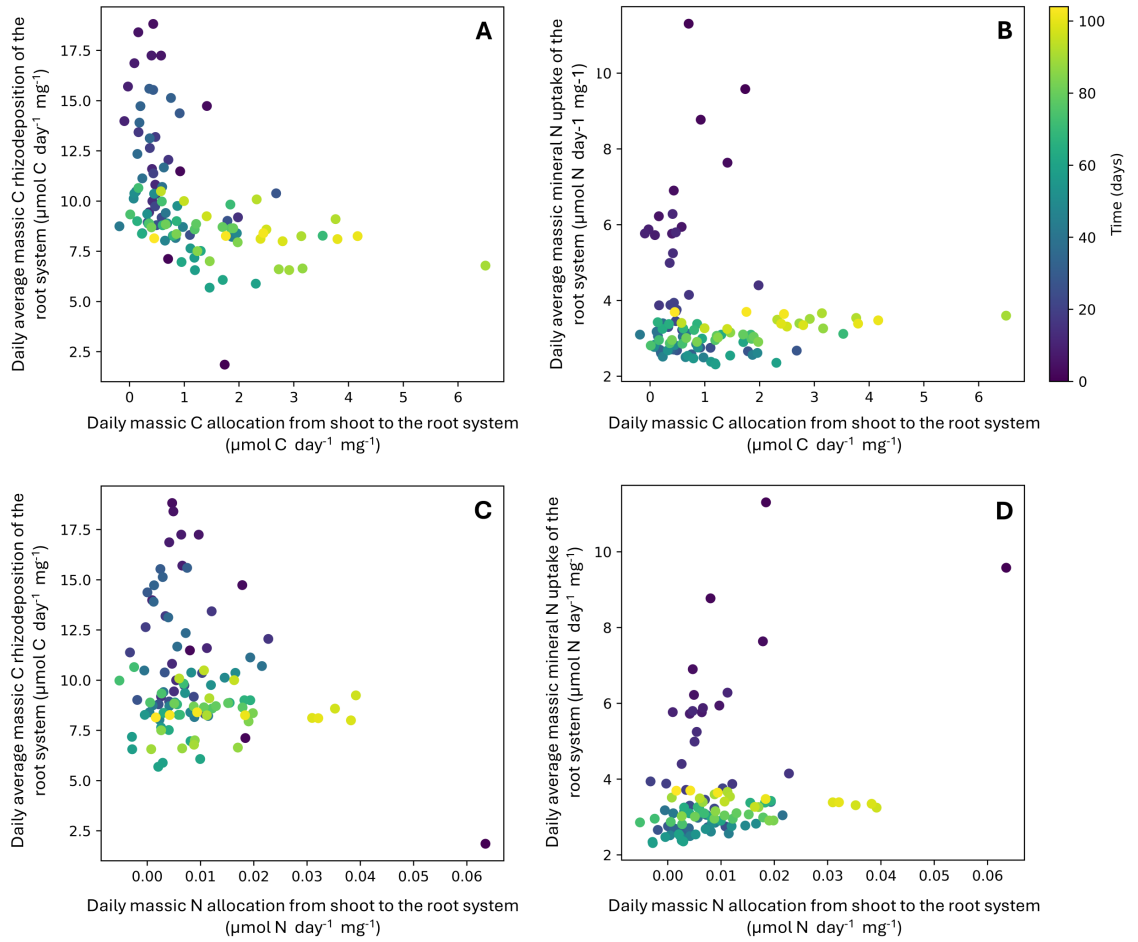

Figure 6.18: Daily average root system massic C rhizodeposition (A & C) and net massic mineral N uptake (B & D) as a function of daily massic C allocation from shoot (A & B) and daily massic N allocation from shoot (C & D) to the root system. All massic flows were normalized by root system total exchange surface. The colors represent days since the simulation started.

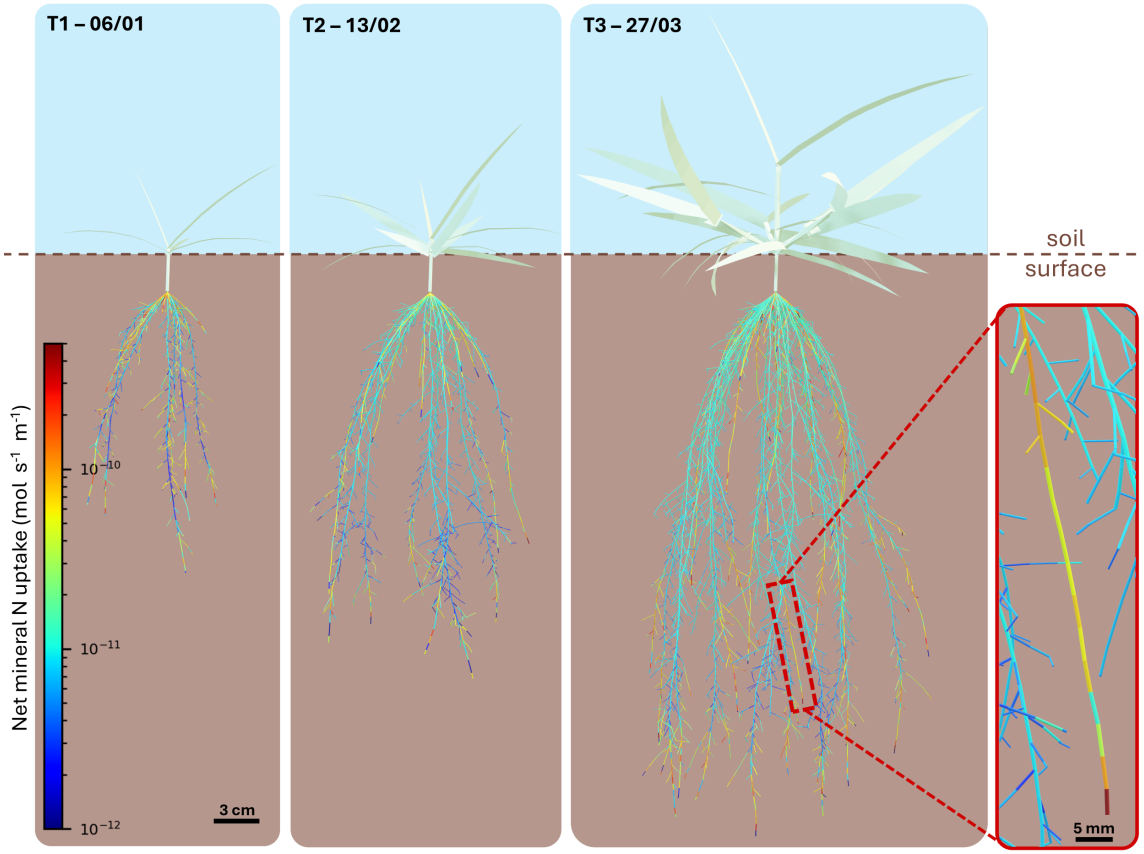

Figure 6.19: Spatial distribution of net mineral N uptake per unit of root length throughout the root system architecture of winter wheat as simulated by Wheat-BRIDGES, shown at 20, 57 and 100 days after simulation started (T1, T2 & T3 respectively). For an interactive video, see geraulttr.github.io/AR_glb_viewer

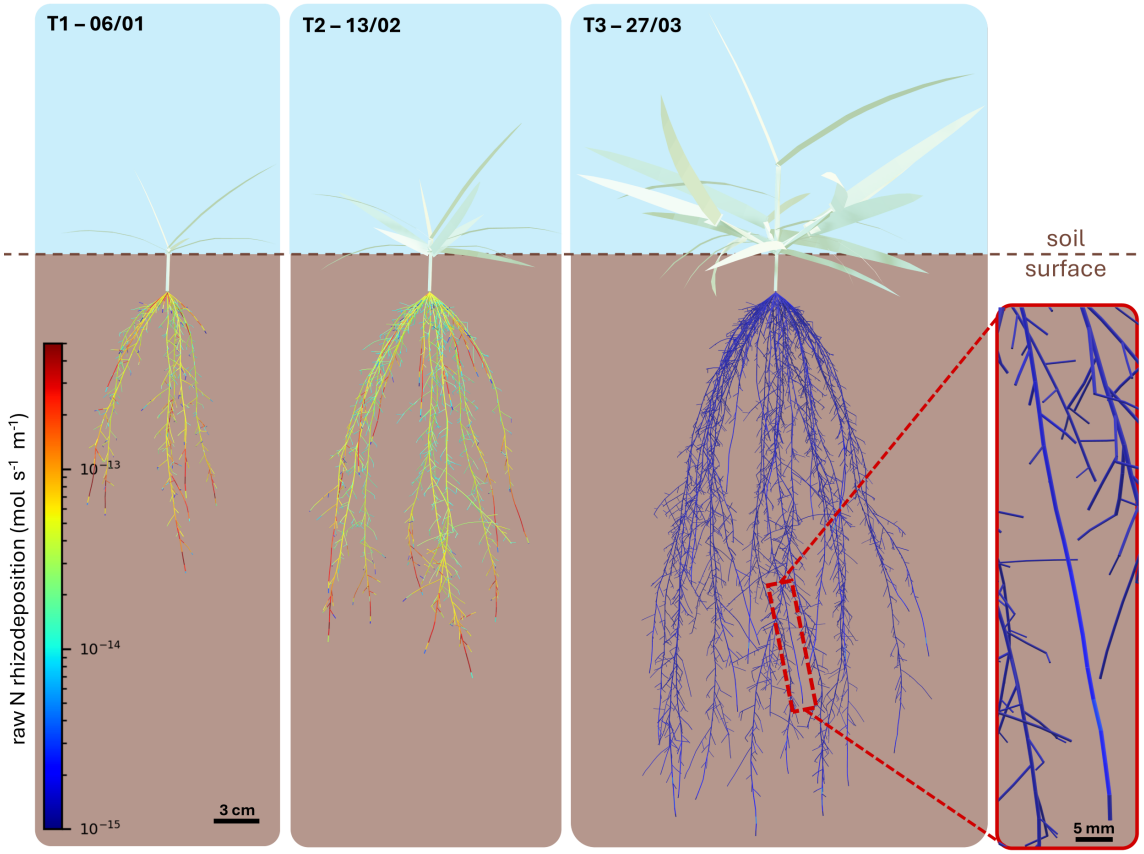

Figure 6.20: Spatial distribution of net N rhizodeposition per unit of root length throughout the root system architecture of winter wheat as simulated by *Wheat-BRIDGES*, shown at 20, 57 and 100 days after simulation started (T1, T2 & T3 respectively). For an interactive video, see geraulttr.github.io/AR_glb_viewer

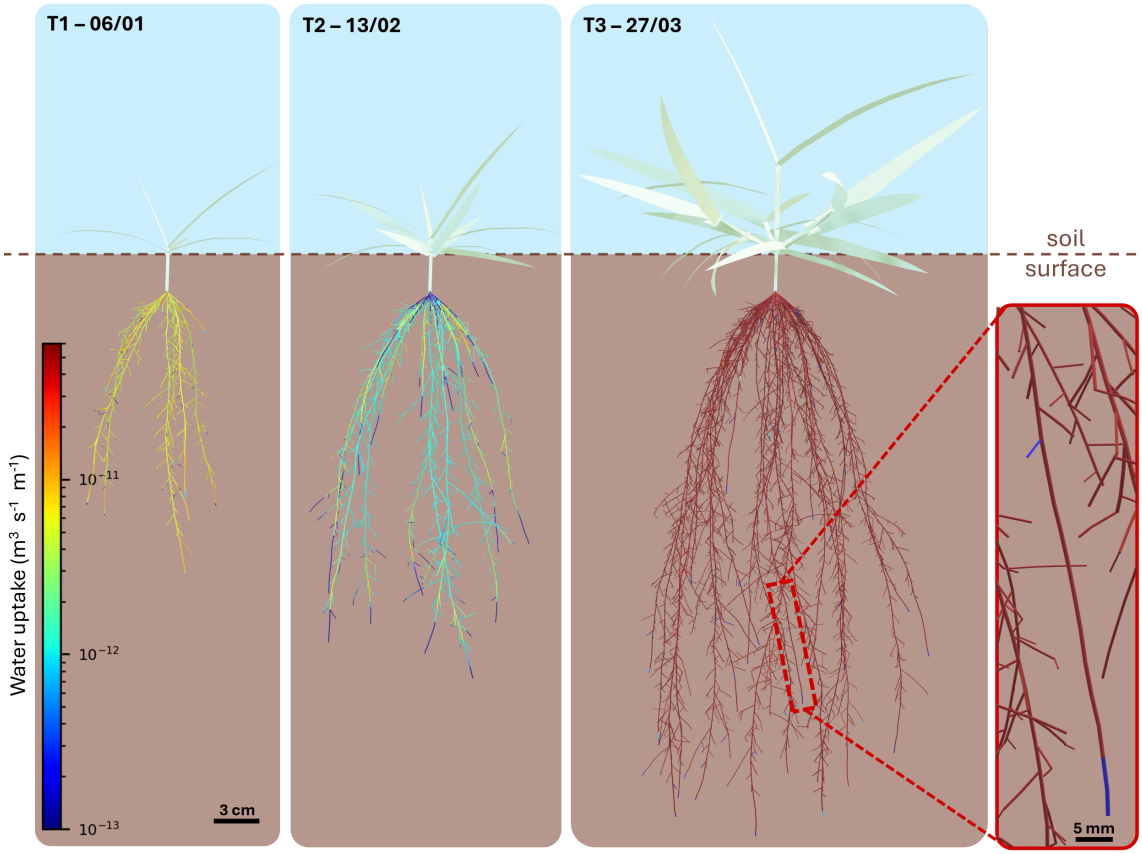

Figure 6.21: Spatial distribution of water uptake per unit of root length throughout the root system architecture of winter wheat as simulated by *Wheat-BRIDGES*, shown at 20, 57 and 100 days after simulation started (T1, T2 & T3 respectively). For an interactive video, see gerault tr.github.io/AR_glb_viewer

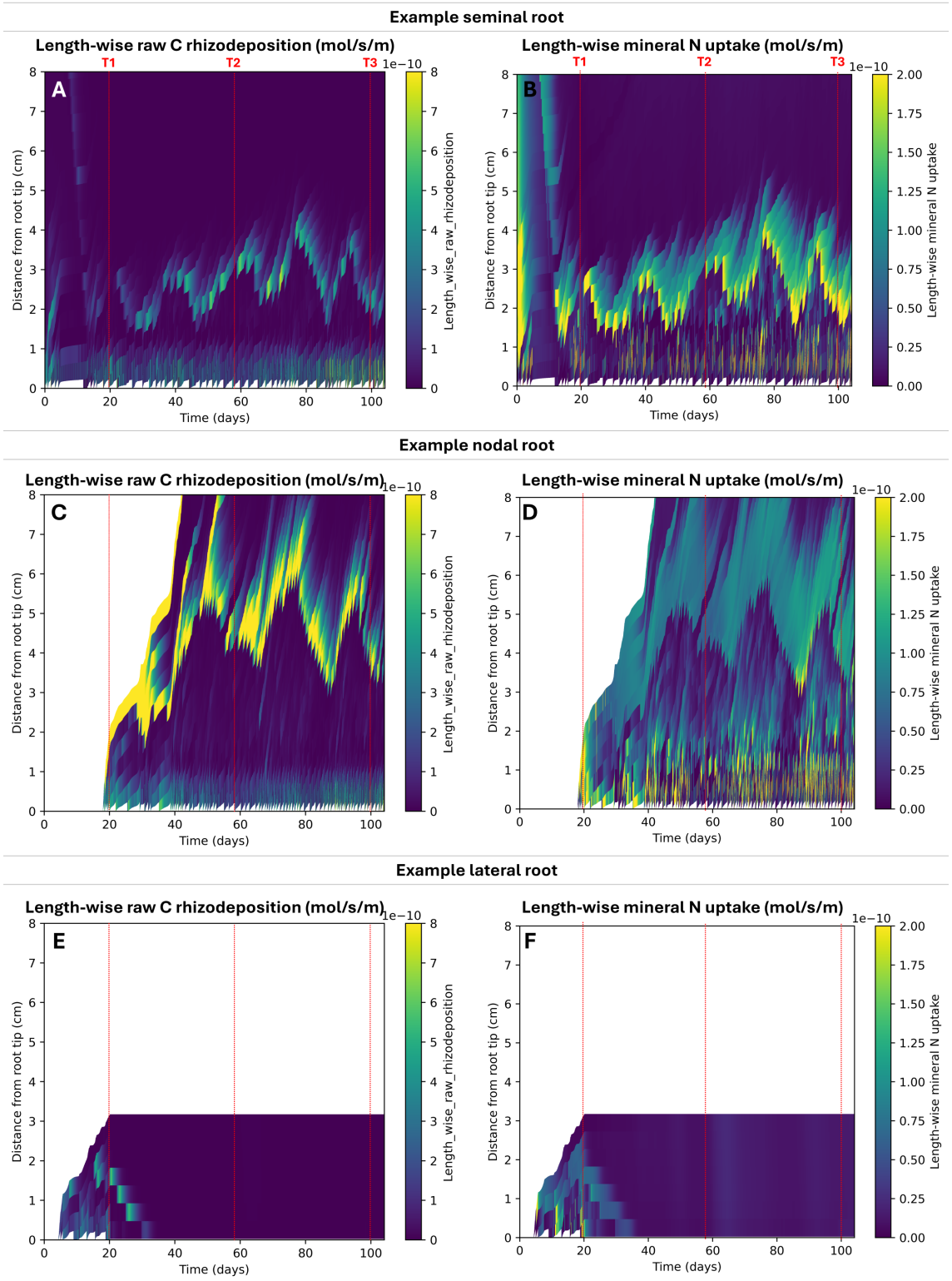

Figure 6.22: Evolution of C rhizodeposition per unit of root length along a single root and across time (A, C, E), and of mineral N uptake per unit of root length along a single root and across time (B, D, F). An example seminal, nodal and lateral root carried by a seminal root are presented.

Supplementary Notes

Supplementary Note 1: *Root-BRIDGES* nitrate patch scenario

A simulation scenario was designed to study the plastic response of the root system to an exposure to a localized nitrate patch. In this objective, *Root-BRIDGES* used in a scenario following the hydroponic growth conditions of Drew and Saker [1975] on wheat. Before studying the plastic response of the root system, we confirmed that simulated dry mass was in close range with experimental measurements (Fig. S6.23). Root growth was then simulated over time for both a control and a nitrate

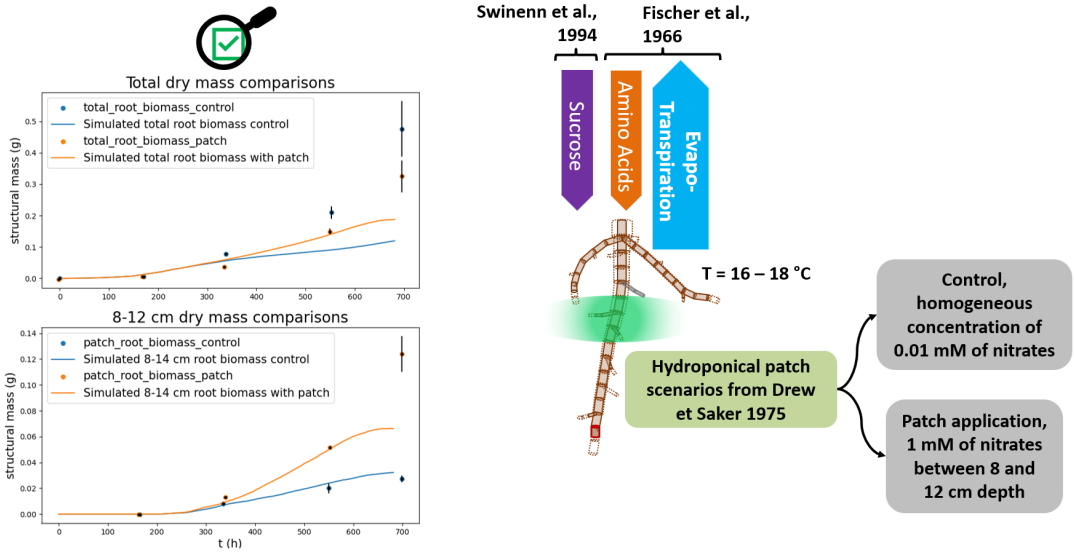

Figure 6.23: Drew and Saker [1975] simulation scenario applied to *Root-BRIDGES*

patch exposure scenario between 8 and 12 cm. The results are summarized in Figure S6.24 and showed an increased N uptake and rhizodeposition in the patch horizon, compared to the control and other root regions. This increase of root-soil exchanges were also associated with an increase in lateral branching intensity which emerged only from the trophic C&N interactions introduced in *Root-BRIDGES*, making increased exchange surface and the multiplication of active apices key determinants of sustained exchanges in this horizon. However, the input C supply to the model was identical for both control and test scenarios, therefore increased root growth negatively impacted the C allocation to rhizodeposition in the patch scenario compared to the control. These results were presented at an oral communication during the international conference ISRR 2024.

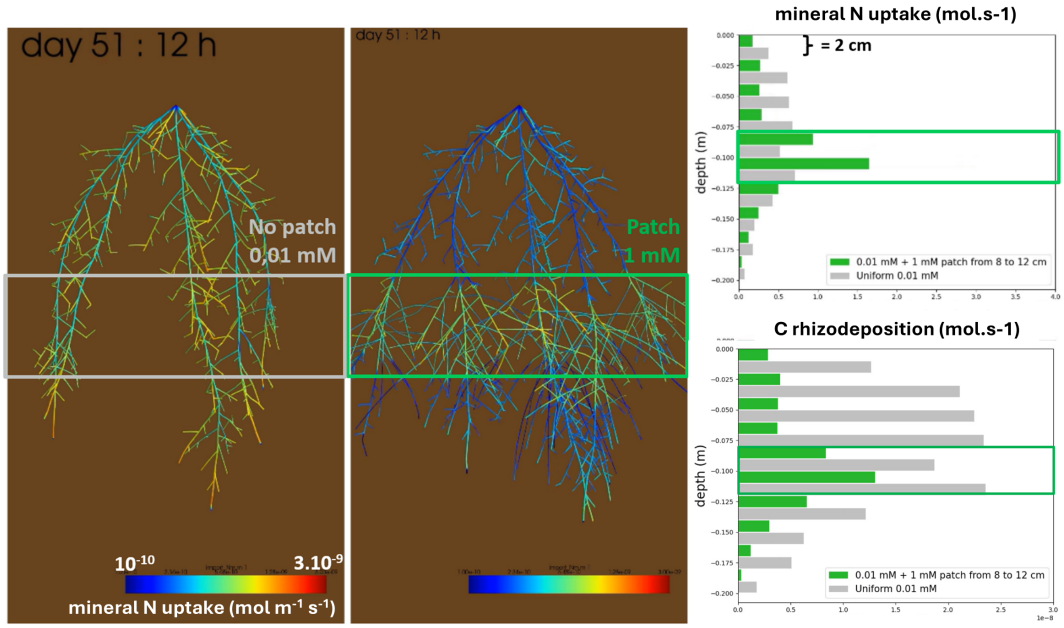

Figure 6.24: Simulation outputs of *Root-BRIDGES* in a nitrate patch scenario inspired from Drew and Saker [1975]

Supplementary Note 2: Clustering the physiological states of FSPM organs

Here we tested an adaption of the method of Ali et al. [2019] to analyze complex FSPM outputs, taking each plant organ multivariate time series at the same level and clustering their *physiological state* to decipher the determinants contrasted organs activity throughout the plant. We combined a Deep Convolutional AutoEncoder with a UMAP projection of the encoded outputs, and with a HDBSCAN clustering of the projection. Each identified cluster was then related to original simulated data by clearly isolating the physiological differences that explained divergence between clusters: which processes or states, where in the plant architecture and at what time did the model simulate a recurrent pattern.

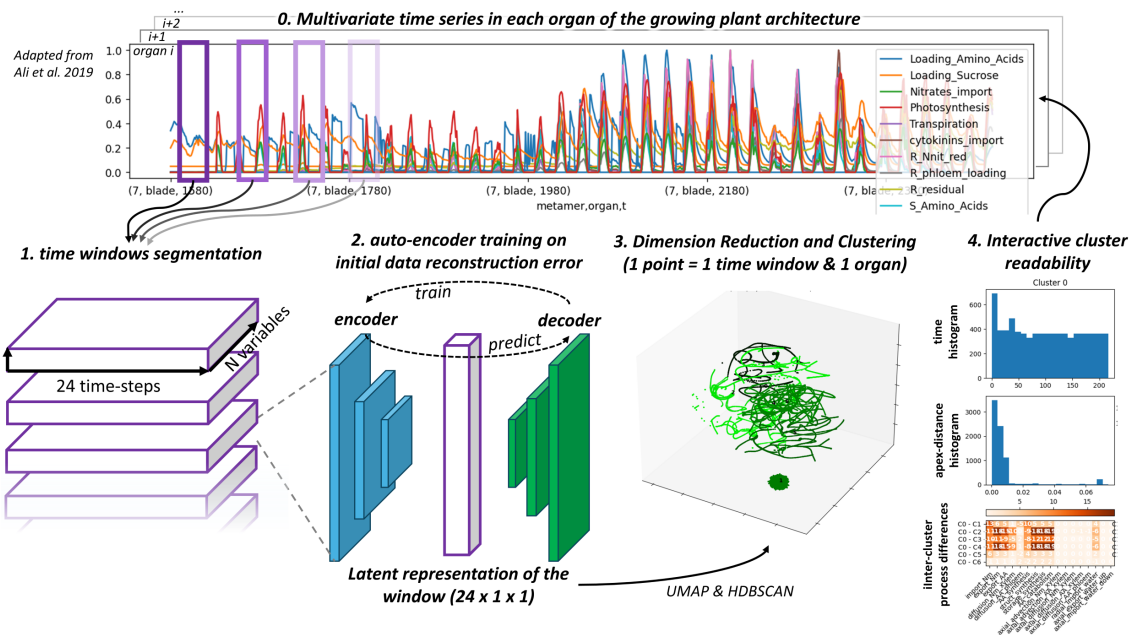

Figure 6.25: Data analysis workflow for FSPM time-series outputs adapted from Ali et al. [2019]. Before the analysis, a preparation step slices output time series in 24h windows for all variables and all organs simultaneously. This dataset of time-windows is then used for the training of a Deep Convolutional AutoEncoder (DCAE, 2). The DCAE is trained to reconstruct initial data, and when the prediction error is low enough, the high-dimensional latent representation of the windows are then projected into a lower dimension space with UMAP, easing the visualization and clustering of each window, e.g. with HDBSCAN (3). Finally, each cluster is related to the original data to define what time, which which organ and which organ explained the divergence between clusters (4).

Chapter 5 Supplementary Material

Supplementary Figures

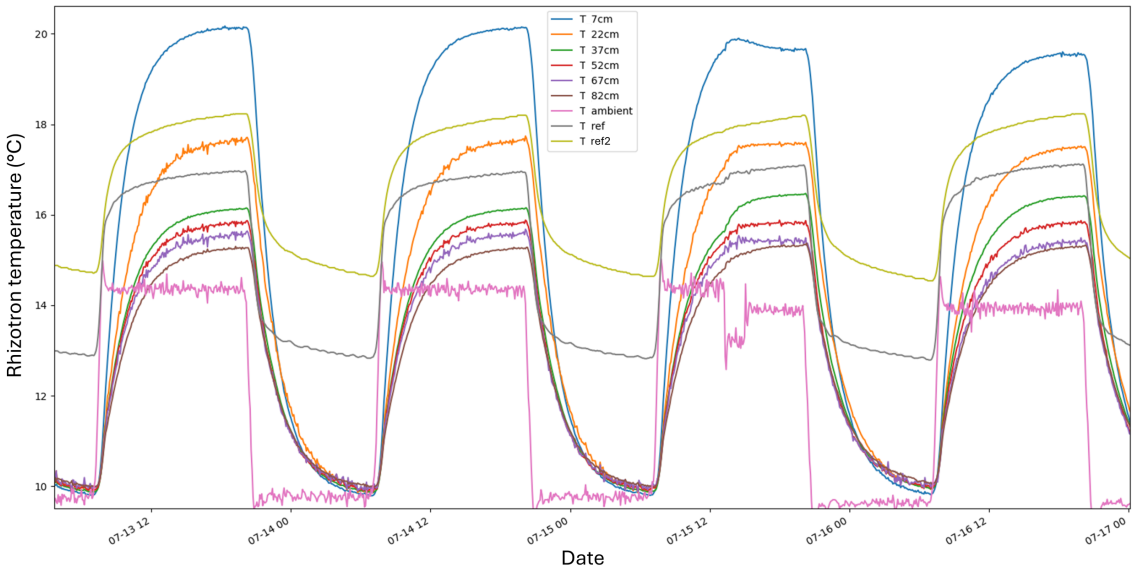

Figure 6.26: Temperature profile along rhizotron horizons (7, 22, 37, 52, 67, 82 cm from soil surface) during 4 example days of Exp. 2. *T ambient* is an additional control sensor monitoring air temperature in a shadowed area, and *T ref* and *T ref2* are internal temperatures of the Campbell acquisition card.

Supplementary Notes

Supplementary Note 1: ^{15}N pulse - labeling with sand patches applied to roots

On the last day of preliminary rhizotron experiment, a localized pulse - labeling using of the root system was tested using 10mM KNO_3 enriched to 10% atom ^{15}N applied to 0.52g dry sand patches over 4cm of root for 4h. Labeled tools, separate pipettes and stringent contamination controls would be used. After the pulse, sand, exposed root segments, exposed axes, and remaining root system were be recovered and shoot axes were rinsed repeatedly (5×1min baths) to remove surface ^{15}N, and then frozen for further isotopic analysis along with shoot organs. Soil was dried at 105°C for 48 h prior isotopic analysis. Isotopic analyses remain to be performed to date to quantify the allocation of ^{15}N in the system and test the feasibility of local N uptake assessment using local labeling through patch application.

université PARIS-SACLAY
ÉCOLE DOCTORALE
Agriculture, alimentation, biologie, environnement, santé (ABIES)

Titre : Étude des régulations de la rhizodéposition et du prélèvement d'azote à différentes échelles à l'aide de la modélisation structure-fonction des plantes. Application au cas d'étude du blé (*Triticum aestivum*)

Mots clés : Exsudation racinaire, FSPM, Couplage aérien-racinaire, Ecophysiologie végétale, Stockage de carbone dans les sols, Blé

Résumé : La rhizodéposition, c'est-à-dire la libération de matières organiques par les racines vivantes, a été identifiée comme un levier pour favoriser la séquestration de carbone dans les sols et l'adaptation des plantes à des conditions environnementales variables. Son intensité varie fortement selon l'âge de la plante et la disponibilité en ressources du sol, suivant des régulations encore mal comprises. La rhizodéposition dépendrait du statut métabolique de la plante, en particulier des échanges de carbone (C) et d'azote (N) au sein de la plante. Son hétérogénéité le long des racines suggère une forte dépendance vis-à-vis de l'architecture racinaire et des caractéristiques anatomiques et métaboliques de chaque segment racinaire. L'absorption de nutriments par les racines étant contrôlée par des facteurs similaires, la rhizodéposition et l'absorption d'azote pourraient co-évoluer dans l'espace et le temps, mais leur variabilité spatiale conjointe et leurs interactions restent largement inexplorées.

Cette thèse a visé à quantifier la variabilité spatiale et temporelle de la rhizodéposition et de l'absorption d'azote, à proposer une interprétation mécaniste de cette variabilité, et à évaluer son importance pour le bilan en C et N de la plante, en prenant le blé comme cas d'étude. Elle s'est appuyée sur des modèles de plantes fonction-structure (FSPM), afin d'étudier les interactions entre architecture, métabolisme et environnement. *Root-CyNAPS*, un nouveau FSPM simulant le métabolisme et le transport de l'azote dans un système racinaire 3D avec une description anatomique détaillée, a été conçu pour analyser la variabilité spatiale de l'absorption et de la rhizodéposition d'azote en lien avec les échanges de C et d'eau. *Root-CyNAPS* a ensuite été couplé à deux FSPM existants, *CN-Wheat*, qui simule la croissance et le fonctionnement C&N du blé en tenant compte d'une architecture aérienne détaillée, et *RhizoDep*, qui simule la croissance et la rhizodéposition du C sur un système racinaire architecturé.

Le couplage de ces trois FSPM, rendu possible par le nouvel outil *MetaFSPM,* a conduit au modèle *Wheat-BRIDGES*. En complément, des essais en rhizotrons ont été conçus pour suivre l'évolution de l'architecture et de l'anatomie du blé au cours du temps et mesurer les flux de rhizodéposition le long des racines.

Les simulations de *Root-CyNAPS* ont montré que la contribution au bilan en N de la plante des régions les plus actives (e.g. pointes racinaires et zones d'émergence des racines latérales) dépend de la disponibilité en N du sol et de l'âge de la plante. *Wheat-BRIDGES* confirme que ces régions actives se caractérisent à la fois par une rhizodéposition et une absorption d'azote accrues, en raison de leur dépendance similaire aux concentrations en métabolites et à l'anatomie racinaire le long d'une racine donnée. Ces simulations montrent aussi qu'approximer ces deux flux à partir de la masse du système racinaire ou du taux de photosynthèse ne permet pas de quantifier précisément leur variabilité au cours du temps. Les résultats expérimentaux obtenus en rhizotrons suggèrent que l'anatomie d'une racine de blé varie peu le long d'un axe et que l'anatomie racinaire influence ces flux principalement via l'évolution de la perméabilité de l'endoderme et de la sénescence corticale. Globalement, les résultats de cette thèse montrent que les concentrations locales en métabolites et la différenciation de l'endoderme sont des déterminants clés de l'évolution de la rhizodéposition et de l'absorption d'azote le long des racines et au cours du temps, conduisant à une co-localisation partielle de ces flux. Les modèles développés dans cette thèse offrent la possibilité d'explorer des interactions complexes dans le système sol–plante–atmosphère et ouvrent de nouvelles perspectives pour identifier des idéotypes ou pratiques agroécologiques permettant d'optimiser la rhizodéposition et/ou l'absorption d'azote par les racines.

université PARIS-SACLAY

ÉCOLE DOCTORALE
Agriculture, alimentation, biologie, environnement, santé (ABIES)

Title : Investigating the multi-scale regulations of rhizodeposition and nitrogen uptake using Functional-Structural Plant Modeling. Application of a framework to winter wheat (*Triticum aestivum*)

Keywords : Root exudation, FSPM, Shoot-root coupling, Plant ecophysiology, Soil carbon sequestration, Wheat

Abstract : Rhizodeposition – the release of organic matters by living roots – has been recognized as a lever for soil carbon sequestration and plant's adaptation to contrasted environments. Yet its magnitude varies widely with plant age and soil resource availability, and the underlying regulations remain unclear. Rhizodeposition may depend on the metabolic status of the plant, in particular on the exchanges of carbon (C) and nitrogen (N) between plant compartments. Its highly heterogeneous distribution along roots suggests a strong dependency on root architecture and on the anatomical and metabolic characteristics of individual root segments. Because nutrient uptake is controlled by similar factors, one may hypothesize that rhizodeposition and N uptake are linked in space and time, but their spatial variability and interactions have remained largely unexplored. This thesis aimed to quantify the spatial and temporal variability of rhizodeposition and N uptake, to provide a mechanistic interpretation of such variability, and to assess its importance in terms of plant C & N balance, using wheat as a case study.

The thesis relied primarily on the use of functional-structural plant models (FSPM), which allow to investigate the interactions between plant architecture, metabolism and environment from organ scale to whole-plant scale. Root-CyNAPS, a new FSPM simulating N uptake, metabolism and transport in a 3D root system with a detailed anatomical description, was developed and used to investigate how N uptake and N rhizodeposition vary along roots and interact with C and water dynamics. Root-CyNAPS was then coupled to two existing FSPMS, i.e. CN-Wheat, which simulates wheat growth in interaction with C, N and water dynamics using a detailed description of shoot organs in 3D, and RhizoDep, which simulates root growth and rhizodeposition in interaction with root C metabolism in a 3D root system. Wheat-BRIDGES, the whole-plant model resulting from the coupling of these three FSPM, was made possible by the development of *MetaFSPM*, a new generic toolkit that facilitates FSPM coupling and inter-comparison. To complement this modeling approach, experiments were conducted in large soil-filled rhizotrons in order to monitor the evolution of wheat architecture and root anatomy over time and to measure rhizodeposition rates along wheat roots.

Root-CyNAPS simulations showed that the contribution of most active root regions - e.g. root tips and sites of lateral root emergence - to plant N balance is highly sensitive to soil N availability and plant age. *Wheat-BRIDGES* simulations confirmed that the same root regions dominate both rhizodeposition and mineral N uptake, with local metabolite concentrations and root anatomy resulting in a co-location of these flows along individual roots. However, differences between root types and age-dependent changes in the root system generate complex dynamics at plant scale, showing that simple approaches such as assuming a proportionality of rhizodeposition or N uptake with root system biomass or C input are not accurate enough. Experimental results obtained in rhizotrons suggested that root anatomical characteristics do not significantly vary along the roots of wheat, aside the evolution of endodermis' apoplastic barrier and cortical senescence. Altogether, the results of this thesis show that local metabolite concentrations and endodermis differentiation are key drivers of rhizodeposition and N uptake evolution along the roots and over time, leading to a partial co-location of these flows. The models developed in this thesis offer the opportunity to explore complex links between C, N and water dynamics in the plant-soil-atmosphere system and to identify new ideotypes or agroecological practices that optimize rhizodeposition and/or root N uptake.